Chapman & Hall/CRC
Mathematical and Computational Biology Series

Normal Mode Analysis

THEORY AND APPLICATIONS TO BIOLOGICAL AND CHEMICAL SYSTEMS

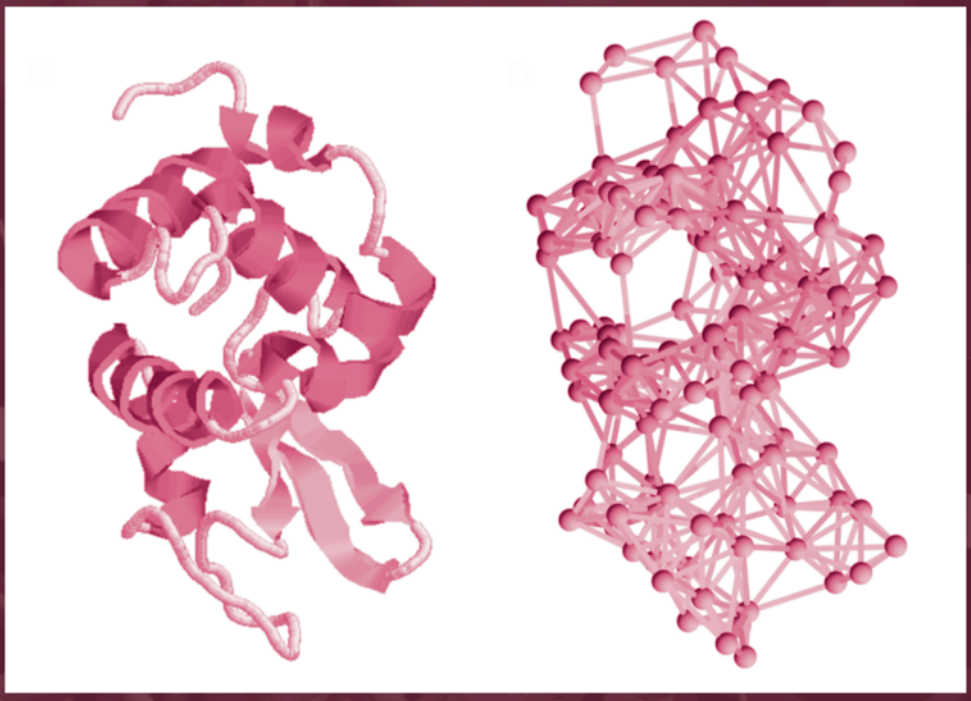

Edited by
Qiang Cui
Ivet Bahar

Chapman & Hall/CRC
Taylor & Francis Group

Chapman & Hall/CRC
Mathematical and Computational Biology Series

Normal Mode Analysis

THEORY AND APPLICATIONS TO BIOLOGICAL AND CHEMICAL SYSTEMS

CHAPMAN & HALL/CRC
Mathematical and Computational Biology Series

Aims and scope:
This series aims to capture new developments and summarize what is known over the whole spectrum of mathematical and computational biology and medicine. It seeks to encourage the integration of mathematical, statistical and computational methods into biology by publishing a broad range of textbooks, reference works and handbooks. The titles included in the series are meant to appeal to students, researchers and professionals in the mathematical, statistical and computational sciences, fundamental biology and bioengineering, as well as interdisciplinary researchers involved in the field. The inclusion of concrete examples and applications, and programming techniques and examples, is highly encouraged.

Proposals for the series should be submitted to one of the series editors above or directly to:
CRC Press, Taylor & Francis Group
24-25 Blades Court
Deodar Road
London SW15 2NU
UK

Chapman & Hall/CRC
Mathematical and Computational Biology Series

Normal Mode Analysis

THEORY AND APPLICATIONS TO BIOLOGICAL AND CHEMICAL SYSTEMS

Edited by
Qiang Cui
Ivet Bahar

Chapman & Hall/CRC
Taylor & Francis Group
Boca Raton London New York

Published in 2006 by
Chapman & Hall/CRC
Taylor & Francis Group
6000 Broken Sound Parkway NW, Suite 300
Boca Raton, FL 33487-2742

Printed in the United States of America on acid-free paper
10 9 8 7 6 5 4 3 2 1

International Standard Book Number-10: 1-58488-472-X (Hardcover)
International Standard Book Number-13: 978-1-58488-472-9 (Hardcover)

Library of Congress Cataloging-in-Publication Data

Catalog record is available from the Library of Congress

informa
Taylor & Francis Group
is the Academic Division of Informa plc.

Visit the Taylor & Francis Web site at
http://www.taylorandfrancis.com

and the CRC Press Web site at
http://www.crcpress.com

Foreword

Normal mode calculations of molecules of biological interest [1–3] were introduced several years after the first molecular dynamics simulation [4]. All of the calculations studied the bovine pancreatic inhibitor, which was the model system used for simulations because of its small size and the availability of a high-resolution crystal structure at that time [5]. It was recognized that normal modes have several important attributes, which made them of interest as a complement to molecular dynamics simulations, even though they approximate the full potential by a harmonic function around a (not necessarily the) minimum energy structure: (a) Unlike molecular dynamics simulations, essentially exact results with no statistical error are obtained; (b) only diagonalization of a matrix is required; and (c) quantization, which is of particular importance for entropy and specific heat calculations, can be introduced in a straightforward manner. A study of the bovine pancreatic inhibitor, for example, showed that above 50 K [2], quantum corrections to the atomic fluctuations are small, although convergence of the entropy to the classical value required much higher temperatures. Relatively little was done with normal mode treatments of biomolecules in subsequent years, with most of the attention focused on molecular dynamics simulations. The latter, which take account of deviations from the harmonic approximation because the full potential is used, provide more correct information, in principle, about the classical dynamics and thermodynamics of macromolecular systems. Moreover, solvent can easily be introduced in an explicit manner. However, one important attribute of normal mode analyses, which has continued to be exploited, is that they provide information about conformation changes in a manner that is often easier to visualize than molecular dynamics simulations. This aspect was recognized very early in a normal mode study of lysozyme, which demonstrated that the lowest mode gave a good description of the hinge closing motion in that molecule [6]. It was also shown in reference [2] that the thermal atomic fluctuations, which contribute to the temperature (B) factors observed in x-ray crystallography, can be estimated by summing over the normal modes at the appropriate temperature and that they approximate, at least in their relative values, those found experimentally and calculated from molecular dynamics simulations.

In the last few years a number of advances have been made that have considerably increased interest in the use of normal modes for the study of biomolecules. One is the use of molecular dynamics for the generation of quasi-harmonic modes [7, 8] or the essentially equivalent extended dynamics

method [9]. In this approach the results of a molecular dynamics simulation are used to construct the equal time fluctuation matrix $\langle x_i\, x_j \rangle$, whose diagonal and off-diagonal terms are interpreted as force constants for the calculation of the associated modes. In this way, some anharmonic effects are included, while the simplicity of the normal modes is maintained. A second development of widespread interest is the introduction of methods for determining the normal modes of very large systems that are difficult to treat by molecular dynamics. One approach applicable to highly symmetric systems is the use of group theory to reduce the size of the matrices that have to be diagonalized [10]; a recent application is to a full treatment of the normal modes of icosahedral viruses (see Van Vlijmen, this volume). An alternative, which also limits the size of the matrices to be diagonalized, is to use an iterative approach (Perahia, this volume). Whether the interesting idea of obtaining normal modes without the Hessian matrix by driving the system at the appropriate frequency (Bowman, this volume) can be extended to large molecules is yet to be determined. Block normal modes [11,12] or so-called elastic models [13] have been found to be surprisingly effective for the study of large systems. In the former the full all-atom potential is used but the size of the matrices that have to be calculated is reduced by treating "blocks" (e.g., consisting of an amino acid or two amino acids) as rigid bodies so that only the translations and rotations contribute to the internal motions of the molecule (see Cui and Olson, this volume). As an example, the application of the methodology to F_1-ATPase [14] has provided useful insights that complement molecular dynamics simulation [15, 16]. The seminal elastic model paper of Tirion [13] used a potential function, which consists of pair-wise interactions between all atoms with an arbitrary cutoff and a scale factor introduced to fit the average B factors (see Bahar, Jernigan, Brooks, and Phillips, this volume). Such simplified models are being widely applied and can be used even in cases when atomic resolution structures are not available (see Ma, this volume). It is interesting to mention in this regard, the paper by de Gennes and Papoular, published in 1969 [17] that suggested the importance of the shape of the molecule in determining its low frequency modes. The ease of use of these "elastic" models, analogous to the program GRASP for electrostatic surface calculations, is likely to make their results an integral part of papers describing structures obtained from x-ray crystallography, nuclear magnetic resonance spectroscopy, and cryo-electron microscopy in the not-too-distant future. The results are of interest primarily for the lowest frequency modes, which correspond to the displacements with the largest amplitudes. One important conclusion that has come from the studies of the approximate modes for large systems is that in many cases where the internal motions have a functional role (e.g., F_1-ATPase [14]), nature has by evolution encoded them in the structure, which is composed of relatively rigid domains connected by flexible hinges. As a consequence of this evolutionary encoding, large structural changes can be achieved with only small displacements of the flexible parts of the molecule (i.e., the hinges), which are reasonably approximated by a few normal modes.

The seductive simplicity of normal mode calculations requires a cautionary note in this volume dedicated to their use. Normal mode modes, when scaled appropriately, provide the amplitudes of the motions around a minimum, an equilibrium property, but they tell us little about the dynamics of the motions involved. In a large molecular complex, the wave number of the modes range from about 0.1 or so to 3000 cm^{-1}, values corresponding to timescales on the order of vibrational periods in the range of nanoseconds to femtoseconds. However, it is known from experiments and simulations that motions of interest may extend into the millisecond to second range. Thus, for example, the suggestion that the lowest frequency modes can be identified with slow exchange phenomena on the microseconds timescale is unlikely to be valid. The identification of a conformational transition with one or a few normal modes tells us something about the inherent flexibility of the molecule but does not provide an understanding of the dynamics of the conformational change, which requires knowledge of the free energy along the reaction coordinate. The primary reason for events on the molecular timescale to take longer than nanoseconds is that there are activation barriers to be surmounted in the conformational change. These, of course, are not included in the normal mode description. Although such timescales cannot be attained directly by present-day molecular dynamics simulations, they are present in the model and can be probed by transition path sampling [18], for example.

If molecular dynamics calculations are made of the temperature dependence of the magnitude of the atomic fluctuations, they have a harmonic behavior (the amplitude varies as $T^{1/2}$) below 150 K or so and above that temperature they increase more rapidly, corresponding to contributions not only from oscillations within a well but also from jumps between wells [19, 20]. Interestingly, the analysis of a series of minima along a molecular dynamics trajectory has shown that the normal modes are surprisingly similar [21]. Extensions of normal mode calculations to include such behavior, as well as anharmonicity in general, are being discussed (see Kitao and Keyes, this volume) but so far a generally useful robust method has not been proposed.

Another aspect of normal modes is that the lowest frequency modes capture elements of the collective motions and can, in principle, be used as reduced bases in molecular dynamics simulations for treating large scale displacements (see Nilges and Liu, this volume). This would be the ideal marriage of the two complementary approaches.

This volume, written by experts in the field, is a very useful addition to the literature concerning the simulation of complex systems. It will serve a role for normal mode studies, which complements that of the volume edited by Becker et al., for molecular dynamics simulations [22]. Both beginners and experts will find helpful information in this volume, though it appears to me to be designed more for the latter. I have enjoyed looking through all the chapters, though I have not been able to mention everyone in this foreword.

Martin Karplus
Strasbourg

References

1. Go, N., T. Noguti, and T. Nishikawa (1983). "Dynamics of a small globular protein in terms of low-frequency vibrational modes." *Proc. Natl Acad. Sci. USA* **b80**: 3696–3700.
2. Brooks, B.R. and M. Karplus (1983). "Harmonic dynamics of proteins: normal modes and fluctuations in bovine pancreatic trypsin inhibitor." *Proc. Natl Acad. Sci. USA* **80**: 6571–6575.
3. Levitt, M., C. Sander, and P.S. Stern (1985). "Protein normal-mode dynamics: trypsin inhibitor, crambin, ribonuclease and lysozyme." *J. Mol. Biol.* **181**: 423–447.
4. McCammon, J.A., B.R. Gelin, and M. Karplus (1977). "Dynamics of folded proteins." *Nature* **267**: 585–590.
5. Deisenhofer, J. and W. Steigemann (1975). "Crystallographic refinement and the structure of the bovine pancreatic trypsin inhibitor at 1.5 Å resolution." *Acta Crystallogr.* **B31**: 238–250.
6. Brooks, B.R. and M. Karplus (1985). "Normal modes for specific motions of macromolecules: application to the hinge-bending mode of lysozyme." *Proc. Natl Acad. Sci. USA* **82**: 4995–4999.
7. Karplus, M. and J.N. Kushick (1981). "Method for estimating the configurational entropy of macromolecules." *Macromolecules* **14**: 325–332.
8. Brooks III, C.L., M. Karplus, and B.M. Pettitt (1998). *Proteins: A Theoretical Perspective of Dynamics, Structure, & Thermodynamics*. *Adv. Chem. Phys.* Vol. LXXI, John Wiley & Sons, New York.
9. Amadei, A., A.B. Linssen, and H.J. Berendsen (1993). "Essential dynamics of proteins." *Proteins* **17**: 412–425.
10. Van Vlijmen, H.W.T. and M. Karplus (2001). "Normal mode analysis of large systems with icosahedral symmetry: application to $(\text{dialanine})_{60}$ in full and reduced basis set implementations." *J. Chem. Phys.* **115**: 691–698.
11. Tama, F., F.X. Gadea, O. Marques, and Y.H. Sanejouand (2000). "Building-block approach for determining low-frequency normal modes of macromolecules." *Proteins* **41**: 1–7.
12. Li, G. and Q. Cui (2002). "A coarse-grained normal mode approach for macromolecules: an efficient implementation and application to Ca(2+)-ATPase." *Biophys. J.* **83**: 2457–2474.
13. Tirion, M.M. (1996). "Low amplitude motions in proteins from a single-parameter atomic analysis," *Phys. Rev. Lett.* **77**: 1905–1908.
14. Cui, Q., G. Li, J. Ma, and M. Karplus (2004). "A normal mode analysis of structural plasticity in the biomolecular motor F_1-ATPase." *J. Mol. Biol.* **340**: 345–372.
15. Ma, J., T.C. Flynn, Q. Cui, A.G.W. Leslie, J.E. Walker, and M. Karplus (2002). "A dynamic analysis of the rotation mechanism for conformational change in F_1-ATPase." *Structure* **10**: 921–931.
16. Bückmann, R.A. and H. Grubmüller (2002). "Nanosecond molecular dynamics simulation primary mechanical energy transfer steps in F_1-ATP synthase." *Nat. Struct. Biol.* **9**: 196–202.
17. de Gennes, P.G. and M. Papoular (1969). "Vibrations de basse fréquence dans certaines structures biologiques." In *Polarization, Matériere et Rayonnement*. Presses Universitaire de France, Paris.

18. Dellago, C., P.G. Bolhuis, F.S. Csajka, and D. Chandler (1998). "Transition path sampling and the calculation of rate constants." *J. Chem. Phys.* **108**: 164–177.
19. Kuczera, K., J. Kuriyan, and M. Karplus (1990). "Temperature dependence of the structure and dynamics of myoglobin: a simulation approach." *J. Mol. Biol.* **213**: 351–373.
20. Elber, R. and M. Karplus (1987). "Multiple conformational states of proteins: a molecular dynamics analysis of myoglobin." *Science* **235**: 318–321.
21. van Vlijmen, H.W.T. and M. Karplus (1999). "Analysis of calculated normal modes of a set of native and partially unfolded proteins." *J. Phys. Chem. B* **103**: 3009–3021.
22. Becker, O.M., A.D. MacKerell, Jr., B. Roux, and M. Watanabe, eds (2001). *Computational Biochemistry and Biophysics*. Marcel Decker, Inc., New York.

Preface

With rapid developments in novel experimental techniques, limits in the resolution, size, and complexity of the chemical and biological systems that can be investigated have been constantly pushed forward. Recent examples include solving the atomic structures of the ribosome, imaging bacterial cell with 3D electron tomography, monitoring the structural dynamics of a single molecular motor and revealing motion of enzyme molecules during catalysis. The availability of these new experimental data poses exciting challenges to the theoretical community for developing novel theoretical and computational techniques that can be used to better interpret experimental results and glean further mechanistic or functional insights. In this book, we focus on a specific technique, normal mode analysis (NMA), that is finding a wide range of applications in the study of chemical and biological problems. Although traditionally used in highly harmonic systems such as small molecules in the gas phase and solid-state materials, creative adaptation and further developments of NMA have demonstrated that it is capable of providing unique insights into the structural and dynamic properties of complex systems. This is vividly illustrated by the contributions here from leading experts in this rapidly developing area.

The book is organized into two general sections. The first section concerns fundamental algorithm developments of NMA at different resolutions and the application of those techniques in the study of biological systems of variable sizes. The second section covers method developments based on or inspired by NMA but going beyond the harmonic approximation inherent in standard NMA techniques.

The first chapter, by Hinsen, gives a concise and incisive introduction to the fundamental physical ideas of NMA and reviews the basic numerical algorithms along with typical observables based on application to proteins. Since NMA formally involves a Hessian matrix inversion process that limits its applicability to large systems, both numerical and approximate methods have been developed to extend the size limit. In Chapter 2, Mouawad and Perahia discuss iterative diagonalization methods that facilitate the solution of large eigenvalue problems in NMA of large protein or protein complexes. In Chapter 3, Rader et al. introduce the elastic network model, which has become tremendously useful for large biomolecules and biomolecular assemblies; the chapter also provides an insightful analysis of why such simplified models work well for complex protein systems. In Chapter 4, Li et al. further compare the elastic model with another coarse-grained NMA techniques for

nucleic acid systems to explore both the applicability and limitations of these methods; in addition, the use of NMA for spectral analysis in proteins using hybrid quantum mechanical and molecular mechanical potentials is also discussed. Chapter 5, by Sanejouand, further illustrates the unique value of different NMA approaches in the study of functional motions in proteins that undergo significant conformational transitions for function. In the next few chapters, various NMA techniques uniquely developed for specific classes of biomolecular systems are discussed and illustrated. Chapter 9 concerns an optimizing elastic network model for studying conformational transitions in ATPases. Chapter 10 involves the development of elastic models for motions of DNA molecules at different length scales. Chapter 11 presents an efficient method that takes advantage of symmetry in the NMA of virus particles.

A unique value of NMA is that a subset of eigenvectors provides a compact description of the intrinsic flexibility of biomolecules, which can be used to better interpret data from various structural biology techniques; this is the theme for three contributions in the book. In Chapter 6, Tama and Brooks discuss the value of NMA in the analysis of low-resolution cryo-electron microscopy data. This important application is also emphasized by Ma in Chapter 7, in addition to the use of NMA in x-ray fiber diffraction refinement. In Chapter 8, Phillips describes coupling NMA and x-ray crystallography in the investigation of protein motions.

An intrinsic approximation in most NMA techniques is the harmonic approximation to the potential energy surface, which needs to be avoided in a more accurate description of complex systems. The second part of the book contains contributions that discuss how to go beyond the harmonic limit but still maintain a NMA framework. In Chapter 12, Kitao compares results from NMA and molecular dynamics analyses of proteins, based on which he and coworkers propose a model for the energy landscape of proteins. In Chapter 14, Kaledin and coworkers introduce a creative approach for evaluating normal modes of interest in biomolecules with molecular dynamics simulations that scale well with the size of the system. In the next two chapters, Fujisaki et al. and Yu and Leitner discuss the problem of vibrational relaxation in liquids and biomolecules and how an NMA framework can be useful in such investigations. In Chapter 13, Keyes presents the theoretical foundation of instantaneous NMA of liquids and how different dynamical properties such as diffusion can be evaluated using the theory. Finally, in the last two chapters, Nilges and Abseher and Liu et al. present innovative computational algorithms that couple NMA and molecular dynamics for efficient sampling of the conformational space of biomolecules, which is a major challenge in the field of biomolecular simulations.

The contributions here illustrate the very spirit of interdisciplinary research, which involves adapting methods from traditionally separated areas for solving the problem of interest. Thus, it is our sincere hope that this book will help not only to stimulate further application and development of NMA-based theoretical and computational methods, but also to inspire young graduate

students to pursue interdisciplinary studies that transverse the boundaries between chemistry, biology, physics, and engineering.

Qiang Cui
Madison, Wisconsin

Ivet Bahar
Pittsburgh, Pennsylvania

Acknowledgments

We thank, in the first place, all of the authors who contributed to this book. This book would not be possible without their enthusiasm, their support, and, most importantly, their scientific achievements and valuable contributions. We also thank Mr. Mark Holliman (System Administrator at the University of Pittsburgh Department of Computational Biology), for maintaining the Web site that facilitated the communication among the authors; Mr. Ron G. Landes (Eurekah.com), for the initial suggestion of editing a book on NMA of macromolecules; and Ms. Jessica Vakili (Taylor and Francis Books), for helping with the production and organization of the chapters. I.B. also acknowledges the enjoyable collaboration with many colleagues, postdocs, and students on elastic network models and normal mode analysis, both at her former (Bogazici University) and current (U of Pittsburgh) institutions, and in particular the inspiring collaboration with Dr. Burak Erman. We are grateful to the National Science Foundation, the National Institutes of Health, and the Department of Energy for the generous support for all of our research and educational work, including this book.

Ivet Bahar

Editors

Dr. Qiang Cui was born in Beijing, China. He went to the University of Science and Technology of China as an undergraduate and obtained his B.S. degree from the Department of Chemical Physics in 1993. He obtained his Ph.D. degree from Emory University in 1997, working with Professor Keiji Morokuma on the theoretical analysis of nonadiabatic chemical reactions and organometallic catalysis. During his postdoctoral years with Professor Martin Karplus at Harvard, he worked on developing hybrid QM/MM methods and applying those techniques to study enzyme catalysis and kinetics. Since 2001, he has been an assistant professor in the Department of Chemistry at the University of Wisconsin in Madison. His major research interests involve theoretical and computational analysis of biophysical and biochemical problems, such as energy transduction in biomolecular motors and pumps, radical reactions in biology, and assembly of protein-nucleic acid complexes.

Dr. Ivet Bahar was born and educated in Istanbul, Turkey, where she completed her B.S. and M.S. degrees in chemical engineering (Bogazici University, 1980 and 1983) and her Ph.D. degree in chemistry (Istanbul Technical University, 1986). She worked at Bogazici University as an assistant, associate, and full professor in the Department of Chemical Engineering (1986–2001) and as director of the Polymer Research Center (1993–2001) at the NIH National Cancer Institute Division of Basic Sciences. She was a visiting scientist for several short-term appointments between 1992 and 2000. She joined the University of Pittsburgh, School of Medicine in 2001 to start a new Center for Computational Biology and Bioinformatics, as a professor in the Molecular Genetics and Biochemistry Department. She is currently a professor and the founding chair of the Department of Computational Biology in the same school. Her research expertise is in modeling and simulations of macromolecular structures and dynamics, and developing new theories and methods for understanding the complex machinery of biomolecular systems. With over 150 research articles, Dr. Bahar has established herself as a prominent investigator in the field of computational biology. She has been an Elected Member of the European Molecular Biology Organization (EMBO) since 2000, and a Principal Member of the Turkish National Academy of Sciences since 1997.

Contributors

Rogher Abseher
Unité de Bio-informatique
Structurale
CNRS URA 2815
Paris, France

Ivet Bahar
Department of Computational Biology
School of Medicine
University of Pittsburgh
Pittsburgh, Pennsylvania

Charles L. Brooks III
Department of Molecular Biology
The Scripps Research Institute
Lo Jolla, California

Alex Brown
Department of Chemistry
University of Alberta
Edmonton, Canada

Joel M. Bowman
Department of Chemistry
and Cherry L Emerson Center
for Scientific Computation
Emory University
Atlanta, Georgia

Lintao Bu
Department of Chemistry
Boston University
Boston, Massachusetts

Chakra Chennubhotla
Department of Computational Biology
School of Medicine
University of Pittsburgh
Pittsburgh, Pennsylvania

Qiang Cui
Department of Chemistry and
Theoretical Chemical Institute
University of Wisconsin-Madison
Madison, Wisconsin

Omar N.A. Demerdash
Department of Chemistry and
Theoretical Chemical Institute
University of Wisconsin-Madison
Madison, Wisconsin

Hiroshi Fujisaki
Department of Chemistry
Boston University
Boston, Massachusetts

Jianbin He
Hefei National Laboratory for Physical
Sciences at Micro-Scale
School of Life Sciences
University of Science and Technology of
China
Hefei, Anhui, China

Konrad Hinsen
Laboratoire Leon Brillouin (CEA-CNRS)
CEA Saclay
Gif-sur-Yvette, France

Robert L. Jernigan
Department of Biochemistry, Biophysics,
and Molecular Biology
Iowa State University
Ames, Iowa

Alexey L. Kaledin
Department of Chemistry
and Cherry L Emerson Center
for Scientific Computation
Emory University
Atlanta, Georgia

Martina Kaledin
Department of Chemistry
and Cherry L Emerson Center
for Scientific Computation
Emory University
Atlanta, Georgia

T. Keyes
Department of Chemistry
Boston University
Boston, Massachusetts

Akio Kitao
Institute of Molecular and Cellular
Bioscience
University of Tokyo
Tokyo, Japan

David M. Leitner
Department of Chemistry and Chemical
Physics Program
University of Nevada
Reno, Nevada

Guohui Li
Department of Chemistry and
Theoretical Chemical Institute
University of Wisconsin-Madison
Madison, Wisconsin

Haiyan Liu
Hefei National Laboratory for
Physical Sciences at Micro-Scale
School of Life Sciences
University of Science and Technology of
China
Hefei, Anhui, China

Jianpeng Ma
Verna and Mars McLean Department of
Biochemistry and Molecular Biology
Baylor College of Medicine and Rice
University
Houston, Texas

Atsushi Matsumoto
Department of Chemistry
Wright–Rieman Laboratories
The State University of New Jersey
Piscataway, New Jersey

Liliane Mouawad
Laboratoire de Biophysique Moléculaire
Institut Curie
Université Paris-Sud
Orsay, France

Michael Nilges
Unité de Bio-informatique
Structurale
CNRS URA 2815
Paris, France

Wilma K. Olson
Quantum Bioinformatics Group
Center for Promotion of Computational
Sciences and Engineering
Japan Atomic Energy Research Institute
Kyoto, Japan

David Perahia
Laboratoire de Modélisation et
d'Ingénierie des Protéines
Institut de Biochimie et de Biophysique
Moléculaire et Cellulaire
Université Paris-Sud
Orsay, France

George N. Phillips, Jr.
Departments of Biochemistry and
Computer Science
University of Wisconsin-Madison
Madison, Wisconsin

A.J. Rader
Department of Computational Biology
School of Medicine
University of Pittsburgh
Pittsburgh, Pennsylvania

Yves-Henri Sanejouand
Laboratoire de Physique
Ecole Normale Supérieure
Lyon, France

Taner Z. Sen
L.H. Baker Center for Bioinformatics and Biological Statistics
Iowa State University
Ames, Iowa

Yunyu Shi
Hefei National Laboratory for Physical Sciences at Micro-Scale
School of Life Sciences
University of Science and Technology of China
Hefei, Anhui, China

John E. Straub
Department of Chemistry
Boston University
Boston, Massachusetts

Florence Tama
Department of Molecular Biology
The Scripps Research Institute
Lo Jolla, California

Herman W.T. van Vlijmen
Computational Drug Design Group
Biogen Idec
Cambridge, Massachusetts

Adam Van Wynsberghe
Department of Chemistry and Theoretical Chemical Institute
University of Wisconsin-Madison
Madison, Wisconsin

Lee-Wei Yang
Department of Computational Biology
School of Medicine
University of Pittsburgh
Pittsburgh, Pennsylvania

Xin Yu
Department of Chemistry and Chemical Physics Program
University of Nevada
Reno, Nevada

Zhiyong Zhang
Hefei National Laboratory for Physical Sciences at Micro-Scale
School of Life Sciences
University of Science and Technology of China
Hefei, Anhui, China

Contents

1

Normal Mode Theory and Harmonic Potential Approximations

Konrad Hinsen

CONTENTS

1.1 Introduction

Normal mode analysis (NMA) has become one of the standard techniques in the study of the dynamics of biological macromolecules. It is primarily used for identifying and characterizing the slowest motions in a macromolecular system, which is inaccessible by other methods. This chapter explains what normal mode analysis is and what one can do with it without going beyond its limit of validity. The focus of this chapter is on proteins, although normal mode analysis can equally well be applied to other macromolecules (e.g., DNA) and to macromolecular assemblies ranging in size from protein–ligand complexes to a whole ribosome.

By definition, normal mode analysis is the study of harmonic potential wells by analytic means. Section 1.2 of this chapter will therefore deal with potential wells and harmonic approximations. Section 1.3 is about normal mode approaches to different physical situations, and Section 1.4 discusses how useful information can be extracted from normal modes.

1.2 Potential Wells

The fundamental restriction of normal mode analysis is its limitation to the study of dynamics in a single potential well. More specifically, normal mode analysis studies motions of small amplitude in a potential well, where "small" means "small enough that the approximations hold." What exactly that means in practice will be discussed later in this section. An immediate consequence is that normal mode analysis is not well suited to the study of conformational transitions, although it can play a complementary role to other techniques in such applications.

The starting point for normal mode analysis is one particular stable conformation of the system that represents a minimum of the potential energy surface. One then constructs a *harmonic approximation* of the potential well around this conformation. This step involves the central approximation of the method, which therefore deserves a more detailed discussion.

A harmonic potential well has the form[1]

$$U(\mathbf{r}) = \tfrac{1}{2}(\mathbf{r} - \mathbf{R}) \cdot \mathbf{K}(\mathbf{R}) \cdot (\mathbf{r} - \mathbf{R}) \tag{1.1}$$

where $\mathbf{R}$ is a $3N$-dimensional vector (N is the number of atoms) describing the stable conformation at the center of the well and $\mathbf{r}$ is an equally $3N$-dimensional vector representing the current conformation. The symmetric and positive semidefinite matrix $\mathbf{K}$ describes the shape of the potential well. A harmonic model for a potential well thus consists of $\mathbf{R}$ and $\mathbf{K}$.

Before we can describe the options for constructing a harmonic approximation, we have to review the properties of potential energy landscapes of proteins. First and foremost, the potential energy landscape of a protein has a multiscale structure (see Figure 1.1). On the length scale on which one typically considers conformations from a structural point of view (0.1 to 10 nm), a stable conformation corresponds to a local minimum of a smooth, slowly varying potential. If several local minima exist, they describe different stable conformations, and are separated by local maxima and saddle points. Looking closer (0.001 to 0.1 nm), one sees that the potential well is not smooth, but has many local minima and energy barriers of smaller height. These are referred to as conformational substates [1–3]. The differences between neighboring conformational substates are, for example, different arrangements of sidechains, whereas a different conformation would imply more important geometrical changes involving the backbone.

By far the most frequently applied method to construct a harmonic potential model consists of starting from an all- or united-atom potential $V(\mathbf{r})$ and an

[1] We limit ourselves to harmonic potentials in Cartesian coordinates. Other coordinates can be used as well, but are less convenient for numerical applications. Note that a potential that is harmonic in one coordinate set is in general *not* harmonic in other coordinates.

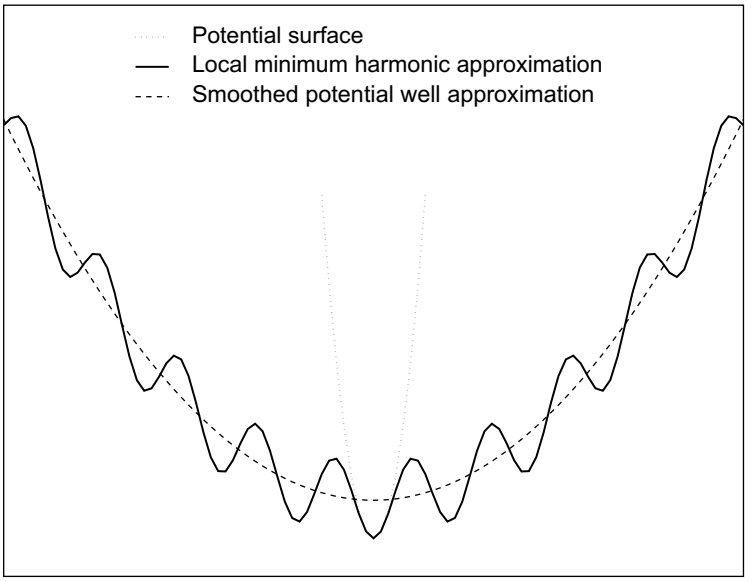

FIGURE 1.1
A schematic one-dimensional view of the potential energy surface of a protein showing two kinds of harmonic approximations: an approximation to a local minimum, and an approximation to the smoothed-out potential well.

experimentally or otherwise obtained initial conformation. An energy minimization algorithm is then applied to find a local minimum $\mathbf{R}_{\min}$ near the initial structure. Finally, the matrix $\mathbf{K}$ is obtained as the second derivative of the potential:

$$\mathbf{K}_{ij} = \left[\frac{\partial^2 U}{\partial \mathbf{r}_i \partial \mathbf{r}_j} \right]_{\mathbf{r}=\mathbf{R}_{\min}} \tag{1.2}$$

The resulting harmonic model is thus an approximation to a conformational substate, valid for very small motions around the local minimum. However, such models have been routinely used in the study of larger amplitude motions, for example, the opening/closing motions that control the access of ligands to the active site in enzymes. Most of the criticism aimed at normal mode analysis concerns this use of a model for a conformational substate beyond its theoretical limit of applicability. However, other kinds of harmonic models exist, as will be shown below, and even the use of conformational substate models can be justified empirically because the outcome of the subsequent normal mode analysis usually yields results that are in agreement with experimental data. The low-energy motions in the local minima and in the global potential must therefore be very similar in shape. This is in fact plausible, because the motions that separate conformational substates and those that characterize large-amplitude motions are very different.

A low-energy motion on a large scale should also be a low-energy motion on a smaller scale.

Alternatively, one can directly construct a harmonic model around a given $\mathbf{R}_{\min}$ (e.g., an experimental conformation) by fitting the remaining parameters to experimental or simulation data. This approach has been used in particular for simplified protein models in which only the C_α atoms are represented explicitly. A reasonable and simplifying assumption is

$$U(\mathbf{r}_1, \ldots, \mathbf{r}_N) = \sum_{\text{all pairs } \alpha,\beta} U_{\alpha\beta}(\mathbf{r}_\alpha - \mathbf{r}_\beta) \tag{1.3}$$

with

$$U_{\alpha\beta}(\mathbf{r}) = \tfrac{1}{2}k(|\mathbf{R}_\alpha - \mathbf{R}_\beta|)(|\mathbf{r}| - |\mathbf{R}_\alpha - \mathbf{R}_\beta|)^2 \tag{1.4}$$

that is, the harmonic potential consists of a sum of pair terms that represent springs whose force constants $k(r)$ decrease with an increasing distance between the two atoms in the configuration that represent the minimum.

Such a potential, with a step function for $k(r)$, was first used with an all-atom model by Tirion [4], who showed that it reproduces the low-frequency end of the density of states rather well. Hinsen [5, 6] then used another variant (with $k(r)$ exponentially decreasing and a reduced description of the backbone by the C_α atoms) for characterizing slow protein motions by dynamical domains. The Anisotropic Network Model [7], although derived in a different way, is also equivalent to a potential of the form (1.3) for the C_α atoms, again with a step function for $k(r)$. As long as only an identification of the low-frequency modes is required, the form of $k(r)$ is indeed not critical.

On the other hand, a quantitative description of a potential well requires a more careful approximation. By fitting to a local minimum (substate) of the Amber 94 force field [8], Hinsen et al. [9] obtained the form

$$k(r) = \begin{cases} 8.6 \times 10^5 \dfrac{\text{kJ}}{\text{mol nm}^3} \cdot r - 2.39 \times 10^5 \dfrac{\text{kJ}}{\text{mol nm}^2}, & \text{for } r < 0.4 \text{ nm} \\ \dfrac{128 \text{ kJ nm}^4/\text{mol}}{r^6}, & \text{for } r \geq 0.4 \text{ nm} \end{cases} \tag{1.5}$$

and found that the global potential well can be described by scaling the local potential well down by a factor that must be evaluated for each protein individually. The special case for $r < 0.4$ nm takes care of nearest neighbors along the backbone, which are strongly bound through the very rigid peptide group. For other pairs, the interaction is mediated mostly by a large number of sidechain atoms. This model has been shown to reproduce the long-time dynamics of proteins remarkably well, as will be shown in Section 1.3.2.

1.3 Normal Modes

The basic idea of normal modes is illustrated in Figure 1.2 for a system with two coordinates, labeled r_1 and r_2. The harmonic potential well shown has two special directions, labeled e_1 and e_2, which correspond to the normal modes. Imagine the potential well as a real bowl in which a small ball moves around. The normal mode directions are special because the ball can move along any one of them back and forth. If it starts along any other direction (say, r_1), then it will be deflected by the potential along the perpendicular direction (r_2) as well, and thus move along both directions. Only the normal mode directions are independent. This independence greatly simplifies the analysis of the motions. In particular, oscillations of the ball along any one of the normal mode directions have a well-defined frequency, which is related to the curvature of the potential along the direction of motion. Any compound motion contains both frequencies. Knowing the normal modes thus permits the explicit evaluation of all possible vibrational frequencies in a system, assuming of course that the system has vibrational dynamics, that is, that friction can be neglected.

There is another important feature of normal modes that can be seen in Figure 1.2. The thick line describes a particular constant energy value. A ball that is dropped from a position on that line will bounce back to the same energy level again (assuming the absence of friction). If the ball moves along the lower normal mode (e_1, the one with the lower curvature and lower oscillation frequency), it can move further away from the minimum at a given energy than if it moved along the higher normal mode. This illustrates that the low normal modes describe large-amplitude motions. In a molecular system, the level of available energy is defined by the temperature.

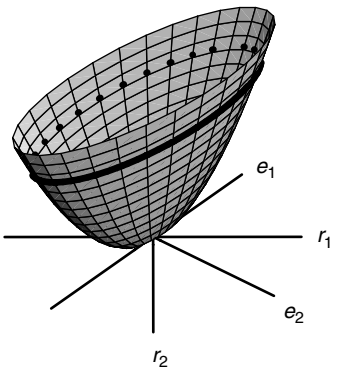

FIGURE 1.2
A two-dimensional harmonic potential well. The two Cartesian coordinate axes of the system are r_1 and r_2, the two normal mode directions are e_1 and e_2.

In the case of a protein with N atoms, there are $3N$ Cartesian coordinates and thus also $3N$ normal mode directions. It is useful to consider the $3N$-dimensional space defined by the $3N$ Cartesian coordinates, which is called configuration space. A $3N$-dimensional vector in this space can either represent a point, that is, a configuration of the protein, or a direction, that is, the change of a configuration. Normal mode vectors represent directions, as do velocity vectors and force vectors. A normal mode vector thus describes in which direction each atom moves, and how far it moves relative to the other atoms. However, a normal mode vector does *not* describe an absolute amount of displacement for any atom. Additional information (e.g., the temperature) is required for fixing the global amplitude of the atomic displacements.

Mathematically, the normal mode vectors are obtained as the eigenvectors $\mathbf{e}_i$ of the matrix $\mathbf{K}$, which are defined by

$$\mathbf{K} \cdot \mathbf{e}_i = \lambda_i \mathbf{e}_i, \quad i = 1, \ldots, 3N \tag{1.6}$$

The $3N$ numbers λ_i are the associated eigenvalues that describe the curvature of the potential along the normal mode directions.

The independence of the normal modes makes it possible to rewrite the harmonic potential in the simpler form

$$U(\mathbf{c}) = \tfrac{1}{2}\mathbf{c} \cdot \mathbf{\Lambda} \cdot \mathbf{c} \tag{1.7}$$

The new interaction matrix $\mathbf{\Lambda}$ is diagonal and has the eigenvalues λ_i as its elements. The new coordinates $\mathbf{c}$ are given by

$$c_i = (\mathbf{r} - \mathbf{R}) \cdot \mathbf{e}_i \tag{1.8}$$

and the original coordinates $\mathbf{r}$ can be recovered through

$$\mathbf{r} = \mathbf{R} + \sum_{i=1}^{3N} c_i \mathbf{e}_i \tag{1.9}$$

Each of the coordinates c_i measures the distance from the minimum along one of the normal mode directions.

More important to us is, however, the physical interpretation of the normal modes. The eigenvalue λ_i describes the energetic cost of displacing the system by one length unit along the eigenvector $\mathbf{e}_i$. Normal mode analysis therefore classifies the possible deformations of a protein by their energetic cost. For realistic potentials, low-energy deformations correspond to *collective* or *delocalized* deformations, whereas high-energy modes are *local* deformations. This is a consequence of the nonlinearity of the interaction terms, plus the fact that short-range interactions (e.g., bond stretching) are stronger than long-range interactions (e.g., electrostatic).

This can be illustrated by a simple example: a linear chain of N equidistant particles, each of which interacts with its two neighbors through a spring of equilibrium length d, the pair potential is then given by Equation (1.4) with $k(r) = k_0$. Displacing a particle in the middle by a distance a causes two pair terms to increase by $\frac{1}{2}k_0a^2$. Displacing a group of ten particles in the middle by the same distance a (all in the same direction) also causes two pair terms to increase, by exactly the same amount. However, we should be comparing $3N$-dimensional displacement vectors of the same length, that is, the same norm in $3N$-dimensional space. Moving a group of M particles as a unit by a distance a yields a displacement vector with a norm of $\sqrt{M}a$. The incurred energy increase is thus proportional to $1/M$, that is, collective motions (large M) are energetically cheaper than local ones. This would not be the case if the potential were linear in the pair distance, local and global motions would then have equal energetic costs. A potential with a less than linear growth would even favor local moves. However, such potentials do not exist at the atomic scale. Finally, global displacements would be penalized if there were strong interactions at longer distances, beyond nearest neighbors. But such situations are not found on the atomic scale, the short-range interactions (the chemical bond structure) are the strongest ones.

When normal mode analysis is applied to an isolated protein, the first six eigenvalues λ_i are zero. They describe the six rigid-body movements of the protein (translation along three independent axes plus rotation around three independent axes) that incur no energetic cost at all. They are usually of no interest and ignored in the analysis, such that "the lowest-energy modes" in practice means "the lowest-energy modes with nonzero energies."

1.3.1 Vibrational Modes

If one assumes that the atoms in a molecule are classical particles, then the equations of motion for a molecule with a harmonic interaction potential of the form (1.1) are given by

$$\mathbf{M} \cdot \ddot{\mathbf{r}} = -\mathbf{K} \cdot (\mathbf{r} - \mathbf{R}) \tag{1.10}$$

The matrix $\mathbf{M}$ is a $3N \times 3N$ diagonal matrix, which contains the masses of the atoms on its diagonal, each mass being repeated three times, once for each of the three Cartesian coordinates. A system with these equations of motion is known as a $3N$-dimensional harmonic oscillator and is discussed in all textbooks on classical mechanics (see, e.g., [10]). We will therefore only give a summary of the solution.

With the introduction of *mass-weighted coordinates*,

$$\tilde{\mathbf{r}} = \sqrt{\mathbf{M}} \cdot \mathbf{r} \tag{1.11}$$

$$\tilde{\mathbf{R}} = \sqrt{\mathbf{M}} \cdot \mathbf{R} \tag{1.12}$$

$$\tilde{\mathbf{K}} = \sqrt{\mathbf{M}}^{-1} \cdot \mathbf{K} \cdot \sqrt{\mathbf{M}}^{-1} \tag{1.13}$$

the equations of motion can be rewritten as

$$\ddot{\tilde{\mathbf{r}}} = \tilde{\mathbf{K}} \cdot (\tilde{\mathbf{r}} - \tilde{\mathbf{R}}) \tag{1.14}$$

The $3N$ independent solutions of these equations have the form

$$\tilde{\mathbf{r}}(t) = \tilde{\mathbf{R}} + \tilde{\mathbf{A}}_i \cos(\omega_i t + \delta_i), \quad i = 1, \ldots, 3N \tag{1.15}$$

where δ_i is an arbitrary phase factor and ω_i and $\tilde{\mathbf{A}}_i$ are the solutions of the eigenvalue equation

$$\tilde{\mathbf{K}} \cdot \tilde{\mathbf{A}}_i = \omega_i \tilde{\mathbf{A}}_i \tag{1.16}$$

This is identical to Equation (1.6) except for the use of the mass-weighted force constant matrix.

The combination of the $3N$-dimensional vector $\mathbf{A}_i$ and the eigenvalue ω_i is known as a vibrational normal mode. Since this was historically the first type of normal mode analysis, and remains the most frequently used one, it is common to use the term "normal mode" for this form only.

The physical interpretation of $\mathbf{A}_i$ and ω_i can be obtained from Equation (1.15): ω_i is a vibrational frequency, and $\mathbf{A}_i$ is an amplitude vector that specifies how far and in what direction each individual atom moves. Vibrational normal mode analysis thus classifies all possible motions around a stable equilibrium state by vibrational frequency. Note that since the range of atomic masses is much smaller than the range of eigenvalues, the difference between energetic (Equation [1.6]) and vibrational (Equation [1.16]) analysis is not very large. Low-frequency modes are therefore to a very good approximation also low-energy modes, and vice versa. For historical reasons (normal mode analysis in chemistry was originally developed for describing the vibrational spectra of small molecules), most published normal mode studies on proteins use vibrational modes, even though the interpretation is often in terms of energetic modes.

Figure 1.3 shows the frequency spectrum of three proteins, crambin, lysozyme, and myoglobin, obtained from vibrational normal mode analysis using a conformational substate approximation to the Amber 94 potential [8]. The main observation is that the three spectra are nearly identical. The reason for this is that most of the modes describe motions that are common to all proteins, ranging from hydrogen vibrations (the well-separated block beyond 85 ps^{-1}) at the high end through internal vibrations of single amino acids down to vibrations of secondary-structure elements (helices, β-sheets). The small differences are due to the different amino acid distributions and different percentages of secondary structure motifs. The motions that are specific to a particular protein, and thus of interest for understanding its function, are at the far lower end of the spectrum.

It should be stressed that this analysis describes only vibrational motion in a conformational substate. There are larger amplitude motions along

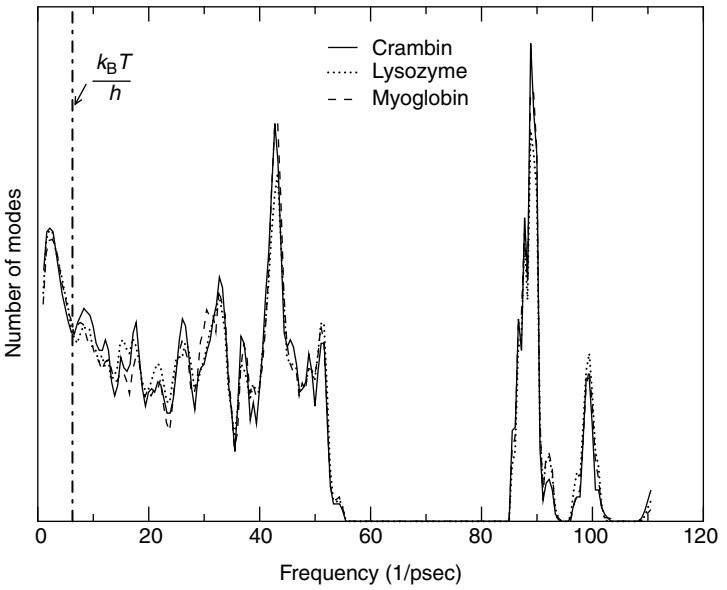

FIGURE 1.3
The vibrational frequency spectrum (number of modes per frequency interval) of three different proteins in a local minimum of the Amber 94 force field. The vertical line indicates the quantum limit for $T = 300$ K.

the lower-frequency modes as well, but they are diffusive, not vibrational. They will be discussed in Section 1.3.2.

It should also be noted that at the high frequency end, quantum effects become important. The criterion for the applicability of classical mechanics is $h\nu \ll k_B T$. At 300 K, this yields $\nu \ll 6$ psec^{-1}, which, as Figure 1.3 shows, is satisfied for only a very small part of the vibrational spectrum. However, since the transformation to normal mode coordinates remains valid in a quantum description, only the dynamic interpretation must be adapted.

1.3.2 Langevin and Brownian Modes

The real large-amplitude motions in proteins traverse many conformational substates. The transition from one conformational substate to the next requires crossing a small energy barrier. At the structural level this means, for example, that some sidechain rearrangements are necessary before the backbone motion can proceed. An explicit treatment of these barrier crossings is not desirable, and also not necessary. One can model such situations by a smoothed-out potential (see Figure 1.1) and replace the barrier crossings by the introduction of friction and random forces into the dynamics. The simplest model involving friction is known as *Langevin dynamics*. It consists

of augmenting Equation (1.10) by two terms:

$$\mathbf{M} \cdot \ddot{\mathbf{r}} = -\mathbf{K} \cdot (\mathbf{r} - \mathbf{R}) - \mathbf{\Gamma} \cdot \dot{\mathbf{r}} + \xi(t) \tag{1.17}$$

The first term, proportional to the velocities, is a friction term, defined by a $3N \times 3N$ matrix $\mathbf{\Gamma}$, called friction matrix, which will be discussed later. The second term describes a random force that satisfies the conditions

$$\langle \xi(t) \rangle = 0 \tag{1.18}$$

$$\langle \xi(t)\xi(t') \rangle = 2k_{\mathrm{B}}T\mathbf{\Gamma}\delta(t - t') \tag{1.19}$$

The second condition specifies that the random force is a white noise signal (i.e., uncorrelated in time) with an amplitude defined to add on average just as much energy to the system as is taken out by the friction term.

A method for solving this equation numerically has been given by Lamm and Szabo [11]. However, it will not be discussed here because a further useful simplification can be made for the case of large-amplitude motions in proteins. In general, Langevin modes describe damped oscillations plus random displacements along a normal mode coordinate. When the friction coefficients are very large, the oscillations become overdamped: the molecule moves slowly back toward its energetic minimum, but reaches it only asymptotically and never swings back. The random displacements become the dominant aspect of the dynamics, and one observes Brownian motion (diffusion) with preferential movements toward the minimum. This is the dynamic behavior that the large-amplitude motions of proteins display. It can be described by the formalism of Brownian Dynamics, which consists of a differential equation (known as the Smoluchowski equation) for the probability distribution of the random displacements. This equation can be solved analytically for a harmonic potential. The derivation is too lengthy to be reproduced here, the reader is therefore referred to Reference 9 and to Section 2.2 of Reference 12. The result is again an eigenvalue problem, this time for the matrix

$$\hat{\mathbf{K}} = \sqrt{\mathbf{\Gamma}}^{-1} \cdot \mathbf{K} \cdot \sqrt{\mathbf{\Gamma}}^{-1} \tag{1.20}$$

that is, a friction-weighted force constant matrix. Its eigenvalues $\hat{\lambda}_i$, $i = 1, \ldots, 3N$, are the relaxation coefficients of the Brownian modes, whose directions are again given by the eigenvectors. If the protein were deformed along Brownian mode k by an amplitude A, and if then the random forces were switched off, the protein would return toward the energetic minimum along the same direction and its position along this direction would be given by $A \exp(-\hat{\lambda}_k t)$.

Like other normal mode techniques, Brownian mode analysis requires a stable conformation of the protein as input and a harmonic model for the global potential well. In addition, a model for the friction matrix $\mathbf{\Gamma}$ is required. Since friction manifests itself already on short time scales, it can be measured

from molecular dynamics (MD) simulations of proteins. With the simplifying assumption that each particle of the protein has an independent friction constant (which implies that $\mathbf{\Gamma}$ is diagonal), it is sufficient to calculate the mean-square displacement of each particle from the simulation trajectory and fit the short-time behavior to a straight line in order to obtain approximate values of the elements of $\mathbf{\Gamma}$. It turns out that the friction constant can be well described by a linear function of the local density in the protein around the particle of interest, averaged over a sphere of 1.5 nm radius [9]. In a typical compact protein, the local density is uniform on that length scale, the variations are thus due to surface effects: for particles near the surface, the sphere contains water, whose density is much smaller than that of the protein itself. The correlation between friction constant and amount of protein matter in the vicinity of the particle is not surprising in view of the explanation of the origin of friction given above, that is, interactions with other atoms in the protein, in particular sidechain atoms. However, the idea that friction is a solvent effect is quite popular in the literature, although it has never been backed by any data.

Several experimentally observable quantities, in particular time correlation functions, can be calculated from Brownian modes analytically [12], which permits the study of protein dynamics at arbitrarily long time scales. Figure 1.4 shows that such a model can yield surprisingly good results. It shows the incoherent intermediate scattering function for a C-phycocyanin dimer from a two-level normal mode calculation (Brownian modes for the long-time dynamics plus vibrational modes for short-time effects) and from a standard MD trajectory. It should be noted that the MD results should tend to the same asymptotic values as the normal modes curves; the fact that they do not indicates that the trajectory of 1.6 nsec is not long enough for sampling all the motions. A look at the relaxation times obtained from the Brownian modes confirms this: the largest relaxation time is 4.5 nsec. The absence of sampling problems is in fact an important advantage of normal mode techniques in the study of slow protein dynamics.

In summary, Brownian mode calculations demonstrate that a very simple harmonic potential with few parameters can reproduce the backbone dynamics of a protein very well if an appropriate dynamical model is chosen. The major limitation is the restriction to motions around a stable energetic minimum.

1.4 Interpretation and Analysis of Normal Modes

In the study of molecular systems, normal modes are used to answer particular scientific questions. In order to draw valid conclusions, it is important to understand the methods and, in particular, their limitations.

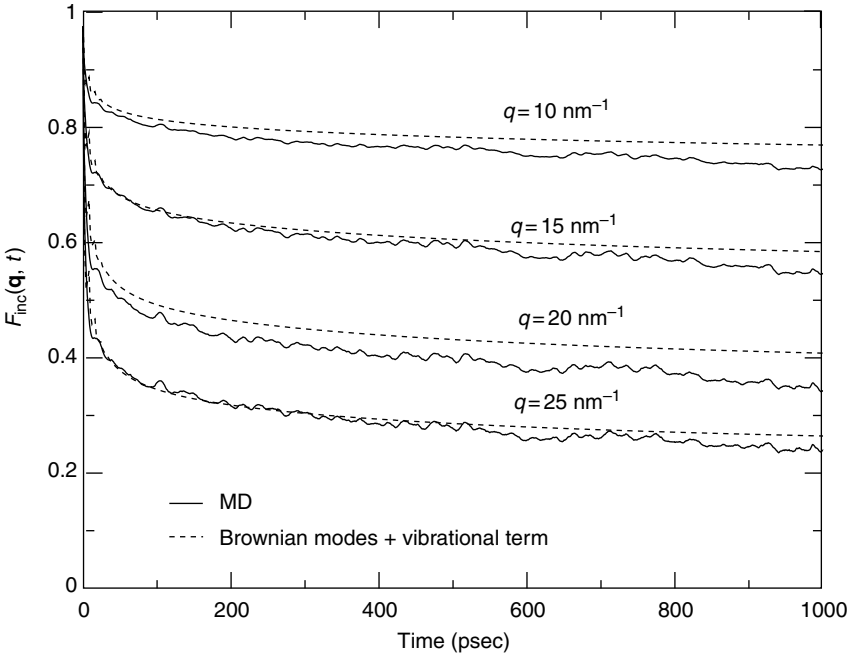

FIGURE 1.4
The incoherent intermediate scattering function $F_{\mathrm{inc}}(\mathbf{q}, t)$, a quantity observable in neutron scattering experiments, calculated from a mixed Brownian/vibrational modes model and from an MD trajectory for a C-phycocyanin dimer. Both calculations are for a coarse-grained model in which a single point mass located at the C_α position represents a whole residue. The normal modes were calculated directly for this model, the MD trajectory was generated from an all-atom simulation.

The applications of normal modes can be broadly classified into two groups. Those in the first group use all modes or a large subset (usually the lowest energy modes) as a convenient analytical representation of the potential well. In that case the only limitations are due to the necessarily approximate nature of the harmonic model, and due to the choice of a subset. The other group contains all analyses that look at the properties of individual modes. In this case, care must be taken to avoid an overinterpretation of the data.

One potential pitfall of single mode analysis is discussing the differences of modes that are nearly equal in energy. In the extreme case of exactly equal energies (the modes are then called degenerate), the modes that come out of a numerical calculation represent arbitrary choices of the algorithm. Any combination of such modes would be an equally valid mode. Interpreting the characteristics of any one such mode or the differences between the degenerate modes is no more meaningful than discussing the differences between motion along the x and the y coordinates in an arbitrarily chosen Cartesian coordinate system. Although this is strictly true only for equal energies, it is also approximately true for approximately equal energies. A small difference

in energy between two modes should be considered a probably unreliable detail of the numerical model, rather than something fundamental about the system being studied. In practice, only a few of the lowest modes in a protein are sufficiently well separated to merit an individual discussion, and even that is not always the case. In all other cases, it is preferable to analyze the coordinate subspace spanned by all modes in a certain range of timescales.

A second pitfall is placing too much importance on the frequency of a mode obtained from a vibrational normal mode calculation. As discussed above, the slow modes that are characteristic of a particular protein and often related to its function show diffusional behavior on long timescales. Vibrational dynamics occurs only inside a conformational substate for a short duration and is rarely of interest. Vibrational normal mode analysis is thus useful mostly for higher frequencies, for example, when comparing to spectroscopic measurements. For assessing the time scales of slow motions, Brownian modes are the appropriate approach.

A very useful approach in the analysis of normal modes is to turn attention away from individual modes and toward the types of motion in the protein that one would like to analyze. For example, one can ask the question: "Which modes (and thus which energies and which time scales) are involved in the rotation of this domain?" Or, turning to higher modes, "Which frequencies are involved in helix bending motions?"

Such questions can be answered using projection methods [13], which are based on an important mathematical property of normal modes: the normal mode vectors $\mathbf{e}_i$ (see Equation [1.6]), being the eigenvectors of a matrix, form a basis of the $3N$-dimensional configuration space of the protein. This means that any vector d in configuration space, and thus any type of motion, can be written as a superposition of normal mode vectors with suitable prefactors p_i, which are the *projections* of $\mathbf{d}$ onto mode i. Mathematically, the projections are defined by

$$p_i = \mathbf{d} \cdot \mathbf{e}_i \tag{1.21}$$

and satisfy the relation

$$\sum_{i=1} 3N p_i^2 = 1 \tag{1.22}$$

because the normal mode vectors form a basis of configuration space. It is therefore possible to interpret p_i^2 as the contribution of mode i (and its associated energy and time scales) to the motion described by $\mathbf{d}$.

Many interesting types of motion are described by more than one degree of freedom. For example, the rigid-body translation of a helix has three degrees

of freedom, one for each independent direction in 3D-space:

$$\mathbf{d}_x = \begin{pmatrix} (0,0,0) \\ \dots \\ (0,0,0) \\ (1,0,0) \\ \dots \\ (1,0,0) \\ (0,0,0) \\ \dots \\ (0,0,0) \end{pmatrix}, \quad \mathbf{d}_y = \begin{pmatrix} (0,0,0) \\ \dots \\ (0,0,0) \\ (0,1,0) \\ \dots \\ (0,1,0) \\ (0,0,0) \\ \dots \\ (0,0,0) \end{pmatrix}, \quad \mathbf{d}_z = \begin{pmatrix} (0,0,0) \\ \dots \\ (0,0,0) \\ (0,0,1) \\ \dots \\ (0,0,1) \\ (0,0,0) \\ \dots \\ (0,0,0) \end{pmatrix} \tag{1.23}$$

The nonzero entries in these vectors correspond to the atoms that make up the helix. For the case of M vectors (in this example we have $M = 3$), the projections are defined as

$$p_i = \frac{1}{\sqrt{M}} \sum_{k=1}^{M} \mathbf{d}_k \cdot \mathbf{e}_i \tag{1.24}$$

such that the sum of p_i^2 is again 1, and p_i can again be interpreted as the quantitative contribution of mode i to the motion under consideration. A convenient graphical representation is a plot of

$$C_k = \sum_{i=6}^{k} p_i^2, \quad k = 1, \dots, 3N \tag{1.25}$$

against k, ω_k (for vibrational modes), or $\hat{\lambda}_k$ (for Brownian modes). This yields a curve that increases from 0 to 1, with the steepest increase in the time scales that contribute most to the type of motion being studied.

An example for such an analysis is shown in Figure 1.5. It is taken from a normal mode study of the dynamics and conformational changes of Ca-ATPase [14] and shows how helix translations and rotations are distributed over the normal modes. In particular, it shows that different helices move on different timescales, and also that some helices have a wider time scale spectrum than others. In the case of Ca-ATPase, the helices near the A domain are characterized by longer timescales and larger amplitudes than the other helices. No explicit time scales were obtained in this calculation, but this would have been possible by performing a Brownian mode analysis (see Section 1.3.2).

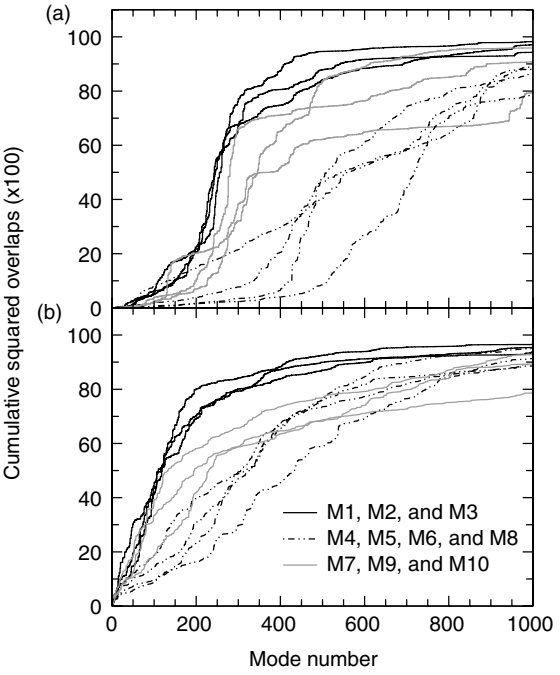

FIGURE 1.5
The cumulative projections C_k (see Equation [1.25]) of rigid-body translations (a) and rotations (b) of the transmembrane helices in Ca-ATPase onto the normal modes. Only translations along and rotations around the helix axes were taken into account. The plot shows the different timescales and amplitudes that characterize the motions of the different helices.

1.5 Conclusion

The goal of this chapter is to give an overview of the harmonic models and normal mode techniques that are used in studying the behavior of proteins. Any such overview is necessarily incomplete, and this chapter is no exception. Quasi-harmonic analysis, which derives a force constant matrix from thermodynamic calculations obtained from an MD trajectory, was left out because it is a technique for analyzing trajectories rather than an independent method. Normal mode calculations on continuous deformable media models were left out as well, because they are of interest mainly to the community of electron microscopists. Other rather specialized techniques have not been mentioned either. Finally, the actual numerical algorithms that are useful for identifying normal modes were not covered because they are either straightforward textbook algorithms (for sufficiently small systems) or specialized techniques discussed in Chapters 17 and 18. As for applications, the possibilities are numerous and the reader can find ample inspiration in the other chapters of this book.

References

1. Frauenfelder, H., Parak, F., and Young, R.D. Conformational substates in proteins, *Ann. Rev. Biophys. Biophys. Chem.*, 17: 451–479, 1988.
2. Elber, R., and Karplus, M. Multiple conformational states of proteins: a molecular dynamics analysis of myoglobin, *Science*, 235: 318–321, 1987.
3. Kitao, A., Hayward, S., and Go, N. Energy landscape of a native protein: jumping-among-minima model, *Proteins*, 33: 496–517, 1998.
4. Tirion, M.M. Low-amplitude elastic motions in proteins from a single-parameter atomic analysis, *Phys. Rev. Lett.*, 77: 1905–1908, 1996.
5. Hinsen, K. Analysis of domain motions by approximate normal mode calculations, *Proteins*, 33: 417–429, 1998.
6. Hinsen, K. Thomas, A., and Field, M.J. Analysis of domain motions in large proteins, *Proteins*, 34: 369–382, 1999.
7. Atilgan, A.R. Durell, S.R. Jernigan, R.L., Demirel, M.C. Keskin, O., and Bahar, I. Anisotropy of fluctuation dynamics of proteins with an elastic network model, *Biophys. J.*, 80: 505–515, 2001.
8. Cornell, W.D., Cieplak, P., Bayly, C.I., Gould, I.R., Merz Jr, K.M., Ferguson, D.M., Spellmeyer, D.C., Fox, T., Caldwell, J.W., and Kollman, P.A. A second generation force field for the simulation of proteins and nucleic acids, *J. Am. Chem. Soc.*, 117: 5179–5197, 1995.
9. Hinsen, K., Petrescu, A.-J., Dellerue, S., Bellissent-Funel, M.C., and Kneller, G.R. Harmonicity in slow protein dynamics, *Chem. Phys.*, 261: 25–38, 2000.
10. Goldstein, H. "*Classical Mechanics*," Addison-Wesley Pub. Co., Reading, MA, 1980.
11. Lamm, G. and Szabo, A. Langevin modes of macromolecules, *J. Chem. Phys.*, 85: 7334–7348, 1986.
12. Kneller, G.R. Inelastic neutron scattering from damped collective vibrations of macromolecules, *Chem. Phys.*, 261: 1–24, 2000.
13. Hinsen, K. and Kneller, G.R. Projection methods for the analysis of complex motions in macromolecules, *Mol. Sim.*, 23: 275–292, 2000.
14. Reuter, N., Hinsen, K., and Lacapre, J.-J. Transconformations of the SERCA1 Ca-ATPase: a normal mode study, *Biophys. J.*, 85: 2186–2197, 2003.

2

All-Atom Normal Mode Calculations of Large Molecular Systems Using Iterative Methods

Liliane Mouawad and David Perahia

CONTENTS

2.1 Introduction

The internal motions of proteins play an important role in their biological function, especially large amplitude motions that may be necessary for

enzymatic activity, allosteric transitions, and various biological processes such as signal transduction, etc.; characterizing these conformational changes is of general concern [1–4]. Molecular dynamics (MD) simulations have played a dominant role since the late 1970s to reveal the internal motions of proteins, however, due to the complex nature of the energy surface and the existence of a tremendously large number of energy minima, this method was not well-adapted to apprehend collective motions. Indeed, the conformational jumps from one minimum to another, taking place on the picosecond time scale [5], correspond to local motions that propagate into larger amplitude ones in a much longer time, as in *liquids*. On the contrary normal mode (NM) analysis appeared to be the most direct way to obtain the large amplitude motions [6,7]. It showed that they may occur in a correlated fashion, all atoms moving together along given directions, without the requirement of important local conformational changes of residues, as in *solids*. These two types of dynamics (MD and NM) raised the question whether the proteins have rather liquid- or solid-like properties [8–10]. Many experimental observations indicated that the predominance of one or the other type depends on the temperature of the system, the harmonic dynamics (i.e., NM) being important at low temperatures (lower than 200 K) and a diffusive type dynamics (i.e., MD), at higher temperatures [11–14].

The NM analysis is based on the harmonic approximation of the potential energy (see Section 2.2), which a priori represents a severe restriction for the protein to undertake large movements. Despite this approximation, low-frequency modes obtained by this method appeared to describe well the wide conformational changes that are observed experimentally [15–19]. NM analysis consists of diagonalizing the Hessian matrix whose elements are the second derivatives of the potential with respect to coordinates. The size of this matrix increases as the square of the number of atoms, which constituted for a long time a serious limitation for this method. Since the 1980s many efforts were devoted to overcome this difficulty by reducing the number of degrees of freedom, which can be done by several ways. The first approach [9,20] was based on the use of dihedral angle space, neglecting the other degrees of freedom, which results in more than tenfold reduction of the Hessian matrix' size. This approach yields a frequency spectrum and directions of motion in agreement with experiments, but still the size of the matrix increases as the square of the dihedral angle's number, which may represent a limitation for its application to very large proteins. Recently several authors [21, 22] considered each residue (or set of residues) as a rigid block having six translation–rotation degrees of freedom (RTB or BNM methods), which reduces drastically the size of the Hessian matrix and consequently the computational time. The quality of the modes depends on the number of residues taken in a block, one residue per block yielding low-frequency modes comparable to those obtained for all degrees of freedom, while increasing this number results in a rapid deterioration of the mode quality.

Another approach is the elastic network model (ENM) proposed originally by Tirion [23]; it is based on a simplified potential where the structure is only maintained by springs between neighboring atoms, which is consistent with

the solid-like nature of proteins. This potential is constructed in a way that corresponds to the minimum energy. Thus, its principal advantage is to avoid energy minimization. However, to calculate the NM for large proteins, the size of the matrix still should be reduced. For that, one may only consider the coordinates of the C_α atoms of the protein as a reduced basis set. Several variants of this model were proposed by Bahar et al. [24, 25], Hinsen [26], and Tama and Sanejouand [19]; they all yield low-frequency modes in a rather good agreement with observed conformational changes, but give unrealistic frequency spectra.

All the methods presented above neglect the coupling between the retained degrees of freedom and those that were ignored, although such a coupling may be important for a detailed description of the conformational change mechanism. Thus, it is important to consider other approaches that take into account all the degrees of freedom. The only way to do so is to use iterative schemes in order to diagonalize the Hessian matrix [27–29]. The interest of such approaches is that no more approximation than the harmonic one is done. These methods will constitute the object of this chapter, but beforehand let us take a look at the theory of NMs.

2.2 Normal Mode Theory

The NM theory is based on the resolution of Newton's equation of motion with the hypothesis that the potential energy function $V(\mathbf{r})$ has a quadratic form [30, 31]. Let us consider the function $V(\mathbf{r})$ of a molecule constituted of N atoms and depending on the mass-weighted Cartesian coordinates $\mathbf{r}$ ($r_1 = \sqrt{m_1}x_1$, $r_2 = \sqrt{m_1}y_1$, $r_3 = \sqrt{m_1}z_1$, $r_4 = \sqrt{m_2}x_2, \ldots$, m_i being the mass of atom i). For small atomic displacements it may be expanded as a Taylor series:

$$V(\mathbf{r}) = V(\mathbf{r}^0) + \sum_{i=1}^{3N} \left(\frac{\partial V}{\partial r_i}\right)_0 (r_i - r_i^0) + \frac{1}{2}\sum_{i,j=1}^{3N} \left(\frac{\partial^2 V}{\partial r_i \partial r_j}\right)_0 (r_i - r_i^0)(r_j - r_j^0) + \cdots \tag{2.1}$$

the index 0 refers to a reference structure that can be chosen to correspond to a minimum of the potential energy function, thus $(\partial V/\partial r_i)_0 = 0$. In addition, the potential energy can be defined relative to this reference structure such that $V(\mathbf{r^0}) = 0$. Moreover, for sufficiently small displacements the terms beyond second order may be neglected, reducing $V(\mathbf{r})$ to the quadratic form:

$$V(\mathbf{r}) = \frac{1}{2}\sum_{i,j=1}^{3N} k_{ij}(r_i - r_i^0)(r_j - r_j^0) \tag{2.2}$$

where $k_{ij} = (\partial^2 V/\partial r_i \partial r_j)_0$ represents the force constant relative to coordinates i and j.

In the matrix notation Equation (2.2) may be expressed as follows:

$$V(\mathbf{r}) = \tfrac{1}{2}\mathbf{r}^{\mathbf{T}}\mathbf{H}\mathbf{r} \tag{2.3}$$

where $\mathbf{r}$ is now the vector constituted of $3N$ coordinate differences $r_i - r_i^0$, $\mathbf{r}^{\mathbf{T}}$ the transpose of $\mathbf{r}$, and $\mathbf{H}$ the $3N \times 3N$ matrix, the elements of which are the force constants k_{ij}.

The kinetic energy K has also a quadratic form expressed by

$$K = \tfrac{1}{2}\dot{\mathbf{r}}^{\mathbf{T}}\mathbf{M}\dot{\mathbf{r}} \tag{2.4}$$

where $\dot{\mathbf{r}}$ is the vector of velocities, that is, the time derivative of $\mathbf{r}$, and $\mathbf{M}$ the matrix of second derivatives of the kinetic energy with respect to velocities. In a Cartesian basis set $\mathbf{M}$ consists of a diagonal matrix whose elements are the atomic masses. In the case of mass-weighted Cartesian coordinates as here, $\mathbf{M}$ reduces to a unit matrix. Introducing Equation (2.3) in the Newton's equation of motion

$$\mathbf{M}\ddot{\mathbf{r}} = -\nabla V(\mathbf{r}) \tag{2.5}$$

in which $\ddot{\mathbf{r}}$ represents the second derivative of $\mathbf{r}$ with respect to time, and $\nabla V(\mathbf{r})$ the first derivative of $V(\mathbf{r})$ with respect to $\mathbf{r}$, one obtains:

$$\mathbf{M}\ddot{\mathbf{r}} + \mathbf{H}\mathbf{r} = 0 \tag{2.6}$$

Equation (2.6) may be resolved by adopting the general form

$$\mathbf{r} = \mathbf{T}\mathbf{u} \tag{2.7}$$

where $\mathbf{T}$ is an orthogonal transformation matrix, that is, $\mathbf{T}^{\mathbf{T}}\mathbf{T} = \mathbf{T}\mathbf{T}^{\mathbf{T}} = \mathbf{1}$, and $\mathbf{u}$ a $3N$ coordinate vector, each element of which having the following time dependence

$$u_k = C_k \cos(\omega_k t + \phi_k) \tag{2.8}$$

where C_k and ϕ_k are the amplitude and the phase at time $t = 0$, respectively, and ω_k is the angular frequency of the kth vibrational mode. The coordinates $u_k$are called *NM coordinates* [31]. Using Equations (2.7) and (2.8) one gets for a given Cartesian coordinate

$$r_i - r_i^0 = \sum_{k=1}^{3N} T_{ik}u_k = \sum_{k=1}^{3N} T_{ik}C_k \cos(\omega_k t + \phi_k) \tag{2.9}$$

where T_{ik} is an element of the matrix $\mathbf{T}$. The set of elements $\{T_{ik}\}$ for a given k, with i running from 1 to $3N$ defines the direction along which all the atoms vibrate in phase with the same frequency. This equation shows that the displacement along a given Cartesian coordinate consists of the superposition of $3N$ vibrational motions.

Introducing the expression of $\mathbf{r}$ from Equation (2.7) in Equation (2.6) and multiplying the latter by $\mathbf{T^T}$ one gets

$$\mathbf{T^T M T \ddot{u}} + \mathbf{T^T H T u} = 0 \tag{2.10}$$

From Equation (2.8), one gets $\ddot{u}_k = -\omega_k^2 u_k$, which can be written in the matrix form

$$\mathbf{\ddot{u}} = -\mathbf{\Lambda u} \tag{2.11}$$

where $\mathbf{\Lambda}$ is a diagonal matrix with elements $\lambda_k = \omega_k^2$. Replacing $\mathbf{\ddot{u}}$ in Equation (2.10) and considering that $\mathbf{M}$ is the unit matrix, this yields:

$$\mathbf{T^T H T} = \mathbf{\Lambda} \tag{2.12}$$

$\mathbf{T}$ is thus a square matrix that diagonalizes $\mathbf{H}$. Each column of $\mathbf{T}$ is an eigenvector $\mathbf{q}_k$ (expressed in the Cartesian basis set) of $\mathbf{H}$ and thus is a *NM vector* associated to a given frequency, ω_k (or eigenvalue, λ_k). All the $3N$ vectors $\{\mathbf{q}_k\}$ are orthonormal thus linearly independent; they form a new basis set defining the NM reference frame for the molecule. In this frame, each of the molecule's structures corresponds to a point whose coordinate along a given direction $\mathbf{q}_k$ is the *NM coordinate* u_k. This is analogous to what is observed for one atom in the three-dimensional Cartesian space, where the atom is a point and its position is determined by its coordinates (x, y, z) along the three vectors of the basis set $\{\mathbf{e}_1, \mathbf{e}_2, \mathbf{e}_3\}$, which are the unit vectors along X, Y, and Z directions. The structure of a molecule consisting of N atoms can be considered as a point in the $3N$-dimensional Cartesian space, where its position is determined by its $3N$-coordinates $(r_1, r_2, \ldots, r_{3N})$ along the $3N$vectors of the basis set $\{\mathbf{X}_1, \mathbf{X}_2, \ldots, \mathbf{X}_{3N}\}$. In the reference frame corresponding to the NMs, the molecule's position is determined by its NM coordinates $(u_1, u_2, \ldots, u_{3N})$ along the basis set $\{\mathbf{q}_1, \mathbf{q}_2, \ldots, \mathbf{q}_{3N}\}$. Notice that, when expressed in the Cartesian space, a normal coordinate describes an internal collective (or localized) change of the structure, except for the first six modes that correspond to global translations and rotations of the molecule with eigenvalues equal to zero.

The calculation of NMs reduces to the diagonalization of the Hessian matrix $\mathbf{H}$. The main difficulty is that, for a large molecule, this matrix becomes too large to be diagonalized by standard diagonalization techniques [32].

2.3 Iterative Methods

2.3.1 Methods Based on the Rayleigh Quotient

Various iterative methods, developed several years ago for obtaining the lowest eigenvalue and eigenvector of a large symmetric matrix $\mathbf{H}$, are based on

the minimization of the *Rayleigh quotient* [33] given by

$$\rho(\mathbf{v}) = \frac{\mathbf{v^T H v}}{\mathbf{v^T v}} \tag{2.13}$$

where $\mathbf{v}$ is a guess vector. In fact $\rho(\mathbf{v})$ is a stationary point (minimum) with respect to any variation in $\mathbf{v}$ if, and only if, $\mathbf{v}$ is the eigenvector of $\mathbf{H}$, and at this point $\rho(\mathbf{v})$ is equal to the corresponding eigenvalue. One may then use steepest descent or conjugate gradient methods to converge to the lowest value of the *Rayleigh constant* for computing the lowest frequency mode. The gradient of $\rho(\mathbf{v})$ is

$$\nabla\rho(\mathbf{v}) = \frac{2(\mathbf{H} - \rho(\mathbf{v})\mathbf{I})\mathbf{v}}{\mathbf{v^T v}} \tag{2.14}$$

where $\mathbf{I}$ is the unit matrix.

As direct minimization is in general computationally costly, other techniques were developed such as the one based on Davidson's modification [34] of Lanczos's algorithm [35], consisting of adding orthonormal correction vectors to $\mathbf{v}$ during successive iterations in order to approach the exact eigenvector.

One inconvenience of this method is that only one mode is obtained, the one corresponding to the lowest eigenvalue. However, the procedure may be extended in order to find the next mode by introducing a modification to the Hessian matrix such that the calculated lowest eigenvalue is shifted to a higher value (root shifting method) [36]. This is achieved by replacing $\mathbf{H}$ by $\mathbf{H} + \beta_1 \mathbf{q_1 q_1^T}$ where β_1 is an arbitrary large value, and $\mathbf{q}_1$ the eigenvector corresponding to the lowest eigenvalue of the unmodified matrix. The vector $\mathbf{q}_1$ remains an eigenvector of the transformed matrix but its eigenvalue is shifted by β_1, all the other eigenvalues and eigenvectors being unchanged.

A similar approach was adapted by Brooks and Karplus [27] to calculate NM for proteins. They applied it to lysozyme to extract the lowest-frequency NM corresponding to the hinge bending motion of the protein.

More recent developments based on Lanczos/Arnoldi factorization [37] for diagonalizing large sparse matrices have been introduced in numerous packages (BLZPACK [38], ARPACK [39], …), allowing to calculate a large number of eigenvalues and eigenvectors. These methods seem to converge rather rapidly to the exact modes, but to our knowledge only BLZPACK was applied to proteins [40] (however, it required large computer memory).

2.3.2 Perturbation Method

Another iterative approach developed by Durand et al. [29] for computing exact NMs for macromolecules uses a perturbation-iteration scheme. In this

approach low resolution modes are first obtained by considering that the protein consists of rigid blocks corresponding each to a given number of residues and having only six translation–rotation degrees of freedom (RTB method mentioned in Section 2.1). In a second step the obtained low-resolution modes are perturbed by high frequency modes explicitly calculated in each block. This is done by coupling low- and high-frequency modes through a perturbation added to the Hessian matrix projected in the space of approximate low-frequency modes. This approach is based on the theory of effective Hamiltonians [41]. It was applied to crambin, a small protein of 46 residues, for which it provided exact low-frequency modes. Larger proteins were not tested, which would have assessed the efficiency of the approach.

2.3.3 Mixed Basis Method

Several years ago we proposed an iterative method of diagonalization in a mixed basis (DIMB) [28, 42] that was implemented in the CHARMM [43] program. The rest of this chapter consists of the presentation of this method because it is at present the only iterative method that is available within a molecular simulation package that proved to be efficient for obtaining a set of low-frequency modes for a very large molecular system.

2.4 The DIMB Method

The DIMB method is based on the principle that approximate low frequency modes may be refined if they are coupled to higher frequency degrees of freedom. It consists, first, of dividing the Hessian matrix in sub-blocks, the low-frequency eigenvectors of diagonal sub-blocks providing the approximate guess vectors that will be refined iteratively. Second, this refinement is made by coupling the guess vectors to high-frequency degrees of freedom, which amounts to taking into account the off-diagonal sub-blocks. These degrees of freedom may be high-frequency NMs; however, the use of these modes is complex and not efficient, especially for large systems [28], so another way to perform such a coupling is to consider subsets of Cartesian coordinate displacements. Indeed, the latter, as it was shown in Equation (2.9), contain implicitly high-frequency motions since they correspond to the superposition of all the low- and high-frequency NM. This coupling proved to be very efficient, so it was adopted in the DIMB method, whose name referred to the mixing of subsets taken from two different basis sets: low-frequency NM and Cartesian coordinates.

In what follows we will describe how to obtain initial guess vectors taken as a first approximation of exact modes and the iterative procedure used to refine them.

2.4.1 Initial Guess Vectors

The Hessian matrix is subdivided in an arbitrary number of sub-blocks:

$$\mathbf{H} = \begin{pmatrix} \mathbf{H^{AA}} & \mathbf{H^{AB}} & \dots \\ \mathbf{H^{BA}} & \mathbf{H^{BB}} & \dots \\ \dots & \dots & \dots \end{pmatrix} \tag{2.15}$$

Each diagonal block ($\mathbf{H^{AA}}, \mathbf{H^{BB}}, \dots$) contains an arbitrary number of elements ($l \times l, k \times k, \dots$, respectively) corresponding to any part of the molecule's structure. Diagonalizing these blocks and redimensioning their eigenvectors yield the set of orthonormal vectors $\{\mathbf{q^A}, \mathbf{q^B}, \dots\}$ as shown in Figure 2.1(a) (for more details see the appendix). Expressing the Hessian matrix in this set of vectors after reorganizing them in the ascending order of their eigenvalues, yields the matrix $\mathbf{Q}$ (see Figure 2.1[b]). The property of this matrix is that it can be partitioned in sub-blocks that depend on the frequency. Diagonalizing only the sub-block $\mathbf{Q^{LL}}$ that corresponds to the lowest frequencies, yields the set of initial guess vectors $\{\mathbf{q}\}_0$, where the subscript stands for iteration number 0.

2.4.2 Iterative Procedure for Obtaining the NMs

In iteration number 1, a subset s_0 from the Cartesian basis, $\{\mathbf{X}\}_{s_0}$, is chosen (see Figure 2.2 and the appendix for the composition of vectors $\mathbf{X}$) and combined with the guess vectors $\{\mathbf{q}\}_0$. Then the mixed set of vectors is orthonormalized to form $\{\mathbf{q}', \mathbf{X}\}_0$, a sub-basis in which the Hessian matrix will be expressed, yielding $\mathbf{Q}_{(1)}$. Notice that the dimension of $\mathbf{Q}_{(1)}$ is much smaller than that of $\mathbf{H}$. The eigenvectors of $\mathbf{Q}_{(1)}$, $\{\mathbf{q}\}_1$, constitute the starting vectors for the second iteration, replacing $\{\mathbf{q}\}_0$ in the procedure. In each iteration step, the set of Cartesian vectors is chosen differently in order to scan the entire set of degrees of freedom of the system. The iteration procedure continues until the eigenvectors converge to exact NMs according to defined criteria.

2.4.3 Convergence Criteria

In iteration I, an eigenvector $\mathbf{q}_{(I)}$of the matrix $\mathbf{Q}_{(I)}$ is considered to be converged to an exact mode if, when it is expressed in the Cartesian reference frame (for more details see the appendix), it is also an eigenvector of the initial Hessian matrix $\mathbf{H}$. A precise evaluation of the convergence is given by [42]:

$$C_q = 1 - \frac{\mathbf{q}_{(I)}^{\mathbf{T}} \mathbf{H} \mathbf{q}_{(I)}}{\left(\mathbf{q}_{(I)}^{\mathbf{T}} \mathbf{H}^{\mathbf{T}} \mathbf{H} \mathbf{q}_{(I)}\right)^{1/2}} \tag{2.16}$$

In this expression, when $\mathbf{q}_{(I)}$ is the correct eigenvector of $\mathbf{H}$, C_q is equal to zero, while when it is very far from it, C_q is close to 1; during successive iterations,

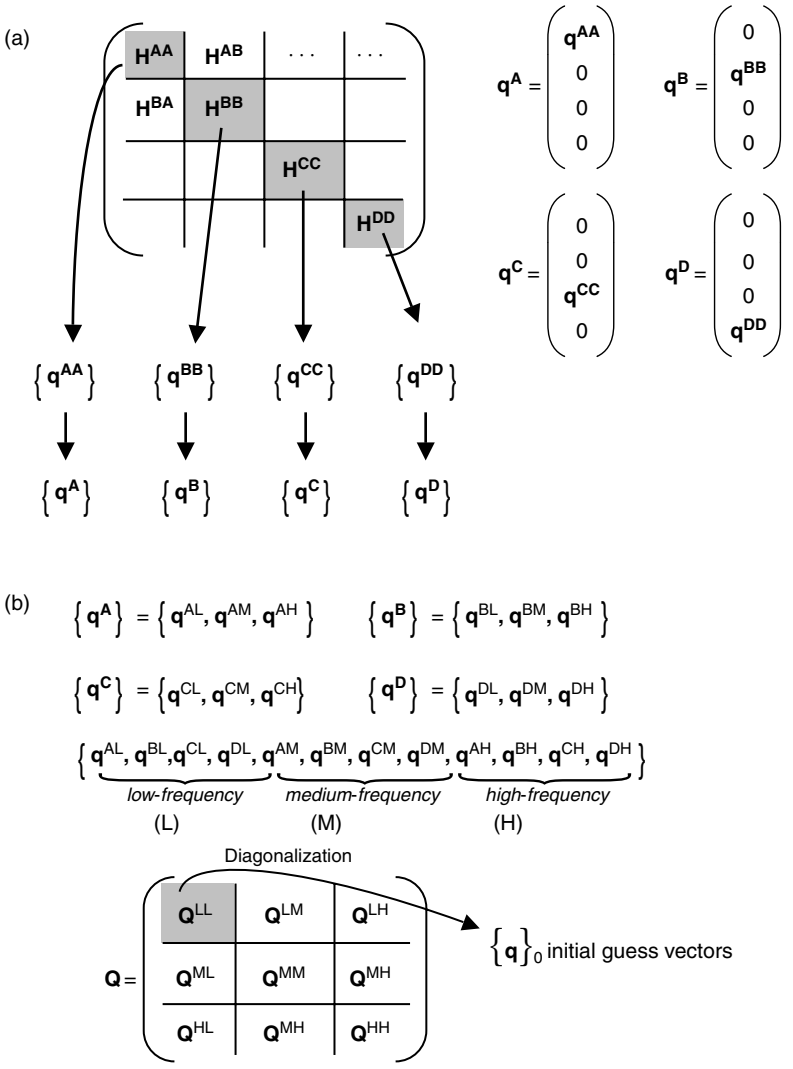

FIGURE 2.1
DIMB method, iteration number 0: (a) The subdivision of the Hessian matrix **H** corresponds to the example of a molecule divided into four parts. Diagonalization of each block ($\mathbf{H}^{AA}$, $\mathbf{H}^{BB}$, $\mathbf{H}^{CC}$, and $\mathbf{H}^{DD}$) yields the sets of eigenvectors $\{\mathbf{q}^{AA}\}$, $\{\mathbf{q}^{BB}\}$, $\{\mathbf{q}^{CC}\}$, and $\{\mathbf{q}^{DD}\}$. The dimensions of these vectors correspond to those of the sub-matrices; therefore, they are completed with zeroes in order to attain the dimension of the entire matrix **H**, yielding sets of vectors $\{\mathbf{q}^{A}\}$, $\{\mathbf{q}^{B}\}$, $\{\mathbf{q}^{C}\}$, and $\{\mathbf{q}^{D}\}$. (b) These vectors are reorganized in their frequencies' ascending order. The Hessian matrix expressed in this basis, **Q**, is divided in its turn into sub-blocks and only $\mathbf{Q}^{LL}$ is diagonalized; a part of its eigenvectors $\{\mathbf{q}\}_0$, corresponding to the lowest-frequency eigenvalues, are the initial guess vectors.

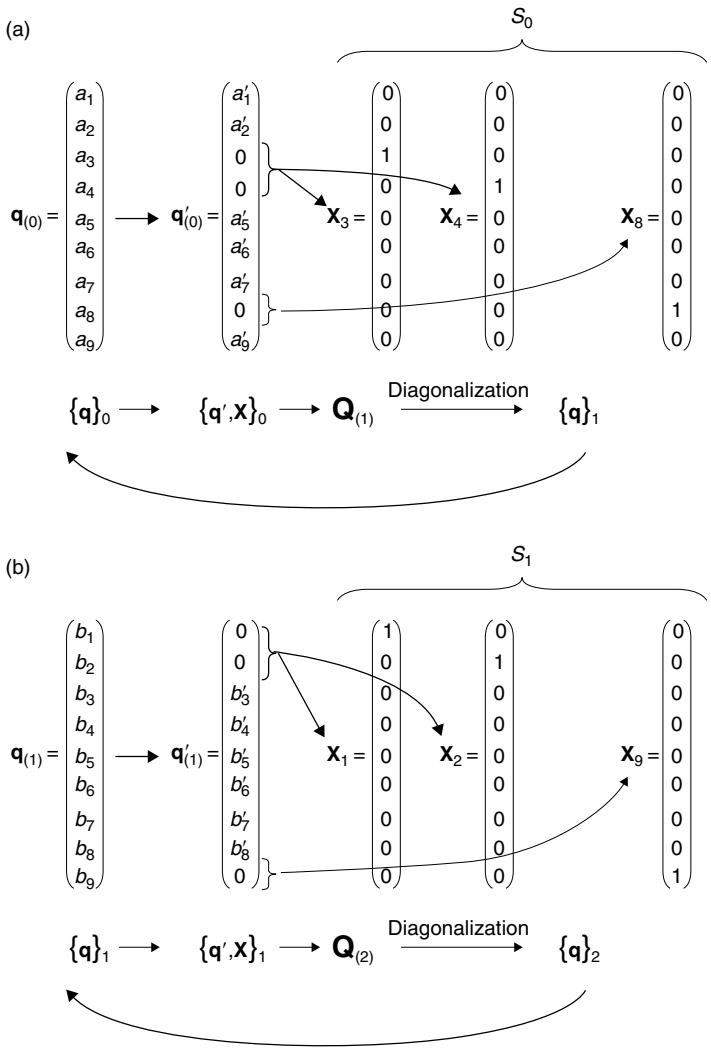

FIGURE 2.2
DIMB method, iterative procedure: example of a 3-atom molecule. (a) In iteration number 1, a selection ($s_0 = 3$) of elements of all the $\{\mathbf{q}\}_0$ vectors are replaced by zeroes in two disjoint regions of the vectors (double-window technique mentioned in the appendix) and orthonormalized, yielding $\{\mathbf{q}'\}_0$. The corresponding Cartesian coordinate basis vectors $\{\mathbf{X}_3, \mathbf{X}_4, \mathbf{X}_8\}$ are combined to $\{\mathbf{q}'\}_0$ to form the mixed basis $\{\mathbf{q}', \mathbf{X}\}_0$. Diagonalization of the Hessian matrix $\mathbf{Q}_{(1)}$ in this sub-basis yields $\{\mathbf{q}\}_1$ vectors that replace $\{\mathbf{q}\}_0$ in the next iteration run. (b) Iteration number 2, in which the s_0 elements are chosen differently, and so on.

C_q will decrease until it reaches zero, but in practice a threshold value is chosen in order to stop the iterative procedure at a given level of precision. It was observed that even for vectors $\mathbf{q}$ close to the NMs, the value of C_q stays high because it is too sensitive to small, nonrepresentative variations of the

vectors; this yields a large number of unnecessary iterations, thus another criterion may be used.

In this new criterion, the eigenvectors are considered to be converged when they do not change significantly during a given number, K, of successive iterations. Therefore at each iteration (I) the calculated eigenvectors $\{\mathbf{q}\}_I$ are projected on those $\{\mathbf{q}\}_{I-1}$ of the previous iteration ($I-1$). We define $(P_{I,I-1})_j$ as the maximum of the projections of all the m calculated vectors $\{\mathbf{q}\}_I$ on the jth vector $\mathbf{q}_{j(I-1)}$:

$$(P_{I,I-1})_j = \max[(\mathbf{q}_{1(I)} \cdot \mathbf{q}_{j(I-1)}), \ldots, (\mathbf{q}_{i(I)} \cdot \mathbf{q}_{j(I-1)}), \ldots, (\mathbf{q}_{m(I)} \cdot \mathbf{q}_{j(I-1)})] \tag{2.17}$$

and $\bar{P}_{I,I-1}$, the average of the maximum projections over all the modes j:

$$\bar{P}_{I,I-1} = \frac{1}{m} \sum_{j=1}^{m} (P_{I,I-1})_j \tag{2.18}$$

Finally, the new convergence criterion

$$C_P = (K-1) - (\bar{P}_{I,I-1} + \bar{P}_{I-1,I-2} + \cdots + \bar{P}_{I-(K-2),I-(K-1)}) \tag{2.19}$$

should be smaller than a threshold value. We observed that for $K = 4$, corresponding to $C_P = 3 - (\bar{P}_{I,I-1} + \bar{P}_{I-1,I-2} + \bar{P}_{I-2,I-3})$, and a threshold value of 10^{-3}, good quality eigenvectors are obtained with reasonable computational time (see Section 2.5).

2.5 Applications of DIMB

The DIMB method has been applied to several proteins of various sizes and shapes (going from BPTI, 58 residues, to ATCase, 2878 residues) [17,28,44,45] and always converged to exact NM [28,42]. Only two test-cases will be presented here, a small protein, neocarzinostatin (NCS, 948 atoms; its pdb identifier: 1NOA) and a middle-size one, human hemoglobin (HbA, 5598 atoms, 2HHB). Both proteins were energy minimized until a root mean square energy gradient of 10^{-4} kcal/mol/Å was reached, before undertaking the calculation of their NMs.

2.5.1 Neocarzinostatin

The modes of NCS were calculated in two ways, either by the DIMB method or by the standard method (SM), that is, the straightforward diagonalization of the entire Hessian matrix, in order to compare the results.

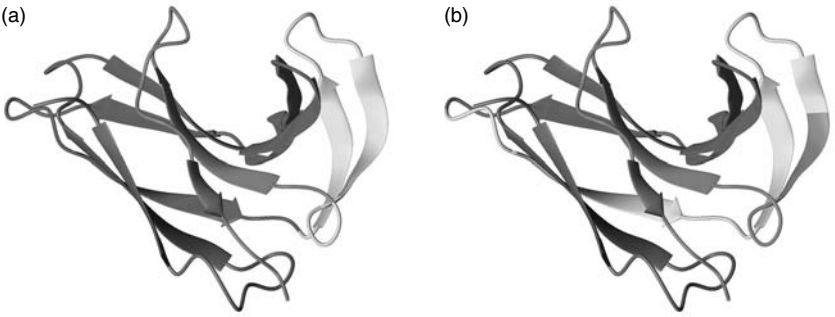

FIGURE 2.3
(See color insert following page 136) Structure of NCS. (a) Partition of the protein according to its secondary structure elements. (b) Subdivision of the protein in four equal parts of 237 atoms without any structural considerations. Each part of the protein is presented by a different color.

2.5.1.1 Comparison between DIMB and the SM

In iteration zero of the DIMB method the Hessian matrix was divided into four diagonal blocks according to the secondary structure elements of NCS, as shown in Figure 2.3(a). Then 20 iterations were carried out to calculate the 50 lowest-frequency modes. The evolution of the frequencies and of the projection of the eigenvectors on those of SM are presented in Figure 2.4(a) and Figure 2.4(b) for the four lowest frequency modes. Moreover, eigenvalues and the projections of eigenvectors for all the calculated modes (except the six translation–rotation modes) are shown in Figure 2.4(c) and Figure 2.4(d) at the first and last iterations (numbers 0 and 20). It is observed that even at iteration 0 one may find an eigenvector with a rather good overlap with a correct mode calculated by SM, as here 86% ($1 - P^{\max} = 0.07$) for mode 7, which is the lowest-frequency internal mode, although its eigenvalue is slightly higher than the correct one (5.7 cm^{-1} instead of 3.6 cm^{-1}). After 20 iterations in the mixed basis, all the modes have converged to a very high precision (with an average relative error of 10^{-4} for the eigenvalues and an average overlap for the eigenvectors of 99.99%). In fact the modes have converged more rapidly, in only 12 iterations, as can be seen in Figure 2.5(a), in which the average of the maximum projections between the two sets of modes is reported with respect to the iteration number, ($\bar{P}_{\mathrm{DIMB,SM}}$ is obtained using Equations [2.17] and [2.18] but instead of modes at iterations I and $I - 1$, the modes were those calculated by DIMB and SM). This observation is corroborated by the convergence criterion C_P (Equation [2.19], Figure 2.5[b]) that is based on the projections of the modes for four successive iterations. On the contrary, the old criterion C_q (Equation [2.16], Figure 2.5[c]) did not reveal the right state of convergence at 20 iterations; it tends to zero only after 32 iterations.

These calculations were performed on a single 2.4 GHz Pentium IV processor for both SM and DIMB methods. The CPU time needed to calculate the 50 lowest-frequency modes by SM was 1.7 min, while 20 iterations of the

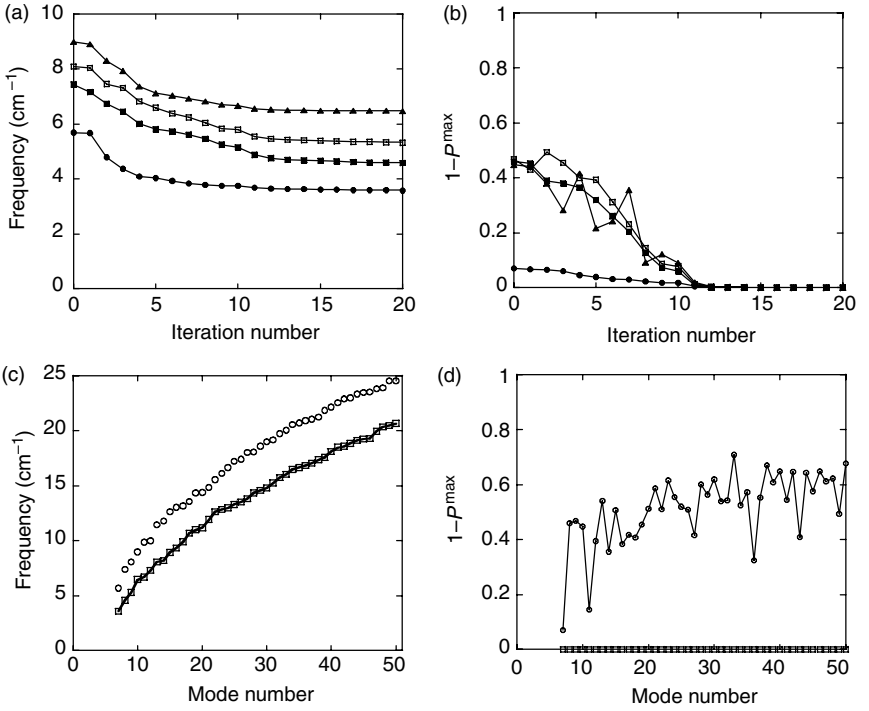

FIGURE 2.4
Comparison between DIMB and SM for NCS. (a) Evolution of the frequencies with respect to the iteration number for the four lowest-frequency modes. (b) $1 - P^{\max}$ for the four lowest-frequency modes, $P^{\max}$ being the maximum of the projections of each mode calculated by DIMB on all those obtained by SM. In (a) and (b), filled circles correspond to mode 7 (the 6 translation–rotation modes are omitted), filled squares to mode 8, open squares to mode 9, and filled triangles to mode 10. (c) The frequency of all the modes calculated by DIMB at iteration 0 (circles) and iteration 20 (open squares) and by SM (solid line). (d) $1 - P^{\max}$ for all the modes calculated by DIMB, at iteration 0 (circles) and iteration 20 (squares).

DIMB method required 2.8 min to calculate the same number of modes. However, if the calculations would have been stopped after only 12 iterations, at which point the modes had already attained good convergence, they would have cost 1.6 min in CPU time.

2.5.1.2 Utilization of DIMB with a Different Partition

The initial partition of the protein determines the quality of the guess vectors and therefore may influence the convergence rate of the modes. To investigate the role of the partition, the Hessian matrix was divided in four equal parts of 237 atoms (Figure 2.3[b]) without any structural considerations. In this partition it happened that the first diagonal block included the entire residues from number 1 to 31 and the nitrogen atom of the peptidic group of residue 32,

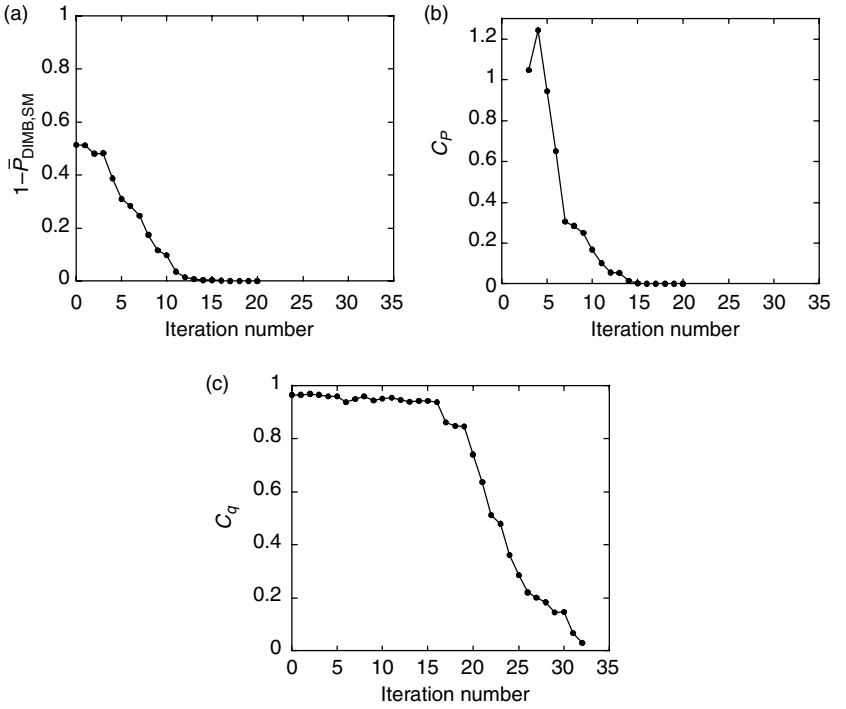

FIGURE 2.5
(a) $1-\bar{P}_{\mathrm{DIMB,SM}}$, $\bar{P}_{\mathrm{DIMB,SM}}$ being the average of the maximum of the projections obtained using Equations (2.17) and (2.18) for modes calculated by DIMB and SM vs. iteration number. It shows that the modes have converged after only 12 iterations. (b) The new convergence criterion, C_P, confirms this observation. (c) The old convergence criterion, C_q, shows that convergence is not reached before 30 iteration steps.

leaving its bonded hydrogen atom isolated in the second block. The existence of similar orphan atoms was observed in other blocks. For these atoms, the bonds connecting them to the rest of the protein are not taken into account in the eigenvectors calculated for the corresponding block, which reduces the quality of the guess vectors. Despite this poor subdivision of the matrix, the eigenvectors still converge after few iterations to the right NMs as shown in Figure 2.6, although not as efficiently as when the secondary structures were taken into account.

2.5.1.3 Coupling Between Backbone Collective Motions and Side-Chains

It is of general interest to know how side-chains motions may be coupled to the overall internal motion of the backbone, because it may have important implications in the function of the protein. Such information can be obtained from the NM analysis when all the atoms are taken into account in the calculation (as in the DIMB method). For comparison, approximate methods that

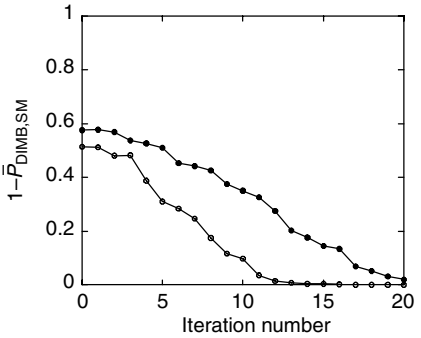

FIGURE 2.6
Comparison of the two ways of partitioning the Hessian matrix in iteration 0 (as shown in Figure 2.3). $1 - \bar{P}_{DIMB,SM}$ vs. iteration number, $\bar{P}_{DIMB,SM}$ being the average of the maximum of the projections. Open circles correspond to the partition in which the secondary structure elements are taken into account (same figure as Figure 2.5[a]) and filled circles to the partition in which the protein is divided in four equal parts.

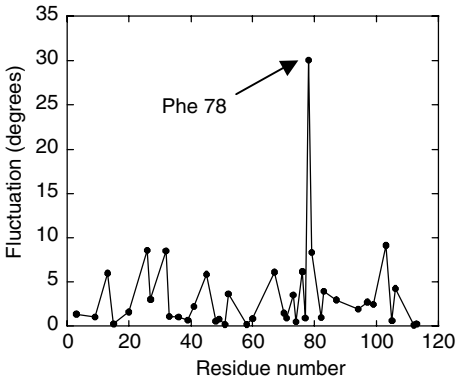

FIGURE 2.7
Fluctuations of the side-chains χ_1 angles of NCS for a maximum displacement of 2 Å along mode number 9.

consider only C_α atoms (as ENM) or rigid-body side-chains (as RTB) do not allow such investigations.

To illustrate the importance of the coupling between side-chains and the collective motions, let us consider once more the case of NCS. The fluctuations of the χ_1 angles of the side-chains were calculated for mode number 9, which corresponded the most to the conformational change involved in ligand-binding. The results, presented in Figure 2.7, showed the prominence of the fluctuations of a single residue, Phe 78, whose side-chain motion is thus coupled to the collective conformational change of the protein. In a more detailed analysis of the dynamics along mode 9 it was observed that the collective backbone motion for opening the binding site of the protein was coupled to

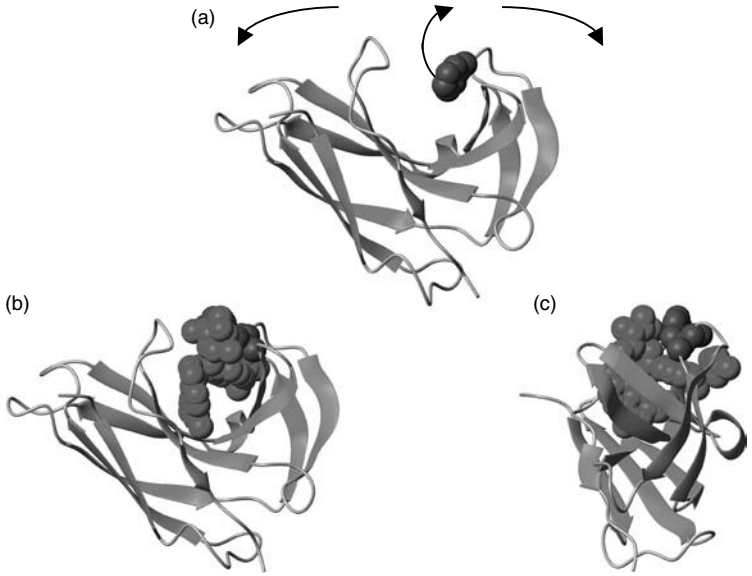

FIGURE 2.8
(See color insert following page 136) Crystal structures of apo (a) and holo-NCS containing a chromophore (b and c); residue Phe 78 is shown in red and the chromophore in green. In (a) the arrows indicate the motion along mode 9, in the opening direction of the cleft, which is coupled to the upward motion of Phe 78. In (b) holo-NCS is presented in the same orientation as (a) while in (c) it is rotated by 90°.

the upward motion of the Phe 78 side-chain (Figure 2.8[a]) and in the opposite direction, the closing of the cleft was accompanied by a downward motion of the side-chain. This indicated that the mentioned residue would play an important role in ligand binding, first by making more accessible the binding site for ligand approach and second, by maintaining the ligand tightly bound to the protein. This deduction is consistent with the observation of both liganded and unbound crystal structures, where residue Phe 78 adopts two different orientations as can be seen in Figure 2.8.

2.5.2 Hemoglobin

Hemoglobin is a tetramer composed of two α chains (141 residues) and two β chains (146 residues), each chain containing a heme molecule. To calculate the 200 lowest-frequency modes of this protein we could not apply the SM because it required more than 1.2 GB RAM, while the DIMB method required only 50 MB. Two ways for subdividing the Hessian matrix were adopted, first in 10 parts without any structural consideration [16,42] (560 atoms for the largest block) and second in 4 parts, each corresponding to a polypeptide chain with its heme (1429 atoms for the largest block). In the former case the calculations were continued for 384 iterations, until the older convergence criterion given by Equation (2.16) reached a value less than 0.06, that is, the

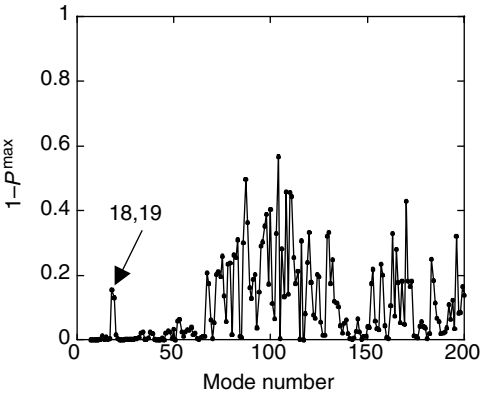

FIGURE 2.9
Comparison between two ways of subdividing the Hessian matrix for hemoglobin. $1 - P^{max}$, P^{max} being the maximum of the projections of all the modes calculated by DIMB after only 12 iterations (partition in four parts corresponding to each chain) on those obtained after 384 iterations (partition in 10 parts of approximately 560 atoms). The latter are assimilated to modes obtained by SM because they converged to a very high precision level.

modes have converged to a high precision level. These modes are considered as the reference ones. In the second method of subdivision, only 12 iterations were carried out, taking 3 h on a single 2.4 GHz processor, and all the vectors were projected on all the reference modes. The maximum of these projections for each reference mode are reported in Figure 2.9, where it can be seen that the first 66 modes (i.e., including all those describing the collective motions) are well-converged. Notice that modes 18 and 19, the projections of which are around 0.85 ($1 - P^{max} \approx 0.15$), are quasi-degenerate modes.

2.6 Concluding Remarks

The three iterative methods presented here converge well to the exact low-frequency NMs. However the methods based on the Rayleigh quotient [27] or on the perturbation approach [29] do not allow the calculation of a large number of low-frequency NM, contrary to DIMB. In the latter the number of calculated modes can be large enough to describe all the interesting motions ranging from the collective movements to those of isolated secondary structures. Therefore DIMB is at present the only method implemented in a molecular simulation package that allows the calculation of a large number of *exact* low-frequency NMs for macromolecules that are too large to be handled by the SM. It is based on the classical force field used in molecular simulations. This is important because it yields the low-frequency spectrum for a given molecule in the same range as that obtained experimentally by neutron scattering or other techniques; therefore the calculated thermodynamic

quantities from these modes come out with reasonable values. Moreover, it allows the calculation of NMs for any type of molecule of biological interest (proteins, nucleic acids, ligands, in which may be included water molecules and ions, …) and their possible assemblies, as far as their parameters are known for MD simulations. In addition, since the all-atom representation is used, it permits the study of the coupling between collective and localized motions as shown in the previous section.

Generally, calculation of NM by either the standard or iterative methods is relatively long compared to approximate methods using simplified force fields, because it requires beforehand the energy minimization to a very low root mean energy gradient ($\leq 10^{-4}$ kcal/mol/Å), which is very time consuming. In addition the DIMB method has been criticized because of the length of its calculation time, but as it was mentioned earlier, the new convergence criterion (Equation [2.19]) shows that in fact, the modes converge much more rapidly than what was reported previously [22,26] by using the old criterion (Equation [2.16]). In fact only few iteration steps are necessary to obtain exact modes and still fewer if the molecule's internal structure is taken into account in the initial subdivision of the Hessian matrix. Nevertheless, the DIMB method offers the possibility to stop the calculations at any desired precision of the modes. Even at iteration zero, the guess vectors may be of the same quality or better than those obtained by approximate methods (ENMs, rigid-blocks approaches, …) for a relatively low calculation time cost (excluding the energy minimization), but with all atoms represented and obtained frequencies of the same order of magnitude as those revealed by experimental spectra.

Moreover, any initial guess vectors may be considered in the DIMB method, either obtained by an arbitrary subdivision of the Hessian matrix in iteration 0 or by introducing in iteration 1 the vectors obtained from another approximate method. Indeed, they all will ultimately converge to exact lowest frequency modes; however, there is a real advantage to choosing guess vectors that are as close as possible to the correct lowest frequency modes in order to increase the convergence rate.

Appendix A Detailed Description of the DIMB Method

A.1 Initial Guess Vectors

The Hessian matrix is subdivided in an arbitrary number of sub-blocks

$$\mathbf{H} = \begin{pmatrix} \mathbf{H^{AA}} & \mathbf{H^{AB}} & \cdots \\ \mathbf{H^{BA}} & \mathbf{H^{BB}} & \cdots \\ \cdots & \cdots & \cdots \end{pmatrix} \tag{2.20}$$

each diagonal block ($\mathbf{H^{AA}}$, $\mathbf{H^{BB}}$, ...) contains an arbitrary number of elements ($l \times l, k \times k, \ldots$, respectively) corresponding to any part of the structure. The diagonalization of these blocks yields the set of eigenvectors $\{\mathbf{q^{AA}}\}$ for $\mathbf{H^{AA}}$, $\{\mathbf{q^{BB}}\}$ for $\mathbf{H^{BB}}$, etc. These vectors should be transformed to have the dimensionality of the entire system ($3N$) by adding zeros to the vectors as shown in Figure 2.1(a). This yields the set of orthonormal vectors $\{\mathbf{q^A}, \mathbf{q^B}, \ldots\}$, which forms a new basis set. In this procedure all the off-diagonal sub-blocks of the Hessian matrix are neglected, although they represent the interactions between different parts of the protein. In order to take into account these interactions, a new basis set consisting of low-frequency NM and some Cartesian coordinates should be adopted as described earlier. So first, one should calculate the low-frequency NM that will be considered as initial guess vectors. For this purpose, the basis set $\{\mathbf{q^A}, \mathbf{q^B}, \ldots\}$ is reorganized in the ascending order of the corresponding eigenvalues $\{\mathbf{q^L}, \mathbf{q^M}, \ldots\}$, as shown in Figure 2.1(b) and the Hessian matrix is expressed in this basis set (it will be denoted $\mathbf{Q}$). The new Hessian matrix is divided in sub-blocks and only the low-frequency one is diagonalized as shown below.

Theoretically, there exists an orthogonal transformation matrix $\mathbf{T}'$ (see Reference 28) such that

$$\mathbf{Q} = \mathbf{T'^T H T'} \tag{2.21}$$

The elements of $\mathbf{Q}$ are the second derivatives of the potential energy function with respect to the coordinates in the basis set $\{\mathbf{q^L}, \mathbf{q^M}, \ldots\}$ and as for matrix $\mathbf{T}$ in Equation (2.12) the columns of $\mathbf{T}'$ are the vectors $\{\mathbf{q^L}, \mathbf{q^M}, \ldots\}$, thus the elements of $\mathbf{T}'$ are of the form $t'_{ij} = \partial X_i / \partial q_j$ where X_i are the Cartesian coordinates. Equation (2.21) is a similarity transformation that preserves the eigenvalues and the eigenvectors when expressed in the Cartesian basis. For a complete basis set $\{\mathbf{q^L}, \mathbf{q^M}, \ldots\}$ of $3N$elements, the $\mathbf{Q}$ matrix is of the same dimension as $\mathbf{H}$. It can be partitioned in sub-blocks that depend on the frequency as shown in Figure 2.1(b). The sub-block corresponding to the lowest frequencies, $\mathbf{Q^{LL}}$, is of an arbitrary size; it depends on the number of modes that is intended to be calculated. In practice, only the $\mathbf{Q^{LL}}$ sub-matrix is calculated using the $\{\mathbf{q^L}\}$ set; then it is diagonalized to yield a reduced basis set $\{\mathbf{q^r}\}$, which is defined in the space of the $\{\mathbf{q^L}\}$ vectors. $\{\mathbf{q^r}\}$ have to be back transformed in order to define them in the initial Cartesian frame using the transformation matrix $\mathbf{T}''$

$$\mathbf{q} = \mathbf{T}''\mathbf{q^r} \tag{2.22}$$

$\mathbf{T}''$ is not a square matrix; it corresponds to a part of $\mathbf{T}'$. Indeed, its columns are only composed by vectors $\{\mathbf{q^L}\}$. From the set of the obtained $\{\mathbf{q}\}$ vectors, only a chosen subset $\{\mathbf{q}\}_0$, corresponding to the lowest eigenvalues, constitutes the initial guess vectors. The subscript stands for iteration number 0.

A.2 Iterative Procedure for Obtaining the NMs

The guess vectors are coupled with subsets of Cartesian coordinates to form mixed basis sets using an iterative procedure. In iteration number 1, let us consider s_0 Cartesian coordinate vectors, $\{\mathbf{X}\}_{s_0}$, that constitute a subset of the Cartesian basis. Each of these vectors corresponds to one degree of freedom although it is constituted of $3N$ elements. Indeed, all the elements are equal to zero except the one that corresponds to the displacement of a given atom along one of the Cartesian axes, whose value is 1 (see Figure 2.2[a]). Let us now consider the set of vectors $\{\mathbf{q}\}_0$ and $\{\mathbf{X}\}_{s_0}$, which should be orthonormal to constitute a reduced basis. Note that each of them is already orthonormal, but this is not the case between the two sets. In order to orthonormalize the whole set $\{\mathbf{q}, \mathbf{X}\}_0$ keeping the vectors $\{\mathbf{X}\}_{s_0}$ unchanged, for each vector $\mathbf{q}$ the components corresponding to Cartesian coordinates of selection s_0 are replaced by zeros, making the modified set $\{\bar{\mathbf{q}}\}_0$ not orthonormal anymore, but orthogonal to the set $\{\mathbf{X}\}_{s_0}$. In order to reorthonormalize the set $\{\bar{\mathbf{q}}\}_0$ by preserving the null components that were introduced, the Gram–Schmidt orthogonalization procedure is used [33], followed by the normalization $\mathcal{N}$. In this procedure the vector $\bar{\mathbf{q}}_i$ is orthogonalized with respect to all the preceeding vectors $\{\bar{\mathbf{q}}_1, \ldots, \bar{\mathbf{q}}_{i-1}\}$:

$$\mathbf{q}'_i = \mathcal{N}\left(\bar{\mathbf{q}}_i - \sum_{k=1}^{i-1} (\mathbf{q}'^{\mathbf{T}}_k \bar{\mathbf{q}}_i)\mathbf{q}'_k\right) \tag{2.23}$$

The Hessian matrix $\mathbf{Q}_{(1)}$ is expressed in the new reduced basis $\{\mathbf{q}', \mathbf{X}\}_0$, using the transformation matrix $\mathbf{T}_{(1)}$ as in Equation (2.21), the columns of $\mathbf{T}_{(1)}$ being the vectors $\{\mathbf{q}', \mathbf{X}\}_0$. Diagonalization of $\mathbf{Q}_{(1)}$ yields the eigenvectors $\{\mathbf{q}\}_1$ which constitute the starting vectors for the second iteration. In each iteration step, the set of Cartesian vectors is chosen differently in order to scan the whole degrees of freedom of the system (Figure 2.2[b]). Different kinds of selections of the Cartesian coordinates may be adopted, but in practice we observed that it is more efficient to choose the Cartesian coordinates that belong to two disjoint regions along the sequence of the molecule; we called it the double-window technique [42]. The iteration procedure continues until the eigenvectors converge to exact NMs.

References

1. Citri, N., Conformational adaptability of enzymes, *Adv. Enzymol.*, 37, 397, 1973.
2. Carreri, G., Gratton, E., and Fasella, P., Enzyme dynamics: the statistical physics approach, *Annu. Rev. Biophys. Bioeng.*, 8, 69, 1979.

3. Gurd, F.R.N., and Rothgeb, M., Motions in proteins, *Adv. Prot. Chem*., 33, 73, 1979.
4. Yon, J.M., Perahia, D., and Ghelis, C., Conformational dynamics and enzyme activity, *Biochimie*, 80, 33, 1998.
5. Elber, R., and Karplus, M., Multiple conformational states of proteins: a molecular dynamics analysis of myoglobin, *Science*, 235, 318, 1987.
6. Go, N., Shape of the conformational energy surface near the global minimum and low-frequency vibrations in the native conformation of globular proteins, *Biopolymers*, 17, 1373, 1978.
7. Brooks, B., and Karplus, M., Harmonic dynamics of proteins: normal modes and fluctuations in bovine pancreatic trypsin inhibitor, *Proc. Natl Acad. Sci. USA*, 80, 6571, 1983.
8. Noguti, T., and Go, N., Collective variable description of small-amplitude conformational fluctuations in a globular protein, *Nature*, 296, 776, 1982.
9. Go, N., Noguti, T., and Nishikawa, T., Dynamics of a small globular protein in terms of low-frequency vibrational modes, *Proc. Natl Acad. Sci. USA*, 80, 3696, 1983.
10. Perahia, D., Levy, R., and Karplus, M., Motions of an alpha helical polypeptide: comparison of molecular and harmonic dynamics, *Biopolymers*, 29, 645, 1990.
11. Frauenfelder, H., Petsko, G., and Tsernoglou, D., Temperature dependent x-ray diffraction as a probe of protein structural dynamics, *Nature*, 280, 558, 1979.
12. Keller, H., and Debrunner, P.G., Evidence for conformational and diffusional mean square displacements in frozen aqueous solutions of oxymyoglobin, *Phys. Rev. Lett*., 54, 68, 1980.
13. Mayo, K.H., Kucheida, D., Parak, F., and Chien, J.C.W., Structural dynamics of human deoxyhemoglobin and hemochrome investigated by nuclear gamma resonance absorption (Mossbauer) spectroscopy, *Proc. Natl Acad. Sci. USA*, 80, 5294, 1983.
14. Smith, J.C., Protein dynamics: comparison of simulations with inelastic neutron scattering experiments, *Quart. Rev. Biophys*., 24, 227, 1991.
15. Marques, O., and Sanejouand, Y.H., The hinge-bending mode in citrate synthase arising from normal mode calculations, *Proteins: Struct. Funct. Genet*., 23, 557, 1995.
16. Mouawad, L., and Perahia, D., Motions in hemoglobin studied by normal mode analysis and energy minimization: evidence for the existence of tertiary T-like, quaternary R-like intermediate structures, *J. Mol. Biol*., 258, 393, 1996.
17. Thomas, A., Field, M.J., and Perahia, D., Analysis of the low frequency normal modes of the R-state of aspartate transcarbamylase and a comparison with the T-state modes, *J. Mol. Biol*., 261, 490, 1996.
18. Jaaskelainen, S., Verma, C.S., Hubbard, R.E., Linko, P., and Caves, L.S.D., Conformational change in the activation of lipase: an analysis in terms of low-frequency normal modes, *Protein Sci*., 7, 1359, 1998.
19. Tama, F., and Sanejouand, Y.-H., Conformational change of proteins arising from normal mode calculations, *Protein Eng*., 14, 1, 2001.
20. Levitt, M., Sander, C., and Stern, P.S., Protein normal-mode dynamics: trypsin inhibitor, crambin, ribonuclease and lysozyme, *J. Mol. Biol*., 181, 423, 1985.
21. Tama, F., Gadea, F.X., Marques, O., and Sanejouand, Y.H., Building blocks approach for determining low-frequency normal modes in macromolecules, *Proteins: Struct. Funct. Genet*., 41, 1, 2000.

22. Li, G., and Cui, Q., A coarse-grained normal mode approach for macromolecules: an efficient implementation and application to Ca(2+)-ATPase., *Biophys. J.*, 83, 2457, 2002.
23. Tirion, M., Large amplitude elastic motions in proteins from a single parameter, atomic analysis, *Phys. Rev. Lett.*, 77, 1905, 1996.
24. Bahar, I., Atilgan, A.R., and Erman, B., Direct evaluation of thermal fluctuations in proteins using a single-parameter harmonic potential, *Fold. Design*, 2, 173, 1997.
25. Atilgan, A.R., Durell, S.R., Jernigan, R.L., Demirel, M.C., Keskin, O., and Bahar, I., Anisotropy of fluctuation dynamics of proteins with an elastic network model, *Biophys. J.*, 80, 505, 2001.
26. Hinsen, K., Analysis of domain motions by approximate normal mode calculations, *Proteins: Struct. Funct. Genet.*, 33, 417, 1998.
27. Brooks, B., and Karplus, M., Normal modes for specific motions of macromolecules: application to the hinge-bending mode of lysozyme, *Proc. Natl Acad. Sci. USA*, 82, 4995, 1985.
28. Mouawad, L., and Perahia, D., Diagonalization in a mixed basis: a method to compute low-frequency normal modes for large macromolecules, *Biopolymers*, 33, 599, 1993.
29. Durand, P., Trinquier, G., and Sanejouand, Y.H., A new approach for determining low-frequency normal modes in macromolecules, *Biopolymers*, 34, 759, 1994.
30. Goldstein, H., *Classical Mechanics*, Addison-Wesley, Reading, MA, 1950.
31. Wilson, E.B., Decius, J.C., and Cross, P.C., *Molecular Vibrations*, McGraw-Hill, New York, 1955.
32. Brooks, B.R., Janezic, D., and Karplus, M., Harmonic analysis of large systems. I. Methodology, *J. Comp. Chem.*, 16, 1522, 1995.
33. Humar, J.L., *Dynamics of Structures*, Prentice Hall, New Jersey, 1990.
34. Davidson, E.R., The iterative calculation of a few of the lowest eigenvalues and corresponding eigenvectors of large real-symmetric matrices, *J. Comp. Chem.*, 17, 87, 1975.
35. Lanczos, C.J., An iteration method for the solution of the eigenvalue problem of linear differential and integral operators, *J. Res. Natl Bur. Stand.*, 45, 255, 1950.
36. Shavitt, I., Bender, C.F., Pipano, A., and Hosteny, R.P., The iterative calculation of several of the lowest or highest eigenvalues and corresponding eigenvectors of very large symmetric matrices, *J. Comp. Phys.*, 11, 90, 1973.
37. Arnoldi, W.E., The principle of minimized iterations in the solution of the matrix eigenvalue problem, *Quart. Appl. Math.*, IX, 17, 1951.
38. Marques, O., BLZPACK: description and user's guide, CERFACS Report TR/PA/95/30, Toulouse, France, 1995.
39. Lehoucq, R.B., Sorensen, D.C., and Yang, C., ARPACK user's guide: solution of *large scale eigenvalue problems with implicitly* restarted Arnoldi methods, 1997, http://www.caam.rice.edu/software/ARPACK.
40. Marques, O., and Sanejouand, Y.H., Protein motions through eigenanalyses: a set of study cases, CERFACS Report TR/PA/95/32, Toulouse, France, 1995.
41. Durand, P., and Malrieu, J.-P., *Ab-Initio Methods in Quantum Chemistry — I*, Lawley, K.P., ed., New York, John Wiley & Sons, 1987, p. 352.
42. Perahia, D., and Mouawad, L., Computation of low-frequency normal modes in macromolecules: improvements to the method of diagonalization in a mixed basis and application to hemoglobin, *Comput. Chem.*, 19, 241, 1995.

43. Brooks, B.R., Bruccoleri, R.E., Olafson, B.D., States, D.J., Swaminathan, S., and Karplus, M., CHARMM: a program for macromolecular energy, minimization, and dynamics calculations, *J. Comp. Chem.*, 4, 187, 1983.
44. Thomas, A., Field, M.J., Mouawad, L., and Perahia, D., Analysis of the low frequency normal modes of the T-state of aspartate transcarbamylase, *J. Mol. Biol.*, 257, 1070, 1996.
45. Thomas, A., Hinsen, K., Field, M.J., and Perahia, D., Tertiary and quaternary conformational changes in aspartate transcarbamylase: a normal mode study, *Proteins*, 34, 96, 1999.

3

The Gaussian Network Model: Theory and Applications

A.J. Rader, Chakra Chennubhotla, Lee-Wei Yang, and Ivet Bahar

CONTENTS

3.1 Introduction

A view that emerges from many studies is that proteins possess a tendency, encoded in their three-dimensional (3D) structures, to reconfigure into

functional forms, that is, each native structure tends to undergo conformational changes that facilitate its biological function. An efficient method for identifying such functional motions is normal mode analysis (NMA), a method that has found widespread use in physical sciences for characterizing molecular fluctuations near a given equilibrium state. The utility of NMA as a physically plausible and mathematically tractable tool for exploring protein dynamics has been recognized for the last 20 years [1, 2]. With recent increase in computational power and speed the application of NMA to proteins has gained renewed interest and popularity.

Contributing to this renewed interest in utilizing NMA has been the introduction of simpler models based on polymer network mechanics. The Gaussian network model (GNM) is probably the simplest among these. This is an elastic network (EN) model introduced at the residue level [3, 4], inspired by the full atomic NMA of Tirion with a uniform harmonic potential [5]. Despite its simplicity, the GNM and its extension, the anisotropic network model (ANM) [6], or similar coarse-grained EN models combined with NMA [7–9], have found widespread use since then for elucidating the dynamics of proteins and their complexes. Significantly, these simplified NMAs with EN models have recently been applied to deduce both the machinery and conformational dynamics of large structures and assemblies including HIV reverse transcriptase [10, 11], hemagglutinin A [12], aspartate transcarbamylase [13], F1 ATPase [14], RNA polymerase [15], an actin segment [16], GroEL-GroES [17], the ribosome [18, 19], and viral capsids [20–22].

Studying proteins with the GNM provides more than the dynamics of individual biomolecules, such as identifying the common traits among the equilibrium dynamics of proteins [23], the influence of native state topology on stability [24], the localization properties of protein fluctuations [25], or the definition of protein domains [26, 27]. Additionally, GNM has been used to identify residues most protected during hydrogen–deuterium exchange [28, 29], critical for folding [30–34], conserved among members of a given family [35], or involved in ligand binding [36].

The theoretical foundations of the GNM will be presented in this chapter, along with a few applications that illustrate its utility. The following questions will be addressed. What is the GNM? What are the underlying assumptions? How is it implemented? Why and how does it work? How does the GNM analysis differ from NMA applied to EN models? What are its advantages and limitations compared to coarse-grained NMA? What are the most significant applications and prospective utilities of the GNM, or the EN models in general?

To this end, the chapter begins with a brief overview of conformational dynamics and the relevance of such mechanical motions to biological function. Section 3.2.1 is devoted to explaining the theory and assumptions of the GNM as a simple, purely topological model for protein dynamics. The casual reader may elect to skip over Sections 3.2.2 to 3.2.4 where the derivation of the GNM is presented using fundamental principles from statistical mechanics. In Section 3.3, attention is given to how the GNM is implemented

(Section 3.3.1), and to what extent it can be or cannot be applied to proteins in general. An interpretation of the physical meaning of both fast and slow modes is presented (Section 3.3.2) with examples for a small enzyme, ribonuclease T1. Section 3.3.3 describes how the GNM differs from the ANM (i.e., from the NMA of simplified EN models) and discusses when the use of one model is preferable to the other. Finally, results are presented in Sections 3.3.4 and 3.3.5 for two widely different applications: specific motions of supramolecular structures and classification of motions in general through the iGNM online database of GNM motions. The chapter concludes with a discussion of potential future uses.

3.1.1 Conformational Dynamics: A Bridge Between Structure and Function

With recent advances in sequencing genomes, it has become clear that the canonical sequence-to-function paradigm is far from being sufficient. Structure has emerged as an important source of additional information required for understanding the molecular basis of observed biological activities. Yet, advances in structural genomics have now demonstrated that structural knowledge is not sufficient for understanding the molecular mechanisms of biological function either. The connection between structure and function presumably lies in *dynamics*, suggesting an encoding paradigm of sequence to structure to dynamics to function.

Not surprisingly, a major endeavor in recent years has been to develop models and methods for simulating the dynamics of proteins, and relating the observed behavior to experimental data. These efforts have been largely impeded, however, by the memory and time cost of molecular dynamics (MD) simulations. These limitations are particularly prohibitive when simulating the dynamics of large structures or supramolecular assemblies.

3.1.2 Functional Motions of Proteins Are Cooperative Fluctuations Near the Native State

While accurate sampling of conformational space is a challenge for macromolecular systems, the study of protein dynamics benefits from a great simplification: proteins have uniquely defined native structures under physiological conditions, and they are functional only when folded into their native conformation. Therefore, while the motions of macromolecules in solution are quite complex and involve transitions between an astronomical number of conformations, those of proteins near native state conditions are much simpler, as they are confined to a subset of conformations, or microstates, near the folded state. These microstates usually share the same overall fold, secondary structural elements, and even tertiary contacts within individual domains. Typical examples are the open and closed forms of enzymes, usually adopted in the unliganded and liganded states, respectively. Exploring the *fluctuation*

dynamics of proteins near native state conditions is a first step toward gaining insights about the molecular basis and mechanisms of their function; and fluctuation dynamics can be treated to a good approximation by linear models — such as NMA.

Another distinguishable property of protein dynamics — in addition to confinement to a small subspace of conformations — is the *collective* nature of residue fluctuations. The fluctuations are indeed far from random, involving the correlated motions of large groups of atoms, residues, or even entire domains or molecules whose concerted movements underlie biological function. An analytical approach that takes account of the collective coupling between all residues is needed, and again NMA emerges as a reasonable first approximation.

3.2 The Gaussian Network Model

3.2.1 A Minimalist Model for Fluctuation Dynamics

Most analytical treatments of complex systems dynamics entail a compromise between physical realism and mathematical tractability. A challenge is to identify the simplest, yet physically plausible, model that retains the physical and chemical characteristics, which are needed for the time and length scales of interest. Clearly, as the size and length scales of the processes of interest increase, it becomes unnecessary to account for many of the microscopic details in the model. The inclusion of these microscopic details could, on the contrary, tend to obscure the dominant patterns characterizing the biological function of interest.

The GNM was proposed by Bahar et al. [3] within such a minimalist mindset to explore the role and contribution of *purely topological constraints*, defined by the 3D structure, on the collective dynamics of proteins. Inspired by the seminal work of Flory and collaborators applied to polymer gels [37], each protein is modeled by an EN (Figure 3.1), the dynamics of which is entirely defined by network topology. The position of the nodes of the EN are defined by the C^{α}-atom coordinates, and the springs connecting the nodes are representative of the bonded and nonbonded interactions between the pairs of residues located within an interaction range, or cutoff distance, of r_c. The cutoff distance is usually taken as 7.0 Å, based on the radius of the first coordination shell around residues observed in PDB structures [38, 39].

3.2.2 GNM Assumes Fluctuations Are Isotropic and Gaussian

If we define equilibrium position vectors of a node, i, by $\mathbf{R}_i^0$, and the instantaneous position by $\mathbf{R}_i$, the fluctuations, or deformations, from this mean position can then be defined by the vector $\Delta\mathbf{R}_i = \mathbf{R}_i - \mathbf{R}_i^0$. The fluctuations

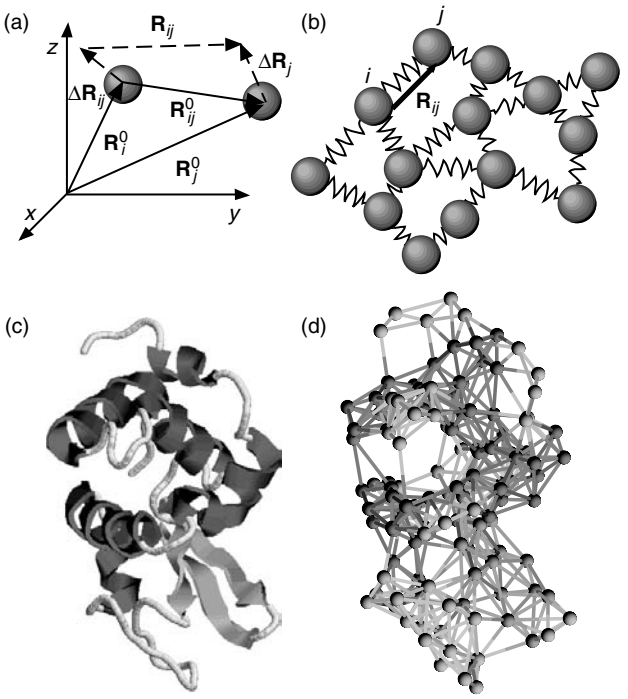

FIGURE 3.1
(See color insert following page 136) Description of the GNM. (a) Schematic representation of the equilibrium positions of the ith and jth nodes, $\mathbf{R}^0_i$ and $\mathbf{R}^0_j$, with respect to a laboratory-fixed coordinate system (xyz). The instantaneous fluctuation vectors, $\Delta\mathbf{R}_i$ and $\Delta\mathbf{R}_j$, are shown by the dashed arrows, along with the instantaneous separation vector $\mathbf{R}_{ij}$ between the positions of the two residues. $\mathbf{R}^0_{ij}$ is the equilibrium distance between nodes i and j. (b) In the EN of GNM every residue is represented by a node and connected to spatial neighbors by uniform springs. These springs determine the $N-1$ degrees of freedom in the network and the structure's modes of vibration. (c) Three dimensional image of hen egg white lysozyme (PDB file 1hel [46]) showing the C^α trace. Secondary structure features are indicated by pink for helices and yellow for β-strands. (d) Using a cutoff value of 10 Å, all connections between C^α nodes are drawn for the same lysozyme structure to indicate the nature of the EN analyzed by GNM.

in the distance vector $\mathbf{R}_{ij}$ between residues i and j, can in turn be expressed as $\Delta\mathbf{R}_{ij} = \mathbf{R}_{ij} - \mathbf{R}^0_{ij} = \Delta\mathbf{R}_j - \Delta\mathbf{R}_i$ (Figure 3.1[a]). By assuming that these fluctuations are *isotropic* and *Gaussian* we can write the potential of the network of N nodes (residues), V_{GNM}, in terms of the components ΔX_i, ΔY_i, and ΔZ_i of $\Delta\mathbf{R}_i$, as

$$V_{\mathrm{GNM}} = \frac{\gamma}{2}\left[\sum_{i,j}^{N}\Gamma_{ij}[(\Delta X_i - \Delta X_j)^2 + (\Delta Y_i - \Delta Y_j)^2 + (\Delta Z_i - \Delta Z_j)^2]\right] \tag{3.1}$$

where Γ_{ij} is the ijth element of the Kirchhoff (or connectivity) matrix of inter-residue contacts defined by

$$\Gamma_{ij} = \begin{cases} -1, & \text{if } i \neq j \text{ and } \mathrm{R}_{ij} \leq r_\mathrm{c} \\ 0, & \text{if } i \neq j \text{ and } \mathrm{R}_{ij} > r_\mathrm{c} \\ -\sum_{j,j\neq i} \Gamma_{ij}, & \text{if } i = j \end{cases} \tag{3.2}$$

and γ is the force constant taken to be uniform for all network springs. Expressing the X-, Y-, and Z-components of the fluctuation vectors $\Delta\mathbf{R}_i$ as three N-dimensional vectors $\Delta\mathbf{X}$, $\Delta\mathbf{Y}$, and $\Delta\mathbf{Z}$, Equation (3.1) simplifies to

$$V_\mathrm{GNM} = \frac{\gamma}{2}[\Delta\mathbf{X}^\mathrm{T}\mathbf{\Gamma}\Delta\mathbf{X} + \Delta\mathbf{Y}^\mathrm{T}\mathbf{\Gamma}\Delta\mathbf{Y} + \Delta\mathbf{Z}^\mathrm{T}\mathbf{\Gamma}\Delta\mathbf{Z}] \tag{3.3}$$

where $\Delta\mathbf{X}^\mathrm{T}$, $\Delta\mathbf{Y}^\mathrm{T}$, and $\Delta\mathbf{Z}^\mathrm{T}$ are the row vectors $[\Delta X_1, \Delta X_2, \ldots, \Delta X_N]$, $[\Delta Y_1, \Delta Y_2, \ldots, \Delta Y_N]$, and $[\Delta Z_1, \Delta Z_2, \ldots, \Delta Z_N]$, respectively. The total potential can alternatively be expressed as

$$V_\mathrm{GNM} = \frac{\gamma}{2}[\Delta\mathbf{R}^\mathrm{T}(\mathbf{\Gamma} \otimes \mathbf{E})\Delta\mathbf{R}] \tag{3.4}$$

where $\Delta\mathbf{R}$ is the $3N$-dimensional vector of fluctuations, $\Delta\mathbf{R}^\mathrm{T}$ is its transpose, $\Delta\mathbf{R}^\mathrm{T} = [\Delta X_1, \Delta Y_1, \ldots, \Delta Z_N]$, $\mathbf{E}$ is the identity matrix of order 3, and $(\mathbf{\Gamma} \otimes \mathbf{E})$ is the direct product of $\mathbf{\Gamma}$ and $\mathbf{E}$, found by replacing each element Γ_{ij} of $\mathbf{\Gamma}$ by the 3×3 diagonal matrix $\Gamma_{ij}\mathbf{E}$. One should note that by construction the eigenvalues for this $3N \times 3N$ matrix, $\Gamma \otimes \mathbf{E}$, are threefold degenerate. This degeneracy arises from the isotropic assumption, further explored in the following section.

3.2.3 Statistical Mechanics Foundations of the GNM

What we are primarily interested in is determining the mean-square (ms) fluctuations of a particular residue, i, or the correlations between the fluctuations of two different residues, i and j. These respective properties are given by

$$\langle \Delta\mathbf{R}_i \cdot \Delta\mathbf{R}_i \rangle = \langle \Delta X_i^2 \rangle + \langle \Delta Y_i^2 \rangle + \langle \Delta Z_i^2 \rangle \tag{3.5}$$

and

$$\langle \Delta\mathbf{R}_i \cdot \Delta\mathbf{R}_j \rangle = \langle \Delta X_i \Delta X_j \rangle + \langle \Delta Y_i \Delta Y_j \rangle + \langle \Delta Z_i \Delta Z_j \rangle \tag{3.6}$$

Thus, if we know how to compute the component fluctuations $\langle \Delta X_i^2 \rangle$ and $\langle \Delta X_i \Delta X_j \rangle$ then we know how to compute the residue fluctuations and their cross-correlations.

In the GNM, the probability distribution of all fluctuations, $P(\mathbf{\Delta R})$ is *isotropic* (Equation [3.7]) and *Gaussian* (Equation [3.8]), that is,

$$P(\mathbf{\Delta R}) = P(\mathbf{\Delta X}, \mathbf{\Delta Y}, \mathbf{\Delta Z}) = p(\mathbf{\Delta X})p(\mathbf{\Delta Y})p(\mathbf{\Delta Z}) \tag{3.7}$$

and

$$\begin{aligned} p(\mathbf{\Delta X}) &\propto \exp\left\{-\frac{\gamma}{2k_{\mathrm{B}}T}\mathbf{\Delta X}^{\mathrm{T}}\mathbf{\Gamma}\mathbf{\Delta X}\right\} \\ &\propto \exp\left\{-\frac{1}{2}\left(\mathbf{\Delta X}^{\mathrm{T}}\left(\frac{k_{\mathrm{B}}T}{\gamma}\mathbf{\Gamma}^{-1}\right)^{-1}\mathbf{\Delta X}\right)\right\} \end{aligned} \tag{3.8}$$

where k_{B} is the Boltzmann constant and T is the absolute temperature. Similar forms apply to $p(\Delta\mathbf{Y})$ and $p(\Delta\mathbf{Z})$. $\Delta\mathbf{X} = [\Delta X_1, \Delta X_2, \ldots, \Delta X_i, \ldots, \Delta X_N]$ is therefore a multidimensional Gaussian random variable with zero mean and covariance $(k_{\mathrm{B}}T/\gamma)\mathbf{\Gamma}^{-1}$ in accord with the general definition [40]

$$W(\mathbf{x}, \boldsymbol{\mu}, \mathbf{\Xi}) = \frac{1}{(2\pi)^{N/2}|\mathbf{\Xi}|^{1/2}}\exp\left\{-\frac{1}{2}(\mathbf{x}-\boldsymbol{\mu})^{\mathrm{T}}\mathbf{\Xi}^{-1}(\mathbf{x}-\boldsymbol{\mu})\right\} \tag{3.9}$$

for multidimensional Gaussian (normal) probability density function associated with a given N-dimensional vector $\mathbf{x}$ having mean vector $\boldsymbol{\mu}$ and covariance matrix $\mathbf{\Xi}$. Here, the term in the denominator, $(2\pi)^{N/2}|\mathbf{\Xi}|^{1/2}$, is the partition function that ensures the normalization of $W(\mathbf{x}, \boldsymbol{\mu}, \mathbf{\Xi})$ upon integration over the complete space of accessible $\mathbf{x}$, and $|\mathbf{\Xi}|$ is the determinant of $\mathbf{\Xi}$. Similarly, the *normalized* probability distribution $p(\Delta\mathbf{X})$ is

$$p(\mathbf{\Delta X}) = \frac{1}{Z_{\mathbf{X}}}\exp\left\{-\frac{1}{2}\left(\mathbf{\Delta X}^{\mathrm{T}}\left(\frac{k_{\mathrm{B}}T}{\gamma}\mathbf{\Gamma}^{-1}\right)^{-1}\mathbf{\Delta X}\right)\right\} \tag{3.10}$$

where $Z_{\mathbf{X}}$ is the partition function given by

$$Z_{\mathbf{X}} = \int \exp\left\{-\frac{1}{2}\left(\mathbf{\Delta X}^{\mathrm{T}}\left(\frac{k_{\mathrm{B}}T}{\gamma}\mathbf{\Gamma}^{-1}\right)^{-1}\mathbf{\Delta X}\right)\right\}\mathrm{d}\mathbf{\Delta X} = (2\pi)^{N/2}\left|\frac{k_{\mathrm{B}}T}{\gamma}\mathbf{\Gamma}^{-1}\right|^{1/2} \tag{3.11}$$

In the GNM, the determinant of the Kirchhoff matrix is zero, and the inverse, $\mathbf{\Gamma}^{-1}$, which scales with the covariance, cannot therefore be directly computed. $\mathbf{\Gamma}^{-1}$ is found instead by eigenvalue decomposition of $\mathbf{\Gamma}$ and reconstruction of the inverse using the $N-1$ nonzero eigenvalues and associated eigenvectors. The same expression in Equation (3.11) is valid for $Z_{\mathbf{Y}}$ and$Z_{\mathbf{Z}}$ such

that the overall GNM partition function (or configurational integral) becomes

$$Z_{\mathrm{GNM}} = Z_X Z_Y Z_Z = (2\pi)^{3N/2} \left| \frac{k_{\mathrm{B}}T}{\gamma} \mathbf{\Gamma}^{-1} \right|^{3/2} \tag{3.12}$$

Now we have the statistical mechanical foundations to write the expectation values of the residue fluctuations, $\langle \Delta X_i^2 \rangle$ and correlations, $\langle \Delta X_i \Delta X_j \rangle$. It can be verified that the $N \times N$ covariance matrix $\langle \Delta \mathbf{X} \Delta \mathbf{X}^{\mathrm{T}} \rangle$ is equal to $(k_{\mathrm{B}}T/\gamma)\mathbf{\Gamma}^{-1}$, using the statistical mechanical average[1]

$$\langle \Delta \mathbf{X} \Delta \mathbf{X}^{\mathrm{T}} \rangle = \int \Delta \mathbf{X} \Delta \mathbf{X}^{\mathrm{T}} p(\Delta \mathbf{X}) \mathrm{d}\Delta \mathbf{X} = \frac{k_{\mathrm{B}}T}{\gamma} \mathbf{\Gamma}^{-1} \tag{3.13}$$

Because

$$\langle \Delta \mathbf{X} \Delta \mathbf{X}^{\mathrm{T}} \rangle = \langle \Delta \mathbf{Y} \Delta \mathbf{Y}^{\mathrm{T}} \rangle = \langle \Delta \mathbf{Z} \Delta \mathbf{Z}^{\mathrm{T}} \rangle = \tfrac{1}{3} \langle \Delta \mathbf{R} \Delta \mathbf{R}^{\mathrm{T}} \rangle \tag{3.14}$$

we obtain

$$\begin{aligned} \langle \Delta \mathbf{R}_i^2 \rangle &= \frac{3k_{\mathrm{B}}T}{\gamma} (\mathbf{\Gamma}^{-1})_{ii} \\ \langle \Delta \mathbf{R}_i \cdot \Delta \mathbf{R}_j \rangle &= \frac{3k_{\mathrm{B}}T}{\gamma} (\mathbf{\Gamma}^{-1})_{ij} \end{aligned} \tag{3.15}$$

as the ms fluctuations of residues and correlations between residue fluctuations. It should be noted that the assumption of *isotropic fluctuations* (Equation [3.8]) is intrinsic to the GNM. Thus the $3N$-dimensional problem (Equation [3.4]) can be reduced to an N-dimensional one described by Equation (3.15).

3.2.4 Influence of Local Packing Density

The diagonal elements of the Kirchhoff matrix, $\mathbf{\Gamma}_{ii}$, are equal to the residue coordination numbers, z_i $(1 \leq i \leq N)$, which represent the degree of the EN nodes in graph theory. Thus z_i is a direct measure of *local packing density* around the ith residue. To better understand this, it is possible to express $\mathbf{\Gamma}$ as a sum of two matrices $\mathbf{\Gamma}_1$ and $\mathbf{\Gamma}_2$, consisting exclusively of the diagonal and off-diagonal elements of $\mathbf{\Gamma}$, respectively. Using these two matrices, $\mathbf{\Gamma}^{-1}$ may

[1]Note that solving Equation (3.13) involves the ratio of the multidimensional Gaussian counterparts for the two integrals $\int \exp\{-ax^2\}\mathrm{d}x = \frac{1}{2}\sqrt{(\pi/a)}$ and $\int x^2 \exp\{-ax^2\}\mathrm{d}x = (\sqrt{\pi}/4)a^{3/2}$ in the range $(0, \infty)$ such that $\langle x^2 \rangle = (\sqrt{\pi}/4)a^{-3/2}/\frac{1}{2}\sqrt{(\pi/a)} = 1/2a$. For the simplest case of a single spring, subject to harmonic potential $\frac{1}{2}\gamma x^2$, $a = \gamma/2k_{\mathrm{B}}T$, and $\langle x^2 \rangle = k_{\mathrm{B}}T/\gamma$.

be written as

$$\begin{aligned}\boldsymbol{\Gamma}^{-1} &= [\boldsymbol{\Gamma}_1 + \boldsymbol{\Gamma}_2]^{-1} = [\boldsymbol{\Gamma}_1(\mathbf{E} + \boldsymbol{\Gamma}_1^{-1}\boldsymbol{\Gamma}_2)]^{-1} = (\mathbf{E} + \boldsymbol{\Gamma}_1^{-1}\boldsymbol{\Gamma}_2)^{-1}\boldsymbol{\Gamma}_1^{-1} \\ &= (\mathbf{E} - \boldsymbol{\Gamma}_1^{-1}\boldsymbol{\Gamma}_2 + \cdots)\boldsymbol{\Gamma}_1^{-1} = \boldsymbol{\Gamma}_1^{-1} - \boldsymbol{\Gamma}_1^{-1}\boldsymbol{\Gamma}_2\boldsymbol{\Gamma}_1^{-1} + \cdots \end{aligned} \tag{3.16}$$

if one assumes that the invariants of the product $(\boldsymbol{\Gamma}_1^{-1}\boldsymbol{\Gamma}_2)$ are small compared to those of the identity matrix, $\mathbf{E}$, which is a valid approximation for protein Kirchhoff matrices. Thus, the information concerning local packing density and distribution of contacts is dominated by the diagonal matrix, $\boldsymbol{\Gamma}_1^{-1}$, which is the leading term in a series expansion for $\boldsymbol{\Gamma}^{-1}$ in Equation (3.16). Consequently, application of Equation (3.15) indicates that $\langle(\Delta\mathbf{R}_i)^2\rangle$ scales with $[\boldsymbol{\Gamma}_1^{-1}]_{ii} = 1/z_i$, to a first approximation. Thus the *local packing density* as described by the coordination numbers is an important structural property contributing to the ms fluctuations of residues [41]. However, these coordination numbers represent only the leading order and not the entire set of dynamics described by Equation (3.15).

3.3 Method and Applications

3.3.1 Equilibrium Fluctuations

The ms fluctuations of residues are experimentally measurable (e.g., x-ray crystallographic *B*-factors, or root mean-square [rms] differences between different models from NMR), and as such, have often been used as an initial test for verifying and improving computational models and methods. Beginning with the original GNM paper [3], several applications have demonstrated that the fluctuations predicted by the GNM are in good agreement with experimental *B*-factors [6, 23, 39, 42–44]. The *B*-factors are related to the expected residue fluctuations and calculated according to

$$B_i = \frac{8\pi^2}{3}\langle(\Delta\mathbf{R}_i)^2\rangle = \frac{8\pi^2 k_B T}{\gamma}[\boldsymbol{\Gamma}^{-1}]_{ii} \tag{3.17}$$

Figure 3.2(a) illustrates the agreement between the *B*-factors predicted by the GNM (solid curve) and those calculated from experimental data (open circles) for an example protein, ribonuclease T1 (RNase T1), where $\boldsymbol{\Gamma}$ has been constructed from the C^α coordinates for RNase T1 deposited in the Protein Data Base (PDB) [45]. Panel B compares the rms fluctuations predicted by the GNM and those observed across the 20 NMR models deposited in the PDB for reduced disulphide-bond formation facilitator (DsbA) [46]. The correlation coefficient between GNM results and experimental data for these two example proteins are 0.769 and 0.823 in the respective panels A and B. An extensive comparison of experimental and theoretical GNM *B*-factors for a series of PDB

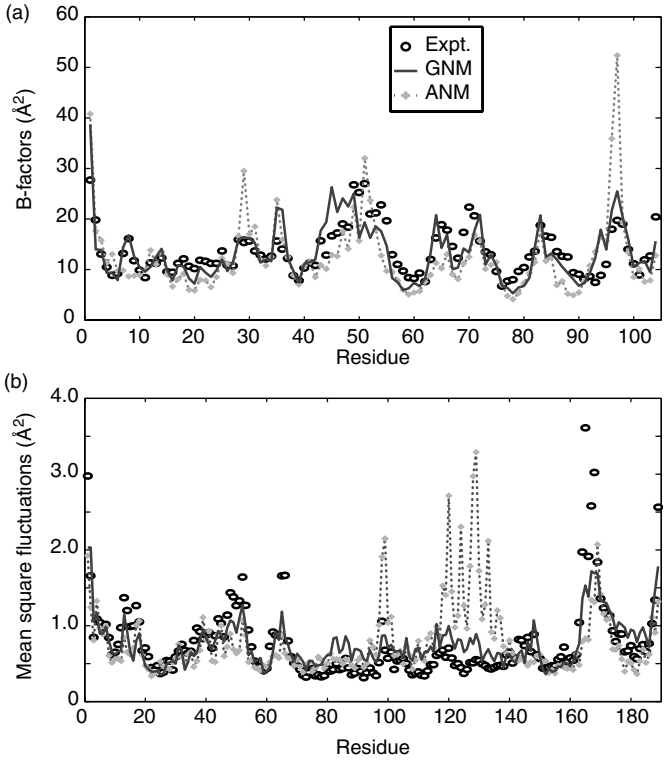

FIGURE 3.2
Comparison of ms fluctuations predicted by GNM and ANM with experimental observations. (a) Experimental x-ray crystallographic *B*-factors (open circles) reported for ribonuclease T1 (PDB file 1bu4 [53]) plotted with calculated values from GNM (solid line) and ANM (dotted line) against residue number. (b) Root mean square deviation between C^{α} coordinates of NMR model structures (open circles) deposited for the reduced disulphide-bond formation facilitator (DsbA) in the PDB file 1a24 [46].

structures by Phillips and coworkers has shown that GNM calculations yield an average correlation coefficient of about 0.65 with experimental *B*-factors provided that the contacts between neighboring molecules in the crystal form are taken into account. The agreement with NMR data is also remarkable, pointing to the consistency between the fluctuations undergone in solution and those inferred from x-ray structures.

3.3.2 GNM Mode Decomposition: Physical Meaning of Slow and Fast Modes

A major utility of the GNM is the ease of obtaining the collective modes of motion accessible to structures in native state conditions. The GNM normal modes are found by transforming the Kirchhoff matrix into a product of

three matrices, the matrix $\mathbf{U}$ of the eigenvectors $\mathbf{u}_i$ of $\mathbf{\Gamma}$, the diagonal matrix $\mathbf{\Lambda}$ of eigenvalues λ_i, and the transpose $\mathbf{U}^{\mathrm{T}} = \mathbf{U}^{-1}$ of the unitary matrix $\mathbf{U}$ as in Equation (3.18).

$$\mathbf{\Gamma} = \mathbf{U}\mathbf{\Lambda}\mathbf{U}^{\mathrm{T}} \tag{3.18}$$

The eigenvalues are representative of the *frequencies* of the individual modes, while the eigenvectors define the *shapes* of the modes. The first eigenvalue, λ_1, is identically zero with the corresponding eigenvector comprised of elements all equal to a constant, $1/\sqrt{N}$, indicative of an absence of internal motions in this *zero* mode. The vanishing frequency reflects the fact that the molecule can be translated rigidly without any potential energy change.

Combining Equations (3.15) and (3.18), the cross-correlations between residue fluctuations can be written as a sum over the $N-1$ nonzero modes ($2 \leq k \leq N$) using

$$\begin{aligned}\langle \Delta\mathbf{R}_i \cdot \Delta\mathbf{R}_j \rangle &= \frac{3k_{\mathrm{B}}T}{\gamma}[\mathbf{\Gamma}^{-1}]_{ij} = \frac{3k_{\mathrm{B}}T}{\gamma}[\mathbf{U}\mathbf{\Lambda}^{-1}\mathbf{U}^{\mathrm{T}}]_{ij} \\ &= \frac{3k_{\mathrm{B}}T}{\gamma}\sum_k [\lambda_k^{-1}\mathbf{u}_k\mathbf{u}_k^{\mathrm{T}}]_{ij}\end{aligned} \tag{3.19}$$

This permits us to identify the correlation, $[\Delta\mathbf{R} \cdot \Delta\mathbf{R}]_k$ contributed by the kth mode as

$$[\Delta\mathbf{R}_i \cdot \Delta\mathbf{R}_j]_k = \frac{3k_{\mathrm{B}}T}{\gamma}\lambda_k^{-1}[\mathbf{u}_k]_i[\mathbf{u}_k]_j \tag{3.20}$$

where $[\mathbf{u}_k]_i$ is the ith element of $\mathbf{u}_k$. Because $\mathbf{u}_k$ is normalized, the plot of $[\mathbf{u}_k]_i^2$ against the residue index, i, yields the normalized distribution of ms fluctuations of residues in the kth mode, shortly referred to as the kth *mode shape* (Figure 3.3[a]). Because the residue fluctuations are related to the experimental temperature (*B*-factors) by Equation (3.17), these elements of $\mathbf{u}_k$ reflect the residue mobilities in the kth mode.

Note that the factor λ_k^{-1} plays the role of a statistical weight, which suitably rescales the contribution of mode k. This ensures that the slowest mode has the largest contribution. In addition to their significant contribution, the slowest motions are in general also those having the highest *degree of collectivity*. Many studies have shown that the shapes of the slowest modes indeed reveal the mechanisms of *cooperative* or *global* motions, and the most constrained residues (minima) in these modes play a critical role, such as a hinge-bending center, that govern the correlated movements of entire domains [10–13, 17, 19, 44, 47–52]. It is important to note that although these motions are slow, they involve substantial conformational changes distributed over several residues. The fastest modes, on the other hand, involve the most tightly packed and hence most severely constrained residues in the molecule. Their high frequency does not imply a definitive conformational change, because they cannot effectively relax within their severely

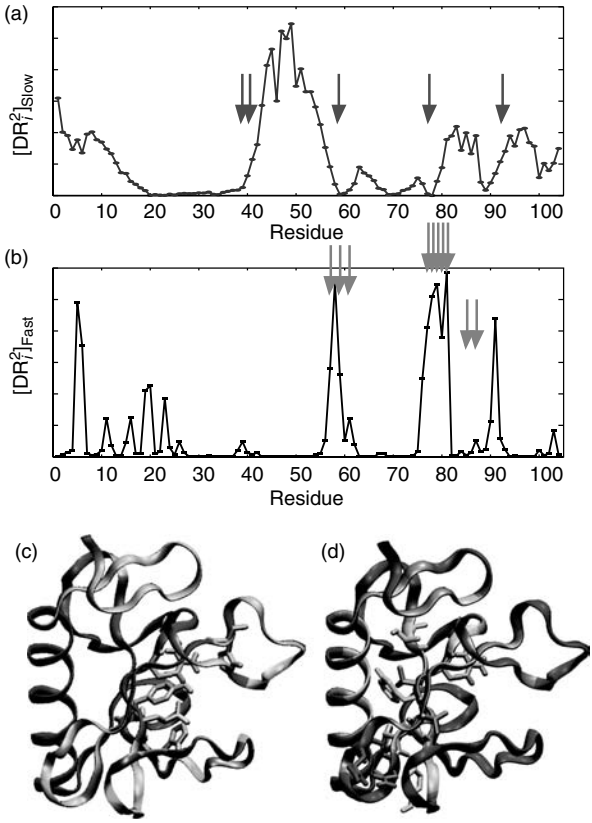

FIGURE 3.3
(See color insert following page 136) Physical meaning of slow and fast modes in GNM. (a) Distribution of squared displacements of residues in the slowest mode as a function of residue index for ribonuclease T1 (RNase T1). The red arrows identify local minima that correspond to five experimentally identified catalytic residues: Tyr38, His40, Glu58, Arg77, and His92. (b) Distribution of squared displacements averaged over the ten fastest modes for the same protein. Here the arrows indicate the residues shown by hydrogen/deuterium exchange to be the most protected and thus important for reliable folding. A majority of these critical folding residues appear as peaks in the fast modes. (c) Color-coded mapping of the slowest mode (a) onto the 3D C^{α} trace of RNase T1 (PDB file: 1bu4 [53]) where red is most mobile and blue least mobile. The side chains of the five catalytic residues are shown in pink surrounding the nucleotide binding cavity. (d) A similar color-coded mapping of the fluctuations of the ten fastest modes (b) onto the C^{α} trace. Here the side chains of the ten most protected residues from hydrogen deuterium exchange experiments are drawn explicitly showing that most of them are calculated to be mobile (red). The images in c and d were generated using VMD [74].

constrained environment. On the contrary, they enjoy extremely small conformational freedom, on a *local* scale, by undergoing fast, but small amplitude fluctuations.

Figure 3.3 illustrates the contrast between the degree of collectivity for the slowest and fastest modes for an example protein, RNase T1. As in this case, the slow modes involve almost the entire molecule as indicated by the

broad, delocalized peaks in panel A. The relative potential motion predicted by this mode is plotted onto the 3D structure in Figure 3.3(c), color-coded such that minima are blue and maxima are red. For RNaseT1, five red arrows are drawn in Figure 3.3(a) to indicate the residues identified as part of the catalytic site (Y38, H40, E58, R77, and H92) [53]. With the exception of H92, these five residues are located near minima in the slow (global) mode shape (Figure 3.3[a]) and their side chains are shown to be spatial neighbors (pink tubes) in the 3D plot of this protein (Figure 3.3[c]).

In contrast, the fastest modes are highly localized, with mode shapes that usually involve only a few peaks, as in Figure 3.3(b). These peaks refer to the residues that have a high concentration of local energy and are tightly constrained in motion. It has been noticed that these residues are often conserved across species and may form the folding nuclei [33, 34, 54]. In the application to RNase T1, the ten most protected residues (57,59,61,77–81,85, and 87), as identified by hydrogen–deuterium exchange experiments [55], are indicated by gold arrows in Figure 3.3(b) and shown with their side chains in the 3D structure, color-coded such that minima are blue and maxima are red (Figure 3.3[d]). As illustrated, many of these residues involve interactions between different strands of the central β-sheet, suggesting their potential involvement in the folding of RNase T1.

3.3.3 What Is ANM? How Does GNM Differ from ANM?

As pointed out in Chapter 1 by Hinsen, ANM analysis is simply an NMA applied to an EN model, the potential of which is defined as [6]

$$V_{\mathrm{ANM}} = \frac{\gamma}{2}\left[\sum_{i,j}^{N} (R_{ij} - R_{ij}^0)^2 H(r_c - R_{ij})\right] \tag{3.21}$$

where $H(r_c - R_{ij})$ is the heavyside step function equal to 1 if the argument is positive, and zero otherwise. $H(r_c - R_{ij})$ selects all residue pairs within the cutoff separation of r_c. In the GNM, on the other hand, the potential is given by

$$V_{\mathrm{GNM}} = \frac{\gamma}{2}\left[\sum_{i,j}^{N} (\mathbf{R}_{ij} - \mathbf{R}_{ij}^0)^2 H(r_c - R_{ij})\right] \tag{3.22}$$

Equation (3.22) looks very similar to Equation (3.21), with the major difference that the vectors $\mathbf{R}_{ij}$ and $\mathbf{R}_{ij}^0$ in Equation (3.22) replace distances (scalars), R_{ij} and R_{ij}^0. This means that the potential, which depended upon the dot product between the fluctuation vectors in the GNM

$$\begin{aligned}(\mathbf{R}_{ij} - \mathbf{R}_{ij}^0) \cdot (\mathbf{R}_{ij} - \mathbf{R}_{ij}^0) &= R_{ij}^2 + (R_{ij}^0)^2 - 2R_{ij}R_{ij}^0 \cos(\mathbf{R}_{ij}, \mathbf{R}_{ij}^0) \\ &= R_{ij}^2 + (R_{ij}^0)^2 - 2(X_{ij}X_{ij}^0 + Y_{ij}Y_{ij}^0 + Z_{ij}Z_{ij}^0)\end{aligned} \tag{3.23}$$

now (in the ANM) depends upon their scalar product

$$\begin{aligned}(R_{ij} - R_{ij}^0)(R_{ij} - R_{ij}^0) &= R_{ij}^2 + (R_{ij}^0)^2 - 2R_{ij}R_{ij}^0 \\ &= R_{ij}^2 + (R_{ij}^0)^2 - 2[X_{ij}^2 + Y_{ij}^2 + Z_{ij}^2]^{1/2} \\ &\quad \times [(X_{ij}^0)^2 + (Y_{ij}^0)^2 + (Z_{ij}^0)^2]^{1/2} \end{aligned} \tag{3.24}$$

Because the scalars R_{ij} and R_{ij}^0 depend upon their components in a nonquadratic form, it is natural to end up with anisotropic fluctuations upon taking the second derivatives of the potential with respect to the displacements along the X-, Y-, and Z-axes as is done in NMA. Using Equations (3.23) and (3.24), the difference between these two potentials is

$$V_{\mathrm{GNM}} - V_{\mathrm{ANM}} = \gamma \left[\sum_{i,j}^{N} R_{ij}R_{ij}^0(1 - \cos(\mathbf{R}_{ij}, \mathbf{R}_{ij}^0))H(r_c - R_{ij}) \right] \tag{3.25}$$

that is, the two potentials are equal only if $\cos(\mathbf{R}_{ij}, \mathbf{R}_{ij}^0) = 1$, that is, $\mathbf{R}_{ij} = \mathbf{R}_{ij}^0$ or $\Delta\mathbf{R}_i = \Delta\mathbf{R}_j$.

Physically, this means that in addition to changes in inter-residue distances (springs), any change in the *direction* of the inter-residue vector $\mathbf{R}_{ij}^0$ is also being resisted or penalized in the GNM potential. On the contrary, the ANM potential depends exclusively on the *magnitudes* of the inter-residue distances and does not penalize any such changes in orientation. It is conceivable that within the densely packed environment of proteins, orientational deformations may be as important as translational (distance) ones, and a potential that takes account of the energy dependence associated with the internal orientational changes (i.e., V_{GNM}) is physically more meaningful than one exclusively based on distances (V_{ANM}). Not surprisingly, ANM has been observed to give rise to excessively high fluctuations compared to the GNM results or experimental data (Figure 3.2), and hence necessitated the adoption of a higher cutoff distance for interactions [6]. With a higher cutoff distance, each residue is connected to more neighbors in a more constrained and consolidated network.

Inasmuch as V_{GNM} is physically more realistic, one might prefer to adopt the GNM, rather than the ANM for a coarse-grained NMA. However, this greater realism comes at a price. Because the GNM describes the dynamics within an N-dimensional configurational space as opposed to a $3N$-dimensional one of ANM, the residue fluctuations predicted by the GNM are intrinsically isotropic. Thus GNM cannot provide information regarding the individual components: $\Delta X^{(k)}$, $\Delta Y^{(k)}$, and $\Delta Z^{(k)}$, of the deformation vectors $\Delta\mathbf{R}^{(k)}$ associated with each mode, k, but rather predicts the magnitudes, $|\Delta\mathbf{R}^{(k)}|$, induced by such deformations. The conclusion is that GNM is more accurate, and should be chosen when evaluating the deformation magnitudes, or the distribution of motions of individual residues. However, ANM is the only

possible (less realistic) model when it comes to assessing the directions or mechanisms of motions. That the fluctuations predicted by the GNM correlate better with experimental *B*-factors than those predicted by the ANM has been observed and confirmed in a recent systematic study of Phillips and coworkers [23]. The dotted curves in Figure 3.2 illustrate the ANM results, and provide a comparison of the level of agreement (with experimental data) usually achieved by the two respective models. The correlation coefficients between the GNM results and experimental data are 0.769 and 0.823 in the panels A and B, respectively, whereas their ANM counterparts are 0.639 and 0.261. We note that the two sets of computed results are themselves correlated (0.756 and 0.454, respectively), which can be expected from the similarity of the underlying models.

3.3.4 Applicability to Supramolecular Structures

A major advantage of the GNM is its applicability to large complexes and assemblies. The size of the Kirchhoff matrix is $N \times N$ for a structure of N residues, as opposed to the size $3N \times 3N$ of the equivalent Hessian matrix for a residue-level EN NMA (or ANM). The resulting computational time requirement for GNM analysis is then about 3^3 times less than for ANM, which in turn is about 8^3 times less than for NMA at atomic scale (assuming eight atoms on the average per residue). This enormous decrease in computational time permits us to use ANM, and certainly GNM, for efficiently exploring the dynamics of supramolecular structures [17, 22].

Due to limitations in computational memory and speed, efforts to analyze large structures of $\sim 10^5$ residues rely upon further coarse-graining of the structure of interest. This is now the standard approach, having been implemented in several forms by various research groups including hierarchical coarse-graining (HCG) [56], discussed below; rotations–translations of blocks (RTB) [57] or block normal mode (BNM) [9]; and substructure-synthesis method (SSM) [58], which are discussed in other chapters of this book.

For both GNM and ANM, it has been demonstrated that an HCG scheme where clusters of residues and their interactions, as opposed to individual pairs of residues, are considered as the EN nodes successfully reproduce the essential features of the full-residue GNM/ANM calculations [56]. The global dynamics of hemagglutinin A were obtained at least two orders of magnitude faster than standard GNM/ANM by coarse-graining to the level of every 40th residue ($N/40$) [56]. Notably, the minima in global mode shapes, which identify key regions coordinating the collective dynamics, were *exactly* reproduced by the $N/40$ coarse-graining.

Figure 3.4 illustrates the application of GNM to the wild type 70S ribosome from *Escherichia coli* [59]. The calculations were performed by considering a single node for each amino acid (on the C^α atom) and each nucleotide (on the *P* atom), yielding a total of 10,453 nodes (residues and nucleotides). Because the diameter of the *A*-form RNA double helix is 20 Å, a larger cutoff distance is

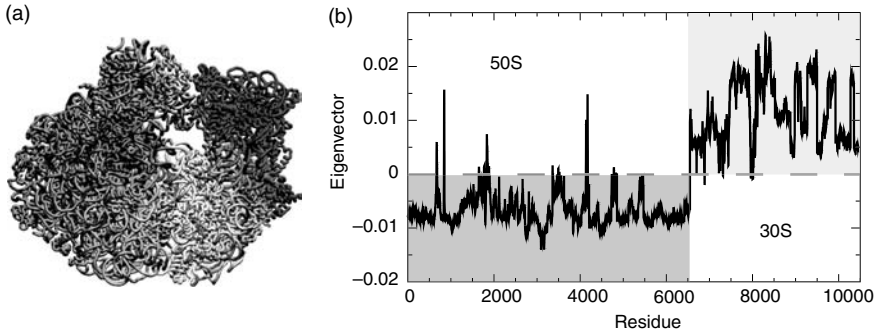

FIGURE 3.4
(See color insert following page 136) Application of GNM to the 70S ribosome structure. The calculations were performed on the wild type 70S ribosome from *E. coli* (PDB files 1pnx and 1pny [59]). (a) The slowest nonzero mode for the 70S ribosome colored from −1 (red) to +1 (blue) is mapped onto the 3D structure indicating a dramatic break at the interface between the two subunits (50S and 30S). This image was generated using VMD [74]. (b) The slowest nonzero mode plotted vs. the residue number. Residues in the 50S subunit (blue) exhibit one direction of motion that is opposed to the motion in the 30S subunit (red).

required to correctly identify base-paired nucleotides solely by their *P*-atom positions [42]. To ensure adequate connectivity, two cutoff distances were adopted, 9.0 Å if both atoms were C^{α} and 21.0 Å if one or both were phosphorous, analogous to our ANM analysis of ribosome [19]. Panels a and b illustrate the slowest (nonzero) mode shape as a color-coded 3D structure and against the residue index. The coloring emphasizes the distinct difference between the motions of the 50S (red) and 30S (blue) subunits in this mode and indicates an anticorrelated motion of one subunit with respect to the other. This type of anticorrelated motion (i.e., ratcheting of one subunit with respect to the other) has been observed by cryo-EM [60].

Recently the dynamics of the HK97 bacteriophage viral capsid has been analyzed using the GNM. Two different forms of the capsid known as the pro-capsid (Prohead II) [2] and mature (Head II) [61] were considered. These structures are comprised of 420 copies of a single protein chain arranged into 12 pentamers and 60 hexamers, which expand from a spherical form (prohead) to icosahedral form (head) during maturation [62]. The GNM results obtained with a coarse-graining of $N/35$ for the first (slowest nonzero) mode of the two forms are shown in Figure 3.5(a) and Figure 3.5(b). These HCG structures have 3072 and 3360 nodes respectively. GNM computations were also performed with the complete sets of 107,520 and 117,600 residues for the respective pro-capsid and mature capsid to examine the conformational changes accompanying maturation [22]. Figure 3.5(c) and Figure 3.5(d) indicate that the slowest nonzero mode for the full capsid matches the $N/35$ results. This mode is asymmetric, yet identifies a region at each pole, pentamer-centered, as the most mobile (red) in each of these calculations.

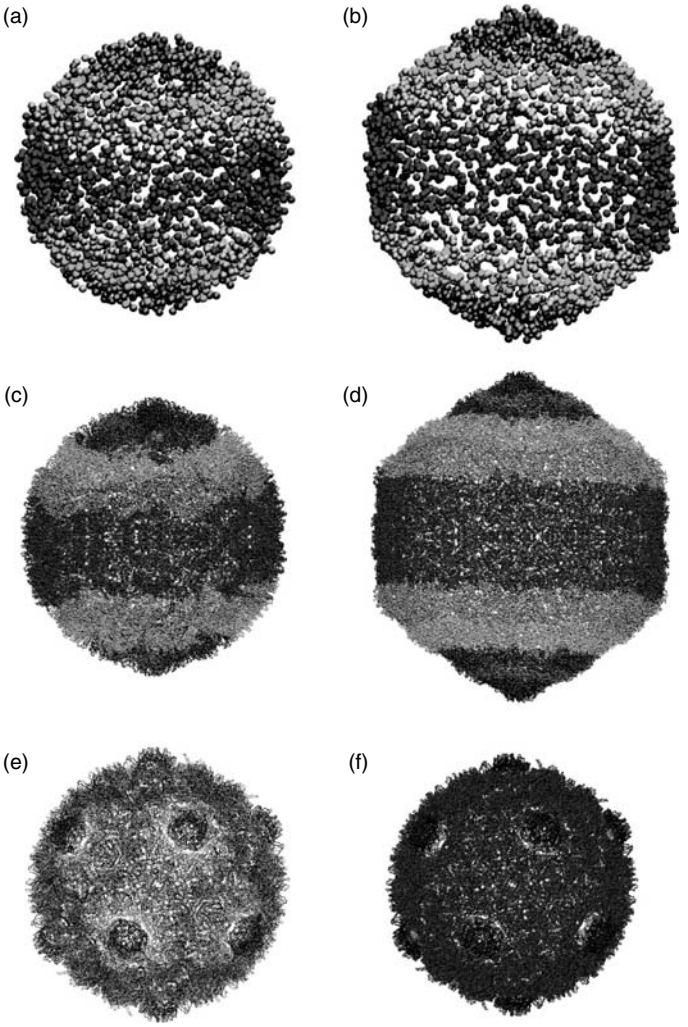

FIGURE 3.5
(See color insert following page 136) Application of GNM to the HK97 bacteriophage viral capsid. (a) The ms fluctuations from the slowest (threefold degenerate) mode for the prohead viral capsid coarse-grained by retaining only every 35th residue are colored from most mobile (red) to least mobile (blue). (b) The results for the slowest (threefold degenerate) mode of the head viral capsid calculated using a similar coarse-grained procedure of retaining every 35th residue. Both identify pentamer-centered regions at opposite poles as the most mobile regions suggesting an expansion or puckering of these residues. (c) The ms fluctuations for the slowest mode calculated over the entire (107,520 residue) prohead capsid structure (PDB file 1if0 [62]) and (d) entire (117,600 residue) head capsid structure (PDB file 1fh6 [61]) also demonstrate this high degree of mobility at the poles. (e) The weighted summation of the 11 slowest modes identifies the 12 pentamers as the most mobile regions responsible for expansion from the prohead to head form. (f) The slowest nondegenerate, symmetric mode, mode 31, also identifies these pentamers as highly mobile. These images were generated using VMD [74].

Due to the large degree of symmetry of the capsid, many of the calculated modes are degenerate, that is, have the same frequencies (eigenvalues). For example, the mode indicated in Figures 3.5(a) to Figure 3.5(d) is threefold degenerate, oriented along a different axis of the capsid. Hence a superposition of these three modes would more accurately describe the global motion of expansion that accompanies maturation. In fact, the superposition of the 11 slowest modes was found to yield icosahedrally symmetric fluctuations and identify the 12 pentamers as the most mobile (red) regions in the capsid (Figure 3.5[e]). Cryo-EM maps of intermediates between the prohead and head conformations indicate a large degree of motion for these pentamers during expansion [63]. It should be noted that the slowest nondegenerate mode, mode 31, is icosahedrally symmetric and also identifies these 12 pentamers as the most mobile regions (Figure 3.5[f]). However, because the frequency of mode 31 is at least three times that of modes 1 through 11, its contribution to the observed structural changes is small relative to that of these slower, asymmetric modes which cooperatively induce a similar set of fluctuation dynamics [22].

3.3.5 iGNM: A Database of GNM Results

With advances in computational methods for characterizing proteins, and with the recognition of the importance of modeling and understanding structural dynamics, a number of groups have recently undertaken the task of generating and making available on the Internet servers or databases for modeling or examining protein motions. One of the earliest attempts in this direction is the Database (DB) of Macromolecular Movements (MolMovDB; http://molmovdb.org/) [64] originally known as the DB of Protein Motions, constructed by Gerstein and collaborators [65]. Currently, about 4400 movies ("morphs") are available in the MolMovDB, generated by interpolating between pairs of known conformations of proteins or RNA molecules. These "morphs" are then used to classify molecules into roughly 178 motion types. Another online calculation tool based on a simplified NMA combined with the rotations–translations of blocks (RTB) algorithm [57] has been developed by Sanejouand's group with a sophisticated webserver interface (elNémo; http://igs-server.cnrs-mrs.fr/elnemo/), which includes up to 100 slowest modes for each studied structure [66]. A similar, yet more extensive work has been conducted in the lab of Wako [67] where the normal modes in the space of dihedral angles have been generated and collected in the ProMode DB (http://cube.socs.waseda.ac.jp/pages/jsp/index.jsp), for nearly 1442 single chain proteins extracted from the PDB. ProMode has been restricted to relatively small proteins (<300 residues) due to the time cost of energy minimization performed prior to NMA. In the same spirit, we have generated a DB of GNM results, iGNM (http://ignm.ccbb.pitt.edu/) [68]. Two major advantages of this DB are (i) motions are predicted, rather than interpolated between two structures, implying that knowledge of a single structure is sufficient to

generate the equilibrium fluctuations and (ii) the completeness of structure-dynamics data generated, since almost all of the existing PDB structures (22,549 PDB files as of September 15, 2003) have been analyzed. One should note that we are still in the process of cleaning and refining the resultant output files as well as augmenting the iGNM DB with newly deposited structures.

The iGNM DB provides information on protein dynamics beyond those experimentally provided by *B*-factors (for x-ray structures) or rms fluctuations (NMR structures). We have developed an Internet-based query system to retrieve information on *B*-factors, GNM mode shapes (eigenvectors corresponding to both the slowest and fastest ends of the vibrational spectrum), ribbon diagrams color-coded according to the residue mobilities, and cross-correlation maps describing the strength and types of correlations between residue fluctuations. The retrieved data are presented using a Chime plug-in (for 3D visualization of molecular structures) and Java applets (for graphical two-dimensional [2D] plots of fluctuation distributions). In addition to retrieving the data stored in the DB, the user has the ability to compute GNM dynamics for newly deposited structures as well as user-generated structures (e.g., from comparative modeling) through an automated online calculation server. The raw data for modes, frequencies, and residue correlations can be downloaded from the iGNM DB. Figure 3.6 illustrates the different types of outputs accessible from the iGNM DB, for phospholipase A2, as an example. For visualization, the residue mobility in the 20 slowest and fastest modes for each protein is mapped onto a ribbon diagram of the 3D structure (Figure 3.6[a]) color-coded from blue (least mobile) to red (most mobile). For slow modes, the blue portion of the molecule indicates the least mobile regions (minima), which are usually relevant to biological function (see Section 3.3.2). Similarly, by selecting the fast modes from the menu, the users are able to view the residues predicted to be critical for folding (maxima) colored red. Figure 3.6(b) illustrates a 2D plot of this same information against residue number for a given mode. Using the Java-applet windows (Figure 3.6[b] insets) the user is able to identify residues of interest, and scale the curves in order to compare multiple modes or different proteins. Figure 3.6(c) demonstrates the case where theoretical (red) and experimental (yellow) *B*-factors are plotted against the residue index simultaneously. The correlation map between the motions of residue pairs is illustrated in Figure 3.6(d). The colors on the map reflect the correlation cosines between the fluctuations of residue pairs — dark blue for anticorrelated (coupled but opposite direction), red for correlated (coupled, same direction), and green for uncorrelated motions.

3.4 Future Prospects

As discussed earlier, EN models in general have proven effective in characterizing large-scale motions in biomolecules. The simplicity of these models

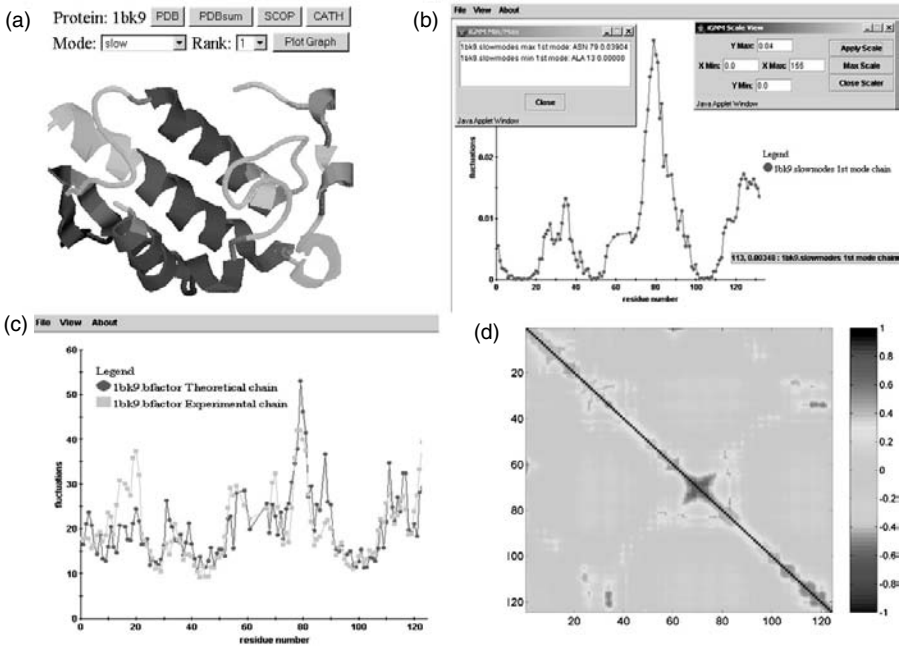

FIGURE 3.6
(See color insert following page 136) Visualization of dynamics data stored in the iGNM DB. The results shown are of the example phospholipase A2 (PDB:1bk9 [75]). (a) The slowest motions (slow1) are color-coded and mapped on structure of 1bk9 in dark blue, green, orange to red in the increasing order of mobility. (b) The window shows the mobility of the slowest mode with scalable range of view, max/min value info window and pop-up tag that shows the residue number and coordinates. (c) The experimental and predicted B factors are compared. (d) The cross-correlation of residue pairs of all modes. The perfect concerted motion (+1) is colored dark red while the perfect anticorrelated motion (−1) is colored dark blue.

sacrifice atomic-level predictions, in favor of performing efficient calculations of large structures, which capture the essential dynamics and functional motions encoded in the native structure. Such models are necessary to infer dynamics and function in an age where structural information about larger and larger complexes outpaces the computational ability to apply traditional atomic-level simulations.

There are at least five major areas in which GNM, or EN models in general, are anticipated to be useful. These include (i) the applications to low resolution structural data (e.g., cryo-EM), both for structure refinement and dynamics assessment [69–71]; (ii) exploring the machinery of supramolecular structures or multi-molecular assemblies including protein–DNA, protein–protein, and membrane protein–lipid complexes [19]; (iii) high throughput examination of the collective dynamics of families of proteins toward extracting common dynamic patterns and design principles selected and conserved across genomes or within subfamilies for functional requirements; (iv) investigation

of unfolding pathways and kinetics by including a temperature dependence for contacts [31, 36, 72]; and (v) integration with more detailed models and simulations [32, 73] (e.g., MD) for efficiently exploring the physical and chemical transitions between different functional forms further discussed in the chapter by Liu and coworkers.

References

1. Go, N., Noguti, T., and Nishikawa, T. Dynamics of a small globular protein in terms of low-frequency vibrational modes, *Proc. Natl Acad. Sci. USA,* 80, 3696, 1983.
2. Brooks, B. and Karplus, M. Harmonic dynamics of proteins: normal modes and fluctuations in bovine pancreatic trypsin inhibitor, *Proc. Natl Acad. Sci. USA,* 80, 6571, 1983.
3. Bahar, I., Atilgan, A.R., and Erman, B. Direct evaluation of thermal fluctuations in proteins using a single-parameter harmonic potential, *Fold. Des.,* 2, 173, 1997.
4. Haliloglu, T., Bahar, I., and Erman, B. Gaussian dynamics of folded proteins, *Phys. Rev. Lett.,* 79, 3090, 1997.
5. Tirion, M.M. Large amplitude elastic motions in proteins from a single-parameter, atomic analysis, *Phys. Rev. Lett.,* 77, 1905, 1996.
6. Atilgan, A.R. et al. Anisotropy of fluctuation dynamics of proteins with an elastic network model, *Biophys. J.,* 80, 505, 2001.
7. Hinsen, K. and Kneller, G.R. A simplified force field for describing vibrational protein dynamics over the whole frequency range, *J. Chem. Phys.,* 111, 10766, 1999.
8. Tama, F. and Sanejouand, Y.H. Conformational change of proteins arising from normal mode calculations, *Protein Eng.,* 14, 1, 2001.
9. Li, G.H. and Cui, Q. A coarse-grained normal mode approach for macromolecules: an efficient implementation and application to Ca2+-ATPase, *Bipohys. J.,* 83, 2457, 2002.
10. Bahar, I. et al. Collective motions in HIV-1 reverse transcriptase: examination of flexibility and enzyme function, *J. Mol. Biol.,* 285, 1023, 1999.
11. Temiz, N.A. and Bahar, I. Inhibitor binding alters the directions of domain motions in HIV-1 reverse transcriptase, *Proteins,* 49, 61, 2002.
12. Isin, B., Doruker, P., and Bahar, I. Functional motions of influenza virus hemagglutinin: a structure-based analytical approach, *Biophys. J.,* 82, 569, 2002.
13. Thomas, A. et al. Tertiary and quaternary conformational changes in aspartate transcarbamylase: a normal mode study, *Proteins,* 34, 96, 1999.
14. Cui, Q. et al. A normal mode analysis of structural plasticity in the biomolecular motor F-1-ATPase, *J. Mol. Biol.,* 340, 345, 2004.
15. Van Wynsberghe, A., Li, G., and Cui, Q. Normal-mode analysis suggests protein flexibility modulation throughout RNA polymerase's functional cycle, *Biochemistry,* 43, 13083, 2004.
16. Ming, D.M. et al. Simulation of F-actin filaments of several microns, *Biophys. J.,* 85, 27, 2003.
17. Keskin, O. et al. Molecular mechanisms of chaperonin groel–groes function, *Biochemistry,* 41, 491, 2002.

18. Tama, F. et al. Dynamic reorganization of the functionally active ribosome explored by normal mode analysis and cryo-electron microscopy, *Proc. Natl Acad. Sci. USA,* 100, 9319, 2003.
19. Wang, Y. et al. Global ribosome motions revealed with elastic network model, *J. Struct. Biol.,* 147, 302, 2004.
20. Tama, F. and Brooks III, C.L. The mechanism and pathway of ph induced swelling in Cowpea Chlorotic mottle virus, *J. Mol. Biol.,* 318, 733, 2002.
21. Tama, F. and Brooks III, C.L. Diversity and identity of mechanical properties of icosahedral viral capsids studied with elastic network normal mode analysis, *J. Mol. Biol.,* 345, 299, 2005.
22. Rader, A.J., Vlad, D.H., and Bahar, I. Maturation dynamics of bacteriophage HK97 capsid, *Structure,* 13, 413, 2005.
23. Kundu, S. et al. Dynamics of proteins in crystals: comparison of experiment with simple models, *Biophys. J.,* 83, 723, 2002.
24. Burioni, R. et al. Topological thermal instability and length of proteins, *Proteins,* 55, 529, 2004.
25. Wu, Y. et al. Universal behavior of localization of residue fluctuations in globular proteins, *Phys. Rev. E.,* 67, 041909, 2003.
26. Kundu, S., Sorensen, D.C., and Phillips Jr., G.N. Automatic domain decomposition of proteins by a Gaussian network model, *Proteins: Struct. Funct. Bioinf.* 57, 725, 2004.
27. Kundu, S. and Jernigan, R.L. Molecular mechanism of domain swapping in proteins: an analysis of slower motions, *Bipohys. J.,* 86, 3846, 2004.
28. Bahar, I. et al. Correlation between native-state hydrogen exchange and cooperative residue fluctuations from a simple model, *Biochemistry,* 37, 1067, 1998.
29. Jaravine, V.A., Rathgeb-Szabo, K., and Alexandrescu, A.T. Microscopic stability of cold shock protein examined by NMR native state hydrogen exchange as a function of urea and trimethylamine n-oxide, *Protein Sci.,* 9, 290, 2000.
30. Ortiz, A.R. and Skolnick, J. Sequence evolution and the mechanism of protein folding, *Bipohys. J.,* 79, 1787, 2000.
31. Micheletti, C., Lattanzi, G., and Maritan, A. Elastic properties of proteins: insight on the folding process and evolutionary selection of native structures, *J. Mol. Biol.,* 321, 909, 2002.
32. Micheletti, C., Carloni, P., and Maritan, A. Accurate and efficient description of protein vibrational dynamics: comparing molecular dynamics and Gaussian models, *Proteins,* 55, 635, 2004.
33. Rader, A.J. and Bahar, I. Folding core predictions from network models of proteins, *Polymer,* 45, 659, 2004.
34. Rader, A.J. et al. Identification of core amino acids stabilizing rhodopsin, *Proc. Natl Acad. Sci. USA,* 101, 7246, 2004.
35. Chen, S.C. and Bahar, I. Mining frequent patterns in protein structures: a study of protease families, *Bioinformatics,* 20, i77–i85, 2004.
36. Micheletti, C. et al. Crucial stages of protein folding through a solvable model: predicting target sites for enzyme-inhibiting drugs, *Protein Sci.,* 11, 1878, 2002.
37. Flory, P.J. Statistical thermodynamics of random networks, *Proc. R. Soc. Lond. A,* 351, 351, 1976.
38. Miyazawa, S. and Jernigan, R.L. Estimation of effective inter-residue contact energies from protein crystal structures: quasi-chemical approximation, *Macromolecules,* 18, 534, 1985.

39. Bahar, I. and Jernigan, R.L. Inter-residue potentials in globular proteins and the dominance of highly specific hydrophilic interactions at close separation, *J. Mol. Biol.,* 266, 195, 1997.
40. Papoulis, A. Sequences of random variables, in *Probability, Random Variables, and Stochastic Processes,* Kogakusha Company, Tokyo, 1965, p. 233
41. Halle, B. Flexibility and packing in proteins, *Proc. Natl Acad. Sci. USA,* 99, 1274, 2002.
42. Bahar, I. and Jernigan, R.L. Vibrational dynamics of transfer RNAs: comparison of the free and synthetase-bound forms, *J. Mol. Biol.,* 281, 871, 1998.
43. Bahar, I. Dynamics of proteins and biomolecular complexes: inferring functional motions from structure, *Rev. Chem. Eng.,* 15, 319, 1999.
44. Keskin, O., Jernigan, R.L., and Bahar, I. Proteins with similar architecture exhibit similar large-scale dynamic behavior, *Biophys. J.,* 78, 2093, 2000.
45. Berman, H.M. et al. The protein data bank, *Nucleic Acids Res.,* 28, 235, 2000.
46. Wilson, K.P., Malcolm, B.A., and Matthews, B.W. Structural and thermodynamic analysis of compensating mutations within the core of chicken egg white lysozyme, *J. Biol. Chem.,* 267, 10842, 1992.
47. Bahar, I. et al. Vibrational dynamics of folded proteins: significance of slow and fast motions in relation to function and stability, *Phys. Rev. Lett.,* 80, 2733, 1998.
48. Jernigan, R.L., Demirel, M.C., and Bahar, I. Relating structure to function through the dominant slow modes of motion of DNA topoisomerase II, *Int. J. Quant. Chem.,* 75, 301, 1999.
49. Jernigan, R.L. et al. Relating the structure of HIV-1 reverse transcriptase to its processing step, *J. Biomol. Struct. Dyn.,* 11, 49, 2000.
50. Keskin, O. et al. Relating molecular flexibility to function: a case study of tubulin, *Biophys. J.,* 83, 663, 2002.
51. Xu, C., Tobi, D., and Bahar, I. Allosteric changes in protein structure computed by a simple mechanical model: hemoglobin T<-> R2 transition, *J. Mol. Biol.,* 333, 153, 2003.
52. Sluis-Cremer, N., Temiz, N.A., and Bahar, I. Conformational changes in HIV-1 reverse transcriptase induced by nonnucleoside reverse transcriptase inhibitor binding, *Curr. HIV Res.,* 2, 323, 2004.
53. Loris, R. et al. Conserved water molecules in a large family of microbial ribonucleases, *Proteins,* 36, 117, 1999.
54. Demirel, M.C. et al. Identification of kinetically hot residues in proteins, *Protein Sci.,* 7, 2522, 1998.
55. Mullins, L.S., Pace, C.N., and Raushel, F.M. Conformational stability of ribonuclease T1 determined by hydrogen–deuterium exchange, *Protein Sci.,* 6, 1387, 1997.
56. Doruker, P., Jernigan, R.L., and Bahar, I. Dynamics of large proteins through hierarchical levels of coarse-grained structures, *J. Comput. Chem.,* 23, 119, 2002.
57. Tama, F. et al. Building-block approach for determining low-frequency normal modes of macromolecules, *Proteins,* 41, 1, 2000.
58. Ming, D. et al. Substructure synthesis method for simulating large molecular complexes, *Proc. Natl Acad. Sci. USA,* 100, 104, 2003.
59. Vila-Sanjurjo, A. et al. X-ray crystal structures of the wt and a hyper-accurate ribosome from *Escherichia coli*, *Proc. Natl Acad. Sci. USA,* 100, 8682, 2003.
60. Frank, J. and Agrawal, R.K. A ratchet-like inter-subunit reorganization of the ribosome during translocation, *Nature,* 406, 318, 2000.

61. Wikoff, W.R. et al. Topologically linked protein rings in the bacteriophage HK97 capsid, *Science,* 289, 2129, 2000.
62. Conway, J.F. et al. Virus maturation involving large subunit rotations and local refolding, *Science,* 292, 744, 2001.
63. Lata, R. et al. Maturation dynamics of a viral capsid: visualization of transitional intermediate states, *Cell,* 100, 253, 2000.
64. Echols, N., Milburn, D., and Gerstein, M. MolMovDB: analysis and visualization of conformational change and structural flexibility, *Nucleic Acids Res.,* 31, 478, 2003.
65. Gerstein, M. and Krebs, W. A database of macromolecular motions, *Nucleic Acids Res.,* 26, 4280, 1998.
66. Suhre, K. and Sanejouand, Y.H. elNemo: a normal mode web server for protein movement analysis and the generation of templates for molecular replacement, *Nucleic Acids Res.,* 32, W610–W614, 2004.
67. Wako, H., Kato, M., and Endo, S. ProMode: a database of normal mode analyses on protein molecules with a full-atom model, *Bioinformatics,* 20, 2035, 2004.
68. Yang L.W., Lin, X., Jursa, C.J., Holliman, M., Rader, A.J., Karimi, H., and Bahar, I. iGNM: A Database of Protein Functional Motions Based on Gaussian Network Model, *Bioinformatics,* 21, 2978–2987, 2005.
69. Ming, D. et al. How to describe protein motion without amino acid sequence and atomic coordinates, *Proc. Natl Acad. Sci. USA,* 99, 8620, 2002.
70. Tama, F., Wriggers, W., and Brooks III, C.L. Exploring global distortions of biological macromolecules and assemblies from low-resolution structural information and elastic network theory, *J. Mol. Biol.,* 321, 297, 2002.
71. Delarue, M. and Dumas, P. On the use of low-frequency normal modes to enforce collective movements in refining macromolecular structural models, *Proc. Natl Acad. Sci. USA,* 101, 6957, 2004.
72. Portman, J.J., Takada, S., and Wolynes, P.G. Microscopic theory of protein folding rates. I. Fine structure of the free energy profile and folding routes from a variational approach, *J. Chem. Phys.,* 114, 5069, 2001.
73. Zhang, Z.Y., Shi, Y.Y., and Liu, H.Y. Molecular dynamics simulations of peptides and proteins with amplified collective motions, *Biophys. J.,* 84, 3583, 2003.
74. Humphrey, W., Dalke, A., and Schulten, K. VMD: visual molecular dynamics, *J. Mol. Graph.,* 14, 33, 1996.
75. Zhao, H. et al. Structure of a snake venom phospholipase A2 modified by p-bromo-phenacyl-bromide, *Toxicon,* 36, 875, 1998.

4

Normal Mode Analysis of Macromolecules: From Enzyme Active Sites to Molecular Machines

Guohui Li, Adam Van Wynsberghe, Omar N.A. Demerdash, and Qiang Cui

CONTENTS

4.1 Introduction

Normal mode analysis (NMA), a simple but powerful approach, finds its value in many research areas including chemistry [1], structural biology [2], and solid-state physics [3, 4]. The basic information available from NMA includes the frequency and direction of motions, which makes NMA valuable in the interpretation (assignment) of experimental data [5] such as spectra and scattering profiles that encode structural and dynamical information.

Historically, NMA has been widely used in small-molecule spectroscopy [1] and the theoretical description of solid dynamics [3, 4], perhaps mainly because the harmonic approximation inherent in NMA is often expected to be valid in those systems. Application of NMA to macromolecules, especially biomolecules, started much later [6–8] due to a number of reasons. First of all, the systems are much larger and more complex; it therefore appeared to be a daunting task to compute a reliable Hessian matrix and solve the corresponding eigenvalue problem. Second, in addition to localized vibrations, biomolecules have diffusive type of motions that are highly anharmonic in nature; it was not clear if NMA would provide a meaningful description. Finally, biomolecules are usually characterized experimentally in solution or more complex media. It was almost certain that the environment would have a major impact on the motion of biomolecules, but it was not clear how such contributions can be incorporated effectively in a NMA framework [9].

Despite those difficulties, many research groups devoted efforts to improving and applying NMA techniques in the context of biomolecular simulations. Through more than two decades of studies, it has now become clear that NMA can be used in very versatile and ingenious ways to extract meaningful information regarding the structural and dynamical properties of biomolecules. The key is to make appropriate approximation(s) that suits the property or experiment observable under investigation; this has been illustrated well by other chapters in the book. In the current chapter, we discuss two classes of NMA studies being pursued in our research group, which probe dramatically different kinds of properties of biomolecules. The first area concerns quantitative characterization of localized vibrations at high frequency (thousands of wave numbers), which report on the structure (and potentially the dynamics) of specific site. The second area deals with semi-quantitative but systematic characterization of soft modes at very low frequency, which reflect the inherent structural flexibility of large biomolecular assemblies [10–13]. Since the modes of interest differ drastically in terms of frequency and character of motion in those two areas of study, different computational techniques need to be employed. In Section 4.2, we concisely summarize methods being developed and refined in our group, and compare these with other techniques available in the literature. In Section 4.3, we use a number of applications to illustrate information uniquely available from NMA calculations in the study of biomolecules. We summarize our findings and comment on future developments in Section 4.4.

4.2 Basic Theories and Implementations

In this section, we first briefly summarize technical details of NMA with hybrid QM/MM potential functions, which are required for the

quantitative description of localized vibrations that report on local structure and dynamics. We then describe a systematic approach for reducing the resolution (and therefore dimension) of NMA, which is well suited for the study of low-frequency motions in large biomolecules or biomolecular assemblies.

4.2.1 NMA with Hybrid QM/MM Potentials

Laser spectroscopy is a class of powerful techniques that are used for probing the structural and dynamical properties of complex molecular systems. In addition to the widely used 1-dimensional (1D) infrared (IR), Raman, and ultraviolet spectroscopies [1, 14, 15], more recent developments in nonlinear (such as 3-photon echo and fifth-order Raman) spectroscopies have provided novel ways of probing the dynamics of liquids and biomolecules with much improved time resolution [16]. For complex molecular systems, the interpretation of spectra is in general challenging and robust theoretical analysis is essential. Central to the simulation of many molecular spectra is the frequency of a particular (set of) chromophore vibration; depending on the level of sophistication, one needs to determine either the distribution of vibrational frequencies along a set of microscopic molecular dynamics trajectories or the time correlation function of the vibrational frequency [16]. The technique we discuss here has been applied by us to only 1D, IR, and Raman spectra calculations, but it is also useful in more sophisticated nonlinear spectroscopy simulations.

The frequency of interest here is often in the range of 1500 cm^{-1} or higher, thus the corresponding mode is expected to be highly localized although the fluctuating environment can perturb the value of the frequency through molecular interactions. Therefore, meaningful simulation of spectra in the condensed phase requires a method that can reliably describe both the electronic structure of the chromophore and the interaction between the chromophore and the environment. In this regard, a hybrid QM/MM framework [17–19] seems most attractive in terms of the balance between accuracy and computational cost: the chromophore and its immediate environment are treated quantum mechanically, whereas atoms further away are described with more approximate methods such as classical force fields (molecular mechanics). Indeed, such methods have been widely applied to the study of catalytic mechanisms in enzymes with substantial success [20–22], and several groups reported applications of QM/MM methods in molecular spectra simulations [23–28].

If only the ground and the first vibrational levels are explicitly involved, a harmonic approximation is often found to be adequate in spectra assignment. In this case, NMA is the method of choice and the major challenge concerns the calculation of the Hessian matrix in a QM/MM framework; the technical details have been discussed in previous work [23], here we summarize the most essential points. One starts with a popular expression of the QM/MM

total energy [17–19],

$$E = \left\langle \Phi \middle| \hat{H}^{\mathrm{QM}} + \hat{H}_{\mathrm{ele}}^{\mathrm{QM/MM}} \middle| \Phi \right\rangle + E_{\mathrm{van}}^{\mathrm{QM/MM}} + E_{\mathrm{bonded}}^{\mathrm{QM/MM}} + E^{MM} \tag{4.1}$$

which indicates that the QM and MM regions interact through electrostatic, van der Waals, and bonded energy terms, among which only the electrostatic term explicitly perturbs the wavefunction of the QM region. Taking the second derivative of the energy expression in Equation (4.1) with respect to nuclear displacements, one obtains a somewhat lengthy formula for the Hessian matrix elements [23, 29]. As discussed in detail in Reference 23, an important point is that one needs to evaluate both the MM derivatives of the one-electron integrals describing QM/MM interactions and the MM derivatives of the molecular orbital (MO) coefficients. The latter arises because displacement of the MM atom influences the QM wavefunction and the effect can be obtained by solving the coupled perturbed Hartree–Fock (CPHF) or coupled perturbed Kohn–Sham (CPKS) equations [29, 30]. Calculations in Reference 23 showed that MM derivatives of MO coefficients make very small contributions to the vibrational frequencies but make notable contributions to the dipole derivatives and therefore IR intensities; we expect a similar situation for other spectra (e.g., Raman) calculations.

Once the Hessian matrix is calculated, the normal modes of the system can be readily obtained by diagonalizing the mass-weighted Hessian through well-established procedures [31]. Algorithms that are useful for large biomolecules have been developed to allow the diagonalization of a partial Hessian localized to the site of interest [27, 28].

For spectra assignment, one needs to estimate the intensity of various vibrations, which can be derived with the appropriate derivatives of molecular properties and the eigenvectors determined from NMA. For linear IR spectroscopy, for example,

$$I_k = \frac{N\pi}{3c^2} \left| \nabla \bar{\mu} \cdot \mathbf{L}_k \right|^2 \tag{4.2}$$

where N is the Avogadro's number, c is the speed of light, $\bar{\mu}$ is the dipole moment of the molecule, and $\mathbf{L}_k$ is the kth eigenvector. The QM/MM methods for computing IR spectra were implemented in the GAMESS–US/CHARMM package [23]; the procedure for computing Raman spectra is being implemented.

In QM/MM calculations, the minimal QM region would normally be the chromophore, but previous calculations have established that for more quantitative results one has to treat the immediate environment of the chromophore (e.g., within hydrogen-bonding distances) with quantum mechanical models also. Alternatively, the immediate QM region can be described with a polarizable molecular mechanical model that has been fine-tuned to treat interactions with the QM region; in this regard, the effective fragment potential approach [32] was found useful in a number of studies. With a polarizable

MM force field, the calculation of the QM/MM Hessian becomes more tedious but the basic principle is the same.

4.2.2 Coarse-Grained NMA with Physical Potentials

In the study of low-frequency modes of large biomolecules or macromolecular assemblies, the nature of the motions (modes) of interest is very different from those described in Section 4.2.1. Here we are mainly concerned with the qualitative character of vibrational motions of the lowest frequencies, because these are often found to correlate well with conformational transitions that occur during the functional cycle of "molecular machines" [10, 12, 13]. It is usually difficult to directly characterize such large-scale collective motions using experimental techniques, which makes NMA a powerful tool that complements structural biology techniques in revealing structure–function relationships of large biomolecular complexes. In addition, NMA can be a useful tool for improving the resolution of x-ray [33], NMR [34], or EM structures (see other chapters in this book) by approximating collective motions.

The fact that only the lowest-frequency modes are of interest makes it possible to develop unique computational algorithms for NMA applications. Since these modes involve the *collective* motion of a large number of atoms, an adequate description can be achieved by reducing the effective dimension of the eigenvalue problem by partitioning the macromolecule into a set of "blocks," where each block can be as small as a single residue or as large as a secondary structure element; the level of coarse-graining depends on the desired level of accuracy and the number of low-frequency modes. The full Hessian is then projected onto a subspace spanned by the basis vectors associated with the coarse-grained blocks. Only the projected Hessian, which has a significantly smaller dimension, needs to be diagonalized

$$\mathbf{H}^{\text{sub}} = \mathbf{P}^{\text{T}}\mathbf{H}\mathbf{P} \tag{4.3}$$

In the original work of Tama et al. [35], the subspace consists of the translational and rotational eigenvectors of the blocks

$$\begin{aligned} P^{\mu}_{J,j\nu} &= \sqrt{m_j/M_J}\,\delta_{\mu\nu}, && \mu = 1,2,3 \\ P^{\mu}_{J,j\nu} &= \sum_{\alpha\beta} (\mathbf{I}_J)^{-1/2}_{(\mu-3),\alpha} \sqrt{m_j}(\mathbf{r}_j - \mathbf{r}^0_J)_\beta \varepsilon_{\alpha\beta\nu}, && \mu = 4,5,6 \end{aligned} \tag{4.4}$$

where J and j label blocks and atoms respectively, and μ labels the translation ($\mu = 1,2,3$) and rotation ($\mu = 4,5,6$) of each block; M_J, $\mathbf{I}_J$, and $\mathbf{r}^0_J$ is the sum of mass, moment of inertia, and center of mass for block J, respectively. The method is thus referred to as "Rotational–translational block" (RTB).

In our implementation [36], we adapted the name "block normal mode" (BNM) for the coarse-graining procedure, because the subspace in general

can be constructed by a set of low-frequency modes of the blocks, *in addition to* their translational and rotational eigenvectors. The advantage of using only the translational and rotational eigenvectors of the blocks is that the expressions are analytical (Equation [4.6]) and no normal mode calculation for the blocks is required; however, accurate results can be expected only when the size of the block is small (e.g., one residue). When the size of the block is large, for example, each block corresponding to a secondary structural element, it is clearly desirable to include low-frequency modes of the blocks.

In the original implementation of Tama et al. [35], the entire atomic Hessian is first constructed and then projected into the RTB subspace (Equation [4.3]). In our implementation [36], the projected Hessian is constructed directly, taking advantage of the block structure of the projection calculation, which completely eliminated the memory or disk required for the storage of the full atomic Hessian. Recently, we have further increased the efficiency of the BNM method by taking advantage of the power of parallel computations and sparsity associated with the Hessian matrix of very large systems (e.g., 30S/50S ribosome) even *after* projection. The projected Hessian matrix ($\mathbf{H}^{\text{sub}}$ in Equation [4.3]) is constructed in a parallel fashion with only elements above a predetermined threshold (10^{-8} kcal/mol Å^2) in Reference 8 and the corresponding Hessian indices stored. The eigenvalues and eigenvectors associated with a desired number of lowest-frequency modes are then determined with an iterative Lanczos algorithm [37, 38] implemented in the PARPACK package [39]. There are several distinct advantages associated with using Lanczos for BNM calculations. First, approximate solutions are available at any step during the recursion and can be systematically improved by more recursive steps. The smallest and largest eigenvalues usually converge much faster than the rest and therefore Lanczos is ideally suited for BNM, where only a small number of low-frequency modes are of interest. Second, the Lanczos algorithm involves simple matrix–vector multiplications and therefore can be made highly efficient for sparse-matrices like the projected Hessian in BNM. Finally, the recursion usually needs only a small number of previous vectors and therefore does not require a large storage space, which is only proportional to the number of eigenvalues to be calculated.

It is of interest to compare the BNM/RTB method to other techniques developed in the literature for NMA of large biomolecules. Although the size of the projected Hessian is similar to those used in the elastic network model [40, 41], the projected Hessian is constructed based on the full Hessian with atomic level of physical interactions. Therefore, we expect that BNM/RTB is in general more robust than the elastic network model that assumes a uniform coupling constant between all atoms within a cutoff (see Section 4.3.2 for further comparisons). We also note that the block partitioning scheme in BNM is somewhat similar to that in the substructure-synthesis method (SSM) proposed recently by Ming et al. in Reference 42, where the "blocks" in BNM are replaced by "substructures" (a term widely used in the literature of mechanics) in SSM. The difference is that the blocks in BNM do not overlap, whereas the "substructures" have overlapping regions in SSM. The modes

of the complete macromolecule are constructed in BNM by diagonalizing a projected Hessian spanned by the eigenvectors of blocks, whereas the modes of the substructures are "synthesized" together with the Rayleigh–Ritz variational principle based on constraints in the overlapping region. The BNM result does not rely on the choice of the overlapping boundary between different substructures as in SSM, and is completely general in terms of block structures and spatial arrangements. The significant advantage of the SSM method, on the other hand, is that it does not require Hessian of the entire molecule. Due to this simplification, SSM is most suited for specific types of substructure arrangements, such as filament systems. For more globular systems, such as the ribosome (see Section 4.3) or virus, BNM is more useful.

4.3 Illustrative Applications

In this section, we briefly discuss applications of the two NMA techniques presented above for various biophysical problems. The main aim is to illustrate the versatility of this simple but unique computational framework; due to limited space, detailed discussions are given elsewhere.

4.3.1 Active Site of Mb–CO

Myoglobin (Mb) has attracted the attention of many authors over the past several decades [43]. The issue that received the most investigation concerns the differentiation between CO and O_2 binding. In the gas phase, compounds involving the heme group bind CO much more strongly than O_2 by a factor of approximately 30,000 (corresponds to a difference of 6.2 kcal/mol in binding energy). In the presence of the protein environment, by contrast, the difference is reduced to a value between 25 ($\sim$1.9 kcal/mol) and 40 ($\sim$2.2 kcal/mol difference in binding energy), depending on the biological source of Mb. During the early period of this long investigation, attention was paid to the steric repulsion between active site residues and the bound ligand, which was based on the x-ray observation that CO in the synthetic models of myoglobin [44] appears to bend away from the typical linear geometry observed in most inorganic compounds. Several x-ray results for the Mb–CO system also indicate a bend in CO arrangement of different degrees [45, 46]. This agreement was recently questioned by a number of groups based on observations from polarized IR [47, 48], ^{13}C, ^{17}O, and ^{57}Fe nuclear magnetic resonance (NMR), ^{57}Fe Mössbauer [49], and Resonance Raman (RR) spectroscopies [50–52], augmented with density functional theory (DFT) calculations on model compounds [53–57]. The most recent high-resolution x-ray structure also showed a nearly linear Fe–C–O geometry [58]. Such a linear Fe–CO arrangement led several groups to conclude that the steric interaction between the bound ligand and

active site residues is not the main origin for the CO/O_2 binding differentiation. Mutagenesis studies from Olson and Phillips among others [43, 59] emphasized the importance of polarity, rather than steric interaction, in the binding site. This concept is supported by various measurements including RR, IR, vibrational echo, and stark spectroscopy, which found correlation between the vibrational frequency and relaxation rate of the bound CO with electrostatic polarization from the protein [60–62].

Central to the interpretation of spectroscopic measurements is the direction of the transition dipole moment, and whether it is aligned with the CO bond vector. Although this issue has been addressed briefly in previous computational studies [63, 64], a rigorous analysis that includes the protein has not been done; this is our goal here.

QM/MM geometry optimization and NMA were performed for the wild type sperm-whale Mb–CO (two different His64 tautermers) and two mutants that have the highest (H64G) and lowest (V68N) measured CO vibrational frequencies [43, 65]. The structures of the mutants were modeled starting from the x-ray result for the wild type Mb–CO (PDB code 1MBC) [45]. The details of calculations are summarized in the footnote of Table 4.1.

The major difference (on a relative scale) between wild type and mutant Mb–CO active site lies in the equilibrium of C–O and Fe–C distances; the former varies from 1.172 Å in H64G to 1.180 Å in V68N. The longer CO distance in the latter is due to the weak hydrogen bonding interaction between CO and the side-chain of N68 introduced by the mutation. The Fe–C distance has an inverse correlation with the C–O distance, as expected from the well-known bonding character of the Fe–CO moiety; it varies from 1.740 Å in V68N to 1.762 Å in H64G. These variations in the bond lengths correlate with C–O and Fe–C stretching frequencies (see below). In all the structures investigated here, the Fe–CO moiety is more or less perpendicular to the heme plane (Figure 4.1).

The calculated vibrational frequencies and IR intensities for the CO stretch in the wild type and a number of mutant Mb–CO are summarized in Table 4.1. Encouragingly, the computed values are in good agreement with experimental results, especially on a relative scale. For instance, the V68N has the lowest CO stretch frequency, which is 1945 and 1922 cm^{-1} from the calculation and experiment, respectively. The H64G mutant and the δ-H64 wild type Mb–CO has the highest CO stretch of 1977 cm^{-1}; the experimental measurement gave values of about 1960 to 1965 cm^{-1}. The ε-H64 wild type has a calculated CO stretch of 1960 cm^{-1}, which is similar to the experimental value of 1941 cm^{-1}. The trend in the CO stretch frequency correlates well with that in the CO equilibrium distance, that is, V68N and H64G have the longest and shortest CO distance, respectively. The IR intensity for the CO stretch is very similar among the structures considered here, the δ-H64-WT and V68N has the smallest and the largest IR intensity of 644 and 788 km/mol, respectively. Interestingly, it was found experimentally that substituting H64 by a Gly induced an increase in the IR intensity of the CO stretch. It should

TABLE 4.1

Active Site Geometry and CO Stretch Vibrational Frequency for the Wild Type and Mutant Myoglobin[a].

Species	FeC (Å)	FeNεH93 (Å)	CO (Å)	∠O–C–Fe (°)	θ_C(°)[b]	ε_d(°)	τ_d(°)[b]	ν_{Fe-C} (cm^{-1})[c]	ν_{CO} (cm^{-1})[c]	I_{CO} (km/mol)
ε-H64-WT	1.747	2.133	1.177	175.7	0.7	4.4	2.6	5xx (508)	1960 (1941)	704
δ-H64-WT	1.760	2.143	1.173	175.1	0.6	2.5	5.7	527	1977 (>1960)	644
H64G	1.762	2.136	1.172	179.3	1.0	2.9	2.6	524 (492)	1977 (1965)	742
V68N	1.740	2.124	1.180	175.7	1.0	3.6	2.6	544 (526)	1945 (1922)	788

[a] The QM part included two diformamidate molecules mimicking the porphine ring and the side-chain of the proximal histidine (H93) plus the iron and CO. The QM atoms were described at the B3LYP level with the valence double zeta basis of Ahlrichs and co-workers (*J. Chem. Phys.* 97, 2571, 1992). The protein environment was described with the polar hydrogen CHARMM19 force field. To approximately account for the solvation effect, a water drop of 16 Å was overlaid at the binding site (centered on the iron atom), and partial charges on the side-chain of exposed charged residues were scaled by an empirical factor of 0.3. Link atoms were introduced to saturate the valence of the boundary QM atoms. During the QM/MM Hessian calculation, 306 MM atoms were included in the MM-CPHF solution, among which 207 atoms were treated with the decoupled approximation.

[b] For the definition of θ_C/τ_d angles, see Scheme 4.1.

[c] Values without parentheses were calculated with QM/MM normal mode analysis; those with parentheses were measured experimentally (for a recent review and collection of measured values, see Reference 22).

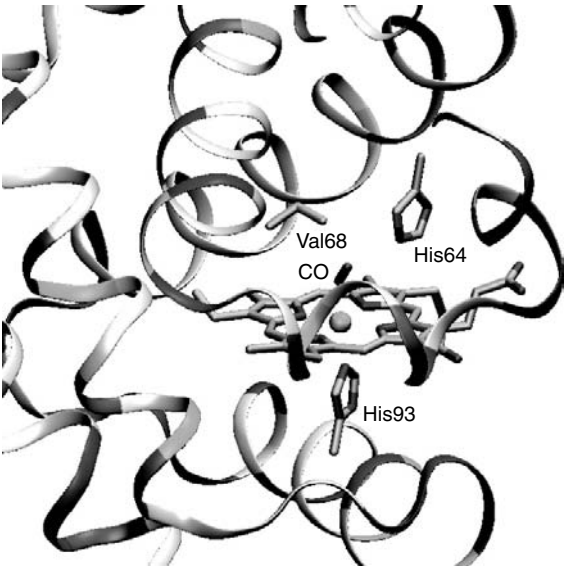

FIGURE 4.1
(See color insert following page 136) Active site of CO bound myoglobin. The heme and CO are shown in the line form, and part of the protein is shown in the ribbon form; the protein is color-coded based on the amino acid type (red — acidic, blue — basic, green — polar, and white — nonpolar).

be noted that the absolute IR intensity is likely to be overestimated with the small basis set used here.

In a number of polarized IR measurements, the angle between CO and the heme normal was estimated [47, 51]. A critical assumption made in those studies is that the transition dipole moment for the CO stretch lies along the CO bond vector. The validity of the assumption was investigated by Spiro et al. with DFT calculations on a small model heme–CO system [63, 64]. It was found that the transition dipole moment is much closer to the Fe–C bond vector than the C–O vector even though the deviation is not large. In the current work, calculation of the IR transition dipole moment (dipole derivative projected onto the CO stretch eigenvector) in the protein gives a similar picture (Scheme 4.1). As shown in Table 4.1, in all the structures considered, the transition dipole forms an angle of 2.5 to 4.4° with the Fe–C vector, and an angle of 2.6 to 5.7° with the CO bond vector. In other words, the assumption made in the IR measurements appears to be valid even in the presence of the protein environment.

Other frequencies that involve CO are also in fair agreement with experimental measurements. For the ε-H64-WT, the calculated Fe–C stretch is calculated to be 520 cm^{-1}, which is in qualitative agreement with the experimental values of 510 cm^{-1}. The Fe–C stretch has the highest value in the V68N mutant, which is 544 and 526 cm^{-1} from the calculation and experiment, respectively. The QM/MM calculation also gave a value of about 600 cm^{-1}

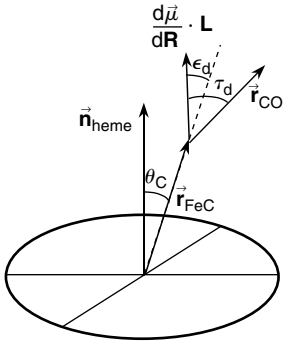

SCHEME 4.1

for the Fe–CO bending modes, whose assignment has been controversial. Our value supports the latest assignment ($\sim$580 cm^{-1}) based on RR study of hemoglobin [66].

4.3.2 Flexibility of Molecular Machines — Comparison between BNM and ANM

As discussed in several chapters of this book, another interesting method for describing the low-frequency motions in large biomolecules is the anisotropic elastic network model (ANM) based on the initial work of Tirion [40, 41]. The physical argument is that the low-frequency collective motions depend essentially on the mass-distribution of atoms in a biomolecule and, therefore, an elastic model without much atomic detail can capture the major character of these motions; the reliability of such elastic approximation is expected to become more robust as the system size increases. Although this appears very reasonable, it is of interest to quantify the agreement between the elastic model and models with more physical atomic interactions so that the level of confidence in applying the elastic model for biological systems can be established. Such comparisons have been made for proteins rather extensively in previous work [41], which in general has found satisfactory agreements, as long as the cutoff is carefully chosen. For another type of important biopolymers, such as nucleic acids, no systematic studies using ANM have been carried out. The performance of simplified models might be different in nucleic acid systems due to different three-dimensional (3D) structures and dominant forces compared to globular proteins. Here we use two ribozymes of very different size, the hammerhead ribozyme and the ribosome, as examples for comparing ANM and atom-based calculations. More detailed analysis compared to MD simulations is given elsewhere.

4.3.2.1 The Hammerhead Ribozyme

The hammerhead ribozyme is an ideal system for studying conformational flexibility because it has been proposed that a major conformational

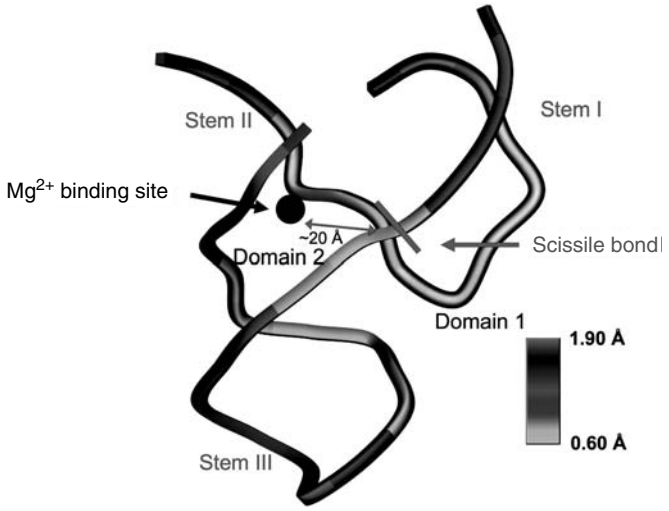

FIGURE 4.2
(See color insert following page 136) Computed RMS fluctuation using classical NMA mapped onto the structure of the hammerhead ribozyme. The structural domains and approximate location of the second metal binding site relative to the scission site are also shown.

change has to occur for the catalysis to proceed. The essential experimental observation is that a Mg^{2+} binding site (A9, also referred to as the P9/G10.1 site), which is nearly 20 Å away from the splicing site in the x-ray structure [67], appears to be crucial to the catalysis; changing the *pro*-R phosphate oxygen in A9 to sulfur abolished the catalytic rate by a factor of 10^3 [68], whereas the splicing activity is largely restored with softer metal ions such as Mn^{2+} that prefers to bind sulfur. Based on this result and a set of abasic mutations [69], Herschlag and coworkers proposed a model in which a significant conformational change from the x-ray structure has to take place to bring the metal at the P9/G10.1 site closer to the splicing site; this corresponds to refolding of domain 2 onto domain 1 (Figure 4.2; see also Reference 69). Although this proposal has not been confirmed by later structural studies [70], and more recent biochemical studies have suggested that the metal ion at the P9/G10.1 site is not within the coordination sphere from the splicing site [71–73], it is of interest to investigate whether the hammerhead ribozyme has noticeable conformational flexibility that is consistent with the major conformational transition proposed in Reference 69. In addition, the small size of the system provides an ideal opportunity to systematically compare collective motions from MD simulations and NMA at various resolutions; here we focus on the comparison between NMA at full atomic level (referred to as "classical NMA"), BNM, and the ANM.

In the classical NMA and BNM calculations, the CHARMM 27 force field for nucleic acids was used [74], with a recently parameterized EEF1 model for nucleic acid systems for an approximate treatment of solvation effect [75, 76].

Starting from the x-ray structure 301D [67], which contained 5 Mg^{2+} ions, the structure was minimized till the root mean square (RMS) gradient dropped below 0.01 kcal/mol Å. In the BNM calculations, each nucleotide or Mg^{2+} ion was taken as a block; in computing the RMS fluctuations, the BNM frequencies were scaled by a factor of 2.35 similar to previous work [36]. In the ANM calculations, two sets of calculations were done with different atoms representing the nodes of the elastic network; only P atoms were used in one set, whereas both the P and the N bonded to the sugar moiety were used in the other. A number of cutoff distances were used that ranged from 18 to 30 Å. Since only low-frequency modes are of interest, only 40 lowest-frequency modes were computed.

To quantify the comparison between different normal mode results, we examined RMS fluctuations, the overlap between eigenvectors and the "spanning coefficients." The latter was defined as the following:

$$S_k = \sum_{i=1}^{M} (\mathbf{L}_{i;\mathrm{BNM/ANM}}^T \bullet \mathbf{L}_{k;\mathrm{NMA}})^2 \tag{4.5}$$

which represents how well the kth classical NMA eigenvector is spanned by M set of BNM or ANM eigenvectors. As discussed in a previous work [36], it is possible that two methods give different eigenvectors but span the same conformational subspace.

The RMS fluctuations from classical NMA calculations are mapped onto the minimized structure in Figure 4.2. As expected, the ends of both RNA chains are floppy and exhibit large degree of flexibility (RMS fluctuations $\sim$1.90 Å). The Stem-III region, which is loosely packed, also has high RMS fluctuations. The domain 1 and 2 regions, by contrast, seem to be well packed through base–pair interactions and exhibit only mild fluctuations on the order of 0.6 Å. Therefore, it seems that although the hammerhead ribozyme is a flexible system overall, the domains implicated in the proposal of Herschlag and coworkers [69] actually form a rather stable core. This suggests that a large conformational transition involving refolding of domain 2 onto domain 1 seems unlikely, although further studies involving more elaborate simulations need to be done to investigate this point.

Moving on to the comparison between different NMA methods, it is seen in Figure 4.3(a) that none of the approximate schemes (BNM and ANM) perform very accurately. The BNM results are in close parallel to the classical NMA. RMS fluctuations throughout the molecule, although BNM seems to systematically overestimate the magnitude of fluctuations. Closer inspection of the vibrational frequencies found that a few lowest frequencies have a somewhat different scaling factor relative to the classical NMA values, as compared to the other modes. Therefore, using the scaling factor that best fitted all frequencies below 60 cm^{-1} over-corrected the lowest BNM frequencies, which resulted in overestimation of the fluctuations. The general agreement between eigenvectors computed from BNM and classical NMA calculations is excellent, as

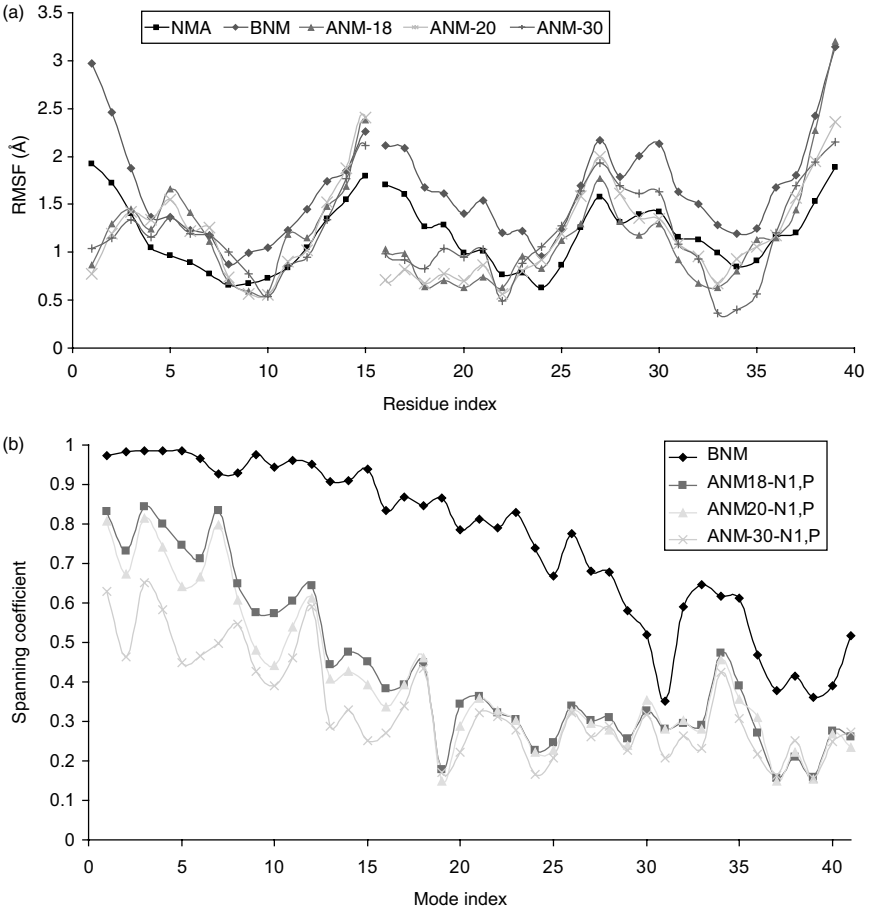

FIGURE 4.3
Comparison between ANM, BNM, and classical NMA for the hammerhead ribozyme. (a) RMS fluctuations and (b) spanning coefficients (Equation [4.5]).

illustrated by the spanning coefficients in Figure 4.3(b) and overlap matrix in Figure 4.4(a) for example, the spanning coefficient is larger than 0.9 for the first 15 modes, and the overlap matrix has a clear diagonal feature that indicates significant overlap between individual pairs of eigenvectors.

The ANM results, somewhat surprisingly, were quite disappointing with all cutoff schemes and choice of nodes in the elastic network; selected results are shown in Figure 4.3 and Figure 4.4. For the RMS fluctuations, even the qualitative trend was not reproduced in any ANM calculations; the ANM results gave significantly damped flexibility in the 5′-termini in both strands and a local peak in fluctuation around C3 (Figure 4.3[a]). The spanning coefficients are substantially smaller than those from BNM calculations; the best agreement was found with both P and sugar-bonded N as elastic nodes

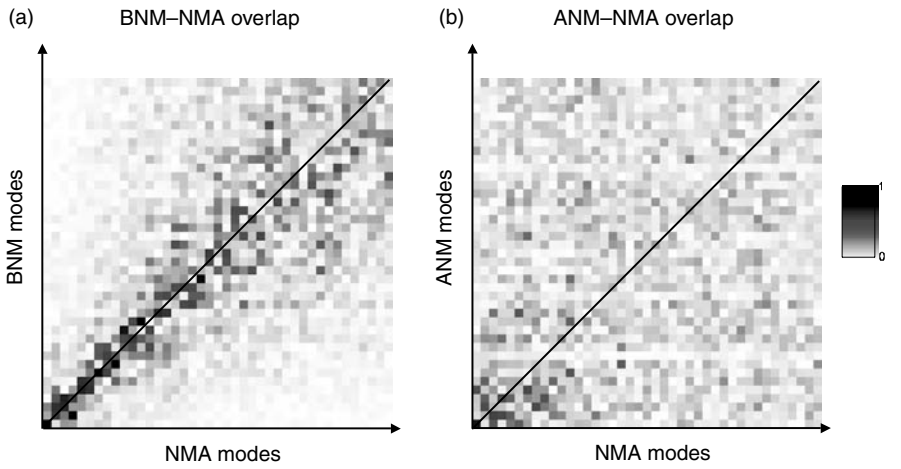

FIGURE 4.4
(See color insert following page 136) Overlap between (a) BNM–NMA and (b) ANM–NMA eigenvectors for the hammerhead ribozyme.

and 18 Å of cutoff, in which only three modes have spanning coefficients larger than 0.8 (Figure 4.3[b]). The overlap matrix is even more devastating (Figure 4.4[b]), which nearly approaches a random distribution.

The results obtained here clearly indicated that the approximations made in the BNM method have very little impact on the quality of the computed low-frequency normal modes for the hammerhead system. By contrast, the simplified ANM model seems to be inaccurate. This is likely due to the fact that the 3D structure of the hammerhead, like many RNA systems, is very different from that of globular proteins. The packing of atoms is less dense, which makes it difficult for a simple elastic network model to capture the essential dynamical features. What remains to be seen is whether the classical NMA results can reproduce collective motions from MD simulations, which include anharmonic contributions. It would also be interesting to see if the limitation in ANM is also observed in larger RNA systems that have more complex secondary/tertiary structural features and in proteins that have highly nonglobular forms such as cytoskeleton filaments. We will report such studies in a separate publication.

4.3.2.2 The 30S and 50S Ribosomes

Obtaining atomic resolution structures for the ribosome [77–80] has been one of the major achievements in structural biology in recent years. However, many studies, such as those using electron microscopy [81], have indicated that the ribosome is a highly dynamical "molecular machine," which should not come as a surprise considering the complex functional cycle of peptide synthesis. A major challenge is to characterize motions that have important

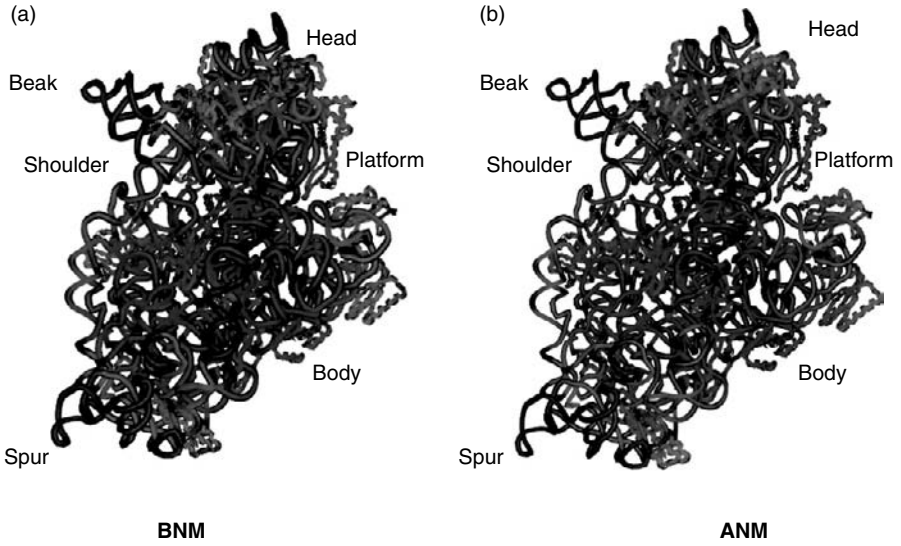

FIGURE 4.5
(See color insert following page 136) Computed RMS fluctuation using (a) BNM and (b) ANM mapped onto the structure of the 30S ribosome subunit (PDB code 1J5E). The red region has higher fluctuations.

functional roles, for which major progress has been made by the ANM model [82, 83], as illustrated in recent publications and in this book. Due to the recent improvements in BNM, it became straightforward to compute the low-frequency modes for systems like the ribosome. This gives us an opportunity to compare the ANM and BNM methods for describing important motions of very large biomolecular assemblies.

We have calculated low-frequency modes of both the 30S and 50S ribosome (PDB code 1J5E and 1JJ2, respectively), which have x-ray structures of 3.05 and 2.4 Å resolution, respectively. The calculation procedures are very similar to those used for the hammerhead. A 10 Å group-based cutoff in electrostatic interactions was used to be consistent with the EEF1 solvation model. This makes the Hessian very sparse, and the sparsity ratio is 141 and 229 even for the projected Hessian for the 30S and 50S ribosome, respectively. In the ANM calculations, the P atoms in the nucleic acids and C_α atoms in the proteins were used as the elastic nodes; similar to previous studies of Tama and Brooks, a cutoff distance of 20 and 16 Å was used for the P and C_α atoms, respectively. As in the hammerhead study, quantities of interest include the RMS fluctuation (Figure 4.5 and Figure 4.6), overlap between eigenvectors (Figure 4.7) and the spanning coefficients (Figure 4.8).

For the overall RMS fluctuations (summed over same number of computed modes in ANM and BNM), the patterns are remarkably similar between ANM and BNM results for both the 30S and 50S ribosomes, except for the relative magnitudes of major peaks. In the 30S ribosome both ANM and BNM

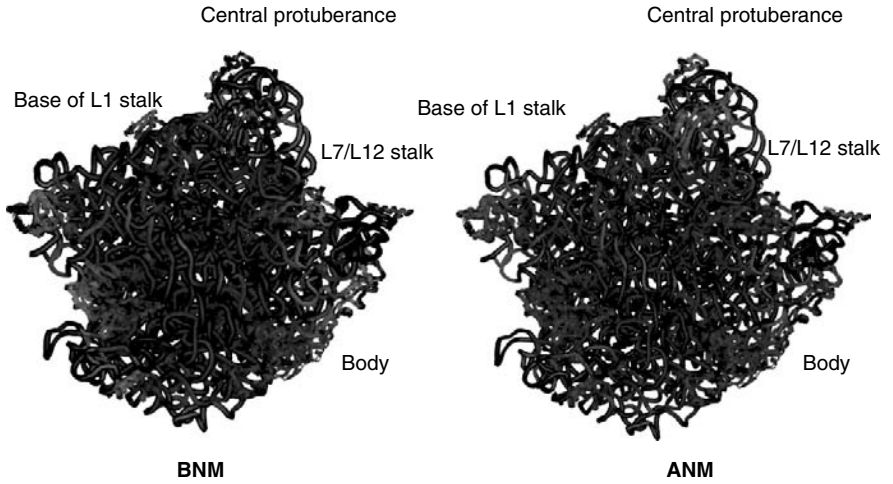

FIGURE 4.6
(See color insert following page 136) Computed RMS fluctuation using (a) BNM and (b) ANM mapped onto the structure of the 50S ribosome subunit (PDB code 1JJ2). The red region has higher fluctuations.

show large RMS fluctuations in the beak, head, platform, spur, and in the region at the base of the spur (Figure 4.5). The high degree of flexibility in the beak, head, and platform is particularly noteworthy, as it appears to be structurally poised to have a role in the translocation of mRNA relative to the ribosome that is essential for translation. This hypothesis is supported by the fact that the mRNA–30S interface is located at the junction of the head, shoulder, and platform, and one can easily envision a role for the immediately adjacent beak, platform, and head in providing a ratchet-like motion that would effect a translocation. Further support for a role for the head in the translocation is given by its binding to domain IV of elongation factor *G*, a GTPase that catalyzes translocation [84]. Regions of high flexibility in the 50S ribosome (Figure 4.6), namely the L7/L12 stalk, base of the L1 stalk, and the central protuberance, also appear to coincide with regions that may be intimately involved in translocation. These regions are adjacent to regions intimately associated with the A, P, and E site of the 30S subunit where mRNA binds. Consistent with a role for the L7/L12 in translocation is the finding that it binds EF to G [84]. Furthermore, the L7/L12 stalk, central protuberance, and L1 stalk were found to be highly flexible in cryoelectron microscopy studies [85]. ANM studies of the 30S and 50S subunits by Wang et al. [83] yielded similar results, with marked flexibility in the beak, spur, and base of the head of the 30S subunit and in the base of the central protuberance, L7/L12 stalk, and L1 stake for the 50S. A notable difference between our data and that of Wang et al. [83] is their finding of flexibility at the bases of the aforementioned 50S structures and base of the head of the 30S, whereas our calculations reveal flexibility in the entirety of these structures.

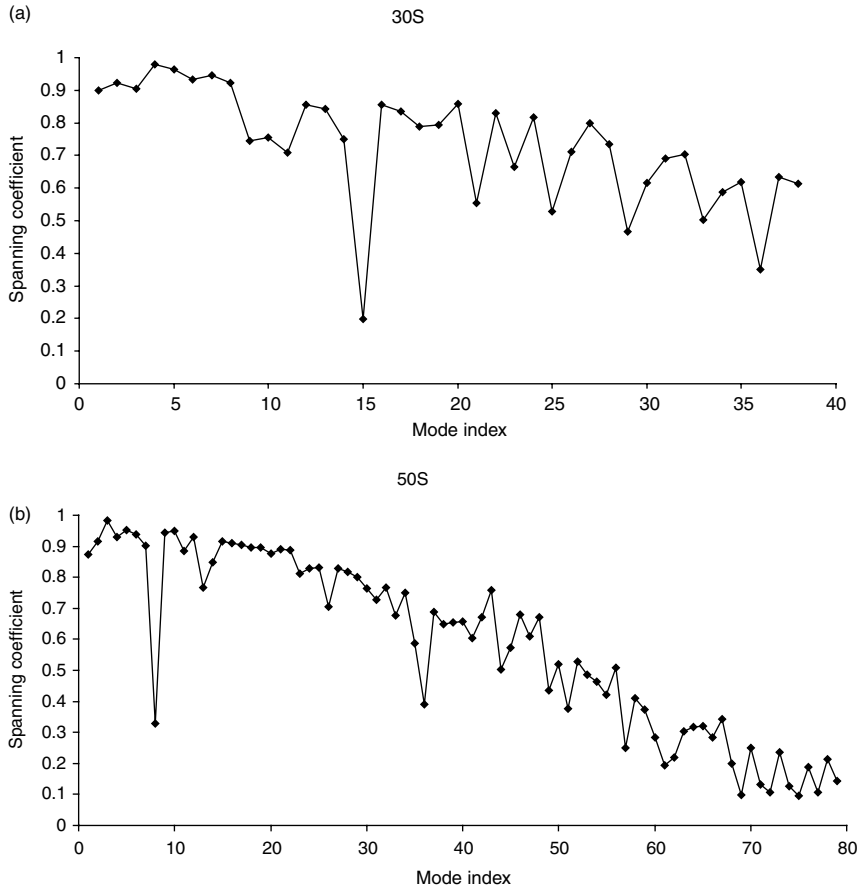

FIGURE 4.7
Spanning coefficients for the BNM modes in terms of ANM modes for the (a) 30S and (b) 50S ribosome subunits.

This discrepancy might be accounted for by the fact that they used a larger *P–P* cutoff distance (24 Å) than this study (20 Å), which would decrease the flexibility.

In terms of eigenvectors (Figure 4.7 and Figure 4.8), the agreement between ANM and BNM results is also quite remarkable considering the complexity of the system. For 30S and 50S, there are about eight BNM modes that have spanning coefficients larger than 0.9; it is interesting that these correspond to the first eight modes in 30S, but not so in the 50S ribosome. The overlap matrix (Figure 4.8) has a much better form compared to that in the hammerhead ribozyme (Figure 4.4). A near diagonal feature is clearly evident that illustrates reasonable overlap between the individual pairs of ANM and BNM eigenvectors, although the feature is much less striking than the overlap between BNM and classical NMA results for the hammerhead.

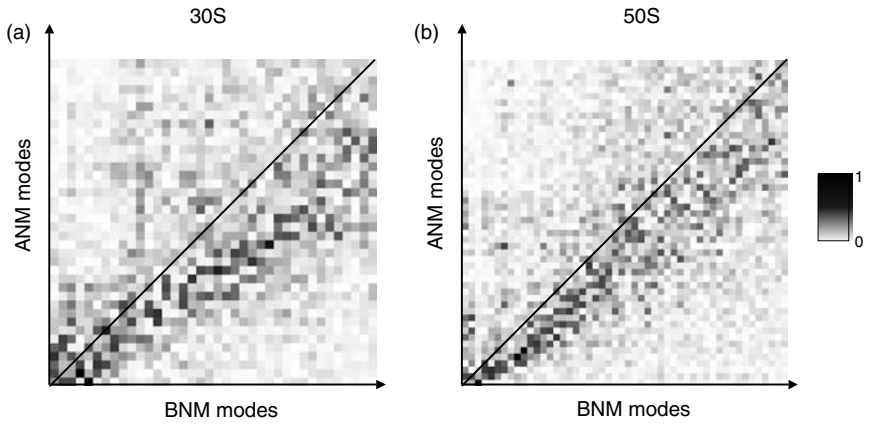

FIGURE 4.8
(See color insert following page 136) Overlap between BNM and ANM eigenvectors for (a) 30S and (b) 50S ribosome subunits.

4.4 Conclusions and Future Perspectives

Two very different methods for computing specific normal modes of interest in biomolecules have been discussed and illustrated with examples. Due to the drastic difference in the nature and frequency of the vibrations, different levels of approximations are appropriate. For computing localized vibrational frequencies, which are useful for characterizing the structural feature of the active site of enzymes, sophisticated treatment of the chromophore electronic structure is important while the environment can be treated more approximately; this gives rise to the QM/MM framework for computing local spectroscopic signature of biomolecules [23]. For analyzing delocalized low-frequency modes, which represent collective flexibility of large biomolecules or biomolecular assemblies, the NMA can be significantly coarse-grained by either reducing the dimension (or resolution) of motion (as in the block NMA [36] or the RTB method [35]) or reducing the resolution of both the potential and motion (as in the elastic network model [40, 41]). Determining whether the coarse-graining procedure is robust or not depends somewhat on the amount of interest and system under study. For large systems of globular shape, previous and current studies suggest that a high degree of coarse-graining, such as in the elastic network model, is useful for describing the overall flexibility. For systems of less globular structure, by contrast, the BNM method that relies on physical interactions is more robust [86]. With the improvements in numerical algorithms, there is essentially no limitation in BNM calculations, provided that a high-resolution structure is available; for low-resolution models, the elastic network model is clearly the only choice.

In terms of future developments, both areas discussed here have plenty of potential. In the QM/MM area, much effort is needed to investigate the appropriate QM size and level for quantitative spectroscopic assignments, in terms of both frequency and intensity. Finding the most efficient protocol to couple such calculations with molecular dynamics simulations would be important for accurate interpretation of nonlinear spectroscopies [16, 87], which are under rapid developments that hold the promise of dramatic improvements in the time resolution for probing biomolecular dynamics. In the study of low-frequency modes, the most exciting possibility concerns using such modes as a basis set to predict unknown conformation of different ligation states (e.g., calcium binding or phosphorylation). Some progress has been made in the context of structure reconstruction based on EM density maps [88], and similar developments can be anticipated with other low-resolution experimental information such as small-angle x-ray scattering [89] or fluorescence-resonance energy transfer (FRET) [90, 91]. Coupled with powerful structural prediction tools [92], meaningful model structures might be generated even in the absence of experimental data, which can serve as powerful guide for the design of future experimental investigations.

Acknowledgments

A.V.W. acknowledges support from the National Science Foundation for a predoctoral fellowship. Q.C. acknowledges support in this area of research from the start-up funding provided by the University of Wisconsin-Madison and a Research Innovation Award from the Research Corporation. Q.C. is an Alfred P. Sloan Research Fellow.

References

1. E.B.J. Wilson, J.C. Decius, and P.C. Cross, *Molecular Vibrations*. New York: Dover Publications, Inc., 1955.
2. C.L. Brooks III, M. Karplus, and B.M. Pettitt, Proteins: a theoretical perspective of dynamics, structure, & thermodynamics. *Adv. Chem. Phys.* 1988; **LXXI**.
3. N.W. Ashcroft and N.D. Mermin, *Solid State Physics*. New York: Hartcourt Brace College Publishers, 1976.
4. B.T.M. Willis and A.W. Pryor, *Thermal Vibrations in Crystallography*. 1975, Cambridge: Cambridge University Press, 1975.
5. B.R. Brooks, D. Janezic, and M. Karplus, Harmonic analysis of large systems: I. Methodology. *J. Comput. Chem.*, 1995; **16**: 1522–1542.

6. N. Go, T. Noguti, and T. Nishkawa, Dynamics of a small globular protein in terms of low-frequency vibrational modes. *Proc. Natl Acad. Sci. USA,* 1983; **80**: 3696–3700.
7. J.A. McCammon et al., The hinge-bending mode in lysozyme. *Nature,* 1976. **262**: 325–326.
8. M. Levitt, C. Sander, and P.S. Stern, Protein normal mode dynamics: trypsin inhibitor, crambin, ribonuclease and lysozyme. *J. Mol. Biol.,* 1985. **181**: 423–447.
9. G. Lamm and A. Szabo, Langevin modes of macromolecules. *J. Chem. Phys.,* 1986. **85**: 7334–7348.
10. J. Ma and M. Karplus, The allosteric mechanism of the chaperonin GroEL: a dynamic analysis. *Proc. Natl Acad. Sci. USA,* 1998. **95**: 8502–8507.
11. F. Tama and Y. Sanejouand, Conformational change of proteins arising from normal mode calculations. *Protein Eng.,* 2001. **14**: 1–6.
12. G. Li and Q. Cui, Analysis of the functional motions in "Brownian molecular machines" with an efficient block normal mode approach. *Biophys. J.,* 2004. **86**: 743–763.
13. Q. Cui et al., A normal mode analysis of structural plasticity in the biomolecular motor F1-ATPase. *J. Mol. Biol.,* 2004. **340**: 345–372.
14. J.R. Ferraro et al., *Introductory Raman Spectroscopy*. 2002, New York: Academic Press.
15. R. Petry, M. Schmitt, and J. Popp, Raman spectroscopy — a prospective tool in the life sciences. *Chem. Phys. Chem.,* 2003. **4**: 14–30.
16. S. Mukamel, *Principles of Nonlinear Optical Spectroscopy*. 1995, New York: Oxford University Press.
17. J. Åqvist and A. Warshel, Simulation of enzyme reactions using valence-bond force-fields and other hybrid quantum-classical approaches. *Chem. Rev.,* 1993. **93**: 2523.
18. M.J. Field, P.A. Bash, and M. Karplus, A combined quantum mechanical and molecular mechanical potential for molecular dynamics simulations. *J. Comput. Chem.,* 1990. **11**: 700–733.
19. J. Gao, Hybrid quantum and molecular mechanical simulations: an alternative avenue to solvent effects in organic chemistry. *Acc. Chem. Res.,* 1996. **29**: 298–305.
20. Q. Cui and M. Karplus, Catalysis and specificity in enzymes: a study of triosephosphate isomerase (TIM) and comparison with methylglyoxal synthase (MGS). *Adv. Protein Chem.,* 2003. **60**: 315–372.
21. J. Gao and D.G. Truhlar, Quantum mechanical methods for enzyme kinetics. *Annu. Rev. Phys. Chem.,* 2002. **53**: 467–505.
22. A. Warshel, Computer simulations of enzyme catalysis: methods, progress and insights. *Annu. Rev. Biophys. Biomol. Struct.,* 2003. **32**: 425–443.
23. Q. Cui and M. Karplus, Molecular properties from combined QM/MM methods. I. Analytical second derivative and vibrational calculations. *J. Chem. Phys.,* 2000. **112**: 1133.
24. M. Nonella, G. Mathias, and P. Tavan, Infrared spectrum of p-benzoquinone in water obtained from a QM/MM hybrid molecular dynamics simulation. *J. Phys. Chem.* A, 2003. **107**: 8638–8647.
25. M. Nonella et al., Structures and vibrational frequencies of the quinones in Rb. sphaeroides derived by a combined density functional/molecular mechanics approach. *J. Phys. Chem.* B, 2003; **107**: 316–322.

26. M. Klahn et al., IR spectra of phosphate ions in aqueous solution: predictions of a DFT/MM approach compared with observations. *J. Phys. Chem.* A, 2004. **108**: 6186–6194.
27. K. Speranskily and M. Kurnikova, Accurate theoretical prediction of vibrational frequencies in an inhomogeneous dynamic environment: a case study of a glutamate molecule in water solution and in a protein-bound form. *J. Chem. Phys.*, 2004. **121**: 1516–1524.
28. H. Li and J.H. Jensen, Partial Hessian vibrational analysis: the localization of the molecular vibrational energy and entropy. *Theo. Chem. Acc.*, 2002. **107**: 211–219.
29. J.A. Pople et al., Derivative studies in Hantrce-Fock and Moller–Plesset Theories. *Int. J. Quant. Chem.*, 1979. **S13**: 255.
30. Y. Yamaguchi et al., *A New Dimension to Quantum Chemistry, Analytical Derivative Methods in ab initio Molecular Electronic Structure Theory*. 1994, Oxford: Oxford University Press.
31. J.E.B. Wilson, J.C. Decius, and P.C. Cross, *Molecular Vibrations*. 1980, New York: Dover Publications, Inc.
32. M.S. Gordon et al., The effective fragment potential method: a QM-based MM approach to modeling environmental effects in chemistry. *J. Phys. Chem.* A, 2001. **105**: 293–307.
33. A.K. Kidera et al., Normal mode refinement: crystallographic refinement of protein dynamic structure: II. Application to human lysozyme. *J. Mol. Biol.*, 1992. **225**: 477–486.
34. D.A. Case, Normal-mode analysis of protein dynamics. *Curr. Opin. Struct. Biol.*, 1994. **4**: 285–290.
35. F. Tama et al., Building block approach for determining low-frequency normal modes of macromolecules. *Proteins: Struct. Funct. Genet.*, 2000. **41**: 1–7.
36. G. Li and Q. Cui, A coarse-grained normal mode approach for macromolecules: an efficient implementation and application to Ca2+-ATPase. *Biophys. J.*, 2002. **83**: 2457–2474.
37. J.K. Cullum and R.A. Willoughby, *Lanczos Algorithms for Large Symmetric Eigenvalue Computations*. 1985, Boston: Birkhauser.
38. C. Lanczos, An iteration method for the solution of the eigenvalue problem of linear differential and integral operations. *J. Res. Natl Bur. Stand.*, 1950. **45**: p. 255.
39. K.J. Maschhoff and D.C. Sorensen, A portable implementation of arpack for distributed memory parallel computers, in *Preliminary Proceedings of the Copper Mountain Conference on Iterative Methods*. 1996.
40. M.M. Tirion, Large amplitude elastic motions in proteins from a single-parameter, atomic analysis. *Phys. Rev. Lett.*, 1996. **77**: 1905–1908.
41. A.R. Atilgan et al., Anisotropy of fluctuation dynamics of proteins with an elastic network model. *Biophys. J.*, 2002. **80**: 505–515.
42. D. Ming et al., Substructure synthesis method for simulating large molecular complexes. *Proc. Natl Acad. Sci. USA*, 2003. **100**: 104–109.
43. B.A. Springer et al., *Mechanisms of ligand recognition in myoglobin. Chem. Rev.*, 1994. **94**: 699–714.
44. J.P. Collman et al., Nature of O_2 and CO binding to metalloporphyrines and heme proteins. *Proc. Natl Acad. Sci. USA*, 1976. **73**: 3333–3337.
45. J. Kuriyan et al., X-ray structure and refinement of carbon-monoxy (Fe-II) myoglobin at 1.5 Å resolution. *J. Mol. Biol.*, 1986. **192**: 133–154.
46. M.L. Quillin et al., High-resolution crystal structures of distal histidine mutants of sperm whale myoglobin. *J. Biol. Chem.*, 1993. **234**: 140–155.

47. M. Lim, T.A. Jackson, and P.A. Anfinrud, Binding of CO to myoglobin from a heme pocket docking site to form nearly linear Fe–CO. *Science,* 1995. **269**: 962–966.
48. D. Ivanov et al., Determination of CO orientation in myoglobin by single-crystal infrared linear dichroism. *J. Am. Chem. Soc.,* 1994. **116**: 4139–4140.
49. T.M. McMahon et al., An experimental and quantum chemical investigation of CO binding to heme proteins and model systems: a unified model based on C-13, O-17, and Fe-57 nuclear magnetic resonance and Fe-57 Mossbauer and infrared spectroscopies. *J. Am. Chem. Soc.,* 1998. **120**: 4784–4797.
50. X. Li and T.G. Spiro, Is bound CO linear or bent in heme-proteins — evidence from resonance Raman and infrared spectroscopic data. *J. Am. Chem. Soc.,* 1988. **110**: 6024–6033.
51. S. Hu, K.M. Vogel, and T.G. Spiro, Deformability of heme protein CO adducts — FT-IR assignment of the FeCO bending mode. *J. Am. Chem. Soc.,* 1994. **116**: 11187–11188.
52. S. Hu, K.M. Smith, and T.G. Spiro, Assignment of protoheme resonance Raman spectrum by heme labeling in myoglobin. *J. Am. Chem. Soc.,* 1996. **118**: 12638–12646.
53. T.G. Spiro and P.M. Kozlowski, Will the real FeCO please stand up? *J. Biol. Inorg. Chem.,* 1997. **2**: 516–520.
54. T.G. Spiro and P.M. Kozlowski, Discordant results on FeCO deformability in heme proteins reconciled by density functional theory. *J. Am. Chem. Soc.,* 1998. **120**: 4524–4525.
55. T. Vangberg, D.F. Bocian, and A. Ghosh, Deformability of Fe(II)CO and Fe(III)CN groups in heme protein models: nonlocal density functional theory calculations. *J. Biol. Inorg. Chem.,* 1997. **2**: 526–530.
56. A. Ghosh and D.F. Bocian, The CO tilting and bending potential energy surface of carbon monoxyhemes. *J. Phys. Chem.,* 1996. **100**: 6363–6367.
57. P. Jewsbury et al., The proximal residue largely determines the CO distortion in carbon monoxy globin proteins — an ab initio study of a heme prosthetic unit. *J. Phys. Chem.,* 1995. **99**: 12677–12685.
58. G.S. Kachalova, A.N. Popov, and J.D. Bartunik, A steric mechanism for inhibition of CO binding to heme proteins. *Science,* 1999. **284**: 473–476.
59. T. Li, M.L. Quillin, and G.N.J. Phillips, Structural determinants of the stretching frequency of CO bound to myoglobin. *Biochemistry,* 1994. **33**: 1433–1446.
60. K.D. Rector et al., Mutant and wild type myoglobin–CO protein dynamics: vibrational echo experiments. *J. Phys. Chem.* B, 1997. **101**: 1468–1475.
61. C.W. Rella et al., Vibrational echo studies of myoglobin–CO. *J. Phys. Chem.,* 1996. **100**: 15620–15629.
62. E.S. Park et al., Vibrational stark spectroscopy in proteins: a probe and calibration for electrostatic fields. *J. Phys. Chem.* B, 1999. **103**: 9813–9817.
63. T.G. Spiro, M.Z. Zgierski, and P.M. Kozlowski, Stereoelectronic factors in CO, NO, and O2 binding to heme from vibrational spectroscopy and DFT analysis. *Coord. Chem. Rev.,* 2001. **219**: 923–936.
64. T.G. Spiro and P.M. Kozlowski, Is the CO adduct of myoglobin bent, and does it matter? *Acc. Chem. Res.,* 2001. **34**: 137–144.
65. J.S. Olson and G.N.J. Phillips, Myoglobin discriminates between O_2, NO, and CO by electrostatic interactions with the bound ligands. *J. Biol. Inorg. Chem.,* 1997. **2**: 544–552.

66. C. Rajani and J.R. Kincaid, Resonance Raman studies of hemoglobin with selectively deuterated hemes. A new perspective on the controversial assignment of the Fe–CO bening mode. *J. Am. Chem. Soc.,* 1998. **120**: 7278–7285.
67. W.G. Scott et al., Capturing the structure of a catalytic RNA intermediate. *Science,* 1996. **274**: 2065.
68. A. Peracchi et al., Involvement of a specific metal ion in the transition of the hammerhead ribozyme to its catalytic conformation. *J. Biol. Chem.,* 1997. **272**: 26822–26826.
69. A. Peracchi et al., A core folding model for catalysis by the hammerhead ribozyme accounts for its extraordinary sensitivity to abasic mutations. *Biochemistry*, 1998. **37**: 14765–14775.
70. C.M. Dunham, J.B. Murray, and W.G. Scott, A helical twist-induced conformational switch activates cleavage in the hammerhead ribozyme. *J. Mol. Biol.,* 2003. **332**: 327.
71. K. Yoshinari and K. Taira, A further investigation and reappraisal of the thiol effect in the cleavage reaction catalyzed by a hammerhead ribozyme. *Nucleic Acids Res.,* 2000. **28**: 1730–1742.
72. K. Suzumura et al., A reappraisal, based on 31P NMR, of the direct coordination of a metal ion with the phosphoryl oxygen at the cleavage site of a hammerhead ribozyme. *J. Am. Chem. Soc.,* 2002. **124**: 8230–8236.
73. Y. Tanaka et al., Nature of the chemical bond formed with the structural metal ion at the A9/G10.1 motif derived from hammerhead ribozyme. *J. Am. Chem. Soc.,* 2004. **126**: 744–752.
74. N. Foloppe and J.A.D. MacKerell, All-atom empirical force field for nucleic acids: 2.) Parameter optimization based on small molecule and condensed phase macromolecular target data. *J. Comput. Chem.,* 2001. **21**: 86–104.
75. T. Lazaridis and M. Karplus, Effective energy function for proteins in solution. *Proteins: Struct. Funct. Genet.,* 1999. **35**: 133.
76. T. Lazaridis and M. Karplus, Effective energy functions for protein structure prediction. *Curr. Opin. Struct. Biol.,* 2000. **10**: 139–145.
77. N. Ban et al., The complete atomic structure of the large ribosomal subunit at 2.4 Å resolution. *Science,* 2000. **289**: 905–920.
78. P.B. Moore and T.A. Steitz, The structural basis of large ribosomal subunit function. *Annu. Rev. Biochem.,* 2003. **72**: 813–850.
79. B.T. Wimberly et al., Structure of the 30S ribosomal subunit. *Nature,* 2000. **407**: 327–339.
80. F. Schluenzen et al., Structure of functionally activated small ribosomal subunit at 3.3. Å resolution. *Cell,* 2000. **102**: 615–623.
81. J. Frank, Single-particle imaging of macromolecules by cryo-electron microscopy. *Annu. Rev. Biophys. Biomol. Struct.,* 2002. **31**: 303–319.
82. F. Tama et al., Dynamic reorganization of the functionally active ribosome explored by normal mode analysis and cryo-electron microscopy. *Proc. Natl Acad. Sci. USA,* 2003. **100**: 9319–9323.
83. Y.M. Wang et al., Global ribosome motions revealed with elastic network model. *J. Struct. Biol.,* 2004. **147**: 302–314.
84. H. Stark et al., Large-scale movement of elongation factor G and extensive conformational change of the ribosome during translocation. *Cell,* 2000. **100**: 301–309.
85. R.K. Agrawal and J. Frank, Structural studies of the translational apparatus. *Curr. Opin. Struct. Biol.,* 1999. **9**: 215–221.

86. A. van Wynsberghe, G. Li, and Q. Cui, Normal mode analysis suggests protein flexibility modulation throughout RNA polymerase's functional cycle. *Biochemistry*, 2004. **43**: 13083–13096.
87. K.A. Merchant et al., Myoglobin-CO substate structures and dynamics: multidimensional vibrational echoes and molecular dynamics simulations. *J. Am. Chem. Soc.*, 2003. **125**: 13804–13818.
88. W. Wriggers and P. Chacon, Modeling tricks and fitting techniques for multiresolution structures. *Structure*, 2001. **9**: 779–788.
89. S. Doniach, Changes in biomolecular conformation seen by small angle x-ray scattering. *Chem. Rev.*, 2001. **101**: 1763–1778.
90. X.W. Zhuang and M. Rief, Single-molecule folding. *Curr. Opin. Struct. Biol.*, 2003. **13**: 88–97.
91. D. Rueda et al., Single-molecule enzymology of RNA: essential functional groups impact catalysis from a distance. *Proc. Natl Acad. Sci. USA*, 2004. **101**: 10066–10071.
92. M.P. Jacobson et al., A hierarchical approach to all-atom protein loop prediction. *Proteins: Struct. Funct. Bioinf.*, 2004. **55**: 351–367.

5

Functional Information from Slow Mode Shapes

Yves-Henri Sanejouand

CONTENTS

5.1 Introduction

The idea that protein functional motions can be well described with a few slow normal modes *only*, probably originates from the seminal study of hen-egg lysozyme hinge-bending motion, by Martin Karplus and coworkers, 30 years ago [1]. Indeed, after the calculation of an adiabatic potential for the angle-bending, found to be approximately parabolic, these authors treated the relative motion of the two structural domains as an angular harmonic oscillator composed of two rigid spheres with moments of inertia corresponding to those of the domains. A vibrational frequency of 4.3 cm^{-1} was obtained, quite close to the lowest-frequency value found afterward, when standard normal mode analysis (NMA) was performed [2,3].

Then, approximate low-frequency (slow) normal modes were obtained in the case of the quite large yeast hexokinase enzyme (nearly 450 amino-acids), using the Raleigh–Ritz method, and compared to the conformational change observed upon inhibitor binding. It was noticed that two of them had strong components along the conformational change [4].

Later on, such a relationship between protein functional motion and slow mode shapes was also observed for proteins whose structural domains (in particular, their limits) cannot be determined easily, like those of citrate synthase [5]. Notably, as one of the more striking examples, it was found that the second lowest-frequency mode of the T-form of hemoglobin is enough for describing two-third of the transition between T- and R-forms [6, 7].

The fact that a protein motion with a high "collective" character, that is, a motion in which many atoms are involved, can be accurately described with a subset of low-frequency modes is not a surprising result because the corresponding (normal) coordinates themselves have such collective character. However, the fact that one, or a few, of them may prove enough for obtaining a fair description of a conformational change was not a priori expected.

For instance, from a physical point of view, the energy function used to compute protein normal modes is an approximate one, and frequency values would be significantly different, if it were possible to compute them at *ab initio* levels. Moreover, low-frequency parts of protein normal mode spectra are usually not characterized by clear gaps. More generally, NMA is based on a small displacements approximation, which amounts to suppose that a protein behaves like a solid does at low temperature, although it is well known that a protein is a somewhat flexible polymer, undergoing many local conformational transitions at room temperature. Furthermore, from a biological point of view, proteins are known to fold and function in a water environment, within a narrow range of pH, temperature, ionic strength, etc., whereas standard NMA is performed *in vacuo*. As a matter of fact, it requires a preliminary energy minimization, which drifts the atoms of the protein up to several Ångstroms away from their positions in the crystallographic structure. As a consequence, the structure studied with standard NMA is a distorted one. Note that, nowadays, this later point can be partly disregarded, thanks to the development of implicit solvent models, like EEF1 [8] or ACE [9, 10], within the frame of the generalized Born approximation. Indeed, some normal mode studies are now being performed with such a kind of description for protein–water interactions [11].

However, recent results have shed some light on this paradox. Notably, it was shown that using a single parameter Hookean potential for taking into account pairwise interactions between neighboring atoms, the so-called elastic network model (ENM) [12–14], yields results in good agreement with those obtained when NMA is performed with standard semi-empirical potentials, as far as low-frequency normal modes are concerned [15–17].

The purpose of the present contribution is to compare protein functional motions and slow mode shapes, as they are obtained with standard NMA or with various, less detailed, approaches, including ENM. Hereafter,

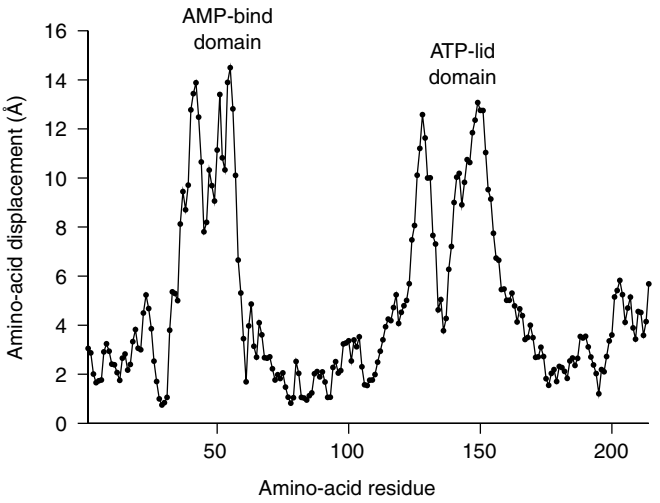

FIGURE 5.1
The conformational change of adenylate kinase upon ligand binding.

approximate methods are described and two cases studied previously [12, 18, 19] are considered in more depth, namely Adenylate Kinase (AdK) and dihydrofolate reductase (DHFR).

5.2 Conformational Change of AdK Arising from NMA

5.2.1 Standard Normal Mode Calculation

Adenylate kinase is a "classic" three-domain enzyme [20]. Upon binding of AdK substrates, ATP and AMP, large-amplitude motions (up to 15 Å; see Figure 5.1) of the two small "AMP-bind" (residues 31 to 72) and "ATP-lid" (residues 119 to 156) structural domains allow for the closure of the active site, as shown in Figure 5.2 in the case of *Escherichia Coli* structures (PDB codes 4AKE and 1ANK).

Standard NMA was done as follows, starting from the "open" form of AdK (Figure 5.2[a]). First, an extensive energy minimization was performed, with the CHARMM package [22], version 27, using extended atoms, the PARAM19 force-field, a distance-dependent dielectric constant, and a 9 Å cutoff for electrostatic interactions. The minimization process was stopped at a gradient root-mean-square (RMS) of 10^{-6} kcal/(mole Å), after nearly 20,000 adopted basis Newton–Raphson (ABNR) steps. At this point, the C_α-RMS deviation from the crystal structure is significant: 1.9 Å. Next, using the VIBRAN module of CHARMM, **F**, the Hessian, that is, the mass-weighted second derivatives of the potential energy matrix, was diagonalized. Because in this case the matrix is not large (matrix order is $3N = 6093$), the standard

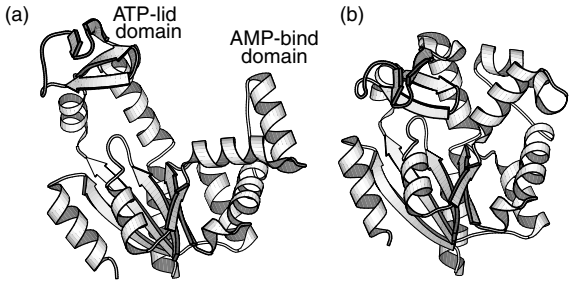

FIGURE 5.2
AdK open (a) and closed (b) conformations, drawn with Molscript [21].

DIAGQ routine available in CHARMM was used [23]. Among the six "zero-frequency" values found, corresponding to the overall translations and rotations of the whole protein, the largest one is close to expected numerical limits, namely 0.0035 cm^{-1}. This means that the minimization process was efficient enough.

5.2.2 Comparison with the Conformational Change

In order to quantify how well a conformational change is described by normal mode j, one can calculate I_j, the scalar product (overlap) between $\mathbf{\Delta x} = \{\Delta x_1, \ldots, \Delta x_k, \ldots, \Delta x_{3N}\}$, the conformational change observed by crystallographers, and $\mathbf{y_j} = \{y_{1j}, \ldots, y_{kj}, \ldots, y_{3Nj}\}$, the jth normal mode of the protein. This is a measure of the similarity between the direction of the conformational change and the one given by mode j. It is obtained as follows [5]:

$$I_j = \mathbf{\Delta x} \cdot \mathbf{y_j} = \frac{\sum \Delta x_k y_{kj}}{\sqrt{\sum \Delta x_k^2}} \tag{5.1}$$

where $\Delta x_k = x_k^{\mathrm{o}} - x_k^{\mathrm{c}}$, x_k^{o} and x_k^{c} are, respectively, the kth atomic coordinate of the protein in the open crystallographic structure and in the closed one. A value of ± 1 for the overlap ($\mathbf{y_j}$ is normalized) means that the direction given by $\mathbf{y_j}$ is identical to $\mathbf{\Delta x}$. From a practical point of view, $\mathbf{\Delta x}$ is calculated after both crystallographic conformations of the protein are superimposed, using standard fitting procedures. Note that Q_{d}, the quality of the motion description, calculated as:

$$Q_{\mathrm{d}} = 100 \sum_{j=1}^{n} I_j^2 \tag{5.2}$$

is equal to 100% when $n = 3N$, that is, when all modes are taken into account, since the $3N$ modes form a complete basis set [24].

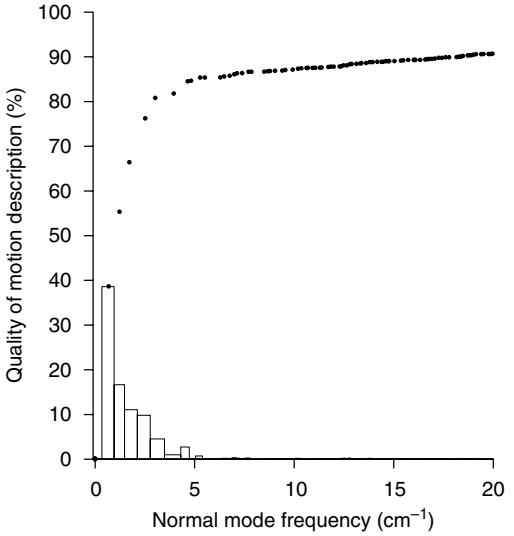

FIGURE 5.3
Description of AdK conformational change with standard normal modes.

In Figure 5.3, Q_d is given for the AdK conformational change shown in Figure 5.2, when more and more low-frequency modes of the open form are added to the description (black circles). The contribution of each normal mode is also shown (white boxes). Note that a single normal mode, the one with lowest frequency ($\nu = 0.68$ cm^{-1}), is enough for describing nearly 40% of the conformational change, whereas the five with lowest frequency modes allow for the description of more than 80% of this motion. Of course, the six zero-frequency modes do not contribute to the description, because overall rigid body motions are removed when the least-square fit of the closed form with respect to the open form is performed.

5.2.3 Effective Number of Modes Required for the Description

In order to determine n_{eff}, the minimum number of modes that are sufficient for accurately describing a conformational change, one can try to evaluate the information contained in the I_j^2s, as follows (a related, recently proposed, quantity was coined "mode concentration" [25]):

$$\log(n_{\text{eff}}) = -\sum^{n} I_j'^2 \log(I_j'^2) \tag{5.3}$$

where

$$I_j'^2 = \frac{I_j^2}{\sum^n I_j^2}$$

The above normalization means that the n low-frequency normal modes considered are supposed to yield the best possible description of the conformational change. In the case of the AdK conformational change, when $n = 3N = 6093$, $n_{\text{eff}} = 14.8$, whereas when $n = 90$, that is, when all modes considered in Figure 5.3 are taken into account, $n_{\text{eff}} = 6.9$. The difference comes from the fact that many modes contribute somehow to the description of the 10% of the conformational change that are not described by the 90 modes with the lowest frequency. Note that 6 to 8 modes describe more than a few percentages of the conformational change each (see Figure 5.3), a figure in good agreement with the latter evaluation of n_{eff}.

5.2.4 RTB Approximation

Owing to its size, diagonalizing the Hessian can be the technically limiting step. Indeed, though the NMA of the small, 58 amino-acids, BPTI protein was performed as early as 1982 [26], 10 years later the largest protein studied at the atomic level of description was still myoglobin, with 153 amino-acids [27], although most interesting proteins are much larger. Since then, efficient algorithms were designed (e.g., DIMB [28]) or adapted to the case of macromolecular assemblies (e.g., the block Lanczos approach [5]) in order to compute the lowest-frequency normal modes, that is, the most informative ones.

Instead of diagonalizing the Hessian, $\mathbf{F}$, as in standard NMA, the principle of the RTB approximation (RTB stands for rotation–translation of blocks) is to diagonalize $\mathbf{F}_{\text{b}}$, a smaller $6n_{\text{b}} \times 6n_{\text{b}}$ matrix defined as follows [18, 29, 30]:

$$\mathbf{F}_{\text{b}} = \mathbf{P}^{\text{t}}\mathbf{F}\mathbf{P} \tag{5.4}$$

where $\mathbf{P}$ is an orthogonal $3N \times 6n_{\text{b}}$ projection matrix built with the vectors describing the six rigid-body rotations and translations of each of the n_{b} blocks the protein is split into. For instance, each block can contain a single amino-acid residue. $\mathbf{U}_{\text{p}}$, the $3N \times 6n_{\text{b}}$ matrix with the $6n_{\text{b}}$ approximate lowest-frequency normal modes of the protein, is then obtained as follows:

$$\mathbf{U}_{\text{p}} = \mathbf{P}\mathbf{U}_{\text{b}}$$

where $\mathbf{U}_{\text{b}}$ is the matrix diagonalizing $\mathbf{F}_{\text{b}}$, $\mathbf{U}_{\text{b}}$ being obtained with standard diagonalization techniques. DIAGRTB, the corresponding Fortran program is available on the web (http://ecole.modelisation.free.fr/modes.html). An efficient, more general, implementation, called BNM (standing for Block Normal Modes) [30], where each block can be treated as a flexible body, in the spirit of dynamical models of the MB(O)ND family [31, 32], is also available in CHARMM [22], since version 32. Note that approximate modes thus obtained can then be refined, for instance, using the effective Hamiltonian theory, as originally proposed [29]. However, as far as slow mode shapes are concerned,

approximate modes are usually so close to exact modes [18, 29] that it is not worth the extra computational cost.

As a matter of fact, the RTB approximation allows for quick calculations of the lowest-frequency modes of large systems described at atomic level [18]. Indeed, when two residues are placed in each block, $\mathbf{F}_\mathrm{b}$ is a $3N_\mathrm{r} \times 3N_\mathrm{r}$ matrix, where N_r is the number of residues. So, it has the same size as matrices diagonalized within the frame of methods based on simplified protein representations, when only C_α atoms are taken into account [12, 13, 17]. When six residues are placed in each block, $\mathbf{F}_\mathrm{b}$ is a $N_\mathrm{r} \times N_\mathrm{r}$ matrix, that is, it has the same size as contact matrices diagonalized within the frame of the fastest method allowing for *B*-factors calculation [16].

Of course, the RTB approximation can only be used for calculating modes in which the so-defined blocks behave almost rigidly. Even in that case, calculated frequencies are found to be higher than exact ones, reflecting the fact that atoms belonging to a given block cannot relax so as to lower the energetical cost of the normal mode motion. However, for frequencies lesser than 40 cm^{-1}, at least when one amino-acid is put in each block, a linear relationship between approximate and exact frequencies holds, that is,

$$\nu_\mathrm{rtb} = d_\mathrm{p} \cdot \nu_\mathrm{s}$$

where ν_s and ν_rtb are frequencies obtained using, respectively, standard approaches or the RTB approximation. In the case of a set of proteins of various sizes, using CHARMM force-field [22] and an 8.5 Å cutoff for electrostatic interactions, it was found that d_p does not depend upon protein size or fold type ($d_\mathrm{p} = 1.7 \pm 0.1$) [18]. This enables us to get fair estimates for exact frequencies, once the approximate ones are known. Note that d_p seems to increase linearly, as a function of the number of amino-acid residues put in each block. Indeed, d_p is nearly equal to 1.7, 2.1, 2.4, and 3.0, when each block contains 1, 2, 3, or 5 residues, respectively. However, in the later case, the linear relationship between ν_s and ν_rtb only holds for frequencies below 15 to 20 cm^{-1} [18]. Note also that d_p depends little upon the details of the electrostatic potential. In the present study of AdK normal modes, where a 9.0 Å cutoff and a distance-dependant dielectric constant are used, d_p is found equal to 1.8 and 3.2, respectively, when each block contains one or five residues.

In Figure 5.4, Q_d, the quality of the motion description (see Equation 5.2), is given for each standard normal mode of AdK when the 100 lowest-frequency approximate modes are taken into account in Equation 5.2 ($n = 100$), as they are calculated with the RTB approximation, with one (black squares) or five (white squares) residues per block (results are also shown when Tirion's modes are used for the description; see Section 5.2.5). With one residue per block, RTB low-frequency modes are able to describe more than 80% of each standard mode of frequency lower than 10 to 15 cm^{-1}. Similar results were obtained previously, in the case of the HIV-1 protease [18]. With five residues per block, the quality of the description drops significantly as the frequency

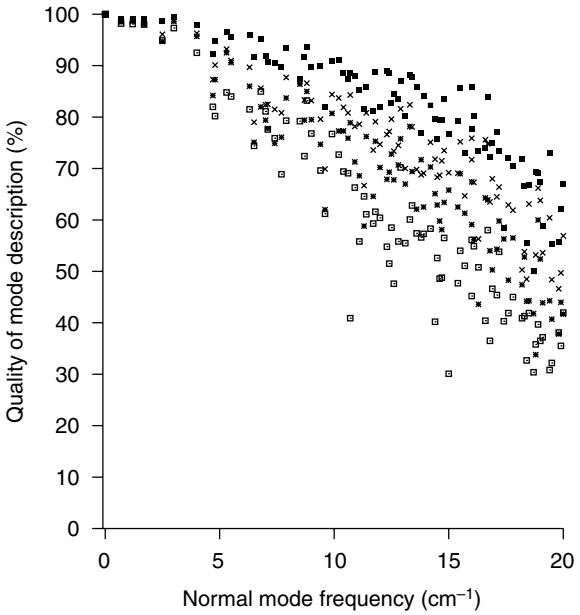

FIGURE 5.4
Quality of the description of each AdK normal mode with 100 approximate ones. Approximate low-frequency modes were calculated as follows: standard Hessian and the RTB approximation, with one (black squares) or five amino-acid residues per block (white squares); Tirion's Hessian (stars); Tirion's Hessian and the RTB approximation (crosses).

of the mode increases, except for the five lowest-frequency modes ($\nu = 0.68$, 1.23, 1.72, 2.52, and 3.02 cm^{-1}).

In Figure 5.5, n_{eff}, the effective number of modes required for the description (see Equation 5.3), is also given for each standard normal mode of AdK, when the 100 lowest-frequency approximate modes are taken into account in Equation 5.3 ($n = 100$), as they are calculated with the RTB approximation. Only the five lowest-frequency standard normal modes can be accurately described with less than five approximate modes. The sixth one ($\nu = 3.95$ cm^{-1}) is well described with $n_{\text{eff}} = 3.5$ modes calculated with the RTB approximation and one residue per block, but $n_{\text{eff}} = 13.8$ when the RTB approximation is used with five residues per block.

5.2.5 Tirion's Approach

Within the frame of the approach proposed by Tirion [15], the standard detailed potential energy function is replaced by

$$E_{\text{p}} = \sum_{d_{ij}^0 < R_{\text{c}}} C(d_{ij} - d_{ij}^0)^2 \tag{5.5}$$

where d_{ij} is the distance between atoms i and j, d_{ij}^0 being the distance between these two atoms in the studied structure. The strength of the potential C is a constant assumed to be the same for all interacting pairs. As such, it has to be set only in order to define energy (and frequency) units. Note that this energy function was designed so that for any chosen configuration the potential energy, E_p, is a minimum of the function ($E_p = 0$). Thus, with such an approach *par définition* NMA does not require any prior energy minimization.

Note also that in Equation 5.5 the sum is restricted to atom pairs separated by less than R_c, which is an arbitrary cutoff parameter. When, as proposed by Bahar et al., only C_α atoms are taken into account [16], a cutoff of 8 to 13 Å can be used [12, 13]. The corresponding ENM [12–14] (C_α-ENM) is enough to study backbone motions, since it proves sufficient for characterizing low-frequency normal modes of proteins. Moreover, it allows for studying proteins of large size on common workstations, using small amounts of CPU time, since, with such a simple model, the matrix to be diagonalized is a $3N_r \times 3N_r$ one. As a matter of fact, with such models, modes of systems as large as the whole ribosome have been calculated on desktop computers [33].

Using this kind of highly simplified potential, as with detailed modes, a few low-frequency normal modes are often found to yield a good description of protein functional motions, especially when the corresponding conformational change has a highly collective character [12, 14, 25]. Thus, results obtained with NMA in the field of low-frequency protein dynamics seem to be of a very good quality even when most atomic details are ignored.

In Figure 5.4 and Figure 5.5, respectively, Q_d, the quality of the motion description and n_{eff}, the effective number of modes required for an accurate description, are given for each standard normal mode of AdK when the 100 lowest-frequency approximate modes are taken into account in Equations 5.2 and 5.3 ($n = 100$), as they are calculated with Tirion's approach. For the sake of comparison, the structure considered is the open form of AdK studied with standard NMA, that is, the energy-minimized one. Here, $R_c = 5$ Å and, as initially proposed [15], all atoms are included in the model. First, the diagonalization of the corresponding Hessian is performed with standard techniques (stars). Next, the RTB approximation is used, with one residue per block (crosses). Note that this kind of calculation can now be performed through the Web, thanks to the ELNEMO Web site of Karsten Suhre (http://igs-server.cnrs-mrs.fr/elnemo/) [34, 35].

Interestingly, within the frame of Tirion's approach, the RTB approximation seems to improve the quality of the description of most, if not all, standard modes considered (see Figure 5.4 and Figure 5.5). This is not an unexpected result, because RTB adds informations to Tirion's model, about amino-acid sizes for instance, through the projection process (see Equation 5.4). Note that in the method originally proposed by Tirion, topological informations were also included in the model through the use of internal coordinates [15]. On the other hand, Tirion's modes yield better descriptions of standard modes than those obtained with detailed potentials, when the

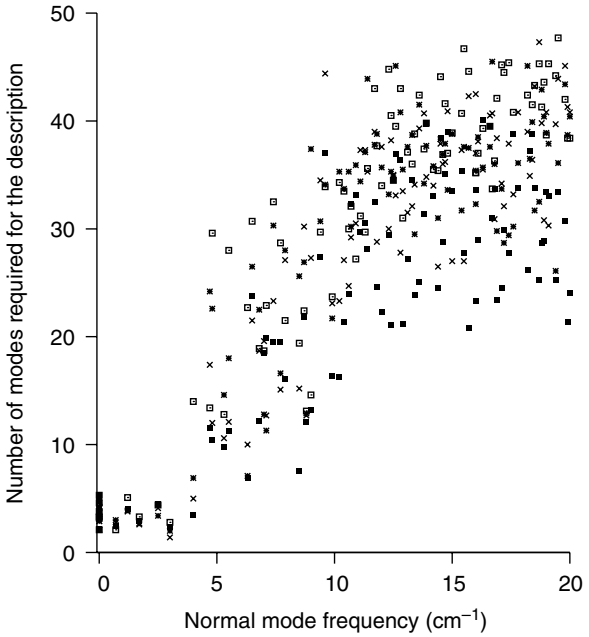

FIGURE 5.5
Minimum number of approximate modes required for an accurate description of each AdK normal mode. Approximate low-frequency modes were calculated as follows: standard Hessian and the RTB approximation, with one (black squares) or five amino-acid residues per block (white squares); Tirion's Hessian (stars); Tirion's Hessian and the RTB approximation (crosses).

latter are obtained with the RTB approximation and five residues per block (see Figure 5.4 and Figure 5.5).

However, with all four approximations, the five lowest-frequency standard normal modes of the open form of AdK are all found to be extremely well described (Q_d over 95%; see Figure 5.4), with a small effective number of approximate modes ($n_{eff} = 5$ or less; see Figure 5.5). This means that these modes are very robust and, specifically, that the subspace spanned by the five corresponding coordinates (the normal coordinates) is almost not perturbed when most atomic details are missing in the protein model. A similar conclusion was also reached in a study of large protein normal modes, through a hierarchy of coarse-grained models [36], as well as in a study using low-resolution structural data [19].

Such results support the idea that the few lowest-frequency modes depend mainly upon the shape of the protein, that is, upon the distribution of its masses in space. As expected, such modes can be described well in terms of relative motions of structural domains of the protein. Reciprocally, when the limits of the domains of a given protein are not obvious, they can be used in order to delineate the domains, as proposed by Hinsen [17].

TABLE 5.1

Quality of the Description of AdK Conformational Change with Low-Frequency Normal Modes, either Standard or Approximate Ones.

Structure	Method	Largest overlap (mode rank)	n_{eff}	Q_{d}(%)
Energy-minimized	Standard	−0.62 (#1)	6.9	91
Energy-minimized	Standard+RTB(1)	0.74 (#1)	4.4	91
Energy-minimized	Standard+RTB(5)	−0.71 (#1)	4.5	91
Energy-minimized	Tirion	−0.75 (#6)	4.8	91
Energy-minimized	Tirion+RTB(1)	−0.77 (#1)	4.3	92
Energy-minimized	C_α-ENM	−0.74 (#1)	4.9	96
Crystallographic	Tirion	0.81 (#9)	3.6	94
Crystallographic	Tirion+RTB(1)	−0.81 (#1)	3.6	95
Crystallographic	C_α-ENM	0.81 (#1)	3.8	97

The normal modes are calculated either for the energy-minimized structure obtained within the frame of the standard approach, or for the initial, crystallographic, structure of the open form. When the RTB approximation is used for diagonalizing the Hessian, the number of amino-acid residues put in each block is given between parentheses.

5.2.6 Description of the Conformational Change with Approximate Modes

In Table 5.1, a summary of the results obtained is given, when the AdK conformational change is compared to the 100 lowest-frequency normal modes obtained with the various methods described above.

Amazingly, results obtained with standard NMA, that is, with the more detailed protein model, are the less spectacular ones. Indeed, the mode that is most involved in the conformational change [37] has an overlap with the conformational change (see Equation 5.1) of −0.62, whereas it has more significant values when approximate modes are considered (up to 0.81). Moreover, the number of modes required for an accurate description of the conformational change, n_{eff} (see Equation 5.3), is significantly smaller when approximate methods are used (down to 3.6, instead of 6.9), whereas the quality of the description with the 100 lowest-frequency modes, Q_{d} (see Equation 5.2), is better (up to 97%, instead of 91%).

One major advantage of the family of methods based on Tirion's approach is that they enable calculating low-frequency modes of the crystallographic structure itself. As mentioned above, during the minimization process required within the frame of standard NMA, the open form of AdK drifts away from the crystal structure by 1.9 Å. As a matter of fact, better results are obtained when normal modes are calculated for the crystallographic structure (see Table 5.1). Note that, in this later case, as far as the description of the conformational change is concerned, the RTB approximation does not improve the modes obtained with Tirion's approach. However, it lowers the rank of the mode found to be the most involved in the conformational change. This is likely to be related to the following artifact, found when Tirion's approach

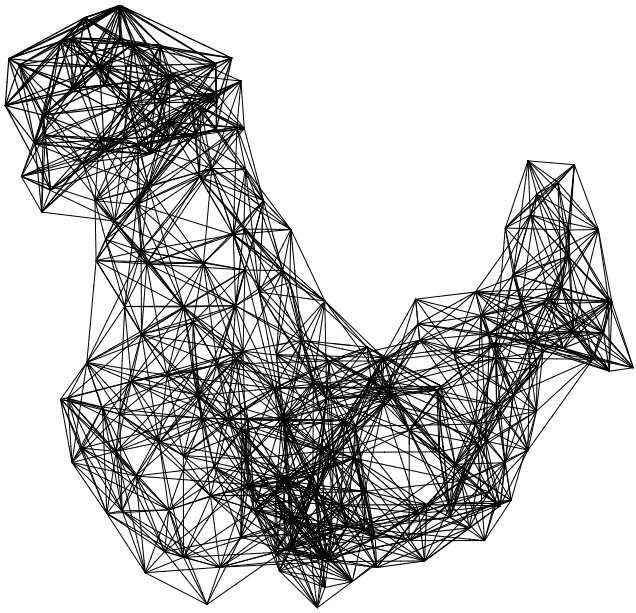

FIGURE 5.6
Elastic network model of the open form of AdK. Harmonic springs are established between C_α atoms less than 10 Å away from each other.

is used as is, namely, as described in Equation 5.5: when a light atom is linked to others by few harmonic springs, it can be found involved in a low-frequency, though localized, normal mode motion. Because when the RTB approximation is used this atom is included in a rigid body, namely, the block this atom is put into, it allows for getting rid of such artifactual low-frequency modes [38]. Note that such artifactual modes can also be obtained with C_α-ENM. Indeed, parts of the polypeptidic chain extending away from most other amino-acids can be observed in crystal structures, in particular at both N- and C-terminal ends. Being linked by few harmonic springs to the rest of the protein, they can also be found involved in the lowest-frequency normal modes calculated for the model. Note that if an atom or a group of atoms is not linked by at least three springs to the rest of the system, this artifact appears as a number of zero-frequency normal modes larger than six.

However, such artifacts are not observed in the case of AdK C_α-ENM, even when modes are calculated for the crystal structure of the open form (see Table 5.1). As a matter of fact, low-frequency modes obtained with the corresponding protein model, that is, without any atomic detail (see Figure 5.6, where $R_c = 10$ Å) yield one of the best descriptions obtained in the present study for the conformational change of AdK (see Figure 5.7, and compare it to Figure 5.3). Notably, a single mode, the lowest-frequency one, is found to be enough for describing 65% of the conformational change.

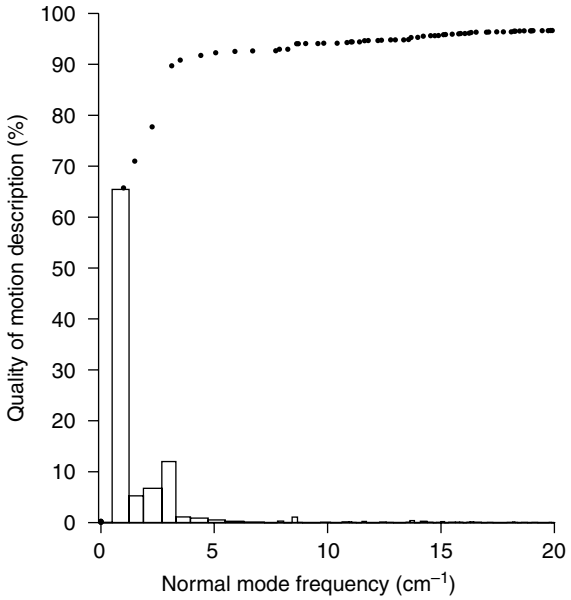

FIGURE 5.7
Description of AdK conformational change with C_α-ENM modes. C was adjusted, so that $\nu(\#1) = 1\ \mathrm{cm}^{-1}$.

This later result has a rather general character. Indeed, in a recent survey of a database [39] of more than 3800 protein motions found in the PDB, Gerstein et al. [25] showed that for nearly half of them a couple of C_α-ENM modes are enough for describing most of the motion.

5.3 Conformational Change of DHFR and NMA

Dihydrofolate reductase, a rather small, 159 amino-acid, protein is the target for the therapeutically important "anti-folate" drugs, such as methotrexate. A significant conformational change occurs when DHFR binds methotrexate [40]. Although changes are small (C_α-RMS $= 0.8$ Å), the motion has a collective character, as shown in Figure 5.8, where the distance between the open (PDB code 5DFR) and the closed (PDB code 4DFR) forms is given for each C_α, as a function of residue number.

All normal mode analyses performed in the case of AdK were also done in the case of the open form of DHFR. A summary of the results obtained when comparing the normal modes of DHFR with its conformational change is given in Table 5.2. As shown in Figure 5.9, low-frequency normal modes obtained with standard approaches do not allow a fair description of the conformational change of DHFR (compare with Figure 5.3 and Figure 5.7).

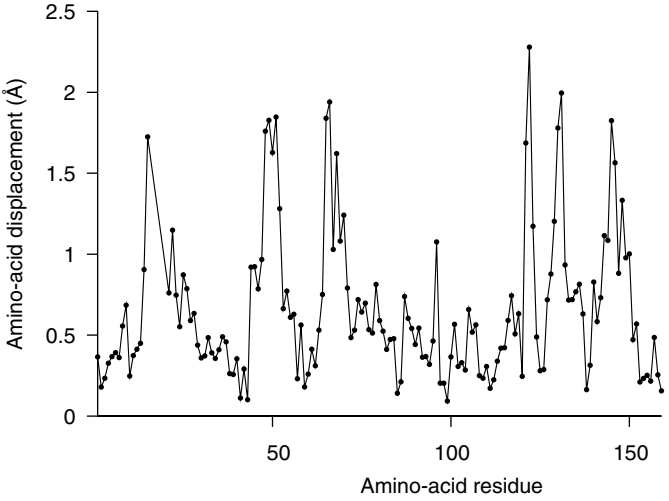

FIGURE 5.8
The conformational change of DHFR.

TABLE 5.2

Quality of the Description of DHFR Conformational Change with Low-Frequency Normal Modes, either Standard or Approximate Ones.

Structure	Method	Largest overlap (mode rank)	n_{eff}	Q_{d}(%)
Energy-minimized	Standard	−0.27 (#3)	32.2	52
Energy-minimized	Standard+RTB(1)	0.36 (#2)	23.9	55
Energy-minimized	Tirion	0.28 (#2)	32.2	46
Energy-minimized	Tirion + RTB(1)	−0.29 (#2)	36.7	52
Energy-minimized	C_α-ENM	0.48 (#1)	21.7	73
Crystallographic	Tirion	0.32 (#2)	20.3	29
Crystallographic	Tirion + RTB(1)	−0.32 (#1)	29.4	39
Crystallographic	C_α-ENM	−0.53 (#1)	8.8	51

The normal modes are calculated either for the energy-minimized structure obtained within the frame of the standard approach, or for the initial, crystallographic one of the open form.

In particular, no single mode is found to be enough for describing more than 7% of the motion. One reason for that could be that preliminary energy minimizations have distorted the structure a lot. Indeed, at the end of the process, the C_α-RMS deviation from the crystal structure is 1.0 Å, that is, a value similar to the C_α-RMS difference between the open and closed forms of DHFR (0.8 Å). When modes are calculated with Tirion's approach, either for the energy-minimized or for the crystal structure, they do not perform better. However, a clear improvment is observed with C_α-ENM modes. In particular, a single mode is found to be enough for describing nearly 25% of

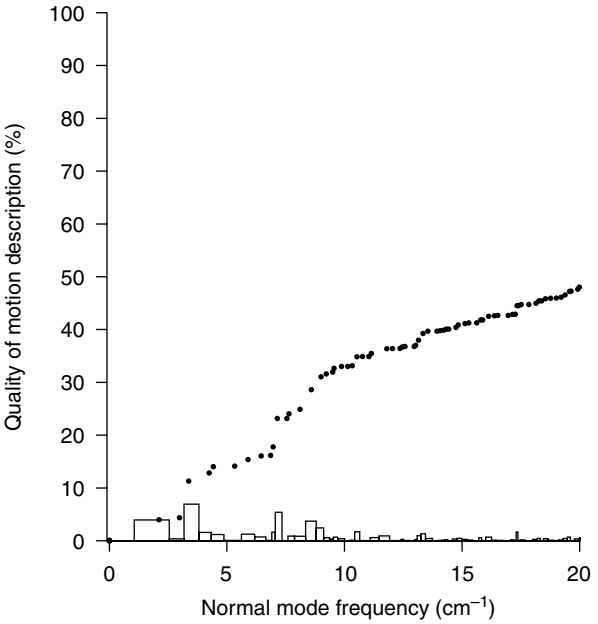

FIGURE 5.9
Description of DHFR conformational change with standard normal modes.

the motion. Further work is required in order to check the general character of such results, but they probably mean that details of the protein description become important either when the protein is small or (and) when the amplitude of the conformational change is not large.

5.4 Applications

Nowadays, one major application of NMA is the identification of potential functional motions of proteins. Here, the main difficulty is that NMA alone cannot tell which is the mode that is most involved in the conformational change (and if there is any). Also, it does not tell anything about the amplitude of the functional motion, which is often much larger than amplitudes predicted by normal mode theory for room temperature motions (typically, 1 to 2 Å). So, attempts to predict conformational changes from NMA have to be backed by experimental data. For instance, it was predicted that, upon Gp120 binding, a conformational change occurs in CD4, the HIV-1 receptor, as a rigid-body motion of domain one (D1), on top of which the virus binds, with respect to domain two (D2). This prediction was based on normal mode calculations [41], and also on the fact that the only mutations of D2 found to lower the affinity of CD4 for Gp120 are located in the two loops of D2

involved in the interface between D1 and D2. Moreover, both loops exhibit large motions in the lowest-frequency modes of CD4 [41], allowing for relative domain displacement in spite of their tight association.

Another kind of application is to use NMA as a check for conformational changes proposed on the basis of nonstructural experimental data (mutagenesis experiments, etc.). If a few normal modes are found involved in the proposed conformational change, this will be in favor of the correctness of the proposal. Such a positive feedback from NMA has, for instance, recently been obtained, in a study of the mechanosensitive channel opening [42].

However, for the years to come, applications that appear to be the most promising ones rely on the use of the lowest-frequency modes of a protein as a (small) set of coordinates along which the structure is perturbed, so as to achieve better agreement with experimental data [34, 43, 44].

5.5 Conclusion

When the functional motion of a protein has a clear collective character [14, 18] and, probably, as illustrated above, when its amplitude is large enough, normal modes can prove useful for studying the mechanical details of the motion. This is due to the fact that the few lowest-frequency modes of a protein are relative motions of structural domains. This fact is not a trivial one, since it also proves helpful to define such structural domains, when their limits are not obvious ones, through the dynamical information provided by these modes [17].

However, perturbing the structure along its lowest-frequency modes appears to be a promising tool in the field of structure refinement [44], especially for fitting atomic structures into low-resolution electron density maps [43] or within the frame of molecular replacement techniques [34], when a protein with a known structure has undergone a large conformational change.

References

1. J.A. McCammon, B.R. Gelin, M. Karplus, and P.G. Wolynes. The hinge-bending mode in lysozyme. *Nature*, 262: 325–326, 1976.
2. B.R. Brooks and M. Karplus. Normal modes for specific motions of macromolecules: application to the hinge-bending mode of lysozyme. *Proc. Natl Acad. Sci. USA*, 82: 4995–4999, 1985.
3. M. Levitt, C. Sander, and P.S. Stern. Protein normal-mode dynamics: trypsin inhibitor, crambin, ribonuclease and lysozyme. *J. Mol. Biol.*, 181: 423–447, 1985.

4. W. Harrison. Variational calculation of the normal modes of large macromolecules: methods and some initial results. *Biopolymers,* 23: 2943–2949, 1984.
5. O. Marques and Y.-H. Sanejouand. Hinge-bending motion in citrate synthase arising from normal mode calculations. *Proteins,* 23: 557–560, 1995.
6. D. Perahia and L. Mouawad. Computation of low-frequency normal modes in macromolecules: improvements to the method of diagonalization in a mixed basis and application to hemoglobin. *Comput. Chem.,* 19: 241–246, 1995.
7. L. Mouawad and D. Perahia. Motions in hemoglobin studied by normal mode analysis and energy minimization: evidence for the existence of tertiary T-like, quaternary R-like intermediate structures. *J. Mol. Biol.,* 258: 393–410, 1996.
8. T. Lazaridis and M. Karplus. Effective energy function for proteins in solution. *Proteins,* 35: 133–152, 1999.
9. M. Schaefer and M. Karplus. A comprehensive analytical treatment of continuum electrostatics. *J. Phys. Chem.,* 100: 1578–1599, 1996.
10. N. Calimet, M. Schaefer, and T. Simonson. Protein molecular dynamics with the generalized Born/ACE solvent model. *Proteins,* 45: 144–158, 2001.
11. G. Li and Q. Cui. Analysis of functional motions in Brownian molecular machines with an efficient block normal mode approach: myosin-II and Ca(2+)-ATPase. *Biophys. J.,* 86: 743–763, 2004.
12. F. Tama and Y.-H. Sanejouand. Conformational change of proteins arising from normal mode calculations. *Protein Eng.,* 14: 1–6, 2001.
13. A.R. Atilgan, S.R. Durell, R.L. Jernigan, M.C. Demirel, O. Keskin, and I. Bahar. Anisotropy of fluctuation dynamics of proteins with an elastic network model. *Biophys. J.,* 80: 505–515, 2001.
14. M. Delarue and Y.-H. Sanejouand. Simplified normal modes analysis of conformational transitions in DNA-dependant polymerases: the elastic network model. *J. Mol. Biol.,* 320: 1011–1024, 2002.
15. M.M. Tirion. Low-amplitude elastic motions in proteins from a single-parameter atomic analysis. *Phys. Rev. Lett.,* 77: 1905–1908, 1996.
16. I. Bahar, A.R. Atilgan, and B. Erman. Direct evaluation of thermal fluctuations in proteins using a single-parameter harmonic potential. *Fold. Design,* 2: 173–181, 1997.
17. K. Hinsen. Analysis of domain motions by approximate normal mode calculations. *Proteins,* 33: 417–429, 1998.
18. F. Tama, F.-X. Gadea, O. Marques, and Y.-H. Sanejouand. Building-block approach for determining low-frequency normal modes of macromolecules. *Proteins,* 41: 1–7, 2000.
19. F. Tama, W. Wriggers, and C.L. Brooks III. Exploring global distortions of biological macromolecules and assemblies from low-resolution structural information and elastic network theory. *J. Mol. Biol.,* 321: 297–305, 2002.
20. S. Hayward. Identification of specific interactions that drive ligand-induced closure in five enzymes with classic domain movements. *J. Mol. Biol.,* 339: 1001–1021, 2004.
21. P. Kraulis. Molscript: a program to produce both detailed and schematic plots of protein structures. *J. Appl. Crystallogr.,* 24: 946–950, 1991.
22. B.R. Brooks, R.E. Bruccoleri, B.D. Olafson, D.J. States, S. Swaminathan, and M. Karplus. CHARMM: a program for macromolecular energy, minimization, and dynamics calculations. *J. Comput. Chem.,* 4: 187–217, 1983.

23. B.R. Brooks, D. Janezic, and M. Karplus. Harmonic-analysis of large systems. 1. Methodology. *J. Comput. Chem.*, 16: 1522–1542, 1995.
24. H. Goldstein. *Classical Mechanics*. Addison-Wesley, Reading, MA, 1950.
25. W.G. Krebs, V. Alexandrov, C.A. Wilson, N. Echols, H. Yu, and M. Gerstein. Normal mode analysis of macromolecular motions in a database framework: developing mode concentration as a useful classifying statistic. *Proteins*, 48: 682–695, 2002.
26. T. Noguti and N. Go. Collective variable description of small-amplitude conformational fluctuations in a globular protein. *Nature*, 296: 776–778, 1982.
27. Y. Seno and N. Go. Deoxymyoglobin studied by the conformational normal mode analysis. I. Dynamics of globin and the heme–globin interaction. *J. Mol. Biol.*, 216: 95–109, 1990.
28. L. Mouawad and D. Perahia. DIMB: Diagonalization in a mixed basis. A method to compute low-frequency normal modes for large macromolecules. *Biopolymers*, 33: 569–611, 1993.
29. P. Durand, G. Trinquier, and Y.H. Sanejouand. A new approach for determining low-frequency normal modes in macromolecules. *Biopolymers*, 34: 759–771, 1994.
30. G. Li and Q. Cui. A coarse-grained normal mode approach for macromolecules: an efficient implementation and application to Ca(2+)-ATPase. *Biophys. J.*, 83: 2457–2474, 2002.
31. H.M. Chun, C.E. Padilla, D.N. Chin, M. Watanabe, V.I. Karlov, H.E. Alper, K. Soosaar, K.B. Blair, O.M. Becker, L.S.D. Caves, R. Nagle, D.N. Haney, and B.L. Farmer. MBO(N)D: a multibody method for long-time molecular dynamics simulations. *J. Comput. Chem.*, 21: 159–184, 2000.
32. J. Elezgaray, G. Marcou, and Y.-H. Sanejouand. Exploring the natural conformational changes of the C-terminal domain of calmodulin. *Phys. Rev. E*, 66: 31908–31915, 2002.
33. F. Tama, M. Valle, J. Frank, and C.L. Brooks III. Dynamic reorganization of the functionally active ribosome explored by normal mode analysis and cryo-electron microscopy. *Proc. Natl Acad. Sci. USA*, 100: 9319–9323, 2004.
34. K. Suhre and Y.-H. Sanejouand. On the potential of normal mode analysis for solving difficult molecular replacement problems. *Act. Cryst. D*, 60: 796–799, 2004.
35. K. Suhre and Y.-H. Sanejouand. Elnémo: a normal mode server for protein movement analysis and the generation of templates for molecular replacement. *Nucleic Acids Res.*, 32: W610–W614, 2004.
36. P. Doruker, R.L. Jernigan, and I. Bahar. Dynamics of large proteins through hierarchical levels of coarse-grained structures. *J. Comput. Chem.*, 23: 119–127, 2002.
37. J. Ma and M. Karplus. Ligand-induced conformational changes in ras p21: a normal mode and energy minimization analysis. *J. Mol. Biol.*, 274: 114–131, 1997.
38. F. Tama. Ph. D. Thesis. Paul Sabatier University, Toulouse (France), 2000.
39. M. Gerstein and W.G. Krebs. A database of macromolecular motions. *Nucleic Acids Res.*, 26: 4280–4290, 1998.
40. C. Bystroff and J. Kraut. Crystal structure of unliganded *Escherichia coli* dihydrofolate reductase. ligand-induced conformational changes and cooperativity in binding. *Biochemistry*, 30: 2227–2239, 1991.
41. Y.-H. Sanejouand. Normal-mode analysis suggests important flexibility between the two N-terminal domains of CD4 and supports the hypothesis of a conformational change in CD4 upon HIV binding. *Protein Eng.*, 9: 671–677, 1996.

42. H. Valadie, J.-J. Lacapere, Y.-H. Sanejouand, and C. Etchebest. Dynamical properties of the Mscl of *Escherichia coli*: a normal mode analysis. *J. Mol. Biol.,* 332: 657–674, 2003.
43. F. Tama, O. Miyashita, and C.L. Brooks III. Flexible multi-scale fitting of atomic structures into low-resolution electron density maps with elastic network normal mode analysis. *J. Mol. Biol.,* 337: 985–999, 2004.
44. M. Delarue and P. Dumas. On the use of low-frequency normal modes to enforce collective movements in refining macromolecular structural models. *Proc. Natl Acad. Sci. USA,* 101: 6957–6962, 2004.

6

Unveiling Molecular Mechanisms of Biological Functions in Large Macromolecular Assemblies Using Elastic Network Normal Mode Analysis

Florence Tama and Charles L. Brooks III

CONTENTS

6.1 Introduction

It is now well established that large-scale rearrangements in proteins are important for a variety of protein functions including catalysis and regulation of activity. The recent developments in experimental methods, especially cryo-electron microscopy (cryo-EM), have revealed that large-molecular assemblies are also highly dynamic. While experiment can provide a tremendous source of information on these dynamical properties, computational methods must be employed to complement experimental observations. Indeed, by using theory to explore (at near-atomic levels of detail) functionally important rearrangements observed in experiments at low-resolution it is possible to gain new insights into the mechanism of these transformations that are presently inaccessible to experiments.

The exploration of molecular motions of biological molecules and their assemblies by simulation approaches such as molecular dynamics has provided significant insights into structure–function relationships for small biological systems. However, the study of large-scale macromolecular assemblies by this technique is limited to relatively short timescales due to the computational complexity of brute-force simulation methods.

Normal mode analysis (NMA) provides an alternative to molecular dynamics for the study of motions of macromolecules. The timescale accessible to theoretical work is extended with NMA, and this approach has been proven extremely useful for studying collective motions of biological systems [1–3]. Exploration of the normal modes of a molecular system can yield insights, at the atomic level, on the mechanism of large-scale rearrangements of proteins–proteins complexes that occur upon ligand–protein binding [4–11]. Studies employing NMA have generally focused on a few large-amplitude/low-frequency normal modes, which are expected to be relevant to function.

Theoretical studies of dynamical properties of biological systems by NMA have been limited to small proteins (up to 300 residues) [12], mainly due to the size of the biological system. The protein model used in such calculations consists of classical point masses, with typically one point per atom, and the energy terms for interactions between atoms are defined by semiempirical force-fields. The use of such force-fields requires an energetically precise

all-atom description of the equilibrium configuration of the macromolecule, which becomes computationally difficult to achieve as the system size increases. However, multi-scale approaches that retain the atomic detail have also seen some success.

Elastic network models can also be used to address these issues [13]. In the elastic network model approach a simplified potential is used to represent the molecule as a set of pseudo-particles that capture the molecule mass distribution. These particles are coupled *via* harmonic springs to provide a description of the system as an elastic net. This model does not necessitate preliminary energy minimization, thereby permitting direct analysis of crystal and NMR coordinates, or even low-resolution structures obtained from electron microscopy [14–17]. Moreover, the reduced representation of the molecule, whereby a single coordinate is used to represent several atoms (e.g., using C_α atoms to represent each residue of a protein) provides a multiscale description that can significantly reduce the computational expense. The elastic network model, in concert with methods that facilitate large diagonalization problems such as the rotation–translation block (RTB) method [18,19] or DIMB [20], have extended studies of dynamics via NMA to very large biological assemblies.

In the following pages, we will review the elastic network model and RTB-based diagonalization techniques used in NMA as well as methods based on NMA for the generations of feasible conformational change pathways between different conformations of biological systems. We will illustrate recent successes of NMA applied to large macromolecular assemblies. Particular focus will be on recent studies of viruses, the ribosome and myosin. In addition, the application of elastic network normal mode analysis to low-resolution structures obtained from cryo-EM will also be presented.

6.2 Theory and Method

6.2.1 Normal Mode Theory

The normal mode method is based on the analytic dynamics of a system whose potential energy is expressed as a quadratic function of atomic displacement about an equilibrium conformation (harmonic approximation) [21]. Specifically, if one expands the potential energy function U around a minimum on the energy surface, r^0, the Hamiltonian of the system is given by

$$H \cong K(\dot{\mathbf{r}}) + E(\mathbf{r}) \cong \frac{1}{2}\sum_n m_n \dot{\mathbf{r}}_n^2 + \frac{1}{2}\sum_{nm} (\mathbf{r}_n - \mathbf{r}_n^0)\left.\frac{\partial^2 E}{\partial \mathbf{r}_n \partial \mathbf{r}_m}\right|_{\mathbf{r}=\mathbf{r}_o} (\mathbf{r}_m - \mathbf{r}_m^0) \quad (6.1)$$

where K represents the kinetic energy, E the potential energy, and $\mathbf{r}_n$ and $\mathbf{r}_n^0$ are the coordinates of atom n.

The dynamics of this system (for all times) now follow from the solution of the eigenvalue problem

$$\mathbf{M}^{-1/2}\nabla^2\mathbf{E}\mathbf{M}^{-1/2}\mathbf{y}_i = \omega_i^2\mathbf{y}_i \tag{6.2}$$

$$y_i^{\mathrm{T}}y_j = \delta_{ij} \tag{6.3}$$

In this expression, $\nabla^2\mathbf{E}$ is the Hessian, which comprises the $3N \times 3N$ matrix of the second derivatives of the potential energy evaluated at $\vec{r} = \vec{r}^0$, the matrix $\mathbf{M}$ contains the atomic masses on its diagonal. The solution is a set of normal modes consisting of an eigenvector $\mathbf{y}_i = (y_i^{1x}, y_i^{1y}, y_i^{1z}, y_i^{2x}, y_i^{2y}, y_i^{2z}, \ldots, y_i^{Nx}, y_i^{Ny}, y_i^{Nz})^{\mathrm{T}}$ and its associated frequency ω_i. The eigenvector gives the direction and relative amplitude of each atomic displacement. For a mode i, all the atoms oscillate at the same frequency, ω_i [21]. The dynamics of the system is described as a linear combination of *independent* normal mode oscillators. The nature of the atomic displacements in the framework of the normal mode representation is then expressed as

$$|\Delta\mathbf{r}_n| = \left|\mathbf{r}_n - \mathbf{r}_n^0\right| = \sum_{i=1}^{3N-6} \frac{A_i}{\omega_i^2} \begin{pmatrix} y_i^{nx} \\ y_i^{ny} \\ y_i^{nz} \end{pmatrix} \tag{6.4}$$

where A_i/ω_i^2 is an arbitrary amplitude for displacement along normal mode i. If the atoms are undergoing thermal fluctuations along each mode, the standard deviation of each atom is given by setting A_i equal to $\sqrt{k_{\mathrm{B}}\,T/m_n}$, here T is the absolute temperature, k_{B} is the Boltzmann constant, and m_n is the atomic mass of atom n. From this equation, it is evident that the largest contribution to the atomic displacement comes from the lowest frequency normal modes. In addition, the lowest-frequency eigenvectors represent the most globally distributed or collective motions, that is, a large number of atoms have significant components $(y_i^{3n-2}, y_i^{3n-1}, y_i^{3n})$, whereas for high-frequency eigenvectors only a few atoms contribute to the Cartesian element $\mathbf{y}_i$.

6.2.2 Multi-Scale Energy Functions Using Elastic Networks

A simplified representation of the potential energy can also be introduced for the NMA of biological systems. In this representation, the biological system is described as a three-dimensional (3D) elastic network based on the equilibrium distribution of atoms [13]. In this elastic network model, amino acids or base pairs may be represented in full atomic detail, or at a more coarse-grained level. For example, at one mass point per residue [22], only C_α atoms [23,24] or more coarse-grained particle-based models [25] may be used to identify the junctions of the network. These junctions are representative of the mass

distribution of the system and are connected together via a simple harmonic restoring force

$$E(\vec{r}_a, \vec{r}_b) = \begin{cases} \frac{k}{2}(|\vec{r}_a - \vec{r}_b| - |\vec{r}_a^0 - \vec{r}_b^0|)^2, & \text{for } |\vec{r}_a^0 - \vec{r}_b^0| \leq R_C \\ 0, & \text{for } |\vec{r}_a^0 - \vec{r}_b^0| > R_C \end{cases} \tag{6.5}$$

where $\vec{r}_a - \vec{r}_b$ denotes the vector connecting pseudo-atoms a and b, the zero superscript indicates the initial configuration of the pseudo-atoms, and R_C is a spatial cutoff for interconnections between the particles. The strength of the potential k is a phenomenological constant assumed to be the same for all interacting pairs; different types of atoms or residues are not assigned different values of k.

The total potential energy of the molecule is expressed as the sum of elastic strain energies:

$$E_{\text{System}} = \sum_{a,b} E(\vec{r}_a, \vec{r}_b) \tag{6.6}$$

Note that this energy function, E, is a minimum for any chosen configuration of any system, thus eliminating the need for minimization prior to NMA. Consequently, NMA can be performed directly on crystallographic or NMR structures [13].

Several studies have shown that this Hookean potential is sufficient to reproduce the low-frequency normal modes of proteins as produced by more complete potential energy functions [24]. The high degree of accord between the modes constructed from these methods suggests that low-frequency normal modes are predominantly a property of the shape of the molecular system [26]. Although this agreement tends to break down at high frequencies, there have been many cases showing that collective motions found in the low-frequency modes well characterize biologically relevant conformational changes [24].

6.2.3 Rotation–Translation Block Method

The application of NMA critically depends on diagonalization of the Hessian and this can be a limiting factor in applying NMA to interesting molecular systems. The RTB method was introduced to reduce the size of the Hessian by introduction of a simple physical idea: a protein or nucleic chain may be viewed as being composed of rigid components linked together, such as residues/bases or group of residues/bases or more extensive segments of structure forming secondary structural elements [18,19]. The combination of rotation and translation of these rigid components should provide a good representation of the low-frequency normal modes of the biological system. Thus in the RTB method, the molecular system is first divided into n_b blocks,

each consisting of one or of a few consecutive residues/base pairs, etc. Then, the lowest-frequency normal modes of the biological system are obtained as a linear combination of the rotations and translations of these blocks.

In standard approaches, the normal modes of the system are calculated through the diagonalization of the Hessian matrix $\nabla^2\mathbf{E}$ (Equation [6.2]). The Hessian is the $3N \times 3N$ matrix of the second derivatives of the potential energy with respect to the mass-weighted coordinates, where N is the number of atoms of the system. In the RTB approach, $\nabla^2\mathbf{E}$, the Hessian being diagonalized is first expressed in a basis defined by the rotational and translational degrees of freedom of n_b blocks. $\mathbf{H}_b$, the projected Hessian, is given by

$$\mathbf{H}_b = \mathbf{P}^{\mathrm{T}}\nabla^2\mathbf{E}\mathbf{P} \tag{6.7}$$

where $\mathbf{P}$ is the orthogonal $3N \times 6n_b$ matrix built with the vectors associated with the local rotations and translations of each block. From the normal modes, $\mathbf{A}_b$, obtained by diagonalizing $\mathbf{H}_b$, which is a $6n_b \times 6n_b$ matrix, the corresponding $(3N)$ atomic displacements are recovered by

$$\mathbf{A}_{\mathrm{P}} = \mathbf{P}\mathbf{A}_b \tag{6.8}$$

Following the above formalism, the actual computational procedure consists of three steps. In the first step, blocks of residues are defined and the six rotation–translation modes of each block α, $\mathbf{U}_\alpha$, are determined and stored. These $6n_b$ vectors form a new basis of small dimension that corresponds to the projector $\mathbf{P}$. In the second step, the Hessian matrix is expressed in this new basis, separately for each coupling or diagonal block, $\mathbf{H}_{\alpha\beta}$

$$\mathbf{H}^b_{\alpha\beta} = \mathbf{U}^{\mathrm{T}}_\alpha \mathbf{H}_{\alpha\beta}\mathbf{U}_\beta \tag{6.9}$$

The set of $n_b^2\mathbf{H}^b_{\alpha\beta}$ block-matrices forms the matrix $\mathbf{H}_b$. The construction of $\mathbf{H}_b$ has minimal memory requirements, since the Hessian corresponding to each block, that is, $\mathbf{H}_{\alpha\beta}$, is first calculated and projected into the rotation–translation matrix. Therefore, during this step, the largest matrix kept in memory corresponds to the size of one block in the 3D coordinates. The RTB method requires only the small dimension vectors $\mathbf{U}_\alpha$ and the small $6n_b \times 6n_b$ $\mathbf{H}_b$ matrix to be stored. In the last step, $\mathbf{H}_b$ is diagonalized with standard methods.

It has been demonstrated that this approach yields very accurate approximations of the low-frequency normal modes of proteins. Studies have also shown that the manner in which the protein is partitioned into blocks has minimal qualitative consequence on the description of the low-frequency normal modes of the system [19].

6.2.4 Multi-Scale NMA Using Elastic Network Hamiltonians and the RTB Method

Combining the elastic network representation of molecular structure and connectivity with the RTB approach for the reduction of the complexity of the normal mode, Hessian permits one to extend the application of normal modes methods for the exploration of conformational deformations and dynamics to assemblies of nearly arbitrary size while maintaining a modest requirement for computer memory and computational time. Thus, these approaches together enable the development and exploration of multi-scale models for the functional motions of large biological machines and assemblies. However, this methodology does not provide an absolute scale of the normal mode eigenvalues, that is, the frequencies of the motions. Instead, only relative values are extracted. To retrieve the absolute value, for example, as could be obtained from a fully atomic representation using a standard force-field incorporating all interatomic interactions, a scaling factor may be deduced by comparing the thermal fluctuations from the elastic network NMA calculations (Equation [6.4]) with those from either simulation or experiment (through Debye–Waller factor) [13,23]. Even though the absolute energy scale/time scale of the molecular motions is distorted in these calculations, the character (directions) of the low-frequency motions is unaffected, thus providing an efficient way to study the nature of large conformational rearrangements of biological systems that are not accessible via molecular dynamics simulation.

6.2.5 Mapping the Pathway of Conformational Change Using NMA

The elucidation of the pathways for conformational changes in macromolecular systems may be useful in the analysis of functional rearrangements in biological systems, providing an atomic-level description of the conformational transition. To generate these pathways, models of intermediate structures between the two known conformational states of the molecule must be developed. This can be approached in a variety of ways from the stand point of modeling [27,28]. The approach that we discuss here is to follow the low-energy normal modes directions of the system between the two end point states. NMA based methods have been already developed to describe conformational change pathways [11,29]. Here an alternative iterative technique is presented [30,31].

6.2.5.1 Linear Interpolation between Endpoints Using Normal Mode Directions

The displacement vector between two endpoint conformation of a molecular system, $\Delta\mathbf{r}$, can simply be expressed as the superposition of displacements

along the normal modes direction of the system

$$\Delta \mathbf{r} = \sum_i \mathbf{y}_i q_i \tag{6.10}$$

where

$$q_i = \mathbf{y}_i \Delta \mathbf{r} \tag{6.11}$$

since the normal mode eigenvectors should span the conformational space. By using some fraction of normal mode coordinate, q_i, of Equation (6.11) for the deformation, Equation (6.10), the intermediate structures can be generated. However, we should note that using the entire mode corresponds to simple Cartesian interpolation. Generally, one finds that a smaller subset of displacements, $\mathbf{q}_i$, along mode $\mathbf{y}_i$ account for the majority of the conformational deformation between two endpoint conformations and this serves as a basis for expressing the possibly functional dynamics of the conformational change. These modes are coincident with a few modes with the lowest frequencies [24].

6.2.5.2 Nonlinear/Iterative Approach

Although the linear interpolation approach just described is often adequate to describe conformational changes in biological systems in some instances, to describe conformational changes between two conformationally distinct states requires a nonlinear description due to the anharmonic character of the energy landscape. The lowest frequency normal mode of the open structure is shown in Figure 6.1 indicates the preferential direction of the conformational change in the vicinity of the structure. However, it is evident that the mode

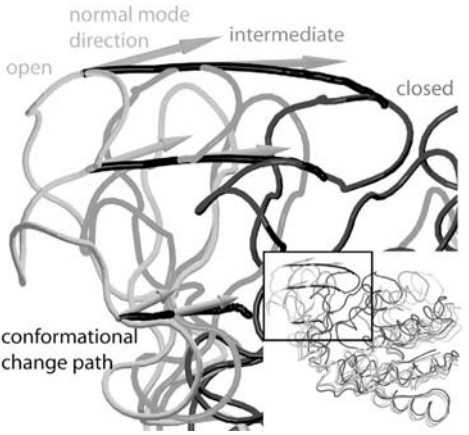

FIGURE 6.1
(See color insert following page 136) Nonlinear conformational change between the open and closed forms of the adenylate kinase the linear normal mode directions.

itself is not adequate to lead the structure to the closed form. The discrepancy arises because the normal modes provide only linear motions even though the conformational change pathway is nonlinear. The direction of the conformational change alters as the structure is deformed from the initial to the final structure as seen in Figure 6.1. Another critical aspect is that displacing too far along the direction given by the lowest frequency modes, inspite of being the globally preferential direction of the conformational change, can induce large distortion in the local structure such as bond distances.

The problems arising from the harmonic approximation employed in the NMA can be ameliorated by performing the NMAs and conformational deformations in an iterative manner [30,31]. Instead of moving the structure from the initial to the final form directly, the deformation is limited to a small amount, and normal modes are recalculated for the deformed structure. In this approach, the conformational change is described by the following iterative procedure: the initial conformation is defined as $C_{\mathrm{I}} = C_0$ and the final state is C_{F}. NMA is performed on C_k with k initially taken at $k = \mathrm{I}$. The vector difference $\Delta\mathbf{r}^k$ between C_k and C_{F} is (re-)evaluated. The structure C_k is displaced along a linear combination of normal modes $\mathbf{y}^k$ toward the final state leading to the next structure C_{k+1}. The amplitude, q_i^k, of the displacements along normal mode i is given by

$$q_i^k = \mathbf{y}_i^k \cdot \Delta\mathbf{r}^k Q \tag{6.12}$$

where Q is a parameter that determines how far the structure is displaced; 0 equals the current coordinates and 1 equals the full projection of the current normal mode coordinates onto C_{F}. This procedure is repeated until some convergence criterion in RMSD between the kth iterate and the final conformation is reached. Figure 6.1 shows the nonlinear conformational change pathway obtained in this procedure.

6.3 Applications

With the methods and algorithms just described in hand, one can tackle the exploration of biological questions related to the conformational reorganization of large macromolecular assemblies. In this section, we present several applications of NMA to large macromolecular assemblies such as viruses, the ribosome, and the muscle protein myosin. In addition, we will illustrate not only how NMA can be used to explore dynamical properties of atomically detailed x-ray structures, but also how the multi-scale methods described above can be used to provide insights to dynamical processes that are characterized by low-resolution experiments. The primary motivation behind the studies described below is to complement experimental observations by exploring, at a near-atomic level, functionally important rearrangements

observed in experiments at low-resolution and to obtain new insights into the mechanism of these transformations that are presently inaccessible to experiments.

6.3.1 Unveiling Molecular Mechanisms of Conformational Changes of Large Macromolecular Assemblies

6.3.1.1 The Mechanism and Pathway of pH Induced Swelling in Cowpea Chlorotic Mottle Virus

Recent advances in structural biology and the large increase in computer power have made possible theoretical studies on systems as large as entire viral capsids of nonenveloped icosahedral viruses. For example, a general kinetic model for the self-assembly of spherical viruses, that includes a nucleation event has been described [32]. Other important aspects regard the assembly and maturation of virus particles. These phenomena involve large-scale rearrangements of the capsid proteins, from swollen or nonspherical shaped forms to the mature spherical icosahedral form [33–36]. The exploration of putative pathways for the conformational changes, which accompany these physical transitions, would be helpful to understand the mechanism associated with the swelling phenomena since it could provide a description of the rearrangements of the subunits at an atomic level and motivate hypotheses for the triggering event.

The large majority of viruses display icosahedral symmetry. This requires at least 60 structural units to complete a shell. However, very few viruses contain only 60 copies of a single capsid protein. Most of the icosahedral viruses display quasi-symmetry, that is, they have $60T$ identical subunits in the shell, where T is the triangulation number [37], which reflects the selection rules for distributing capsomers (hexamers and pentamer) on a surface lattice.

One example of such a system that we have examined is the Cowpea Chlorotic Mottle Virus (CCMV). The capsid is made up of 180 proteins that form a 286 Å diameter icosahedral shell with $T = 3$ quasi-symmetry. Native CCMV is stable around pH 5.0. At pH 7.0 and with low ionic strength, the particles undergo a concerted transition to a swollen form where the average size of the particle has increased by roughly 10% [36]. Presumably swelling only occurs when Ca^{2+} ions, which binds at the quasi-3-fold axes, is first removed. Structures of native and swollen forms have been determined by x-ray crystallography and cryo-EM [38], respectively, thus a comparison of our calculations with experimental results will be possible.

An elastic network was constructed from the 28620 C_α atoms of CCMV with a cutoff of 8 Å to define the C_α–C_α based network connectivity. For the computation of the lowest frequency normal modes using the RTB method, each block was made of one of the proteins comprising the asymmetric subunit. Thus a total of 180 blocks was considered and the matrix to be diagonalized was 1,080 × 1,080, instead of 85,860 × 85,860 when diagonalization was done in the full Cartesian space. We note that in this calculation since each

protein is treated as a block, conformational changes within each individual protein are not allowed. Nevertheless, this approach should be a reasonable approximation since the experimental cryo-electron density map of the swollen particle was only at 28 Å and does not reveal large rearrangements within each protein [38].

Normal mode analysis performed on icosahedral viruses gives modes that are degenerate and nondegenerate. For the nondegenerate normal modes, the motion of each asymmetrical unit is exactly the same because this mode adheres to the icosahedral symmetry of the whole system. Experimental studies of viruses have suggested that the swollen or provirion capsids also adhere to icosahedral symmetry. Therefore, to study swelling phenomena pathway, in the absence of experimental data suggesting symmetry-breaking pathways, it seems most appropriate to explore pathways that obey the implied symmetry and thus limit our considerations to the fully symmetric normal modes.

Starting from the native form of CCMV, we displaced the structure along the direction given by the nondegenerate low-frequency normal modes and intermediate structures were created. Since we performed NMA only on a C_α representation, all-atom structures were created by rigidly superimposing the atomically detailed subunit structures onto the C_α framework. These structures were compared to the experimental density map of the swollen CCMV by computing the *R*-factor. For one mode, we observed a decrease of the R-factor value from 72 to 49%. Such a decrease of the *R*-factor indicates that this normal mode is actually similar to the direction followed by CCMV during the swelling process. This mode, referred to as a "breathing mode" (Figure 6.2[a]), corresponds to an overall expansion of the virus particle. We were able to improve the *R*-factor value by displacing the structure presenting the lowest *R*-factor (49%) along three other non-degenerate normal modes. Compared to the breathing mode, these modes make a more limited contribution to the conformational change and they correspond mainly to rearrangements between the subunits. The final *R*-factor was 45 and 43.8 after minimization of the protein interfaces in the presence of icosahedral symmetry, and the final structure fits the experimental map of the swollen CCMV quite well (Figure 6.2[b]).

These structures provide feasible pathways for the swelling process. In this case, a linear pathway is a reasonable approximation due to the symmetrical properties of virus structure. To obtain more information on the origin of the swelling process, the all-atom intermediate structures were energy minimized and the approximate association energies for each unique interface were calculated [39,40]. The interfacial energies should reflect how each protein–protein interface changes during the swelling process. We observed that the dimeric interactions are well preserved in the swollen form, while pentameric interactions nearly disappear. We also noticed that the association energy around the quasi-3-fold axis is lost very early in the swelling process, which suggests that the residues triggering the swelling may be located at quasi-3-fold interface. A closer examination of the residues interacting at the quasi-3-fold axis and their contribution to the association energy reveals that

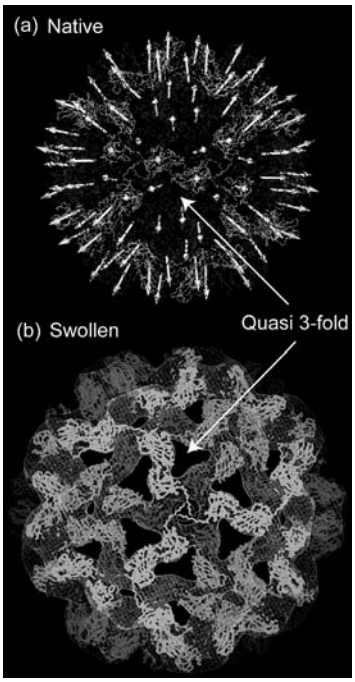

FIGURE 6.2
(See color insert following page 136) Elastic NMA of the viral capsid proteins of CCMV. (a) Amplitude and direction of motion for CCMV as obtained from expansion along the breathing mode. (b) Electron density fitting with the estimated model for swollen CCMV as obtained from NMA. All the graphics were produced using VMD [62].

residues sensitive to a change in the pH (acidic residues, ASP, and GLU) have a significantly lower contribution to the association energy after expansion. Since the swelling process is driven by a change in pH, pKa calculations were performed for the acidic residues present at the quasi-3-fold axis in the native CCMV and for intermediate structures along the swelling pathway. The pKa calculations pointed to one specific residue, GLU 81, with a pKa higher than expected (>7). In the native state, this acidic residue interacts with two other acidic residues of the adjacent subunits that comprise the quasi-3-fold symmetry axis. When the pH increases from 5 to 7, GLU 81 becomes deprotonated, which results in repulsive interactions with these two other acidic residues. The repulsive interactions would be sufficient to trigger the swelling process of CCMV.

Extension of this study to a variety of viruses comprising different sizes and quasi-equivalence symmetries reveals that the pentameric units generally have higher flexibility and may move as independent units against the others capsomers. This general behavior indicates that viral capsids, if needed, can accomplish transition between conformations that might have different shape using the specific character of the pentameric unit's flexibility [41].

6.3.1.2 Dynamic Reorganization of the Functionally Active 70S Ribosome

The ribosome is a macromolecular machine that performs protein synthesis by translating the genetic information residing on the mRNA into a specific sequence of amino acids. The ribosome is made from more than 50 proteins and several elements of ribosomal RNA (rRNA) that are arranged in two unequal subunits, the large (50S) and the small (30S) subunits. The two subunits join together on an mRNA molecule to form the 70S active complex and interact via a network of intermolecular bridges [42–44]. These bridges are components critical to the maintenance of the overall architecture of the 70S complex. The tRNA molecules responsible for carrying the particular amino acid moieties to be added to the nascent protein chain are located in the intersubunit void between the 30S and 50S subunits. There are three distinct stages in protein synthesis: the initiation, the elongation, and the termination. Each of these stages involves the binding of several factors (intiation factor, elongation factor, termination factor) which induce conformational rearrangements of the ribosome.

One of the key mechanical steps during the elongation cycle is the translocation process, in which the tRNA molecules move from the A-aminoacyl and P-peptidyl site into the P- and E-exit site. This process is promoted by binding of the elongation factor G protein (EF-G) and subsequent GTP hydrolysis. Large conformational rearrangements of the ribosome occur during this process, which consists of a ratchet-like rotation of the two ribosomal subunits [45]. Several other rearrangements such as the large displacement of the L1 stalk [46], rearrangement of the L7/L12 stalk, and domain movement in the 30S subunit were also experimentally observed [47]. We studied the rearrangements of the ribosome using the theoretical methods of elastic network NMA to provide a near-atomic level description of these structural rearrangements linking motions obtained from the NMA to experimental observations.

An elastic network model was constructed based on the 5.5 Å x-ray map [48] of the 70S ribosome from *Thermus thermophilus* [26]. Phosphate and C_α atom positions were taken for the junctions of the elastic network. In our calculations, we considered two cutoff distances to delimitate the junctions within the network. We used a cutoff of 20 Å for the P–P and P–C_α interactions and 16 Å for the C_α–C_α interactions in the x-ray structure. These values were based on the distance distribution functions between C_α–C_α, C_α–P and P–P positions. NMA was performed using the RTB method for which five consecutive C_α or P atoms were assigned to a block, the block boundaries were constructed such that atoms from different subunits were not included in the same blocks.

The lowest frequency modes obtained from the elastic network of the 70S structure of the ribosome show a number of motions that may have potential functional relevance [26]. In particular, two of these motions show similarity with rearrangements that have been elucidated by means of experimental techniques. To complement experimental information, these modes were analyzed in detail.

Our NMA of the ribosome shows a mode that corresponds well to the ratchet-like motions observed experimentally. We observed a rotation of the 30S relative to the 50S subunit similar to that described by Frank et al. based on single particle cryo-EM structural data [45]. This rotation leads to relatively large conformational rearrangement of several parts of the ribosome such as the stalk base in the 50S subunit and the head and the shoulder in the 30S subunit, which are known to interact with EF-G (see Figure 6.3). These observations suggest a mechanical coupling between the binding sites of EF-G and the ratchet-like motion.

The underlying mechanism of the ratchet-like motion can be examined using one mode from the NMA. First, helix 27 of the 16S RNA, for which base pair rearrangements are known to promote large rearrangements of the ribosome, emerges as a part of the axis of the rotation of the 30S subunit. Thus, this detailed analysis of the conformational rearrangements may have

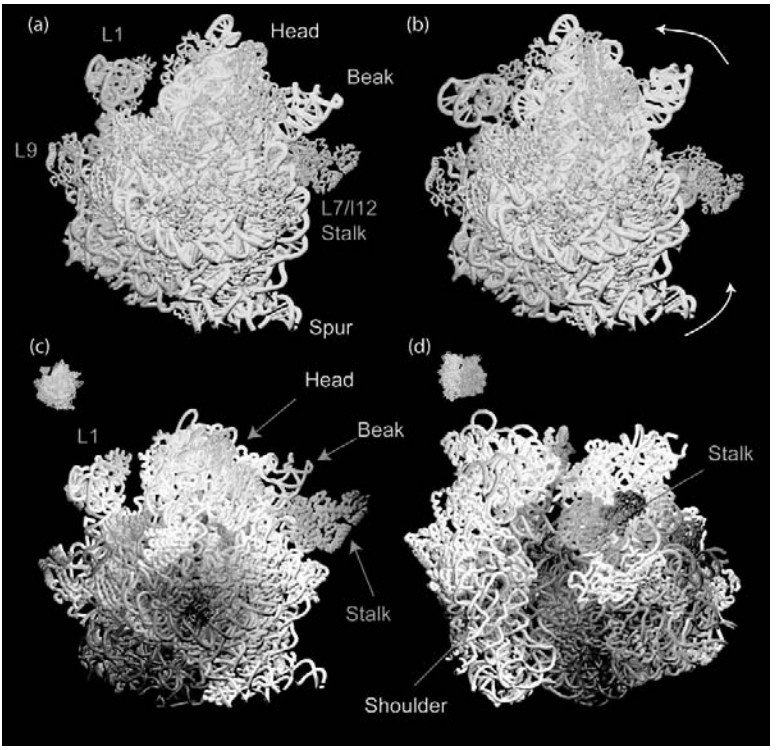

FIGURE 6.3
(See color insert following page 136) Elastic network NMA of the 70S ribosome. (a) The x-ray structure of the 70S ribosome (the 30S subunit in yellow and the 50S in blue). (b) Rearrangements of the 70S ribosome after displacement along the ratchet-like mode. (c) and (d) Two different views, as indicated by thumbnails, of the atomic displacements along the ratchet-like mode. The atoms are colored according to their amplitude along the mode. The scale ranges from red (largest conformational rearrangements) to blue (no motions).

provided a rationalization for this experimental observation; since base pair rearrangements affect the center of rotation of the subunit, large conformational change may occur. Second, two types of bridges emerge from our study. Two peripheral bridges connecting the 30S and 50S subunits are found to facilitate the conformational switching by being flexible, whereas others are very rigid, and serve to maintain the integrity of the architecture during the ratchet-related conformational change. Third, we observe that the positions of the tRNAs are affected by the ratchet like motion. In particular, weaker contacts are observed between the ribosome and tRNA in the A site, indicated by increasing distance between interacting pairs of atoms. The change in the interactions between the ribosome and the tRNAs suggests that the rotation may facilitate the movement of the tRNAs through the inter-subunit space, by optimizing their positions for the translocation process that occurs upon GTP hydrolysis once EF-G is bound.

Another interesting motion observed through our NMA, which complements recent experimental observations [46,49,50], is the large displacement of the L1 stalk in a manner that opens/closes the inter-subunit space (see Figure 6.4). This motion is correlated with small rearrangements in the A, P, and E sites, which implicates this region in the binding and shuttling of tRNA at the E site.

Using the iterative NMA based method, we were able to define a feasible conformational change pathway for the ratchet-like motion of the ribosome. The amplitude of displacements along the ratchet-like normal modes was calibrated to match the experimentally observed amplitude of conformational change seen in the cryo-EM structures [45]. Using the structures generated from NMA, in collaboration with members of the McCammon group, we also recently investigated how the electrostatic properties of the ribosome

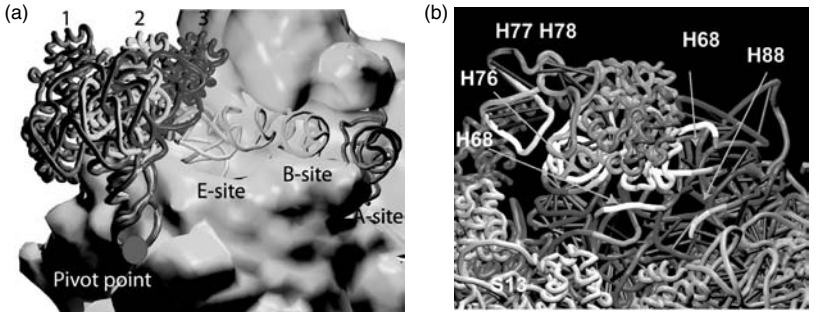

FIGURE 6.4
(See color insert following page 136) Elastic network NMA of the 70S ribosome. The structural rearrangements of the L1 stalk along the mode 1. (a) This displacement occurs around a pivotal point and several positions of the L1 stalk along this mode are represented (1) the outer, (2) x-ray structure, (3) the inner. (b) The magnitude of the structural rearrangements correlated with the L1 stalk motion, with red color indicating large motion and blue color indicating no motion. Small rearrangements are observed in H68, which is connected with H69. H69 is known to interact with the tRNA at A, P, and E sites.

are altered by these conformational changes [51]. Our analysis revealed that there are regions of positive potential around the A-site tRNA in the initial structure, which may help keep the tRNA in place. Upon completion of the ratchet-like motion, the channel between the 30S and 50S domains of the ribosome is wider and more negative. This change in electrostatic potential may make it easier for the tRNA molecules to translocate. In addition, the region around the L1 protein is positively charged, supporting the idea that L1 may interact with the negatively charged E-site tRNA during its release from the ribosome.

6.3.1.3 Myosin II ATPase Inhibition

Myosin is a molecular motor that performs its motile functions on actin filaments. Myosin II is found in both muscle and nonmuscle cells. Phosphorylation of smooth muscle and nonmuscle myosin II serves two purposes. It turns on the actin stimulated ATPase activity and it modifies myosin solubility. Dephosphorylated myosin (10S) is soluble and adopts a folded rod-like domain. Phosphorylation leads to a conformational change to an extended form (6S) that is competent for filament assembly at physiological ionic strength [52]. Similar conformational changes are observed with heavy meromyosin (HMM), a soluble 2-headed fragment of myosin [53]. The mechanism of formation of the inhibited state is still unexplained by static structural models obtained from cryo-EM experiments [53], in particular, how the two heads of the S1 domain fold backward onto the S2 (dimerization domain) and how the arrangement of the two heads can destabilize the filaments.

To address these fundamental questions about the functioning and inhibition of myosin, the conformational transition from the activated state of smooth muscle HMM to its inhibited state was investigated using elastic network NMA [54]. An atomic model for the inhibited structure was obtained by building a high-resolution structure into a 3D image [53] (see Figure 6.5). The 3D image reveals an asymmetrical interaction (head–head) between the S1 domains, but the position of S2 was unclear. For the active state, no structure is available. It is known that the active state is symmetrical and the rod domain (S2) adopts a coiled-coil structure. However, the number of residues that should be uncoiled at the S1–S2 junction is not known. Thus, we have constructed several hypothetical models for the active state with 0, 14, 21, or 28 residues uncoiled at the S1–S2 junctions (see Figure 6.5) and examined which model of uncoiled junction best conforms to other experimental data.

We employed an iterative NMA conformational interpolation method (see Equation [6.12]) to create a conformational pathway between the activated and inhibited states. In our calculations only the 40 lowest-frequency normal modes were considered and the structure was displaced along the 10 largest amplitude normal modes. Q was chosen to be relatively small, $Q = 0.025$ (see Equation [6.12]) in order to avoid large distortion in the structures, and approximately 400 iterations were used to move from the initial to the final state. The target structure does not include coordinates of the S2 domain.

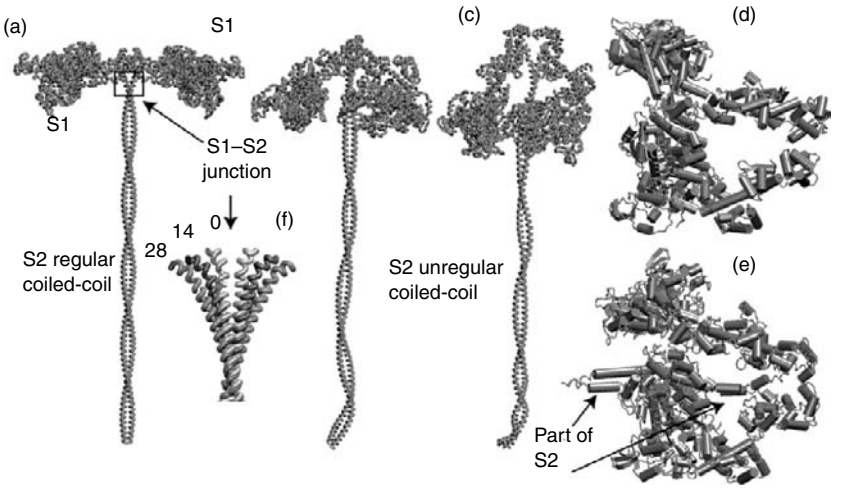

FIGURE 6.5
Elastic network NMA of myosin II from heavy meromyosin (HMM). (a) The initial (activated-state) model, (b) our intermediate structure for the transition from active to inhibited HMM (c) the final structure obtained from iterative NMA, (d) S1 domains of the target structure which was modeled by Wendt et al. [53], (e) S1 domains of the final structure obtained from iterative NMA, (f) modeled S1–S2 junction with 0, 14, and 28 uncoiled residues.

Although S2 contributes to the normal modes of the initial structure, it does not contribute to the vector difference $\Delta \mathbf{r}^k$ used to define the transition pathway. Thus, the movements of S2 obtained in this analysis result from the movements of the myosin heads toward the target structure.

The analysis of the final structures obtained from this iterative procedure indicates that at least 14 but not more than 21 residues of S2 at its junction with S1 must be uncoiled to obtain a smooth conformational transition and to have the correct spatial placement of S1 and S2 domains of the inhibited conformation. Lengths of uncoiled helix greater or shorter than these leads to decoupling of the head (S1) and tail (S2) domain or severe strain remaining localized at the S1–S2 junction. Both yield models that poorly conform to the final state. Since S2 was not present in the target structure, its position was essentially extrapolated from the resulting normal modes. In our final structure the S2 domain is between the two heads (see Figure 6.5), as it was determined by conventional EM, and, at the same time, positions the S2 domain near densities in 3D reconstructions of smooth muscle HMM and 10S myosin [52,53]. Furthermore, the simulations show that the transition between the symmetrical active-state myosin to the asymmetrical inhibited-state induce distortions throughout the S2 domain, which provides, for the first time, a mechanism to explain changes in myosin solubility due to dephosphorylation. Such distortions produced in a sufficient number of myosin molecules would destabilize the filament, as the tight filament packing of S2 domains of assembling myosin that is possible with a regular coiled-coil is disrupted.

As the myosin is released from the filaments, further folding into the 10S conformation occurs until all the myosin is dissolved.

6.3.2 Exploration of Global Distortions and Interpretation of Low-Resolution Structural Information

Large biomolecular assemblies are difficult to study by x-ray crystallography. The recent developments in electron microscopy have produced a growing number of low-resolution structures of such large assemblies. In particular, large conformational changes of macromolecular complexes have been characterized by cryo-EM [55]. Nevertheless, despite the amount of available low-resolution structural information, few theoretical methods have been developed to assist the interpretation of inferred dynamical transitions. In this section, we present the first application of NMA to study global distortions of biological systems from low-resolution structure and a new procedure for the flexible fitting of high-resolution structures into low-resolution electron densities.

6.3.2.1 Global Distortions of Biological Molecules from Low-Resolution Structural Information

Until recently, reduced representations of proteins for NMA were limited to the use of C_α atoms. Greater reductions in the representation have been considered in the study of the influenza virus hemagglutinin [25]. NMAs based on elastic network models from coarse-grained structures containing $N/2, N/10, N/20$, and $N/40$ (where N is the number of residues) C_α atoms were performed, and it was shown that with coarse-graining it continued to capture the slow dynamics of proteins with high accuracy. Since highly reduced representations are sufficient to provide dynamical information on x-ray and NMR protein structures, studies of dynamical properties of low-resolution image data, as for example from cryo-EM, should be possible if one develops a discrete representation of the density.

This objective can be achieved by taking advantage of the vector quantization approach, which is a clustering technique that provides a robust means to develop a discrete reduced representation of continuous 3D data [56,57]. In this approach, the shape of the biological object is encoded in so-called codebook vectors that identify the structural features of the system. Using the elastic network model and the codebook vectors as a representation of the electron density map, it is possible to perform NMA for a low-resolution structure. To test whether this methodology provides a good description of the dynamical properties of biological systems, several proteins that are known to undergo a large conformational change have been studied.

Several elastic network models were constructed from simulated low-resolution EM density maps with different levels of complexity, that is, number of codebook vectors, for the discretized representation. In the elastic

network model, an important parameter is the cutoff, since it determines the number of interactions between each junction of the network. It has been shown that when only the C_α atoms are used, the best results are obtained with an 8 to 10 Å cutoff, which roughly corresponds to the second peak in the distribution of C_α–C_α separations. When we use such reduced representations, where in some cases only 30% of the total number of residues are considered, codebook vectors are sparsely distributed and the distance between each point in these models is significantly larger than the mean C_α–C_α distance in proteins. Thus, in order to choose the cut-off value appropriate for the reduced representation, it is first necessary to establish the distribution of codebook-vector center—codebook-vector center separations, then the and the elastic network model can be constructed by choosing a cutoff distance that just exceeds the second peak in the distribution.

Figure 6.6 illustrates that the global preferential directions for the conformational change is well reproduced from discrete representations of a low-resolution map for the example of adenylate kinase [14]. Similar results were observed by Ming et al. [16]. These studies show that the global dynamical properties of a biological object can be extracted not only from high x-ray crystallographic data but also from low-resolution structural data. This work opens the door for further studies aimed at understanding the mechanical properties for large assemblies for which experimental data from cryo-EM is available for different functional states.

Indeed, applications of this methodology to experimental data revealed functionally important rearrangements of several macromolecular assemblies [15]. NMA based on a discrete representation of an EM map of the ribosome at 25 Å resolution can capture a motion similar to the ratchet-like reorganization observed by cryo-EM experiment [45] and NMA of the 70S atomic structure [26]. In the case of the *Escherichia coli* RNA polymerase, the lowest frequency normal mode obtained from a discretized representation of the low-resolution structure at 15 Å reveals a large conformational rearrangement of the clamp domains that is consistent with several studies [58,59]. Finally, NMA performed from a discretized representation of a map at 27 Å resolution of the chaperonin CCT suggests large flexibility of the apical domain, which is involved in the substrate binding. This result is in agreement with the known structural variability of the chaperonin [60].

6.3.2.2 Flexible Fitting of Atomic Structures into Low-Resolution Electron Density Maps

The fitting of a known x-ray structure into low-resolution structural data from electron microscopy or other lower-resolution methods can provide a deeper understanding of the low-resolution data. However, since biological systems are highly dynamic, in some cases the conformation of the known x-ray structure does not correspond to the conformation of the low-resolution map. Thus, it is necessary to take into account the flexibility of the system

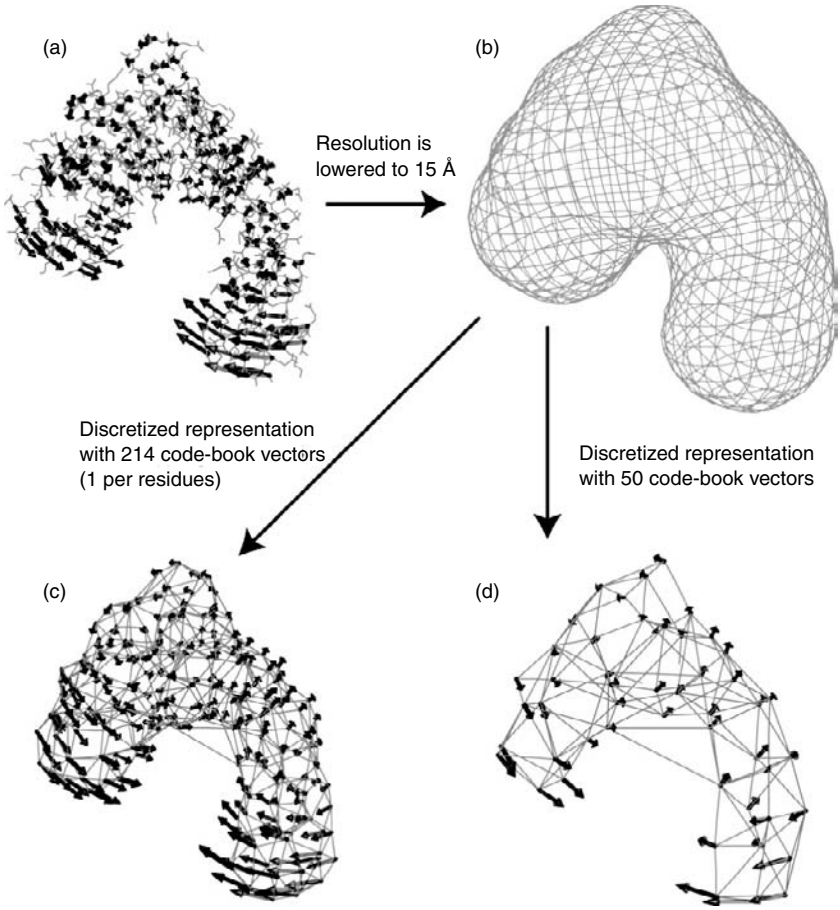

FIGURE 6.6
Elastic network NMA on low resolution structures: amplitude and direction of motion for the normal mode that has the highest similarity with the conformational changed observed in the adenylate kinase (a,c,d). (a) X-ray structure, (b) low-resolution structure of the adenylate kinase. Discretized representations of the adenylate kinase with (c) 214 codebook vectors, and (d) 50 codebook vectors. The NMA was carried out with a cut-off of 12 and 18 Å, respectively.

during the fitting. We propose that low-frequency distortions from NMA can be used as search directions in structure refinement protocols.

We recently developed a new program for flexible fitting based on iterative normal mode analysis (NMFF) [30]. For the fitting of a high-resolution structure into low-resolution structural data, it is necessary to maximize the correlation coefficient:

$$\text{c.c.} = \frac{\sum_{ijk} \rho^{\exp}(i,j,k)\rho^{\text{sim}}(i,j,k)}{\sqrt{\sum_{ijk} \rho^{\exp}(i,j,k)^2 \sum_{ijk} \rho^{\text{sim}}(i,j,k)^2}} \tag{6.13}$$

where $\rho^{\exp}(i,j,k)$ is the target experimental density map and $\rho^{\mathrm{sim}}(i,j,k)$ is a given map simulated from the deformed x-ray structure. In the case of myosin it was possible to determine the exact amplitude for each normal mode since a conformational difference vector was known; such information is not available if the target is a low-resolution electron density map. In order to overcome this problem, we developed a protocol to guide the choice of the relevant normal modes.

To choose the normal mode that increases the correlation coefficient and to determine the modes to be followed, we can calculate the gradient of the correlation coefficient $F_i = \partial$ c.c.$/\partial q_i$ for each mode $\mathbf{y}_i$. The gradient can be derived analytically. The absolute value of the gradient indicates how each mode will increase the correlation coefficient, whereas the sign determines the direction that needs to be followed along each mode. The magnitude of the displacement can be set to be proportional to the gradient:

$$q_i = \lambda F_i \tag{6.14}$$

where λ is a parameter that is chosen to make suitable displacements that expedite convergence while minimizing local distortions. This refinement process is equivalent to a steepest descent/ascent optimization of the correlation coefficient in the normal mode coordinate space.

During the maximization process, we also use a Newton–Raphson type algorithm near a maximum of the correlation coefficient. In this case, we need to calculate the second derivative, or Hessian, of the correlation coefficient. From this, the approximate best amplitude to displace the structure along each mode is given as:

$$\mathbf{q} = \mathbf{H}^{-1}\mathbf{F} \tag{6.15}$$

where $\mathbf{F} = \{F_k\}, \mathbf{H} = \{\partial \text{ c.c.}/\partial q_i \partial q_j\}$ is the Hessian, and $\mathbf{q}$ is the amplitude of displacement.

Our iterative procedure combines steepest ascent and Newton–Raphson techniques to optimize displacements of the x-ray structures along the 20 lowest-frequency normal modes to achieve high correlation between the experimental cryo-EM map and the modeled structure. At each step, the structure is displaced along the five modes with the largest gradient/Hessian. The procedure is performed until convergence of the correlation coefficients. To evaluate the performance of our approach, several proteins that undergo large conformational changes have been examined. Results indicate that NMFF provides an accurate and fast alternative method for the flexible fitting of high-resolution structure into a low-resolution density map determined by electron microscopy. Additionally, we have demonstrated that lower resolution (multi-scale) structural models, that is, C_α based models, can also be used for the normal mode searching in lieu of fully atomic models with little loss of overall accuracy [30].

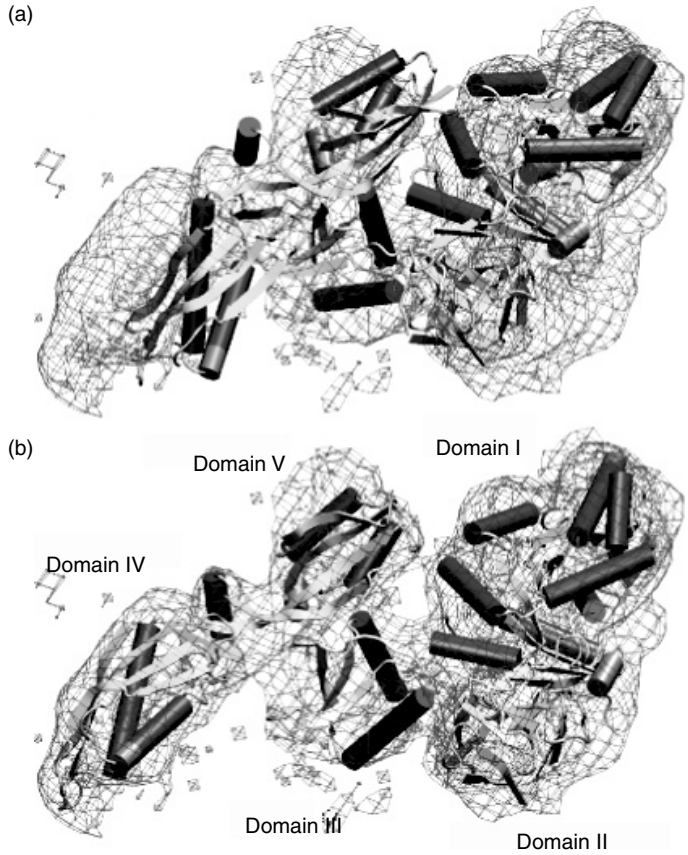

FIGURE 6.7
(See color insert following page 136) Flexible fitting using all-atoms at 10 Å resolution of Elongation G bound to the ribosome with NMFF. Rigid-body fitted structure (with Situs package) [56] into simulated EM map of the other conformational state. (b) The final flexibly fitted structure.

This methodology was then successfully applied to experimental cryo-EM maps for three biological systems with different degrees of complexity [61]. In each case, there were experimental data suggesting that a large conformational change was needed to fit the known x-ray structure of the biomolecule or molecular complex into the cryo-EM map. We explored the conformational change of a single protein, EF-G bound to the ribosome [46]. As we can see in Figure 6.7(a), after initial rigid body fitting some regions of the density remain unaccounted for. Figure 6.7(b) illustrates the structure after flexible fitting, using all atoms, in which significant improvement of the fit to the density is observed. The flexible fitting reveals large rearrangements between the domains II, IV, and V. In particular, we observe a large displacement (up to 20 Å) of domain IV, which is correlated with rotations of domains II and V.

NMFF was also shown to be successful in flexibly fitting complex macromolecular assembly such as the *E. coli* RNA polymerase [58] and protein assemblies such as the protein capsid of CCMV [38]. The latter system is peculiar since it exhibits icosahedral symmetry. Thus, our application to this system addresses the imposition of symmetry constraints during the flexible fitting/refinement of the high-resolution structure.

6.4 Conclusions

The combination of the elastic network model and the RTB approach have enabled the extension of applications of NMA to large macromolecular assemblies. These initial applications have focused on a range of assemblies and aimed to provide a better understanding of their functional motions, that is, the swelling transition of CCMV, the ratchet-like motion of the ribosome, and the conformational transition between active and inhibited myosin II. In addition, NMA of discretized representations of 3D data, such as that arising from cryo-EM map, provides predictive insight into conformational changes of large biomolecular assemblies. Finally, NMA provides a tool for the flexible fitting of high-resolution structures into low-resolution structural data.

Elastic network NMA based on coarse-grained x-ray structure or discrete representation of continuous 3D data successfully predicts many dynamical properties of several large macromolecular assemblies. Here, the detailed atomic interactions present in a standard force-field are replaced by a simple harmonic restoring force between the junctions of the network, and the essential properties captured by this model are the shape of the macromolecular assembly and the connectivity of its underlying structural framework. Thus, these studies show that a key to understanding the function of biological systems appears to lie in the shape-dependent dynamical properties of their complex architecture. These observations support the idea that Nature builds robustness into the functioning of these machines by assembling particular shapes, and that it is this shape, which dominates the character of the most facile motions, used in achieving function in such assemblies.

Acknowledgments

The authors are thankful to the many people who have collaborated with them in these projects. In particular, their interactions with P. Chacon, J. Frank, R. Konecny, J.A. McCammon, O. Miyashita, Y.H. Sanejouand, K.A. Taylor, J. Trylska, M. Valle, and W. Wriggers are gratefully acknowledged. Financial support from the National Institutes of Health to the Center for Multiscale Modeling Tools for Structural Biology-MMTSB (RR12255) is greatly appreciated.

References

1. Go, N., Noguti, T., and Nishikawa, T., *Proc. Natl Acad. Sci. USA* 80, 3696, 1983.
2. Brooks, B.R., and Karplus, M., *Proc. Natl Acad. Sci. USA* 80, 6571, 1983.
3. Levitt, M., Sander, C., and Stern, P.S., *J. Mol. Biol.* 181, 423, 1985.
4. Harrison, W., *Biopolymers* 23, 2943, 1984.
5. Brooks, B.R., and Karplus, M., *Proc. Natl Acad. Sci. USA* 82, 4995, 1985.
6. Gibrat, J.F., and Go, N., *Proteins* 8, 258, 1990.
7. Seno, Y., and Go, N., *J. Mol. Biol.* 216, 95, 1990.
8. Seno, Y., and Go, N., *J. Mol. Biol.* 216, 111, 1990.
9. Marques, O., and Sanejouand, Y.H., *Proteins* 23, 557, 1995.
10. Perahia, D., and Mouawad, L., *Comput. Chem.* 19, 241, 1995.
11. Mouawad, L., and Perahia, D., *J. Mol. Biol.* 258, 393, 1996.
12. Case, D.A., *Curr. Opin. Struct. Biol.* 4, 285, 1994.
13. Tirion, M.M., *Phys. Rev. Lett.* 77, 1905, 1996.
14. Tama, F., Wriggers, W., and Brooks, III, C.L., *J. Mol. Biol.* 321, 297, 2002.
15. Chacon, P., Tama, F., and Wriggers, W., *J. Mol. Biol.* 326, 485, 2003.
16. Ming, D., Kong, Y.F., Lambert, M.A., Huang, Z., and Ma, J.P., *Proc. Natl Acad. Sci. USA* 99, 8620, 2002.
17. Ming, D.M., Kong, Y.F., Wakil, S.J., Brink, J., and Ma, J.P., *Proc. Natl Acad. Sci. USA* 99, 7895, 2002.
18. Durand, P., Trinquier, G., and Sanejouand, Y.H., *Biopolymers* 34, 759, 1994.
19. Tama, F., Gadea, F.X., Marques, O., and Sanejouand, Y.H., *Proteins* 41, 1, 2000.
20. Mouawad, L., and Perahia, D., *Biopolymers* 33, 599, 1993.
21. Goldstein, H., *Classical Mechanics*, 2nd ed., Addison-Wesley Pub. Co., Reading, MA, 1980.
22. Hinsen, K., *Proteins* 33, 417, 1998.
23. Bahar, I., Atilgan, A.R., and Erman, B., *Fold. Des.* 2, 173, 1997.
24. Tama, F., and Sanejouand, Y.H., *Protein Eng.* 14, 1, 2001.
25. Doruker, P., Jernigan, R.L., and Bahar, I., *J. Comput. Chem.* 23, 119, 2002.
26. Tama, F., Valle, M., Frank, J., and Brooks III, C.L., *Proc. Natl Acad. Sci. USA* 100, 9319, 2003.
27. Schlitter, J., Engels, M., Kruger, P., Jacoby, E., and Wollmer, A., *Mol. Simulat.* 10, 291, 1993.
28. Guilbert, C., Perahia, D., and Mouawad, L., *Comput. Phys. Commun.* 91, 263, 1995.
29. Xu, C.Y., Tobi, D., and Bahar, I., *J. Mol. Biol.* 333, 153, 2003.
30. Tama, F., Miyashita, O., and Brooks III, C.L., *J. Mol. Biol.* 337, 985, 2004.
31. Miyashita, O., Onuchic, J.N., and Wolynes, P.G., *Proc. Natl Acad. Sci. USA* 100, 12570, 2003.
32. Zlotnick, A., Aldrich, R., Johnson, J.M., Ceres, P., and Young, M.J., *Virology* 277, 450, 2000.
33. Conway, J.F., Wikoff, W.R., Cheng, N., Duda, R.L., Hendrix, R.W., Johnson, J.E., and Steven, A.C., *Science* 292, 744, 2001.
34. Canady, M.A., Tihova, M., Hanzlik, T.N., Johnson, J.E., and Yeager, M., *J. Mol. Biol.* 299, 573, 2000.
35. Tuma, R., Tsuruta, H., Benevides, J.M., Prevelige, P.E., and Thomas, G.J., *Biochemistry* 40, 665, 2001.
36. Bancroft, J.B., Hills, G.J., and Markman, R., *Virology* 31, 354, 1967.

37. Caspar, D.L.D., and Klug, A., *Cold Spring Harbor Symp. Quant. Biol.* 27, 1, 1962.
38. Speir, J.A., Munshi, S., Wang, G.J., Baker, T.S., and Johnson, J.E., *Structure* 3, 63, 1995.
39. Reddy, V.S., Giesing, H.A., Morton, R.T., Kumar, A., Post, C.B., Brooks, C.L., and Johnson, J.E., *Biophys. J.* 74, 546, 1998.
40. Reddy, V.S., Natarajan, P., Okerberg, B., Li, K., Damodaran, K.V., Morton, R.T., Brooks, C., and Johnson, J.E., *J. Virol.* 75, 11943, 2001.
41. Tama, F., and Brooks III, C.L., Diversity and identity of mechanical properties of icosahedral viral capsids studied with elastic network normal mode analysis, *J. Mol. Biol.*, 345, 299–314, 2005.
42. Cate, J.H., Yusupov, M.M., Yusupova, G.Z., Earnest, T.N., and Noller, H. F., *Science* 285, 2095, 1999.
43. Gabashvili, I.S., Agrawal, R.K., Spahn, C.M., Grassucci, R.A., Svergun, D.I., Frank, J., and Penczek, P., *Cell* 100, 537, 2000.
44. Frank, J., Verschoor, A., Li, Y., Zhu, J., Lata, R.K., Radermacher, M., Penczek, P., Grassucci, R., Agrawal, R.K., and Srivastava, S., *Biochem. Cell. Biol.* 73, 757, 1995.
45. Frank, J., and Agrawal, R.K., *Nature* 406, 318, 2000.
46. Valle, M., Zavialov, A., Sengupta, J., Rawat, U., Ehrenberg, M., and Frank, J., *Cell* 114, 123, 2003.
47. Carter, A.P., Clemons, W.M., Jr., Brodersen, D.E., Morgan-Warren, R. J., Hartsch, T., Wimberly, B.T., and Ramakrishnan, V., *Science* 291, 498, 2001.
48. Yusupov, M.M., Yusupova, G.Z., Baucom, A., Lieberman, K., Earnest, T.N., Cate, J.H., and Noller, H.F., *Science* 292, 883, 2001.
49. Harms, J., Schluenzen, F., Zarivach, R., Bashan, A., Gat, S., Agmon, I., Bartels, H., Franceschi, F., and Yonath, A., *Cell* 107, 679, 2001.
50. Gomez-Lorenzo, M.G., Spahn, C.M., Agrawal, R.K., Grassucci, R.A., Penczek, P., Chakraburtty, K., Ballesta, J.P., Lavandera, J.L., Garcia-Bustos, J.F., and Frank, J., *EMBO J.* 19, 2710, 2000.
51. Trylska, J., Konecny, R., Tama, F., Brooks III, C.L., and Mccammon, J.A., Ribosome motions modulate electrostatic properties, *Biopolymers*, 74, 423–31, 2004.
52. Liu, H.J., Qu, C.X., Johnson, J.E., and Case, D.A., *J. Struct. Biol.* 142, 356, 2003.
53. Wendt, T., Taylor, D., Trybus, K.M., and Taylor, K., *Proc. Natl Acad. Sci. USA* 98, 4361, 2001.
54. Tama, F., Feig, M., Liu, J., Brooks III, C.L., and Taylor, K.A., The requirement for mechanical coupling between head and S2 domains in smooth muscle myosin ATPase regulation and its implications for dimeric motor function, *J. Mol. Biol.* 345, 837–54, 2004.
55. Saibil, H.R., *Nat. Struct. Biol.* 7, 711, 2000.
56. Wriggers, W., and Birmanns, S., *J. Struct. Biol.* 133, 193, 2001.
57. Wriggers, W., Milligan, R.A., and McCammon, J.A., *J. Struct. Biol.* 125, 185, 1999.
58. Darst, S.A., Opalka, N., Chacon, P., Polyakov, A., Richter, C., Zhang, G.Y., and Wriggers, W., *Proc. Natl Acad. Sci. USA* 99, 4296, 2002.
59. Cramer, P., Bushnell, D.A., and Kornberg, R.D., *Science* 292, 1863, 2001.
60. Llorca, O., Martin-Benito, J., Ritco-Vonsovici, M., Grantham, J., Hynes, G.M., Willison, K.R., Carrascosa, J.L., and Valpuesta, J.M., *EMBO J.* 19, 5971, 2000.
61. Tama, F., Miyashita, O., and Brooks III, C.L., *J. Struct. Biol.* 147, 315, 2004.
62. Humphrey, W., Dalke, A., and Schulten, K., *J. Mol. Graph.* 14, 33, 1996.

7

Applications of Normal Mode Analysis in Structural Refinement of Supramolecular Complexes

Jianpeng Ma

CONTENTS

7.1 Introduction

From several decades of computational research in structural biology and biophysics [1, 2], it is now well established that functions of biological macromolecules involve substantial structural motions, which can occur in a wide range of length scales [1, 2], for example, from vibrations of chemical bonds to global conformational changes of supramolecular complexes. However, molecular motions often impose difficulties in experimental structural determination as they tend to compromise the precision of the measurement. Meanwhile, due to the nature of instruments and molecular systems, experimental structural data are obtained in varying resolution scales, for

example, from atomic coordinates provided by x-ray crystallography to low- to intermediate-resolution electron density maps from, for example, electron cryomicroscopy (cryo-EM). For certain systems, especially supramolecular complexes, the errors in resolution are further augmented by the motions intrinsic to the complexes. The only way to overcome the errors imposed by motions is to use computational methods to model the structural flexibility in the process of structural refinement against experimental measurement. Therefore, a challenge in modern computational biophysics is to develop new methods of expanded capacity to efficiently model biomolecular motions in such a wide distribution of length and resolution scales.

Harmonic modal analyses are effective ways for analyzing molecular motions. The most frequently used ones are normal mode analysis (NMA) [3] and quasi-harmonic analysis [4], which is closely related to a method called essential dynamics [5]. Mathematically, all these modal analyses are eigenvalue problems that provide a complete basis set of modes from which any arbitrary molecular deformation can be expressed as a linear combination. Since modal analyses are harmonic approximations, they are particularly effective when elastic (harmonic) properties of molecules are concerned. From numerous computational studies, it is known that large-scale elastic deformational motions of biomolecules can be well described by low-frequency vibrational modes of the structures (typical samples can be found in References 6–21). Therefore, in practice, it is desirable to study biomolecular dynamics by filtering out the less important high-frequency motions and focusing on those dominating low-frequency components.

In recent years, significant advance has been made in methodology development of NMA [22]. It has provided a substantially enhanced capacity for studying large-scale biomolecular dynamics. In this chapter, a brief outline is given for some of those new methods that were developed to study dynamics at multi-length and multi-resolution scales. Emphases are given to the important applications of the new methods to assisting experimental structural determination.

This chapter is a concise review with a focused scope and our apology goes to the colleagues whose work is not explicitly referred to in this limited space.

7.2 Methods of NMA

7.2.1 Basic Theory of NMA

In the standard NMA [1, 3, 9], the potential surface of a given molecular structure is treated as quadratic in the vicinity of an energy minimum (harmonic approximation). The motions of the molecule are then decomposed into a set of independent harmonic vibrational modes, that is, normal modes, by which the overall molecular motions can be described as a linear combination. The normal modes are also referred to as molecular deformational modes.

They can be determined by computationally diagonalizing second-derivative matrix, **H**, of the total potential function with a matrix transformation, $\mathbf{H} = \mathbf{U}\Lambda\mathbf{U}^{-1}$, where **U** is an orthogonal matrix with its columns representing the eigenvectors of **H** and Λ is a diagonal matrix that contains the eigenvalues of **H**, or force constants of the harmonic modes. The eigenvectors determine the directionality of modes and the eigenvalues are related to frequencies of vibration. For a nonlinear system that contains N atoms, totally there are $3N - 6$ vibrational modes.

From numerous studies, it has been firmly established that only a very small set of low-frequency modes makes dominant contributions to biologically important conformational dynamics that are often of large amplitudes and are concerted. An outstanding example is the molecular chaperonin GroEL [7], an ATP-driven supramolecular motor complex, in which the nature of the functionally important *en bloc* domain motions was very successfully captured by NMA.

A fundamentally important fact that emerged from NMA is that many proteins, especially the large molecular complexes, have evolved to utilize their intrinsic structural flexibility, as manifested in low-frequency normal modes, to facilitate the conformational changes required for functions. This is probably because, mechanically it simply costs the least amount of energy to alter a molecular conformation to fulfill a certain function.

7.2.2 Elastic NMA

In recent years, a different type of NMA, called elastic NMA based on an elastic network often formed by C_α positions [23, 24], was introduced to study protein dynamics. The most frequently used one is also called anisotropic network model (ANM) [25]. It is essentially a standard NMA [3] based on a simplified pairwise harmonic potential function [26] applied to the C_α-based network with a single phenomenological force constant γ that can be set to be the same for all pairs. The mathematical form of the potential function is

$$V = (\gamma/2)\sum_i \sum_j \sigma_{ij}(|\mathbf{r}_{ij}| - |\mathbf{r}_{ij}^0|)^2, \quad \sigma_{ij} = \begin{cases} 1, & |\mathbf{r}_{ij}^0| \le r_c \\ 0, & |\mathbf{r}_{ij}^0| > r_c \end{cases},$$

where $|\mathbf{r}_{ij}|$ and $|\mathbf{r}_{ij}^0|$ are the instantaneous and equilibrium values (or initial values from the coordinates) of pairwise distance between the ith and the jth C_α atoms, respectively. The cutoff effect of the interaction is specified by the value of σ_{ij}, which is the Heaviside step function. This form of potential function was introduced by Tirion [26]. Its functional form resembles that of chemical bond in commonly used molecular mechanics potential function [27], that is, the harmonic potential is proportional to the square of the scalar difference of the instantaneous and the equilibrium lengths of the pair distance. The absolute value of γ in ANM is irrelevant to the calculation and is often set

to 1.0. A distinct advantage of ANM is that it treats the initial coordinates as the equilibrium coordinates. This feature avoids the lengthy initial energy minimization required in all atom-based NMA that sometimes significantly distorts structures [3]. Despite the fact that the potential function for ANM [25, 26] is drastically simplified and bears no resemblance to real molecular mechanics force field [27], studies have shown that the method can faithfully describe the patterns of motion for low-frequency modes of protein structures [17–19, 21, 25, 28–32].

However, the elastic NMA has an inherent weakness referred to as "tip effect." In systems that have certain structural components, the "tips," sticking out of the main body, for example, an isolated surface loop or simply a thinner region, tip effect could lead to pathological behaviors in some modes presumably due to imbalance of elastic forces among neighboring harmonic oscillators. In those modes, the magnitudes of displacement of the points in eigenvectors at or around the tips are much larger than those of the rest of the system, but with perfectly normal-looking eigenvalues. Since the eigenvectors of normal modes are normalized, the abnormally large magnitudes of displacement of the "tips" make the rest of the system essentially static. To make the matter worse, it is usually impossible to predict which modes have tip effect. But generally speaking, the higher-frequency modes have a larger tendency to have more severe tip effect. Although in a case-by-case situation, one might be able to ease such an effect, to our best knowledge, systematic ways are unavailable for overcoming this problem. In practice, if one is only interested in very few lowest-frequency modes for functional interpretation, the tip effect may be minimal since those modes are usually less likely to have tip effects. But in cases where a small set of continuous low-frequency modes are needed, the tip effect could become a major issue because it is almost inevitable that some of the modes in that small set will have some degrees of tip effect.

7.3 Structural Refinement in Cryo-EM Measurement

7.3.1 NMA Based on Low-Resolution Density Maps

In experiments, structural information comes at various resolutions. This is especially true for supramolecular complex structures determined by methods such as cryo-EM technique. For these systems, modelling motions based on structural data from which no atomic coordinates can be built is a challenge for computational study. This challenge was met by the development of quantized elastic deformational model (QEDM) by us [33] and by others as well [34], one very important advance in the field of NMA in recent years. Without the knowledge of atomic coordinates and amino-acid sequence, QEDM successfully allows one to compute low-frequency normal modes based on low-resolution (as low as 20 to 30 Å) density maps.

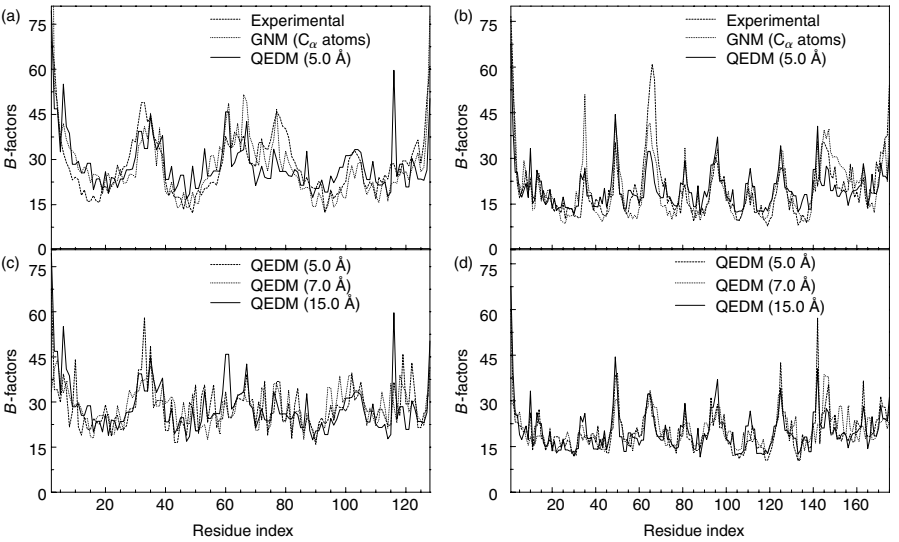

FIGURE 7.1
Comparison of computed and experimental *B*-factor curves, (a) and (c) for 2CCY; (b) and (d) for 1AQB. In (a) and (b), GNM uses the C_α positions, and QEDM uses 5 Å electron density map. In (c) and (d), QEDM is applied to electron density maps of 5, 7, and 15 Å resolutions. *B*-factors on the centroids of Voronoi cells computed at low resolutions by QEDM were mapped onto the C_α atoms based on a distance averaging method, that is, the average *B*-factors on the centroids within 1.9 Å (half of the nearest C_α–C_α distance along the polypeptide chain) from a particular C_α atom is assigned to that C_α atom. Every *B*-factor curve is normalized against the experimental one by matching the areas underneath the two curves. The cutoff distance was 6.8 Å. (Adopted from Ming, D., Kong, Y., Lambert, M., Huang, Z., and Ma, J., *Proc. Natl Acad. Sci. USA*, **99**, 8620 [2002].)

In QEDM, the concept of elastic NMA is applied to a set of points that are chosen to discretize the density maps. The positions of these points have no correlation with the positions of real atoms. They can be the grid points used for storing the density maps [35], or the ones determined by vector quantization method [36–38]. As shown in the original methodology papers [33, 34], the number of points can vary significantly and the only requirement is that it is large enough to effectively represent the overall shape of the molecule. This feature enables the calculation of modes for extremely large systems, in which cases the number of points much smaller than that of C_α atoms could be used to extract the overall features of low-frequency motions. It was shown that both the profiles of thermal fluctuation and directionality of low-frequency modes can be computed by QEDM almost as faithfully as what one can do with atomic coordinates at a wide range of resolutions [33, 34]. In Figure 7.1(a) and (b), the experimentally determined *B*-factor profiles for two arbitrarily selected proteins are plotted together with those computed by QEDM using density maps at 5.0 Å resolution and those by GNM based on the known C_α

positions [23]. The positions of peaks and valleys are matched strikingly well. It was also shown that the features of *B*-factor profiles calculated by QEDM are very insensitive to the resolution of the maps. At 15 Å or even lower resolutions, one can still get pretty good *B*-factor profiles [33] (Figures 7.1[c] and 7.1[d]) that match the experimentally determined ones.

A rather unique application of QEDM was to compute the mechanical elastic properties of large molecular systems based on low-resolution cryo-EM density maps. In one case, QEDM was employed to compute the differential flexibility of two key components of bacterial flagellum, filament, and hook [39], which is partially responsible for the mechanism of the motor. The dimensionless twist-to-bend ratio (*EI*/*GJ*) of the filament and hook was computed. The results indicate that within each structure bending is favored over twisting. The two ratios, along with data from experimental measurements, allowed one to propose a theoretical Young's modulus (*E*) for the hook. The value seems to be orders of magnitude smaller than experimentally determined Young's moduli for the filament and thus provides quantitative evidence for linking compliance in the flagellum mainly to the hook.

Another particularly important application of QEDM to supramolecular complexes is on human fatty acid synthase (FAS) [40], which is a crucial enzyme in fat metabolism and its malfunction is involved in many diseases [41–44]. The molecule is a huge enzymatic complex with extraordinarily large structural flexibility as required by its functions. The application of QEDM to the 19-Å cryo-EM density maps [45] successfully revealed the deformations of the structure [40]. It was found that the most significant molecular motions are the rigid body movements around the structural hinges as described by the four lowest-frequency modes. In mode 7, the motion is primarily around the inter-subunit hinge (Figure 7.2[a]). Each subunit moves as a rigid body and the dimer undergoes a see-saw-like bending around the pseudo 2-fold symmetry axis in the plane of the dimer. In mode 8, it describes an out-of-plane twisting, nearly perpendicular to mode 7, between two rigid subunits around the inter-subunit hinge (Figure 7.2[b]). The combination of modes 7 and 8 would allow the two subunits to make large-scale motions around the inter-subunit hinge. Mode 9 (Figure 7.2[c]) and mode 10 (Figure 7.2[d]) reveal the motions around the two intra-subunit hinges. Furthermore, for this particular system, the computationally predicted conformers were confirmed by experiments for the first time [46] (also see Section 7.3.4).

Just like the C_α-based elastic NMA, the success of QEDM hinges on an important fact that, in biomolecular dynamics, the features of low-frequency deformational motions are not sensitive to the local structural connectivity, rather they are predominantly influenced by the overall shape, or the mass distribution, of the molecule, which can be depicted by the low-resolution density maps. It is clear that QEDM significantly extends one's capability of modeling molecular motions, especially those of supramolecular complexes, to an unprecedented level and opens a new horizon for NMA. For many large

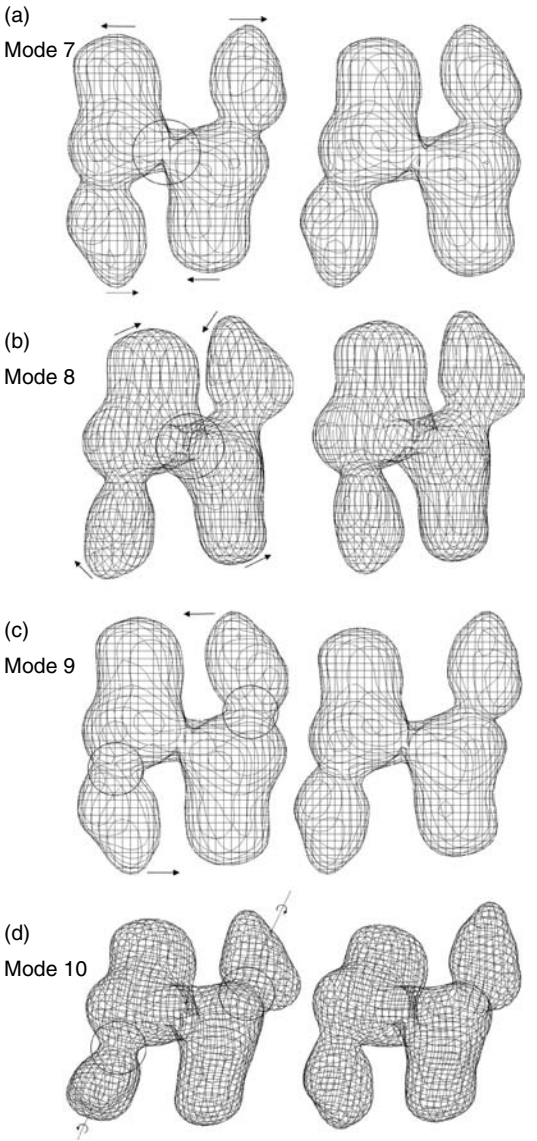

FIGURE 7.2
The motional patterns of the first four lowest-frequency deformational modes: mode 7 (a), 8 (b), 9 (c), and 10 (d). Note, the first six modes are zero modes corresponding to global translation and rotation of the entire molecule. For each mode, two opposite conformations (left and right) during harmonic vibration are shown to illustrate the direction of the motion. The amplitude of the motion was arbitrarily chosen for visual clarity. The arrows are used to indicate the directions of the motions. The larger circles in (a) and (b) indicate the intersubunit hinge and the smaller circles in (c) and (d) indicate the intrasubunit hinges. The dotted lines in (d) indicate the longest axes of the subunits. (Adopted from Ming, D., Kong, Y., Wakil, S.J., Brink, J., and Ma, J., *Proc. Natl Acad. Sci. USA*, **99**, 7895 [2002].)

systems, the method offers a way to reliably compute the global deformational motions at almost any experimentally accessible resolutions in real space. Since the birth of the method [33, 34], there have been many applications of QEDM on very large molecular complexes [40, 47–49] with many more surely to come in future.

7.3.2 QEDM-Assisted Cryo-EM Structural Refinement

Similar to x-ray crystallography and many other structural determination methods, the conformational heterogeneity of biomolecules severely impairs one's ability to reach high resolution by single-particle cryo-EM technique. The structural heterogeneity within the particle population due to the inherent flexibility of the proteins in solution can lead to smearing out of the cryo-EM averaging. At this point, this issue is mainly manifested in extraordinarily flexible systems such as FAS, in which case the cryo-EM reconstruction was only able to reach 19 Å [45] although the actual data extended to a much higher resolution. In the near future, given the dynamic nature of biological systems, the conformational heterogeneity is expected to become a major limiting factor for resolution of many systems once the resolutions of cryo-EM are high enough. To cope with such a problem, in a recent study of FAS [46], a major effort has been made to develop a computational strategy in conjunction with NMA [40] to separate the heterogeneous data such that structurally homogeneous particle images can be grouped to achieve higher resolution reconstructions within each group [50].

In a standard cryo-EM single model refinement, a set of projections of an initial 3D model is generated [51, 52]. Each raw particle image is aligned to each projection in 2D and grouped with the projection it is most similar to. The particles grouped with each projection are then mutually aligned to each other and averaged together. This produces a class-average from the raw particle data corresponding to each projection image. Since the 3D orientation of the projections is known, the orientation of the class averages is also known. The class averages are used to construct a new 3D model, which is used to seed the next iteration of refinement.

In the study of FAS [46], the two end-point conformers of the first two vibrational modes (modes 7 and 8 shown in Figures 7.2[a] and 7.2[b]) and the original structure were used (totally $n = 5$ models) as initial models for the multirefinement algorithm as developed in EMAN [52] (Figure 7.3). As usual, the particles are classified based on the projection they are the most similar to, however, now one ends up with n class-averages for each orientation, which can be used to produce n new 3D models to seed the next round of iterative refinement. Not only does this technique yield n refined 3D models, but it also produces n subsets of the raw particle data that were associated with each of the 3D models.

This very simple method produced very encouraging results. However, a potential criticism of this method is that it could potentially bias the final

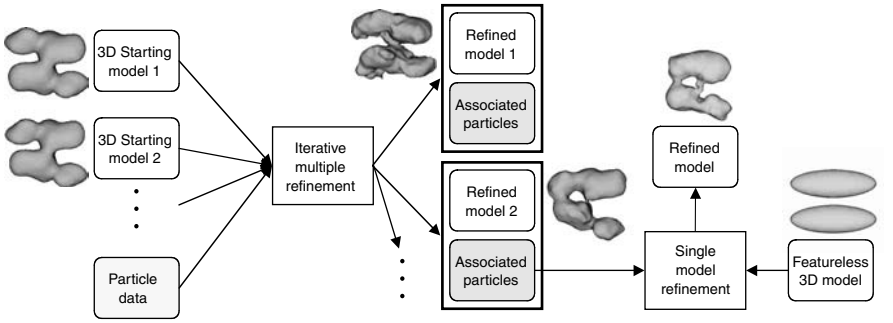

FIGURE 7.3
A flow diagram of the second test used to verify that structurally consistent subpopulations were determined from the raw heterogeneous particle data set. A featureless model (right) was refined against the particle data used to generate refined model 2. The result of this refinement appears to be in the same structural substate as refined model 2.

results to look like the initial models, even if there was no true structural heterogeneity in the data [53]. In other words, one may be extracting false features from the noise present in the raw particle images by imposing biased initial models. To demonstrate that this is not the case, a number of validation tests were designed to assure that the refined model from the subset image particles is genuine. First, if the conformational variation exists and is strongly represented in the data, it should be possible to generate conformational substates without requiring accurate initial 3D models. Toward this end, a multireference refinement was performed, but rather than starting with QEDM-derived models, a single averaged structure seeded with a low level of noise was used to produce several nearly identical and featureless starting models. This refinement did, indeed, produce structures with variations very similar to what was predicted by QEDM. However, due to the much larger differences between the initial models and the final structures, this refinement took substantially longer time to converge. An additional test is to take the subpopulation of particles used to generate one of the final models in the QEDM-based refinement, and to refine these particles against the original featureless two ellipsoidal model (Figure 7.3). This computational experiment again produced a structure similar to the original normal-mode-based structure that was used to group the images, demonstrating that the models produced using the QEDM-based refinement are not biased by the initial models, but are actually represented by the experimental data.

At current stage, QEDM-assisted cryo-EM refinement is not yet suited for every system. Several technical difficulties need to be overcome before the method can become a routine structural refinement procedure. For example, when the raw particle images are grouped into subgroups based on different molecular conformational states, each subgroup will naturally have fewer particles, which itself limits the resolutions. Therefore, a larger set of total particle images is required in order for each subgroup to have enough

particles for high-resolution reconstruction. Moreover, there is no unique way to determine the magnitudes of displacement of modes in generating the initial searching models. In principle, a complex molecule can have a continuous distribution of vibrational amplitude even along a single normal mode. It is merely an approximation to select a small number of extreme conformers along the modal displacement vector as representative searching models. Finally, in many cases, it is not clear what are the optimal ways of combining different modes. This is because combination of even a small set of modes can result in a very large number of conformers that can all be used for initial searching models. When there are only a limited number of particle images, a large number of initial searching models could impose severe difficulties.

Although still with these difficulties, the concept involved in QEDM-assisted cryo-EM refinement harbors hope for facilitating structural determination by cryo-EM to high resolutions. In a related issue, normal modes were also recently used to guide flexible docking of crystal structures into cryo-EM density maps [54]. There will certainly be more new methodology developments along this line in the foreseeable future.

7.4 Structural Refinement in Fiber Diffraction

7.4.1 NMA at Length Scales of Several Microns

Long filamentous systems in cells play important roles for cellular functions. From the computational point of view, the length of those filaments, which can be as long as several microns, prevents them from being studied by any conventional methods at atomistic details. To cope with this problem, a specific computational method called substructure synthesis method (SSM) [55] was developed to determine modes at very long length scales. In SSM, a given structure is treated as an assemblage of substructures, which can be domains, subunits, or large segments of biomolecules. NMA is first applied to the single substructure to obtain a set of substructure modes. Then, substructures are connected together to generate a longer structure of desired length. This is achieved by a set of geometric constraints for compatibility at the interfaces of neighboring substructures. Figure 7.4 illustrates a 1D example for the implementation of SSM: in fusing two identical segments together, one of the two boundary points (c and a′) are equalized (sacrificed) in the process of synthesis. The efficiency of SSM lies in the fact that the method only deals with an eigenvalue problem for a much smaller substructure. The low-frequency vibrational modes of the longer structure are determined from substructure modes according to Rayleigh–Ritz principle [56]. For periodically repeating systems, the desired length of final structure can be reached by combining a hierarchical synthesis scheme (HSS) with SSM.

SSM was applied to simulating F-actin filaments, which are widely involved in cytoskeletal support, cell transport, and contractile events in all eukaryotic

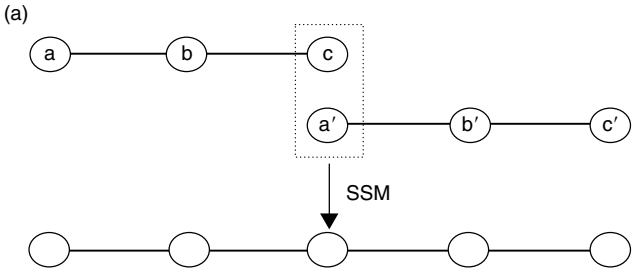

FIGURE 7.4
A schematic illustration of SSM when fusing two 3-mass-point chains together. One of the two boundary points (c and a′) is equalized (sacrificed) during synthesis. (Adopted from Ming, D., Kong, Y., Wu, Y., and Ma, J., *Biophys. J.*, **85**, 27 [2003].)

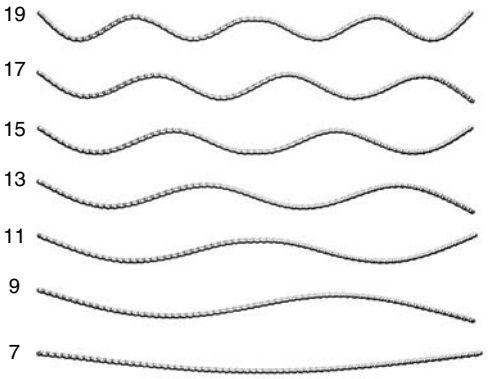

FIGURE 7.5
The motional patterns of several lowest-frequency bending modes for the 4.6 μm F-actin filament calculated by SSM–HSS. The indices of the modes are marked. The even indices are the ones that degenerate to the displayed one. The 7th mode is the lowest-frequency mode. (Adopted from Ming, D., Kong, Y., Wu, Y., and Ma, J., *Biophys. J.*, **85**, 27 [2003].)

cells [57]. The monomeric form of actin is called G-actin that exists in nonionic solutions. It has a molecular weight of 41 kD. In the presence of salt, actin monomers polymerize into a double-stranded helical polymer called F-actin [58]. It is known from experimental evidence [59] that a substantial portion of dynamic properties of F-actin resides in the elasticity of the filaments. Therefore, a harmonic analysis of dynamics of F-actin filaments is useful for understanding of the mechanical elastic properties of actin filaments.

The vibrational modes of F-actin filaments of 4.6 μm from the substructure modes of a single repeat that consisted of 13 G-actin subunits was successfully calculated [60]. To achieve that, SSM was used, in conjunction with HSS, to simplify the calculation for periodically repeating F-actin filaments. Figure 7.5 shows patterns of several lowest-frequency bending modes. SSM–HSS is proven to be an effective way to scale up the microscopic dynamic

information from atomistic simulations to a wide range of near macroscopic length scales [60].

7.4.2 Fiber Diffraction Refinement Based on Long-Range Normal Modes

One very significant application of long-range normal modes for biological fibers determined by SSM is in the refinement of structural models against fiber diffraction data [61, 62]. There are many filamentous systems in cell whose structures can only be studied by fiber diffraction [63]. Examples range from simple polypeptides, polynucleotides, and polysaccharides, to cytoskeletal filaments and filamentous viruses.

In fiber diffraction, the fiber specimens align axially, but not azimuthally, so that the diffraction patterns are cylindrically averaged. Such an average leads to a much more limited number of independent diffractions comparing with those of a single crystal with a similar size of asymmetric unit. The lack of sufficient data prevents one from refining the Cartesian coordinates of every atom in the fibers. Therefore, it is very important to choose a proper set of parameters for effective structural refinement [64]. Moreover, in traditional fiber refinement methods, fibers are assumed to be straight helices. However, in reality, biological fibers, such as DNA or F-actin, are usually flexible and are likely to deviate from perfect helical systems. All kinds of static and dynamic disordering of fibers such as bending, twisting, and stretching are likely to contribute to the modulation of diffraction patterns. Therefore, effects should be included in refinement because otherwise it can lead to severe mistreatment of errors.

From what was described in the previous section, collective long-range deformations of a filament, such as bending, twisting, and stretching, can be effectively described by normal modes [60, 65]. Therefore, they are the natural choices as refinement parameters. A distinct advantage of using normal modes as refinement parameters is that a very small set of parameters (modes) can effectively model the dynamic deformations of fibers in the fiber diffraction refinement. In practice, it was assumed that deformations occur within the periodic repeat of the filaments (helical unit cell) with a certain defined length. As a result, the straight rigid filament model used in traditional refinement methods was replaced by wave-like conformations.

The method was applied to the refinement of F-actin model against fiber diffraction data [61]. In the traditional model of F-actin, the Holmes model [66], filaments have two right-handed helical strands that twist around each other with a rise of 27.5 Å and a rotation angle of -166.15° per monomer around the filament axis. The minimum repeat of the double-stranded helix has 13 subunits (the 13-subunit repeat).

The refinement was focused on the effects of long-range filamentous deformation, which were separated from those of local deformation by treating the four-domains of G-actin as rigid bodies. Several runs of refinement were performed against the fiber diffraction data [66] using

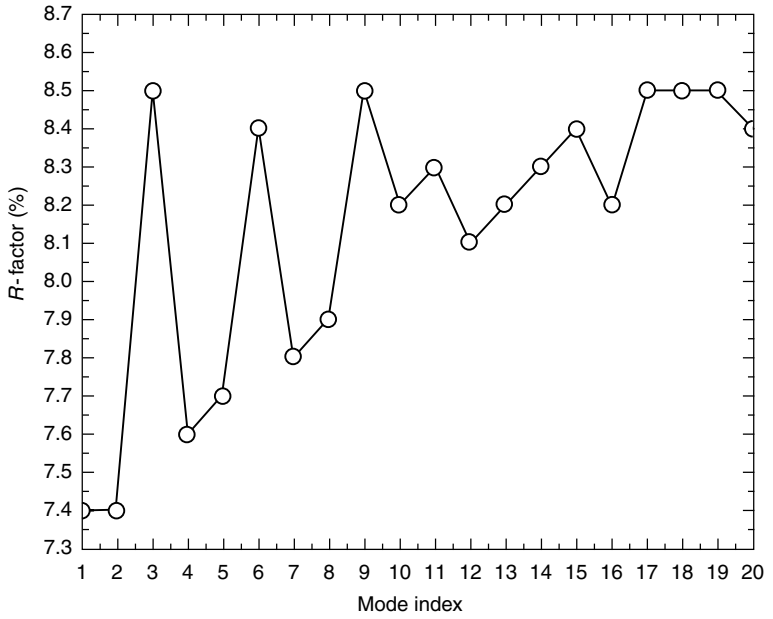

FIGURE 7.6
Refinement results by each of the first 20 lowest-frequency vibrational modes as a function of the mode index. The refinement was based on the normal modes calculated for a 13-subunit repeat using ANM. The ceiling of the figure is the value of *R*-factor of the standard Holmes model (8.7%), the starting point of this study. (Adopted from Wu, Y. and Ma, J., *Biophys. J.*, **86**, 116 [2004].)

various assemblies of G-actin subunits as helical unit cells. Within the helical unit cells, the helical symmetry was disregarded and all atoms were treated in a unique way. F-actin filaments were assumed to deform periodically in terms of the helical unit cells.

First, the low-frequency modes of a 13-subunit repeat were computed using C_α-based ANM [25]. Then, each individual low-frequency mode was used as a refinement parameter (Figure 7.6). All the first 20 lowest-frequency modes tested reduced the *R*-factor to various degrees (the ceiling of the figure is the *R*-factor of the standard Holmes model 8.7%), whereas the two perpendicular bending modes 1 and 2 resulted in the lowest *R*-factor (7.4%). All of the first 11 lowest-frequency modes are bending modes with shortening wavelengths, with the exception that modes 3 and 6 are twisting modes and mode 9 is a stretching mode. These results suggest that the very low-frequency bending modes of F-actin filament make the dominant contributions to the improvement of structure refinement. Furthermore, the bending modes calculated by SSM for longer repeating units can further improve the refinement [61].

In addition to the refinement by a single mode as described above, runs of refinement were also performed to find out how a combination of multiple modes improves the refinement. The combination of several low-frequency

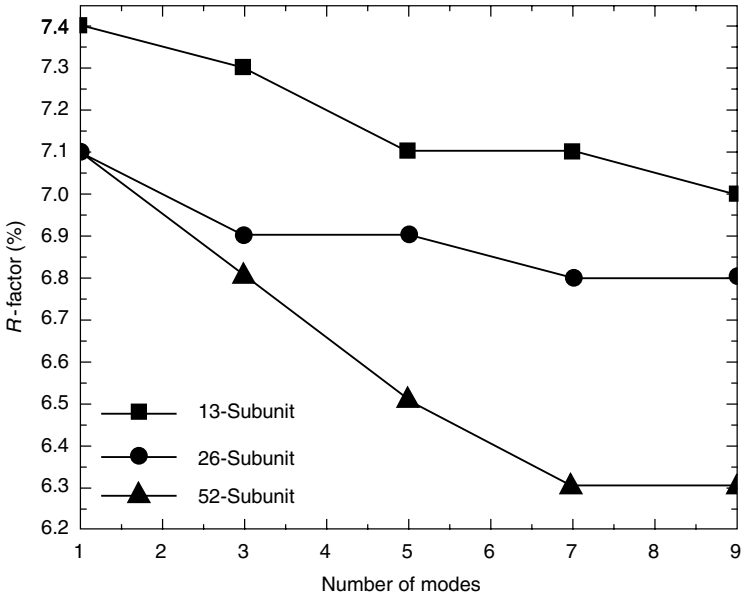

FIGURE 7.7
Refinement results using various sizes of repeats as helical unit cells with a combination of multiple low-frequency normal modes. (Adopted from Wu, Y. and Ma, J., *Biophys. J.*, **86**, 116 [2004].)

modes further decreased the *R*-factor. For example, the use of 9 modes in the refinement resulted in an *R*-factor of 7.0% (Figure 7.7). With larger helical unit cells (26- and 52-subunit repeats), the trends of changes in *R*-factor were consistent, that is, they monotonically decrease as the number of modes used in refinement increases. The best values of *R*-factor were 6.8% for the 26-subunits and 6.3% for the 52-subunits using 7 to 9 lowest-frequency modes.

In summary, these results clearly suggest that a substantial portion of refinement errors in fiber diffraction of F-actin comes from long-range deformations, in particular bending, of the filaments. Therefore, effects of these long-range deformations should be properly accounted for in the refinement to avoid mistreatment of errors. SSM-based normal mode refinement provides an effective way of doing so with only a small set of long-range modes as adjustable parameters, thus preventing the potential over-fitting problem.

Acknowledgments

The author gratefully acknowledges support from the American Heart Association, the Robert Welch Foundation, the National Science Foundation Career Award, and the National Institutes of Health. The author is also a recipient of

the Award for Distinguished Young Scholars Abroad from National Natural Science Foundation of China.

References

1. Brooks III, C.L., Karplus, M., and Pettitt, B.M., Proteins: a theoretical perspective of dynamics, structure, and thermodynamics, *Adv. Chem. Phys.*, **71**, 1 (1988).
2. McCammon, J.A. and Harvey, S., *Dynamics of Proteins and Nucleic Acids*, Cambridge University Press, Cambridge (1987).
3. Brooks, B.R., Janezic, D., and Karplus, M., Harmonic analysis of large systems. I. Methodology, *J. Comput. Chem.*, **16**, 1522 (1995).
4. Janezic, D., Venable, R.M., and Brooks, B.R., Harmonic analysis of large systems. III. Comparison with molecular dynamics, *J. Comput. Chem.*, **16**, 1554 (1995).
5. Amadei, A., Linssen, A.B.M., and Berendsen, H.J.C., Essential dynamics of proteins, *Proteins*, **17**, 412 (1993).
6. Ma, J. and Karplus, M., Ligand-induced conformational changes in *ras* p21: a normal mode and energy minimization analysis, *J. Mol. Biol.*, **274**, 114 (1997).
7. Ma, J. and Karplus, M., The allosteric mechanism of the chaperonin GroEL: a dynamic analysis, *Proc. Natl Acad. Sci. USA*, **95**, 8502 (1998).
8. Brooks, B. and Karplus, M., Normal modes for specific motions of macromolecules: application to the hinge-bending mode of lysozyme, *Proc. Natl Acad. Sci. USA*, **82**, 4995 (1985).
9. Levitt, M., Sander, C., and Stern, P.S., Protein normal-mode dynamics: trypsin inhibitor, crambin, ribonuclease and lysozyme, *J. Mol. Biol.*, **181**, 423 (1985).
10. Seno, Y. and Go, N., Deoxymyoglobin studied by the conformational normal mode analysis II. The conformational change upon oxygenation, *J. Mol. Biol.*, **216**, 111 (1990).
11. Seno, Y. and Go, N., Deoxymyoglobin studied by the conformational normal mode analysis. I. Dynamics of globin and the heme–globin interaction, *J. Mol. Biol.*, **216**, 95 (1990).
12. Thomas, A., Field, M.J., and Perahia, D., Analysis of the low-frequency normal modes of the R state of aspartate transcarbamylase and a comparison with the T state modes, *J. Mol. Biol.*, **261**, 490 (1996).
13. Thomas, A., Field, M.J., Mouawad, L., and Perahia, D., Analysis of the low frequency normal modes of the T-state of aspartate transcarbamylase, *J. Mol. Biol.*, **257**, 1070 (1996).
14. Thomas, A., Hinsen, K., Field, M.J., and Perahia, D., Tertiary and quaternary conformational changes in aspartate transcarbamylase: a normal mode study, *Proteins*, **34**, 96 (1999).
15. Li, G. and Cui, Q., A coarse-grained normal mode approach for macromolecules: an efficient implementation and application to Ca(2+)-ATPase, *Biophys. J.*, **83**, 2457 (2002).
16. Cui, Q., Li, G., Ma, J., and Karplus, M., A normal mode analysis of structural plasticity in the biomolecular motor F(1)-ATPase, *J. Mol. Biol.*, **340**, 345 (2004).
17. Xu, C., Tobi, D., and Bahar, I., Allosteric changes in protein structure computed by a simple mechanical model: hemoglobin T<–>R2 transition, *J. Mol. Biol.*, **333**, 153 (2003).

18. Wang, Y., Rader, A.J., Bahar, I., and Jernigan, R.L., Global ribosome motions revealed with elastic network model, *J. Struct. Biol.*, **147**, 302 (2004).
19. Keskin, O., Bahar, I., Flatow, D., Covell, D.G., and Jernigan, R.L., Molecular mechanisms of chaperonin GroEL–GroES Function, *Biochemistry*, **41**, 491 (2002).
20. Tama, F. and Sanejouand, Y.H., Conformational change of proteins arising from normal mode calculations, *Protein Eng.*, **14**, 1 (2001).
21. Tama, F. and Brooks III, C.L., The mechanism and pathway of ph induced swelling in cowpea chlorotic mottle virus, *J. Mol. Biol.*, **318**, 733 (2002).
22. Ma, J., New advances in normal mode analysis of supermolecular complexes and applications to structural refinement, *Curr. Protein Pept. Sci.*, **5**, 119 (2004).
23. Bahar, I., Atilgan, A.R., and Erman, B., Direct evaluation of thermal fluctuations in proteins using a single-parameter harmonic potential, *Fold. Des.*, **2**, 173 (1997).
24. Haliloglu, T., Bahar, I., and Erman, B., Gaussian dynamics of folded proteins, *Phys. Rev. Lett.*, **79**, 3090 (1997).
25. Atilgan, A.R., Durell, S.R., Jernigan, R.L., Demirel, M.C., Keskin, O., and Bahar, I., Anisotropy of fluctuation dynamics of proteins with an elastic network model, *Biophys. J.*, **80**, 505 (2001).
26. Tirion, M.M., Large amplitude elastic motions in proteins from a single-parameter, atomic analysis, *Phys. Rev. Lett.*, **77**, 1905 (1996).
27. MacKerell, A.D., Bashford, D., Jr., Bellott, M., Dunbrack, R.L., Jr., Evanseck, J.D., Field, M.J., Fischer, S., Gao, J., Guo, H., Ha, S., Joseph-McCarthy, D., Kuchnir, L., Kuczera, K., Lau, F.T.K., Mattos, C., Michnick, S., Ngo, T., Nguyen, D.T., Prodhom, B., Reiher, I., W.E., Roux, B., Schlenkrich, M., Smith, J.C., Stote, R., Straub, J., Watanabe, M., JWiorkiewicz-Kuczera, J., Yin, D., and Karplus, M., All-atom empirical potential for molecular modeling and dynamics studies of proteins, *J. Phys. Chem.*, **B102**, 3586 (1998).
28. Doruker, P., Jernigan, R.L., and Bahar, I., Dynamic of large proteins through hierarchical levels of coarse-grained structures, *J. Comput. Chem.*, **23**, 119 (2002).
29. Hinsen, K., Analysis of domain motions by approximate normal mode calculations, *Proteins*, **33**, 417 (1998).
30. Tama, F., Valle, M., Frank, J., and Brooks III, C.L., Dynamic reorganization of the functionally active ribosome explored by normal mode analysis and cryo-electron microscopy, *Proc. Natl Acad. Sci. USA*, **100**, 9319 (2003).
31. Kim, M.K., Jernigan, R.L., and Chirikjian, G.S., An elastic network model of HK97 capsid maturation, *J. Struct. Biol.*, **143**, 107 (2003).
32. Kundu, S., Melton, J.S., Sorensen, D.C., and Phillips, G.N., Jr., Dynamics of proteins in crystals: comparison of experiment with simple models, *Biophys. J.*, **83**, 723 (2002).
33. Ming, D., Kong, Y., Lambert, M., Huang, Z., and Ma, J., How to describe protein motion without amino-acid sequence and atomic coordinates, *Proc. Natl Acad. Sci. USA*, **99**, 8620 (2002).
34. Tama, F., Wriggers, W., and Brooks, C.L., Exploring global distortions of biological macromolecules and assemblies from low-resolution structural information and elastic network theory, *J. Mol. Biol.*, **321**, 297 (2002).
35. Doruker, P. and Jernigan, R.L., Functional motions can be extracted from on-lattice construction of protein structures, *Proteins*, **53**, 174 (2003).
36. Gray, R.M., Vector quantization, *IEEE ASSP Mag.*, **1**, 4 (1984).
37. Martinetz, T.M., Berkovich, S.G., and Schulten, K.J., "Neural-gas" network for vector quantization and its application to time-series prediction, *IEEE Trans. Neural Networks*, **4**, 558 (1993).

38. Makhoul, J., Roucos, S., and Gish, H., Vector quantization in speech coding, *Proc. IEEE*, **73**, 1551 (1985).
39. Flynn, T.C. and Ma, J., Theoretical analysis of twist/bend ratio and mechanical moduli of bacterial flagellar hook and filament, *Biophys. J.*, **86**, 3204 (2004).
40. Ming, D., Kong, Y., Wakil, S.J., Brink, J., and Ma, J., Domain movements in human fatty acid synthase by quantized elastic deformational model, *Proc. Natl Acad. Sci. USA*, **99**, 7895 (2002).
41. Stoops, J.K., Ross, P., Arslanian, M.J., Aune, K.C., Wakil, S.J., and Oliver, R.M., Physicochemical studies of the rat liver and adipose fatty acid synthetases, *J. Biol. Chem.*, **254**, 7418 (1979).
42. Stoops, J.K. and Wakil, S.J., Animal fatty acid synthetase. A novel arrangement of the beta-ketoacyl synthetase sites comprising domains of the two subunits, *J. Biol. Chem.*, **256**, 5128 (1981).
43. Stoops, J.K., Wakil, S.J., Uberbacher, E.C., and Bunick, G.J., Small-angle neutron-scattering and electron microscope studies of the chicken liver fatty acid synthase, *J. Biol. Chem.*, **262**, 10246 (1987).
44. Singh, N., Wakil, S.J., and Stoops, J.K., On the question of half- or full-site reactivity of animal fatty acid synthetase, *J. Biol. Chem.*, **259**, 3605 (1984).
45. Brink, J., Ludtke, S.J., Yang, C.Y., Gu, Z.W., Wakil, S.J., and Chiu, W., Quaternary structure of human fatty acid synthase by electron cryomicroscopy, *Proc. Natl Acad. Sci. USA*, **99**, 138 (2002).
46. Brink, J., Ludtke, S.J., Kong, Y., Wakil, S.J., Ma, J., and Chiu, W., Experimental verification of conformational variation of human fatty acid synthase as predicted by normal mode analysis, *Structure (Camb.)*, **12**, 185 (2004).
47. Kong, Y., Ming, D., Wu, Y., Stoops, J.K., Zhou, Z.H., and Ma, J., Conformational flexibility of pyruvate dehydrogenase complexes: a computational analysis by quantized elastic deformational model, *J. Mol. Biol.*, **330**, 129 (2003).
48. Beuron, F., Flynn, T.C., Ma, J., Kondo, H., Zhang, X., and Freemont, P.S., Motions and negative cooperativity between p97 domains revealed by cryoelectron microscopy and quantized elastic deformational model, *J. Mol. Biol.*, **327**, 619 (2003).
49. Chacon, P., Tama, F., and Wriggers, W., Mega-dalton biomolecular motion captured from electron microscopy reconstructions, *J. Mol. Biol.*, **326**, 485 (2003).
50. Carazo, J.M., Accessing information on the conformational flexibility of molecular machines, *Structure*, **12**, 170 (2004).
51. Ludtke, S.J., Jakana, J., Song, J.L., Chuang, D., and Chiu, W., A 11.5 Å single particle reconstruction of GroEL using EMAN, *J. Mol. Biol.*, **314**, 253 (2001).
52. Ludtke, S.J., Baldwin, P.R., and Chiu, W., EMAN: semiautomated software for high-resolution single-particle reconstructions, *J. Struct. Biol.*, **128**, 82 (1999).
53. Grigorieff, N., Resolution measurement in structures derived from single particles, *Acta Crystallogr. D*, **56**, 1270 (2000).
54. Tama, F., Miyashita, O., and Brooks, III, C.L., Normal mode based flexible fitting of high-resolution structure into low-resolution experimental data from cryo-EM, *J. Struct. Biol.*, **147**, 315 (2004).
55. Ming, D., Kong, Y., Wu, Y., and Ma, J., Substructure synthesis method for simulating large molecular complexes, *Proc. Natl Acad. Sci. USA*, **100**, 104 (2003).
56. Temple, G. and Bickley, W.G., *Rayleigh's Principle and its Applications to Engineering*, Dover, New York (1956).
57. Chen, H., Bernstein, B.W., and Bamburg, J.R., Regulating actin-filament dynamics *in vivo*, *Trends Biochem. Sci.*, **25**, 19 (2000).

58. Oda, T., Makino, K., Yamashita, I., Namba, K., and Maeda, Y., Distinct structural changes detected by x-ray fiber diffraction in stabilization of F-actin by lowering pH and increasing ionic strength, *Biophys. J.*, **80**, 841 (2001).
59. Yasuda, R., Miyata, H., and Kinosita, K., Jr., Direct measurement of the torsional rigidity of single actin filaments, *J. Mol. Biol.*, **263**, 227 (1996).
60. Ming, D., Kong, Y., Wu, Y., and Ma, J., Simulation of F-actin filaments of several microns, *Biophys. J.*, **85**, 27 (2003).
61. Wu, Y. and Ma, J., Refinement of F-actin model against fibre diffraction data by long-range normal modes, *Biophys. J.*, **86**, 116 (2004).
62. Wu, Y. and Ma, J., Normal-mode-based refinement of an F-actin model against fibre diffraction data, *Fibre Diff. Rev.*, **12**, 25 (2004).
63. Stubbs, G., Development in Fibre Diffraction, *Curr. Opin. Struct. Biol.*, **9**, 615 (1999).
64. Wang, H. and Stubbs, G., Molecular dynamics in refinement against fibre diffraction data, *Acta Crystallogr. A*, **49**, 504 (1993).
65. ben-Avraham, D. and Tirion, M.M., Dynamic and elastic properties of F-actin: a normal-modes analysis, *Biophys. J.*, **68**, 1231 (1995).
66. Holmes, K.C., Popp, D., Gebhard, W., and Kabsch, W., Atomic model of the actin filament, *Nature*, **347**, 44 (1990).

8

Normal Mode Analysis in Studying Protein Motions with X-Ray Crystallography

George N. Phillips, Jr.

CONTENTS

8.1 Introduction

Traditional x-ray crystallography has provided prodigious amounts of information on protein and nucleic acid structures, revealing intricate details for many biological activities. In most cases, however, it is the subtle or sometimes not so subtle dynamic behavior of these structures that contains the essence of their function. Allostery, induced fit, and key conformational changes are alterations in the structures that allow proteins to catalyze reactions, transport ligands, or regulate systems. Thus, it is not only the form that determines function, but also the way in which the form changes in time.

Collectively, we are moving beyond static pictures of biological structures to a point where dynamic descriptions are necessary for defining mechanisms of function including catalysis (Benkovic and Hammes-Schiffer 2003). Dynamics are much harder to study than the static aspects of structures, or even the "energy landscape" of possible states (Bryngelson et al. 1995; Frauenfelder 1995). The classical chemists' idea that Arrhenius' law applies for enzyme-mediated catalysis or substrate binding is limited. We know that the complexity of proteins and the multiple processes involved in substrate

binding, distortion, and release impose multiple barriers that do not equate to simply achieving a transition state (Ansari et al. 1994). New connections are needed in our understanding of the relationships between sequence, structure, dynamics, and function.

According to the Haldane–Pauling theory, any complex between a protein and substrates that stabilizes the transition state of a reaction will accelerate the rate of reaction (Haldane 1930; Pauling 1946). This principle has been verified as being a good first order approximation by the generation of antibody-based enzymes (Schultz and Lerner 1995; Ulrich et al. 1997). However, there are documented differences between the catalytic efficiencies of abzymes and enzymes. As pointed out by Hilvert (2000), if rate acceleration ($-\log KT_s$) is plotted against chemical proficiency ($\log k_{cat}/k_{uncat}$) for a representative set of reactions, the result shows that abzyme reactions cluster in the lower left quadrant of the plot, corresponding to the poorest catalysts, whereas enzymatic reactions are much more effective. The K_m values are roughly comparable in all of these systems. The best antibodies approach the effectiveness of the least efficient enzymes, but it should be noted that the corresponding reactions often involve conversions of relatively activated substrates (e.g., the hydrolysis of aryl esters).

Forming a specific stabilization of the transition state is likely to be only part of the design of naturally selected, efficient enzymes. Another feature is the channeling of thermal energy into modes of motion that can contribute to one or more necessary steps in a catalytic cycle. Induced fit binding, thermal fluctuations that overlap the transition state, and structural fluctuations that lead to binding or even unbinding events can all be a part of the selection process for better chemical efficiency. The number of failures in abzyme development (proteins that bind transition state analogs well but do not have activity) is not reported. The abzyme examples that do work may be ones with a small dynamic requirement, with even that having been selected by the combinatorial or other approaches to abzyme discovery.

The application of dimensionality reduction methods, namely principle component analysis, to macromolecular structural data was first described by Garcia (1992) to identify large-amplitude modes of fluctuations in macromolecular dynamics simulations. Principle component analysis and its correlates have also been used to identify and study protein conformational substates (Romo et al. 1995; Caves et al. 1998; Kitao and Go 1999) as a possible method to extend the timescale of molecular dynamics simulations (Amadei et al. 1993; Amadei et al. 1996) and as a method to perform conformational sampling (de Groot et al. 1996a,b). The validity of the method has also been established by comparison with experimentally derived data (de Groot et al. 1998; Haliloglu and Bahar 1999). An alternative approach to determine collective modes for proteins uses normal mode analysis (Levy and Karplus 1979; Go et al. 1983; Levitt et al. 1985) and was also extended as a basis for modeling the flexibility of larger molecules (Zacharias and Sklenar 1999).

As pointed out by Go and also others (Go et al. 1983; Go 1990), the large amplitude, low-frequency modes of motion of a protein contribute significantly

to the entropy of the system, and must therefore be understood if any connections are to be made with experimental thermodynamic measurements. Classification of modes and their use in describing or predicting key conformational changes is also taking hold. Gerstein and his group have done a superb job of mining examples from the PDB and adding dynamic interpretations and explanations (Gerstein and Krebs 1998). Increasingly specific connections between dynamics and function were found, as a result of studies, including those on cyclophilin A (Eisenmesser et al. 2002) and the signaling protein NtrC (Volkman et al. 2001) using NMR, and theoretical studies on alphalytic protease (Miller and Agard 1999; Ota and Agard 2001), hemagglutinin (Isin et al. 2002), tubulin (Keskin et al. 2002), and photosynthetic reaction centers (Balabin and Onuchic 2000) and others.

There are numerous examples that indicate that modes of motion in proteins occur along closure pathways resulting from ligand binding (Miller and Agard 1999; Ota and Agard 2001; Roccatano et al. 2001; Tama and Sanejouand 2001). Many other studies relate simplified normal modes to function, illustrating the value of the approach (e.g., Ma and Karplus 1998; Doruker et al. 2002). There is a growing awareness and discussion of the role of dynamics in catalysis (Benkovic and Hammes-Schiffer 2003) and new experimental and theoretic tools are needed. Clearly more insight is needed before enzymes can be well understood or designed *de novo*. The effect of protein motions on the drug design process has also been noted (Teodoro and Kavraki 2003). The problem of allowing for induced-fit in computational searches for lead compounds is still largely unsolved. Members of my laboratory have been contributing by trying to reduce the space of local protein dynamics to a manageable dimensionality once the motions are understood (Teodoro et al. 2003).

Experimental determinations of the detailed dynamics of proteins are more difficult than obtaining a static model of the average structure. At present there are only a few techniques that can yield information about both the structure and the deviations from the average. X-ray crystallography can provide very detailed information about relatively small amplitude fluctuations, but is limited by the requirement that the crystalline lattice retain order during an experiment. Crystals can be subjected to time-resolved experiments (Moffat 1998; Schotte et al. 2003), but the range of applications is limited to reactions that can be triggered by light or trapped by clever manipulations (Stoddard 1998). Usually crystallographic studies reveal amplitudes, but not time constants of displacements. NMR spectroscopy can provide information about dynamics of particular regions of a protein, but it has limitations on interpretation depending on whether the dynamics can be defined as slowly or quickly exchanging (Kay 1998; Kempf and Loria 2003). More recently, it has been found that mass spectrometry coupled with hydrogen/deuterium exchange with proteolysis allows relative solvent accessibility changes to be determined (Engen and Smith 2001; Lanman and Prevelige 2004). This technique may be slightly more indirect but shows strong promise.

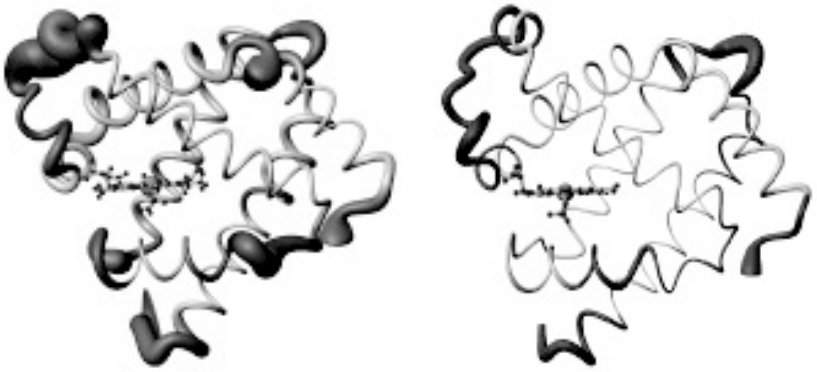

FIGURE 8.1
(See color insert following page 136) Comparison of the variation within an ensemble derived from NMR (left) and x-ray crystallography (right). The plot shows an expanded backbone representation in proportion to the RMS deviations within each ensemble. The regions of mobility overlap well.

The experimental techniques mentioned above give complementary information about dynamics. A comparison of the dynamics of myoglobin as determined by NMR and crystallography is also possible by building two ensembles. Figure 8.1 shows one ensemble derived from five different crystal forms (and hence different packing forces) of sperm whale myoglobin (Phillips 1990; Zhang et al. in preparation) compared with the ensemble generated by NMR methods (Osapay et al. 1994). Although the amplitudes seem to be on somewhat different scales, the regions of the protein that are most mobile are highly correlated. The variation among members of the x-ray ensemble is greater than that derived from *B*-factors of any individual structure determination, but the trends are remarkably similar. Thus it seems NMR and crystallography produce similar patterns of dynamic regions in this case.

The same experimental technique that has given us so many structures over the years, x-ray crystallography, also contains the potential to study the molecular dynamics of these biological structures. Surprisingly, however, the crucial component of the x-ray data needed for such dynamical studies, the diffuse scattering, is usually treated as noise and discarded (Clarage and Phillips 1997). One can argue for the complete refinement of macromolecular structure and dynamics in crystals, utilizing all of the available x-ray scattering data, namely, the high resolution Bragg reflections and the diffuse scattering between Bragg peaks. In addition to the average structure, the result of this expanded refinement will be a picture of the conformational states available to a macromolecule, knowledge indispensable for correlating molecular structure and dynamics with biochemical function. The effect of the crystal lattice on dynamics must be part of the analysis. Starting from some of my early work on myoglobin (Phillips 1990), we know that crystal contacts can locally dampen the flexibility of the protein in regions of crystal contacts. Since the percentage of water in the crystals is about the same as

the percentage of water in cells, the contacts with neighbors may be more regular in crystals, but not more numerous or extreme.

The basis of the methods stems from Born and von Karman (1912) theory, which has worked well for ionic solids and other crystals. Modern physical lattice dynamics includes quantum effects, but the classical spring-like methods seem to work well for many aspects of protein structure, and many researchers believe quantum effects can be ignored, at least for now, due to the larger size of proteins and their more macroscopic properties. Simplified normal mode analysis would seem appropriate here.

8.2 Comparison of Theory and Diffraction Experiment

The dynamic behavior of proteins in crystals can be calculated by these simple models and compared with experiments. The Gaussian network model (GNM) and a simplified version of the crystallographic translation–libration screw (TLS) model were used to calculate mean square fluctuations of C_α atoms for 114 proteins from two nonredundant sets of proteins whose structures have been determined by x-ray crystallography (Kundu et al. 2002). The GNM describes a protein as an elastic network of alpha carbons attached by Hookean springs where the atoms fluctuate about their mean positions (Haliloglu et al. 1997). The Kirchhoff, or valency–adjacency matrix of such a structure is constructed. A quantity proportional to the mean-square fluctuations of each atom, and the cross-correlation fluctuations between different atoms are the diagonal and off-diagonal elements, respectively, of the pseudo inverse of the Kirchhoff matrix. The "inverse" can be expressed as a sum of eigenvectors. Initial comparisons of calculations with displacement parameters from crystallography were encouraging (Bahar et al. 1997). Kundu et al. (2002) calculated correlation coefficients between the theoretical predictions and experiment for an extensive set of proteins. The GNM method gave excellent correlation with experimental measurement with an average correlation coefficient of 0.59. It has the added benefit of being able to calculate correlations between the fluctuations of pairs of atoms. By incorporating the effect of neighboring molecules in the crystal the correlation was further improved to a correlation coefficient of 0.66. The GNM model does better than the rigid body libration model in predicting atomic displacements in proteins (Kuriyan and Weis 1991), and is further able to compute cross-correlations between different atoms, which takes us toward understanding the oft-invoked and sometime mystical "conformational change." Recent techniques using a simplified harmonic potential on all atoms or C_α atoms or vector fields (Hinsen 2000) allow the calculation of not only amplitudes but also directions of protein motions in crystals for even very large protein complexes.

TLS methods have been used successfully to define the directions and magnitudes of collective motions of predefined set of atoms (see Winn et al. 2001)

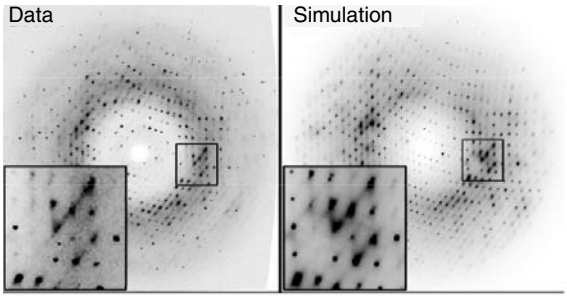

FIGURE 8.2
Illustration of effects of coupled motions on crystal diffraction and the ability to calculate both Bragg and diffuse components. Data (left): 30 sec still exposure from calmodulin at room temperature. Measurements of the intensities of sharp Bragg peaks were used to refine multiple-conformer structural models. Simulation (right): exposure calculated using a simple anisotropic liquid-like model for motions, using our program XCADS. The parameters obtained from the diffuse-scattering refinement not only yielded the best correlation coefficient with the data, but also produced the best simulated diffraction images. (Reprinted from Wall, M.E., J.B. Clarage and G.N. Phillips [1997]. *Structure* **5**: 1599–1612. With permission.)

and the resulting tensors can be converted easily to thermal ellipsoids for a conventional illustration of each atom's motion (Howlin et al. 1993). One problem with the approach is the requirement for manual choosing of the set of atoms in a group. Using GNM or other simplified normal mode analysis, it is possible to automatically identify the domain (segments) for collective motion analysis. This method uses graph theoretic methods, which state that the first nonzero eigenvector of the Kirchoff or Laplacian matrix, also known as the Fiedler (1975) vector, cuts the protein into the best two collectively moving groups on the basis of the sign of the eigenvector component for each atom or amino acid. The method has been implemented and compared with manual or other methods of domain assignment and seems to work extremely well (Kundu et al. 2004).

Analysis of diffuse x-ray scattering has been applied to a variety of systems in my laboratory including tropomyosin (Chacko and Phillips 1992), tRNA (Kolatkar et al. 1994), aspartate amino transferase (unpublished), calmodulin (Wall et al. 1997), and myoglobin (Clarage et al. 1995). Other laboratories have also made significant contributions (e.g., Clarage et al. 1992; Benoit and Doucet 1995; Thune and Badger 1995; Hery et al. 1998). Given an appropriate model for motions, it is possible to produce slices of calculated and experimentally determined diffraction patterns that showed remarkable agreement, one of which is shown in Figure 8.2. All motions in a lattice may not be exactly the same as motions in the cellular milieu, but there is mounting evidence that the lattice does not change the fundamental modes.

Prior work on effects of the crystal lattice on protein dynamics leads directly to the idea of calculating the Bragg and diffuse scattering arising from coupled displacements. Compared to the usual Bragg formalism, there will be slight differences when couplings are included, and the predicted diffuse

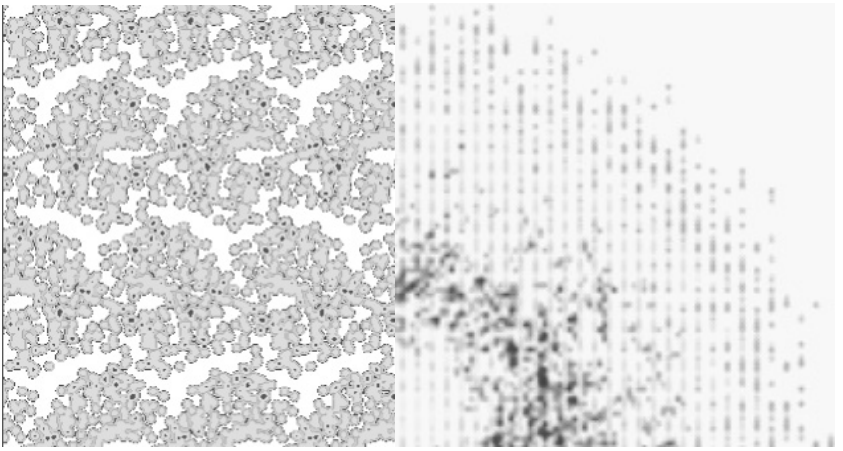

FIGURE 8.3
(See color insert following page 136) On the left is a constructed segment of a 3D lattice of a crystal of the enzyme, adenylate kinase, and on the right is the calculated reciprocal-space slice showing the calculated Bragg and diffuse x-ray scattering assuming independent motions within each molecule.

scattering will also come naturally from the calculations. Both Bragg and diffuse scattering are affected by these couplings and should be incorporated in modern crystallographic theory.

8.3 Effect of Displacements on the Bragg Peaks

One general form of the diffraction equation in terms of the scattering vector, $\mathbf{Q}$, and locations of atoms, $\mathbf{R}_{lk}$ is

$$I(\mathbf{Q}) = FF^* = \left(\sum_{lk}^{N} f_{kQ} e^{i\mathbf{Q}\cdot\mathbf{R}_{lk}}\right)\left(\sum_{l'k'}^{N} f^*_{k':Q} e^{-i\mathbf{Q}\cdot\mathbf{R}_{l'k'}}\right)$$

where the sum is over l, l' unit cells and k, k' atoms within each unit cell. $\mathbf{R}_{lk}$ can be written as the vector sum of the average position and a displacement

$$\mathbf{R}_{lk} = \mathbf{r}_{lk} + \mathbf{u}_{lk}$$

The average over time scales longer than the x-ray frequency and over the space of the mosaic block of crystal (the so-called ideally imperfect crystal because the lattice defects are uniformly distributed in a long range sense) then becomes

$$I(\mathbf{Q}) = \sum_{lk}\sum_{l'k'} f_{kQ} f^*_{k':Q} e^{i\mathbf{Q}\cdot(\mathbf{r}_{lk}-\mathbf{r}_{l'k'})} \langle e^{i\mathbf{Q}\cdot(\mathbf{u}_{lk}-\mathbf{u}_{l'k'})}\rangle$$

which, using the usual approximation for the averaged exponential term, reduces to

$$I(\mathbf{Q}) = \sum_{lk} \sum_{lk'} f_{kH} \mathrm{e}^{-Q^2\langle u_{lk}^2\rangle/2} f_{k'Q}^* \mathrm{e}^{-Q^2\langle u_{lk'}^2\rangle/2} \mathrm{e}^{i\mathbf{Q}\cdot(\mathbf{r}_{lk}-\mathbf{r}_{lk'})} \mathrm{e}^{Q^2\langle u_{lk}u_{lk'}\rangle}$$

where $\mathbf{Q}$ is the scattering factor and Q its magnitude. This form applies to a full anisotropic treatment, but for the sake of discussion of the ramification of the last term, it can be rewritten for isotropic displacements in a crystal, leading to the common Bragg approximation. Allowing for correlated motions of atoms k and k' within the unit cell, the equation becomes:

$$I(\mathbf{H}) = \sum_{k} \sum_{k'} f_{kH} \mathrm{e}^{-(2\pi H)^2\langle u_k^2\rangle/2} f_{k'H}^* \mathrm{e}^{-(2\pi H)^2\langle u_{k'}^2\rangle/2} \mathrm{e}^{i2\pi\mathbf{H}\cdot(\mathbf{r}_k-\mathbf{r}_{k'})} \mathrm{e}^{(2\pi H)^2\langle u_k u_{k'}\rangle}$$

where $\mathbf{H}$ is the reciprocal lattice vector and H its magnitude. Thus for two atoms in the structure with the same u (or B-factor) whose movements are correlated, the contribution by this pair to the intensity is "full strength," that is, all the Debye–Waller type terms cancel, leaving only the interference term involving the coordinates. This will apply to the entire diffraction pattern including both the Bragg spots and diffuse scattering. Of course, there will be a resolution dependent fall off in the overall diffraction pattern, because there are lattice and intermolecular uncoupled motions. But there will also remain effects for atoms with different B-factors or somewhat less coupled motions. This is a second order effect and its manifestations will depend on the extent of the coupling and the maintenance of the coherence among neighboring unit cells. (Note that the equation reduces to the standard form when motions are assumed to be uncorrelated, as the last term becomes unity.)

Since there are many correlated motions in protein crystals, this is likely to be a noticeable effect when comparing calculated and experimental intensities and could account for some of the problems in protein crystallography in getting experimental and calculated intensities to agree to each other within experimental error. The effect is not expected to be large in cases where the mosaic block size is large, but the change in intensity distributions is in the right direction to explain why many protein crystals appear to be slightly twinned based on intensity distributions, even when their standard Bragg analysis seemed not to require explicit treatment of the twinning.

This result suggests that both an improvement in agreement between theory and experiment and additional information about correlated movements can be obtained from Bragg diffraction data. One can calculate the diffraction patterns for known structures using both the usual Bragg approximation, and including the additional term for comparison. In principle, the correlated movements between atoms should be extractable from the diffraction data. It is impossible, however, for the complete set of $k(k-1)/2$ possible correlation terms to be determined directly by refinement, since the number of terms exceeds the number of observed x-ray spots! However, one can envision

using constraints in a refinement, much like prior knowledge of bond lengths, angles, planarity, etc. is used in standard protein structure refinements. Different types of coupling models, including GNM, simplified normal modes, liquid-like potentials, TLS, etc. can be tested.

8.3.1 Normal Mode Predictions of X-Ray Diffuse Scattering

Diffuse scattering analysis requires the inclusion of more than one unit cell of the crystal. A recent algorithm for calculating simplified normal modes makes it possible to include very large structures (Hinsen et al. 1999) and the code, the Molecular Modeling Toolkit (MMTK) has been made available (Hinsen 2000). Since MMTK includes both a simplified potential function and a Fourier-based vector field description of the couplings, the "normal modes" of an entire block of a protein crystal with several unit cells on a side can be included within the range of current 64-bit computer processors. One could also use CHARMM (Brooks and Karplus 1983) to construct "crystals" of proteins that employ cyclic boundary conditions as an additional constraint on the modes and employ the block normal mode approach (Tama et al. 2000) as implemented in a modified version of CHARMM (Li and Cui 2002). Using the simplified potential functions, the wave vector-associated modes comprising the first Brillouin zone in Born–von Karman theory (Willis and Pryor 1975) could be computed. Once the modes of protein motions are defined, the results can be used to calculate the Bragg and diffuse diffraction according to the equations above. These calculations would allow the connections between structure and dynamics in protein crystals. The diffuse scattering analysis will allow a comparison between the theory and experiment in a direct way.

The calculation of the diffuse scattering can be incrementally increased in sophistication, starting with the somewhat ad hoc model described by Caspar and coworkers (Clarage et al. 1992) and by Wall et al. (1997) using an anisotropic pair correlation function with a long-range and a short-range regime for the correlations. Alternative formulations have also been proposed by Go and coworkers (Mizuguchi et al. 1994). After one calculates the lattice dynamics from the basic structure using the MMTK or CHARMM-based methods, it is possible to use the following expression from Wall (1996) with the large amplitude modes. The atomic displacements can be expanded in terms of the crystalline modes, so that

$$\mathbf{u}_{kl} = \sum_{\mathbf{g}s} a_{s,\mathbf{g}} \mathbf{e}_{ks,\mathbf{g}} \mathbf{e}^{i(\mathbf{g}\cdot R_l - \omega_s(\mathbf{g})t)}$$

where $\mathbf{e}_{ks,\mathbf{g}}$ is the complex polarization vector for atom k in branch s with lattice wave vector, $\mathbf{g}$, $a_{s,\mathbf{g}}$ is the amplitude, and ω_s is the frequency. The first-order expression for the Bragg and diffuse components can be derived from equations given above, ignoring for these purposes the second order effect of

covariance on the Bragg scattering, to be

$$I_{\text{Bragg}} = \mathrm{e}^{-(1/2)\mathbf{q}\cdot(V_k+V_{k'})\cdot\mathbf{q}} I_{\text{o}}(\mathbf{q})$$

and

$$I_{\text{diffuse}} = \sum_{\mathbf{g},s}\sum_{l,l'} \mathrm{e}^{i(\mathbf{g}+\mathbf{q})\cdot(\mathbf{R}_l-\mathbf{R}_{l'})} \sum_{k,k'} f_k f_{k'} \mathrm{e}^{i\mathbf{q}\cdot(\mathbf{r}_\mathbf{k}-\mathbf{r}_{\mathbf{k}'})} \mathrm{e}^{-(1/2)\mathbf{q}\cdot(V_k+V_{k'})\cdot\mathbf{q}}$$
$$\times\ \mathbf{q}\cdot[|a_{s,\mathbf{g}}|^2 \mathbf{e}_{ks,\mathbf{g}}\mathbf{e}_{k's,\mathbf{g}}]\cdot\mathbf{q}$$

where V_k is the variance matrix for atom k (same for k'), $I_{\text{o}}(\mathbf{q})$ is the standard, unperturbed Bragg intensity, and the scattering factors, r_k and R_l are the displacements for the kth atom and the lth unit cell, the scattering factors f_k are presumed real here. This expression reduces directly to the liquid-like motion of Clarage et al. if displacements are assumed to be equivalently distributed (Wall 1996). Coupled with the ability to calculate the modes, this allows for a direct comparison of calculated motions and experimental data.

Because qualitative inspection of the diffuse scattering of many protein crystals reveals streaks that would correspond to transverse displacements of waves (Clarage and Phillips 1997), one would hypothesize that the calculations will show this. The alternative, compression waves, would not be expected to be present in large amplitudes if the theory is to match the experimental observations.

8.4 Complete Refinement Strategies

The generalized crystallographic target function for refinement of structures should be defined as the mean square difference of all measured intensities for *all* reciprocal space points, R, on either the raw pixel level or the Gibbs lattice-sampled pattern, both of which include Bragg and diffuse intensities. Note that amplitudes alone cannot be used, for there is no analog of a structure factor in diffuse scattering; in fact, squaring the scattering amplitude is crucial to defining the double-sum over atoms, which in turn leads to terms involving pair-correlations. To optimize the fit one must first describe a model for the disorder, which then defines the explicit form of the correlations.

This more complete approach is less "ad hoc" than previous efforts by me and others, and in principle provides just what is needed: all the positions, displacements, and correlations. A disadvantage is the great number of parameters in the displacement covariance matrix (whose diagonal elements correspond to the standard B-values, and whose off-diagonals contain the cross-correlations between atom pairs) or its normal mode-based equivalent. The number of free parameters is certainly larger than even the extended set of

observations collected on the Gibbs lattice. One is therefore led to explore several ways to reduce the complexity of the problem. This is where the simplified mode calculations or the use of TLS-like rigid body definitions (Harris et al. 1992; Howlin et al. 1993; Winn et al. 2001) with sound methods for division of the molecule into groups enter the picture. It seems best to make use of *all* the diffraction data instead of using only the Bragg approximation in describing a structure and its deviations. The impact will be variable. For "tight" proteins the dynamics will be small in amplitude and largely "uncoupled" on a large scale and little if any new insight would be likely to result. For more complex systems where differentially coupled motions are retained in the crystal lattice, new insight about mechanisms of actions will result.

Abstractions of the structure of proteins has led to the identification of a plethora of motifs, usually visualized as static icons of underlying function, rather than dynamic ones. We are now increasingly appreciating the fact that the interconversion between states, and the relaxations of structure as biological recognition events occur is just as much a part of molecular biology as the starting structures. If we can discover new ways to observe these events, the result will be a richer picture of structure and dynamics and their connections to function.

Acknowledgments

This work was supported by the Vilas Trust, through a University of Wisconsin Vilas Associate award to the author. The author also acknowledges the help of Jason McCoy, Bog Stec, and Wei Zhang for the preparation of figures.

References

Amadei, A., A.B. Linssen, and H.J. Berendsen (1993). "Essential dynamics of proteins." *Proteins* **17**: 412–425.

Amadei, A., A.B. Linssen, B.L. de Groot, D.M. van Aalten, and H.J. Berendsen (1996). "An efficient method for sampling the essential subspace of proteins." *J. Biomol. Struct. Dyn.*, **13**: 615–625.

Ansari, A., C.M. Jones, E.R. Henry, J. Hofrichter, and W.A. Eaton (1994). "Conformational relaxation and ligand binding in myoglobin." *Biochemistry* **33**: 5128–5145.

Bahar, I., A.R. Atilgan, and B. Erman (1997). "Direct evaluation of thermal fluctuations in proteins using a single-parameter harmonic potential." *Fold. Des.*, **2**: 173–181.

Balabin, I.A. and J.N. Onuchic (2000). "Dynamically controlled protein tunneling paths in photosynthetic reaction centers." *Science* **290**: 114–7.

Benkovic, S.J. and S. Hammes-Schiffer (2003). "A perspective on enzyme catalysis." *Science* **301**: 1196–1202.

Benoit, J.P. and J. Doucet (1995). "Diffuse scattering in protein crystallography." *Quart. Rev. Biophys.* **28**: 131–169.

Born, M. and T. von Karman (1912). *Phys. Zeit.* **13**: 297.

Brooks, B. and M. Karplus (1983). "Harmonic dynamics of proteins: normal modes and fluctuations in bovine pancreatic trypsin inhibitor." *Proc. Natl Acad. Sci. USA* **80**: 6571–6575.

Bryngelson, J.D., J.N. Onuchic, N.D. Socci, and P.G. Wolynes (1995). "Funnels, pathways, and the energy landscape of protein folding: a synthesis." *Proteins* **21**: 167–195.

Caves, L.S., J.D. Evanseck, and M. Karplus (1998). "Locally accessible conformations of proteins: multiple molecular dynamics simulations of crambin." *Protein Sci.* **7**: 649–666.

Chacko, S. and G.N. Phillips, Jr. (1992). "Diffuse x-ray scattering from tropomyosin crystals." *Biophys. J.* **61**: 1256–1266.

Clarage, J.B., M.S. Clarage, W.C. Phillips, R.M. Sweet, and D.L. Caspar (1992). "Correlations of atomic movements in lysozyme crystals." *Proteins* **12**: 145–157.

Clarage, J.B. and G.N. Phillips, Jr. (1997). "Analysis of diffuse scattering and relation to molecular motion." *Meth. Enzymol.* **277**: 407–432.

Clarage, J.B., T. Romo, B.K. Andrews, B.M. Pettitt, and G.N. Phillips, Jr. (1995). "A sampling problem in molecular dynamics simulations of macromolecules." *Proc. Natl Acad. Sci. USA* **92**: 3288–3292.

de Groot, B.L., A. Amadei, R.M. Scheek, N.A. van Nuland, and H.J. Berendsen (1996a). "An extended sampling of the configurational space of HPr from *E. coli*." *Proteins* **26**: 314–322.

de Groot, B.L., A. Amadei, D.M. van Aalten, and H.J. Berendsen (1996b). "Toward an exhaustive sampling of the configurational spaces of the two forms of the peptide hormone guanylin." *J. Biomol. Struct. Dyn.* **13**: 741–751.

de Groot, B.L., S. Hayward, D.M. van Aalten, A. Amadei, and H.J. Berendsen (1998). "Domain motions in bacteriophage T4 lysozyme: a comparison between molecular dynamics and crystallographic data." *Proteins* **31**: 116–127.

Doruker, P., R.L. Jernigan, and I. Bahar (2002). "Dynamics of large proteins through hierarchical levels of coarse-grained structures." *J. Comput. Chem.* **23**: 119–127.

Eisenmesser, E.Z., D.A. Bosco, M. Akke, and D. Kern (2002). "Enzyme dynamics during catalysis." *Science* **295**: 1520–1523.

Engen, J.R. and D.L. Smith (2001). "Investigating protein structure and dynamics by hydrogen exchange MS." *Anal. Chem.* **73**: 256A–265A.

Fiedler, M. (1975). "A property of eigenvectors of non-negative symmetric matrices and its application to graph theory." *Czechoslovak Math. J.* **25**: 619–633.

Frauenfelder, H. (1995). "Complexity in proteins." *Nat. Struct. Biol.* **2**: 821–823.

Garcia, A.E. (1992). "Large-amplitude nonlinear motions in proteins." *Phys. Rev. Lett.* **68**: 2696–2699.

Gerstein, M. and W. Krebs (1998). "A database of macromolecular motions." *Nucleic Acids Res.* **26**: 4280–4290.

Go, N. (1990). "A theorem on amplitudes of thermal atomic fluctuations in large molecules assuming specific conformations calculated by normal mode analysis." *Biophys. Chem.* **35**: 105–112.

Go, N., T. Noguti, and T. Nishikawa (1983). "Dynamics of a small globular protein in terms of low-frequency vibrational modes." *Proc. Natl Acad. Sci. USA* **80**: 3696–3700.

Haldane, J.B.S. (1930). *Enzymes*. New York, Longmans, Green & Co.

Haliloglu, T. and I. Bahar (1999). "Structure-based analysis of protein dynamics: comparison of theoretical results for hen lysozyme with x-ray diffraction and NMR relaxation data." *Proteins* **37**: 654–667.

Haliloglu, T., I. Bahar, and B. Erman (1997). "Gaussian dynamics of folded proteins." *Phys. Rev. Lett.* **79**: 3090–3093.

Harris, G.W., R.W. Pickersgill, B. Howlin, and D.S. Moss (1992). "The segmented anisotropic refinement of monoclinic papain by the application of the rigid-body TLS model and comparison to bovine ribonuclease A." *Acta Crystallogr. B* **48**: 67–75.

Hery, S., D. Genest, and J.C. Smith (1998). "X-ray diffuse scattering and rigid-body motion in crystalline lysozyme probed by molecular dynamics simulation." *J. Mol. Biol.* **279**: 303–319.

Hilvert, D. (2000). "Critical analysis of antibody catalysis." *Annu. Rev. Biochem.* **69**: 751–793.

Hinsen, K. (2000). "The molecular modeling toolkit: a new approach to molecular simulations." *J. Comp. Chem.* **21**: 79–85.

Hinsen, K., A. Thomas, and M.J. Field (1999). "Analysis of domain motions in large proteins." *Proteins* **34**: 369–382.

Howlin, B., S.A. Butler, D.S. Moss, G.W. Harris, and H.P.C. Driessen (1993). "Tlsanl–Tls parameter-analysis program for segmented anisotropic refinement of macromolecular structures." *J. Appl. Crystallogr.* **26**: 622–624.

Isin, B., P. Doruker, and I. Bahar (2002). "Functional motions of influenza virus hemagglutinin: a structure-based analytical approach." *Biophys. J.* **82**: 569–581.

Kay, L.E. (1998). "Protein dynamics from NMR." *Nat. Struct. Biol.* **5**: 513–517.

Kempf, J.G. and J.P. Loria (2003). "Protein dynamics from solution NMR: theory and applications." *Cell. Biochem. Biophys.* **37**: 187–211.

Keskin, O., S.R. Durell, I. Bahar, R.L. Jernigan, and D.G. Covell (2002). "Relating molecular flexibility to function: a case study of tubulin." *Biophys. J.* **83**: 663–680.

Kitao, A. and N. Go (1999). "Investigating protein dynamics in collective coordinate space." *Curr. Opin. Struct. Biol.* **9**: 164–169.

Kolatkar, A., J.B. Clarage, and G.N. Phillips, Jr. (1994). "Analysis of diffuse scattering from yeast initiator tRNA crystals." *Acta Crystallogr. D* **50**: 210–218.

Kundu, S., J.S. Melton, D.C. Sorensen, and G.N. Phillips, Jr. (2002). "Dynamics of proteins in crystals: comparison of experiment with simple models." *Biophys. J.* **83**: 723–732.

Kundu, S., D.C. Sorensen, and G.N. Phillips, Jr. (2004). "Automatic domain decomposition of proteins by a Gaussian network model." *Proteins* **57**: 725–733.

Kuriyan, J. and W.I. Weis (1991). "Rigid protein motion as a model for crystallographic temperature factors." *Proc. Nat Acad. Sci. USA* **88**: 2773–2777.

Lanman, J. and P.E. Prevelige, Jr. (2004). "High-sensitivity mass spectrometry for imaging subunit interactions: hydrogen/deuterium exchange." *Curr. Opin. Struct. Biol.* **14**: 181–188.

Levitt, M., C. Sander, and P.S. Stern (1985). "Protein normal-mode dynamics: trypsin inhibitor, crambin, ribonuclease and lysozyme." *J. Mol. Biol.* **181**: 423–447.

Levy, R.M. and M. Karplus (1979). "Vibrational approach to the dynamics of an alpha-helix." *Biopolymers* **18**: 2465–2495.

Li, G. and Q. Cui (2002). "A coarse-grained normal mode approach for macromolecules: an efficient implementation and application to Ca(2+)-ATPase." *Biophys. J.* **83**: 2457–2474.

Ma, J. and M. Karplus (1998). "The allosteric mechanism of the chaperonin GroEL: a dynamic analysis." *Proc. Natl Acad. Sci. USA* **95**: 8502–8507.

Miller, D.W. and D.A. Agard (1999). "Enzyme specificity under dynamic control: a normal mode analysis of alpha-lytic protease." *J. Mol. Biol.* **286**: 267–278.

Mizuguchi, K., A. Kidera, and N. Go (1994). "Collective motions in proteins investigated by x-ray diffuse scattering." *Proteins* **18**: 34–48.

Moffat, K. (1998). "Time-resolved crystallography." *Acta Crystallogr. A* **54**: 833–841.

Osapay, K., Y. Theriault, P.E. Wright, and D.A. Case (1994). "Solution structure of carbonmonoxy myoglobin determined from nuclear magnetic resonance distance and chemical shift constraints." *J. Mol. Biol.* **244**: 183–197.

Ota, N. and D.A. Agard (2001). "Enzyme specificity under dynamic control II: principal component analysis of alpha-lytic protease using global and local solvent boundary conditions." *Protein Sci.* **10**: 1403–1414.

Pauling, L. (1946). "Molecular architecture and biological reactions." *Chem. Eng. News* **24**: 1375–1377.

Phillips, G.N., Jr. (1990). "Comparison of the dynamics of myoglobin in different crystal forms." *Biophys. J* **57**: 381–383.

Roccatano, D., A.E. Mark, and S. Hayward (2001). "Investigation of the mechanism of domain closure in citrate synthase by molecular dynamics simulation." *J. Mol. Biol.* **310**: 1039–1053.

Romo, T.D., J.B. Clarage, D.C. Sorensen, and G.N. Phillips, Jr. (1995). "Automatic identification of discrete substates in proteins: singular value decomposition analysis of time-averaged crystallographic refinements." *Proteins* **22**: 311–321.

Schotte, F., M. Lim, T.A. Jackson, A.V. Smirnov, J. Soman, J.S. Olson, G.N. Phillips, Jr., M. Wulff, and P.A. Anfinrud (2003). "Watching a protein as it functions with 150-ps time-resolved x-ray crystallography." *Science* **300**: 1944–1947.

Schultz, P.G. and R.A. Lerner (1995). "From molecular diversity to catalysis: lessons from the immune system." *Science* **269**: 1835–1842.

Stoddard, B.L. (1998). "New results using Laue diffraction and time-resolved crystallography." *Curr. Opin. Struct. Biol.* **8**: 612–618.

Tama, F., F.X. Gadea, O. Marques, and Y.H. Sanejouand (2000). "Building-block approach for determining low-frequency normal modes of macromolecules." *Proteins* **41**: 1–7.

Tama, F. and Y.H. Sanejouand (2001). "Conformational change of proteins arising from normal mode calculations." *Protein Eng.* **14**: 1–6.

Teodoro, M.L. and L.E. Kavraki (2003). "Conformational flexibility models for the receptor in structure based drug design." *Curr. Pharm. Des.* **9**: 1635–1648.

Teodoro, M.L., G.N. Phillips, Jr., and L.E. Kavraki (2003). "Understanding protein flexibility through dimensionality reduction." *J. Comput. Biol.* **10**: 617–634.

Thune, T. and J. Badger (1995). "Thermal diffuse x-ray scattering and its contribution to understanding protein dynamics." *Prog. Biophys. Mol. Biol.* **63**: 251–276.

Ulrich, H.D., E. Mundorff, B.D. Santarsiero, E.M. Driggers, R.C. Stevens, and P.G. Schultz (1997). "The interplay between binding energy and catalysis in the evolution of a catalytic antibody." *Nature* **389**: 271–275.

Volkman, B.F., D. Lipson, D.E. Wemmer, and D. Kern (2001). "Two-state allosteric behavior in a single-domain signaling protein." *Science* **291**: 2429–2433.

Wall, M.E. (1996). *Diffuse Features in X-Ray Diffraction from Protein Crystals (Staphylococcal nuclease, Image Processing)*. Princeton, NJ, Princeton, p. 167.

Wall, M.E., J.B. Clarage, and G.N. Phillips (1997). "Motions of calmodulin characterized using both Bragg and diffuse x-ray scattering." *Structure* **5**: 1599–1612.

Willis, B.T.M. and A.W. Pryor (1975). *Thermal Vibrations in Crystallography*. London; New York, Cambridge University Press.

Winn, M.D., M.N. Isupov, and G.N. Murshudov (2001). "Use of TLS parameters to model anisotropic displacements in macromolecular refinement." *Acta Crystallogr. D* **57**: 122–133.

Zacharias, M. and H. Sklenar (1999). "Harmonic modes as variables to approximately account for receptor flexibility in ligand–receptor docking simulations: application to DNA minor groove ligand complex." *J. Comp. Chem.* **20**: 287–300.

9

Optimizing the Parameters of the Gaussian Network Model for ATP-Binding Proteins

Taner Z. Sen and Robert L. Jernigan

CONTENTS

9.1 Introduction

The elastic network models of coarse-grained proteins have demonstrated their success in representing the overall motions of proteins, and particularly

the slowest most important motions derived from normal mode analysis. The elastic network model's superior performance in comparison to results from atomic molecular dynamics must originate in its better representation of the cooperativity within protein structures. Generally atomic interaction potentials would have less overall cohesiveness. The elastic network models, by having large numbers of interconnections, many of which are evident in the large domain motions of the slowest modes of motion, provides a clear and simple model of protein cohesiveness. Until now, these interactions represented by springs have all been treated as identical. If a model is to represent the cohesiveness properly, then the question arises as to whether this is being done in the best way. Are the protein cores being represented in too rigid a way? Or are the surface residues not sufficiently rigid? Motions computed for the slow important motions might be affected by these issues. Here we are exploring some range of changes to the ways in which the spring constants are formulated, by making them depend on the local packing density in the simplest way, in terms of the number of each residue's close interactions.

We also examine the cutoff distance dependence of spring constants for the adenosine triphosphate (ATP)-binding protein set. The cutoff distance establishes the packing density of the studied protein because it determines the number of neighbors each residue has. The cutoff distance was optimized against the experimental *B*-factors for a large set of protein by Kundu et al. [1]. Note that our data set of six proteins is not intended to obtain statistically tested results, but rather to provide initial insights regarding the effects of packing density for the case of ATP-binding proteins.

9.2 Methods

9.2.1 Proteins

A small high-resolution protein set is comprised of the ATP-binding proteins available in the Brookhaven protein data bank (pdb) [2], having different sizes and with domains belonging to different CATH superfamilies [3, 4]. This set consists of three protein pairs, each having an unbound form and an ATP-bound conformer. (1) The human cyclin-dependent kinase 2, (a) for the unbound conformer (pdb code 1HCL [5], resolution 1.8 Å) and (b) for its ATP-bound conformer (pdb code 1HCK [6], resolution 1.9 Å). These proteins each consist of 294 residues. (2) The 5′-nucleotidase from *Escherichia Coli*, (a) for the unbound conformer (pdb code 1USH [7], resolution 1.73 Å) and (b) the ATP-bound conformer (pdb code 1HP1 [8], resolution 1.7 Å). The proteins each consist of 516 residues. (3) The gamma subunit of phosphoinositide 3-kinase (a) for the unbound conformer (pdb code 1E8Y [9], resolution 2 Å) and (b) for the ATP-bound conformer (pdb code 1E8X [9], resolution 2.2 Å). These proteins each consist of 841 residues. In the last protein pair, the origins

TABLE 9.1

RMSD between Conformers of the Same Protein With and Without ATP.

Conformers	RMSD (Å)
1HCL/1HCK	0.33
1USH/1HP1	0.15
1E8Y/1E8X	1.41

of the two proteins are different. 1E8Y is a human protein; whereas 1E8X is a porcine protein. The root-mean-square-distance (RMSD) between these two proteins is 1.41 Å (Table 9.1). This group of proteins has been chosen to show the effect of protein size in the elastic network calculations.

The ATP-binding sites for the protein pairs have major distinctive differences as can be seen in Figure 9.1. For both kinases, the ATP binding site is buried inside the protein; therefore when the ATP ligand is bound, it establishes substantial numbers of contacts with the protein. In the case of the 5′-nucleotidase, however, the ATP-binding site is located on the surface, and has fewer contacts. The number and the type of contacts between ATP and the proteins are obtained using the LPC (ligand–protein contacts) software developed by Sobolev et al. [10]. According to the distance calculations between atoms, not only do the kinases achieve more contacts with ATP, but they also create more hydrogen bonds with the ligands than does the 5′-nucleotidase protein; there are 16 and 13 hydrogen bonds in the cases of 1HCK and 1E8X and only nine hydrogen bonds in the case of 1HP1.

For the RMSD calculations, the protein pairs are structurally aligned using ProFit v2.2 (Martin, A.C.R., http://www.bioinf.org.uk/software/profit/) [11] over the coordinates of C^{α} atoms.

9.2.2 Gaussian Network Model

The theory of the Gaussian network model (GNM) can be found elsewhere in detail [12, 13] and in the chapter "Gaussian network model: theory and applications" by Rader et al. in this book. The underlying concept of the original GNM treatment is to represent the cohesiveness of the proteins by establishing sufficient number of strings with uniform fixed-value spring constants between all close pairs of residues. In this treatment, each residue is represented as a point (or node) positioned at its C^{α} atom. There are two parameters, the cutoff distance R_c and spring constant: the cutoff distance R_c determines whether two residues are connected with a spring, that is, in contact, without differentiating between bonded and nonbonded interactions. These contacts are expressed in a contact matrix, and the pseudoinverse of

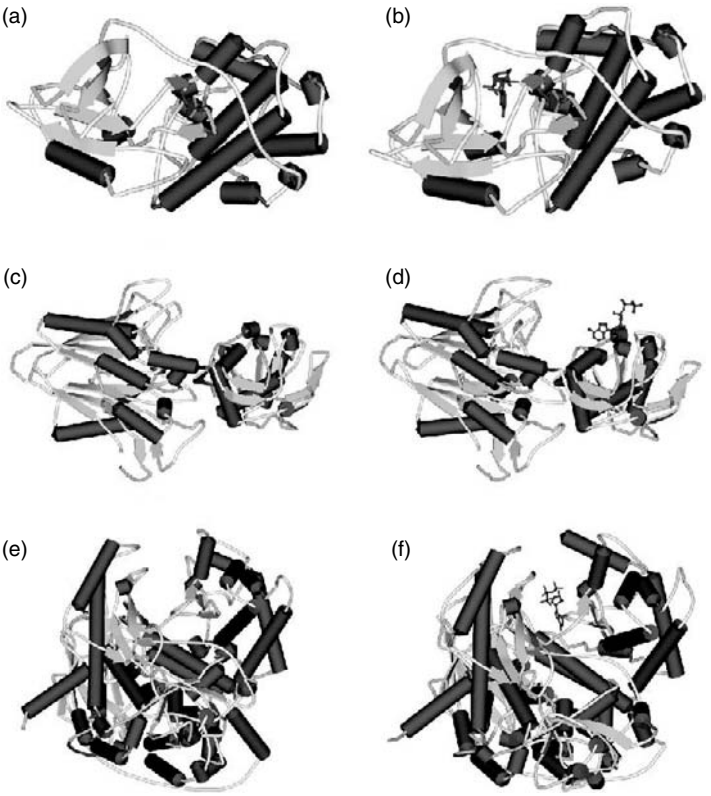

FIGURE 9.1
(See color insert following page 136) Three-dimensional representations of representative ATP-binding proteins (a) 1HCL, (b) 1HCK, (c) 1USH, (d) 1HP1, (e) 1E8Y, and (f) 1E8X. The proteins are colored according to their secondary structures using Accelrys DS ViewerPro 5.0. The ATP-bound conformers are shown in the right column. Their unbound counterpart is in the left column. ATP molecules are given with blue stick representations.

this matrix (since the zero eigenvalue corresponding to the external degree of freedom must be eliminated) is obtained with singular value decomposition (SVD). The diagonal of the pseudoinverse of the contact matrix provides mean-square fluctuations for each node, which in turn may be compared with the experimental Debye–Waller temperature factors (*B*-factors), generally available in the pdb files.

The computed mean-square fluctuations can be decomposed meaningfully into normal modes by using appropriate eigenvalues during calculations. The smallest eigenvalues provide the global or collective motions that correspond to the conformational rearrangements of the protein on the largest scale. In contrast, the largest eigenvalues correspond to noncollective modes influenced mainly by local effects. In terms of the overall motions, only the large domain motions make significant contributions.

In this work, the protein residues are represented by single nodes, and likewise the ATP molecule is represented by one node placed at the C4* atom. For other proteins, best results are usually achieved when the nodes represent similar volumes of protein, that is, similar numbers of atoms, but the details of the representation for a small molecule in the context of a much larger protein often do not have so much effect on the important large domain motions, except to influence the direction of a motion [14,15].

9.2.3 Spring Constants

In the original GNM treatment, the spring constants between each pair of residues are defined all to be identical. Hinsen [16] employed distance-dependent spring constants, whose magnitudes fall off exponentially. Here in an exploratory attempt to improve protein dynamics predictions, we introduced novel alternative types of spring constants by creating a dependence upon the number of contacts for each residue, so as to make the protein more heterogeneous. Different interacting pairs can now have different spring constants, reflecting their packing environments. For this purpose, the following constants are employed:

$$k_{ij}^{1} = 1 \tag{9.1}$$

$$k_{ij}^{2} = \frac{1}{n_i^C} + \frac{1}{n_j^C} \tag{9.2}$$

$$k_{ij}^{3} = \frac{1}{\sqrt{n_i^C \times n_j^C}} \tag{9.3}$$

$$k_{ij}^{4} = \left(\frac{1}{n_i^C}\right)^{0.5} + \left(\frac{1}{n_j^C}\right)^{0.5} \tag{9.4}$$

$$k_{ij}^{5} = \frac{(n_i^C + n_j^C)}{2} \tag{9.5}$$

$$k_{ij}^{6} = \sqrt{n_i^C \times n_j^C} \tag{9.6}$$

where k_{ij} represents the spring constant between nodes i and j. For simplicity, $k = i$ will be used throughout the text to denote the use of a spring constant, where i ranges from 1 to 6 for the defined springs in Equations (9.1) to (9.6). n_i^C is the number of contacts for the ith node. Note that form 1 is the original version, independent of the number of neighbors, 2 to 4 have weaker cooperativity than 1, and 5 to 6 have enhanced cooperativity for dense packing.

9.2.4 Correlation Coefficient

Generally, our criterion for choosing parameters will be based on the extent of agreement of the computed fluctuations with the experimental *B*-factors. For this purpose, we use the linear correlation coefficient calculated as follows:

$$C = \frac{\sum_{i=1}^{N} (x_i - \bar{x})(y_i - \bar{y})}{\sqrt{\sum_{i=1}^{N} (x_i - \bar{x})^2 \cdot \sum_{i=1}^{N} (y_i - \bar{y})^2}} \tag{9.7}$$

In this equation, N is the number of nodes, x_i and $\bar{x}$ are the mean-square residue fluctuations as calculated by GNM and their mean over all residues. Similarly, y_i and $\bar{y}$ are the experimentally determined *B*-factors and their mean. This linear correlation coefficient is a straightforward way to analyze the extent of linear dependence between any two quantities. Its value can range between 1 and -1, where the limiting values 1 and -1 correspond to perfect correlation and perfect anticorrelation. However, this coefficient has its limitations. The linear correlation coefficient only captures how two quantities track together in their deviations from the mean without any reference to their relative amplitudes. Therefore, this parameter only provides information regarding the relative up and down patterns.

9.3 Results

9.3.1 Conformational Changes

Each protein pair is aligned structurally as described in Section 9.2. The RMSD calculated after the structural alignments are shown in Table 9.1. The RMSD values of the 1HCL/1HCK and 1USH/1HP1 pairs are small compared to that of the 1E8X/1E8Y pair. The distances between conformers for each residue are also calculated separately to locate the regions of largest conformational changes.

For the 1HCL/1HCK pair, the distances between corresponding residues in the conformers larger than 1 Å are seen for the following residues: G13, T14, T26, R36, Y159, and T160. Among those residues, T26 is located on a loop on the protein surface away from the binding site, which explains its high mobility. G13 and T14 are in the binding pocket and establish hydrogen bonds with ATP. These two residues clearly undergo conformational changes specifically to accommodate the binding of the ATP. The other residues, R36, Y159, and T160, are situated on two surface loops, which directly interact with G13 and T14, so the conformational changes in these three residues could be induced by the rearrangements of G13 and T14 positions at the ATP-binding site. For the 1USH/1HP1 pair, the largest distance between corresponding residues is 0.87 Å for residue K321, and the other distances

are all less than 0.6 Å. The small amplitude of conformational changes may be attributed to the characteristically exposed surface binding of the ATP ligand. For the 1E8Y/1E8X pair, the global conformational rearrangements observed may be due to the different origins of the proteins. The largest changes occur at the *C*-terminal in the residues F1087 to L1092. Changes larger than 1 Å are only seen for surface residues, rather than in the vicinity of the binding sites.

9.3.2 Pair Distribution Functions

Since the cutoff distance is as crucial as the spring constant for the protein dynamics predictions, the issue of which structural features are captured with a given cutoff distance becomes of primary importance. To understand where the residues are located with respect to one another, pair distribution functions are useful. The pair distribution function is calculated by (1) assuming each node as a center, (2) calculating the distances between the central node and other nodes, and (3) repeating this procedure for each node followed by averaging. By defining bins of constant size and counting how many node pairs fall into each bin, the distribution of the relative positions of nodes with respect to one another can be obtained. Therefore, the peaks in this function represent average node shells around each central node. Figure 9.2 shows the pair distribution functions for 1E8Y and 1E8X as representatives.

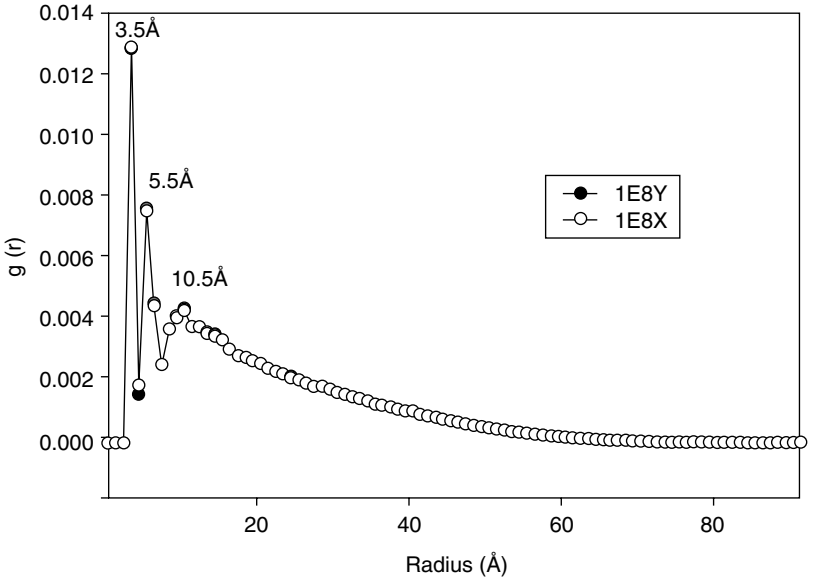

FIGURE 9.2
The pair distribution functions of 1E8Y and 1E8X with bins of size 1 Å.

Since the bin step size is taken as 1 Å, the first peak at 3.5 Å shows the relative node density in the range of 3 and 4 Å. This first peak captures the sequence neighbors with their C^{α}–C^{α} virtual bond length of 3.8 Å. Two additional peaks are clearly visible at 5.5 and 10.5 Å in Figure 9.2. When a cutoff distance needs to be chosen to model the protein interactions, the pair distribution function provides a guideline by revealing the relative positions of two nodes with respect to one another. An interesting feature of Figure 9.2 is that it shows nearly identical behavior for both 1E8Y and 1E8X, a similarity also observed for the other two pairs of proteins. This similarity could have been anticipated from the low values of RMSD between conformers. Although the pair distribution function can be used a guideline to choose the cutoff distance, the function fails to capture the details of interactions between nodes. Consequently, further analysis is necessary to understand how the cutoff distance affects the quality of the protein dynamics predictions. We use the values of the correlation coefficient as a means to improve our predictions.

9.3.3 Correlations

Table 9.2 shows the linear correlation coefficients between the experimental *B*-factors and the mean-square fluctuations obtained with the elastic network calculations. The correlation coefficients are calculated at various cutoff distances and for various spring constants. As the cutoff distance determines the nonzero elements of the contact matrix, it also influences the overall strength of cooperativity for connections in a given protein. For some cases, the correlation coefficients couldn't be calculated, since the singular value decomposition algorithm [17] failed to converge during the diagonalization of the contact matrix. This failure may originate in the algorithm. These cases are designated with dashes in the tables.

For any spring constant, the cutoff distance of 5 Å usually yields low correlations (data not shown). This inadequacy can be clearly explained by the pair distribution functions. As discussed earlier, the cutoff distance of 5 Å would only capture the first shell of nodes that corresponds almost exclusively to sequence neighbors. Therefore, at this cutoff value, neither long-range interactions, nor secondary structure information can be factored out in the contact matrix. As a result of this, the GNM with $R_c = 5$ Å does not predict experimental *B*-factors well.

9.3.4 Correlation Coefficients at Different Cutoff Distances and Spring Constants

The correlation coefficients as a function of cutoff distances and spring constants are shown in Figures 9.3(a) to (c) for the three proteins in their unbound forms. Generally, the correlation coefficient is largest in the range of R_c from

TABLE 9.2

Correlation Coefficients — the Left Side Is for Proteins Without ATP and the Right Side for Proteins With ATP.

(a)			1HCL				(b)		1HCK			
Å	***k*=1**	***k*=2**	***k*=3**	***k*=4**	***k*=5**	***k*=6**	***k*=1**	***k*=2**	***k*=3**	***k*=4**	***k*=5**	***k*=6**
7	0.70	0.73	0.73	0.73	0.63	0.63	0.58	0.60	0.60	0.60	0.51	0.51
10	0.67	0.64	0.64	0.67	0.66	0.65	0.58	0.57	0.57	0.58	0.57	0.56
13	0.66	0.59	0.59	0.64	—	—	0.59	0.53	0.53	0.58	0.59	—
15	0.66	0.58	0.59	0.64	0.66	0.5	0.61	0.54	0.56	0.60	—	—
17	0.65	0.57	0.58	0.63	—	—	0.61	0.54	0.56	0.59	—	—
20	0.64	0.57	0.59	0.63	—	—	0.56	0.53	0.54	0.56	—	—
25	0.57	0.52	0.53	0.56	—	—	0.47	0.44	0.45	0.47	—	—
30	0.49	0.45	0.45	0.48	—	—	0.40	0.36	0.36	0.39	—	—
			1USH						**1HP1**			
Å	***k*=1**	***k*=2**	***k*=3**	***k*=4**	***k*=5**	***k*=6**	***k*=1**	***k*=2**	***k*=3**	***k*=4**	***k*=5**	***k*=6**
7	0.73	0.74	0.74	0.74	0.70	0.69	0.77	0.78	0.78	0.78	0.72	0.72
10	0.70	0.69	0.69	0.70	0.69	0.68	0.74	0.74	0.74	0.74	0.72	—
13	0.67	0.64	0.64	0.67	—	—	0.69	0.68	0.68	0.70	0.68	—
15	0.67	0.63	0.63	0.67	—	0.66	0.69	0.66	0.66	0.69	—	—
17	0.68	0.62	0.62	0.67	—	—	0.69	0.65	0.65	0.69	—	—
20	0.70	0.62	0.62	0.68	—	—	0.70	0.64	0.64	0.69	—	—
25	0.70	0.61	0.62	0.68	—	—	0.71	0.62	0.63	0.69	—	—
30	0.70	0.61	0.63	0.68	—	—	0.71	0.62	0.63	0.69	—	—
			1E8Y						**1E8X**			
Å	***k*=1**	***k*=2**	***k*=3**	***k*=4**	***k*=5**	***k*=6**	***k*=1**	***k*=2**	***k*=3**	***k*=4**	***k*=5**	***k*=6**
7	0.56	0.57	0.58	0.58	0.48	0.47	0.69	0.75	0.75	0.73	0.58	0.56
10	0.71	0.69	0.69	0.72	0.65	0.64	0.70	0.74	0.74	0.73	0.59	0.57
13	0.72	0.69	0.69	0.72	—	0.66	0.73	0.73	0.73	0.76	—	—
15	0.70	0.69	0.69	0.72	—	—	0.74	0.74	0.74	0.77	0.64	0.62
17	0.69	0.69	0.69	0.71	—	—	0.75	0.76	0.76	0.78	—	—
20	0.68	0.70	0.69	0.70	—	—	0.78	0.79	0.78	0.80	—	—
25	0.65	0.67	0.67	0.67	—	—	0.77	0.80	0.80	0.79	—	—
30	0.62	0.62	0.62	0.63	—	—	0.73	0.77	0.76	0.75	—	—

7 to 10 Å, and then decreases with increasing cutoff distances. In the case of 1E8Y, this peak range extends even to 13 Å. The correlation coefficients do not always decrease after reaching a peak: for 1USH, the correlation coefficient starts increasing again at higher cutoff distances, but never reaches the level of the 7–10 Å peak that captures the second and even a part of the third coordination shells of nodes. Correlation coefficients also show a peculiar behavior with the use of different spring constants. In all three cases, the original spring

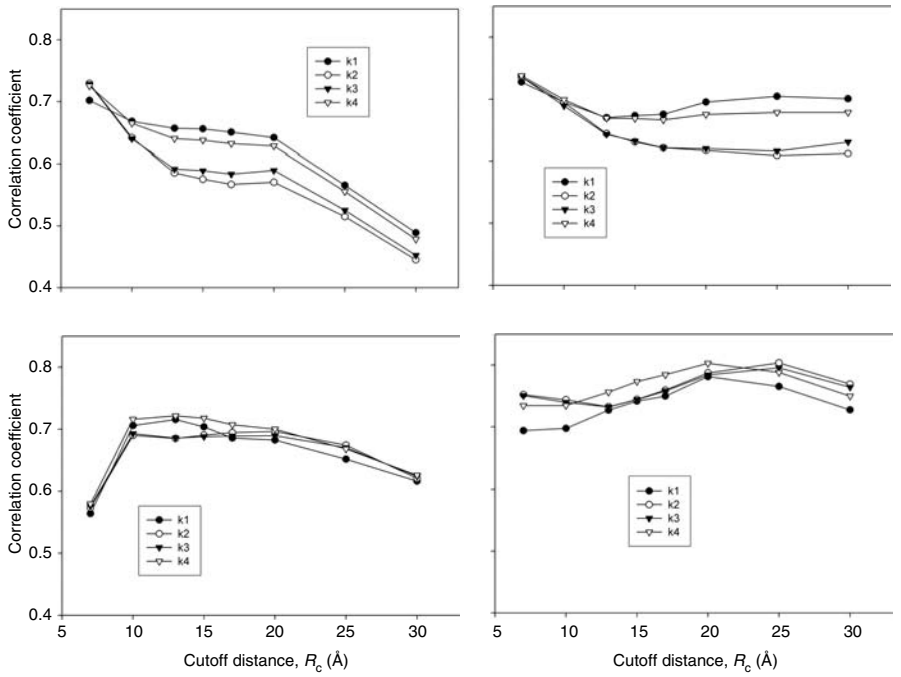

FIGURE 9.3
The correlation coefficients at different cutoff distances R_C for (a) 1HCL, (b) 1USH, (c) 1E8Y, and (d) 1E8X.

constant, $k = 1$, which excludes any dependence on the number of contacts each node interacts with, outperforms other spring constants over a wide range of cutoff distances except in the 7–10 Å range. In this range $k = 4$ is similar or slightly more successful for 1E8Y in predicting the mean-square fluctuations. Figure 9.3(d) shows the correlation coefficients for the case of 1E8X, with ATP included in the calculations as an additional single node. For this protein, the correlation coefficient shows a peak not at the range of 7–10 Å, but instead in the 20–25 Å range. This peak region is specific only for 1E8X: the remaining ATP-bound proteins, 1HP1 and 1HCK, show peaks around 7 and 15 Å, respectively. The structural origin of this peculiar shift in peak positions is not clear.

9.3.5 Cases of Highest Correlations

The cutoff distances and the spring constants yielding the highest correlations are summarized in Table 9.3. The spring constant $k = 4$ in almost all cases outperforms other spring constants except for the protein 1HCK, which gives best correlation with the fixed spring constant.

TABLE 9.3

Conditions That Give the Highest Correlations for Each Protein.

Best	k	R_C (Å)	Correlation
1HCL	4	7	0.73
1USH	4	7	0.74
1E8Y	4	13	0.72
1HCK	1	15	0.61
1HP1	4	7	0.78
1E8X	4	20	0.80

The cutoff distances that correspond to highest correlations show a wide range from 7 to 20 Å. The cutoff distance that provides the highest correlation seems to be protein-specific, at least for the limited set of proteins employed in this study.

9.3.6 Mean-Square Fluctuation Predictions for the Cases That Show Highest Correlations

The benchmark for the predictive power of the elastic network models is its ability to reproduce the experimentally determined fluctuations, or *B*-factors. Figure 9.4 shows a comparison of *B*-factors with fluctuations predicted by GNM for the three unbound proteins for highest correlations. Figure 9.4(a) shows the case of 1HCL where GNM consistently captures the profile and the magnitudes of the *B*-factors. The GNM predictions of fluctuations successfully demonstrate a similar overall shape over almost the range of the whole protein. In Figure 9.4(b), the predicted and experimental fluctuations for the protein 1USH are in good agreement. Most of the highly mobile residues that demonstrate large fluctuations are successfully predicted by GNM. In the case of 1E8Y in Figure 9.4(c), although the experimental fluctuation profile is very rough, GNM results show a high linear correlation of 0.72, identifying most of the highly mobile regions. Of course some minor discrepancies may be caused by inter-molecular interactions in the crystal and these have not been considered here [1].

9.3.7 Comparison of Fluctuations for Different Spring Constants

Although the correlations between experimental and theoretical mean-square fluctuations are satisfactory, information as to how the theoretical fluctuation calculations are influenced by the spring constants may nonetheless be useful to indicate how to better predict protein dynamics. Figures 9.5(a) and (b) compare theoretical fluctuation predictions for the case of 1HP1 at 7 and 35 Å cutoff distances for a series of spring constants. For improved

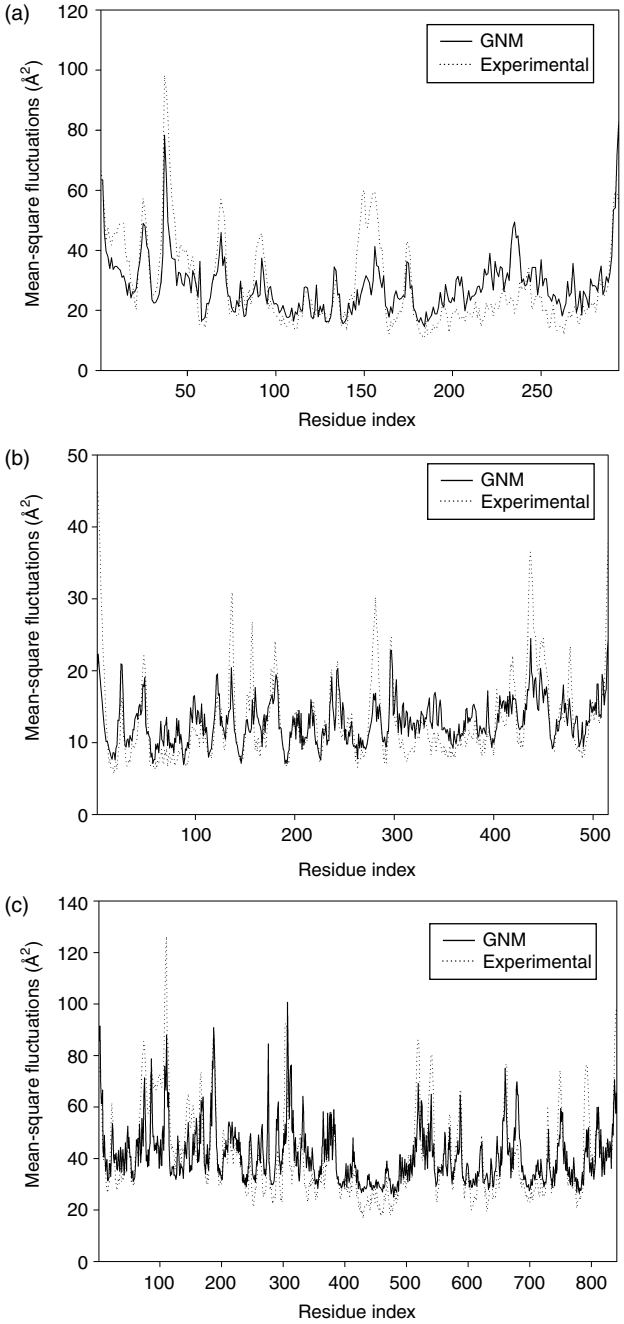

FIGURE 9.4
Comparison of mean-square fluctuations and experimental *B*-factors for the case of spring constant type $k = 4$ at (a) $R_c = 7$ Å for 1HCL, (b) $R_c = 7$ Å for 1USH, and (c) $R_c = 13$ Å for 1E8Y.

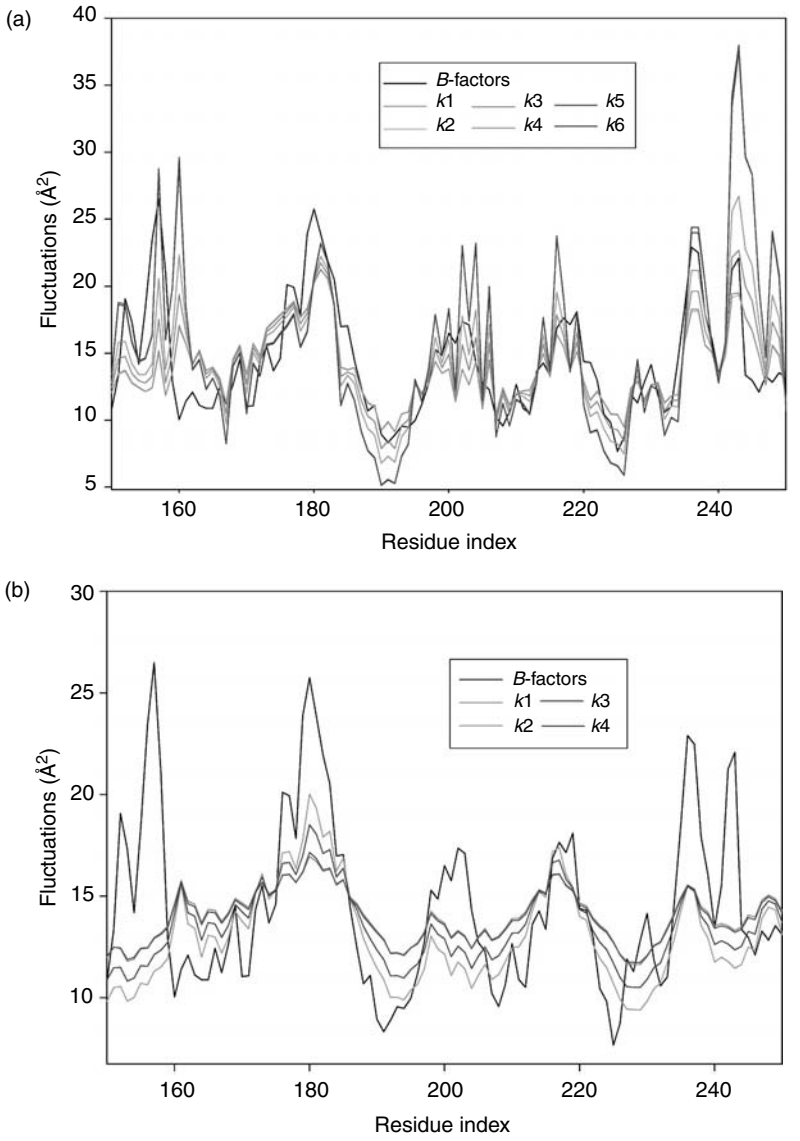

FIGURE 9.5
(See color insert following page 136) Comparison of mean-square fluctuations with *B*-factors for 1HP1 with different spring constants at (a) 7 Å and (b) 35 Å cutoff distances.

visualization, only a range of residues are shown. Interestingly, the fluctuation predictions for different spring constants all follow a similar pattern, demonstrating highly similar maxima and minima profiles at a given cutoff distance. This behavior is limited not only to the protein 1HP1, but also has been observed for the other proteins in the data set. This surprising result

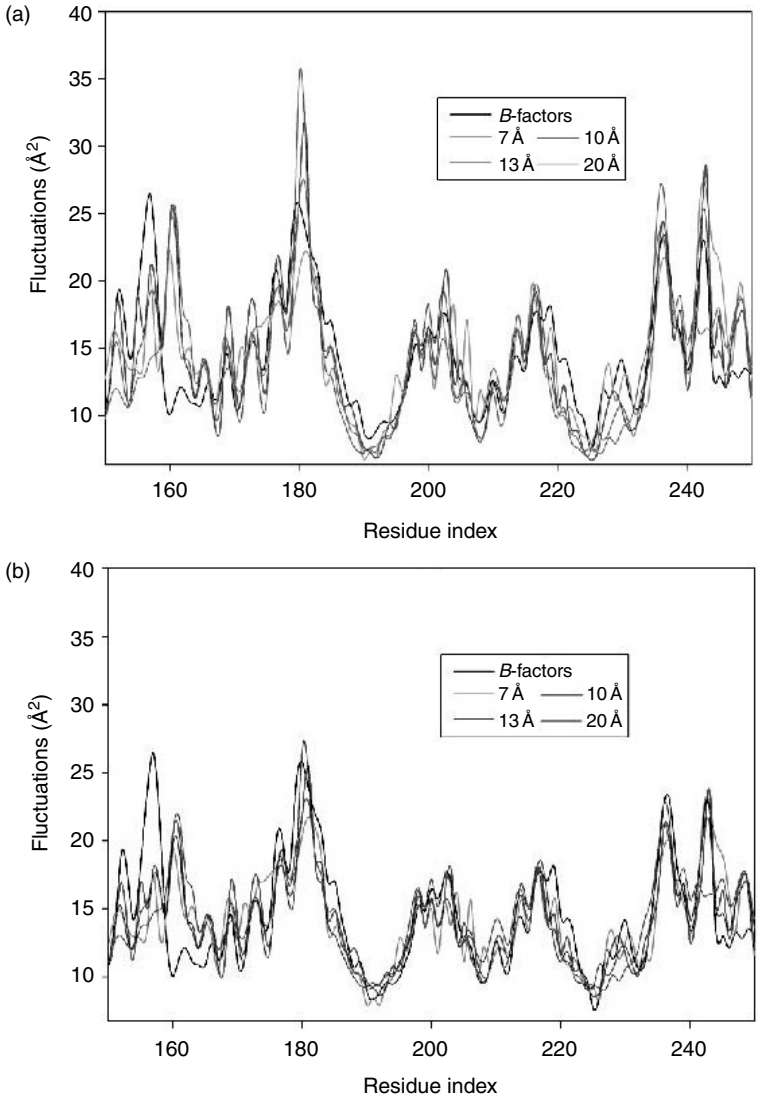

FIGURE 9.6
(See color insert following page 136) Comparison of mean-square fluctuations in the case of 1HP1 at (a) $k = 1$ and (b) $k = 4$.

emphasizes the significance of the state of connectivity between the nodes in fluctuation predictions, rather than the type or strength of connectivity. This result suggests that the global modes of motion are not so strongly influenced by the spring constants. However, this point requires further analysis and it is beyond the scope of the present work. Notably, the longer cutoff distance yields significantly smoother curves.

9.3.8 Comparison of Fluctuations at Different Cutoff Distances

Since the spring constants based on the number of contacts do not substantially influence the *B*-factor predictions, the next step is to analyze the effect of cutoff distances on the predictions. Figures 9.6(a) and (b) show these comparisons in the case of 1HP1 for the spring constants of type $k = 1$ and $k = 4$. Figures 9.6(a) and (b) illustrate that the fluctuations with cutoff distances ranging from 7 to 25 Å follow the same overall pattern. Overall, the cutoff distance seems to be the parameter that affects the correlation between experimental and theoretical fluctuations most, significantly more than do the spring constants.

9.4 Conclusion

The GNM provides a powerful tool to predict protein domain dynamics. In this work, we have analyzed the effect of two important parameters of this model, cutoff distance and spring constant, on the correlation coefficients between experimental *B*-factors and theoretical predictions of mean-square fluctuations. These parameters have been tested for the data set of three protein pairs of ATP-binding proteins. It has been found that the correlation coefficients show distinct dependences on both parameters. Interestingly, the fluctuation patterns for different spring constants show strong similarities, with an overall suggestion that springs ought to be slightly weaker, as in Equation (9.4). The observed strong dependence on cutoff distance is a more significant problem. One possible origin of this dependence could be the differences in sizes among the amino acids. It might be appropriate to introduce springs that are residue type dependent and in the simplest way to make the cutoff distances depend on the sizes of the residue types.

References

1. Kundu, S., Melton, J.S., Sorensen, D.C., and Phillips, G.N., Dynamics of proteins in crystals: comparison of experiment with simple models, *Biophys. J.*, 83, 723–732, 2002.
2. Berman, H.M., Westbrook, J., Feng, Z., Gilliland, G., Bhat, T.N., Weissig, H., Shindyalov, I.N., and Bourne, P.E., The protein data bank, *Nucleic Acids Res.*, 28, 235–242, 2000.
3. Orengo, C.A., Michie, A.D., Jones, S., Jones, D.T., Swindells, M.B., and Thornton, J.M., CATH — a hierarchic classification of protein domain structures, *Structure*, 5, 1093–1108, 1997.
4. Pearl, F.M.G., Lee, D., Bray, J.E., Sillitoe, I., Todd, A.E., Harrison, A.P., Thornton, J.M., and Orengo, C.A., Assigning genomic sequences to CATH, *Nucleic Acids Res.*, 28, 277–282, 2000.

5. Schulze–Gahmen, U., Brandsen, J., Jones, H.D., Morgan, D.O., Meijer, L., Vesely, J., and Kim, S.H., Multiple-modes of ligand recognition — crystal-structures of cyclin-dependent protein-kinase-2 in complex with ATP and 2 inhibitors, olomoucine and isopentenyladenine, *Proteins*, 22, 378–391, 1995.
6. Schulze–Gahmen, U., DeBondt, H.L., and Kim, S.H., High-resolution crystal structures of human cyclin-dependent kinase 2 with and without ATP: bound waters and natural ligand as guides for inhibitor design, *J. Med. Chem.*, 39, 4540–4546, 1996.
7. Knofel, T. and Strater, N., X-ray structure of the *Escherichia coli* periplasmic 5′-nucleotidase containing a dimetal catalytic site, *Nat. Struct. Biol.*, 6, 448–453, 1999.
8. Knofel, T. and Strater, N., Mechanism of hydrolysis of phosphate esters by the dimetal center of 5′-nucleotidase based on crystal structures, *J. Mol. Biol.*, 309, 239–254, 2001.
9. Walker, E.H., Pacold, M.E., Perisic, O., Stephens, L., Hawkins, P.T., Wymann, M.P., and Williams, R.L., Structural determinants of phosphoinositide 3-kinase inhibition by wortmannin, LY294002, quercetin, myricetin, and staurosporine, *Mol. Cell*, 6, 909–919, 2000.
10. Sobolev, V., Sorokine, A., Prilusky, J., Abola, E.E., and Edelman, M., Automated analysis of interatomic contacts in proteins, *Bioinformatics*, 15, 327–332, 1999.
11. Mclachlan, A.D., Rapid comparison of protein structures, *Acta Crystallogr.*, A38, 871–873, 1982.
12. Bahar, I., Atilgan, A.R., and Erman, B., Direct evaluation of thermal fluctuations in proteins using a single-parameter harmonic potential, *Fold. Des.*, 2, 173–181, 1997.
13. Haliloglu, T., Bahar, I., and Erman, B., Gaussian dynamics of folded proteins, *Phys. Rev. Lett.*, 79, 3090–3093, 1997.
14. Sluis–Cremer, N., Temiz, N.A., and Bahar, I., Conformational changes in HIV-1 reverse transcriptase induced by nonnucleoside reverse transcriptase inhibitor binding, *Curr. HIV Res.*, 2, 323–332, 2004.
15. Temiz, N.A. and Bahar, I., Inhibitor binding alters the directions of domain motions in HIV-1 reverse transcriptase, *Proteins*, 49, 61–70, 2002.
16. Hinsen, K., Analysis of domain motions by approximate normal mode calculations, *Proteins*, 33, 417–429, 1998.
17. Press, W.H., Flannery, B.P., Teukolsky, S.A., and Vetterling, W.T., *Numerical Recipes in Fortran*. Cambridge University Press, Cambridge, UK, 1992.

10

Effects of Sequence, Cyclization, and Superhelical Stress on the Internal Motions of DNA

Atsushi Matsumoto and Wilma K. Olson

CONTENTS

10.1 Introduction

The large-scale fluctuations of DNA are key to understanding kinetically complicated molecular events, such as the ease of the long, double helical polymer snaking through the pores of a gel or closing into a loop between separately bound regulatory proteins. DNA loop formation is implicated, in turn, in a number of important biological processes, including the regulation of transcription [1, 2] and the organization of chromatin [3–5]. The base-pair sequence plays a critical role in these processes, helping to guide the overall folding of the chain molecule [6–8] and determining the responses of the double helix to superhelical stress, References 9 and 10.

Recently, we developed a new computational approach for studying the dynamic properties of relatively long DNA molecules without losing track of the local sequence-dependent features of the double helix [11–13]. We make use of a dimeric representation of DNA, which incorporates the known effects of base sequence on the intrinsic structure and the elastic deformability of the constituent dinucleotide steps [14]. The rest states of each dimer are described by six independent step parameters, which specify the preferred orientation and displacement of neighboring base-pair planes (Figure 10.1). The set of rest states and the range of local conformational fluctuations are governed by knowledge-based harmonic energy functions deduced from the mean values and dispersion of step parameters observed in DNA crystal structures. The sugar–phosphate backbone is treated implicitly in the potential energy but is incorporated explicitly as a rigid nucleotide appendage in the kinetic energy. The description of the collective motions of DNA in terms of base-pair steps builds upon general formulations developed by others to express the normal modes of proteins in terms of internal chemical coordinates [15–18].

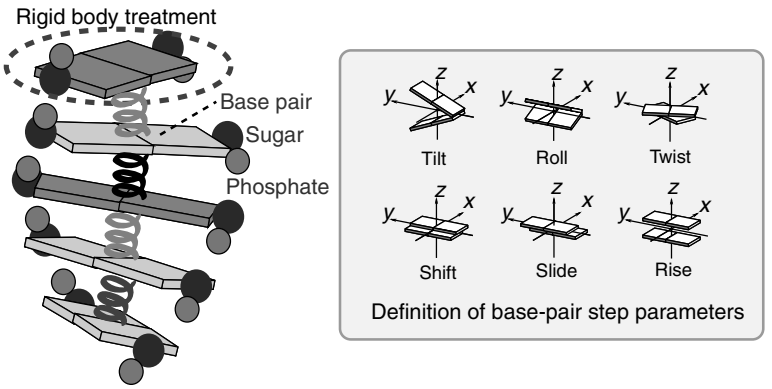

FIGURE 10.1
Schematic representation of DNA helical structure, local elastic deformability, and base-pair step parameters used in the normal-mode analysis of polymeric DNA.

The coarse-grained representation of DNA makes it possible to study the motions of much longer molecular fragments than can be treated with traditional, higher resolution (atomic or torsion angle) treatments, that is, chains roughly an order of magnitude longer than the DNA examined in earlier normal-mode calculations [19–23]. The low-resolution model of DNA also provides a straightforward way to deduce the effects of local structure and deformability on the configurational properties of polymeric sequences.

This chapter focuses on the subtle relationship between DNA base sequence and collective polymeric motions gleaned from the normal-mode analysis of representative double helical molecules. The local, sequence-dependent conformational propensities become important as the contributions of base-pair steps accumulate with the increase of chain length, introducing notable structural variability in molecules of lengths relevant to protein-mediated DNA looping. Here we briefly summarize the DNA model and computational approach. We compare the properties of ideal, naturally straight DNA molecules and naturally curved duplexes, both in the open, linear form and when the structure of the chain is restrained by long-range physical or chemical forces. We highlight the changes in global molecular mobility that accompany ring closure and dissect the effects of intrinsic dimeric structure and local conformational freedom on the dominant normal modes. We focus on sequence contexts, which enhance or repress the global bending, torsion, and stretching of long chain fragments, thereby illustrating ways to "engineer" the macroscopic properties of DNA at the base-pair level. We also discuss the interplay of superhelical stress and the natural coupling of local conformational variables on the large-scale configurational rearrangements of closed circular molecules and the direct physical micromanipulation of single linear chains.

10.2 Methodological Overview

10.2.1 Molecular Representation

Normal-mode analyses of proteins and nucleic acids are usually performed in Cartesian or dihedral angle space. In the case of nucleic acids, there is an even simpler way to describe three-dimensional molecular motion. Because each base or base pair can be approximated as a rigid body, molecular structure can be described in terms of the relative positions and orientations of complementary bases or successive base pairs. Here the base pairs are treated as rigid objects and the six base-pair step parameters — three angular variables called Tilt, Roll, and Twist and three variables called Shift, Slide, and Rise with dimensions of distance [24] — are used as independent conformational degrees of freedom (Figure 10.1). The description of nucleic acid structure is not complete, however, without specification of the sugar–phosphate backbone. We therefore treat each DNA strand as a chain of

nucleotide 5′-monophosphates, with each residue fixed in the *B*-form and related to its sequential neighbors by a given set of local base-pair step parameters (Figure 10.1). This treatment drastically reduces the number of variables needed to describe the helical structure and is key to the successful study of long DNA molecules. The step parameters are defined according to the formulation of El Hassan and Calladine [25], and the backbone is incorporated by superposition of a 5′-nucleotide fragment from the canonical *B*-DNA fiber diffraction model [26] on each base.

10.2.2 DNA Force Field

The conformational potential energy V is a sum of independent contributions from all DNA base-pair steps. The energy of each dimer, V_{XY}, is expressed as a sum of elastic terms over the six base-pair step parameters [14]:

$$V_{XY} = \frac{1}{2}\sum_{i=1}^{6}\sum_{j=1}^{6} f_{ij}(\theta_i - \theta_i^u)(\theta_j - \theta_j^u) \tag{10.1}$$

Here the subscript XY refers to one of the ten unique dinucleotide steps, the $\theta_i (i = 1, 2, \ldots, 6)$ correspond to the instantaneous Tilt, Roll, Twist, Shift, Slide, and Rise at the given step, the θ_i^u denote the equilibrium values of the step parameters in the undeformed reference state, and the f_{ij} are force constants impeding dimeric deformations.

The sugar–phosphate backbone and the surrounding aqueous solvent, that is, charged phosphate groups, water molecules, and counterions, are implicitly treated in the elastic energy terms. The omission of these atoms introduces no serious errors when duplex deformations are limited to energies of the order of $k_B T$, where k_B is the Boltzmann constant and T the temperature in Kelvin.

We consider two types of molecules (i) ideal, naturally straight *B*-DNA chains in which the planes of neighboring base pairs are perfectly parallel ($\theta_1^u = \theta_2^u = 0°$) and (ii) chains that form closed, smoothly deformed minicircles in their equilibrium rest states. The bending components $(\theta_1^\circ, \theta_2^\circ)$ at each base-pair step in the latter molecules are described by a 10-bp repeating pattern of the form,

$$\theta_1^\circ = \left(\frac{360°}{n_B}\right)\cos(36(m - 0.5)); \quad \theta_2^\circ = \left(\frac{360°}{n_B}\right)\cos(36(m - 0.5) + 90) \tag{10.2}$$

where n_B, the number of base pairs, is a multiple of ten, and m denotes the sequential dimer position (see below). The values of Tilt and Roll used as references in the calculation of energy are the same as the values of Tilt and Roll of the natural minicircle, that is, $\theta_1^u = \theta_1^\circ$ and $\theta_2^u = \theta_2^\circ$.

Values of the intrinsic Twist (θ_3^u) are assumed to be independent of sequence and are assigned a range of values consistent with known environmentally induced changes, such as the dependence of helical twist on temperature [27, 28] or ionic strength [29]. The intrinsic displacement of base pairs is restricted to Rise, that is, $\theta_4^u = \theta_5^u = 0$ Å and $\theta_6^u = 3.4$ Å.

Unless otherwise noted, the elastic constants are chosen to mimic the properties of an ideal elastic rod. The variation of individual step parameters is thus assumed to be independent of one another, so that all off-diagonal elastic terms, $f_{ij}(i \neq j)$, in Equation (10.1) are zero. Bending deformations are isotropic and chosen such that the persistence length of the linear chain is 500 Å [30], that is, $f_{ii} = k_B T/\langle \Delta\theta_i^2 \rangle$, where $\langle \Delta\theta_1^2 \rangle^{1/2} = \langle \Delta\theta_2^2 \rangle^{1/2} = 4.7°$. The root-mean-square variation in Twist, $\langle \Delta\theta_3^2 \rangle^{1/2}$, is set to 4° based on estimates of the fluctuations of helical twist in supercoiled DNA involving considerations of the residual writhe in closed circular structures [31–33]. The force constants of the displacement variables — $\langle \Delta\theta_4^2 \rangle^{1/2} = \langle \Delta\theta_5^2 \rangle^{1/2} = \langle \Delta\theta_6^2 \rangle^{1/2} = 0.1$ Å — are assigned values large enough to prevent local spatial translations. The model is therefore comparable to the representation of DNA used in the theory of an ideal, inextensible elastic rod [34, 35] and can be compared with the predicted normal modes. More realistic treatment of the double helical molecule can be obtained through appropriate changes of the intrinsic structural parameters and elastic constants.

10.2.3 Kinetic Energy

The total kinetic energy K is expressed in quadratic form in terms of $\dot{\theta}_i$, the first derivative of θ_i with respect to time, and the weighted "mass" coefficients h_{ij}:

$$K = \frac{1}{2} \sum_{ij} h_{ij} \Delta\dot{\theta}_i \Delta\dot{\theta}_j \tag{10.3}$$

Here the double summation extends over all combinations of base-pair step parameters, that is $6(n_B - 1)$, step parameters in an open, linear DNA or $6n_B$ parameters in a cyclic molecule. The kinetic energy coefficients incorporate the mass m_a and the Cartesian coordinates $\boldsymbol{r}_a$ of all atoms a in the DNA through the relationship:

$$h_{ij} = \sum_a m_a \left(\frac{\partial \mathbf{r}_a}{\partial \theta_i} \right) \left(\frac{\partial \mathbf{r}_a}{\partial \theta_j} \right) \tag{10.4}$$

We take advantage of published analytical expressions for the $(\partial \mathbf{r}_a/\partial\theta_i)$ to evaluate the h_{ij}. The set of rigid-body parameters used to relate neighboring base-pair planes is identical in form to the variables used by others [16, 17] to describe the relative global positions and orientations of different molecules. The internal atomic motions of DNA are effectively separated from the overall rotations and translations of the molecule by expressing the atomic

displacements in terms of an embedded coordinate frame, chosen according to the Eckart condition [36] to minimize the mass-weighted square atomic displacement of DNA [37] in its equilibrium rest state and in a state where one of the step parameters is altered from its minimum energy value [15].

10.2.4 Normal Modes

If the $\Delta\theta_i$ and $\Delta\dot{\theta}_i$ are collected respectively in the vectors $\mathbf{\Theta}$ and $\dot{\mathbf{\Theta}}$, the equations of motion simplify to:

$$\mathbf{H}\Delta\ddot{\mathbf{\Theta}} + \mathbf{F}\Delta\mathbf{\Theta} = \mathbf{0} \tag{10.5}$$

with a periodic solution of the form:

$$\Delta\theta_i = \sum_n A_{in}\alpha_n \cos(\omega_n t + \delta_n) \tag{10.6}$$

Here $\mathbf{F}$ is a collective pseudo-diagonal matrix of elastic force constants and $\mathbf{H}$ is constructed from the terms in Equation (10.4). The fluctuations of each step parameter $\Delta\theta_i$ at time t are thereby expressed as a linear combination of harmonic oscillators, the energies of which are proportional to the square of the nth normal-mode frequency, ω_n^2. The contribution of each mode to the variation of individual step parameters decreases rapidly with increase in ω_n, so that relatively few (low frequency) modes are responsible for the large-scale deformations of the molecule. The contributions of individual step parameters $\Delta\theta_i$ to each of the modes can be determined from the frequency ω_n, phase angle δ_n, and amplitude α_n of the normal mode of interest and the eigenvector components A_{in} obtained by solving the equations of motion.

10.2.5 Imposed Superhelical Stress

The Twist of DNA is assigned values such that, when the molecule is covalently closed into a circle, the normalized sum of the equilibrium Twist, $\sum_{n_B} \theta_3^\circ/360^\circ$, over all n_B base-pair steps is an integer. Here θ_3° is set to 36° and n_B to 200. The normalized sum, which is equal to 20, is the linking number Lk of the closed ring, that is, the number of times the two strands of the double helix wrap around one another. If there are no spatial constraints on the ends of the chain, the variation of intrinsic Twist θ_3^u converts the circular equilibrium structure to a helical configuration [30, 38–40]. If the chain ends are also covalently linked, the total increase or decrease of intrinsic Twist relative to the unligated structure, $\Delta Tw^\circ = (\theta_3^\circ - \theta_3^u)n_B/360^\circ$, imposes torsional stress on the naturally circular molecule. Such a molecule is said to be supercoiled and is characterized by a linking number difference ΔLk equal to ΔTw°.

In practice, the ends of circular molecules are held in place by a restraint energy, E_r, given as a sum over N distance restraints:

$$E_r = \sum_{l=1}^{N} k_l (d_l - d_l^\circ)^2 \tag{10.7}$$

The parameter k_l is an arbitrarily chosen spring constant, d_l is the instantaneous distance between two points on which a distance restraint is placed, and d_l° is the desired separation distance. Three distance restraints, placed on the origins and two coordinate axes of terminal base pairs, are used to enforce DNA ring closure. A single restraint on the separation of base-pair origins is used to limit the end-to-end extension of stretched, linear chains. Because the restraint energy is close to zero after energy minimization, the dimeric contributions from Equation (10.1) dominate the total energy.

10.3 Dominant Modes

10.3.1 Comparative Spectra

We start with a comparative analysis of the dominant (lowest frequency) normal modes of four DNA molecules — a pair of open, linear chains and a pair of circularized molecules — each chain inextensible, 200 bp in chain length, and capable of ideal isotropic bending. One of the DNAs in each pair is intrinsically straight and the other closes naturally into a circle in its equilibrium rest state. We classify the motions, following Matsumoto and Gō [23], on the basis of the global structural changes revealed through computer visualization of the eigenvectors associated with each mode and expressed by Equation (10.6). The dominant bending and twisting modes of the linear molecules are represented by the upper set of spectra in Figure 10.2 and those of the cyclic molecules by the lower set.

10.3.2 Linear DNA

Each of the pure (planar) bending modes of the naturally straight linear molecules (dashed lines at the left of the uppermost spectrum in Figure 10.2) is doubly degenerate, describing mutually perpendicular motions of equivalent energy. The superposition of these modes leads to the global isotropic bending characteristic of an ideal elastic rod. The bending modes of the unligated DNA circle, by contrast, are not degenerate: it is energetically more costly to bend the curved molecule out of the plane of the minimum energy structure than to deform it in the plane of the equilibrium configuration (note the higher frequency bending modes represented by light gray lines associated with each lower frequency [dashed] bending mode in the spectrum). Moreover,

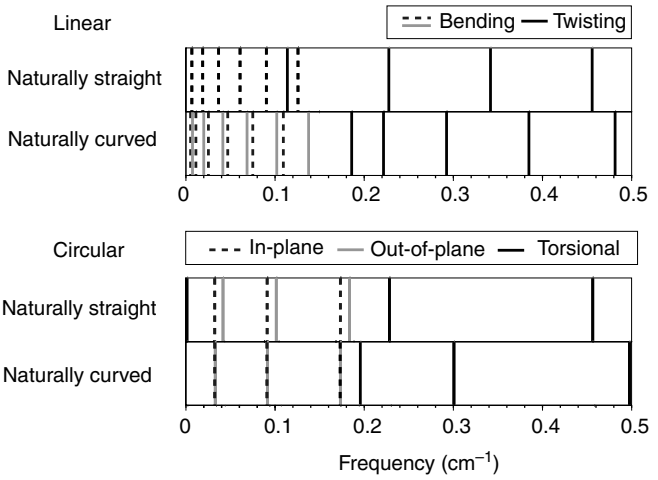

FIGURE 10.2
Comparative spectra of the lowest frequency bending and twisting modes of 200-bp open, linear DNA, and circular molecules, which are perfectly straight or naturally curved at equilibrium and are subject to an ideal elastic potential. The terms in- and out-of-plane distinguish the different types of global bending exhibited by the covalently closed molecules. The terms twisting and torsion are used interchangeably to describe the net rotation of molecular fragments or the rotation of the molecule as a whole.

as frequency increases, the out-of-plane distortions of the naturally curved molecule become higher in energy and the in-plane distortions become lower in energy than the corresponding deformations of the straight chain.

The twisting modes of the linear molecules (solid black lines in Figure 10.2) are higher in frequency, more widely spaced, and even more sensitive to intrinsic DNA structure than the bending modes. The lowest torsional frequency of the naturally straight molecule is significantly lower in value than that of the curved chain. The localized buildup of Twist associated with this mode has no effect on the overall shape of the naturally straight DNA but forces the curved molecule out of its natural plane. Interestingly, Twist plays virtually no role in the extra "free" (0.189 cm^{-1}) torsional mode of the curved DNA chain (see Section 10.3.3). The energy differences between corresponding torsional modes of the unligated straight and curved chains decrease at higher frequency.

10.3.3 Circular DNA

The collective motions of the circular molecules, both of which are torsionally relaxed ($\theta_3^\circ = \theta_3^u = 36°$), show three types of large-scale deformation, namely in-plane, out-of-plane, and torsional deformations. It should be noted that the only truly pure normal mode of the torsionally relaxed circular molecules is the in-plane bending motion. Out-of-plane bending of the closed polymer always involves torsion and local bending deformations accompany

the global torsional motions. Concerted changes in local bending, rather than twisting, over a 10-bp helical repeat, give rise to the lowest (near zero) frequency "free" torsional mode of the covalently closed molecule constructed of naturally straight DNA. The DNA retains a circular shape, with the molecule rotating freely about its helical axis in this mode. As is clear from the spectral alignment in Figure 10.2, the torsional frequencies of the natural minicircle formed upon ligation of the intrinsically curved DNA are much higher than those of the cyclized, naturally straight chain. The conformational mechanism, which takes base pairs from the inside to the outside of the circle, places a greater energy penalty on the natural minicircle, fixing the rotational setting of the molecule. The free spinning of DNA about its global helical axis cannot be detected in the internal reference frame of the linear, naturally straight molecule, but is observed in the unligated circle, at a slightly lower frequency compared to its cyclic equivalent (0.189 vs. 0.195 cm^{-1}). A number of the higher-frequency torsional modes observed in the open, linear form have no counterpart in the cyclic molecules, presumably, because of the boundary constraints of covalent bond formation. Such modes are expected to occur and other modes, which are illustrated here, are expected to vanish if the ends of the molecule are constrained by the binding of a twisting agent, that is, if the imposed superhelical stress is concentrated at a single base-pair step.

The in-plane bending modes of the cyclic DNA molecules generate elliptical shapes and the out-of-plane modes produce cuplike distortions (see inset in Figure 10.4). As is clear from Figure 10.2, ring closure increases the energetic cost, that is, frequencies, of global bending compared to linear DNA. In contrast to the isotropic deformations of its unligated counterpart, the ease of in- and out-of-plane bending differs in circles made up of naturally straight DNA. The frequencies of in- and out-of-plane deformations are virtually identical, however, in the closed naturally circular molecule. The latter frequencies are roughly equivalent to the frequency of in-plane bending of the cyclized naturally straight chain (Figure 10.2). The differences in the out-of-plane bending modes of naturally circular vs. naturally straight DNA rings arise from different patterns of local conformational motion. While the uptake of Twist, $\Delta\theta_3$, is uniformly zero for the out-of-plane deformations of the naturally straight DNA, it assumes nonzero values for the corresponding changes in the natural minicircle (formed from curved DNA). By contrast, the patterns of local conformational fluctuations underlying the in-plane modes are similar for the two types of closed molecules.

10.4 Role of Intrinsic Structure

10.4.1 Intrinsic Bending and Single-Molecule Stretching

Mechanical constants, which describe the overall elastic behavior of linear DNA, can be obtained by substituting the computed normal-mode

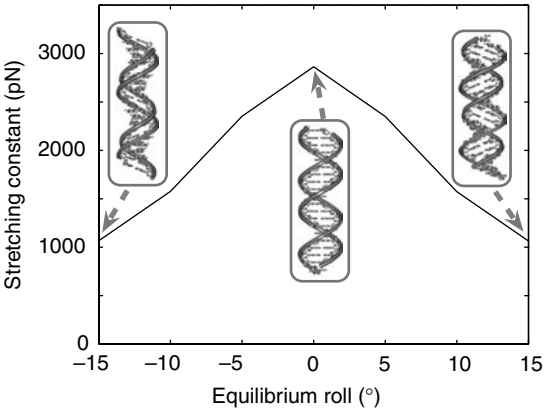

FIGURE 10.3
Computed variation of the mechanical stretching constant as a function of the equilibrium Roll angle θ_2^u of an ideal, naturally straight DNA chain. The molecular insets, generated with MolScript [64], illustrate equilibrium rest states with positive, zero, and negative intrinsic Roll.

frequencies in classical expressions for the normal modes of an ideal elastic rod [41]. For example, the stretching constant (Young's modulus) Y is given by $(2\nu_n^s)ML/n^2$, where ν_n^s is the computed frequency of the nth stretching mode, M is the total mass of the molecule, and L is the length of the DNA helical axis. Substitution of the computed stretching frequency of a 200-bp extensible, naturally straight DNA molecule, in which the translational force constants are assigned values mimicking the observed dispersion of Shift, Slide, and Rise in high resolution structures ($\langle\Delta\theta_4^2\rangle^{1/2} = 0.61$ Å, $\langle\Delta\theta_5^2\rangle^{1/2} = 0.61$ Å, and $\langle\Delta\theta_6^2\rangle^{1/2} = 0.22$ Å), however, fails to account for the values of Y deduced from single-molecule manipulations of DNA (3 vs. 1.0 to 1.4×10^3 pN) [42–45]. Global extension of an ideal, naturally straight molecule occurs exclusively through changes in Rise, the energetically stiffest step parameter, which describes the axial, that is, van der Waals' separation of neighboring base-pair planes. Other lower energy dimer deformations contribute to the extension and compression if the equilibrium structure deviates from its ideal rest state (see below).

Starting from the ideal, naturally straight polymer, we introduce an identical nonzero equilibrium Roll value (θ_2^u) at every dimer step and compute the normal modes and stretching constant. Because the choice of θ_2^u alters the helical contour length as well as the normal-mode frequencies, the change of mechanical constants in Figure 10.3 reflects the slight compression of the double helical axis brought about by the assumed nonzero equilibrium Roll, for example, ca. 4% reduction in contour length for $\theta_2^u = \pm 10°$, as well as the natural global stretching motions. The major contributions to Y in this example arise, however, from the change in normal-mode frequencies.

As depicted in the inset to Figure 10.3, the base pairs of DNA structures with nonzero θ_2^u are inclined with respect to the helical axis. The displacement

of neighboring base pairs in the direction of inclination, that is, variation of Slide, adds naturally to the global stretching. Because Slide is a much "softer" conformational variable than Rise [14], global stretching is energetically enhanced with increase (or decrease) of θ_2^u. The mechanical stretching constant consequently decreases, attaining values comparable to those extracted from experiment for $\theta_2^u = \pm 10$ to 15°. In other words, when the base-pair planes are perpendicular to the helical axis, along which the stretching motion takes place, energetically costly deformations via Rise result in a large elastic constant. When the equilibrium Roll angle deviates from zero, stretching takes place by lower energy conformational routes with a concomitant decrease in the mechanical constant. Thus, the base pairs of the mixed sequence DNA used in single-molecule stretching experiments may not lie perpendicular to the direction of stretching, or may reorient upon forced extension as predicted in atomic simulations [46].

10.4.2 Intrinsic Curvature and DNA Ring Puckering

We next consider a series of closed, naturally curved molecules of varying intrinsic curvature, but all of the same chain length ($n_B = 200$ bp), planar in their undeformed open configuration, and torsionally relaxed. When the condition of a uniform double helical repeat of 10 bp per turn is satisfied, the closed, torsionally relaxed, circular molecule with curvature $\kappa^\circ = 2\pi/3.4n_B = 0.009$ Å^{-1} is a minimum energy configuration. Figure 10.4 reports the dependence of the frequencies of the lowest in-plane and out-of-plane bending deformations on the ratio of curvature $q = \kappa^u/\kappa^\circ$ in a series of molecules, which form natural minicircles of different chain lengths.

The variation of the computed normal modes agrees closely with the theoretical dependence on q [35]. The degeneracy of the in-plane and out-of-plane modes is evident from the superposition of o and + symbols, which are overlaid on the predicted variation of frequencies (solid and dashed curves, respectively). As noted above, the frequency of the out-of-plane bending mode is higher than that of the in-plane mode if the molecule is naturally straight ($q = 0$), but is of comparable magnitude if the DNA forms a natural minicircle ($q = 1$). The ease of out-of-plane bending becomes greater than that of in-plane deformation, that is, of lower frequency and lower energy, if q is greater than 1.06, a threshold value determined by the choice of elastic constants. In other words, molecules that are more strongly bent and cyclize into smaller rings than the natural minicircle, show a natural tendency to fluctuate out of the plane of the 200-bp circle. Indeed, when $q = 2$ and the molecule is closed into a circle two times the length of its equilibrium rest state, the barrier to out-of-plane deformations is removed, and the frequency of the mode is close to zero. Thus, DNA loops of a few hundred base pairs can be forced to adopt puckered, out-of-plane configurations by incorporating sequences, such as those reported by Cloutier and Widom [47], which naturally close

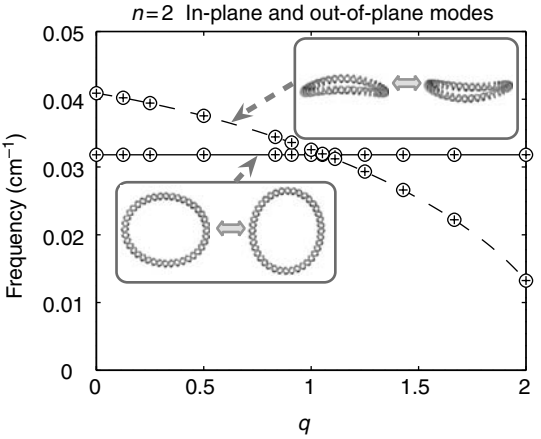

FIGURE 10.4
Normal-mode frequencies of the lowest $n = 2$ in- and out-of-plane bending modes of naturally circular molecules that are closed into chains of 200 bp. Data are reported as a function of the ratio $q = \kappa^u/\kappa^\circ$ of the intrinsic curvature κ^u to the curvature κ° of the minimum energy configuration of the natural minicircle. The degeneracy of modes is evident from the computed frequencies, which are distinguished by o and + symbols and compared with the theoretically predicted frequencies [34, 35] (shown respectively by smooth unbroken and broken curves). The molecular insets, generated with MolScript [64], illustrate the two types of global motion.

into tight circles. By contrast, the frequencies of the in-plane modes of the torsionally relaxed minicircles are constant over the above range of q.

10.4.3 Intrinsic Curvature and Enzyme Cutting Patterns

In order to mimic the effect of a bound protein on the natural motions of DNA, we introduce a short naturally curved chain fragment into a covalently closed molecule otherwise made up of naturally straight DNA. The binding of proteins often induces significant bending in DNA and is known to influence large-scale properties of closed molecules. For example, the presence of the *Escherichia coli* catabolite activator protein (CAP) on a 284-bp minicircle precludes access of the DNA cutting enzyme, DNase I, to parts of the duplex, other than the CAP binding site, that can be reached in the absence of CAP [9].

Here a curved insert is assigned the position-dependent, intrinsic bending components (Equation [10.2]) that characterize an ideal 200-bp natural minicircle. These changes in equilibrium rest state are made only at dimer steps within the selected region of curvature. All other steps of the duplex retain the intrinsic step parameters of a naturally straight molecule, and both curved and straight dimer steps are governed by the same ideal elastic potential. As anticipated, a 5- to 11-bp insert of curved DNA raises the lowest frequency "free" torsional mode to values greater than zero (blackened circles on the left half of Figure 10.5). Precise identification of the torsional mode is complicated

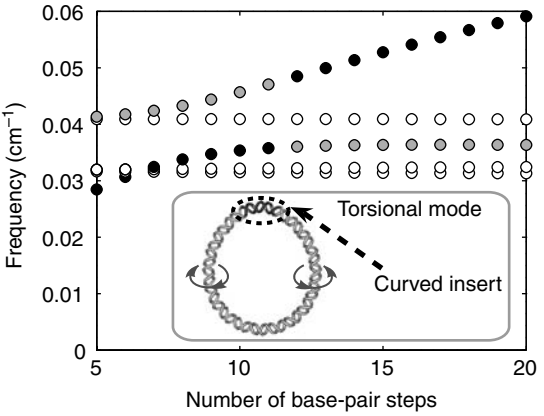

FIGURE 10.5
Spectrum of the five lowest frequency normal modes as a function of the chain length, in base pairs, of a curved insert in a 200-bp torsionally relaxed circular DNA, which is otherwise naturally straight in its equilibrium state. The curved inserts are assigned the same force constants as other dimer steps. The intrinsic step parameters of the insert are assigned the repeating pattern associated with a 200-bp natural minicircle. The dominant torsional modes of the different chains are highlighted by filled circles. The molecular inset, generated with MolScript [64], illustrates the overall twisting of the closed DNA molecule with a 20-bp curved fragment. Circles filled in black correspond to the dominant torsional mode in chains with a specified curved inset and circles filled in gray to the second most important mode.

by the mixed character of motions in the modified duplex. Two of the five lowest frequency modes between 0.02 and 0.06 cm^{-1} (denoted by the circles filled in black and gray) show a mixture of out-of-plane bending and global torsional motions.

The restrictions on global motion imposed by a curved insert are further enhanced by increasing the length of the perturbed fragment. As evident from Figure 10.5, where the five lowest normal-mode frequencies are reported for curved inserts of 5 to 20 bp, the frequencies of the two aforementioned mixed torsional modes increase with added base-pair steps. The dominant torsional mode with the largest average degree of rotation around the helical axis, shown by blackened circles in the figure, increases in frequency as the length of the insert is increased. With inserts of 5 bp, the dominant torsional frequency falls below the pure in-plane and out-of-plane bending modes and has some out-of-plane bending character. By contrast, when 20 bp of the minicircle are naturally curved, the frequency exceeds those of the pure bending modes, but still retains some out-of-plane bending character. The motions of the latter DNA are illustrated schematically in Figure 10.5.

Regardless of the choice of mode, the frequency of torsional motion of a closed duplex with a curved insert is clearly increased over that of a circular chain without such a fragment. The enzyme cutting properties of CAP-bound DNA minicircles [9] are thus clarified. In the absence of protein (curved insert), the energy of "free" torsional motion is low and no single orientation of the

closed duplex is preferred over any other. Thus, all sites are equally accessible to a ligand such as DNase I, which contacts the (outer) convex surface of its bent double helical target [48, 49]. The introduction of local curvature restricts rotation of the DNA as a whole about its helical axis, favoring the minimum energy configuration and limiting access to residues located on the inside of the ring.

10.5 Role of Sequence-Dependent Deformability

10.5.1 Dimer Deformability and Large-Scale Anisotropy of Linear DNA

The interplay between local and large-scale conformational motions found from base-pair level analyses of DNA normal modes suggests new ways in which one might "engineer" the macroscopic properties of long polymers from the perspective of dimer deformability. For example, one can take advantage of the enhanced deformability of pyrimidine–purine steps [14] in combination with the periodic fluctuations of Roll and Tilt, which underlie the low-frequency bending modes of DNA to design regular polymers that are intrinsically straight in the equilibrium state (at 0 K), yet, which bend in a preferred direction at ambient temperatures.

We illustrate this large-scale anisotropy in Figure 10.6 with the two lowest frequency bending modes of a series of intrinsically straight poly d(A_mT_m) sequences where m is half the length of the repeating unit, that is, $m = 1$

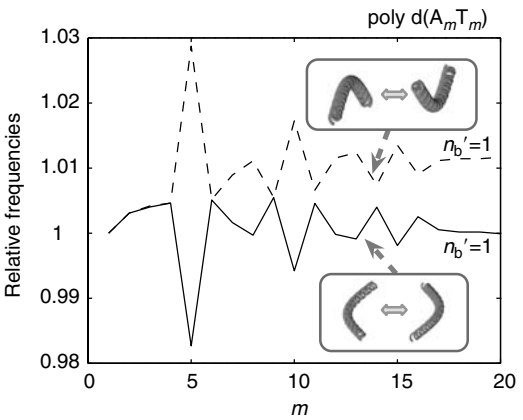

FIGURE 10.6
The first ($n_b = 1$) and second ($n_{b'} = 1$) lowest global bending frequencies (solid and dashed lines, respectively), plotted as a function of m, in a series of intrinsically straight 120-bp poly d(A_mT_m) chains, which are subject to a sequence-dependent elastic potential [14]. Frequencies are normalized with respect to the lowest bending frequency of the poly d(AT) alternating copolymer ($m = 1$). The molecular insets, generated with MolScript [64], illustrate the orthogonal directions of bending of the linear chain.

corresponds to the alternating poly d(AT) copolymer with a 2-bp repeating unit and $m = 5$ to the poly d(A_5T_5) block copolymer with a 10-bp sequential repeat. To emphasize the influence of sequence-dependent deformability on global properties, we assign an ideal, naturally straight rest state to all dimers. We employ elastic constants deduced from the variation of base-pair steps in high-resolution protein–DNA crystal structures [14] and consider 120-bp sequences with $m = 1$ to 20. As is clear from the figure, the degeneracy of bending frequencies that is characteristic of large-scale isotropic bending breaks down for particular sequential repeats, namely at $m = 5$, 7, 8, and 10–20, where the frequencies are no longer equivalent. The DNA in these cases bends more easily in the direction of the lower frequency mode than in the roughly perpendicular direction of the higher frequency mode (see molecular inset in Figure 10.6).

Thus, even a naturally straight chain will bend in a preferred direction if intrinsically flexible and stiff dimer steps are spaced at half-turn increments, that is, ca. 5 bp apart, on opposite sides of the double helix. Chains with such features are more likely to associate with strategically placed, up- or downstream proteins in a hairpin loop structure, and are expected to experience more difficulty in snaking through the pores of a gel. This picture of intrinsic global mobility differs from conventional "static" interpretations [50,51] of the anomalously slow gel mobilities of certain DNA sequences based on the intrinsic equilibrium structure of the constituent base-pair steps.

10.5.2 Dimer Deformability and Rotational Positioning of Circular DNA

In order to gain understanding of the effects of local base-pair deformability on the properties of cyclic DNA molecules, we examined a simple polymeric sequence with T · A base pairs replacing A · T base pairs at two sites along a cyclized 200-bp poly dA · poly dT chain. Each base-pair substitution introduces two new dimer steps in the closed duplex, that is, an AT immediately followed by a TA in the closed d($TA_{m-1}TA_{199-m}$) sequence. Here the DNA is again assumed to be naturally straight in its equilibrium rest states and is subject to fluctuations at the dimeric level based on the observed distributions of base-pair parameters in protein–DNA complexes [14].

As is clear from Figure 10.7, the distance m between altered sites has a remarkable effect on the lowest torsional frequency. The computed frequency assumes a maximum if the altered sites are separated by a multiple of 5 bp, regardless of the distance of separation along the chain contour. That is, a comparable increase in frequency, with a concomitant enhancement of the energy barrier to "free" global rotational motion, occurs whether either the two TA steps are sequentially close or on the opposite sides of the closed duplex. A minimum in frequency is also repeated every 5 bp, but is offset from the maxima in Figure 10.7 by 2 to 3 bp. Here too, the minimum values do not depend on the distance between altered base pairs.

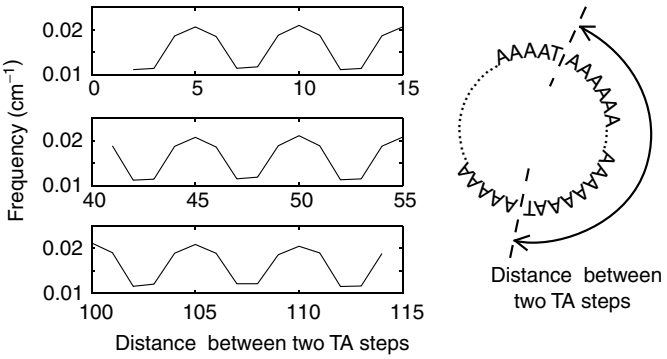

FIGURE 10.7
Lowest ($n = 0$) torsional frequency, as a function of the sequential distance, m, between altered A·T→T·A base pairs, of a torsionally relaxed poly d($TA_{m-1}TA_{199-m}$) closed duplex, which is naturally straight in its equilibrium rest state and subject to a sequence-dependent elastic potential [14]: (top) $2 \leq m \leq 15$, when the modified sites are close to one another; (bottom) $100 \leq m \leq 115$, when the sites are on opposite sides of the circle; (middle) $41 \leq m \leq 55$, when the sites are separated by intermediate distances.

Thus, chain deformability also contributes to the rotational positioning of DNA and the relative accessibility of cutting enzymes and other chemical agents to the inner and outer surfaces of DNA loops and minicircles.

10.6 Role of Conformational Coupling

10.6.1 Roll–Slide Interdependence and Supercoiling of Circular DNA

Slight over- or undertwisting of a DNA circle introduces subtle changes in the computed normal-mode frequencies. The in-plane bending motions of supercoiled chains are consistently lower in frequency (energy) and the out-of-plane motions are consistently higher in value than the corresponding modes of the relaxed circle, with the differences becoming more pronounced as the frequencies of the modes increase. The in- and out-of-plane bending deformations of the supercoiled rings, however, are not pure, that is, the normal modes are combinations of pure in-plane and pure out-of-plane bending modes.

Figure 10.8 reports the decrease in the lowest (predominantly in-plane) bending frequencies of a 200-bp circular molecule made up of naturally straight DNA as a function of imposed intrinsic Twist θ_3^u. The computed bending modes of idealized molecules are represented by discrete points and connected by solid lines. The superposition of symbols (open circles and plus signs) highlights the degeneracy of the configurational fluctuations.

The frequency of deformation drops precipitously if the intrinsic Twist is changed slightly beyond the illustrated range, approaching a value of zero if θ_3^u is changed by $\pm 2.2°$, the critical values in the present model associated with the interchange of the circular and Figure 8 minimum energy rest states

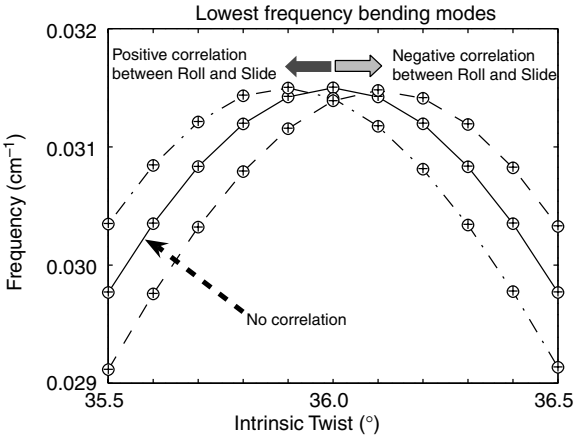

FIGURE 10.8
Lowest normal-mode bending frequencies, plotted as a function of intrinsic Twist θ_3^u, of circular DNA molecules, which are naturally straight in the equilibrium rest state. Chains governed by an ideal elastic potential (points connected by solid lines) are compared with chains that are also subject to the positive or negative coupling of Roll and Slide, where f_{25} is -0.233 or 0.233, respectively. The degeneracy of the modes is evident from the computed frequencies, which are distinguished by o and + symbols.

[52]. The very low frequency of such modes indicates that the energetic cost of deforming the over- or undertwisted circle into a different shape is negligible in these regions of θ_3^u. Both in- and out-of-plane bending deformations contribute to the changes in molecular shape at the critical values.

In contrast to the symmetric effects of over- and undertwisting on bending frequency found for a minicircle subject to ideal elastic deformations, comparable increases or decreases in θ_3^u have different effects on a more realistically closed duplex with base-pair step parameters obeying the conformational coupling characteristic of known structures, that is, nonzero $f_{ij}(i \neq j)$ in Equation (10.1). The normal-mode frequencies of such molecules are shifted to the right or left of the values which characterize the ring described by an ideal elastic force field (points connected by broken lines in Figure 10.8). In these examples, Roll and Slide are assigned a covariance $\langle \Delta\theta_2 \Delta\theta_5 \rangle$ based on the observed dispersion, $|\langle \Delta\theta_2 \Delta\theta_5 \rangle| = (1/2)(\langle \Delta\theta_2^2 \rangle \langle \Delta\theta_5^2 \rangle)^{1/2}$, and the sign of correlation seen in DNA crystal data [14]. The elastic constants are obtained by inversion of the assumed covariance matrix (see Reference 14 for details).

If Roll and Slide are correlated such that the increase of Roll leads to a decrease of Slide and vice versa, that is, $\langle \Delta\theta_2 \Delta\theta_5 \rangle < 0$, $f_{25} = +0.233$, the maximum value of the lowest bending frequency occurs at an imposed Twist of 36.1°, a value that *undertwists* the molecule (because θ_3°, the step parameter in the torsionally relaxed circle, is less than θ_3^u; see Section 10.2.5). (Positive values of f_{ij} allow for the concomitant increase in Roll and decrease in Slide observed in the majority of base-pair steps [14].) The maximum shifts to lower values of θ_3^u characteristic of overtwisted DNA if Roll and Slide obey a positive

correlation ($\langle \Delta\theta_2 \Delta\theta_5 \rangle > 0$, $f_{ij} = -0.233$) such as that found in a few base-pair steps, including AA dimers.

The shift in frequencies in Figure 10.8 alters, albeit slightly, the values of imposed Twist at which the normal-mode frequencies approach zero, that is, the critical values of θ_3^u at which the large-scale transition between circular and Figure-8 forms take place. The transition occurs as θ_3^u approaches 33.8° or 38.2° in the ideal natural minicircle. Because the frequencies are symmetric with respect to the equilibrium Twist ($\theta_3^\circ = 36.0°$) of the torsionally relaxed configuration, the difference between the smaller critical value (33.8°) and θ_3° is equal to that of the larger one (38.2°). The shift in frequencies when Roll and Slide are negatively correlated makes both critical values larger. As a result, the difference between the smaller critical value and θ_3° is less than that of the larger one. Given the smaller difference of the former, the large-scale configurational transition in such chains is expected to take place more easily when θ_3^u is decreased rather than increased, that is, overtwisted rather than undertwisted. The preferred direction of transition occurs via the increase of θ_3^u, that is, undertwisting, if Roll–Slide coupling is positive.

The asymmetric uptake of supercoiling in naturally occurring DNA may reflect the interplay of conformational variables like Roll and Slide in combination with the sequence-dependent variation of equilibrium Twist. (The mean values of dimer steps in *B*-DNA structures span the range 31 to 40° with a mean generic sequence average of 36° [53].) Most naturally occurring DNA is undertwisted, that is, negatively supercoiled [54]. The shift in bending frequencies computed when Roll and Slide exhibit positive correlations may contribute to the observed tendency of the closed duplex to unwind. Interestingly, no other pair of step parameters has a comparable effect on the computed bending frequencies. More realistic representation of the chain molecule, such as sequence-dependent anisotropic bending, does not affect the general effects of coupling. Changes in intrinsic step parameters, however, shift the state of minimum energy and have more pronounced effects on the tendency of the closed duplex to over- or underwind.

10.6.2 Twist–Rise Coupling and Overstretching of Linear DNA

Values of the global twisting rigidity of DNA derived from recent single-molecule studies of over- and undertwisted molecules, which are stretched to full extension [55] are much higher (by a factor of 1.1 to 1.5) than values deduced from earlier solution measurements [32, 56–59]. The low-frequency twisting modes of model DNA polymers subject to comparable external constraints provide a structural rationalization for these differences. The global twisting constant, which can be obtained by substituting the computed normal-mode twisting frequencies in the standard expression [41] for the normal modes of an ideal elastic rod, is dominated by the lowest-frequency twisting ($n = 1$) mode. The increase in frequency of the latter mode is thus

TABLE 10.1

Effect of Local Conformational Coupling on the Lowest Frequency Normal Twisting Modes and Global Torsional Constant of a 100-bp Ideal, Naturally Straight DNA Molecule[a].

Coupled variables	ν_l^{o} cm^{-1}	ν_l^{eq} cm^{-1}	ν_l^{str} cm^{-1}	$\nu_l^{eq} - \nu_l^{o}$ (%)	$\nu_l^{str} - \nu_l^{o}$ (%)	R^b
Ideal DNA[c]	0.1886	0.1886	0.1886	0.00	−0.01	1.05
Tilt–Roll	0.1887	0.1887	0.1886	0.00	−0.01	1.05
Tilt–Twist	0.1882	0.1882	0.1895	0.00	+0.71	1.06
Tilt–Shift	0.1886	0.1886	0.1886	0.00	−0.01	1.05
Tilt–Slide	0.1886	0.1886	0.1886	0.00	−0.01	1.05
Tilt–Rise	0.1886	0.1886	0.1888	0.00	+0.08	1.05
Roll–Twist	0.1874	0.1874	0.1905	0.00	+1.65	1.08
Roll–Shift	0.1886	0.1886	0.1886	0.00	−0.01	1.05
Roll–Slide	0.1887	0.1887	0.1886	0.00	−0.01	1.05
Roll–Rise	0.1887	0.1887	0.1897	0.00	+0.54	1.06
Twist–Shift	0.1881	0.1881	0.1873	0.00	−0.45	1.04
Twist–Slide	0.1882	0.1882	0.1866	0.00	−0.87	1.03
Twist–Rise	0.1845	0.1971	0.1971	**+6.83**	**+6.87**	1.20
Shift–Slide	0.1887	0.1887	0.1886	0.00	−0.01	1.05
Shift–Rise	0.1886	0.1886	0.1881	0.00	−0.30	1.04
Slide–Rise	0.1886	0.1886	0.1882	0.00	−0.22	1.05
Roll–Twist, Twist–Rise	0.1866	0.1992	0.2023	**+6.72**	**+8.41**	1.23
Twist–Slide, Twist–Rise	0.1862	0.1987	0.1971	**+6.72**	**+5.87**	1.18
Roll–Twist, Twist–Slide	0.1906	0.1906	0.2045	0.00	**+7.28**	1.21
Roll–Twist, Twist–Slide, Twist–Rise	0.1845	0.1969	0.2123	**+6.75**	**+15.09**	1.39

[a] Equilibrium rest state: $\theta_1^u = 0°$, $\theta_2^u = 0°$, $\theta_3^u = 36°$, $\theta_4^u = 0$ Å, $\theta_5^u = 0$ Å, and $\theta_6^u = 3.4$ Å; DNA chains subject to the following global constraints: ν_l^{o}, unrestrained chain ends; ν_l^{eq}, ends restrained to equilibrium length; ν_l^{str}, chain ends stretched by 5%.

[b] Ratio of torsional constants $R = C^{str}/C^{o}$ of stretched chains compared to the corresponding DNA molecules with unrestrained ends. Torsional constants estimated from the lowest torsional frequency, that is, $C = (2L\nu_n^t)^2 I_M/n^2$, where I_M is the moment of inertia per unit length around the twisting axis [41].

[c] Chain with independent parameters.

indicative of an increase in the twisting constant. (The global twisting rigidity is proportional to the square of the normal-mode twisting frequency.)

The frequency of the dominant global twisting mode of a series of 100-bp DNA homopolymers with different local conformational properties and global constraints on chain ends is listed in Table 10.1. The reference molecule is assigned the intrinsic step parameters and elastic constants of an ideal naturally straight duplex. In other chains, the base-pair step parameters are assumed to be correlated. All pairs of correlations, for which, $\langle \Delta\theta_i \Delta\theta_j \rangle = \langle \Delta\theta_j \Delta\theta_i \rangle \neq 0$, are considered, one at a time, as well as selected combinations of two or three pairs of conformational correlations.

The normal-mode twisting frequencies ν_l^o, which are obtained from calculations without restraint on the end-to-end distance, are compared in Table 10.1 with the frequencies ν_l^{eq} of chain ends restrained to their full equilibrium extension and the frequencies ν_l^{str} of chains that are stretched 5% beyond the end-to-end length of the equilibrium structure. The spring constant k of the energy term (Equation [10.7]) used to restrain chain ends is equated to $k_B T/\langle \Delta \text{Rise}^2 \rangle$. That is, the restraint energy placed on chain ends is comparable to the interaction associated with the deformation of Rise at a single base-pair step.

According to the tabulated data, the largest change in twisting frequency due to the end-to-end restraint occurs when Twist–Rise conformational correlations are considered in the potential energy function (5th column). Smaller changes in frequency accompany the incorporation of Roll–Twist or Twist–Slide interactions in the slightly overstretched chains (6th column). The normal-mode frequency increases much more if two or three parameters are coupled. The combination of Roll–Twist and Twist–Slide is striking, because each of the correlations alone does not change the frequency very much, yet when combined, the increase of frequency is fairly large. When the Twist–Rise correlation is included with this combination, the frequency is especially large (last entry in Table 10.1). The computed increase in the elastic constant under these conditions is equivalent to that observed in recent physical studies of single, fully extended DNA molecules [55].

10.7 Summary

The DNA discussed in this review is comparable in length to the loops that are formed by various regulatory proteins and enzymes that bind in tandem to sequentially distant parts of the long chain molecule [1, 2]. The influence of intrinsic structure, such as, natural curvature vs. ideal extension, on the global motions of the molecules presented here thus provides insight into how DNA loops of several hundred base pairs might respond to changes in nucleotide sequence and environmentally induced superhelical stress. The sequence of base pairs determines the degree of intrinsic curvature, local deformability, and other conformational properties of the double helical molecule [60–62]. Changes in chemical environment perturb the equilibrium rest state [27–29] and effect transformations of the *B*-DNA duplex to alternate helical forms [63].

Here we show that covalently closed DNA duplexes with natural curvature are torsionally stiffer than minicircles, which are made up of naturally straight DNA (Figure 10.2). While naturally straight DNA rotates freely about its global helical axis, there is a barrier impeding large-scale helical twisting of curved DNA. Even a short, naturally curved insert locks the rotational setting of a covalently closed molecule, which is otherwise naturally straight (Figure 10.5). Segments that lie on the outer face of the circularized structure are accessible to DNA cutting enzymes but those on the inside are

hidden. Cyclic DNA molecules with base-pair deformability appropriately phased with the double helical repeat also restrict "free" torsional motions (Figure 10.7). Even a naturally straight, linear chain will bend in a preferred direction if intrinsically flexible and stiff dimer steps are spaced at half-turn increments, that is, ~5 bp apart, on opposite sides of the double helix (Figure 10.6).

The degree of intrinsic curvature also governs global bending. Closed DNA molecules that are strongly bent show a natural tendency to fluctuate out of the plane and chains made of naturally straight DNA deform more easily in the plane of a circle (Figure 10.4). The barrier opposing global bending of the natural minicircle lowers significantly when the molecule is over- or undertwisted (Figure 10.8). The frequency, or, energy, of global bending decreases in value upon supercoiling, and if the imposed stress is sufficiently large, global configurational rearrangements take place.

At the polymeric level, the local conformational features included in the dimeric DNA model bring structural insights not possible with conventional elastic treatments. The calculations reported here show how the natural coupling of local conformational variables affects the global motions of DNA. The synchronous variation of Twist and Rise increases the global twisting constant substantially, providing a structural perspective on the micromanipulation of individual molecules (Table 10.1). Successful correspondence of the computed stretching modulus with experimental data requires that the DNA base pairs be inclined with respect to the direction of stretching or reoriented upon forced extension (Figure 10.3). Chain extension is thereby effected by low energy transverse motions, which vary the overlap but preserve the strong van der Waals' stacking of neighboring base-pair planes. The computed stretching constant significantly exceeds observed values if the DNA is pulled in a direction perpendicular to the base-pair planes.

Acknowledgments

Support of this work through U.S.P.H.S. grant GM34809 and the New Jersey Commission on Science and Technology (Center for Biomolecular Applications of Nanoscale Structures) is gratefully acknowledged. Computations were carried out at the Rutgers University Center for Computational Chemistry.

References

1. Adhya, S., Multipartite genetic control elements: communication by DNA loop, *Annu. Rev. Genet.*, 23, 227, 1989.
2. Schleif, R., DNA looping, *Annu. Rev. Biochem.*, 61, 199, 1992.

3. Dillon, N., Trimborn, T., Strouboulis, J., Fraser, P., and Grosveld, F., The effect of distance on long-range chromatin interactions, *Mol. Cell*, 1, 131, 1997.
4. Bazett-Jones, D.P., Côté, J., Landel, C.C., Peterson, C.L., and Workman, J.L., The SWI/SNF complex creates loop domains in DNA and polynucleosome arrays and can disrupt DNA–histone contacts within these domains, *Mol. Cell. Biol.*, 19, 1470, 1999.
5. Ringrose, L., Chabanis, S., Angrand, P.-O., Woodroofe, C., and Stewart, A.F., Quantitative comparison of DNA looping *in vitro* and *in vivo*: chromatin increases effective DNA flexibility at short distances, *EMBO J.*, 18, 6630, 1999.
6. Laundon, C.H. and Griffith, J.D., Curved helix segments can uniquely orient the topology of supertwisted DNA, *Cell*, 52, 545, 1988.
7. Yang, Y., Westcott, T.P., Pedersen, S.C., Tobias, I., and Olson, W.K., The effect of sequence-directed bending on DNA supercoiling, *Trends Biochem. Sci.*, 20, 313, 1995.
8. Chirico, G. and Langowski, J., Brownian dynamics simulations of supercoiled DNA with bent sequences, *Biophys. J.*, 71, 955, 1996.
9. Lavigne, M., Kolb, A., Yeramian, E., and Buc, H., CRP fixes the rotational orientation of covalently closed DNA molecules, *EMBO J.*, 13, 4983, 1994.
10. Zhou, H.J., Zhang, Y., OuYang, Z.C., Lindsay, S.M., Feng, X.Z., Balagurumoorthy, P., and Harrington, R.E., Conformation and rigidity of DNA microcircles containing *waf1* response element for p53 regulatory protein, *J. Mol. Biol.*, 306, 227, 2001.
11. Matsumoto, A. and Olson, W.K., Sequence-dependent motions of DNA: a normal mode analysis at the base-pair level, *Biophys. J.*, 83, 22, 2002.
12. Matsumoto, A., Tobias, I., and Olson, W.K., Normal mode analysis of circular DNA at the base-pair level. 1. Comparison of computed motions with the predicted behavior of an ideal elastic rod, *J. Chem. Theor. Comp.*, 1, 117, 2005.
13. Matsumoto, A., Tobias, I. and Olson, W.K., Normal mode analysis of circular DNA at the base-pair level. 2. Large-scale configurational transformation of a naturally curved molecule, *J. Chem. Theor. Comp.*, 1, 130, 2005.
14. Olson, W.K., Gorin, A.A., Lu, X.-J., Hock, L.M., and Zhurkin, V.B., DNA sequence-dependent deformability deduced from protein–DNA crystal complexes, *Proc. Natl Acad. Sci., USA*, 95, 11163, 1998.
15. Noguti, T. and Gō, N., Dynamics of native globular proteins in terms of dihedral angles, *J. Phys. Soc. Jpn.*, 52, 3283, 1983.
16. Braun, W., Yoshioki, S., and Gō, N., Formulation of static and dynamic conformational energy analysis of biopolymer systems consisting of two or more molecules, *J. Phys. Soc. Jpn.*, 53, 3269, 1984.
17. Higo, J., Seno, Y., and Gō, N., Formulation of static and dynamic conformational energy analysis of biopolymer systems consisting of two or more molecules — avoiding a singularity in the previous method, *J. Phys. Soc. Jpn.*, 54, 4053, 1985.
18. Levitt, M., Sander, C., and Stern, P.S., Protein normal-mode dynamics: trypsin inhibitor, crambin, ribonuclease, and lysozyme, *J. Mol. Biol.*, 181, 423, 1985.
19. Tidor, B., Irikura, K.K., Brooks, B.R., and Karplus, M., Dynamics of DNA oligomers, *J. Biomol. Struct. Dynam.*, 1, 231, 1983.
20. Garcia, A.E. and Soumpasis, D.M., Harmonic vibrations and thermodynamic stability of a DNA oligomer in monovalent salt solution, *Proc. Natl Acad. Sci. USA*, 86, 3160, 1989.

21. Ha Duong, T. and Zakrzewska, K., Calculation and analysis of low frequency normal modes for DNA, *J. Comp. Chem.*, 18, 796, 1997.
22. Lin, D., Matsumoto, A., and Gō, N., Normal mode analysis of a double-stranded DNA dodecamer d(CGCGAATTCGCG), *J. Chem. Phys.*, 107, 3684, 1997.
23. Matsumoto, A. and Gō, N., Dynamic properties of double-stranded DNA by normal mode analysis, *J. Chem. Phys.*, 110, 11070, 1999.
24. Diekmann, S., Dickerson, R.E., Bansal, M., Calladine, C.R., Hunter, W.N., Kennard, O., Lavery, R., Nelson, H.C.M., Olson, W.K., Saenger, W., Shakked, Z., Sklenar, H., Soumpasis, D.M., Tung, C.-S., von Kitzing, E., Wang, A.H.-J., and Zhurkin, V.B., Definitions and nomenclature of nucleic acid structure parameters, *J. Mol. Biol.*, 205, 787, 1989.
25. El Hassan, M.A. and Calladine, C.R., The assessment of the geometry of dinucleotide steps in double-helical DNA: a new local calculation scheme, *J. Mol. Biol.*, 251, 648, 1995.
26. Chandrasekaran, R. and Arnott, S., The structures of DNA and RNA helices in oriented fibers, in *Landolt-Börnstein Numerical Data and Functional Relationships in Science and Technology, Group VII/1b, Nucleic Acids*, Saenger, W., ed., Springer-Verlag, Berlin, 1989, p. 31.
27. Wang, J.C., Variation of the average rotation angle of the DNA helix and the superhelical turns of closed cyclic lambda DNA, *J. Mol. Biol.*, 43, 25, 1969.
28. Depew, R.E. and Wang, J.C., Conformational fluctuations of DNA helix, *Proc. Natl Acad. Sci. USA*, 72, 4275, 1975.
29. Anderson, P. and Bauer, W., Supercoiling in closed circular DNA: dependence upon ion type and concentration, *Biochemistry*, 17, 594, 1978.
30. Olson, W.K., Marky, N.L., Jernigan, R.L., and Zhurkin, V.B., Influence of fluctuations on DNA curvature. A comparison of flexible and static wedge models of intrinsically bent DNA, *J. Mol. Biol.*, 232, 530, 1993.
31. Shore, D. and Baldwin, R.L., Energetics of DNA twisting. I. Relation between twist and cyclization probability, *J. Mol. Biol.*, 170, 957, 1983.
32. Horowitz, D.S. and Wang, J.C., Torsional rigidity of DNA and length dependence of the free energy of DNA supercoiling, *J. Mol. Biol.*, 173, 75, 1984.
33. Frank-Kamenetskii, M.D., Lukashin, A.V., Anshelevich, V.V., and Vologodskii, A.V., Torsional and bending rigidity of the double helix from data on small DNA rings, *J. Biomol. Struct. Dynam.*, 2, 1005, 1985.
34. Coleman, B.D., Lembo, M., and Tobias, I., A new class of flexure-free torsional vibrations of annular rods, *Meccanica*, 31, 565, 1996.
35. Tobias, I., A theory of thermal fluctuations in DNA miniplasmids, *Biophys. J.*, 74, 2545, 1998.
36. Eckart, C., Some studies concerning rotating axes and polyatomic molecules, *Phys. Rev.*, 47, 552, 1935.
37. McLachlan, A.D., Least squares fitting of two structures, *J. Mol. Biol.*, 128, 74, 1979.
38. Tobias, I. and Olson, W.K., The effect of intrinsic curvature on supercoiling — predictions of elasticity theory, *Biopolymers*, 33, 639, 1993.
39. Dubochet, H., Bednar, J., Furrer, P., Stasiak, A.Z., and Stasiak, A., Determination of the DNA helical repeat by cryo-electron microscopy, *Struct. Biol.*, 1, 361, 1994.
40. Tobias, I., Thermal fluctuations of small rings of intrinsically helical DNA treated like an elastic rod, *Philos. Trans. R. Soc.* 362, 1387, 2004.
41. Strutt (Baron Rayleigh), J.W., *Theory of Sound*, Dover Publications, London, 1945, Chap. 7.

42. Smith, S.B., Cui, Y., and Bustamante, C., Overstretching B-DNA: the elastic response of individual double-stranded and single-stranded DNA molecules, *Science*, 271, 795, 1996.
43. Baumann, C.G., Smith, S.B., Bloomfield, V.A., and Bustamante, C., Ionic effects on the elasticity of single DNA molecules, *Proc. Natl Acad. Sci. USA*, 94, 6185, 1997.
44. Wang, M., Yin, H., Landick, R., Gelles, J., and Block, S.M., Stretching DNA with optical tweezers, *Biophys. J.*, 72, 1335, 1997.
45. Bouchiat, C. and Mezard, M., Elasticity model of a supercoiled DNA molecule, *Phys. Rev. Lett.*, 80, 1556, 1998.
46. Kosikov, K.M., Gorin, A.A., Zhurkin, V.B., and Olson, W.K., DNA stretching and compression: large-scale simulations of double helical structures, *J. Mol. Biol.*, 289, 1301, 1999.
47. Cloutier, T.E. and Widom, J., Spontaneous sharp bending of double-stranded DNA., *Mol. Cell.*, 14, 355, 2004.
48. Suck, D. and Oefner, C., Structure of DNase I at 2.0 Å resolution suggests a mechanism for binding to and cutting DNA, *Nature*, 321, 620, 1986.
49. Lahm, A. and Suck, D., DNase I-induced DNA conformation. 2 Å structure of a DNase I-octamer complex, *J. Mol. Biol.*, 221, 645, 1991.
50. Calladine, C.R., Collis, C.M., Drew, H.R., and Mott, M.R., A study of electrophoretic mobility of DNA in agarose and polyacrylamide gels, *J. Mol. Biol.*, 221, 981, 1991.
51. Brukner, I., Sanchez, R., Suck, D., and Pongor, S., Trinucleotide models for DNA bending propensity: comparison of models based on DNaseI digestion and nucleosome packaging data, *J. Biomol. Struct. Dynam.*, 13, 309, 1995.
52. Le Bret, M., Catastrophic variation of twist and writhing of circular DNAs with constraint, *Biopolymers*, 18, 1709, 1979.
53. Gorin, A.A., Zhurkin, V.B., and Olson, W.K., B-DNA twisting correlates with base pair morphology, *J. Mol. Biol.*, 247, 34, 1995.
54. Bauer, W.R., Structure and reactions of closed duplex DNA, *Annu. Rev. Biophys. Bioeng.*, 7, 287, 1978.
55. Bryant, Z., Stone, M.D., Gore, J., Smith, S.B., Cozzarelli, N.R., and Bustamante, C., Structural transitions and elasticity from torque measurements on DNA, *Nature*, 424, 338, 2003.
56. Barkley, M.D. and Zimm, B.H., Theory of twisting and bending of chain macromolecules; analysis of the fluorescence depolarization of DNA, *J. Chem. Phys.*, 70, 2991, 1979.
57. Thomas, J.C., Allison, S.A., Apellof, C.J., and Schurr, J.M., Torsion dynamics and depolarization of fluorescence of linear macromolecules. II. Fluorescence polarization anisotropy measurements on a clean viral ϕ29 DNA, *Biophys. Chem.*, 12, 177, 1980.
58. Hurley, I., Osei-Gyimah, P., Archer, S., Scholes, C.P., and Lerman, L.S., Torsional motion and elasticity of the deoxyribonucleic acid double helix and its nucleosomal complexes, *Biochemistry*, 21, 4999, 1982.
59. Millar, D.P., Robbins, R.J., and Zewail, A.H., Torsion and bending of nucleic acids studied by subnanosecond time-resolved fluorescence depolarization of intercalated dyes, *J. Chem. Phys.*, 76, 2080, 1982.
60. Trifonov, E.N., DNA in profile, *Trends Biochem. Sci.*, 16, 467, 1991.
61. Crothers, D.M., Drak, J., Kahn, J.D., and Levene, S.D., DNA bending, flexibility, and helical repeat by cyclization kinetics, *Meth. Enzymol.*, 212, 3, 1992.

62. Hagerman, P.J., Straightening out the bends in curved DNA, *Biochim. Biophys. Acta*, 1131, 125, 1992.
63. Ivanov, V.I., Minchenkova, L.E., Minyat, E.E., and Schyolkina, A.K., Cooperative transitions in DNA with no separation of strands, *Cold Spring Harbor Symposium, Quant. Biol.*, 47, 243, 1983.
64. Kraulis, P.J., MolScript: a program to produce both detailed and schematic plots of protein structures, *J. Appl. Cryst.*, 24, 946, 1991.

11

Symmetry in Normal Mode Analysis of Icosahedral Viruses

Herman W.T. van Vlijmen

CONTENTS

11.1 Introduction

In the past 20 years, many atomic structures of icosahedral viruses have become available. The VIPER database [1] currently lists 74 x-ray structures and 11 cryo-electron microscopy (cryo-EM) structures, corresponding to 65 different virus types and additional strain variations. In most structures only the virus protein capsid is present, whereas the RNA (or DNA) that is encapsulated by the capsid is not resolved. The icosahedral virus capsid consists of 60 or more identical subunits, called protomers, which in turn are made up of a number of identical or nonidentical proteins often called viral proteins (VPs).

Computational analyses of virus capsid structures have included molecular dynamics (MD) calculations to study the binding of small molecules [2, 3],

Poisson–Boltzmann calculations to study the structural basis of pH sensitivity [4], and normal mode (NM) calculations to study swelling pathways [5]. Because of the large size of these viruses all these calculations were simplified to reduce the complexity. The first MD studies were restricted to fully symmetric motions in which only one protomer is simulated and neighboring protomers are copies generated by icosahedral symmetry operations [2]. A different series of MD studies by Post and coworkers focused on a small molecule ligand binding site in rhinovirus in which only residues in a spherical region around the binding site were allowed to move [3,6–8]. The study of the pH-dependent stability of foot-and-mouth disease virus was reduced in complexity by calculating the electrostatic interactions between two protomers only [4]. Two NM studies on icosahedral viruses have been published, both of which included a full virus capsid. These, otherwise extremely large calculations, were greatly simplified by allowing the individual VPs to move as rigid bodies only [5], or by allowing symmetric motions only [9].

All these simplifications significantly limit the relevance of the results with respect to the full virus capsid. To allow only fully symmetric motions [2, 9] the virus only explores a small fraction $\left(\frac{1}{60}\text{th}\right)$ of its available phase space, as the motion of a single protomer determines the motion of the complete system in this approach. Focusing on a small flexible region around a binding site within a large fixed structure [3] allows the simulation of local effects, but if the property to be studied involves larger scale motions, the results are not representative of the full virus. To use the interaction between two protomers as a model for all interprotomer interactions in the system, [4] ignores potentially significant multibody effects.

The previously published NM studies on icosahedral viruses analyzed conformational changes of cowpea chlorotic mottle virus (CCMV) [5] and bacteriophage HK97 [9], respectively. For CCMV, the x-ray structure of the native form was used to calculate NMs of the virus. The NMs were compared to the cryo-EM structure of the swollen form of CCMV to propose potential pathways of virus swelling. The HK97 study calculated the symmetric NMs of a simplified atomic representation to predict a pathway of virus maturation. As mentioned earlier, both NM studies required significant simplifications to enable the calculations to be done with currently available computer power. The motions allowed in the CCMV study were rigid body motions of the individual VPs, resulting in dynamics analogous to tectonic plate motions. It is likely that internal flexibility of the VPs plays a significant role in large-scale motions of the system, and thus it would be desirable to be able to include more of the natural degrees of freedom in a NM calculation. The HK97 study only included fully symmetric motions, which constitute less than 2% of the motions of the system, and a full treatment of all motions would be a more complete representation of the dynamics of the system.

The symmetry of icosahedral viruses enables a great simplification of the NM calculation without any loss of accuracy. The approach uses the fact that the matrix of second derivatives of the potential energy (the Hessian) of a symmetric system is inherently symmetric [10]. By using methods developed

in group theory the Hessian is expressed in "symmetry coordinates," which results in the Hessian becoming block-diagonal.

Because of this transformation, the size of the Hessian to be diagonalized is reduced from $60N \times 60N$ (where N is the number of degrees of freedom per protomer) to five blocks of sizes $5N \times 5N$, $4N \times 4N$, $3N \times 3N$, $2N \times 2N$, and $N \times N$, respectively. Since the memory use of a NM calculation scales as N^2 and CPU time scales approximately as N^3 [11], the symmetry method enables a large increase in N without sacrificing any accuracy. The approach is completely general and any protomer basis set can be used as long as it can be expressed in Cartesian coordinate displacements. These include, for instance, the C_α-only basis set used in the elastic network model [12, 13], the rigid block basis sets of the rotation–translation block (RTB) model [14], and internal coordinate basis sets such as a dihedral basis set.

The symmetry coordinate method has been applied to systems with circular symmetry such as the gramicidin channel dimer [15] and the tobacco mosaic virus protein disk (17-mer) [16]. For systems with icosahedral symmetry the method has been applied to buckminsterfullerene [17, 18], as a proof of concept to an artificial $(\text{Dialanine})_{60}$ system [19], and recently to icosahedral virus capsids [20, 21].

Here we describe the results of the NM calculations of the $(\text{Dialanine})_{60}$ system and several icosahedral virus capsids. The $(\text{Dialanine})_{60}$ system is a useful proof of concept calculation since it contains all types of intra- and intermolecular forces that are present in much larger icosahedral viruses, and because it allows a direct comparison between a full regular NM calculation and a calculation using symmetry coordinates. The calculations of icosahedral virus capsids focus on general NM properties such as frequency spectra, calculated fluctuations, and displacements of individual NMs. The symmetry method has great potential in the study of dynamic icosahedral virus properties such as large-scale conformational changes associated with cell entry, reversible swelling, or viral maturation. Another application is the study of the stabilizing effects of small molecule binding to the capsid conformation, which is thought to be entropic in nature [8, 22]. In addition, it has recently been shown that NMs can be used to improve the accuracy of cryo-EM structures of icosahedral viruses [23].

11.2 Methods

11.2.1 Theory

The computationally most expensive step in a NM calculation of a large system is the diagonalization of **F**, the mass-weighted Hessian matrix of second derivatives of the potential energy [11]. Since **F** grows quadratically with the size of the molecule, NM calculations on large systems are often prohibitive because of memory and CPU time requirements. For systems

with internal symmetry, group theoretical methods allow a simplification of the form of **F**, resulting in a block-diagonal form **S** that is much easier to diagonalize [10]. Detailed reviews of the group theoretical methods have been published elsewhere [16, 19, 21, 24]. The key step in the simplification of **F** is a change from a Cartesian basis to a symmetry coordinate basis, which is done by the following matrix operations:

$$\mathbf{S} = {}^{\mathrm{t}}\mathbf{\Phi}\mathbf{F}\mathbf{\Phi} \tag{11.1}$$

where t denotes transposition and $\mathbf{\Phi}$ is the matrix of orthonormal symmetry coordinates $\phi^k_{p,s}$ that are defined by the type of symmetry of the system. The $\phi^k_{p,s}$ coordinates are obtained by application of projection operators $\hat{P}^p_{ss}$ to an arbitrary function $\mathbf{U}_k$ of the coordinates of the symmetric system. The projection operators are defined as

$$\hat{P}^p_{st} = \sum_{g \in G} \tau^{p*}_{st}(g)\boldsymbol{T}(g), \quad s,t = 1, s_p \tag{11.2}$$

where $\tau^{p*}_{st}(g)$ is the complex conjugate of the sth row and tth column of the matrix $\boldsymbol{\tau}^p(g)$, which is defined by the irreducible representation (irrep) p of the symmetry group G containing p_G irreps. Matrices $\boldsymbol{\tau}^p(g)$ with dimensions $s_p \times s_p$ for the icosahedral group were described previously [17]. $\boldsymbol{T}(g)$ are the rotation matrices of all (n_G) symmetry operations g of G, which are the regular Cartesian rotation matrices if the function $\mathbf{U}_k$ is expressed in a Cartesian basis. There are 60 rotation matrices for the icosahedral group. Let $\{\mathbf{u}_k; k = 1, N\}$ be an orthonormal basis of subunit 1, for example, a full Cartesian basis where N equals three times the number of atoms. Alternatively, $\mathbf{u}_k$ can be a reduced basis set, where component i of each $\mathbf{u}_k$ vector corresponds to the coefficient of the ith degree of freedom of the full Cartesian basis. We define N functions of the symmetric multimer $\{\mathbf{U}_k; k = 1, N\}$, where $\mathbf{U}_k = (\mathbf{u}_k, \mathbf{0}, \ldots, \mathbf{0})$. Every $\mathbf{U}_k$ vector is 60 times the length of a $\mathbf{u}_k$ vector. When the diagonal projection operators $\hat{P}^p_{ss}$ are applied to all $\mathbf{U}_k$,

$$\phi^{p,s}_k = \hat{P}^p_{ss}\mathbf{U}_k \quad (k = 1, N) \tag{11.3}$$

we obtain $s_p \times N$ basis functions $\phi^{p,s}_k$ for each irrep of the symmetry group. The total number of basis functions obtained this way is $n_G \times N$ and the transformation is orthogonal.

Using orthogonality properties of the $\boldsymbol{\tau}^p(g)$ matrices the elements of the matrix **S** (Equation [11.1]) are given by [19]

$$\mathbf{S}^{ps,\pi\sigma}_{k,\kappa} = {}^{\mathrm{t}}\boldsymbol{u}_k \left[\frac{n_G}{s_p} \sum_{M=1}^{n_G} \tau^p_{s\sigma}(M)\mathbf{F}_{1M}\boldsymbol{T}(M) \right] \boldsymbol{u}_\kappa \delta_{s\sigma}\delta_{p\pi},$$
$$(k, \kappa = 1, N;\ \ p, \pi = 1, p_G;\ \ s, \sigma = 1, s_p) \tag{11.4}$$

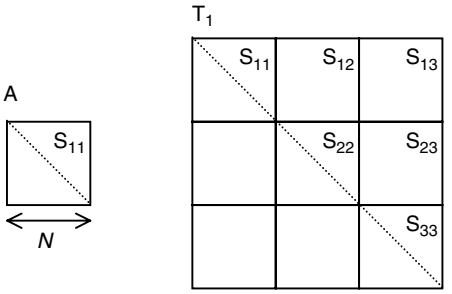

FIGURE 11.1
Diagrammatic representations of the symmetry-based Hessians **S** for irreps A and T_1. The matrices are shown in upper diagonal form since they are symmetric. The entries of the matrices are calculated according to Equation (11.4), which results in the following sums: Irrep A: $\mathbf{S}^{1,1}_{k,\kappa} = {}^{t}\boldsymbol{u}_k\left[(60/1)\sum_{M=1}^{60}\tau^{A}_{11}(M)\mathbf{F}_{1M}\boldsymbol{T}(M)\right]\boldsymbol{u}_\kappa$; Irrep T_1: $\mathbf{S}^{l,\lambda}_{k,\kappa} = {}^{t}\boldsymbol{u}_k\left[(60/3)\sum_{M=1}^{60}\tau^{T_1}_{l\lambda}(M)\mathbf{F}_{1M}\boldsymbol{T}(M)\right]\boldsymbol{u}_\kappa$, where the indices l and λ correspond to the S subscripts in the diagram.

where $\mathbf{F}_{1M}$ is the block of the full mass-weighted Hessian **F** corresponding to the interaction of subunit 1 with subunit M, the indices k and κ sum over all N degrees of freedom, p and π sum over all irreps, s and σ sum over all entries in the matrices $\tau^p(g)$, and δ is the Kronecker delta.

Thus far, the method is general for any point symmetry group. The degree of reduction in complexity in going from matrix **F** to **S** depends on the symmetry of the system. For systems with z-fold circular symmetry and N degrees of freedom per subunit, the Hessian transforms from a $(z \times N)^2$ sized matrix to a block-diagonal matrix containing one matrix of size $(N)^2$ and $(z-1)/2$ matrices of size $(2N)^2$ for odd numbers of z, and two matrices of size $(N)^2$, and $(z-2)/2$ matrices of size $(2N)^2$ for even numbers of z.

Systems with icosahedral symmetry transform from a $(60N)^2$-sized matrix to a block-diagonal matrix containing one matrix of size $(N)^2$, two of size $(3N)^2$, one of size $(4N)^2$, and one of size $(5N)^2$, which can all be diagonalized separately. These matrices correspond to the irreps A, T_1/T_2, G, and H, of the icosahedral symmetry group. The largest matrix that needs to be diagonalized is 12 times smaller in linear dimension, resulting in an approximate diagonalization speedup of 12^3 = 1,723-fold. Figure 11.1 shows diagrams of the transformed Hessians for the A and T_1 irreps.

The A irrep represents fully symmetric motions, and all other irreps correspond to asymmetric motions that are degenerate. For instance, for every NM contained in the T_1 irrep (3-fold degeneracy) there are two additional modes with identical frequency and identical displacements that are rotated with respect to the first NM. The T_2, G, and H irreps have 3-, 4-, and 5-fold degeneracies, respectively. The number of modes represented by the symmetric A irrep form only a small fraction ($\frac{1}{60} = 1.7\%$) of the complete NM spectrum of the icosahedral system.

After diagonalization, the Cartesian displacements of the NMs can be reconstructed, which allows the calculation of NM fluctuations, cross-correlations,

and trajectories. The Cartesian atomic displacement vectors y_i^j of subunit j due to symmetry mode i of irrep A are given by

$$y_i^j = \tau_{11}^A(g_j)\boldsymbol{T}(g_j)\sum_{k=1}^{N}\boldsymbol{u}_k z_{i,k}^A \tag{11.5}$$

where g_j is the rotation corresponding to subunit j, $\mathbf{u}_k$ $(k = 1, N)$ is the orthonormal basis set of subunit 1, and $z_{i,k}^A$ is the kth entry of symmetry mode i of irrep A. For the other irreps the expression for the Cartesian displacement y_i^j is more complex, due to the form of the corresponding block in the transformed Hessian **F** (Figure 11.1). For instance, the expression for the T_1 irrep is

$$\begin{aligned} y_i^j = {} & \tau_{11}^{T_1}(g_j)\boldsymbol{T}(g_j)\sum_{k=1}^{N}\boldsymbol{u}_k z_{i,k}^{T_1} + \tau_{12}^{T_1}(g_j)\boldsymbol{T}(g_j)\sum_{k=1}^{N}\boldsymbol{u}_k z_{i,(N+k)}^{T_1} \\ & + \tau_{13}^{T_1}(g_j)\boldsymbol{T}(g_j)\sum_{k=1}^{N}\boldsymbol{u}_k z_{i,(2N+k)}^{T_1} \end{aligned} \tag{11.6}$$

The expressions for the T_2, G, and H irreps are analogous and contain 3, 4, and 5 terms, respectively. After obtaining Cartesian displacement, vectors of all NM standard methods can be used to calculate trajectories, atomic fluctuations, and cross-correlations [11].

11.2.2 Calculation Details

The methods to calculate NMs using circular and icosahedral symmetry bases and to obtain fluctuations, cross-correlations, and trajectories, were implemented in the program Chemistry at Harvard Molecular Mechanics (CHARMM) (version 28) [25], which was used to calculate all results presented in this chapter.

An artificial icosahedral system consisting of 60 dialanine subunits (called $[\text{Dialanine}]_{60}$) was constructed to verify the symmetry-based calculations by comparing the results to a full standard diagonalization [19].

The capsid structures of poliovirus (Mahoney strain), rhinovirus 16, and CCMV, were obtained from the protein data bank (PDB) database [26] (PDB entries 1vbd, 1aym, and 1cwp, respectively). All calculations were done using the polar hydrogen PARAM19 parameter set [27] in CHARMM. The virus protomer structures were energy minimized in the presence of nine adjacent protomers, using the IMAGE facility in CHARMM, which places symmetric images of the protomer around itself. During the minimizations and NM calculations we used a distance-dependent dielectric constant of $2r$ (r is the distance between atoms in Å) to account for solvent screening, and a nonbonded cutoff distance of 7.5 Å.

Since a full Cartesian basis set was too large to be handled by the available computer memory, we used a basis set that includes all dihedral angles of the system with the exception of the peptide bonds, which were assumed rigid. In addition, the six vectors representing uniform translations and rotations were added for every chain in the protomer. For example, the poliovirus protomer contains five chains: vp1, vp2, vp3, vp4, and a bound ligand. The total size of the protomer basis set of poliovirus was 3,438, which is significantly smaller than a full Cartesian basis set (24,252). The maximum Hessian to be diagonalized is therefore $(5 \times 3,428)^2$, which uses approximately 1.2 gigabyte (GB) of computer memory. The memory requirement for a full diagonalization with this dihedral basis set would have been $144 \times 1.2 = 172$ Gbytes. For comparison we also used RTB basis sets method with rigid blocks of two residues each (basis set size 2,556), or rigid blocks corresponding to complete protein chains in the protomer (basis set size 30).

Calculations were done on SGI computers with R10000 and R14000 processors. CPU times for the largest system, poliovirus, were approximately 27 h for the A irrep to 43 h for the H irrep. Most of the CPU time is spent in the calculation of the transformed Hessian **S** (Equation [11.1]).

11.3 Results

11.3.1 $(\text{Dialanine})_{60}$

We applied the symmetry method to the artificial $(\text{Dialanine})_{60}$ system to be able to confirm that the obtained results are identical to those obtained from a regular NM calculation [19]. The features that were compared were the NM frequencies, displacements, and fluctuations. Figure 11.2 shows the structure of the minimized $(\text{Dialanine})_{60}$ system. The regular NM calculation of the system took 12 min on an SGI R10000 processor, whereas the symmetry-based calculations were much faster, that is, 0.1 sec for the A irrep, 0.2 sec for T_1 and T_2 irrep, 0.4 sec for G irrep, and 0.5 sec for the H irrep. A comparison of the NM frequencies shows that they are identical up to the fourth decimal place (Table 11.1). Round-off differences between the full matrix calculation and the much smaller symmetry matrices calculations are the cause of the small differences beyond the fourth decimal.

The NM displacements of the A irrep are fully symmetric and nondegenerate, that is, identical for all 60 subunits, and the results from both methods could be easily compared by calculating the vector inner product between the atomic displacements. The displacements were identical up to at least six significant figures (inner product $>0.999\,998$). For the degenerate NMs (all other irreps), the displacements from the NM obtained from the symmetry method should be expressable as a linear combination of the set of modes with identical frequencies from the full calculation. This was confirmed as the total squared inner product of the symmetry method mode with the degenerate

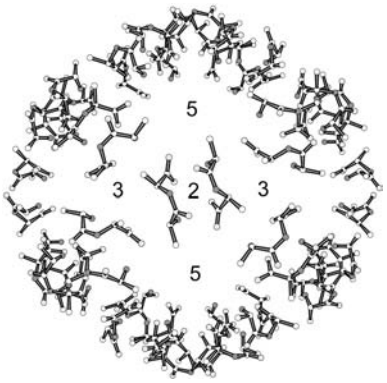

FIGURE 11.2
Symmetrically minimized structure of the $(Dialanine)_{60}$ system. The numbers represent five of the symmetry axes, labeled by their symmetry level. The 10 subunits in the back are omitted for clarity. Hydrogens are not shown.

TABLE 11.1

Comparison of the NM Frequencies (in cm^{-1}) from Full and Symmetry Calculations.

Full	A	T_1	T_2	G	H
8.541 953 (5)					8.541 912
9.030 711 (3)			9.030 643		
9.927 437 (4)				9.927 345	
11.230 868 (5)					11.230 826
12.960 291 (3)			12.960 120		
13.298 421 (4)				13.298 819	
17.217 847 (5)					17.214 828
19.146 540 (5)					19.146 528
20.921 159 (4)				20.921 062	
22.822 960 (1)	22.822 952				

modes from the full calculation added up to exactly one in all cases. As a final check we compared the atomic fluctuations of the system from the full and symmetry-based calculations and found that they were identical. These results therefore confirmed that our implementation was correct and that the results are equivalent.

11.3.2 Poliovirus

The C_α-trace of the minimized structure of poliovirus is shown in Figure 11.3. Minimization of the protomer in the presence of symmetry images resulted in relatively small conformational changes (RMSD C_α atoms 2.3 Å). Most of the difference is due to a uniform shrinkage of the capsid, which has a diameter of about 300 Å (shrinkage of less than 2%). The shrinkage is small on a relative

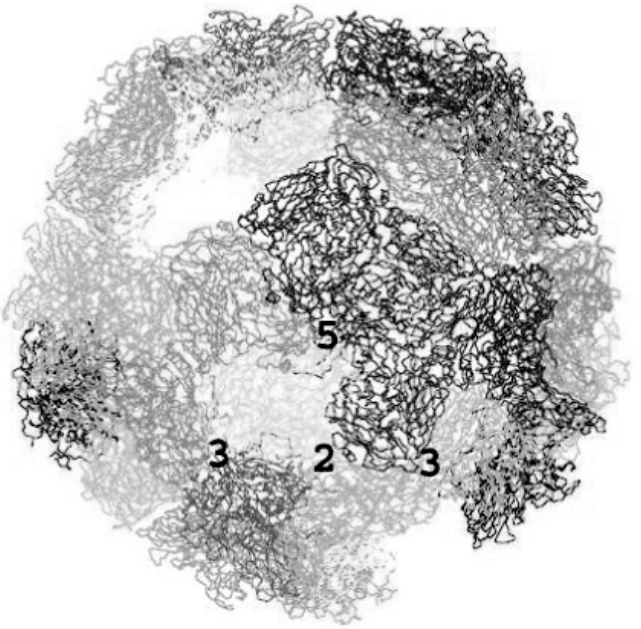

FIGURE 11.3
(See color insert following page 136) Top view of the C_α-trace of the poliovirus capsid, in which protomers are shown in different colors. The locations of a 2-fold, two 3-fold, and a 5-fold symmetry axis are indicated.

scale, but highlights one of the potential drawbacks of NM analysis with a standard molecular mechanics potential energy function. The shrinkage could be caused by approximations of electrostatics, the absence of RNA in the structure, or the fact that minimization corresponds to the annealing of a structure that is basically a hollow shell.

Every protomer of poliovirus contains 8,084 atoms in a polar hydrogen representation, and thus the full capsid contains $60 \times 8,084 = 485,040$ atoms, or 1,455,120 degrees of freedom in a full Cartesian basis set. A standard NM calculation would need over 8 Terabytes (TB) of computer memory to store the Hessian, and the CPU time to complete the calculation would be unacceptably long. The use of the symmetry method with a full Cartesian basis set is still a very large calculation with a maximum Hessian size (corresponding to the H irrep) of more than 58 GB. Although the fully symmetric modes of the A irrep could be calculated with a full Cartesian basis (memory requirement of 2.3 GB), we decided to use various reduced basis sets to describe the flexibility of the virus. The most complete basis set used was the set of all dihedral angles excluding the dihedrals of the peptide bonds, extended with the uniform rotation/translation motions of all separate protein chains and small molecule. This resulted in a protomer basis set size of 3,438 vectors. The second basis set was the RTB basis set using a block size of 2 residues (2,556 vectors). The most simplified basis set included only the uniform rotation/translation

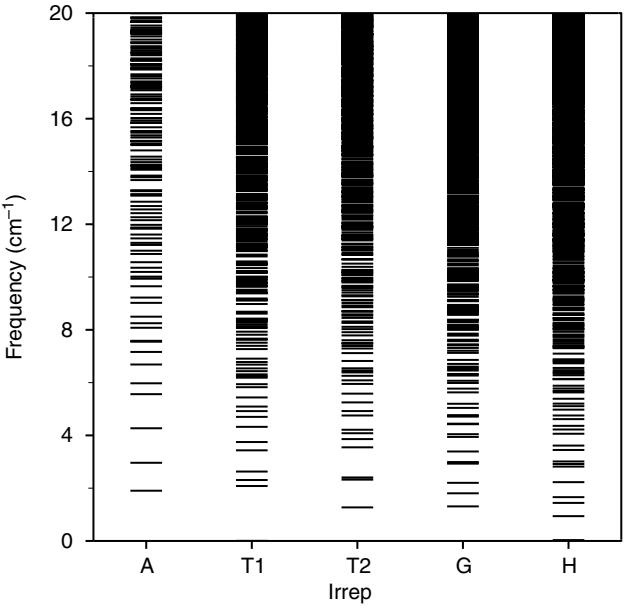

FIGURE 11.4
Frequency spectra of the NMs of poliovirus using a full dihedral basis set. The five columns correspond to the five different irreducible representations of the icosahedral symmetry group.

motions of all separate protein chains (vp1 to vp4) and small molecules (total of 30 vectors). This last basis set corresponds to the basis set used in the previously reported CCMV NM study [5].

As described in Section 11.2, the NMs of the virus capsid are grouped into five irreps: A, T_1, T_2, G, and H. Memory requirements for the different irreps with the dihedral basis set were 47 Megabytes (MB), 425 MB, 756 MB, and 1.2 GB, for the A, T_1/T_2, G, and H irreps, respectively.

Figure 11.4 shows the frequency spectra up to 20 cm^{-1} of the NMs of the different irreps for the full dihedral angle basis set. The H irrep contains the lowest frequency NM with a frequency of 0.94 cm^{-1}, which corresponds to 28.2 GHz and a period of approximately 35 psec. This value is very close to the estimated frequencies for an elastic sphere model of a virus particle with a radius of 150 Å [28, 29]. The lowest fully symmetric mode (A irrep) has a frequency of 2 cm^{-1}. As expected from group theoretical arguments [10], the six uniform translational and rotational motions are present as two near-zero frequencies in the T_1 irrep. Since the T_1 irrep is 3-fold degenerate, these two frequencies correspond to six uniform motions, which is the correct number for three-dimensional nonlinear molecules. The density of the frequency spectrum is increasingly higher for the A, T_1/T_2, G, and H irreps. Because the A, T_{1s}/T_2, G, and H irrep frequencies correspond to 1-, 3-, 4-, and 5-fold degenerate NMs, a comparison of the density of states of the different irreps shows an even larger dominance of the nonsymmetric NMs (Figure 11.5).

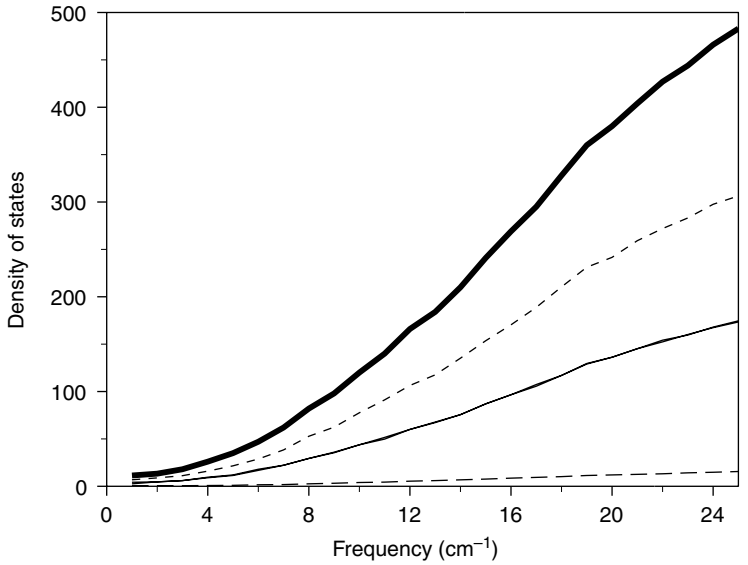

FIGURE 11.5
Density of states calculated from the frequency spectra in Figure 11.4. The density was calculated at every integer frequency and averaged over a window of 5 cm^{-1}. The A, T_1/T_2, G, and H irreps are represented by dashed, solid, short-dashed, and thick lines, respectively.

The overall character of the NMs can be illustrated with displacement vectors attached to their corresponding atoms. Because of the large number of atoms even in a C_α-only representation, we present virus capsids and show the average displacement vectors per vp protein in every protomer. We omitted displacements of the vp4 protein for clarity. It should be noted that although the displacements shown suggest rigid body motions of the individual vp proteins, they are in fact fully flexible. The direction of the motions will be in the opposite direction after half a period of oscillation of the NMs. The first three modes of the A, T_1, T_2, G, and H irreps are illustrated in Figure 11.6. Figure 11.6 shows the displacements of the lowest frequency A irrep NM. The NM is fully symmetric (as are all A irrep modes) and can be described as a uniform radial expansion and contraction motion. This motion is very similar to the spheroidal motion with $l = 0$ in vector spherical harmonics of an elastic sphere [30]. The second A irrep NM is characterized by an in- and outward motion of the structural region around the 5-fold axis also known as the mesa [31] (Figure 11.6). The third A irrep mode consists of corkscrew rotations of pentameric modules around the 5-fold axis without any significant swelling or shrinking of the capsid (Figure 11.6). In the first NM of the T_1 irrep, the mesa are also projected outward significantly, although not simultaneously. Describing the capsid as a sphere with a northern and southern hemisphere the motion consists of alternating expansions and contractions of opposite hemispheres. The second T_1 NM also has alternating expansions and contractions of the hemispheres, but the motions are more

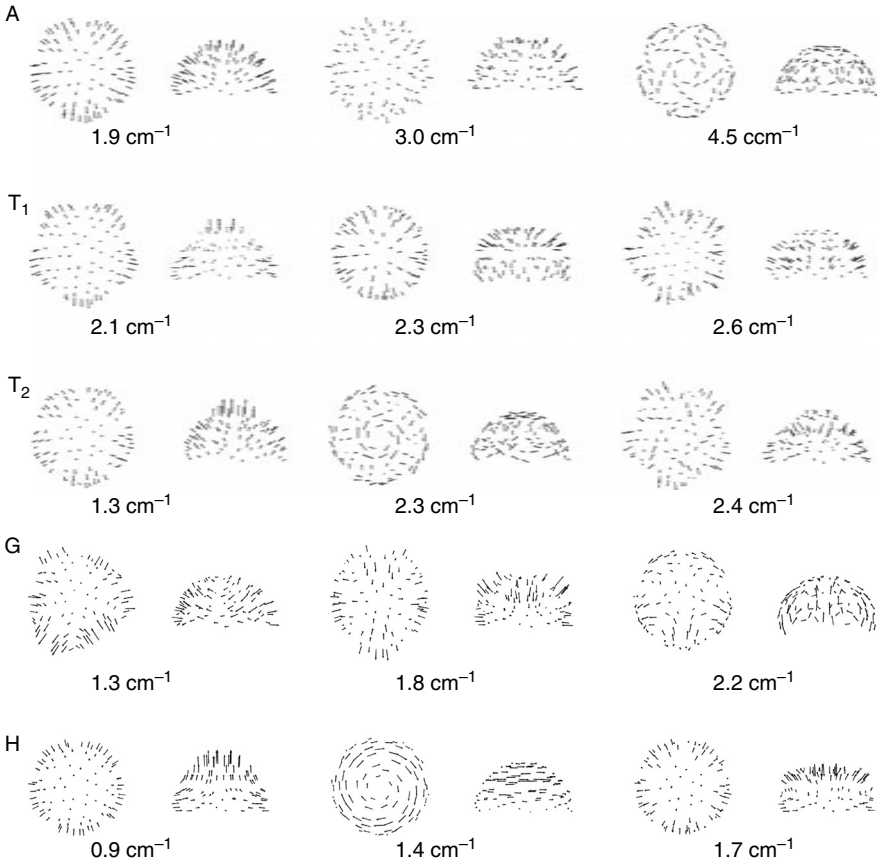

FIGURE 11.6
Top and side views of the first three NM displacements of poliovirus half capsid for all five irreps. The C_α-traces are omitted for clarity. The orientation of the top views is identical to Figure 11.3, and the side views are rotated by 90˚.

uniform. The third T_1 mode has a predominantly toroidal character (motions in plane) in which pentamers are deformed. The first T_2 mode consists of an alternating inward and outward projection of the mesa area around the 5-fold axis on one hemisphere combined with uniform deformation of the capsid (Figure 11.6[g] and Figure 11.7[a]). The second T_2 mode is also a predominantly toroidal mode with three nodes in the latitude direction (including the one at the pole), so that motions in the north and south pole area are in the same direction, and motions around the equator are in opposite direction. This motion corresponds to the third toroidal motion ($l = 3$) in vector spherical harmonics. The third T_2 mode is a complex mode with an outward projection of the mesa. The first G mode consists of an alternating north and south hemisphere motion in which the area around the 2-fold and 3-fold axes is moving outward. The second G mode is complex and contains outward motions of the

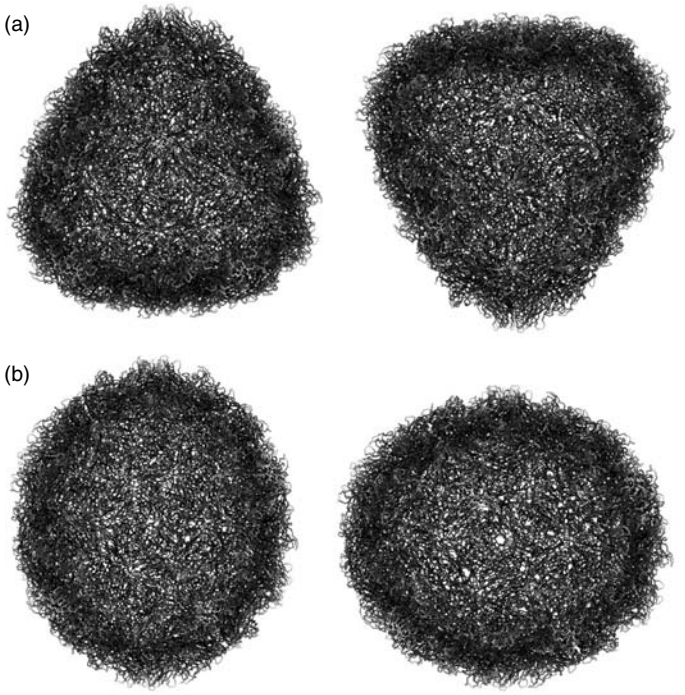

FIGURE 11.7
(a) Shapes of the poliovirus capsid at the two extremes of the first NM of the T_2 irrep. (b) Same as part(a) for the second H irrep NM.

2-fold axes. The third G mode is a complex toroidal mode. The first H mode can be described as a football mode in which the capsid sphere deforms into a football-shaped ellipsoid. This motion also has a direct counterpart in vector spherical harmonics (spheroidal motion with $l = 2$). The second H mode is toroidal and has two nodes in the latitude direction, with the hemispheres moving in opposite directions (toroidal mode with $l = 2$ in vector spherical harmonics). The third H mode projects the mesa simultaneously outward at both poles.

After inspection of the lowest frequency NMs of the different irreps, it appears that some of the motions directly correspond to the individual standing waves that are solutions to the vector spherical harmonics of an elastic sphere. Other motions are clearly influenced by the structural detail of the capsid, for example, the mesa around the 5-fold axis and the canyon that is located around the mesa probably cause many of the low-frequency modes to have significant outward motions of the mesas in which the canyon area functions as a hinge.

We compared the results of the dihedral basis set and we also used two alternative basis sets. The second set was an RTB basis set containing uniform rotation/translation motions of 2-residue blocks, and is smaller (2,556 vectors)

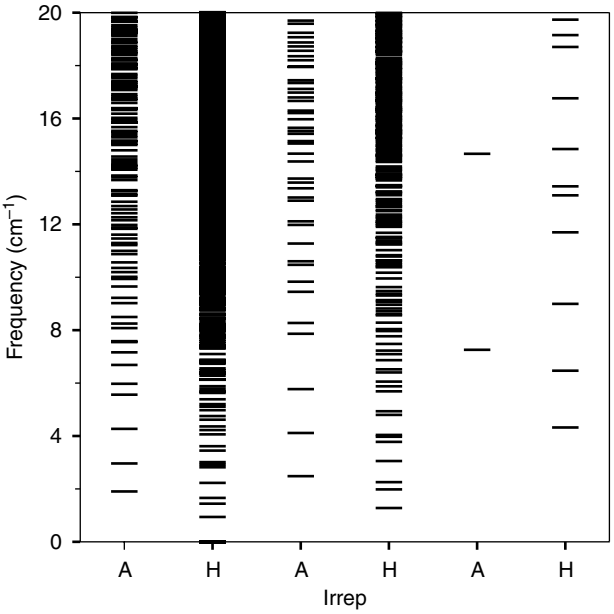

FIGURE 11.8
Frequency spectra of the A and H irrep NMs of poliovirus using three different basis sets. Columns 1 and 2 correspond to the full dihedral basis set also shown in Figure 11.4, columns 3 and 4 correspond to the 2-residue RTB basis set, and columns 5 and 6 to the complete chain RTB basis set.

than the dihedral basis set (3438 vectors). The third basis set that was used had uniform rotation/translation motions for individual chains (vp1, vp2, vp3, vp4, ligand), and contained 30 vectors only. With a basis set of 30 vectors it is possible to do a regular NM calculation without using the symmetry coordinate transformation, and the results would be identical to those obtained here. This approach was used in the NM study of CCMV swelling, where the basis set for the protomer consisted of 18 basis set vectors [5]. The use of the RTB basis sets increased the frequencies of the NMs as a result of the more rigid representation of the system (Figure 11.8). Although the general character of some of the modes such as the uniform breathing mode of the A irrep is also represented in some of the RTB modes, the lack of flexibility significantly affects the details of the motions. When using the third basis set for poliovirus, a protomer of almost 1000 residues is represented by five rigid blocks and therefore any motion that requires flexibility in the protomers themselves will be severely impeded. The effect of using different basis sets on the calculated atomic fluctuations is illustrated in Figure 11.9 for the vp1 protein. The calculated fluctuations are compared to the experimental fluctuations extracted from the crystallographic temperature factors. The results from the dihedral basis set are clearly correlated with the experimental values, although not all fluctuation details are reproduced. The fact that the overall level of

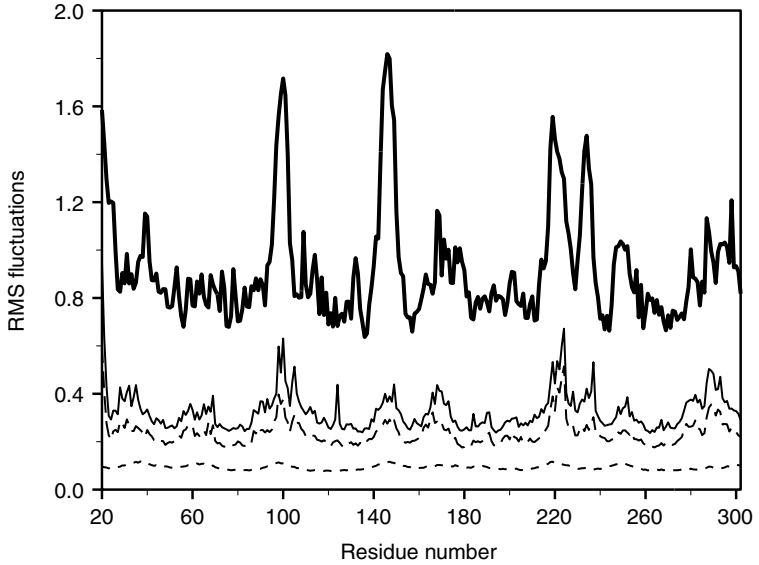

FIGURE 11.9
Residue-averaged fluctuations of poliovirus for vp1. The fluctuations based on crystallographic temperature factors are shown in thick lines, those based on NMs with the full dihedral basis set in thin lines, the RTB basis set with block size of two residues in long-dashed lines, and the RTB basis set with full vp protein block size in short-dashed lines.

fluctuations is lower than that in the experiment is caused by various factors [32]. NM calculation with a full Cartesian basis would result in lower frequencies (and correspondingly larger fluctuations), and bring the NM fluctuations even closer to the experimental values. The fluctuations resulting from the 2-residue RTB basis set are smaller in absolute value but have a pattern similar to the results from the dihedral basis set. In contrast, the fluctuations resulting from the third basis set have few features, and it is clear that many details are lost.

11.3.3 Rhinovirus and CCMV

We also calculated the NMs for rhinovirus 16 and CCMV using dihedral basis sets. The minimizations of the rhinovirus structure resulted in relatively small conformational changes (RMSD C_α atoms 1.8 Å). For CCMV significantly larger changes were seen after minimization (RMSD C_α atoms 6.5 Å). These changes consisted of an overall shrinking of the capsid combined with relatively small loop changes in the A capsid proteins that surround the 5-fold symmetry axis [5]. The capsid structure of CCMV contains larger holes than the structures of poliovirus and rhinovirus, and this may well be the main cause of the shrinking of the CCMV capsid upon energy minimization. Frequency spectra of the NM calculations using dihedral basis

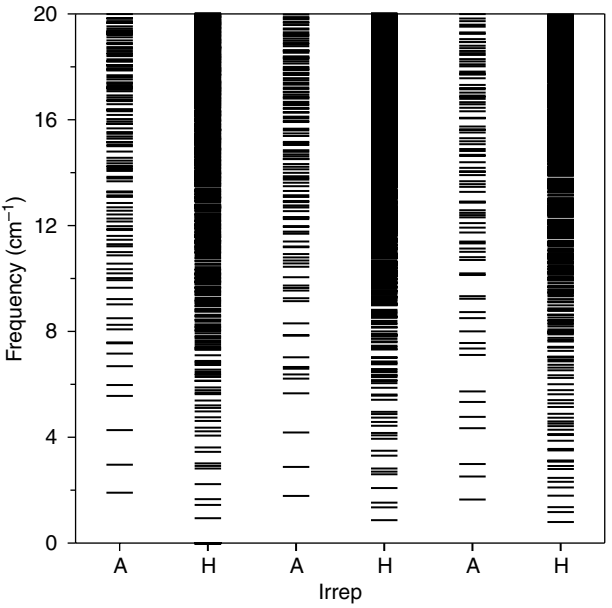

FIGURE 11.10
Comparison of frequency spectra of the A and H irrep NMs of poliovirus (columns 1 and 2), rhinovirus (columns 3 and 4), and CCMV (columns 5 and 6).

sets for irreps A and H of poliovirus, rhinovirus, and CCMV, are shown in Figure 11.10. The density of NM frequencies and lowest calculated frequencies (0.87 cm^{-1} for rhinovirus, 0.80 cm^{-1} for CCMV) are comparable to those obtained for poliovirus. The general character of the displacements of the NMs of rhinovirus and CCMV are also similar to those observed for poliovirus. For the first several NMs of the different irreps the motions correspond to those shown for poliovirus in Figure 11.6. The motions at the residue level or secondary structure element level of the different viruses are still significantly different as the detailed structural features and residue types differ between the viruses.

11.4 Discussion

NM calculations with full dihedral flexibility on icosahedral viruses have been made possible by application of group theory methods. This approach maintains the same level of accuracy as the full calculation but speeds up the calculation more than thousandfold. A $(\text{Dialanine})_{60}$ icosahedral system was used to verify that all NM results were equivalent to a regular NM calculation. In the applications to the viruses we used a full atomic model of the structure and included all dihedral angles except the ones corresponding to the peptide

bonds, which are known to be very rigid. More computer memory will soon allow virus NM calculations with a full Cartesian basis set. The size of the full poliovirus system was 485,040 atoms and the total number of degrees of freedom of the system that were included in the calculation was 205,680 (60 times 3,428). As far as we know, this is the largest NM calculation for a biomolecule reported to date.

Incorporation of full dihedral flexibility in the NM calculation is important for a correct description of the motions in viral capsids. For example, the binding site of small molecules in the capsid is located in the hinge region of the structure. Since a large part of the hinge is located within vp1, any model that represents the vp1 protein as a rigid body would not accurately represent hinge flexibility. In addition, the ability of this method to calculate both symmetric and asymmetric motions allows for a more complete description of the mobility of the system.

The method was implemented in the program CHARMM, which makes it possible to easily use a variety of basis sets and force field parameters. The symmetry method is general and any basis set (full or reduced) can be used as long as the components of the vectors correspond to the coefficients of a full Cartesian basis set (see Section 11.2).

For example, it would be straightforward to use the elastic network model [13]. The elastic network model itself constitutes a large simplification of the system, but it still cannot be used for a virus without the symmetry method due to the large size of the system. The basis set is attractive for use with viruses, since the system does not have to be energy minimized before the NM calculation is done. As described in the results, minimizations of the virus capsids may lead to significant deviations (6.5 Å for CCMV) from the crystal structure and it is not known how this affects the results.

Various experimentally determined properties of virus capsids provide interesting areas of application of NM analysis. These include large scale conformational changes from native to expanded capsids during the process of cell entry [31, 33, 34] or caused by changes in pH [35]. It is likely that the accuracy of fitting atomic structures into cryo-EM density improves as more accurate low-frequency NMs are used in the procedure [23].

NM analysis can also be used to study the structural origins of the ligand-induced conformational changes that occur in poliovirus at sites remote from the ligand binding site [36]. The capsid stabilization of poliovirus and rhinovirus by small molecules has been suggested to result from entropic effects [3, 22]. We can now directly calculate the entropy of icosahedral systems by using the NM frequencies [37], and a comparison of systems with and without bound ligands will provide additional information on the nature of the stabilization effect.

The cryo-EM structure of the swollen CCMV is icosahedrally symmetric, and thus symmetric breathing modes, in particular the first NM of the A irrep, have the largest degree of overlap with this conformational change [5]. Other conformationally altered structures of icosahedral viruses such as those of poliovirus and rhinovirus are also symmetric [31, 33]. However, the fact that

the conformationally altered particle is icosahedrally symmetric does not mean that the pathway from the native conformation is necessarily symmetric. For instance, in the changes associated with cell entry the RNA of the virus exits the capsid, and this occurs most likely through an opening in the capsid [33, 38]. The conformation of the capsid at which the RNA exits is unlikely to be fully symmetric, and thus asymmetric NMs may provide insight into those parts of the capsid that are most likely to open up. Symmetric motions make up less than 2% of the motions of the virus capsid, and it is therefore also more likely that many conformational changes occur through asymmetric states.

Fully flexible all-atom NM analyses of icosahedral viruses have become possible by application of group theory. There also exist many systems with circular symmetry where the application of these methods can significantly reduce the complexity of the NM calculation. The recent increase in structural information of viruses and other symmetric systems from x-ray crystallography and cryo-EM provides a large set of potential applications for NM analysis in the field of large system dynamics.

Acknowledgments

Discussions with Martin Karplus and James Hogle are gratefully acknowledged. I thank Andrej Šali for the use of the ASGL plotting program.

References

1. Reddy, V.S. et al., Virus Particle Explorer (VIPER), a website for virus capsid structures and their computational analyses. *J. Virol.*, 2001, **75**: 11943–11947.
2. Lau, W.F. and B.M. Pettitt, Dynamics of an oxazole compound bound to a common cold virus. *J. Am. Chem. Soc.*, 1989, **111**: 4111–4113.
3. Phelps, D.K. and C.B. Post, Molecular dynamics investigation of the effect of an antiviral compound on human rhinovirus. *Protein Sci.*, 1999, **8**: 2281–2289.
4. van Vlijmen, H.W.T. et al., Titration calculations of foot-and-mouth disease virus capsids and their stabilities as a function of pH. *J. Mol. Biol.*, 1998, **275**: 295–308.
5. Tama, F. and C.L. Brooks, III, The mechanism and pathway of pH induced swelling in cowpea chlorotic mottle virus. *J. Mol. Biol.*, 2002, **318**: 733–747.
6. Phelps, D.K. and C.B. Post, A novel basis of capsid stabilization by antiviral compounds. *J. Mol. Biol.*, 1995, **254**: 544–551.
7. Phelps, D.K., P.J. Rossky, and C.B. Post, Influence of an antiviral compound on the temperature dependence of viral protein flexibility and packing: a molecular dynamics study. *J. Mol. Biol.*, 1998, **276**: 331–337.
8. Phelps, D.K., B. Speelman, and C.B. Post, Theoretical studies of viral capsid proteins. *Curr. Opin. Struct. Biol.*, 2000, **10**: 170–173.
9. Kim, M.K., R.L. Jernigan, and G.S. Chirikjian, An elastic network model of HK97 capsid maturation. *J. Struct. Biol.*, 2003 **143**: 107–117.

10. Wilson, E.B., Jr., J.C. Decius, and P.C. Cross, *Molecular Vibrations. The Theory of Infrared and Raman Vibrational Spectra*. New York: McGraw-Hill, 1955.
11. Brooks, B.R., D. Janežic, and M. Karplus, Harmonic analysis of large systems. I. Methodology. *J. Comput. Chem.*, 1995, **16**: 1522–1542.
12. Tirion, M.M., Large amplitude elastic motions in proteins from a single-parameter, atomic analysis. *Phys. Rev. Lett.*, 1996, **77**: 1905–1908.
13. Bahar, I., A.R. Atilgan, and B. Erman, Direct evaluation of thermal fluctuations in proteins using a single-parameter harmonic potential. *Fold. Des.*, 1997, **2**: 173–181.
14. Durand, P., G. Trinquier, and Y.H. Sanejouand, A new approach for determining low-frequency normal modes in macromolecules. *Biopolymers*, 1994, **34**: 759–771.
15. Roux, B. and M. Karplus, The normal modes of the gramicidin-A dimer channel. *Biophys. J.*, 1988, **53**: 297–309.
16. Simonson, T. and D. Perahia, Normal modes of symmetric protein assemblies. Application to the tobacco mosaic virus protein disk. *Biophys. J.*, 1992, **61**: 410–427.
17. Weeks, D.E. and W.G. Harter, Rotation–vibration spectra of icosahedral molecules. II. Icosahedral symmetry, vibrational eigenfrequencies, and normal modes of buckminsterfullerene. *J. Chem. Phys.*, 1989, **90**: 4744–4771.
18. James, G., The representation theory for buckminsterfullerene. *J. Algebra*, 1994, **167**: 803–820.
19. van Vlijmen, H.W.T. and M. Karplus, Normal mode analysis of large systems with icosahedral symmetry: application to (Dialanine)60 in full and reduced basis set. *J. Chem. Phys.*, 2001, **115**: 691–698.
20. van Vlijmen, H.W.T. and M. Karplus, Normal mode calculations of icosahedral viruses with full dihedral flexibility by use of molecular symmetry. *J. Mol. Biol.*, 2005, **350**: 528–542.
21. van Vlijmen, H.W.T., Ph.D. Thesis, *Structure, Dynamics, and Thermodynamics of Proteins*. Cambridge: Harvard University, 1997.
22. Tsang, S.K. et al., Stabilization of poliovirus by capsid-binding antiviral drugs is due to entropic effects. *J. Mol. Biol.*, 2000, **296**: 335–340.
23. Tama, F., O. Miyashita, and C.L. Brooks, III, Flexible multi-scale fitting of atomic structures into low-resolution electron density maps with elastic network normal mode analysis. *J. Mol. Biol.*, 2004, **337**: 985–999.
24. Lyubarskii, G.Y., *The Application of Group Theory in Physics*. New York: Pergamon Press, 1960.
25. Brooks, B.R. et al., CHARMM: a program for macromolecular energy, minimization, and dynamics calculations. *J. Comput Chem.*, 1983, **4**: 187–217.
26. Berman, H.M. et al., The protein data bank. *Nucleic Acids Res.*, 2000, **28**: 235–242.
27. Neria, E., S. Fischer, and M. Karplus, Simulation of activation free energies in molecular systems. *J. Chem. Phys.*, 1996, **105**: 1902–1921.
28. Ford, L.H., Estimate of the vibrational frequencies of spherical virus particles. *Phys. Rev. E*, 2003, **67**: 051924.
29. Saviot, L. et al., Comment on "Estimate of the vibrational frequencies of spherical virus particles". *Phys. Rev. E*, 2004, **69**: 023901.
30. Arfken, G.B. and H. Weber, *Mathematical Methods for Physicists*, 5th ed. New York: Academic Press, 2000.
31. Belnap, D.M. et al., Molecular tectonic model of virus structural transitions: the putative cell entry states of poliovirus. *J. Virol.*, 2000, **74**: 1342–1354.
32. Brooks, C.L., III, M. Karplus, and B.M. Pettitt, Proteins. A theoretical perspective of dynamics, structure, and thermodynamics. *Advances in Chemical Physics*, eds. I. Prigogine and S.A. Rice, Vol. LXXI. New York: John Wiley & Sons, 1988.

33. Hewat, E.A., E. Neumann, and D. Blaas, The concerted conformational changes during human rhinovirus 2 uncoating. *Mol. Cell*, 2002, **10**: 317–326.
34. Conway, J.F. et al., Virus maturation involving large subunit rotations and local refolding. *Science*, 2001, **292**: 744–748.
35. Liu, H. et al., Pseudo-atomic models of swollen CCMV from cryo-electron microscopy data. *J. Struct. Biol.*, 2003, **142**: 356–363.
36. Hiremath, C.N. et al., Ligand-induced conformational changes in poliovirus-antiviral drug complexes. *Acta Crystallogr. D*, 1997, **53**: 558–570.
37. Tidor, B. and M. Karplus, The contribution of vibrational entropy to molecular association. The dimerization of insulin. *J. Mol. Biol.*, 1994, **238**: 405–414.
38. Hogle, J.M., Poliovirus cell entry: common structural themes in viral cell entry pathways. *Annu. Rev. Microbiol.*, 2002, **56**: 677–702.

12

Extension of the Normal Mode Concept: Principal Component Analysis, Jumping-Among-Minima Model, and Their Applications to Experimental Data Analysis

Akio Kitao

CONTENTS

12.1 Introduction

The nature of the protein dynamics is often stated complex and anharmonic. However, the framework of the normal mode analysis (NMA), in which protein dynamics is described as a linear combination of collective variables and harmonic multidimensional energy surface is assumed, is of great use to elucidate complex dynamics of proteins. The reason of this statement will be threefold. First, collective description of protein dynamics, a key concept of the NMA, has been applied successfully to a number of protein systems

(see, reviews [1–5]). Small number of large-amplitude modes dominantly determines atomic fluctuation of proteins. Since protein dynamics takes place extremely anisotropic, it can be efficiently described by an appropriate set of collective variables. Furthermore, the concepts of "important subspace" [6] and "essential subspace" [7] propose the possibility that "important" or "essential" protein motions take place in a dimensionally small subspace spanned by a subset of collective variables. Second, NMA is useful as an idealized reference to investigate real complex systems. Although anharmonic aspects of protein dynamics draw attention, a large number of degrees of freedom can be approximated to be harmonic [7–14]. Anharmonic degrees of freedoms in protein dynamics were discussed by examining the deviation from purely harmonic systems. Third, very low-frequency normal modes are relevant to protein function. This has been believed for years, and the concept of "dynamic domain" recently succeeded in finding evident examples [15–19]. This has been achieved by comparing conformational variations observed in crystal structures to conformational fluctuations calculated by NMA, molecular dynamics (MD), and principal component analysis (PCA).

In this chapter, some extensions of NMA and applications of NMA concepts to investigate protein dynamics in the native state are introduced. For this purpose, we describe PCA [7, 9, 10, 20]. Langevin mode analysis (LMA) [21, 22] and Jumping-among-minima model (JAM) [3, 14], and discuss the anharmonic nature of protein energy landscape. Also, some applications of NMA concept to the analysis experimental data, the applications in nuclear magnetic resonance (NMR) [23], x-ray crystallography [24, 25], and neutron scattering [10, 26, 27], are focused.

12.2 Collective-Mode Description of Protein Dynamics

A key concept of the NMA is that a set of atomic or internal coordinates of the system is expressed as a linear combination of normal mode coordinates. Let us introduce a mass-weighted atomic coordinate set, $\{q_i(t)\}$. This coordinate set at time t can be written as a column vector $\mathbf{q}(t)$ as

$$\{q_i(t)\} = \mathbf{q}(t) = \begin{pmatrix} \vdots \\ (m_n)^{1/2}\mathbf{r}_n(t) \\ \vdots \end{pmatrix} = \begin{pmatrix} \vdots \\ (m_n)^{1/2}x_n(t) \\ (m_n)^{1/2}y_n(t) \\ (m_n)^{1/2}z_n(t) \\ \vdots \end{pmatrix} \tag{12.1}$$

where m_n and $\mathbf{r}_n(t) = (x_n(t), y_n(t), z_n(t))^t$ are the mass and the position vector of the nth atom ($n = 1, \ldots, N$) in Cartesian coordinates, respectively. The mass-weighted position vector $\mathbf{q}(t)$ consists of $3N$ elements. The element

$q_i(t)$ is given by the linear combination of collective-mode variables, $\boldsymbol{\sigma}(t) = \{\sigma_\alpha(t)\}$, as

$$q_i(t) = \sum_\alpha v_{i\alpha}\sigma_\alpha(t) \tag{12.2}$$

where $v_{i\alpha}$ is the matrix element of the $3N \times 3N$ matrix $\mathbf{V} = \{v_{i\alpha}\}$, which is the transformation matrix from Cartesian coordinate to a certain collective coordinate. In the NMA, it is called "normal mode eigenvector." The matrix $\mathbf{V}$ should be chosen to satisfy an orthonormal condition,

$$\mathbf{V}^{\mathrm{t}}\mathbf{V} = \mathbf{I} \tag{12.3}$$

where $\mathbf{I}$ is the $3N \times 3N$ unit matrix. Equations (12.2) and (12.3) indicate that the collective-mode representation is the orthonormal transformation of the Cartesian coordinate to the other collective coordinate. The matrix $\mathbf{V}$ specifies how atomic coordinates are transformed to new collective coordinate. This is a general aspect of collective description of the protein dynamics not only valid for the NMA but also for other treatment, for example, PCA. Since no information is lost in this transformation, we can choose an appropriate coordinate set to observe target quantity effectively. Normal mode coordinate and the other possible coordinates are described below.

12.3 Principal Component Analysis

The PCA is described in the framework similar to normal mode but more generally. The matrix $\mathbf{V}$ is defined as the eigenvector matrix of the second moment matrix (or variance–covariance matrix) of the atomic Cartesian coordinates, $\mathbf{A}$. $\mathbf{V}$ is determined as the solution of the standard eigenvalue problem:

$$\mathbf{AV} = \mathbf{V}\boldsymbol{\zeta} \tag{12.4}$$

where $\boldsymbol{\zeta} = \{\zeta_\alpha\}$ is a diagonal matrix of the eigenvalues whose elements represent mean-square fluctuation (MSF) along the direction of the corresponding eigenvectors. Matrix $\mathbf{A}$ is defined as

$$\mathbf{A} = \{a_{ij}\} = \{\langle (q_i - \langle q_i \rangle)(q_j - \langle q_j \rangle)\rangle\} \tag{12.5}$$

The second moment matrix can be obtained by various sources, for example, trajectories of MD simulations and Monte Carlo simulation, various conformations deposited in Protein Data Bank for given L conformations. Suppose a sample of mass-weighted atomic coordinates are given as a $3N \times L$ matrix, $\mathbf{Q} = \{(L-1)^{-1/2}\Delta q_{il}\}$, where $\Delta q_{il} = q_{il} - \langle q_i \rangle$, and the indexes i (=1, ..., $3N$) and l (=1, ..., L) represent indexes of coordinates and conformations. For time-dependent samples determined by MD, Δq_{il} is given as $\Delta q_{il} = \Delta q_i(t_l)$ for time

series $t = t_1, \ldots, t_l, \ldots, t_L$. Then, the $3N \times 3N$ matrix $\mathbf{A}$ is determined as

$$\mathbf{A} = \mathbf{Q}\mathbf{Q}^{\mathrm{t}} \tag{12.6}$$

If internal motion of the system is to be observed, external motion can be removed from $\mathbf{Q}$ by satisfying Eckart condition [28]. This condition can be satisfied if each instantaneous coordinate is best-fit to a reference coordinate, which is often chosen to be the average coordinate set $\{\langle q_i \rangle\}$ determined self-consistently. If the second moment matrix is determined, $\mathbf{V}$ and $\boldsymbol{\zeta}$ are obtained by Equation (12.4). For internal motion, the rank of the second moment matrix is a minimum of $3N - 6$ and L. Also, please note that atomic coordinates to be considered in the analysis can be chosen depending on the purposes, for example, C^{α} atoms, backbone atoms, all atoms, etc.

The atomic coordinate is expressed as a linear combination of a new coordinate set $\boldsymbol{\sigma}(t_l) = \{\sigma_\alpha(t_l)\}$ at time t_l as shown in Equation (12.2). In this case, $\{\sigma_\alpha(t_l)\}$ is termed principal mode variable. From Equation (12.2), it is determined by the projection of $\mathbf{q}(t_l)$ onto the axes of principal modes $\mathbf{V}$ as $\boldsymbol{\sigma}(t_l) = \mathbf{V}^t\mathbf{q}(t_l)$ or,

$$\Sigma = \mathbf{V}^{\mathrm{t}}\mathbf{Q} \tag{12.7}$$

where $\sigma_\alpha(t_l)$ is written by a $3N \times L$ matrix $\boldsymbol{\Sigma} = \{\sigma_{\alpha l}\}$. The principal mode variable $\sigma_\alpha(t_l)$ can be scaled by the root-mean-square fluctuation (RMSF) along the axis of the αth principal mode, that is, the square root of the corresponding eigenvalue ζ_α. The matrix of scaled variables $\mathbf{U}^t$ is given by

$$\mathbf{U}^t = \boldsymbol{\zeta}^{-1/2}\Sigma = \boldsymbol{\zeta}^{-1/2}\mathbf{V}^t\mathbf{Q} \tag{12.8}$$

The condition

$$\mathbf{U}^{\mathrm{t}}\mathbf{U} = \mathbf{I} \tag{12.9}$$

is easily derived by using (12.3), (12.4), (12.6), and (12.8).

Projection of the MD and Monte Carlo (MC) trajectories of human lysozyme onto normal mode space was successful in explaining the anharmonicity in a single conformational substate [8]. However, the projection onto the principal mode space is a more efficient way to observe intersubstate transitions [12]. Two important features, transitions between substates and solvent effects, are clearly revealed by the attempt to project an MD trajectory onto the principal coordinate space [9]. By projecting an MD trajectory of melittin in water onto the two-dimensional space spanned by the largest- and second largest-amplitude principal modes, a transition from one substate to another is very clearly seen. The motion along these coordinates involves a bending of the molecule. In early 1990s, conformational transitions in the subspace spanned by few principal components (PCs) were reported in the cases of melittion [9], Met-enkephaline [29], crambin [20], bovine pancreatic trypsin inhibitor (bpti) [10], and hen-egg lysozyme [7]. PCA has now become a standard tool to investigate important motions of biological molecules [5].

Singular value decomposition (SVD) can be also used for this analysis. The SVD is a set of techniques by which any $I \times J$ matrix $\mathbf{B}$ can be decomposed into a product of three matrices as $\mathbf{B} = \mathbf{CDE}^t$, where the matrix $\mathbf{D}$ is $J \times J$ diagonal matrix with positive or zero elements (the singular values), and $\mathbf{C}$ and $\mathbf{E}$ are $I \times J$ and $J \times J$ matrices orthonormalized as $\mathbf{C}^t\mathbf{C} = \mathbf{I}$ and $\mathbf{E}^t\mathbf{E} = \mathbf{E}\mathbf{E}^t = \mathbf{I}$, respectively. The decomposition is proved by the theorem of linear algebra. Using SVD, the matrix $\mathbf{Q}^t$ can be decomposed as,

$$\mathbf{Q}^t = \mathbf{U}\boldsymbol{\zeta}^{1/2}\mathbf{V}^t \tag{12.10}$$

The matrices $\mathbf{Q}^t$, $\mathbf{U}$, $\boldsymbol{\zeta}^{1/2}$, and $\mathbf{V}$ correspond to $\mathbf{B}$, $\mathbf{C}$, $\mathbf{D}$, and $\mathbf{E}$, respectively. Therefore the dimensions of the matrices I and J are equal to L and $3N$, respectively. By inserting the relation (12.10) into (12.6), Equation (12.4) is obtained. As shown here, both PCA and SVD give identical results although they are termed differently. SVD has an advantage that three-step calculations in PCA, preparing the second moment matrix, diagonalization, and projection, can be done in one step. SVD is numerically more demanding in the case $L \gg 3N$, because the size of the matrix to be stored in computer memory may become extremely large.

The PCA is a general method of multivariable analysis. When PCA was applied to the MD trajectory by Levy et al., it was termed "quasi-harmonic" [30], probably because the focus was on the anharmonic aspects of protein dynamics. The term "PCA" was used in Reference 9 because the projection of MD trajectory onto dominant subspace was more emphasized. The term "essential dynamics (ED)" is also used to represent a few dominant anharmonic PC modes [7]. García et al. called dominant principal coordinates "molecule optimal dynamic coordinates" (MODC) [31]. These analyses share essentially the same concept, apart from some details, for example, atoms considered, mass-weighted or not, etc.

Normal mode analysis can be understood as one particular case of PCA. In the place of the second moment matrix $\mathbf{F} = \{f_{ij}\} = \{\partial^2 E/\partial q_i \partial q_j\}$, the second derivative of potential energy, that is, Hessian matrix, is employed to determine the matrix $\mathbf{V}$.

$$\mathbf{FV} = \mathbf{V}\boldsymbol{\lambda} \tag{12.11}$$

The eigenvalue matrix $\boldsymbol{\lambda}$ is related to the angular frequency of the normal modes ω_α as $\boldsymbol{\lambda} = \{\lambda_\alpha\} = \boldsymbol{\omega}^2 = \{\omega_\alpha^2\}$. Since the second moment matrix is calculated from the Hessian matrix as $\mathbf{A} = k_\mathrm{B}T\mathbf{F}^{-1}$, we get the relation

$$\zeta_\alpha = \frac{k_\mathrm{B}T}{\omega_\alpha^2} \tag{12.12}$$

Multidimensional scaling (MDS) is an alternative approach to analyze the given sample $\mathbf{Q}$. In this case, the $L \times L$ matrix

$$\mathbf{R} = \mathbf{Q}^{\mathrm{t}}\mathbf{Q} \tag{12.13}$$

is diagonalized. The eigenvalue $\boldsymbol{\zeta}$ and eigenvector $\mathbf{U} = \mathbf{Q}^{\mathrm{t}}\mathbf{V}\boldsymbol{\zeta}^{-1/2}$ (see Equation [12.8]) are identical with that in (12.4) and (12.10), respectively. This is easily derived by using Equations (12.3), (12.4), (12.6), and (12.13) as,

$$\begin{aligned}\mathbf{U}^{\mathrm{t}}\mathbf{R}\mathbf{U} =& (\boldsymbol{\zeta}^{-1/2}\mathbf{V}^{\mathrm{t}}\mathbf{Q})(\mathbf{Q}^{\mathrm{t}}\mathbf{Q})(\mathbf{Q}^{\mathrm{t}}\mathbf{V}\boldsymbol{\zeta}^{-1/2}) \\ =& \boldsymbol{\zeta}^{-1/2}(\mathbf{V}^{\mathrm{t}}\mathbf{Q}\mathbf{Q}^{\mathrm{t}}\mathbf{V})(\mathbf{V}^{\mathrm{t}}\mathbf{Q}\mathbf{Q}^{\mathrm{t}}\mathbf{V})\boldsymbol{\zeta}^{-1/2} = \boldsymbol{\zeta}\end{aligned} \tag{12.14}$$

The orthonormality of $\mathbf{U}$ is already shown in Equation (12.9). Equation (12.14) indicates that PCA and MDS give the same eigenvalues. Troyer and Cohen applied MDS to investigate energy landscape of bpti [32].

12.4 Langevin Mode

Langevin mode is a natural extension of NMA to include solvent effect on multidimensional harmonic energy surface. It has been proposed by Lamm and Szabo [21] and was applied to Crambin and DNA hexamer by Kottalam and Case [22]. In Langevin mode, we need to introduce the mass-weighted friction matrix $\boldsymbol{\Gamma}$ in addition to the second derivative matrix $\mathbf{F}$. A $3N \times 6N$ eigenvector matrix $\mathbf{W}$ and a $6N \times 6N$ diagonal eigenvalue matrix $\boldsymbol{\xi}$ are determined by the relations

$$\mathbf{F}\mathbf{W} + \boldsymbol{\Gamma}\mathbf{W}\boldsymbol{\xi} + \mathbf{W}\boldsymbol{\xi}^2 = 0 \tag{12.15}$$

$$\mathbf{W}^t\boldsymbol{\Gamma}\mathbf{W} + \boldsymbol{\xi}\mathbf{W}^{\mathrm{t}}\mathbf{W} + \mathbf{W}^{\mathrm{t}}\mathbf{W}\boldsymbol{\xi} = \boldsymbol{\xi} \tag{12.16}$$

The relation (12.15) and (12.16) correspond to (12.11) and (12.3) in NMA, respectively. The matrix elements of $\mathbf{W}$ and $\boldsymbol{\xi}$ are complex numbers. If the element ξ_α, the eigenvalue of the αth Langevin mode, has both real part and imaginary part, these values determine the damping factor and oscillatory frequency, respectively. Therefore, the mode is underdamping. If ξ_α is a real number, the mode is overdamping mode. In the NMA limit ($\boldsymbol{\Gamma} \to 0$), these matrices become

$$\mathbf{W} = \frac{1}{\sqrt{2}}(\mathbf{V}, \mathbf{V}) \tag{12.17}$$

$$\boldsymbol{\xi} = \begin{pmatrix} \pm i\omega & O \\ O & \pm i\omega \end{pmatrix} \tag{12.18}$$

where ω is the matrix of normal mode frequency.

A practical problem is how the friction $\mathbf{\Gamma}$ is to be determined. Based on hydrodynamic theory, the friction can be derived from Oseen tensor and its extensions [33]. In these models, $\mathbf{\Gamma}$ is determined for the given viscosity, radius of particle, and interparticle distances. However, the effective friction matrix determined from MD simulation in water was found to be rather different from those calculated from these hydrodynamic treatments [9]. To reproduce spectral density calculated from the MD trajectory in water, simpler treatment was sufficient [10]. In this case, the off-diagonal elements are set to be zero and the diagonal elements are constant. In other words, spectrum was reproduced well with the combination of independent Langevin oscillators. It was also shown that friction effect on low-frequency collective motions is evidently protein dependent [14]. Estimated friction coefficients are 20 ± 10, 47 ± 10, and $100 \pm 10\ \mathrm{cm}^{-1}$ for human lysozyme, bpti, and melittin, whose molecular weights are 14700, 6520, and 2580, respectively. This tendency against size of proteins is qualitatively explained by the relation between translational friction coefficient γ and solvent viscosity η, $\gamma = 6\pi a\eta/m$, which is known as Stokes–Einstein law. Here the mass m and radius a should be considered as those of domain or whole molecule rather than that of each atom in protein, because large-amplitude modes concerned are global motion. Solvent viscosity η is constant, and the factor $a/m \propto m^{-2/3}$ decreases rapidly as protein size increases. Since the overdamping of the mode occurs if the condition $\gamma > 2\omega_\alpha$ is satisfied, the number of overdamping modes decreases as the protein size is larger.

12.5 Conservation and Convergence of Collective Variables

As far as we have learned from published papers, it is safe to say that few modes (say 10 to 50) mainly determine total atomic fluctuation of proteins by ~80% for a given length of simulation trajectory. More number of modes is necessary to describe fluctuations of nucleic acids because they are softer and less anisotropic than proteins. The question here is whether the determined subset of modes is useful to understand protein dynamics. Physical time length of MD is often much shorter than the time scale of the phenomena of interest. Within the limited simulation time, conformational space cannot be sufficiently sampled. Therefore, the results of PCA clearly depend on the length of the simulation. However, as mentioned in the introduction, a small subset of large-amplitude collective variables is expected to conserve within a certain range, as has been proposed as the concepts of "important subspace" [6] and "essential subspace" [7]. In the normal mode refinement of crystallographic protein structure [6], a subset of low-frequency normal modes were used as a basis set to describe internal motions. In the case of human lysozyme, 100 normal modes were sufficient. Hundred normal modes occupy 16% and 1.6% of the internal degrees of freedom in dihedral angle space and in all-atom

Cartesian coordinate space, respectively (for more details see Section 12.8). The subspace spanned by these collective variables is called important subspace as mentioned earlier. By using PCA of 900-psec trajectory of hen-egg lysozyme, Amadei et al. [7] concluded that the ED can be described by less than ten modes [7]. The essential subspace, which is spanned by these modes, is smaller than the important subspace in dimension. The point is whether a subset of collective variables, which is determined by the limited simulation time often shorter than functional time scale, is conserved. Another point is that how many degrees of freedoms are necessary to span a conserved subspace. This can be examined by comparing an eigenvalue matrix of PCA, $\mathbf{V} = \{v_{i\alpha}\}$, with another set determined separately, $\mathbf{V}' = \{v'_{j\beta}\}$, whose column vectors $\mathbf{V}_\alpha$ and $\mathbf{V}'_\beta$ are eigenvectors of PC modes. The inner product of two eigenvectors

$$c_{\alpha\beta} = \mathbf{V}_\alpha (\mathbf{V}'_\beta)^{\mathrm{t}} = \sum_{i=1}^{3N} v_{i\alpha} v'_{i\beta} \tag{12.19}$$

represents the amount of correlation between two vectors. If $c_{\alpha\beta}$ is close to unity, the αth eigenvector $\mathbf{V}_\alpha$ resembles the βth eigenvector $\mathbf{V}'_\beta$. The number of variables needed to describe a subset of $\mathbf{V}_\alpha$ can be examined by changing the number M in the following equations

$$P_\alpha(M) = \sum_{\beta=1}^{M} c_{\alpha\beta}^2 \tag{12.20}$$

$$\bar{P}(M) = \frac{1}{M} \sum_{\alpha=1}^{M} P_\alpha(M) = \frac{1}{M} \sum_{\alpha=1}^{M} \sum_{\beta=1}^{M} c_{\alpha\beta}^2 \tag{12.21}$$

If $P_\alpha = 0.9$ for $M = 120$, this indicates that $\mathbf{V}_\alpha$ is described by a subset of 120 PC modes in $\mathbf{V}'$ by 90%. $\bar{P}(M)$ represents the extent of overlap between two subspaces spanned by each M of PC modes.

Balsera et al. [34] carried out MD simulation of G-action and PCA of two consecutive 235-psec trajectories. In this article, a subspace spanned by 10, 50, and 300 PC modes out of totally 1275 modes determined by one set of 235-psec C^α atom trajectory overlaps the corresponding subspace of another trajectory by less than 20, 50, and 70%, that is, $\bar{P}(10) < 0.2$, $\bar{P}(50) = 0.5$, and $\bar{P}(300) = 0.7$, respectively, while a set of random vectors overlap by about 25% when 300 modes are employed. They concluded that small number of modes (say 1%) do not have predictive power for the longtime behavior of proteins although such modes dominantly contribute to total fluctuations. Similar results were reported in the reference [14], but viewpoints and conclusions were rather different. In this article, 1-nsec MD of human lysozyme was carried out and PCA of ten overlapping trajectories of lengths 100 to 1000 psec. When the large-amplitude PC modes of 1000-psec MD were compared to those of 200-psec, P_α values were 0.35 to 0.5 for $M = 30$ and 0.7 to 0.8 for $M = 300$, where $M = 30$

and 300 correspond to 0.5 and 5% of the total all-atom degrees of freedom, respectively. In this simulation, large conformational change was observed in the middle of the simulation. Therefore, first few PC modes of the 1000-psec MD represent the large conformational change not found in 200-psec MD. It was concluded that a very small subset of PC modes determined from short MD, for example, first 10 PC mode, cannot predict the direction of future large-amplitude mode but it is expected to occur in the subspace spanned by a larger subset, for example, 300 PC modes. This number roughly corresponds to important subspace. Contrarily, Amadei et al. [35] reported that simulations of a few hundreds of picoseconds are, in general, sufficient to provide a stable subspace that the largest 10 eigenvectors compose. The difference is probably caused by the fact that the characteristic time of anharmonic motion strongly depends on protein. If so, it is safer to use the subspace spanned by hundreds of principal modes rather than a few modes. Hess reported that PCA results of high-dimensional random diffusion can appear as pseudo correlated motion in large-amplitude principal modes [36, 37]. The projections of random diffusion are predicted to be cosines. The resemblance to cosines was suggested to be the indicator of insufficient sampling.

12.6 Anharmonicity of Energy Landscape and JAM Model

Since the real energy landscape is anharmonic, the second moments along the principal modes are different from those expected from the normal modes. In other words, the relation given by (12.12) does not hold true. However, we can introduce "effective frequency" of the αth principal mode, $\omega_\alpha^{\text{eff}}$, as [9]

$$\omega_\alpha^{\text{eff}} = \sqrt{\frac{k_B T}{\zeta_\alpha}} \tag{12.22}$$

Although the real energy surface along the principal mode is not necessarily parabolic, this quantity gives the coarse grained information of energy surface if it is approximated to be parabolic. The difference between ω_α and $\omega_\alpha^{\text{eff}}$ is a measure to examine the anharmonicity of real energy landscape. However, because the eigenvectors of normal mode is not necessarily the same as that of PC mode, it is difficult to judge if the difference between ω_α and $\omega_\alpha^{\text{eff}}$ originates from either anharmonicity of energy surface or difference of two vectors. The anharmonicity factor ρ_α introduced in Reference 12 gives a better measure to define the extent of anharmonicity as,

$$\rho_\alpha = \left(\frac{\zeta_\alpha}{\zeta_\alpha^{\text{har}}}\right)^{1/2} = \left(\frac{\zeta_\alpha}{\sum_{\beta=1}^{3N-6} c_{\alpha\beta}^2 (k_B T/\omega_\beta^2)}\right)^{1/2} \tag{12.23}$$

where $c_{\alpha\beta}$ in (12.23) is defined for the PC mode vector $\mathbf{V}_\alpha$ and the normal mode vector $\mathbf{V}'_\beta$. The denominator in (12.23) represents the second moment expected from the normal mode along the direction of the PC mode vector $\mathbf{V}_\alpha$. In the case of bpti, the fraction of anharmonic modes ($\rho_\alpha > 1$) determined by united-atom is 11.7%, which can be rescaled to 7.4% in all-atom model [12]. For other modes, the anharmonicity factor is ∼1, which means that more than 90% of the degrees of freedom have nearly harmonic energy surface. In the case of human lysozyme, the fraction of the anharmonic modes are 5% [14]. The fraction of anharmonic modes roughly corresponds to the important subspace well conserved during the simulation.

The main source of the anharmonicity originates from multiple minima of the energy landscape. As a simple extension of PCA to consider the multiple minima problem, the JAM model has been proposed [14]. Consider the case where K conformations consisting of $\mathbf{Q}$ are classified into K groups. Although arbitrary classification is valid in the following derivations, physical meaning is given if conformations in each group are chosen to be located within the same catchment region of an energy minimum. Let n_k be the number of conformations in the kth group, and the average $\langle\cdots\rangle_k$ is taken over n_k conformations in the kth group. The second moment matrix in equation (12.5) can be divided into two terms

$$\begin{aligned} a_{ij} &= \sum_{k=1}^{K} f_k(\langle q_i\rangle_k - \langle q_i\rangle)(\langle q_j\rangle_k - \langle q_j\rangle) + \sum_{k=1}^{K} f_k\langle(q_i - \langle q_i\rangle_k)(q_j - \langle q_j\rangle_k)\rangle_k \\ &= a_{ij}^{\mathrm{JAM}} + \sum_{k=1}^{K} f_k a_{ij}^k \\ &= a_{ij}^{\mathrm{JAM}} + \langle a_{ij}^k\rangle_{f_k} \end{aligned} \tag{12.24}$$

where

$$L = \sum_{k=1}^{K} n_k, \quad f_k = \frac{n_k}{L} \tag{12.25}$$

and $\langle\cdots\rangle_{f_k}$ denotes an average weighted by f_k. The first and second terms in the right-hand side of Equation (12.24) come from JAM motions and fluctuations around each minimum, respectively. These two terms are also the second moment matrices. In case hierarchical model is to be used, the matrix a_{ij}^k can be divided further by repeating the same operation in Equation (12.24). In this model, $q_i(t)$ can be given as

$$q_i(t) = \sum_{\chi=1}^{O} v_{i\chi}^{\mathrm{JAM}}\sigma_\chi^{\mathrm{JAM}}(t) + \sum_{k=1}^{K}\sum_{\varepsilon=1}^{P} v_{i\varepsilon}^k\sigma_\varepsilon^k(t) \quad (O \le K, P \le 3N-6) \tag{12.26}$$

where $\{\sigma_\chi^{\mathrm{JAM}}(t)\}$ and $\{\sigma_\varepsilon^k(t)\}$ represent JAM mode variables and principal mode variable of the intra-substate motion around the kth energy minimum. The integers O and P represent the numbers of degrees of freedom that are necessary to describe JAM motion and intra-substate motion around energy minimum, respectively. The matrices $\{v_{i\chi}^{\mathrm{JAM}}\}$ and $\{v_{i\varepsilon}^k\}$ are determined as the eigenvectors of the matrices $\{a_{ij}^{\mathrm{JAM}}\}$ and $\{a_{ij}^k\}$, respectively.

This model was applied to the analysis of 1 nsec MD trajectory of human lysozyme in water. As a physical model of the lowest-level substate, "protein rotamer state" was introduced. The protein rotamer state is defined as that all the main-chain and side-chain rotamers in protein are in the same states. From the analysis of intra-substate motion, each conformational subspace is shown to be nearly harmonic and mutually similar. By examining the anharmonicity factor and the shapes of the probability distribution functions, three types of modes are identified (a) multiply-hierarchical modes, (b) singly-hierarchical modes, and (c) harmonic modes. Harmonic modes have parabolic energy surface whose anharmonicity factors are $\sim$1. The multiply- and singly-hierarchical modes showed that anharmonicity factors are greater than one. Along the axis of the multiply-hierarchical modes, different levels of energy barriers coexist (see Figure 12.1 and Table 12.1 for details). The multiply-hierarchical modes correspond to large-amplitude PC modes, which are found to be important in proteins to function [5].

12.7 Application of JAM Concept

One of the important features revealed by the JAM model is that protein dynamics along large-amplitude principal modes take place mainly as the transitions among conformational subspace. Current computer power is still not sufficient to observe the large transitions many times within the limited simulation time. However, fast vibrational motion within a substate converges relatively fast. Let A be an arbitrary dynamical variable. Suppose the average of A with the subspace k, $\langle A\rangle_k$, is determined by the short simulation. In the JAM model, the ensemble average of A, $\langle A\rangle$, can be given by

$$\langle A\rangle = \sum_{k=1}^{M} f_k \langle A\rangle_k \tag{12.27}$$

where f_k is the statistical weight of the substate and M the number of substates. If a certain experimentally observable or determinable quantity Q_i is defined as a functional of $\langle A\rangle$, we have

$$Q_i \equiv Q_i[\langle A\rangle] \tag{12.28}$$

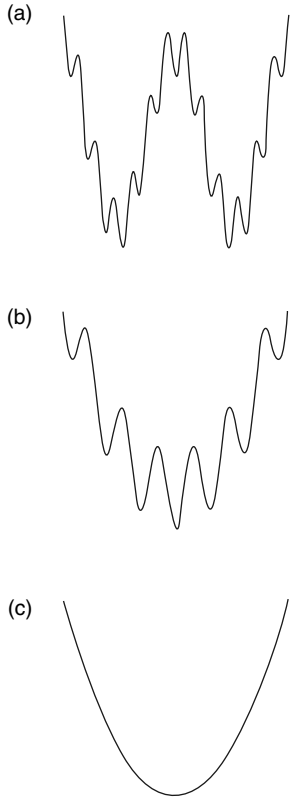

FIGURE 12.1
Free energy surface is schematically shown for (a) multiply-hierarchical, (b) singly-hierarchical, and (c) harmonic modes, respectively. (Reproduced from Kitao A., Hayward S., and Go N. *Proteins*, 33, 496, 1998. With permission.)

In the JAM model, Q_i is rewritten as

$$Q_i = Q_i \left[\sum_{k=1}^{M} f_k \langle A \rangle_k \right] \tag{12.29}$$

In this method, the ensemble average within a substate k, $\langle A \rangle_k$, is obtained by MD simulation or normal mode with a force field. The statistical weights f_k are determined so as to minimize the difference between a set of experimentally determined quantities and that of the calculated ones. Once a set of f_k is obtained, ensemble averages of other quantities, for example, the second moment matrix, can be calculated.

This idea was used to determine the dynamic structure of a protein based on NMR relaxation parameters [23]. In this case the statistical weights are fitted to reproduce NMR order parameter, S^2. Order parameters were calculated using

TABLE 12.1

Principal Mode Category.

	Multiply-hierarchical mode	**Singly-hierarchical mode**	**Harmonic mode**
Principal mode #	1–30	31–300	301–6117
Probability distribution	NonGaussian multiple peak	Gaussian like single peak	Gaussian
Anharmonicity factor	>2	>1	~1
% in # of modes	0.5	4.5	95.0
% in total MSF	82.1	15.0	2.9
RMSF (Å)	>0.08	0.08–0.015	0.015>
Packing topology	Significant change	No change	No change
Fluctuation of dihedral angles	Large change in both main chains and side chains	Large change mainly in surface side chains	Small change

Source: Reproduced from Kitao A., Hayward S., and Go N. *Proteins* 33, 496, 1998. With permission.

the averaging scheme of our JAM model, which is based on the method by Henry and Szabo [38], as the following: The order parameter, S, is given by

$$S^2 = \left\langle r_{nm}^{-6} \right\rangle^{-1} \left[\frac{3}{2} tr\left(\langle \Phi \rangle \right)^2 - \frac{1}{2} \left(tr \langle \Phi \rangle \right)^2 \right] \tag{12.30}$$

The element of the tensor $\Phi(t)$ is defined as

$$\Phi_{\alpha\beta}(t) = \frac{1}{r_{nm}^3(t)} \frac{\{r_{nm}(t)\}_\alpha \{r_{nm}(t)\}_\beta}{r_{nm}^2(t)} \tag{12.31}$$

where $r_{nm}(t) = |\mathbf{r}_{nm}(t)| = |\mathbf{r}_n(t) - \mathbf{r}_m(t)|$ and the vector $\mathbf{r}_{nm}(t)$ is a bond vector between two atoms, that is, proton and nitrogen atoms. In the JAM model, Equation (12.30) can be rewritten as

$$S^2 = \langle r_{nm}^{-6} \rangle^{-1} \left[\frac{3}{2} \mathrm{tr} \left(\sum_{k=1}^{M} f_k \langle \Phi \rangle_k \right)^2 - \frac{1}{2} \left(\mathrm{tr} \sum_{k=1}^{M} f_k \langle \Phi \rangle_k \right)^2 \right] \tag{12.32}$$

The average of tensor Φ within the kth substate, $\langle \Phi \rangle_k$, is determined from a molecular simulation. Once a set of f_k is determined, various quantities, such as directions and amplitudes of atomic fluctuations, can be obtained. Figure 12.2 shows the results of the dynamic NMR refinement of human CD2. The dominant modes determined were found to resemble the structure change upon counter-receptor binding.

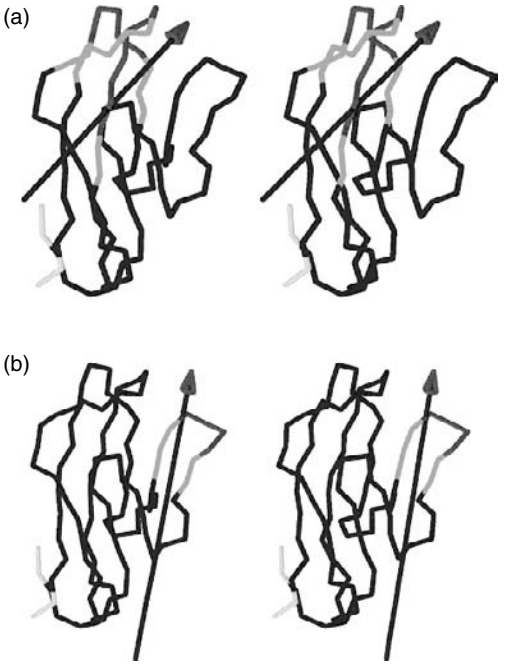

FIGURE 12.2
(See color insert following page 136) Dynamic domain motions in (a), the first and (b) second JAM mode in free human CD2. The residues shown in blue, red, and green represent fixed-domain, moving-domain, and bending residues, respectively, as determined by DynDom (Hayward S., and Berndsen H.J. *Proteins*, 30, 144, 1998). The arrows represent the axes of domain motions. The moving-domains rotate around these axes. The figure created by using the programs DynDom (de Groot B.L., Hayward S., van Aalten D.M., Amadei A., and Berendsen H.J. *Proteins*, 31, 116, 1998) and Rasmol (Sayle R., and Milner-White E.J. *Trends Biochem. Sci.*, 20, 374, 1995). (Reproduced from Kitao A., and Wagner G. *Proc. Natl Acad. Sci. USA*, 97, 2064, 2000. With permission.)

12.8 Application of the Normal Mode Concept to the Dynamics Crystallographic Refinement

Isotropic *B*-factor refinement is the most popular crystallographic refinement method in protein structure determination. In the *B*-factor refinement, atomic motion is assumed to be isotropic. Anisotropic *B*-factor refinement requires more parameters to be determined. The number of parameters can be highly reduced in the normal mode refinement [6, 24, 25, 39] by using normal modes as a basis set of fitting parameters although atomic fluctuations are treated anisotropically. In the formulation by Kidera and Go [39], the second moment of nonmass-weighted Cartesian coordinate of nth atom, the 3×3 matrix $\langle \Delta\mathbf{r}_n \Delta\mathbf{r}_n^{\mathrm{t}} \rangle$, is given by the sum of the internal motion

expressed by the normal mode basis set and the external rigid-body motion in translation/liberation/screw (TLS) model as

$$\langle \Delta \mathbf{r}_n \Delta \mathbf{r}_n^{\mathrm{t}} \rangle = \left(\varphi_n^{\mathrm{I}}\right)^{\mathrm{t}} \Xi^{\mathrm{I}} \varphi_n^{\mathrm{I}} + \left(\varphi_n^{\mathrm{E}}\right)^{\mathrm{t}} \Xi^{\mathrm{E}} \varphi_n^{\mathrm{E}} \tag{12.33}$$

where φ_n^{I} is a $K \times 3$ submatrix of nonmass-weighted normal mode eigenvector, that is, the basis set of fitting to consider internal motion, and K is the number of normal mode variables employed in the refinement. The matrix φ_n^{E} is a 6×3 matrix employed as the basis set of translational and librational motion in TLS model [40]. The matrix Ξ^{I} is a $K \times K$ matrix whose elements are fitting parameters. The maximum number of independent parameters is $\frac{1}{2}K(K+1)$, however, only a small number of off-diagonal elements are practically employed to reduce the number of parameters. Ξ^{E} is a 6×6 matrix, parameters for external motion and the number of independent parameters is 21. These parameters for internal and external motions are determined to reproduce experimental determined electron density map.

Using the normal mode refinement, the internal motion of human lysozyme in its crystal environment is reported to be highly anisotropic. Determined atomic fluctuations were in good agreement with those determined by normal mode [6]. Joti et al. studied nonlinear temperature dependence of atomic fluctuations of human lysozyme in crystal and analyzed the details of the "glass transition," also termed glasslike transition or dynamical transition, at around 150 to 200 K [41]. They classified the temperature dependence of the Debye–Waller factor into three types, harmonic, glassy, and shifted, as shown in Figure 12.3. They also showed that anisotropic protein motion in crystal is well predicted by anisotropic network model (ANM) [42].

12.9 Neutron Scattering

Neutron scattering experiments essentially measure the total dynamic structure factor, $S(\mathbf{k}, \omega)$, where $\mathbf{k}$ and ω correspond to the momentum and energy transfers between incident neutron and sample, respectively. This spectrum can be calculated by molecular simulation relatively easily because it is related to time correlation function directly and the time range of spectrum overlaps with simulation time range. Incoherent and coherent scattering give the information on auto- and cross-correlation, respectively. Because the incoherent scattering length of hydrogen is one order of magnitude larger than the coherent scattering length of all the other atoms in protein, coherent contribution is negligibly small, that is, $S(\mathbf{k}, \omega) \approx S_{\mathrm{inc}}(\mathbf{k}, \omega)$, if particular treatment is not done in experiment. $S_{\mathrm{inc}}(\mathbf{k}, \omega)$ can be defined as the Fourier transform of a time correlation function, the intermediate scattering

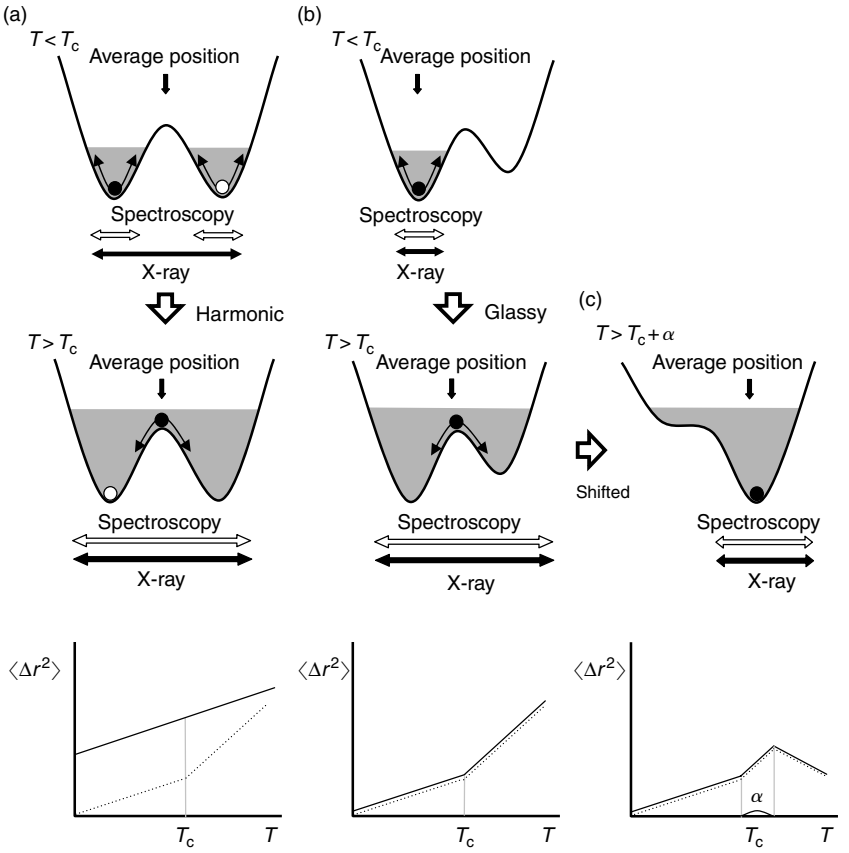

FIGURE 12.3
A schematic explanation of the temperature dependence of the Deby–Waller factors observed in x-ray diffraction (solid line) and incoherent spectroscopy (dotted line). (a) Harmonic response. When all the conformational substates are occupied throughout the temperature range, a glass transition is not observed in x-ray diffraction but is observed in incoherent experiments. (b) "Glassy" response. When a certain substate is not occupied at low temperature but are occupied at high temperatures, dynamic transition may be observed even in x-ray diffraction after "glassy" transition. (c) "Shifted" response. When the temperature is further increased after "glassy" transition, large coordinate shifts at some loci that diminish the population in the original position at low temperatures are observed. In this case, the MSF decrease again after the "glassy" transition. (Reproduced from Joti Y., Nakasako M., Kidera A., and Go N. *Acta Crystallogr. D*, 58, 1421, 2002. With permission.)

function, $I_{\mathrm{inc}}(\mathbf{Q}, t)$:

$$S_{\mathrm{inc}}(\mathbf{k}, \omega) = \frac{1}{2\pi} \int_{-\infty}^{+\infty} \mathrm{d}t \exp(-i\omega t)\, I_{\mathrm{inc}}(\mathbf{k}, t) \tag{12.34}$$

$$I_{\mathrm{inc}}(\mathbf{k}, t) = \sum_n b_{\mathrm{inc},n}^2 \langle \exp(-i\mathbf{k} \cdot \mathbf{r}_n(0)) \exp(i\mathbf{k} \cdot \mathbf{r}_n(t)) \rangle \tag{12.35}$$

where $b_{\mathrm{inc},n}$ and $\mathbf{r}_n(t)$ are the incoherent atomic scattering length and position vector of atom, respectively. Analytical solution can be obtained from Equations (12.34) and (12.35) in the case of NMA [26]. The spectrum can also be calculated easily from MD trajectory and LMA in classical treatment.

The comparison between experimental and calculated spectra has been started from 1980s (see review [26]). The main problem was that the spectrum in the low-frequency region ($<$50 cm^{-1}) differed significantly. The normal mode gives relatively high density in this frequency range, whereas the density decreases as the frequency goes lower in experiment. This incompatibility was reasonably explained by considering the environmental effect as friction [10]. If frictional effect is considered as Langevin mode, the spectral density becomes lower than expected in normal mode in low-frequency region because low-frequency normal modes overdamp [9].

Recent high-resolution measurement enables us to compare experimental and simulated spectra in more detail [27]. Possibility of adjusting force–field parameters from the comparison was suggested. Since strong neutron source projects are ongoing, it is expected to get information that is more useful in the near future by the combination of neutron scattering experiment and molecular simulation.

12.10 Concluding Remarks

Normal mode concept and its extensions are very useful to investigate protein dynamics. As shown in this chapter, they are useful not only for simulation itself and for the analysis of simulation data, but also to analyze various experimental data and to get more detailed information of protein energy landscape. Although normal mode concept is quite simple, it still has potentiality to extend to other future analysis.

References

1. Case D.A. Normal mode analysis of protein dynamics. *Curr. Opin. Struct. Biol.*, 4, 285, 1994.
2. Hayward S. and Go N. Collective variable description of native protein dynamics. *Annu. Rev. Phys. Chem.*, 46, 223, 1995.
3. Kitao A. and Go N. Investigating protein dynamics in collective coordinate space. *Curr. Opin. Struct. Biol.*, 9, 164, 1999.
4. Hayward S. Normal mode analysis of biological molecules. In *Computational Biochemistry and Biophysics*. Becker O.M., MacKerell A.D.J., Roux B., and Watanabe M., Editors. Marcel Dekker, Inc., New York, 2001, p. 153.
5. Berendsen H.J. and Hayward S. Collective protein dynamics in relation to function. *Curr. Opin. Struct. Biol.*, 10, 165, 2000.

6. Kidera A., Inaka K., Matsushima M., and Go N. Normal mode refinement: crystallographic refinement of protein dynamic structure. II. Application to human lysozyme. *J. Mol. Biol.,* 225, 477, 1992.
7. Amadei A., Linssen A.B.M., and Berendsen H.J.C. Essential dynamics of proteins. *Proteins,* 17, 412, 1993.
8. Horiuchi T. and Go N. Projection of Monte Carlo and molecular dynamics trajectories onto the normal mode axes: human lysozyme. *Proteins,* 10, 106, 1991.
9. Kitao A., Hirata F., and Go N. The effects of solvent on the conformation and the collective motions of protein: normal mode analysis and molecular dynamics simulation of melittin in water and in vacuum. *Chem. Phys.,* 158, 447, 1991.
10. Hayward S., Kitao A., Hirata F., and Go N. Effect of solvent on collective motions in globular protein. *J. Mol. Biol.,* 234, 1207, 1993.
11. Hayward S., Kitao A., and Go N. Harmonic and anharmonic aspects in the dynamics of bpti: a normal mode analysis and principal component analysis. *Protein Sci.,* 3, 936, 1994.
12. Hayward S., Kitao A., and Go N. Harmonicity and anharmonicity in protein dynamics: a normal mode analysis and principal component analysis. *Proteins,* 23, 177, 1995.
13. Janezic D., Veneble R.M., and Brooks B.R. Harmonic analysis of large systems. III. Comparison with molecular dynamics. *J. Comput. Chem.,* 16, 1554, 1995.
14. Kitao A., Hayward S., and Go N. Energy landscape of a native protein: jumping-among-minima model. *Proteins,* 33, 496, 1998.
15. Hayward S., Kitao A., and Berendsen H.J. Model-free methods of analyzing domain motions in proteins from simulation: a comparison of normal mode analysis and molecular dynamics simulation of lysozyme. *Proteins,* 27, 425, 1997.
16. Wriggers W. and Schulten K. Protein domain movements: detection of rigid domains and visualization of hinges in comparisons of atomic coordinates. *Proteins,* 29, 1, 1997.
17. Hayward S. and Berendsen H.J. Systematic analysis of domain motions in proteins from conformational change: new results on citrate synthase and T4 lysozyme. *Proteins,* 30, 144, 1998.
18. de Groot B.L., Hayward S., van Aalten D.M., Amadei A., Berendsen H.J. Domain motions in bacteriophage T4 lysozyme: a comparison between molecular dynamics and crystallographic data. *Proteins,* 31, 116, 1998.
19. Hayward S. Structural principles governing domain motions in proteins. *Proteins,* 36, 425, 1999.
20. Garcia A.E. Large-amplitude nonlinear motions in proteins. *Phys. Rev. Lett.,* 68, 2696, 1992.
21. Lamm G. and Szabo A. Langevin modes of macromolecules. *J. Chem. Phys.,* 85, 7334, 1986.
22. Kottalam J. and Case D.A. Langevin modes of macromolecules: applications to crambin and DNA hexamers. *Biopolymers,* 29, 1409, 1990.
23. Kitao A. and Wagner G.A. Space–time structure determination of human CD2 reveals the CD58-binding mode. *Proc. Natl Acad. Sci. USA,* 97, 2064, 2000.
24. Kidera A., and Go N. Refinement of protein dynamic structure: normal mode refinement. *Proc. Natl Acad. Sci. USA,* 87, 3718, 1990.
25. Diamond R. On the use of normal modes in thermal parameter refinement: theory and application to the bovine pancreatic trypsin inhibitor. *Acta Crystallogr.,* A46, 425, 1990.

26. Smith J.C. Protein dynamics: comparison of simulations with inelastic neutron scattering experiments. *Quat. Rev. Biophys.*, 24, 227, 1991.
27. Goupil-Lamy A.V., Smith J.C., Yunoki J., Parker S.F., and Kataoka M. High-resolution vibrational inelastic neutron scattering: a new spectroscopic tool for globular proteins. *J. Am. Chem. Soc.*, 119, 9268, 1997.
28. Eckart C. Some studies concerning rotating axes and polyatomic molecules. *Phys. Rev.*, 47, 552, 1935.
29. Abagyan R. and Argos P. Optimal protocol and trajectory visualization for conformational searches of peptides and proteins. *J. Mol. Biol.*, 225, 519, 1992.
30. Levy R.M., Srinivasan A.R., Olson W.K., and McCammon J.A. Quasi-harmonic method for studying very low frequency modes in proteins. *Biopolymers*, 23, 1099, 1984.
31. Garcia A.E. and Harman J.G. Simulations of Crp:$(Camp)_2$ in noncrystalline environments show a subunit transition from the open to the closed conformation. *Protein Sci.*, 5, 62, 1996.
32. Troyer J.M. and Cohen F.E. Protein conformational landscapes: energy minimization and clustering of a long molecular dynamics trajectory. *Proteins*, 23, 97, 1995.
33. Rotne J. and Prager S. Variational treatment of hydrodynamic interaction in polymers. *J. Chem. Phys.*, 50, 4831, 1969.
34. Balsera M.A., Wriggers W., Oono Y., and Schulten K. Principal component analysis and long time protein dynamics. *J. Phys. Chem.*, 100, 2567, 1996.
35. Amadei A., Ceruso M.A., and Di Nola A. On the convergence of the conformational coordinates basis set obtained by the essential dynamics analysis of proteins' molecular dynamics simulations. *Proteins*, 36, 419, 1999.
36. Hess B. Convergence of sampling in protein simulations. *Phys. Rev. E*, 65, 031910, 2002.
37. Hess B. Similarities between principal components of protein dynamics and random diffusion. *Phys. Rev. E*, 62, 8438, 2000.
38. Henry E.R. and Szabo A. Influence of vibrational motion on solid state line shapes and NMR relaxation. *J. Chem. Phys.*, 82, 4753, 1985.
39. Kidera A. and Go N. Normal mode refinement: crystallographic refinement of protein dynamic structure. I. Theory and test by simulated diffraction data. *J. Mol. Biol.*, 225, 457, 1992.
40. Schomaker V. and Trueblood K.N. On the rigid-body motion of molecules in crystals. *Acta Crystallogr. B*, 24, 63, 1968.
41. Joti Y., Nakasako M., Kidera A., and Go N. Nonlinear temperature dependence of the crystal structure of lysozyme: correlation between coordinate shifts and thermal factors. *Acta Crystallogr. D*, 58, 1421, 2002.
42. Atilgan A.R., Durell S.R., Jernigan R.L., Demirel M.C., Keskin O., and Bahar I. Anisotropy of fluctuation dynamics of proteins with an elastic network model. *Biophys. J.*, 80, 505, 2001.
43. Sayle R. and Milner-White E.J. Rosmol: biomolecular graphics for all. *Trends Biochem. Sci.*, 20, 374, 1995.

13

Imaginary-Frequency, Unstable Instantaneous Normal Modes, the Potential Energy Landscape, and Diffusion in Liquids

T. Keyes

CONTENTS

13.1 Introduction

An elementary definition is that normal modes are dynamically independent linear combinations of coordinate displacements, representing a direction in the relevant configuration space. Each mode obeys a wave equation in time, that is, it executes harmonic motion; the time dependence of each original coordinate is expressed as a sum of harmonic oscillations with different frequencies.

A harmonic system is rigorously described by normal modes. Physically challenging problems are anharmonic. However, in many instances harmonic approximations are possible, and extremely valuable. The truncation of an expansion of the total potential energy, $U(\boldsymbol{r})$, at second order in the displacements, $\delta\boldsymbol{r}$, of the coordinates from a minimum of U is the standard procedure. The approximations are useful so long as the system remains close to the minimum, which, if the potential well is truly confining, can mean forever. The example most relevant to the current discussion is a crystal at low temperature.

In a remarkable article [1], Rahman et al. made the harmonic expansion of U about snapshot configurations of an atomic glass, taken from molecular dynamics simulation; such configurations *are not minima of the potential*. Consequently, the curvature of U is negative along some normal mode directions, leading to imaginary frequencies and *unstable* modes. Substitution of Im $-\omega$ into textbook harmonic formulae leads to unphysical divergences. The resolution, of course, is that the system does not remain near the expansion point, but moves away along the unstable directions, invalidating the ill-behaved expressions. The question of how to use these unusual modes remains.

Rahman et al. simply ignored the small number of Im $-\omega$ and calculated what is probably the most important dynamical quantity in atomic fluids, the velocity correlation function, as if the system were truly harmonic; excellent agreement with simulation was obtained. In a harmonic system the self-diffusion constant, D, the integral of the velocity correlation, vanishes. However, if D is small, as in a glass, the true velocity correlation may be well represented by one with $D = 0$. In addition, they speculated that the number of Im $-\omega$ might be correlated with D, as both vanish in the harmonic case.

Developing a theory of transport coefficients, for example, D or the shear viscosity η, in supercooled, glass-forming liquids [2] is an outstanding problem in physical chemistry. The dynamic range between room temperature and the glass transition is approximately 15 decades! Both theory and simulation become problematic below the mode-coupling [3] temperature, T_c, where D extrapolates to zero from above, and relaxation has slowed by typically 3 to 4 decades from room temperature. Rereading Rahman et al. in 1988,

it appeared to me [4–6] that the unstable modes were an interesting, novel basis for a theory of transport, and my students and I subsequently spent considerable effort developing the idea. In this work, the Im $-\omega$ are employed with no reference to harmonic dynamics. Later, I realized that LaViolette and Stillinger [7] had discussed the number of unstable modes as an indicator of melting in 1985.

Diffusion is now routinely described in terms of the unstable instantaneous normal modes (INM), as the normal modes of snapshot, nonminimum configurations have [8] come to be named. More generally, liquids at low temperature are described [9, 10] in terms of the potential energy landscape (PEL), the topology of the total potential energy, $U(\boldsymbol{r})$, regarded as a surface over the $3N$ coordinates of a system of N atoms. The stationary points of order K are important "waypoints" on the landscape. Minima have $K = 0$, ordinary transition states have $K = 1$, and $K > 1$ corresponds to higher-order saddles. Reaction pathways for diffusion lead from minima to transition states, and thence to connected neighbor minima.

A Kth order stationary point has K unstable modes, establishing the intimate connection between the PEL and the unstable INM. The connection extends to diffusion. For example, in a low temperature "hopping" mechanism, the system spends long periods near a local minimum, with occasional activated passages over transition states to neighbor minima. Obviously the activation is signaled by the presence of an Im $-\omega$, where there had been none, and it might be hoped that the number of Im $-\omega$ could express the frequency of barrier crossing, and thence diffusion. There is no reason why the same ideas could not be applied to other aspects of dynamics, but so far the focus has been on diffusion, and the discussion here will maintain that priority. Furthermore, we will consider classical diffusion only, although the importance of the transition states, and hence Im $-\omega$, must hold for the quantum case as well.

In general, dynamical problems are more difficult than equilibrium problems. A central aim of nonequilibrium statistical mechanics is to express dynamics in terms of equilibrium averages. Most static (thermodynamic) averages at low temperature are dominated by contributions of configurations near the minima. Dynamics, however, is determined by the reaction pathways, transition states, and barriers on the PEL. How [11] can such information be found in a static average reflecting properties of the minima? The most fundamentally important aspect of the INM theory of diffusion is that, despite the obvious dynamical association, *unstable mode properties are static averages that get no contributions from the minima by construction*.

In the following, I will describe the current state of the connection between imaginary frequency, unstable modes, and relaxation dynamics in liquids. The basic idea that D can be expressed with the unstable modes has stood up to the most rigorous analysis. However, despite the efforts of many groups, there is no agreement on a single definitive theory of the underlying physics. Much remains to be done.

13.2 Unstable Modes and Diffusion

The INM are the eigenfunctions of the Hessian, the matrix of second derivatives of $U(\boldsymbol{r})$ with respect to the mass-weighed coordinates, evaluated at an instantaneous liquid configuration. The frequencies are the square roots of the eigenvalues. Away from a minimum (notably at a transition state) some of the modes are unstable. The fraction of unstable modes, denoted f_{u}, is a measure of anharmonicity, as is D; we will argue that these two anharmonic quantities are related.

The averaged distribution of unstable frequencies, or density of states, is denoted as $\langle \rho_{\mathrm{u}}(\omega) \rangle$. In plotting the full (Re and Im frequencies) density of states, the Im $-\ \omega$ are conventionally represented as negative-ω, and the distribution is normalized to unity. One may do the same for translational, rotational, etc. densities of states. Here we will simply use positive ω, with the understanding that it means $|\omega|$. Then the integral of $\langle \rho_{\mathrm{u}}(\omega) \rangle$ equals f_{u}.

For molecules one might calculate, by an appropriate projection method [12], the fraction of unstable translational modes out of all translational modes, since D is a property of center-of-mass translation. As a consequence of being calculated away from a minimum, the INM depend [13] upon the choice of coordinates. The question of the optimal choice remains unresolved. In the following, we will assume that atomic Cartesian coordinates are adequate for molecular systems.

Motion in most of the $3N$ directions on the PEL is impossible, with a sharp increase in U as molecules repel in the densely packed liquid. Unstable directions with downward curvature of U are special and lie along the reaction pathways for diffusion. La Nave et al. [14–16], have argued very simply, that diffusion occurs in a $3Nf_{\mathrm{u}}$-dimensional subspace of the $3N$-dimensional PEL, which indeed predicts $D \propto f_{\mathrm{u}}$, regardless of the details.

A detailed INM theory of D requires three steps:

1. A theory of $\langle \rho_{\mathrm{u}}(\omega) \rangle$ or f_{u}
2. A related theory of D
3. Consequent establishment of the connection between D and the unstable modes

Step 1 allows deduction of PEL properties, a subject of interest in its own right, by interpreting simulated $\langle \rho_{\mathrm{u}}(\omega) \rangle$ with the theory. In [5,10], a statistical–mechanical theory based upon the stationary points of the PEL, it is not necessary to calculate the Hessian for some applications. The instantaneous configuration may be mapped to, or associated with, the nearest stationary point. The order, K, is equal to the number of unstable modes, and $f_{\mathrm{u}} = \langle K \rangle / 3N$.

Because of the roughness and complexity of the PEL, "nondiffusive" Im $-\omega$ [5] exist, which are absent from tractable models and have nothing to do with

diffusion. At this point it is desirable to clarify some terminology and basic concepts. A truly harmonic system has no diffusion and no Im $-\omega$. Note that a parabolic barrier is sometimes called harmonic, but in the present context upward curvature, for confinement, is implied. The presence of some types of anharmonicity, for example, through the functional form of a smooth confining potential, need not change the situation. Another type of anharmonicity, for example, a "bump" on the surface of a global well, will introduce Im$-\omega$ but maintain $D = 0$; this constitutes a nondiffusive mode. Transition states on the PEL are physically linked to diffusion, represent strong anharmonicity, and possess Im $-\omega$. A theory of D should be based upon modes associated with the transition states or reaction coordinates for diffusion — not the "bumps."

Consequently, there is a very important additional step 4 "diffusive" unstable modes must be extracted from numerically determined $\langle \rho_{\rm u}(\omega) \rangle$, for input to the theories. We now describe two approaches to Steps 1 to 3, and the matter of the nondiffusive modes will be addressed in the next section.

13.2.1 Statistical Mechanics on the PEL

Stillinger et al. [10, 17] observed that any liquid configuration may be mapped to a local minimum of the PEL, named inherent structure (IS) with energy $U_{\rm m}$, by steepest descent minimization. Correspondingly, each minimum has a basin of attraction; the landscape is composed of the basins. They further suggested that the canonical configurational integral be written as a sum of the contributions of the basins. The partition function, Q, is then fully described by the distribution in energy, $\Omega(U_{\rm m})$, of the IS and by the averaged basin-constrained partition function, $\langle Q_{\rm m}(U_{\rm m}, T) \rangle$, for basins with $U_{\rm m}$ (used as the zero of energy)

$$Q(T) = \int dU_{\rm m} \Omega(U_{\rm m}) \langle Q_{\rm m}(U_{\rm m}, T) \rangle {\rm e}^{-\beta U_{\rm m}} \tag{13.1}$$

where $\beta = 1/k_{\rm B}T$. The vibrational free energy, $A_{\rm vib}(U_{\rm m}, T)$, is defined by the relation, $\langle Q_{\rm m}(U_{\rm m}, T) \rangle \equiv \exp(-\beta A_{\rm vib}(U_{\rm m}, T))$. The volume, V, or density, ρ, dependence of significant quantities in the canonical ensemble, is left implicit.

13.2.1.1 The Partition Function and the Im $-\omega$ *Density of States*

To facilitate a theory of the unstable modes, we [5] proposed that the PEL be partitioned into the basins of all the stationary points, not just the minima. Here we further develop that idea. A basin defined by the Stillinger IS-mapping can be further decomposed into subbasins with the stationary point mapping [18–20]. The basin-constrained $Q_{\rm m}$, for a particular minimum, is then itself a sum

$$Q_{\rm m} = Q_{\rm mm} + \sum_{\rm s \in m} Q'_{\rm ms} {\rm e}^{-\beta(U_{\rm s} - U_{\rm m})} \tag{13.2}$$

where $Q_{\rm mm}$ or $Q'_{\rm ms}$ is calculated in the subbasin belonging to the minimum or to the saddle s.

The basin of attraction of a saddle will overlap several IS-basins; the basin of a one dimension transition state forms subbasins in the IS-basins of the minima to the left and to the right. Thus we write

$$Q'_{\rm ms} = \frac{1}{m(s)} Q_{\rm ms} \tag{13.3}$$

where $m(s)$ is the number of minima whose basins "share" the saddle, and $Q_{\rm ms}$ is calculated in the entire basin of the saddle, not just the subbasin it forms with the IS-basin of a particular minimum. Then,

$$Q(T) = Q_{\rm m}(T) + Q_{\rm s}(T) = \int dU_{\rm m} \Omega(U_{\rm m}) {\rm e}^{-\beta U_{\rm m}} [\langle Q_{\rm mm}(U_{\rm m}, T)\rangle + S'(U_{\rm m}, T)] \tag{13.4}$$

where $S'(U_{\rm m}, T)$ is the saddle sum averaged over basins with minimum energy near $U_{\rm m}$

$$S'(U_{\rm m}, T) = \left\langle \sum_{\rm s\in m} \frac{1}{m(s)} Q_{\rm ms} {\rm e}^{-\beta \Delta U_{\rm s}} \right\rangle (U_{\rm m}, T) \tag{13.5}$$

and $\Delta U_{\rm s} = U_{\rm s} - U_{\rm m}$.

With the saddles introduced explicitly a useful approximation to the density of states may be written down immediately. Writing both $f_{\rm u}(T)$ and $\langle \rho_{\rm u}(\omega, T)\rangle$ in the form

$$X(T) = \int dU_{\rm m} \Omega(U_{\rm m}) {\rm e}^{-\beta U_{\rm m}} \bar{X}(U_{\rm m}, T)/Q(T) \tag{13.6}$$

we have

$$\langle \bar{\rho}_{\rm u}(\omega, U_{\rm m}, T)\rangle = \left\langle \sum_{\rm s\in m} \frac{1}{3Nm(s)} Q_{\rm ms} {\rm e}^{-\beta \Delta U_{\rm s}} \rho_{\rm u,s}(\omega) \right\rangle (U_{\rm m}, T) \tag{13.7}$$

where $\rho_{\rm u,s}(\omega)$ is the nonnormalized distribution of unstable frequencies for a particular saddle, s; its integral is $K_{\rm s}$, so

$$\bar{f}_{\rm u}(U_{\rm m}, T) = \left\langle \sum_{\rm s\in m} \frac{K_{\rm s}}{3Nm(s)} Q_{\rm ms} {\rm e}^{-\beta \Delta U_{\rm s}} \right\rangle (U_{\rm m}, T) \tag{13.8}$$

To put the focus on frequency, we introduce the total distribution of unstable frequencies of all the saddles associated with a minimum,

$$n_{\rm m}(\omega) = \sum_{\rm s\in m} \rho_{{\rm u},s}(\omega) \tag{13.9}$$

which integrates to $\sum_{s\in m} K_s$. Then

$$\langle \bar{\rho}_u(\omega, U_m, T)\rangle = \left\langle \frac{1}{3Nm(s)} Q_{ms} e^{-\beta \Delta U_s} \right\rangle (\omega, U_m, T)\langle n_m(\omega, U_m)\rangle \tag{13.10}$$

For a single minimum, the contribution of a particular saddle to the frequency-dependent average of saddle quantities is weighted, at a particular ω, by the value of $\rho_{u,s}(\omega)$. An average over minima with values near U_m is also taken. We have assumed that the average over minima of the product of $n_m(\omega)$ with the frequency-dependent saddle average may be factorized. As discussed in Section 13.2.1.4, the number of saddles connected to a minimum diverges in the thermodynamic limit and each quantity becomes self-averaging. Furthermore, different functions $\rho_{u,s}(\omega)$ will be found for different configurations within the domain of a single saddle. In $d = 1$, the single unstable frequency decreases to zero from its value at the transition state as the inflection point, the border of the saddle basin, is approached. Thus, we regard $\rho_{u,s}(\omega)$ as a best representation of the entire saddle basin.

In the same spirit, note that extracting a mean, effective saddle order from the sum in Equation (13.8) leaves the same sum, S' (Equation [13.5]), that enters the partition function,

$$\bar{f}_u(U_m, T) = \frac{K^e(U_m, T)}{3N} S'(U_m, T) \tag{13.11}$$

Thus, we define a frequency-dependent saddle sum

$$S'(\omega, U_m, T) = \left\langle \frac{1}{m(s)} Q_{ms} e^{-\beta \Delta U_s} \right\rangle (\omega, U_m, T) \frac{1}{K^e(U_m, T)} \langle n_m(\omega, U_m)\rangle \tag{13.12}$$

such that $S'(U_m, T) = \int d\omega S'(\omega, U_m, T)$, and so

$$\langle \bar{\rho}_u(\omega, U_m, T)\rangle = \frac{K^e(U_m, T)}{3N} S'(\omega, U_m, T) \tag{13.13}$$

In the thermodynamic limit the most probable IS energy, denoted $U_m(T)$, dominates all the U_m-integrals. Putting everything together yields

$$Q(T) = Q_m(T)(1 + S(T)) \tag{13.14}$$

$$\langle \rho_u(\omega, T)\rangle = \frac{K^e(T)}{3N} S(\omega, T)/(1 + S(T)) \tag{13.15}$$

where

$$S(\omega, T) = S'(\omega, T)/Q_m(T) \tag{13.16}$$

$S(T) = \int d\omega S(\omega, T)$, and for a function of both U_m and T, $f(T) = f(U_m(T), T)$; we have dropped the angle brackets on the Q. Finally, integrating

Equation (13.15) and eliminating S in terms of f_u

$$\langle \rho_u(\omega, T) \rangle = (K^e(T)/3N) - (f_u(T))S(\omega, T) \tag{13.17}$$

The maximum value of f_u is $K^e(T)/3N$, attained when the system is always near a saddle. It is important to distinguish between K^e, which is an average over saddles only in the saddle sum, and $\langle K \rangle$, the average order of the stationary point to which the thermal configuration maps, including $K = 0$ minima; $K^e > \langle K \rangle$.

The above represents an attempt at a somewhat more careful derivation of the unstable density of states than the one in Reference 6. There we proposed the "equivalent minima model," in which the connected saddle sum S', the number of connected saddles $s(m)$, and the partition function for a minimum subdomain Q_{mm} are independent of m. That is, the local landscape looks the same from all minima. In addition, we let all saddles have the same K and $m(s)$, and a given saddle have the same ω for all unstable directions. Then a saddle may be indexed by its unique ω, and Equations (13.14) to (13.16) immediately reduce to their counterparts in Reference [5] — indeed we have deliberately put them in the same form. The quantity $\langle n_m(\omega, T) \rangle / \langle K(T) \rangle$ becomes $n(\omega)$ from Reference 5, the distribution in frequency of saddles, normalized to $s(m)$.

The central role of the saddle sum, S, emphasizes the intimate connection between unstable modes and the saddles on the PEL. Observing an unstable mode with frequency ω requires that the one-dimensional coordinate exists on the PEL, expressed by $\langle n_m(\omega) \rangle$, and that the system visits the saddle to which it belongs, largely governed by $\langle (1/m(s)) Q_{ms} e^{-\beta \Delta U_s} \rangle (\omega, T)/Q_m(T)$; these are the components of S.

13.2.1.2 The Composite Landscape

It is difficult to make much progress with the PEL viewpoint without recognizing the *composite* nature of the landscape. Correlations in liquids are short ranged, except near the critical point or possibly the glass transition. However, in the $3N$-dimensional configuration space, every displacement in principle involves motions of all the atoms, which might appear to imply high collectivity. The way out of this apparent contradiction is to recognize that the liquid may be regarded [21] as a collection of N_r weakly interacting local regions containing $z \sim O(1)$ atom each, with well defined local landscapes.

The stationary points of the PEL are built-up [5] from the local states — this is explicit in the [22, 23] random energy model. The entire system changes its state when a region changes its local state [17], so IS transitions involve small numbers of neighbor molecules. A simple, useful viewpoint is that a Kth order saddle arises when K local regions are on local first-order saddles. Consequently, $\langle K \rangle, K^e \sim O(N)$, and [5, 19, 20, 24], the energy spacing of saddles of adjacent order is characteristic of the activation energy of a single local region. From Equation (13.15), it is seen that the former condition is required to have $\langle \rho_u(\omega) \rangle$ an intensive quantity.

Thinking in terms of the PEL without the composite picture, one might imagine that there are large fluctuations in the number of Im $-\omega$ associated with the IS transitions. However, with many local regions independently moving from minimum to saddle to minimum, it is seen that the fluctuations become negligible as usual for large N_r.

A simple alternative to working out the combinatorics of the composite landscape, which we will follow, is to assume that $\langle \rho_u(\omega, T) \rangle$ may be calculated in a single local region. It is plausible that the dominant saddles in a local region are ordinary transition states, $K = 1$. Then replacing K_s in the saddle sum by a mean value is not an additional approximation. The results derived above still hold, with the substitutions $K^e = 1$, $N = z$, $m(s) = 2$, and $\langle n_m(\omega, T) \rangle / K^e(T) \to s(T) n(\omega, T)$, where $s(T) \sim O(1)$ is the averaged number of transition states connected to a minimum in a local region, and $n(\omega)$ is now the normalized distribution of their unstable frequencies. Then

$$\langle \rho_u(\omega, T) \rangle = \frac{1}{3z} S(\omega, T)/(1 + S(T)) \tag{13.18}$$

where

$$S(\omega, T) = \tfrac{1}{2} G(\omega, T) s(T) \langle n(\omega, T) \rangle / Q_m(T) \tag{13.19}$$

and

$$G(\omega, T) = \langle Q_{ms} e^{-\beta \Delta U_s} \rangle (\omega, T) \tag{13.20}$$

alternatively,

$$\langle \rho_u(\omega, T) \rangle = ((3z)^{-1} - f_u(T)) S(\omega, T) \tag{13.21}$$

13.2.1.3 The Functional Form of the Density of States

For sufficiently large T at constant density, the Boltzmann factor in $G(\omega, T)$ is equal to unity and the distribution of unstable frequencies and the basin-constrained saddle partition function take on the properties characteristic of the "top of the landscape" [25, 26]. Thus, the density of states has a high-T limiting form, $\langle \rho_u(\omega, T = \infty) \rangle$. As T is decreased, the Boltzmann factor will cut off the contributions of saddles with higher activation energy, and saddles with a given ω will acquire different Q_{ms}, changing the ω-dependence of $G(\omega, T)$ and hence that of $\langle \rho_u(\omega, T) \rangle$. Thus [27],

$$\langle \rho_u(\omega, T) \rangle = a(T) G(\omega, T) \langle \rho_u(\omega, T = \infty) \rangle \tag{13.22}$$

where all the ω-independent factors are swept into $a(T)$. We expect that, to a good approximation, G reflects the averaged Boltzmann factor.

Empirically, simulated densities of states are fit well [27] by the form

$$-\ln[\langle \rho_u(\omega, T) \rangle / \omega] = a_1(T) + (a_2 \omega^2 / T)^{a_3(T)} + f_\infty(\omega) \tag{13.23}$$

where f_∞ describes the high-T frequency dependence and a_2 is T-independent. The density of states contains an explicit factor of ω, removed on the left-hand side of Equation (13.23), arising from the Jacobian in the transformation from eigenvalues to frequencies (square root). In the theory, it is contained in $n(\omega)$.

With some high-T data for an estimate of $\langle \rho_u(\omega, T = \infty) \rangle$, which may be refined [27] iteratively, the coefficients are easily determined from simulation data. If the dominant T-dependence of the ω-dependence is indeed due to the Boltzmann factor, comparing the theory and the empirical function, a plausible estimate is

$$\ln[\langle e^{-\beta \Delta U_s} \rangle(\omega, T)] = -(a_2 \omega^2 / T)^{a_3(T)} \tag{13.24}$$

In principle, Equation (13.24) contains a large amount of information about the microscopic barriers on the PEL. If barrier height fluctuations are small, $\ln[\langle e^{-\beta \Delta U_s} \rangle(\omega, T)] = -\beta \langle \Delta U_s(\omega, T) \rangle$. Further assuming that $\langle \Delta U_s(\omega, T) \rangle = c_1(T) + c_2 \omega^2$, corresponding to a simple $d = 1$ model with larger curvature corresponding to higher barriers, and c_1 being the energy above the minimum at the inflection point where $\omega = 0$, one obtains $a_3 = 1$. In fact, this is the case in unit-density Lennard–Jones (LJ) above the melting point [28], and approximately [29] for the [30] center-of-mass modes, which we have proposed as diffusive in supercooled CS_2. The exponent a_3 rises to ≈ 2 as T falls below T_c in unit-density LJ, and we have interpreted this [27] in terms of growing roughness (barrier height fluctuations) on the lower regions of the PEL. The crossover of a_3 from 1 to 2 was also found [31] in molten salts.

A calculation [32] of the averaged distribution of unstable frequencies in the $d = 1$ soft potential model indeed yields $a_3 = 1$ at high T and $a_3 = 2$ as $T \to 0$. The two limiting behaviors are associated with low and high local stress, with symmetric and asymmetric potential energy profiles along the reaction coordinates, respectively. A linear combination of the corresponding two terms is [33] a good alternative to Equation (13.23) as a fit to simulation data at all T.

We argued [6] that analysis of $f_u(T)$ could reveal the distribution of barrier heights, and obtained plausible results in unit-density LJ. A related approach was given by Straub and Thirumalai [34] and applied to biomolecules. It would be a wonderful development if vital PEL information, intimately tied to dynamics, could be reliably deduced from normal mode analysis. The analysis needs to be repeated with all diffusive modes, however. Our simple idealizations are not capable of interpreting data influenced by nondiffusive modes.

13.2.1.4 The Escape Rate and D

The self-diffusion coefficient is influenced by the global structure of the PEL. However, simple local relations between $D(T)$ and $R(T)$, the averaged rate of escape of the system from a basin, are worth exploring. The "IS Markov

approximation" [35, 36], $D(T) = \langle(\delta R)^2\rangle R(T)/6N$, where $\langle(\delta R)^2\rangle$ is the mean-square displacement of successive IS, is quantitatively accurate below T_c in the unit-density LJ liquid. This makes sense because the dynamical mechanism below T_c is expected to be long stays in the basins with infrequent transitions, so memory of earlier transitions is lost. An alternative [37], based on the idea that a transition randomizes the velocity correlation, gives $D/T \propto \langle\omega_m^{-2}\rangle R_{loc}$ at low T, where R_{loc} is calculated for a single local region. The entire system rate is extensive and $\langle(\delta R)^2\rangle$ is $\sim O(1)$ because only the molecules in one local region move in a transition. In the composite picture, R_{loc} is intensive and $R(T) = N_r R_{loc}(T)$. Either way, D is intensive.

In low-dimensional models involving motion among sites (analogous to IS) with widely varying properties there are large differences between the mean escape rate and the inverse mean waiting time. However, because a minimum must be connected to saddles corresponding to rearrangements in all N_r local regions, the number of saddles connected to a minimum diverges in the thermodynamic limit. The mean waiting time in a specific IS is then equal [23] to the inverse of a self-averaging sum over $s(m)$ contributions, which is just the averaged rate. That is, rate and inverse time are equivalent in $3N$ dimensions. We now calculate $R(T)$ in a way that emphasizes its connection to $\langle\rho_u(\omega, T)\rangle$.

Barrier crossing has been extensively studied in one dimension. The rate, denoted r, of crossing a specific barrier is conveniently referred [38] to the transition state theory expression with the correction factor κ

$$r = \kappa(\omega_s)\left(\frac{\omega_m}{2\pi}\right)e^{-\beta\Delta U_s} \tag{13.25}$$

where ω_m and ω_s are the normal mode frequencies for the reaction coordinate evaluated at the minimum and at the transition state, respectively. For one-dimensional reaction coordinates in higher dimensions, one must multiply by the cross section at the barrier top and divide by the cross section at the minimum. The cross sections are essentially the contributions to the configurational integral of the perpendicular degrees of freedom, and express the entropic effects. Multiplying and dividing by the lengths which give the contribution of the reaction coordinate itself, and noting that the momentum integrals in Q are the same for minimum and saddle, the rate is seen to contain the basin-constrained partition functions,

$$r = \frac{\ell_m Q_{ms}}{\ell_s Q_{mm}}\kappa(\omega_s)\left(\frac{\omega_m}{2\pi}\right)e^{-\beta\Delta U_s} \tag{13.26}$$

The harmonic approximation is very useful for stable coordinates, $\ell_m = (2\pi k_B T/m_e\omega_m^2)^{1/2}$, where m_e is an effective mass.

Consistent with the calculation of $\langle\rho_u(\omega)\rangle$ we are considering local regions with first-order saddles, in which case a single ω suffices for a saddle index. The total local rate R_{loc}, the sum of the contributions of all the connected

transition states, may be expressed as a frequency integral. Then, using the harmonic ℓ_m and invoking the dominance of the most probable IS energy, the fully averaged rate is

$$R(T) = N_r(k_B T/2\pi m_e)^{1/2} \int d\omega \frac{\kappa(\omega)}{\ell_s(\omega)} G(\omega, T) s(T) \langle n(\omega, T)\rangle / Q_m(T) \quad (13.27)$$

The crucial observation is that the PEL quantities in Equation (13.27) are those entering $S(\omega, T)$, which determines $\langle \rho_u(\omega)\rangle$. Using Equations (13.18) to (13.21) and multiplying and dividing by f_u to obtain a normalized distribution of unstable frequencies we find

$$R(T) = N_r \frac{(2k_B T/\pi m_e)^{1/2}}{((3z)^{-1} - f_u(T))} \left[\int d\omega \frac{\kappa(\omega)}{\ell_s(\omega)} (\langle \rho_u(\omega)\rangle / f_u) \right] f_u \quad (13.28)$$

Equation (13.28) involves several approximations, and it is still not clear what to use for κ and ℓ_s. Previously [29] we have considered transition state theory ($\kappa = 1$) and the low-friction limit of Kramers theory. Little is known about ℓ_s. We tried [29] simply applying the harmonic formula for stable modes, although there is no justification. There is no natural cutoff to the integral over an unstable degree of freedom and the extent of the saddle region should enter.

The essential observations for the exploitation of Equation (13.28) are as follows. In supercooled liquids Arrhenius or "super (stronger than)-Arrhenius" [10] T-dependence of transport coefficients swamps any weak, for example, power law, behavior. Everything multiplying the integral has weak T-dependence if $3z f_u \ll 1$, which is so in the interesting low-T regime. The ratio, $\kappa(\omega)/\ell_s(\omega)$, will be some low power of ω times additional explicit and implicit weak functions of T. Once constants are taken out, the integral in the square brackets will be given by a low moment of the normalized unstable distribution, for example, $\langle \omega_u \rangle$, which is also weakly T-dependent. Thus the strong $\boldsymbol{T}$-dependence of the escape rate, which will dominate over a broad dynamic range as in supercooled liquids, is determined by the unstable fraction $\boldsymbol{f_u}$.

Further approximations are required to obtain D. The IS-Markov approximation yields

$$D(T) = \frac{\langle (\delta R)^2 \rangle (k_B T/2\pi m_e)^{1/2}}{(1 - 3z f_u(T))} \left[\int d\omega \frac{\kappa(\omega)}{\ell_s(\omega)} (\langle \rho_u(\omega)\rangle / f_u) \right] f_u \quad (13.29)$$

and the strong T-dependence of D is that of f_u.

Other linear [37] relations $D(R)$ will modify the details but not this fundamental conclusion. Nonlinear relations [39] confirm the crucial role of f_u, but allow D to have a significantly different strong T-dependence. Above T_c weak T-dependence such as that found in simple kinetic theories is important. The approach of Reference 37 does a remarkable job [40] of describing

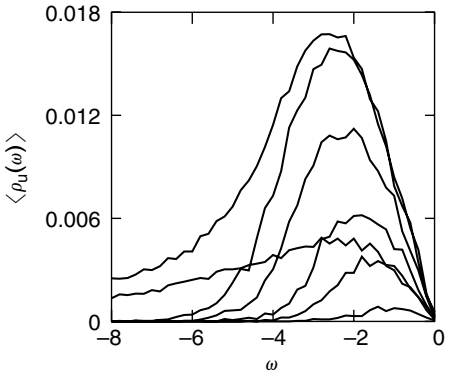

FIGURE 13.1
Center-of-mass and projected translational unstable densities of states vs. ω (psec^{-1}) for CS_2, $P = 1$ atm. Two projected densities, with distinctive broad high-$(-\omega)$ tails extending beyond the left boundary of the figure, are shown for 298 (top) and 135 K. The narrower COM densities, top to bottom, are 298, 244, 193, 165, and 135 K.

unit-density LJ from below T_c to very hot (melting is $T_m \approx 1.8$ reduced LJ units) $T = 20$. Any attempt to describe $T > T_c$ must consider that, at constant density, both D/T and f_u reach constant plateau values at high T. Thus, for example, $D/T \propto f_u$ is a plausible relation while $D \propto f_u$ is not, although both are essentially equivalent in the deeply supercooled regime.

The directions that lead from a minimum to a transition state, the reaction pathways for diffusion, have a special role in diffusion. Observing an Im $-\omega$ depends both on the existence of these directions, and the probability that the system visit them, expressed by the saddle sum S. This is the physical reason behind the connection of D and f_u. The argument works even in the entropic transport case, $\exp(-\beta \Delta U_s) \approx 1$, where a discussion of energy barrier crossing makes no sense — the system must nonetheless visit the "zero barrier" reaction pathways both to exhibit unstable modes and to diffuse.

Perhaps the most comprehensive test [29] of our basic idea is a simulation study of seven densities and eight temperatures of normal and supercooled liquid CS_2, covering almost three decades of D. For a molecular system, diffusive translational modes must be somehow defined. As will be discussed in Section 13.3, both of these aims are well met by analyzing a Hessian of center-of-mass derivatives only. Figure 13.1 shows how simply projecting onto a translation leaves a broad, weakly T-dependent nondiffusive tail, while the center-of-mass modes lack the tail and vanish beautifully with decreasing T.

We first tried $D(T, \rho) = c(\rho) f_u(T, \rho)$ and $D(T, \rho) = c'(\rho) \langle \omega_u(T, \rho) \rangle f_u(T, \rho)$, the latter being approximately derived [29] from low-friction Kramers theory. Both gave excellent fits, with the latter being slightly better at the normal freezing density, 1.46 g/cc, and the two lower densities, and vice versa for the four higher densities. Nevertheless, as T decreases $\langle \omega_u \rangle$ becomes virtually constant, with the two formulae equivalent, and $D(T, \rho) =$

TABLE 13.1

Parameters in Equations (13.30) and (13.31).

ρ (g/cc)	1.42	1.44	1.46	1.485	1.51	1.534	1.55
α	1.012	1.009	0.990	0.919	0.905	0.907	0.905
c''	1.11	1.19	1.20	1.02	0.98	1.19	1.19
γ	0.981	0.962	0.945	0.914	0.908	0.878	0.878

$c'(\rho)\langle\omega_u(T,\rho)\rangle f_u(T,\rho)$ is the best overall description. We investigated the possibility of a nonlinear relation $D(f_u)$ with a third fit

$$D(T,\rho) = c''(\rho)(\langle\omega_u(T,\rho)\rangle f_u(T,\rho))^{\alpha} \tag{13.30}$$

which gave both $\alpha \approx 1$ and, for D in Å/psec, $c'' \approx 1$; thus we also considered

$$D(T,\rho) = (\langle\omega_u(T,\rho)\rangle f_u(T,\rho))^{\gamma} \tag{13.31}$$

The results of the fitting are shown in Table 13.1. The best representation $D(f_u)$ is very close to linear. It is remarkable that Equation (13.31), with no multiplicative constant and a single parameter, provides a nearly quantitative description of diffusion. The quality of the unstable mode theory can be seen in a master plot of $\ln(D)$ vs. $\langle\omega_u\rangle f_u$ for all 56 data points in Figure 13.2. Clearly for the entire temperature and density range, determining the *static* average $\langle\rho_u(\omega)\rangle$ is a viable alternative to the *dynamic* calculation of the mean-square displacement. This validates the basic theoretical idea and is a significant point for the ongoing challenge of simulating deeply supercooled liquids, where dynamics is much more difficult than statics. Since $f_u(T)$ is the frequency integral of $\langle\rho_u(\omega,T)\rangle$, its functional form (Section 13.2.1.3) allows a PEL interpretation of the T-dependence of D, another outstanding question.

13.2.2 The Random Energy Model

Unstable modes and dynamics are conveniently analyzed within a random energy model (REM) of liquids [5, 22, 23], which provides a detailed realization of the composite landscape. A simple analytic expression for f_u results, reducing the dependence of the theory upon computer simulation and numerical analysis. We proceed analogously to the protein REM of Bryngelson and Wolynes [41]. A local region has a ground state with fixed energy and ν excited states with random energies. Neighbor regions have a fixed interaction if they are both in the ground state and a random interaction otherwise. In this manner the states of the entire system, their energies, and their distribution $G(U)$ are built-up from local contributions. Varying basin-constrained

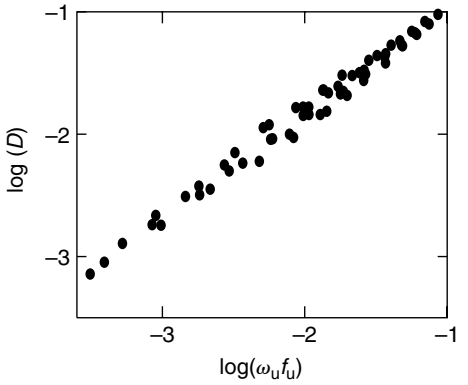

FIGURE 13.2
Log–log INM master plot for seven densities and eight temperatures of liquid CS_2.

partition functions have not been incorporated, so the statistical weight of a state is determined entirely by the Boltzmann factor. The REM is indeed a model, not an approximation to a formally exact starting point, and additional desired features must be put in by hand.

Assuming that dynamics consists of a series of local rearrangements, each state of the entire system might be connected to νN_r neighbors, the number reachable by a change in a single region. However, since not all pairs of states in a local region need be connected, we let [23] the number of connected neighbors, denoted N_{cn}, equal $c\nu N_r$, anticipating that the connectivity fraction $c < 1$.

13.2.2.1 The Fraction of Unstable Frequencies, Dynamics, and T_c

The states of the REM are identified with all the stationary points. This is a different viewpoint from that taken in the intuitive discussion of the composite landscape, where only minima entered. In Reference 41 it was suggested that a minimum is a REM state with all the connected neighbors at higher energy. We made [5] the obvious generalization that a Kth order stationary point has K neighbors with lower energy and $N_{cn} - K$ with higher energy. It is then easy to calculate f_u (so far there are no frequencies in the REM)

$$f_u(U) = p_c^<(U) = \int_{-\infty}^{U} dU' G_c(U'; U) \tag{13.32}$$

where $G_c(U'; U)$ is the energy distribution of states connected to a state with energy U. The fraction of unstable modes for states with energy U is equal to the probability, $p_c^<$, that a connected neighbor has a lower energy. In the thermodynamic limit, $f_u(T) = f_u(U(T))$.

With a physically motivated approximation to $G_c(U';U)$ we found [23]

$$f_u(T) = \frac{1}{2}\left(1 - erf\left(\frac{\delta}{2T}\right)\right) \overset{T\to 0}{\Longrightarrow} \frac{T}{\delta\sqrt{2\pi}} e^{-\delta^2/(4T^2)} \tag{13.33}$$

where $\delta \sim O(1)$ is the width of the distribution of local state random energies. Equation (13.33) exhibits super-Arrhenius behavior with activation energy $E_{act} = \delta^2/4T$. At high T, $f_u \to 1/2$, because at that point the thermal energy approaches the center of the symmetric Gaussian density of states where $p^< = p^> = 1/2$. The averaged saddle order obeys $\langle K\rangle = N_{cn} f_u$. The maximum possible order of an individual saddle is N_{cn}, while the maximum of the thermal average is $N_{cn}/2$. In a liquid the maximum order is the dimension of the configuration space, $3N$, but $N_{cn} = 3N(c\nu/3z) \leq 3N$. Thus, the REM incorporates a coarse-graining, expressed by the factor $(c\nu/3z)$, in that only directions that lead to new states are kept.

Making [41] a simple Metropolis *anzatz* for the rate of transitions among the states, and dividing R into contributions from neighbors with lower and higher energy, $R^<$ and $R^>$, one immediately sees that $R^< = R_0 N_{cn} f_u$, where R_0 is the baseline rate absent any barrier. There is no Boltzmann factor for a downward transition, and $N_{cn} f_u$ is simply the number of states with lower energy. This is the most transparent possible relation $R(f_u)$. More elaborate arguments yield $R^> \propto f_u$, and again we believe generally that $D \propto R$. Thus the REM provides a second derivation of the essential result, $D \propto f_u$.

Transitions among the minima do not provide a useful dynamical description above T_c, and it has been suggested [19, 20, 24] that one should consider "saddle dynamics." Since the REM states include the minima and the saddles, our second derivation may help explain why $D \propto f_u$ still holds above T_c, when D is no longer [35] proportional to the escape rate from the minima.

If T_c is the point where D extrapolates to zero from above and $D \propto f_u$, then [42] T_c may be determined from f_u. Careful analysis of Equation (13.33) yields [23] the estimate, $T_c \approx 0.26\delta$. Furthermore, it is seen that plotting $\langle K\rangle/N_{cn}$ vs. T/δ will allow data on different materials to be represented by a master curve; δ and N_{cn} are determined by fitting the number of diffusive unstable modes to N_{cn} times Equation (13.33). Figure 13.3 demonstrates the master plot for $\langle K\rangle$ in unit-density LJ and the number of center-of-mass modes for our seven densities of CS_2. The data collapse is essentially perfect above T_c. The calculated parameters are given in Table 13.2. With increasing density in CS_2, δ increases from 236 to 486 K. The maximum saddle order or number of connected neighbors is remarkably constant between the two materials and among the different densities. Correspondingly, the coarse-graining factor, $c\nu/3z = c\nu N_r/3N$, equals 0.21 for LJ and 0.23 to 0.22 for CS_2; about 20% of directions lead to new states.

Since $\delta \propto T_c$, a master curve is also predicted with use of the independent variable T/T_c. This has been verified very recently by Angelani et al. [43] for soft spheres with several power-law potentials.

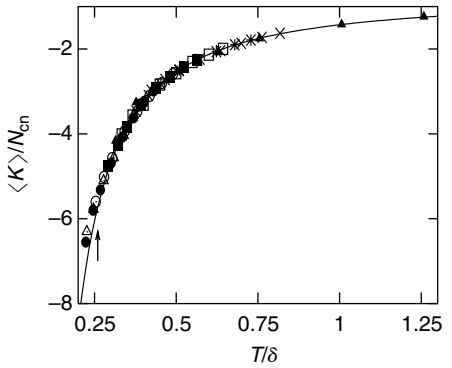

FIGURE 13.3
Natural log-linear REM/INM master curve of fractional saddle order $\langle K \rangle / N_{cn}$ and simulation data vs. dimensionless temperature T/δ , $N = 108$, unit-density LJ (solid triangles) and seven densities of CS_2. Arrow denotes T_c.

TABLE 13.2

Parameters for Master Plot.

Liquid	δ	N_{cn}	$cv/3z$	T_c
$LJ(1\ \text{atom}/\sigma^3)$	$1.59\ \epsilon$	66	0.21	0.41ϵ
CS_2(1.420 g/cc)	236 K	74	0.23	61 K
CS_2(1.440 g/cc)	265 K	71	0.22	69 K
CS_2(1.460 g/cc)	300 K	71	0.22	78 K
CS_2(1.485 g/cc)	343 K	71	0.22	89 K
CS_2(1.51 g/cc)	394 K	71	0.22	102 K
CS_2(1.534 g/cc)	448 K	71	0.22	116 K
CS_2(1.551 g/cc)	486 K	71	0.22	126 K

All systems are $N = 108$ and density is within parentheses.

For unit-density LJ the value $T_c = 0.41$ is in reasonable agreement with what we have published [44], 0.47, but somewhat lower. For CS_2, 1.46 g/cc, 78 K is very close to our estimate [45] of 75 K. However, the data that gave the original T_c are represented very accurately by Equation (13.33). The different T_c arise from fitting data over different temperature ranges. Fitting simulation data to Equation (13.33) and then using $T_c \approx 0.26\delta$ is a good way to obtain consistent T_c on different materials, from simulations covering different temperature ranges and densities.

13.2.2.2 The Configurational Entropy S_c

The configurational entropy is given by Boltzmann's equation, $S_c = k_B \ln(\Omega(T))$, where $\Omega(T)$ is the number of thermally accessible states. It is a static quantity, easily calculated from the unconditional distribution $G(U)$ in the REM, which is believed [21] relevant to dynamics in supercooled liquids.

It cannot be overemphasized that expressing dynamics in terms of statics is a primary goal of nonequilibrium statistical mechanics. Equation (13.32) provides a simple, intuitive way to understand how D and S_c are related. Roughly, the states with energy less than the thermal energy, which determine f_u and thus D, are also the accessible states. As T is decreased and most of the connected neighbor states lie above the thermal energy, both f_u and S_c decrease according to simple REM formulae.

Using our approximate connected neighbor distribution we found [23]

$$\ln(f_u(T)) = 0.65z(S_c(T)/N) - (1.16 + 0.65\ln(\nu)) \tag{13.34}$$

The linear relation between diffusive $\ln(f_u)$ and (S_c/N) had been earlier discovered in simulation studies of water [14, 15] and SiO_2 [16] by La Nave et al. [46]. The slopes (which were determined by fitting the data provided by Emelia La Nave) are 0.96, $z \approx 1.5$ and 16.2, $z \approx 25$, respectively [46]. The conclusion that silica is more collective than water is reasonable, but such a small z is puzzling for water. The theory is in a preliminary stage, but we now know how to begin interpreting the "La Nave plot."

13.3 Diffusive and Nondiffusive Unstable Modes

Tractable landscape models are simple, with unstable modes directly linked to the reaction pathways for diffusion. They cannot provide a literal representation of the PEL, which is rough and too complex to be visualized, with nondiffusive modes. As mentioned earlier, a bump on the surface of a multidimensional harmonic well is also a region of Im $-\omega$, obviously not related to diffusion. Consequently, the INM theories under discussion should not be directly compared to simulation. Our optimistic point of view is that one may proceed nevertheless by extracting *diffusive* unstable modes, regarded as arising from a PEL which has been simplified to the level of available theories. They should be representative of the regions close to the reaction pathways. Center-of-mass modes in CS_2 [29, 30] have already been mentioned, and now we discuss the matter of diffusive modes in general.

In 1993, we observed [5] that a substantial number of unstable modes persisted in the unit-density LJ crystal, where $D \approx 0$; these modes are obviously nondiffusive. The relation $D \propto f_u$ has too weak T-dependence, and does not show the drop to $\approx$0 upon solidification, although the discontinuity is substantial. We wrote: *We therefore suggest that the excess value Δf_u, the difference between f_u in the liquid and in the crystal, is a better indication of barrier crossing than is f_u itself. In other words, f_u in the crystal expresses anharmonicities in the minima, while f_u in the supercooled liquid contains the contributions of the anharmonicities plus that of barrier crossing. Thus, replacement of f_u with Δf_u should make our association of unstable modes with barrier crossing more correct.* The problem of the nondiffusive modes, and the appropriate way to deal with it, was part

of the agenda from the very beginning of INM theory. The original suggestion of employing Δf_u has not been much pursued, although it remains perfectly valid.

The density of states in Equation (13.23) contains explicit exponential T-dependence. After performing the ω integral to obtain f_u, however, only a power law remains. Arrhenius or super-Arrhenius T-dependence of D, an essential feature of supercooled liquids, might still be found in $\exp(-a_1(T))$, but such was not the case in unit-density LJ. Our second attempt to isolate the diffusive modes was to postulate [6] that they are the unstable modes with $|\omega|$ above a lower cutoff, denoted ω_c. Then, $D \propto \exp(-(a_2\omega_c^2/T)^{a_3(T)})$, further associating super-Arrhenius with $a_3 > 1$. The resulting f_u gave [6] a quantitative representation of D in unit-density LJ.

13.3.1 Potential Energy Profile Based Methods

By calculating the potential energy as the system is moved from the instantaneous configuration along an INM eigenfunction, one may calculate [47] a one-dimensional potential energy profile. The profiles may be categorized as single well (SW), double well (DW), and shoulder — a shoulder in a global single well. Stable modes are essentially pure SW, while unstable modes are of DW and shoulder type. A "three flavor" theory [48] results, replacing the two flavor version with Re $-$ ω and Im $-$ ω. Bembenek and Laird noted [49] that the DW, which naturally present a picture of barrier crossing, are obvious candidates for diffusive modes. The shoulders are obvious candidates for the aforementioned nondiffusive bumps. However, they also noted that, in unit-density LJ and in smooth spheres, the DW did not reproduce the strong T-dependence of D at low T.

Bembenek and Laird found that the DW modes exhibit a lower $|\omega|$ cutoff, validating our original hypothesis. Collectivity of the INM, that is, delocalization, is maximal as $|\omega| \to 0$, and minimal (local) at the high-$|\omega|$ extremes. They proposed that the delocalized DW modes are diffusive, and found them to vanish below a characteristic temperature identified with the glass transition; the proposal remains speculative. Analytic calculations in the soft potential model [32] verify the existence of the cutoff.

The success of first schemes for diffusive modes is material-dependent. Ribeiro and Madden [31] found that the DW modes were not notably superior to all the Im $-$ ω in molten salts; with no attempt to identify diffusive modes D is $\propto f_u$. While simply taking DW modes does not work very well in atomic liquids, or [48] CS_2, it provides a superb description of water. An additional translational projection is not even necessary, probably because strong coupling of translation and rotation makes them equivalent. With the DW, Sciortino and Tartaglia [42] obtained the same T_c as was found by analyzing diffusion data. La Nave et al. [14, 15] demonstrated a master plot of $\ln(D)$ vs. f_u, which collapsed data for six densities and five temperatures on a single curve; they also refined the INM estimate of T_c. This study, and ours [29] on

CS_2, are the two most rigorous tests extant of the relation of unstable modes and diffusion.

The excellence of the center-of-mass modes [29] for describing diffusion in CS_2, superior to the DW prescription, has already been mentioned. The rotations are highly anharmonic, in ways that have nothing to do with diffusion. However, projecting onto translation, or projecting the DW onto translation does not eliminate their contribution. A mode that is mainly a nondiffusive rotation still enters the density of states if it has any translational component, and corrupts the diffusive modes. Use of the center-of-mass Hessian eliminates the rotations from step one.

It is not surprising that the DW are more useful in some systems than in others — the surprise is that they are useful at all. The eigenfunctions used to calculate the one-dimensional profiles that classify the modes into the three flavors are calculated at the snapshot configuration. They are not updated as the atoms are moved, and quickly deviate from the true reaction pathways, with a strong increase in U as atoms are pushed close together in a dense liquid. Thus, [48, 50] only a small part of the profile near the origin is meaningful. A DW requires that the system start near the barrier top, so downward curvature in both directions will be apparent before the unphysical rise in U begins. Barrier heights estimated from the DW profiles are [48] too small, since the curves turn upward before the true minima are reached. Conversely, no profile that starts close to a minimum, with upward curvature in both directions, ever turns over to form a DW, as will happen for a reaction pathway.

It is thus seen that the flavors are really indicators of progress along the reaction pathway. DW and SW arise from normal coordinates along which the snapshot configuration is near a barrier top or near a minimum, respectively. Similar reasoning shows that shoulder modes result from bad reaction coordinates following when the snapshot is near an inflection point. Thus the lower cutoff on the DW is explained; if the system is near the inflection point, where $|\omega| = 0$, a shoulder mode, not a DW, is recorded.

With the new perspective, a different argument may be made that the DW are diffusive. The modes closest to the barrier tops best characterize the saddles, and give the directions in which the smallest displacement will lead to a new IS.

13.3.2 Landscape Based Methods

13.3.2.1 Escape Modes

In a simple scenario, minimizing configurations obtained by moving away from the top of a DW profile in both directions would lead to two different, connected neighbor IS. Gezelter et al. [51] showed that in some cases the same IS is found in both minimizations, and named the corresponding modes "false barriers." They used this observation to criticize the entire unstable mode approach to diffusion. Using it to find better diffusive modes was left

[15, 16, 52] to the Rome group, who defined the diffusive "escape" modes as the DW minus the false barriers.

In water D follows f_{esc} even better than f_{dw}. An essentially perfect representation of D is attained [15] by subtracting f_{esc}(ice), that is, the original suggestion [5] of Δf_u. Similarly good results are found [16] in silica, including reproduction of the fragile-to-strong transition. The good performance of the escape modes in two substances is significant and encouraging, given the patchwork of different schemes for different materials discussed so far.

In fitting D to a best power law, the results cited are $D \propto (f_{esc})^2$ in water [15] and $D/T \propto (f_{esc})^{1.3}$ in SiO_2 [16]. This nonlinearity could be due to effects described in [39] the generalized REM, or to the presence of weak T-dependence not expressed by f_{esc}. One immediately notes the appearance of D/T for SiO_2. In CS_2 with the center-of-mass modes we found $D \propto (\langle\omega_u\rangle f_u)^{1.0}$. However, leaving out the unstable frequency leads to a power of 1.4 at the lowest density. Attempting a representation of D/T would give a different power. The value of α is not meaningful unless enough decades are available to swamp the weak T-dependence.

13.3.2.2 Saddle Order

The minima of the squared gradient, $|\nabla U|^2$, include all the stationary points on the PEL, minima and saddles [19]. It has been pointed out [53] that the minima actually found in liquids are not usually true saddles (inflection points in $d = 1$). However, the "false saddles" have similar properties to the true saddles, so we regard all the minima of $|\nabla U|^2$ as generalized stationary points.

Just as minimization of U associates an instantaneous configuration with an IS, minimization of $|\nabla U|^2$ yields an associated generalized stationary point [19, 20]. It is then possible to calculate the averaged saddle order, $\langle K(T)\rangle$; dividing by $3N$ gives the fractional order, $\langle k(T)\rangle$, analogous to f_u. Since taking contributions to f_u from nearby saddles only can be regarded as simplifying the PEL, emphasizing features related to the reaction pathway and diffusion, $\langle k(T)\rangle$ is a plausible diffusive unstable fraction.

Investigations in "modified LJ" and in the binary LJ mixture [19, 20] have established that $\langle k(T)\rangle$ extrapolates to zero at the same temperature as that of D, that is, the static average $\langle k(T)\rangle$ may be analyzed to determine the dynamical T_c. One might further say [19, 20, 24] that the system occupies the borders of the IS basins on the PEL above T_c (K finite) and is close to the minima ($K \to 0$) below T_c.

13.3.2.3 Partial Minimization

Minimization algorithms proceed in a stepwise fashion, and any quantity calculated from the configuration may be evaluated as a function of the number of steps, n. We found [54] that the problematic unstable modes in the LJ crystal are removed by 3 to 4 steps, while unstable modes in the liquid, after an initial sharp drop, persist for tens of steps (Figure 13.4).

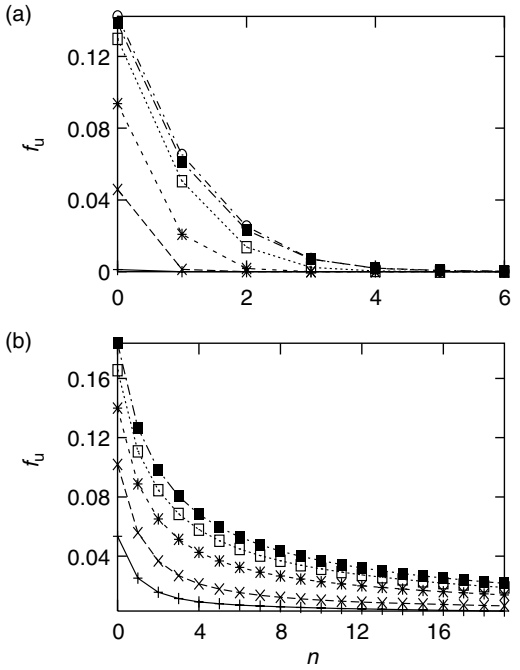

FIGURE 13.4
The fraction of imaginary frequency modes in unit-density LJ vs. the number n of conjugate gradient minimization steps for (a) the crystal ($T = 0.4$, 0.8, 1.2, 1.6, 1.7, and 1.75) and (b) the supercooled liquid ($T = 0.4$, 0.8, 1.2, 1.6, and 2.0), with T increasing from bottom to top.

If nondiffusive modes in the liquid are anything like those in the crystal it is clearly suggested that they are eliminated by the first few steps and one should seek a relation between D and $f_u(n), n \approx 3{-}4$. The value of n employed to represent D must include the sharp drop in nondiffusive Im $-\omega$ but avoid larger n where diffusive modes are removed as well. A systematic procedure is to fit $f_u(n)$ for the supercooled states to a double exponential, $f_u(n) = f_f * \exp(-k_f * n) + f_{dif} * \exp(-k_{dif} * n)$, to account for fast ($f$) nondiffusive and slow diffusive decay with n. The coefficient f_{dif}, represents the fraction of diffusive unstable modes.

Figure 13.5 shows $f_{dif}, f_u(3), f_u(4), D/T$, and [19, 24] $\langle k \rangle$ in unit-density LJ; liquid and crystal data are included. With most of the data from above T_c comparison with D/T is essential, so all quantities will have a high-T plateau. A superb representation of D/T, including vanishing in the crystal, is achieved with $f_u(3)$, $f_u(4)$, or f_{dif}; f_{dif} lies between $f_u(3)$ and $f_u(4)$, and is closer to $f_u(4)$. The saddle fraction falls below the others at the lowest T. Analysis of $D(T)$ gives $T_c = 0.48$. Values obtained from different calculations with $f_u(n)$ are $T_c(4) = 0.47$, $T_c(dif) = 0.46$, and (inset in Figure 13.5) $\lim_{n\to\infty} T_c(n) = 0.47$.

We believe that the PEL features that cause nondiffusive modes occur far from the reaction pathways and are associated with large gradients.

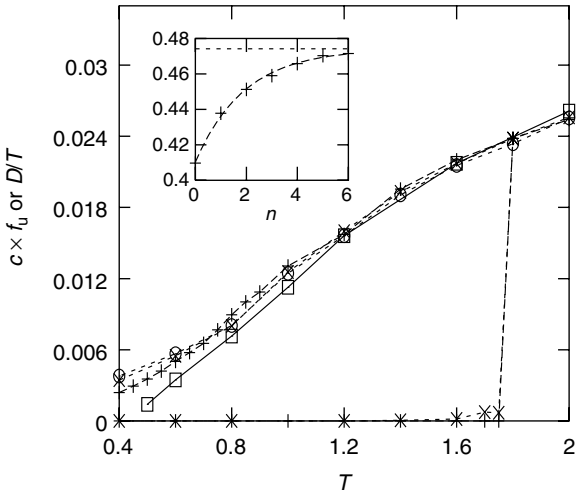

FIGURE 13.5
Comparison of $D/T(+)$, $0.34\, f_{\rm dif}$ ($\bigcirc$), $0.375 f_{\rm u}(4)$ ($\times$) (liquid and crystal) and $0.44\langle k\rangle$ ($\square$). Inset is the minimization-step number dependence of $T_{\rm c}^{\rm inm}(n)$.

By contrast, gradients along the reaction pathways are small or, as a transition state is approached, vanishing. Since minimization algorithms utilize the gradient, the first few steps act to quench the nondiffusive modes and bring the system close to a reaction pathway, while the subsequent steps approach a minimum along the pathway. Partial minimization simplifies the apparent landscape to a large extent such that the original one-dimensional idea linking D and $f_{\rm u}$ applies.

13.4 Summary and Conclusions

Our thesis is that the rate of slow relaxation in liquids is a function of the number, or fraction, of unstable modes. Focusing on diffusion, then, there is a relation $D(f_{\rm u}(T))$. Additional T-dependence, which clearly exists, is assumed to be weak in the sense of not influencing an Arrhenius plot covering several decades.

Three independent arguments, all invoking the intimate connection between unstable modes and reaction pathways on the PEL, lead to a linear relation:

1. A statistical mechanical theory of the unstable density of states, which is then seen to contain the information needed to express the rate of escape from a local minimum.

2. A dynamical random energy model of motions among saddles and minima in which a state with K neighbors of lower energy is a Kth order saddle.
3. A simple physical argument that for liquids diffusive motion in most directions is impossible, and the unstable eigenfunctions are the rare exceptions.

For 1 and 2 we must also argue that D is proportional to the rate of escape R. The three derivations cover both $T < T_c$ and $T > T_c$. Of course, there are many approximations and a nonlinear relation is also possible [39].

The best tests of the theory [14, 29] involve about three decades of D, with most of the data above T_c. Under these circumstances "weak" T-dependence is important. More fundamentally, a diffusive unstable fraction must be employed. Then, essentially perfect INM representations of D have been achieved. If a scheme for diffusive modes that is broadly applicable emerges from the current suggestions, one may hope to calculate D via an equilibrium (Monte Carlo) simulation in a liquid that is too slow for dynamical simulation (molecular dynamics). This would be the culmination of the entire enterprise.

The unstable density of states is a rich source of landscape information in its own right. It would be very interesting if the coefficient a_3 in Equation (13.23) could be interpreted in an unambiguous fashion. A crucial problem for the Stillinger thermodynamic formalism is evaluation of the anharmonic vibrational free energy. I am hopeful that the inherently anharmonic unstable modes can be used in that problem, leading to INM *thermodynamics*.

Acknowledgment

This work has been supported by the National Science Foundation.

References

1. A. Rahman, M. Mandell, and J.P. McTague, Molecular dynamics study of an amorphous Lennard–Jones system at low temperature, *J. Chem. Phys.* 64, 1564 (1976).
2. C. A. Angell, Formation of glasses from liquids and biopolymers, *Science* 267, 1924 (1995).
3. W. Goetze and L. Sjogren, Relaxation processes in supercooled liquids, *Rep. Prog. Phys.* 55, 241 (1992).
4. G. Seeley and T. Keyes, Normal mode analysis of liquid state dynamics, *J. Chem. Phys.* 91, 5581 (1989).
5. B. Madan and T. Keyes, Unstable modes in liquids: density of states, potential energy, and heat capacity, *J. Chem. Phys.* 98, 3342 (1993).

6. T. Keyes, Unstable modes in supercooled and normal liquids; density of states, energy barriers, and self diffusion, *J. Chem. Phys.* 101, 5081 (1994); T. Keyes, The instantaneous normal mode approach to liquid state dynamics, *J. Phys. Chem.* 101, 2921 (1997).
7. R. LaViolette and F. Stillinger, Multidimensional geometric aspects of the solid–liquid transition in simple substances, *J. Chem. Phys.* 83, 4079 (1985).
8. R.M. Stratt, The instantaneous normal modes of liquids, *Acc. Chem. Res.* 28, 201, (1995).
9. M. Goldstein, Viscous liquids and the glass transition: a potential energy barrier picture, *J. Chem. Phys.* 51, 3728 (1969).
10. F.H. Stillinger, A topographic view of supercooled liquids and glass formation, *Science* 267, 1935 (1995).
11. D. Kivelson, private communication.
12. P. Moore and T. Keyes, Normal mode analysis of liquid CS_2; velocity correlation functions and self diffusion constants, *J. Chem. Phys.* 100, 6709 (1994).
13. Wu-Xiong Li, T. Keyes, R. Murry, and J.T. Fourkas, Non-cartesian coordinates for instantaneous normal mode theory of atomic liquids, *J. Chem. Phys.* 109, 1096 (1998); R. Murry, J.T. Fourkas, Wu-Xiong Li, and T. Keyes, Molecular coordinates for instantaneous normal mode calculations. I. Coordinate dependence, *J. Chem. Phys.* 110, 10410 (1999); R. Murry, J.T. Fourkas, Wu-Xiong Li, and T. Keyes, Molecular coordinates for instantaneous normal mode calculations. II. Application to CS_2 and triatomics, *J. Chem. Phys.* 110, 10423 (1999).
14. E. La Nave, A. Scala, F. Starr, F. Sciortino, and H.E. Stanley, Instantaneous normal mode analysis of supercooled water, *Phys. Rev. Lett.* 84, 4605 (2000).
15. E. La Nave, A. Scala, F. Starr, H.E. Stanley, and F. Sciortino, Dynamics of supercooled water in configuration space, *Phys. Rev. E* 64, 036102 (2001).
16. E. La Nave, H.E. Stanley, and F. Sciortino, Configuration space connectivity across the fragile-to-strong transition in silica, *Phys. Rev. Lett.* 88, 035501 (2002).
17. F.H. Stillinger and T.A. Weber, Dynamics of structural transitions in liquids, *Phys. Rev. A* 28, 2408 (1983); F.H. Stillinger and T.A. Weber, Packing structures and transitions in liquids and solids, *Science* 228, 983 (1984).
18. F.H. Stillinger and T.A. Weber, Point defects in BCC crystals; structures, transition kinetics, and melting implications, *J. Chem. Phys.* 81, 5095 (1984).
19. L. Angelani, R. Di Leonardo, G. Ruocco, A. Scala, and F. Sciortino, Saddles in the energy landscape probed by supercooled liquids, *Phys. Rev. Lett.* 85, 5356 (2000).
20. K. Broderix, K.K. Bhattacharya, A. Cavagna, A. Zippelius, and I. Giardina, Energy landscape of a Lennard–Jones liquid: statistics of stationary points, *Phys. Rev. Lett.* 85, 5360 (2000).
21. G. Adam and J.H. Gibbs, On the temperature dependence of cooperative relaxation properties in glass-forming liquids, *J. Chem. Phys.* 43, 139 (1965).
22. T. Keyes, Entropy, dynamics and instantaneous normal modes in a random energy model, *Phys. Rev. E* 62, 7905 (2000).
23. T. Keyes, J. Chowdhary, and J. Kim, Random energy model for dynamics in supercooled liquids: N-dependence, *Phys. Rev. E* 66, 051110 (2002).
24. A. Cavagna, Fragile vs. strong liquids: a saddles ruled scenario, *Europhys. Lett.* 53, 490 (2001).
25. S. Sastry, P. Debenedetti, and F.H. Stillinger, Signatures of distinct dynamical regimes in the energy landscape of a glass-forming liquid, *Nature* 393, 554 (1998).

26. C.A. Angell, B. Richards, and V. Velikov, Simple glass forming liquids: their definitions, fragilities and landscape excitation profiles, *J. Phys. Condens. Matter* 11, A75 (1999).
27. T. Keyes, G. Vijayadamodar, and U. Zurcher, An instantaneous normal mode description of relaxation in supercooled liquids, *J. Chem. Phys.* 106, 4651 (1996).
28. G. Vijayadamodar and A. Nitzan, On the application of instantaneous normal mode analysis to long time dynamics of liquids, *J. Chem. Phys.* 103, 2169 (1995).
29. Wu-Xiong Li and T. Keyes, Instantaneous normal mode theory of diffusion and the potential energy landscape: application to supercooled liquid CS_2, *J. Chem. Phys.* 111, 5503 (1999).
30. Wu-Xiong Li and T. Keyes, Pure translation instantaneous normal modes: imaginary frequency contributions vanish at the glass transition in CS_2, *J. Chem. Phys.* 111, 5503 (1999).
31. M. Ribeiro and P.A. Madden, Unstable modes in ionic melts, *J. Chem. Phys.* 108, 3256 (1998).
32. U. Zurcher and T. Keyes, Anharmonic potentials in supercooled liquids: the soft-potential model, *Phys. Rev. E* 55, 6917 (1997).
33. U. Zurcher and T. Keyes, Soft modes in glass forming liquids; the role of local stress, p. 82, *Supercooled Liquids; Advances and Novel Applications* (American Chemical Society, 1997), book based on the Symposium on Supercooled Liquids, ACS National Meeting, Orlando, FL, 1996, ed., J.T. Fourkas.
34. J.E. Straub and D. Thirumalai, Exploring the energy landscape in proteins, *Proc. Natl Acad. Sci. USA* 90, 809 (1993); J.E. Straub and J. Choi, Extracting the energy barrier distribution of a disordered system from the instantaneous normal mode density of states: application to peptides and proteins, *J. Phys. Chem.* 98, 10987 (1994).
35. T. Keyes and J. Chowdhary, Inherent-structure dynamics and diffusion in liquids, *Phys. Rev. E* 64, 032201 (2001).
36. T. Keyes and J. Chowdhary, The potential energy landscape and mechanisms of diffusion in liquids, *Phys. Rev. E* 65, 041106 (2002).
37. R. Zwanzig, On the relation between self-diffusion and viscosity of liquids, *J. Chem. Phys.* 79, 4507 (1983).
38. J.E. Straub, M. Borkovec, and B.J. Berne, Non-Markovian activated rate processes: comparison of current theories with numerical simulation data, *J. Chem. Phys.* 84, 1788 (1986); J.E. Straub, M. Borkovec, and B.J. Berne, Numerical simulation of rate constants for a two degree of freedom system in the weak collision limit, *J. Chem. Phys.* 86, 4296 (1987).
39. M. Sasai, Energy landscape picture of supercooled liquids: application of a generalized random energy model, *J. Chem. Phys.* 118, 10651 (2003).
40. T. Keyes, Normal mode theory of diffusion in liquids for a broad temperature range, *J. Chem. Phys.* 103, 9810 (1995).
41. J. Bryngelson and P.G. Wolynes, Intermediates and barrier crossing in a random energy model (with applications to protein folding), *J. Phys. Chem.* 93, 6902 (1989).
42. F. Sciortino and P. Tartaglia, Harmonic dynamics in supercooled liquids: the case of water, *Phys. Rev. Lett.* 78, 2385 (1997).
43. L. Angelani, C. De Michele, G. Ruocco, and F. Sciortino, Saddles and softness in simple model liquids, *J. Chem. Phys.* 121, 7533 (2004).
44. J. Chowdhary and T. Keyes, Conjugate gradient filtering of instantaneous normal modes, saddles on the energy landscape, and diffusion in liquids, *Phys. Rev. E* 65, 026125 (2002).

45. J. Kim, T. Keyes, and W. Li, Probes of heterogeneity in rotational dynamics: application to supercooled liquid CS_2, *Phys. Rev. E* 67, 021506 (2003).
46. Emelia La Nave, private communication
47. R. Cotterill and J. Madsen, Localized fluidity modes and the topology of the constant potential-energy hypersurfaces of Lennard–Jones matter, *Phys. Rev. B* 33 262 (1986).
48. Wu-Xiong Li, T. Keyes, and F. Sciortino, Three-flavor instantaneous normal mode formalism: diffusion, harmonicity, and the potential energy landscape in CS_2, *J. Chem. Phys.* 108, 252 (1998).
49. S. Bembenek and B.B. Laird, Instantaneous normal modes and the glass transition, *Phys. Rev. Lett.* 74, 936 (1995).
50. M. Ribeiro and P.A. Madden, Instantaneous normal mode prediction for cation and anion diffusion, *J. Chem. Phys.* 106, 8616 (1997).
51. J. Gezelter, E. Rabani, and B. Berne, Can imaginary instantaneous normal mode frequencies predict barriers to self-diffusion? *J. Chem. Phys.* 107, 4618 (1997).
52. C. Donati, F. Sciortino, and P. Tartaglia, Role of the unstable directions in the equilibrium and aging dynamics of supercooled liquids, *Phys. Rev. Lett.* 85, 1464 (2000).
53. J. Doye and D. Wales, Saddle points and dynamics of Lennard–Jones clusters, solids, and supercooled liquids, *J. Chem. Phys.* 116, 3777 (2002).
54. J. Chowdhary and T. Keyes, Finding diffusive directions in supercooled liquids by partial minimization of the potential energy, *Physica A* 314, 575 (2002).

14

Driven Molecular Dynamics for Normal Modes of Biomolecules without the Hessian, and Beyond

Martina Kaledin, Alexey L. Kaledin, Alex Brown, and Joel M. Bowman

CONTENTS

14.1 Introduction

In recent years, great progress has been made in the development of highly sophisticated, accurate computational methods to study the structure and reactions of small molecules. The application of these methods to biological macromolecules (e.g., proteins and nucleic acids) faces enormous challenges due to computational demands. Knowledge of the atomic motions and their

collective or correlated character in proteins plays an important role in understanding their biological functions [1], and thus approximate computational methods are used to simulate the protein dynamics, for example, molecular dynamics (MD) and normal mode analysis (NMA).

Molecular dynamics simulations can produce the motions of individual molecules in models of solids, liquids, and gases. The key idea is to describe how positions, velocities, and orientations change with time [2]. In theoretical studies of proteins and nucleic acids, these represent a realistic description of molecular motion, including small and large structural fluctuations and conformational transitions. The early MD applications were limited to biological molecules *in vacuo*. The advent of new supercomputer technologies and recent theoretical developments are making it possible to study biomolecules in solution and to extend the simulations to times on the order of nanoseconds [1]. The well-known limitations of MD are due to the approximate nature of the force fields and the absence of quantum effects.

NMA has long been used as a tool for interpreting vibrational spectra of small molecules [3, 4]. The frequencies obtained from NMA can be directly related to experimental infrared (IR) and Raman measurements, and the derived normal modes can be used in characterizing the dynamic behavior of molecules. Although NMA is a quantum method, it is approximate, because only the harmonic motion of the system around a single potential minimum is taken into account. Qualitative and semi-quantitative estimates can be made for many properties of macromolecules, such as the magnitude of atomic fluctuations, displacement covariance matrix, and vibrational entropy [5, 6]. However, there are a number of bottlenecks associated with an application of NMA to biomolecular systems that contain more than 10,000 atoms. In particular, the calculation and storage of the mass-weighted second derivative matrix (Hessian) scales quadratically with the size of the system and the diagonalization scales as the cube of the dimension of the Hessian.

For very large molecular systems in which straightforward diagonalization is not feasible due to limited computational resources, it is still possible to obtain a small number of modes by using iterative diagonalization approaches [7–9], however, this approach still requires the complete Hessian. In proteins low-frequency modes are particularly interesting because they are related to functional properties [10]. To date, approximate coarse-grained protein models [11, 12] have been developed to address this region of the spectrum. Various methods to performed NMA and quasi-harmonic analysis of large molecular systems in full and reduced Cartesian bases, have been described [5, 13, 14].

In our previous study [15] we introduced the driven Molecular Dynamics (DMD) method to perform NMA without a calculation of the Hessian matrix. We demonstrated how frequencies and normal modes could be obtained, and the method was validated on two small molecules and several advantages of this method over the conventional Hessian-based methods for very large systems were noted. Recently, we applied DMD to a 20-residue protein and concluded that this method has considerable potential for the study of large

systems, where the Hessian-based method is not feasible [16]. In this chapter, we review the algorithm of the DMD method and discuss its application to the same protein, Trp-cage. We examine properties calculated from DMD frequencies and normal modes and compare them to those obtained from standard NMA.

Another important advantage of DMD over the Hessian-based NMA is the ability to study the dynamics beyond the harmonic region. One can rigorously quantify such fundamental phenomena as anharmonic motion and mode coupling, which are relevant to studying functional properties of biological macromolecules. A particularly useful application of anharmonic DMD is simulation of so-called two-dimensional infrared (2D-IR) experiments broadly aimed at studying energy transfer in time and frequency domains. In this chapter, we present new results of a small peptide, dialanine, and show how DMD can be readily extended to explore the dynamical motions of relevance to these experiments.

14.2 Driven Molecular Dynamics

14.2.1 Theory

Harmonically driven MD calculations were reported in the 1970s and early 1980s to simulate multiphoton absorption in the IR [17, 18]. In those studies, applied to diatomic molecules, the external driving force was not aimed at determining normal modes, but at creating a highly excited molecule. Following the basic characteristic of normal modes, a classical system executing small amplitude motion about a minimum, can be driven resonantly at the normal mode frequency of the unperturbed system. The DMD method employs an external, sinusoidal driving term that can be used to scan the spectrum in a continuous wave fashion and determine resonant absorptions, which are the normal mode frequencies for weak signals [15]. The molecular motions, induced by driving at resonant frequencies, correspond to the normal mode vibrations.

The Hamiltonian of a molecular system in a DMD simulation consists of the molecular Hamiltonian, H_0 and a driving term $U(\mathbf{q}, t; \omega)$

$$H(\mathbf{p}, \mathbf{q}, t; \omega) = H_0(\mathbf{p}, \mathbf{q}) + U(\mathbf{q}, t; \omega) \tag{14.1}$$

where $\mathbf{q}$ and $\mathbf{p}$ represent the $3N$ atomic Cartesian coordinates and momenta, respectively. In this equation, $H_0 = T + V$, where T is the kinetic energy and V is the molecular potential. The driving term depends only on internuclear distances r_{ij} and is given by

$$U(\mathbf{q}, t; \omega) = \sum_{i<j} \lambda_{ij} r_{ij} \sin(\omega t) \tag{14.2}$$

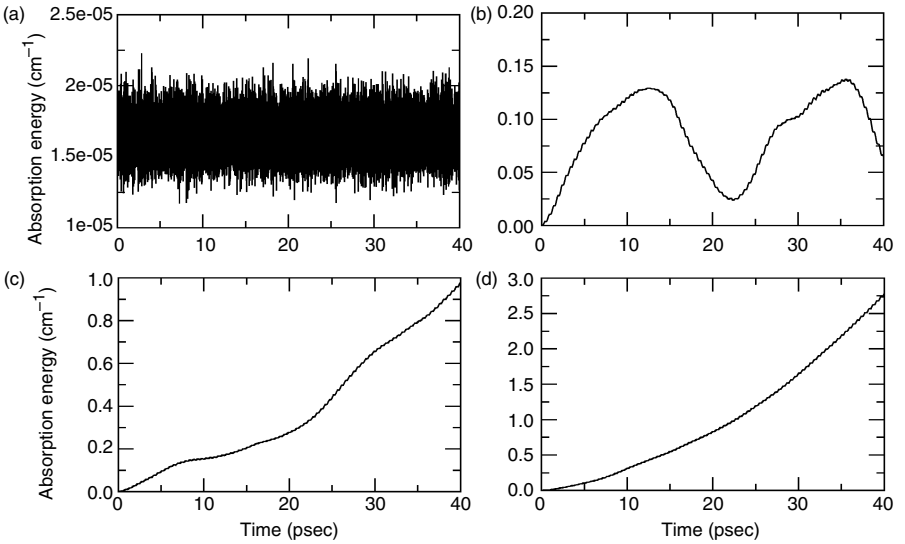

FIGURE 14.1
Example of energy profiles for Trp-cage protein: (a) nonabsorbing high-frequency mode ($\omega =$ 2000 cm^{-1}), (b) nonabsorbing low-frequency mode ($\omega = 33.5$ cm^{-1}), (c) moderately absorbing mode ($\omega = 35.0$ cm^{-1}), and (d) strongly absorbing mode ($\omega = 36.5$ cm^{-1}).

where λ_{ij} are the small coupling constants. Hamilton's equations of motion for Cartesian coordinate α of atom i are

$$\begin{aligned} \frac{\partial H}{\partial p_{\alpha,i}} &= \dot{q}_{\alpha,i} = \frac{p_{\alpha,i}}{m_i}, \\ -\frac{\partial H}{\partial q_{\alpha,i}} &= \dot{p}_{\alpha,i} = -\frac{\partial V}{\partial q_{\alpha,i}} - \sum_{j \neq i} \lambda_{ij} \frac{\alpha_i - \alpha_j}{r_{ij}} \sin(\omega t), \\ i &= 1, \ldots, N, \quad \alpha = x, y, z \end{aligned} \tag{14.3}$$

If, as assumed, ω is a normal mode frequency, then the system should respond to the driving force by executing motion that is a specific linear combination of Cartesian displacements corresponding to the *nth* normal mode, provided the driving is not too hard, that is, the motion remains in the small amplitude limit. The absorption measure that we adopt is the average total internal energy of the molecule after a finite time of driving, which is given by

$$\langle E \rangle = \frac{1}{t} \int_0^t H_0(\tau)\, \mathrm{d}\tau \tag{14.4}$$

At nonresonant frequencies, the absorbed energy is small and oscillatory with time, while on resonance it increases rapidly with time (Figure 14.1). The absorption energy is also a good measure for estimating the stability of the

calculation with respect to the driving force. This issue is discussed in further detail in Section 14.3.

14.2.2 Computational Implementation

The driving term and its derivative (Equations [14.2] and [14.3]), which are easy to evaluate, can be readily incorporated into any MD simulation program. We implemented the driving scheme into the fourth-order velocity Verlet integration program of TINKER [19]. TINKER is a user-friendly classical dynamics program package that was developed specifically for modeling biopolymers. It has the ability to use several common force field parameter sets, and it includes a variety of algorithms for geometry optimization, NMA, potential surface scanning, and solvation effects.

The scanning procedure to obtain the normal mode frequencies and corresponding normal mode vibrations is straightforward. The system is initially at rest at the equilibrium structure. The driving force is chosen to be weak enough so that excitation restricted to the harmonic potential. During the simulation the absorption energy (Equation [14.4]) is monitored to identify a resonant frequency. For each frequency the trajectory is propagated for several picoseconds. The spectrum is scanned with a uniform step $\Delta\omega$. The normal mode vectors for the resonant frequencies are calculated from the mass-weighted coordinates obtained from any time in the trajectory, after significant absorption of energy has occurred. If the frequencies alone are known, for example, from a spectral analysis of the velocity autocorrelation function, they can be used directly with DMD to obtain the normal mode vectors by driving exactly at the known frequencies. The usual mass-scaled, normalized normal modes can be obtained from the Cartesian coordinates of each atom. The components of the mass-scaled normal mode are given by

$$y_{\alpha,i} = \frac{m_i^{1/2}(q_{\alpha,i} - q_{\alpha,i}^{(0)})}{\sqrt{\sum_{\alpha=x,y,z}^{i=1,N} m_i (q_{\alpha,i} - q_{\alpha,i}^{(0)})^2}} \tag{14.5}$$

where $q_{\alpha,i}^{(0)}$ is the reference value of coordinate $q_{\alpha,i}$ and m_i is the mass of atom i.

14.3 Applications

14.3.1 The Harmonic Limit: Trp-Cage

The efficiency and accuracy of DMD was tested on a 20-residue protein (304 atoms) Trp-cage [20] (PDB code: 1L2Y). In both NMA and DMD simulations, the potential function of Trp-cage was described with the assisted model building and energy refinement (AMBER) force field ff98 parameter set for nucleic acids [21]. The structure was energy-minimized by quasi-Newton nonlinear optimization [22] until the RMS gradient was less

than 10^{-6} kcal mol^{-1} Å^{-1}. The structural and dynamical properties of this molecule, such as *B*-factors, root-mean square (RMS) fluctuations, vibrational entropy, and cross-correlations coefficients were calculated using the DMD method and compared to ones from standard NMA [16]. All calculations were carried out *in vacuo*.

14.3.1.1 The Driving Parameter λ

The driving parameter λ_{ij} in Equation (14.2) determines the strength of the driving force. For simplicity, we choose λ_{ij} to be the same for all interatomic distances. The driving force applied to all interatomic distances ensures that all normal modes will be excited. At a resonant frequency the molecule absorbs energy monotonically, as the trajectory propagates, and at some point it can exceed the harmonic limit. In the case of comparison of properties derived from the frequencies and normal modes for the two methods (DMD and standard NMA), it is desirable to keep molecular vibration in the small amplitude region. Driving beyond the harmonic limits is another feature of the DMD method, since it offers the study of coupled anharmonic motion. We discuss this issue in Section 14.3.2.

We tested several driving parameters by analyzing the average absorption energy as a function of frequency [16]. We decreased the driving parameter until the shape of the function did not change. Finally we chose the driving parameter $\lambda = 0.04$ cm^{-1}/Å for the 5 psec simulation. This convergence test is important to identify spurious absorption peaks at very low frequencies.

14.3.1.2 Spectral Density and Resolution

The frequency spectrum was determined in a simple way by a uniform scan in the range from 0 to 4000 cm^{-1}. The choice of a frequency step size is essentially dictated by the frequency resolution. In most of the DMD calculations presented here, the Trp-cage frequency spectrum is scanned with a frequency step size equal to 1 cm^{-1}, each trajectory is propagated up to 5 psec with a 0.5 fsec integration step, unless stated otherwise.

The Trp-cage spectrum from DMD calculations along with the power spectrum obtained by the Fourier transform of the velocity autocorrelation function, generated in a standard MD simulation are shown in Figure 14.2. Also the results from the standard NMA are included. Unlike the discrete frequencies in NMA, the frequency distributions in the MD and DMD simulations are quasi-continuous. In order to better compare the discrete Hessian NM spectrum with the MD and DMD densities, the Hessian normal mode distribution has been represented as a sum of Gaussians with a resolution corresponding to the Fourier transform limit of a 5 psec trajectory. These three spectra are not strictly equivalent; however, they should agree in the positions of the peaks, and there is good agreement on the scale of resolution of this figure. All spectra have been normalized so that the highest peak value is equal to one.

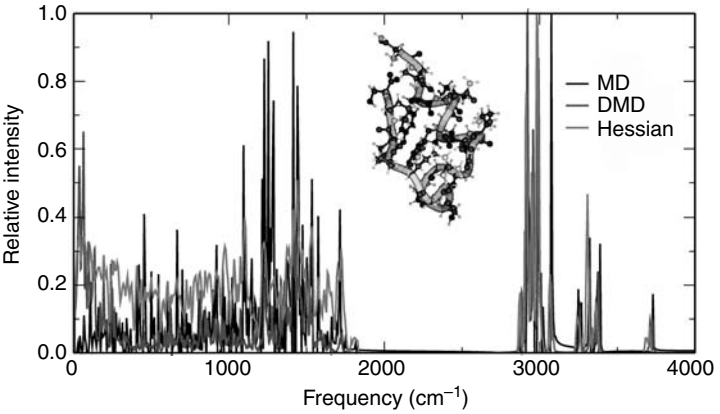

FIGURE 14.2
(See color insert following page 136) Distributions of frequencies calculated by standard NMA (Hessian), MD simulations with and without the driving terms (DMD and MD, respectively). In the Trp-cage structure the backbone trace is shown as a yellow tube.

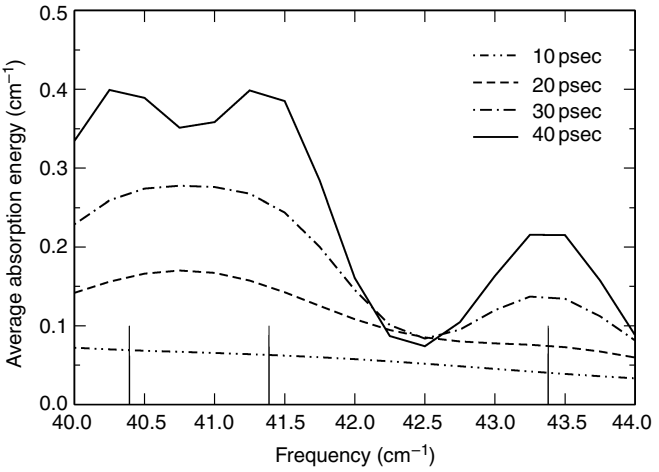

FIGURE 14.3
Resolution power of the DMD method. (a) The frequency spectrum was scanned with a step 0.25 cm^{-1} and the driving parameter $\lambda = 0.0004$ cm^{-1}Å^{-1}. The Hessian normal modes are shown as sticks at 40.4, 41.4, and 43.4 cm^{-1}.

The resolving power of the DMD method is shown in Figure 14.3. As seen, there are three normal mode frequencies in the range from 40 to 44 cm^{-1} that are separated by 1 to 2 cm^{-1}. The spectrum was scanned with a 0.25 cm^{-1} step and $\lambda = 0.0004$ cm^{-1}/Å, and each trajectory was run for up to 40 psec. As the trajectory was propagated, we monitored the average absorption energy. The resolving power of DMD increases significantly in going from 10 to 40 psec.

TABLE 14.1

Comparison of the Computed Normal Mode Eigenvalues and Eigenvectors from DMD Calculation and Standard NMA.

Hessian	DMD	Overlap[a]	Hessian	DMD	Overlap[a]
8.72	8.75	0.997	31.97	32.00	0.992
10.70	10.75	0.973	34.89	35.00	0.991
15.60	15.75	0.954	36.67	36.75	0.997
17.10	17.00	0.987	40.39	40.25	0.772
21.60	21.50	0.936	41.39	41.25	0.995
23.74	23.75	0.989	43.38	43.25	0.987
25.78	25.75	0.987	45.33	45.25[b]	0.697
27.80	27.75	0.956	47.89	48.00	0.996
29.24	29.25	0.988			

[a] Overlap is defined as a dot product between the normalized Hessian and DMD normal mode vectors.
[b] The average absorption energy for this mode is very low at 40 psec and therefore the overlap is low. DMD simulation was performed up to 40 psec with 0.25 cm^{-1} frequency step and $\lambda = 0.0004$ cm^{-1} $Å^{-1}$.

After 30 psec the two peaks separated by 2 cm^{-1} are clearly resolved. To resolve the peaks separated by 1 cm^{-1}, the trajectory has to be propagated for up to 40 psec.

To quantify how a given DMD normal mode compares with the Hessian normal modes, the overlap between the two corresponding vectors can be calculated. Resolved DMD normal mode frequencies and their overlaps with the normal mode frequencies from standard NMA for the lower part of the spectrum (up to 50 cm^{-1}) are collected in Table 14.1. In most cases the overlap is more than 0.95, indicating good accuracy of DMD normal modes. Only at 40 cm^{-1}, the density of DMD normal modes is higher and overlap is only 0.77. In such a case, the DMD method provides normal mode vectors, which are mixed, showing characteristics of the eigenvectors of desired frequency as well as those of the neighboring frequencies. To resolve these frequencies, the trajectory has to be propagated for longer time and scanned with a very small frequency step. Note that for longer propagation time smaller driving parameters should be used, to preserve small amplitude behavior. Longer propagation time results in increase of CPU, so it is important to determine whether typical properties from a NMA can be accurately obtained with a "low resolution" scan of the frequencies. In the next section we demonstrate that average molecular properties of proteins, such as RMS fluctuations and *B*-factors can be obtained accurately even from a very low resolution DMD calculation.

14.3.1.3 Atomic Fluctuations

The DMD normal modes for the resonant frequencies are calculated from the Cartesian coordinates that are obtained from the trajectory, anytime after

significant absorption of energy has occurred. Using these normal modes and the frequencies, several properties can be calculated. The magnitude of atomic fluctuations is sensitive to the value of the vibrational frequencies. The widely used classical expression for the atomic fluctuation of atom k is given by [5]

$$\langle \Delta x_k^2 \rangle = k_B T \sum_{i=1}^{3N-6} \frac{|y_{ki}|^2}{M_k \omega_i^2} \tag{14.6}$$

where ω_i is the frequency of mode i, y_{ki} is the corresponding projection of normal mode i on the Cartesian coordinates of atom k, and M_k is mass. Since the present implementation of DMD does not resolve exact NM frequencies but resonant frequencies extracted from the uniform scan of the spectrum, the sum in Equation (14.6) can be formally replaced by an integral

$$\langle \Delta x_k^2 \rangle = \frac{k_B T}{M_k} \frac{\int_0^{\omega_{\max}} (1/\omega^2) W(\omega) (y_k(\omega))^2 \mathrm{d}\omega}{\int_0^{\omega_{\max}} (W(\omega)/N_f) \mathrm{d}\omega} \tag{14.7}$$

where $W(\omega)$ is a weighting function (see below). The integral in the denominator of Equation (14.7) is a normalization factor, where N_f equals the number of normal modes ($3N - 6$ for N atoms). In evaluating the integrals a simple discretization scheme is used: the weight factors $W(\omega)$ are 0 for nonabsorbing frequencies and 1 for absorbing ones. In the present case, $\omega_{\max}$ is 4000 cm^{-1}.

At nonresonant frequencies, the absorbed energy of the molecule is small and oscillatory with time. In our calculations, the oscillatory baseline was about 10^{-4} (of a normalized integrated spectrum), and all driving frequencies, exceeding this threshold value are considered as absorbing frequencies. With this condition, Equation (14.7) reverts back to a discrete form

$$\langle \Delta x_k^2 \rangle = \frac{N_f}{N_m} k_B T \sum_{i=1}^{N_m} \frac{|y_{ki}|^2}{M_k \omega_i^2} \tag{14.8}$$

where N_m is the number of absorbing frequencies. We tested the integrated values with respect to the threshold value and found stable and accurate results relative to the exact ones, provided the threshold was low enough so that N_m was about twice larger [16] than N_f. With this condition, very few true normal modes are missed in the above equation. There will be approximate copies of normal modes appearing in the sum; however, the normalization in this sum approximately (and evidently accurately) accounts for this.

Measures of atomic fluctuations of Trp-cage protein obtained with 5 psec DMD simulation are collected in Table 14.2 and compared to the exact results. For most properties the error is 10% or less. (If exact normal mode frequencies are used, the agreement of the DMD and Hessian results is nearly perfect. The error is 2%.) The RMS fluctuations averaged over the heavy atoms (C, N, and O) are in the range 0.36 to 0.58 Å; backbone atoms tend to have smaller fluctuations, and side chain atoms tend to have larger fluctuations. There is

TABLE 14.2

RMS Fluctuations $[\langle \Delta r_k^2 \rangle]^{1/2}$ in Å.

	DMD			Hessian		
Method	**Mean**[a]	**Minimum**	**Maximum**	**Mean**[a]	**Minimum**	**Maximum**
All atoms	0.48 (0.19)	0.21	1.47	0.51 (0.21)	0.24	1.59
Backbone	0.36 (0.11)	0.21	0.61	0.36 (0.10)	0.24	0.58
Side chains	0.51 (0.21)	0.23	1.47	0.55 (0.23)	0.28	1.59
N	0.40 (0.14)	0.21	1.20	0.42 (0.15)	0.25	1.34
C	0.44 (0.10)	0.21	1.10	0.44 (0.10)	0.24	1.22
O	0.45 (0.09)	0.29	0.75	0.49 (0.12)	0.29	0.89
H	0.53 (0.15)	0.23	1.47	0.58 (0.16)	0.30	1.59
C_α	0.37 (0.11)	0.21	0.61	0.37 (0.11)	0.26	0.58

[a] The numbers are averages over all Trp-cage atoms for a particular class.
Numbers in parentheses are standard deviations.

an increase in the magnitude of the fluctuations as one goes from the center of the protein out toward the terminal groups.

The atomic fluctuations are related to temperature-dependent crystallographic factors (*B*-factors) according to the well-known expression

$$B_k = 8\pi^2 \frac{\langle \Delta r_k^2 \rangle}{3} \tag{14.9}$$

Figure 14.4 shows the *B*-factors at $T = 300$ K for all atoms and α-carbon atoms of the Trp-cage protein calculated from the Hessian normal modes (Equation [14.6]) and the DMD normal modes (Equation [14.8]). The agreement between the standard Hessian and DMD simulations is very good, lending support to the use of DMD method for further investigation of protein dynamics.

14.3.1.4 Correlation of Atomic Motion

Cross-correlation coefficients are a general indication of the degree of the collective motion in protein. The cross-correlation coefficient between atoms *k* and *j* is defined as [1]

$$C_{kj} = \frac{\langle \Delta r_k \cdot \Delta r_j \rangle}{(\langle \Delta r_k^2 \rangle \langle \Delta r_j^2 \rangle)^{1/2}} \tag{14.10}$$

These coefficients range from a value of -1 (completely anticorrelated motions) to a value of $+1$ (completely correlated motions). They reflect correlation of displacements along a straight line. In other words, two atoms moving exactly in phase and with the same period, but along perpendicular lines will have a cross-correlation of zero. Initially, the calculation was done

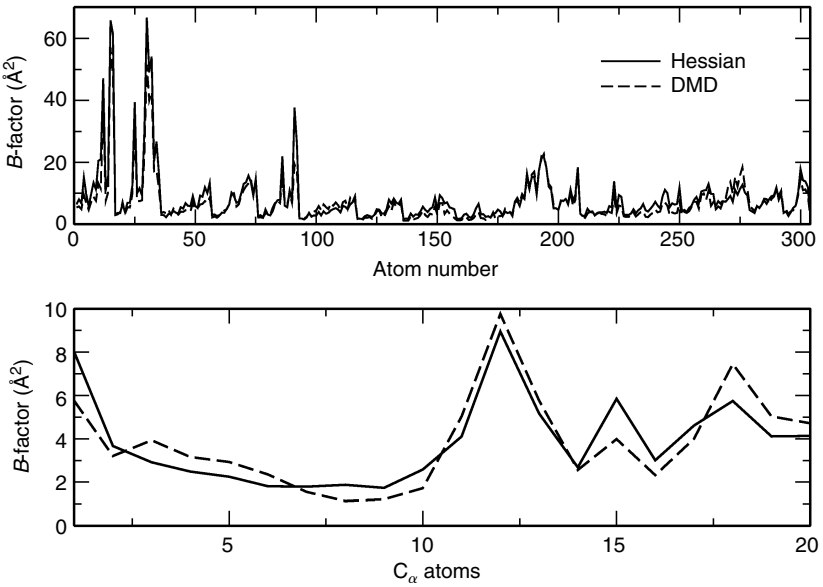

FIGURE 14.4
A comparison of *B*-factors calculated by NMA (Hessian) and low resolution DMD simulation at $T = 300$ K for all atoms and C_α atoms of Trp-cage.

using the 1 cm^{-1} low resolution DMD data set of frequencies and modes; however, the results were not in satisfactory agreement with an exact normal mode calculation. The reason for this is that cross-correlation coefficients are sensitive to the orientation of modes, and thus accuracy of these modes is essential. For most proteins, accurate values of $\langle \Delta x_k^2 \rangle$ can be obtained with as few as 30 lowest-frequency normal modes. Indeed, it has been shown that low-frequency normal modes of proteins, with frequencies under 30 cm^{-1}, are responsible for most of their atomic displacements [23]. In a different set of DMD calculations we carried out the driving at exact normal mode frequencies up to 200 cm^{-1}. Using these, we calculated the cross-correlations of the fluctuations of all backbone C_αs and did obtain accurate cross-correlations coefficients, plotted in Figure 14.5(b) next to the exact normal mode results. Obviously, a finer scanning grid and longer time trajectory are needed. Figure 14.5(c) is a result of the high resolution (40 psec simulation) DMD scan performed up to 100 cm^{-1} with 0.25 cm^{-1} frequency step. There is good agreement with the exact results in Figure 14.5(a).

14.3.1.5 Entropy

Dynamical techniques are useful for understanding the internal motions of complex systems as well as for evaluating thermodynamic properties. As far as proteins (and other biomolecules) are concerned, the computational

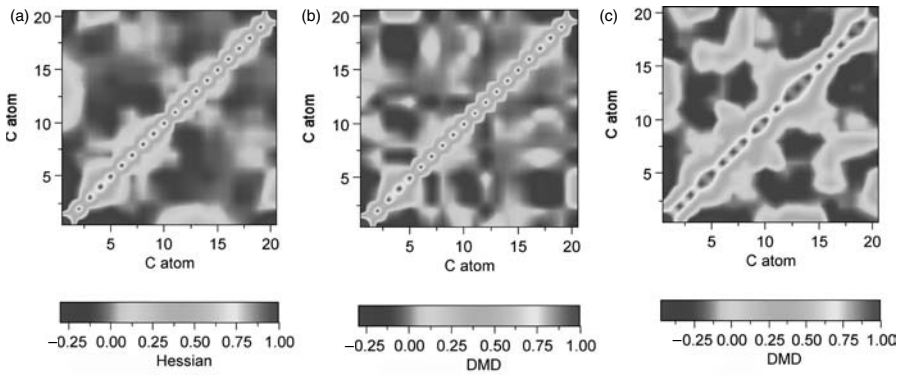

FIGURE 14.5
(See color insert following page 136) Cross-correlation maps for C_α atoms from (a) Hessian normal modes and frequencies, (b) DMD normal modes at exact Hessian frequencies, and (c) DMD normal modes at frequencies obtained from the high resolution DMD calculation.

estimate of entropy is of basic interest in protein folding and ligand binding. In this chapter, we test the calculation of the absolute entropy of Trp-cage using the driven MD approach. The resonant frequencies obtained from the same 5 psec simulation are used in the standard expression for the entropy [1], modified for the number of absorbing frequencies (factor N_f/N_m, see Equations [14.6] to [14.8])

$$S_v = \frac{N_f}{N_m} \sum_j^{N_m} \left[\frac{\hbar\omega_j}{T(e^{\hbar\omega_j/k_B T} - 1)} - k_B \ln(1 - e^{(-\hbar\omega_j/k_B T)}) \right] \tag{14.11}$$

For example, the DMD (Hessian) absolute values of entropy of Trp-cage for temperatures 300, 500, and 1000 K are 0.807 (0.820), 1.293 (1.286), and 2.154 (2.159) kcal mol^{-1}, respectively. As seen, the two methods are in very good agreement.

14.3.2 Beyond the Harmonic Limit: Dialanine

In the previous section we validated the DMD method on Trp-cage protein. All calculations were carried out within the harmonic limit. We calculated several properties based on DMD normal mode frequencies and corresponding normal mode vectors. The results were in very good agreement with the ones calculated using standard NMA method. In our previous study [16], we already discussed the possibility to extend the DMD method beyond the harmonic limit. Mild driving (small λ) is used to extract the normal modes; harder driving can be used to study anharmonic effects. Again, the DMD method has to be tested first on small benchmark systems. From the

earlier study we know that Trp-cage spectrum is congested from overlapping peaks associated with different structural domains. In order to understand the anharmonic processes better, we decided to study a smaller molecular system, dialanine, for which experimental results have also been reported [24]. Here we study anharmonic coupling between the two amide-I oscillators of dialanine in the gas phase. The potential function of dialanine was described with the chemistry of Harvard molecular mechanics (CHARMM)27 force field parameter set [25, 26]. In order to describe the bond stretching in a more realistic fashion, we use the Morse potential function (according to the option available in TINKER). As was done for Trp-cage protein, the structure was optimized until the RMS gradient was less than 10^{-6} kcal mol^{-1} Å^{-1}.

14.3.2.1 Anharmonic Driving of Interatomic Distances

We first determined the normal modes of dialanine using TINKER with the harmonic and Morse descriptions of the bond stretching. According to NMA, most of the contribution to the amide-I band is from the CO stretch [24]. Using the standard harmonic force field, we obtained amide-I frequencies 1677.3 and 1683.9 cm^{-1}, which are similar to those reported earlier [24]. The mode that gives rise to the higher frequency transition is localized more on the acetyl end of dialanine, while the lower frequency amide-I mode arises mainly from the amino end. With the Morse-type potential the resulting amide-I normal mode frequencies are 1674.7 and 1712.3 cm^{-1}, respectively.

By increasing the driving parameter λ to perform hard driving, we observe red shifts in absorption spectra. The resulting anharmonic modes can then be analyzed. We performed uniform frequency scan in the range 1600 to 1750 cm^{-1} with a step size of 1 cm^{-1}. Each trajectory was run up to 20 psec. Figure 14.6 shows absorption energy profiles for the two CO stretches for the indicated λ parameters in the range from 0.4 to 40 cm^{-1} Å^{-1}. As seen, with increasing λ, the absorption energy grows monotonically, reaching thousands of wave numbers. For $\lambda > 4\,\text{cm}^{-1}\,\text{Å}^{-1}$, there are noticeable red shifts observed along with substantial broadening of the lines. The effects of the red shift and line broadening are more dramatic for λ in the range 30 to 40 cm^{-1} Å^{-1}. Certainly, harder driving induces both large amplitude motion and interactions of neighboring units. Frequency shifts are mostly generated by internal vibrational interactions between amide and other modes. As expected, normal modes and absorption frequencies for $\lambda < 4$ cm^{-1} Å^{-1} are in very good agreement with the ones obtained by standard NMA. For $\lambda < 4$ cm^{-1} Å^{-1}, the overlap between the DMD and Hessian normal modes is about 0.98, while in the anharmonic case the overlap substantially decreases due to the mode coupling.

It is important to mention that the above discussion is for driving of interatomic distances. Therefore, the intensities in the spectrum are not proportional to the transition dipole moments but to the average absorbed energy,

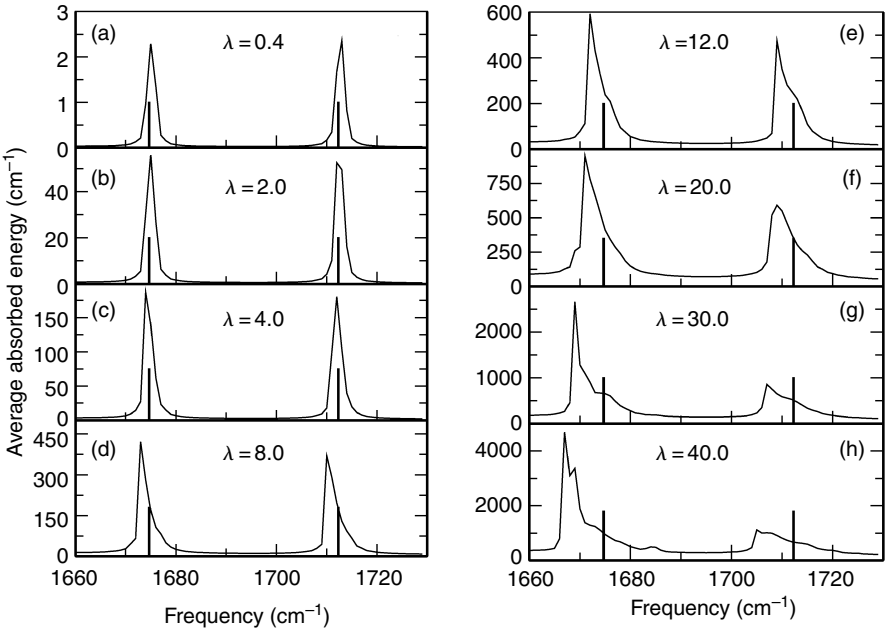

FIGURE 14.6
Dialanine spectrum in the range 1660 to 1730 cm^{-1}. The two peaks correspond to CO stretch. Hessian values are shown as sticks at 1674.7 and 1712.3 cm^{-1}. The driving parameters λ are in $cm^{-1}/Å$ units.

and they reflect the resonance. In the next section, we extend the DMD method for interaction of the molecule with the electric field.

14.3.2.2 Electric Dipole-Driven Dynamics

In order for a particular vibrational mode to absorb electromagnetic radiation, the vibrational motion associated with that mode must produce a change in the dipole moment of the molecule. To simulate IR absorption experiments, we implemented a dipole-driving scheme into TINKER. Here, the driving term (see Equation [14.2]) is given by

$$U(\mathbf{q}, t; \omega) = \vec{\varepsilon}(t; \omega) \cdot \vec{\mu}(\mathbf{q}) \tag{14.12}$$

where $\vec{\varepsilon}(t; \omega)$ is the frequency and time-dependent electric field vector. $\vec{\mu}(\mathbf{q})$ is the electric dipole of the molecule, whose first derivative with respect to the Cartesian coordinates enters the equations of motion of Section 14.2.

In preliminary tests, we observed that mild driving with sinusoidal dipole-driving term does produce the correct IR spectrum for Trp-cage and dialanine [27]. Here, we employ pulsed driving, which is of particular relevance to 2D-IR experiments used for determining a variety of structural and energetic properties of molecules. In our calculations here, a Gaussian pulse

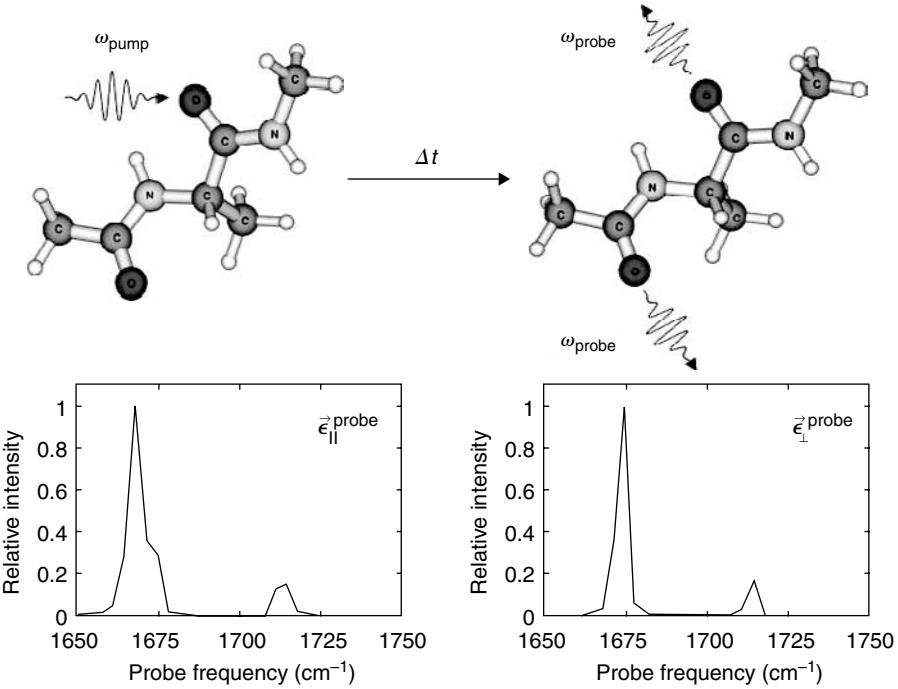

FIGURE 14.7
(See color insert following page 136) Scheme of the 2D-IR experiment for dialanine using the DMD dipole-driving method. The spectrum and structure was recorded at $\Delta t = 4.0$ psec with perpendicularly polarized pump and probe pulses.

centered at frequency ω is used

$$\vec{\varepsilon}(t;\omega) = \vec{\varepsilon}_0 e^{-(t-t_0)^2/2\Delta\tau^2} \cos[\omega(t-t_0)] \tag{14.13}$$

where $\vec{\varepsilon}_0$ determines the direction and strength of the electric field, and t_0 is an arbitrary reference time. Technically, the driving begins (laser is on) at $t = -2t_0$ and finishes (laser is off) at $t = 0$. The reference time is adjusted so that the field starts off with a small intensity (typically 5% of the maximum), rises to the maximum, and dies off at the same small intensity.

The sequence of excitation, time delay, and "probing" (depicted in Figure 14.7 for dialanine) is simulated as follows. The system is initially at rest at the equilibrium structure. For a given pump frequency ω, the electric field is given by Equation (14.13). After the pulse is turned off, the system evolves for a period of time (Δt), and then the system is "probed." In the absence of anharmonicities the dynamics is trivial and, in fact, one dimensional since a harmonic oscillator continues to absorb at a single frequency (no detuning) and does not "communicate" with other normal modes. However, in real systems, anharmonicities play an important role in the dynamics.

The "probe" spectrum is obtained theoretically by calculating the Fourier transform of the dipole–dipole correlation function averaged over the spatial orientations of the field

$$C(t;\Delta t) = \langle \vec{\mu}(\Delta t) \cdot \vec{\mu}(t+\Delta t) \rangle \tag{14.14}$$

where Δt is a time delay between the pump pulse and the probing. Thus, only a single electric field pulse is used in these calculations. The classical dependence of dipole μ is determined and saved. The averaging is done to reflect the molecule's random orientation in the laboratory frame. This requires integrating several dipole-driven trajectories with the field direction uniformly sampled on a coarse spherical polar grid (typically 3 polar and 6 azimuthal angles, resulting in 18 orientations). Controlling the orientation of the dipole with respect to the pump can simulate polarization-specific experiments. A parallel response is measured by projecting the dipole onto the direction of the pump field, while a perpendicular response is obtained by taking the dipole's component orthogonal to the field. 2D spectra can be obtained by scanning the pump frequency and collecting spectra for each pump frequency. Another dimension can be introduced by varying the time delays between the driving and probing.

As an example, we study the IR absorption spectrum of dialanine for a fixed pump field. In the simulated experiment, a Gaussian pump pulse (bandwidth 40 cm^{-1}, full width at half maximum $\sim$220 fsec) centered at frequency 1675 cm^{-1} with the field strength of 0.13 V/Å is used to excite the system. The total energy absorbed is roughly 1400 cm^{-1}. The probed spectrum is shown in Figure 14.7, in the range from 1650 to 1750 cm^{-1}(with resolution 3 cm^{-1}). The spectra were recorded at a time delay of 4 psec with the polarization of the probe pulse parallel and perpendicular to the polarization of the pump pulse. The two peaks correspond to amino end (lower amide-I) and acetyl end (higher amide-I) CO stretches. A qualitatively different picture can be observed in the two cases of pump-probe polarization. The parallel response shows significant red shifts and line broadening in both modes, while the perpendicular response is still relatively harmonic. It is evident that there is strong anisotropy present in dipole transitions of dialanine.

14.4 Summary and Conclusions

Driven MD offers a simple classical scheme for extracting the vibrational normal modes without an explicit knowledge of the second derivative matrix, the Hessian. The standard setup and diagonalization of the Hessian is replaced by a resonant excitation of the molecule (at a frequency ω) using a sinusoidal time-dependent perturbation. To solve the dynamics, one only needs to propagate a single classical trajectory for a given frequency, under conditions

of mild driving, scanning the frequency, and locating the resonances, that is, the normal mode frequencies, thus determine the harmonic spectrum. The normal mode vectors are extracted from instantaneous atomic displacements along the trajectory at an identified resonance.

In the application to Trp-cage protein presented here, we showed in several critical tests that DMD is a competitive alternative to conventional matrix diagonalization. Unlike Hessian-based methods, the CPU effort in DMD scales linearly with the number of atoms for a given force field, while the active memory and disk storage are representative of standard MD. The quality of the normal modes, both the frequency and spatial motion, can be optimized by a careful analysis of the absorbed energy and atomic displacements along the trajectory. The DMD approach provides an accurate description of averaged quantities such as atomic fluctuations and entropy in comparison to the Hessian normal mode results, even from low resolution data. For more detailed properties, such as cross-correlation coefficients, accurate results require driving at exact normal mode frequencies or performing a fine scan. Obviously, to obtain these frequencies in a straightforward scan would be computationally very time consuming, but favorable for parallel computation. A variety of spectral deconvolution methods could also be applied to the spectrum. Another approach to obtain accurate frequencies is to use the velocity autocorrelation function from a standard MD calculation with popular signal processing methods (e.g., filter diagonalization techniques [28, 29] and harmonic inversion schemes [30, 31]).

Perhaps the most attractive feature of DMD, and a clear advantage over Hessian techniques, is the ability to include anharmonic effects directly into the driving scheme. This flexibility allows for simulation of interesting experiments in vibrational spectroscopy. Using an electric field as an active medium for dipole-driven dynamics, we studied field response and the ensuing time-dependent energy transfer in dialanine. Extending these *in vacuo* simulations to liquid phase is straightforward and is a subject of ongoing work.

A few final remarks are in regards to future developments and computational efficiency of DMD. It is, in principle, possible to combine DMD as described in this chapter with an electronic structure algorithm to yield a so-called direct ab initio DMD mechanism. If made practical, such a merger would be a tremendous step forward in biological macromolecule dynamics, allowing to carry out studies of systems for which force fields are either thought to be inaccurate or simply not available. However, even the most efficient and scalable electronic structure methods, such as the popular QM/MM [32] and linear scaling DFT approaches [33], cannot produce thousands of energies (and gradients) on the fly in a short time, as required by an MD algorithm. An alternative way to combine the two pieces would be to generate the Hessian using an electronic structure method and use it as a force field in the dynamics. One would obtain the eigenvalues and corresponding eigenvectors of the raw Cartesian Hessian using DMD. Of course, the anharmonic effects are missing, but that could actually be an advantage if one were interested purely in extracting the normal modes. All the interferences and

line broadening due to mode coupling are eliminated by definition of the Hessian. We are currently pursuing this development on a number of related applications.

Acknowledgments

We thank Professor A. Roitberg (University of Florida) for discussions and for suggesting the test with Trp-cage protein. JMB thanks the National Science Foundation (NSF CHE-0131482) for financial support.

References

1. Brooks, C.L. III, Karplus, M., and Pettitt, B.M., Proteins: a theoretical perspective of dynamics, structure, and thermodynamics, *Adv. Chem. Phys.*, 71, 1, 1988.
2. Haile, J.M., *Molecular Dynamics Simulation, Elementary Methods*, John Wiley & Sons, New York, 1992.
3. Herzberg, G., *Molecular Spectra and Molecular Structure II. Infrared and Raman Spectra of Polyatomic Molecules*, Van Nostrand, New York, 1945.
4. Wilson, E.B., Decius, J.C., and Cross, P.C., *Molecular Vibrations,* McGraw-Hill, New York, 1955.
5. Brooks, B.R., Janezic, D., and Karplus, M., Harmonic analysis of large systems. I. Methodology, *J. Comput. Chem.*, 16, 1522, 1995.
6. Ma, J. and Karplus, M., The allosteric mechanism of the chaperonin GroEL: a dynamic analysis, *Proc. Natl Acad. Sci. USA,* 95, 8502, 1998.
7. Marques, O. and Sanejouand, Y., Hinge-bending motion in citrate synthase arising from normal mode calculations, *Proteins,* 23, 557, 1995.
8. Mouawad, L. and Perahia, D., Diagonalization in a mixed basis: a method to compute low-frequency normal-modes for large macromolecules, *Biopolymers,* 33, 599, 1993.
9. Parlett, B.N., *The Symmetric Eigenvalue Problem*, Prentice Hall, Englewood Cliffs, NJ, 1980.
10. Durand, P., Trinquier, G., and Sanejouand, Y.H., New approach for determining low-frequency normal-modes in macromolecules, *Biopolymers,* 34, 759, 1994.
11. Tama, F., Gadea, F.X., Marques, O., and Sanejouand, Y., Building-block approach for determining low-frequency normal modes of macromolecules, *Proteins,* 41, 1, 2000.
12. Li, G. and Cui, Q., A coarse-grained normal mode approach for macromolecules: an efficient implementation and application to Ca^{2+}-ATPase, *Biophys. J.*, 83, 2457, 2002.
13. Janezic, D. and Brooks, B.R., Harmonic analysis of large systems. II. Comparison of different protein models, *J. Comput. Chem.*, 16, 1543, 1995.
14. Janezic, D., Venable, R.M., and Brooks, B.R., Harmonic analysis of large systems. III. Comparison with molecular dynamics, *J. Comput. Chem.*, 16, 1554, 1995.

15. Bowman, J.M., Zhang, X., and Brown, A., Normal-mode analysis without the Hessian: a driven molecular-dynamics approach, *J. Chem. Phys.*, 119, 646, 2003.
16. Kaledin, M., Brown, A., Kaledin, A.L., and Bowman, J.M., Normal mode analysis using the driven molecular dynamics method: II. An application to biological macromolecules, *J. Chem. Phys.*, 121, 5646, 2004.
17. Christoffel, K.M. and Bowman, J.M., Classical trajectory studies of multi-photon and overtone absorption of HF, *J. Phys. Chem.*, 85, 2159, 1981.
18. McDonald, J.D. and Marcus, R.A., Classical trajectory study of internal energy distributions in unimolecular processes, *J. Chem. Phys.*, 65, 2180, 1976.
19. TINKER: software tools for molecular design, Version 4.1, Washington University School of Medicine, June 2003, available from http://dasher.wustl.edu/tinker.
20. Neidigh, J.W., Fesinmeyer, R.M., and Andersen, N.H., Designing a 20-residue protein, *Nat. Struct. Biol.*, 9, 425, 2002.
21. Cornell, W.D., Cieplak, P., Bayly, C.I., Gould, I.R., Merz, K.M. Jr., Ferguson, D.M., Spellmeyer, D.C., Fox, T., Caldwell, J.W., and Kollman, P.A., A second generation force field for the simulation of proteins, nucleic acids, and organic molecules, *J. Am. Chem. Soc.*, 117, 5179, 1995; Cheatham, T.E. III, Cieplak, P., and Kollman, P.A., A modified version of the Cornell et al. force field with improved sugar pucker phases an helical repeat, *J. Biomol. Struct. Dyn.*,16, 845, 1999.
22. Nocedal, J. and Wright, S.J., *Numerical Optimization*, Springer-Verlag, New York, 1999 (Section 9.1).
23. Brooks, B.R. and Karplus, M., Normal modes for specific motions of macromolecules: application to the hinge-bending mode of lysosome, *Proc. Natl Acad. Sci. USA*, 82, 4995, 1985.
24. Gnanakaran, S. and Hochstrasser, R.M., Conformational preferences and vibrational frequency distributions of short peptides in relation to multidimensional infrared spectroscopy, *J. Am. Chem. Soc.*, 123, 12886, 2001.
25. Foloppe, N. and MacKerell, Jr., A.D. All-atom empirical force field for nucleic acids: I. Parameter optimization based on small molecule and condensed phase macromolecular target data, *J. Comput. Chem.*, 21, 86, 2000.
26. MacKerell, A.D., Jr., Bashford, D., Bellott, R.L., Dunbrack, R.L., Jr., Evanseck, J.D., Field, M.J., Fischer, S., Gao, J., Guo, H., Ha, S., Joseph-McCarthy, D., Kuchnir, L., Kuczera, K., Lau, F.T.K., Mattos, C., Michnick, S., Ngo, T., Nguyen, D.T., Prodhom, B., Reiher, W.E., III, Roux, B., Schlenkrich, M., Smith, J.C., Stote, R., Straub, J., Watanabe, M., Wiorkiewicz-Kuczera, J., Yin, D., and Karplus, M., All-atom empirical potential for molecular modeling and dynamics studies of proteins, *J. Phys. Chem. B*, 102, 3586, 1998.
27. Kaledin, M., Kaledin, A.L., and Bowman, J.M. (work in progress).
28. Wall, M.R. and Neuhauser, D., Extraction, through filter-diagonalization, of general quantum eigenvalues or classical normal mode frequencies from a small number of residues or a short-time segment of a signal. I. Theory and application to a quantum-dynamics model, *J. Chem. Phys.*, 102, 8011, 1995.
29. Da Silva, A.J.R., Pang, J.W., Carter, E.A., and Neuhauser, D., Anharmonic vibrations via filter diagonalization of ab initio dynamics trajectories, *J. Phys. Chem. A*, 102, 881, 1998.
30. Main, J., Dando, P.A., Belkic, D., and Taylor, H.S., Decimation and harmonic inversion of periodic orbit signals, *J. Phys. Math. Gen.*, 33, 1247, 2000.
31. Kunikeev, S.D. and Taylor, H.S., Saving measurement time in ^{13}C NMR spectroscopy, *J. Phys. Chem. A*, 108, 743, 2004.

32. Gao, J., Methods and applications of combined quantum mechanical and molecular mechanical potentials, in *Reviews in Computational Chemistry,* Lipkowitz, K.B. and Boyd, D.B. (Eds.), VCH Publishers, New York, 1995, Vol. 7, p. 119.
33. Schwegler, E. and Challacombe, M., Linear scaling computation of the Hartree–Fock exchange matrix, *J. Chem. Phys.*, 105, 2726, 1996; Li, X.S., Millam, J.M., Scuseria, G.E., Frisch, M.J., and Schlegel, H.B., Density matrix search using direct inversion in the iterative subspace as a linear scaling alternative to diagonalization in electronic structure calculations, *J. Chem. Phys.*, 119, 7651, 2003.

15

Probing Vibrational Energy Relaxation in Proteins Using Normal Modes

Hiroshi Fujisaki, Lintao Bu, and John E. Straub

CONTENTS

15.1 Introduction

The harmonic (or normal mode (NM)) approximation has been a powerful tool for the analysis of few and many-body systems where the essential

dynamics of the system consists of small oscillations about a well-defined mechanically stable structure. The concept of NMs is appealing in science because it provides a simple view for complex systems such as solids and proteins. Though it had been believed that NMs may be too simplistic to analyze the dynamics of proteins, it is by no means always true; the experimental data of neutron scattering for proteins (*B*-factor) indicate that the fluctuations for each residue are well represented by a simplified model using NMs [1]. It was also shown that such a large-amplitude motion as the hinge-bending motion in a protein is well described by a NM [2]. Importantly, NMs have been used to refine the x-ray structures of proteins [3]. Recently, large proteins or even protein complexes can be analyzed by using NMs [4–6].

In this chapter, we are concerned with vibrational energy relaxation (VER) in a protein. This subject is related to our understanding of the functionality of proteins. At the most fundamental level, we must understand the energy flow (pathway) of an injected energy, that is channeled to do useful work. Due to the advance of laser technology, time-resolved spectroscopy can detect such energy flow phenomena experimentally [7]. To interpret experimental data, and to suggest new experiments, theoretical approaches and simulations are essential as they can provide a detailed view of VER. However, VER in large molecules itself is still a challenging problem in molecular science [8]. This is because VER is a typical many-body problem and estimations of quantum effects are difficult [9]. There is a clear need to test and compare the validity of the existing theoretical methods.

We here employ two different methods to estimate the VER rate in a protein, cytochrome c (see Section 15.2 for details). One is the classical equilibrium simulation method [10] with quantum correction factors (QCFs) [11, 12]. The second is the reduced model approach [13], which has been recently employed by Leitner's group [14, 15]. The latter approach is based on NM concepts, which describes VER as energy transfers between NMs mediated by nonlinear resonance [16]. We conclude with a discussion of the validity and applicability of such approaches.

15.2 Cytochrome c

Cytochrome c (cyt c) is one of the most thoroughly physicochemically characterized metalloproteins [17, 18]. It consists of a single polypeptide chain of 104 amino acid residues and is organized into a series of five α-helices and six β-turns. The heme active site in cyt c consists of a 6-coordinate low-spin iron that binds His18 and Met80 as the axial ligands. In addition, two cysteines (Cys14 and Cys17) are covalently bonded through thioether bridges to the heme (see Figure 15.1). Crystal structures of cyt c show that the heme group, which is located in a groove and almost completely buried inside the protein, is nonplanar and somewhat distorted into a saddle-shape geometry.

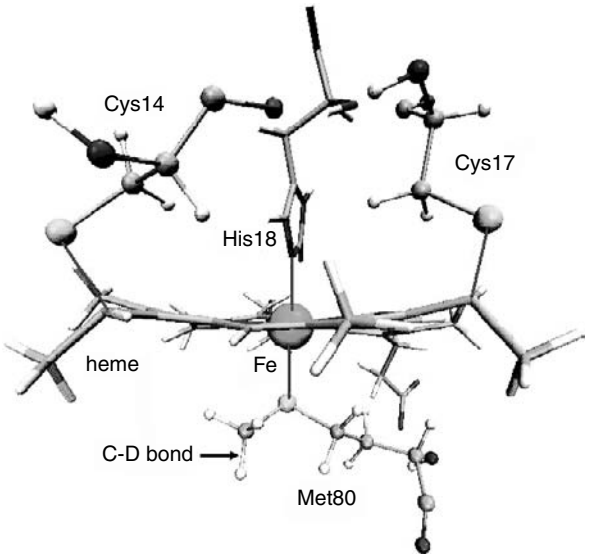

FIGURE 15.1
(See color insert following page 136) The structure of cytochrome c in the vicinity of the heme group, showing the thioether linkages and nonplanar heme geometry.

The reduced protein, ferrocytochrome c (ferrocyt c), is relatively compact and very stable, due to the fact that the heme group is neutral.

The vibrational mode we have chosen for study is the isotopically labeled CD stretch in the terminal methyl group of the residue Met80, which is covalently bonded to Fe in heme (see Figure 15.1). Our simulation model approximates the protein synthesized by Romesberg's group, [19] though their protein contains three deuteriums in Met80 (Met80-3D). The CH and CD stretching bands are located near 3000 and 2200 cm^{-1}, respectively. In contrast with the modeling of photolyzed CO in myoglobin [10], essentially a diatomic molecule in a protein "solvent," we are interested in the relaxation of a selected vibrational mode of a protein. As a result, the modeling is more challenging: There is no clean separation between the system and bath modes because the CD bond is strongly connected to the environment.

15.3 QCF Approach

The classical Landau–Teller–Zwanzig (LTZ) theory of VER is attractive in that it allows us to base our estimate of the VER rate on a classical force autocorrelation function that contains the interaction coupling between the system and bath modes to all orders. The Hamiltonian for such a system is of the Caldeira–Leggett–Zwanzig form, where "bath" coordinates are represented as NMs of

the *bath alone*.[1] The relaxing oscillator is introduced as a local "system" mode, coupled to the bath at all orders, including "bilinear" coupling.

Efforts have been made to introduce quantum effects through the use of "QCFs." The dynamics of the classical system are computed, and the quantum effects are added *a posteriori* in a manner that accounts for the equilibrium quantum statistical distribution of the contributing quantum mechanical degrees of freedom. This approach is summarized below and applied to estimate the rate of VER for the CD bond in the terminal methyl group of Met 80 in cyt c.

15.3.1 Fermi's Golden Rule

Our starting point for computing the rate of VER of the CD stretching mode in cyt c is Fermi's "golden rule" formula. The vibrational population relaxation rate can be written as [13, 20]

$$\frac{1}{T_1} = \frac{\tanh(\beta\hbar\omega_S/2)}{\beta\hbar\omega_S/2}\int_0^\infty dt\cos(\omega_S t)\zeta_{\rm qm}(t) = \frac{\tanh(\beta\hbar\omega_S/2)}{\beta\hbar\omega_S/2}\tilde{\zeta}_{\rm qm}(\omega_S) \tag{15.1}$$

where the force–force correlation function $\zeta_{\rm qm}(t)$ is defined as

$$\zeta_{\rm qm}(t) = \frac{\beta}{2m_S}\langle\mathcal{F}(t)\mathcal{F}(0) + \mathcal{F}(0)\mathcal{F}(t)\rangle_{\rm qm} \tag{15.2}$$

its Fourier transform is $\tilde{\zeta}_{\rm qm}(\omega)$, $\mathcal{F}(t)$ is the quantum mechanical force applied to the system mode considered, m_S is the system (reduced) mass, ω_S is the system frequency, β is an inverse temperature, and the above bracket means a quantum mechanical average. Note that in the classical limit $\hbar \to 0$, the prefactor in front of the integral in Equation (15.1) becomes unity, and the expression reduces to the well-known classical VER formula. The issue is that this limit does not represent well the VER for high frequency modes because of quantum effects (fluctuation), whereas it is difficult to calculate $\zeta_{\rm qm}(t)$.

Rather than using the population relaxation rate $1/T_1$, we could compute the rate of transition between pairs of vibrational quantum states

$$k^{\rm qm}_{n\to n-1} = \frac{2n}{\beta\hbar\omega_S[1+e^{-\beta\hbar\omega_S}]}\tilde{\zeta}_{\rm qm}(\omega) \tag{15.3}$$

where n is the vibrational quantum number. In the limit that $\beta\hbar\omega_S \gg 1$ as we consider here, the splitting between vibrational levels is large compared with

[1] As shown below, the *classical* LTZ formula can be considered as a classical limit of the quantum mechanical population relaxation rate $1/T_1$. This result is derived by using *both* Fermi's golden rule and Bader–Berne theory [20]. Though the transition rate $k_{n\to n-1}$ itself can be derived without any assumption on the bath Hamiltonian, the Bader–Berne result stems from the assumption that the bath Hamiltonian is an ensemble of harmonic oscillators.

the thermal energy. At equilibrium, the system oscillator will be ground state dominated, and we find that

$$\frac{1}{T_1} \simeq \frac{2\tilde{\zeta}_{\rm qm}(\omega_S)}{\beta\hbar\omega_S} \simeq k^{\rm qm}_{1\to 0} \tag{15.4}$$

For such a system, we are free to consider the rate of vibrational relaxation in terms of the ensemble averaged relaxation rate $1/T_1$ or the microscopic rate constant $k^{\rm qm}_{1\to 0}$ — the results will be equivalent.

In the limit that $\beta\hbar\omega_S \to 0$, on the other hand, the splitting between states becomes much smaller than the thermal energy and the results are *not* equivalent. The rate constant $k^{qm}_{1\to 0}$ diverges, while the population relaxation rate $1/T_1$ is well behaved

$$\frac{1}{T_1} \simeq \tilde{\zeta}_{\rm qm}(\omega_S) \tag{15.5}$$

In this chapter, we will present our results in terms of $1/T_1$.

15.3.2 Quantum Correction Factor

While $\zeta_{\rm qm}(t)$ is difficult to compute for all but the simplest systems, it is often possible to compute the classical analog

$$\zeta_{\rm cl}(t) = \frac{\beta}{m_S}\langle \mathcal{F}(t)\mathcal{F}(0)\rangle_{\rm cl} \tag{15.6}$$

for highly nonlinear systems consisting of thousands of atoms. The above bracket denotes a classical ensemble average. The challenge is to relate the quantum mechanical correlation function to its classical analog. An approach explored by Skinner et al. has proved to be quite productive [12]. It involves relating the spectral density of the quantum system to that of the analogous classical system as

$$\tilde{\zeta}_{\rm qm}(\omega_S) = Q(\omega_S)\tilde{\zeta}_{\rm cl}(\omega_S) \tag{15.7}$$

where $Q(\omega_S)$ is referred to as the "QCF." The QCF must obey detailed balance $Q(\omega) = Q(-\omega)e^{\beta\hbar\omega}$ and satisfy the "classical" limit that as $\beta\hbar\omega$ becomes small, the QCF approaches unity. Using this result, we may rewrite Equation (15.1) as

$$\frac{1}{T_1^{\rm QCF}} \simeq \frac{Q(\omega_S)}{\beta\hbar\omega_S}\tilde{\zeta}_{\rm cl}(\omega_S) \tag{15.8}$$

Note that the classical VER rate is defined as $1/T_1^{\rm cl} \equiv \tilde{\zeta}_{\rm cl}(\omega_S)$.

The QCF for a one phonon relaxation mechanism is

$$Q_{\rm H}(\omega) = \frac{\beta\hbar\omega}{1 - e^{-\beta\hbar\omega}} \tag{15.9}$$

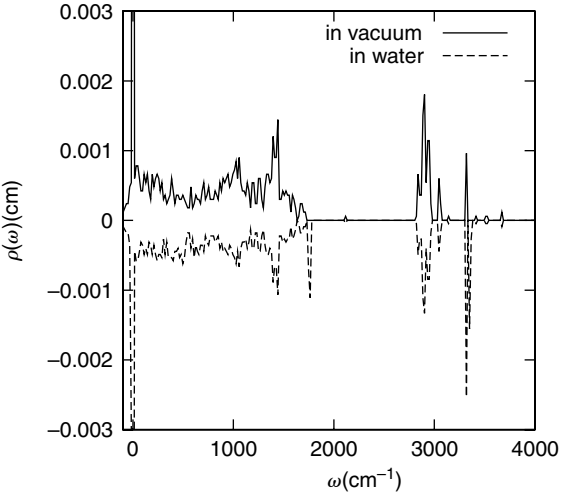

FIGURE 15.2
Density of states $\rho(\omega)$ for cyt c in vacuum (solid line) and in water (dashed line) at 300 K calculated by INM analysis.

However, as the CD stretching mode falls in the transparent region of the DOS (Figure 15.2), a 1:1 Fermi resonance (linear resonance) is not the possible mechanism of VER. As such, the lowest order mechanism available for the VER of the CD mode should involve two phonons.

We have employed Skinner's QCF approach for two-phonon relaxation [12]. If the two-phonon mechanism assumes that two lower frequency bath modes, having frequencies ω_A and $\omega_S - \omega_A$, are each excited by one quantum of vibrational energy, the appropriate QCF is

$$Q_{\mathrm{HH}}(\omega_S) = Q_{\mathrm{H}}(\omega_A) Q_{\mathrm{H}}(\omega_S - \omega_A) \tag{15.10}$$

Alternatively, if the assumed two-phonon mechanism is one that leads to the excitation of one bath vibrational mode of frequency ω_A, with the remaining energy $\hbar(\omega_S - \omega_A)$ being transferred to lower frequency bath rotational and translational modes, the appropriate QCF is

$$Q_{\mathrm{H\text{–}HS}}(\omega_S) = Q_{\mathrm{H}}(\omega_A) \sqrt{Q_{\mathrm{H}}(\omega_S - \omega_A)} \mathrm{e}^{\beta\hbar(\omega_S - \omega_A)/4} \tag{15.11}$$

The functions Q_{H}, Q_{HH}, $Q_{\mathrm{H\text{–}HS}}$ are called the harmonic, harmonic–harmonic, and harmonic–harmonic–Schofield QCF, respectively.

15.3.3 NM Calculations for Cyt c

To compute the QCF requires a knowledge of, or guess at, the mechanism of VER. Likely bath modes must be identified and a combination

of those modes must meet a resonance condition enforced by the conservation of energy in the transition. The candidate modes are identified using quenched normal mode (QNM) or instantaneous normal mode (INM) calculations.

In Figure 15.2, we show the density of states (DOS) for cyt c in vacuum and in water at 300 K. These are the INM spectra, so they contain some negative (actually imaginary) components. The basic structure of this DOS is similar to that of other proteins such as myoglobin [10, 16]. The librational and torsional motions are embedded in lower frequency regions below 2000 cm^{-1}, and vibrational motions are located in higher frequency regions around 3000 cm^{-1}. There is a transparent region between 2000 and 3000 cm^{-1}; the peak due to the CD mode falls in this region near 2200 cm^{-1}. The VER of this CD mode is our target in this study. Note, furthermore, that the spectra in vacuum and in water are very similar. This indicates that water solvent might not affect the simulation results. This conjecture will be confirmed below.

15.3.4 Application to VER of the CD Bond in Cyt c

Bu and Straub [11] employed the QCF approach to estimate the VER rate of a CD bond in the terminal methyl group of Met80 in cyt c (Figure 15.1). Their calculations were done using the program Chemistry at HARvard Mechanics (CHARMM) [21], and cyt c was surrounded by water molecules at 300 K. In this work, we have used molecular dynamics simulations of cyt c *in vacuum* at 300 K to compute the classical autocorrelation function for the force acting on the same CD bond. The results have been used to make estimates of both $1/T_1^{\mathrm{cl}}$ and $1/T_1^{\mathrm{QCF}}$.

In Figure 15.3, the force autocorrelation function and its power spectrum are shown for four different trajectories. We have observed that the force fluctuation and the magnitude of the power spectrum for cyt c in vacuum is very similar to those computed for cyt c in water. We conclude that the effects of water on the VER rate are negligible. With the CD bond frequency $\omega_S = 2133\ \mathrm{cm}^{-1}$, we find $1/T_1^{\mathrm{cl}} = \tilde{\zeta}_{\mathrm{cl}}(\omega_S) \simeq 1\ \mathrm{psec}^{-1}$, that is, the classical VER time is about 1 psec.

To apply QCFs for two-phonon relaxation, Equations (15.10) and (15.11) to this situation, we need to know ω_A. We have found that the CD mode is strongly resonant with two lower frequency modes, 1655th (685.48 cm^{-1}) and 3823rd (1443.54 cm^{-1}) modes because $|\omega_S - \omega_{1655} - \omega_{3823}| = 0.03\ \mathrm{cm}^{-1}$. We might be able to choose $\omega_A = 1443.54$ or 685.48 cm^{-1}.

In Figure 15.4, we show the ω_A dependence of the normalized QCF, that is, $\tilde{Q} = Q/(\beta\hbar\omega_S) = T_1^{\mathrm{cl}}/T_1^{\mathrm{QCF}}$ at 300 K and at 15 K. If we choose $\omega_A = 1443.54\ \mathrm{cm}^{-1}$ at 300 K, $\tilde{Q} = 2.3$ for the harmonic–harmonic QCF and 2.8 for the H–HS QCF. Thus, we have $T_1^{\mathrm{QCF}} = T_1^{\mathrm{cl}}/\tilde{Q} = 0.3 \sim 0.4$ psec. It is interesting to note $\tilde{Q}$ at 15 K varies significantly depending on the QCF employed. We will discuss this feature in Sec. 15.4.4.

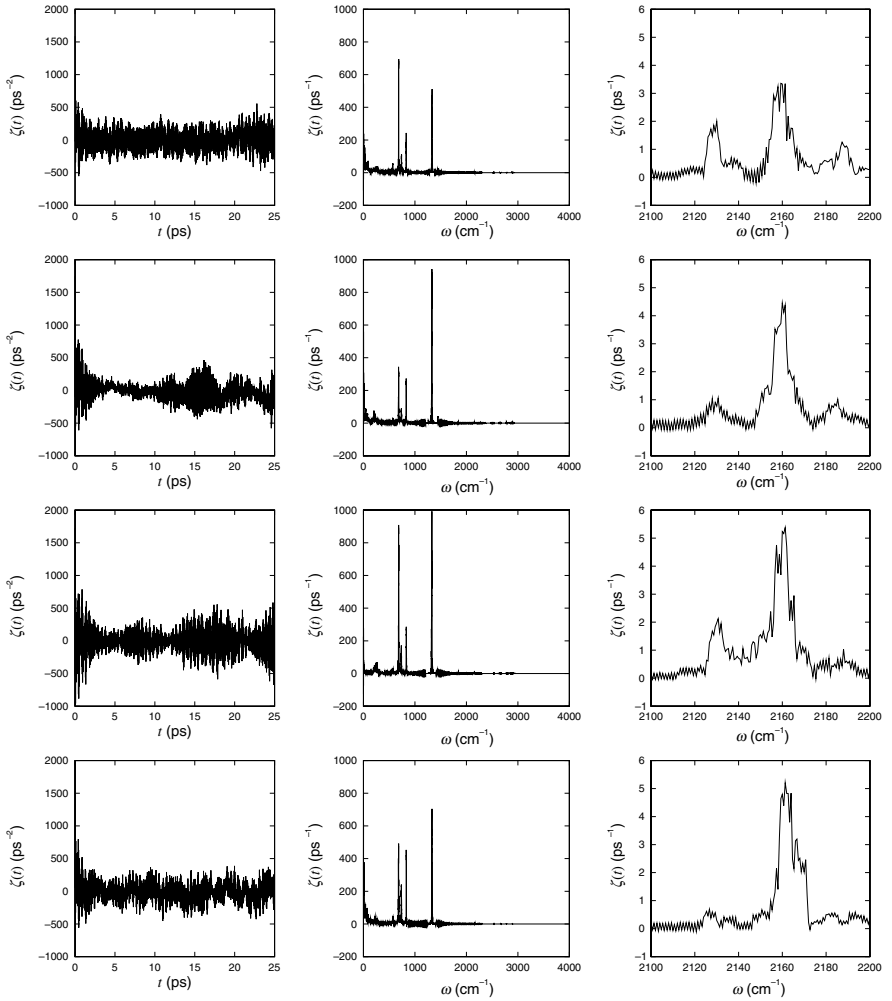

FIGURE 15.3
Left: Classical data for the force–force correlation function. Middle: Fourier spectra for the correlation function. Right: Magnification of the middle figures around the CD bond frequency. These data are taken from four different trajectories of the equilibrium simulation.

15.3.5 Fluctuation of the CD Bond Frequency

We have discussed the fluctuation of the frequency for the CD bond [11]. In the equilibrium simulation, the INM analysis has been employed for each instant of time to generate a time series $\omega_{\mathrm{CD}}(t)$ for the CD bond frequency. From this time series, we can calculate the frequency autocorrelation function

$$C(t) = \overline{\delta\omega_{\mathrm{CD}}(t)\delta\omega_{\mathrm{CD}}(0)} = \frac{1}{T}\int_0^T d\tau\,\delta\omega_{\mathrm{CD}}(t+\tau)\delta\omega_{\mathrm{CD}}(\tau) \tag{15.12}$$

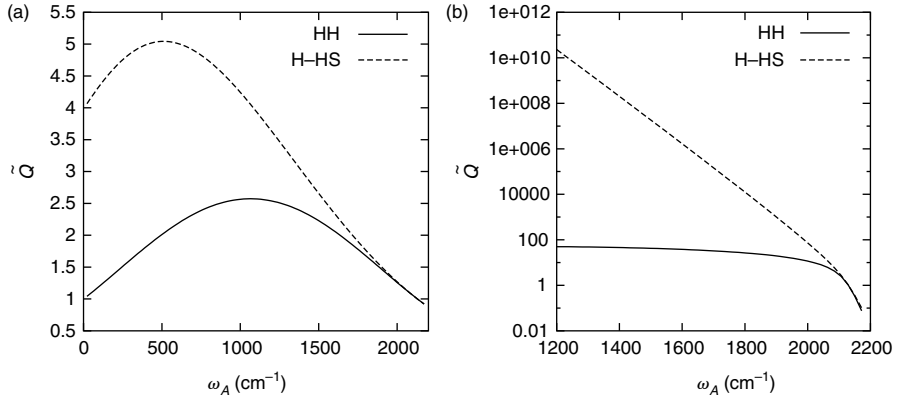

FIGURE 15.4
Normalized HH and H–HS QCF at 300 K (a) and at 15 K (b) as a function of the bath mode frequency ω_A.

where the overline means a long time (T) average, and $\delta\omega_{\mathrm{CD}}(t) = \omega_{\mathrm{CD}}(t) - \overline{\omega_{\mathrm{CD}}(t)}$. The correlation time is defined as

$$\tau_c = \frac{1}{(\Delta\omega)^2}\int_0^\infty C(t)dt \tag{15.13}$$

where $(\Delta\omega)^2 = C(0)$. From Figure 15.5, we found $\Delta\omega \simeq 8.5$ cm^{-1} and $\tau_c \simeq 0.2$ psec. Since $\Delta\omega\tau_c \ll 1$, according to Kubo's analysis [22], the line shape should be homogeneously broadened, that is, its shape is Lorentzian. We also confirmed that the potential barrier of the methyl group to rotate is significantly greater than the thermal energy (barrier height $\simeq 3$ kcal/mol $>$ thermal energy $\simeq 0.6$ kcal/mol).

These results support the validity of employing a NM type study of VER in cyt c as the structure of cyt c is rather rigid around the CD bond and the dynamics of the bond, on the scale of VER, should be well modeled by NMs. Of course, to describe VER among NMs, we must include nonlinear coupling terms. In the next section, we discuss this reduced model approach for VER in cyt c.

15.4 Reduced Model Approach

The QCF approach is attractive in that it allows us to base our estimate of the VER rate on a force autocorrelation function that contains the nonlinearity of the coupling between the system and bath modes to all orders. To obtain an estimate of the VER based on a more accurate representation of the system's quantum dynamics, we expand the potential as a Taylor series in the NMs of the system and bath. In this representation, the system and bath coordinates are "NMs;" to second order in the expansion of the potential energy,

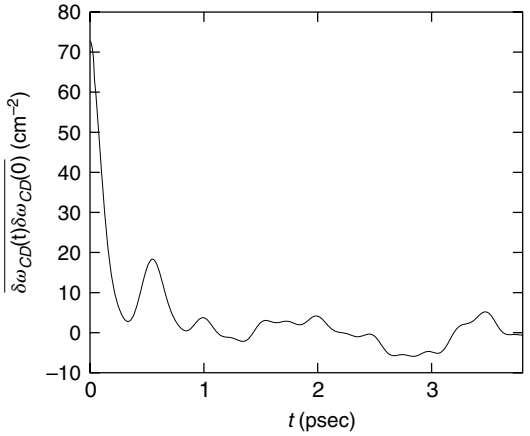

FIGURE 15.5
The frequency autocorrelation function calculated from the instantaneous normal mode analysis. The data up to 20 psec were used to calculate the correlation function.

the system and bath modes are uncoupled and noninteracting. The interaction "coupling" between the system and bath modes first appears at third order. In this section, we describe a perturbation theory estimate of the rate of VER of the CD mode that represents the system–bath coupling to lowest, third order in the system and bath coordinates.

15.4.1 Reduced Model for a Protein

The reduced model approach utilizes the NM picture of a protein, expanding the residual term perturbatively as [23]

$$\mathcal{H} = \mathcal{H}_S + \mathcal{H}_B + \mathcal{V}_3 + \mathcal{V}_4 + \cdots \tag{15.14}$$

$$\mathcal{H}_S = \frac{p_S^2}{2} + \frac{\omega_S^2}{2} q_S^2 \tag{15.15}$$

$$\mathcal{H}_B = \sum_k \frac{p_k^2}{2} + \frac{\omega_k^2}{2} q_k^2 \tag{15.16}$$

$$\mathcal{V}_3 = \sum_{k,l,m} G_{klm} q_k q_l q_m \tag{15.17}$$

$$\mathcal{V}_4 = \sum_{k,l,m,n} H_{klmn} q_k q_l q_m q_n \tag{15.18}$$

Thus the force applied to the system mode is

$$\mathcal{F} = -\frac{\partial \mathcal{V}}{\partial q_S} = -3 \sum_{k,l} G_{S,k,l} q_k q_l - 4 \sum_{k,l,m} H_{S,k,l,m} q_k q_l q_m + \cdots \tag{15.19}$$

where we have used the permutation symmetry of G_{klm} and H_{klmn}. If it is enough to include the lowest order terms proportional to G_{klm}, substituting them into Fermi's golden rule Equation (15.1), we can derive an approximate VER rate as [13]

$$\frac{1}{T_1} \simeq \frac{1}{m_S \hbar \omega_S} \frac{1 - \mathrm{e}^{-\beta\hbar\omega_S}}{1 + \mathrm{e}^{-\beta\hbar\omega_S}} \sum_{k,l} \left[\frac{\gamma \zeta_{k,l}^{(+)}}{\gamma^2 + (\omega_k + \omega_l - \omega_S)^2} + \frac{\gamma \zeta_{k,l}^{(+)}}{\gamma^2 + (\omega_k + \omega_l + \omega_S)^2} + \frac{\gamma \zeta_{k,l}^{(-)}}{\gamma^2 + (\omega_k - \omega_l - \omega_S)^2} + \frac{\gamma \zeta_{k,l}^{(-)}}{\gamma^2 + (\omega_k - \omega_l + \omega_S)^2} \right] \tag{15.20}$$

where we have included a width parameter γ to broaden a delta function, and defined the following:

$$\zeta_{k,l}^{(+)} = \frac{\hbar^2}{2} \frac{(A_{k,l}^{(2)})^2}{\omega_k \omega_l} (1 + n_k + n_l + 2 n_k n_l) \tag{15.21}$$

$$\zeta_{k,l}^{(-)} = \frac{\hbar^2}{2} \frac{(A_{k,l}^{(2)})^2}{\omega_k \omega_l} (n_k + n_l + 2 n_k n_l) \tag{15.22}$$

$$A_{k,l}^{(2)} = -3 G_{S,k,l} \tag{15.23}$$

$$n_k = 1/(e^{\beta\hbar\omega_k} - 1) \tag{15.24}$$

15.4.2 Maradudin–Fein Formula

There exists another well-known formula to describe the VER rate, the Maradudin–Fein (MF) formula [24, 14],

$$W = W_{\mathrm{decay}} + W_{\mathrm{coll}} \tag{15.25}$$

$$W_{\mathrm{decay}} = \frac{\hbar}{2 m_S \omega_S} \sum_{k,l} \frac{(A_{k,l}^{(2)})^2}{\omega_k \omega_l} (1 + n_k + n_l) \frac{\gamma}{\gamma^2 + (\omega_S - \omega_k - \omega_l)^2} \tag{15.26}$$

$$W_{\mathrm{coll}} = \frac{\hbar}{m_S \omega_S} \sum_{k,l} \frac{(A_{k,l}^{(2)})^2}{\omega_k \omega_l} (n_k - n_l) \frac{\gamma}{\gamma^2 + (\omega_S + \omega_k - \omega_l)^2} \tag{15.27}$$

with a width parameter γ. Note that Equations (15.20) and (15.25) are equivalent in the limit of $\gamma \to 0$ as shown by Kenkre et al. [25]. However, they disagree with a finite width parameter such as $\gamma \sim 100\ \mathrm{cm}^{-1}$. In this chapter,

we use the MF formula and consider its classical limit ($\hbar \to 0$) defined as

$$W^{\mathrm{cl}}_{\mathrm{decay}} = \frac{1}{2m_S\beta\omega_S} \sum_{k,l} \frac{(A^{(2)}_{k,l})^2}{\omega_k\omega_l} \left(\frac{1}{\omega_k} + \frac{1}{\omega_l}\right) \frac{\gamma}{\gamma^2 + (\omega_S - \omega_k - \omega_l)^2} \tag{15.28}$$

$$W^{\mathrm{cl}}_{\mathrm{coll}} = \frac{1}{m_S\beta\omega_S} \sum_{k,l} \frac{(A^{(2)}_{k,l})^2}{\omega_k\omega_l} \left(\frac{1}{\omega_k} - \frac{1}{\omega_l}\right) \frac{\gamma}{\gamma^2 + (\omega_S + \omega_k - \omega_l)^2} \tag{15.29}$$

We note some properties of the formula: $W_{\mathrm{decay}} \geq W^{\mathrm{cl}}_{\mathrm{decay}}$ and $W_{\mathrm{coll}} \leq W^{\mathrm{cl}}_{\mathrm{coll}}$, which is derived from

$$\frac{1/(e^x - 1) + 1/(e^y - 1)}{1/x + 1/y} \geq 1 \tag{15.30}$$

$$\frac{1/(e^x - 1) - 1/(e^y - 1)}{1/x - 1/y} \leq 1 \tag{15.31}$$

for $x, y > 0$. We can define an effective QCF as

$$Q_{\mathrm{eff}} = \frac{W}{W^{\mathrm{cl}}} = \frac{W_{\mathrm{decay}} + W_{\mathrm{coll}}}{W^{\mathrm{cl}}_{\mathrm{decay}} + W^{\mathrm{cl}}_{\mathrm{coll}}} \tag{15.32}$$

This should be compared with the normalized QCFs [$\tilde{Q} = Q(\omega_S)/(\beta\hbar\omega_S)$] found in the literature.

15.4.3 Third-Order Coupling Elements

To apply the MF theory to the case of CD bond relaxation in cyt c, we must numerically compute the third-order coupling elements. As the protein has more than 10^3 modes, there are more than 10^6 third-order coupling elements representing the coupling of the "system" CD bond to the "bath" modes of the surrounding protein and solvent.

We have employed the finite difference approximation

$$A^{(2)}_{mn} = -\frac{1}{2} \frac{\partial^3 V}{\partial q_S \partial q_m \partial q_n} \simeq -\frac{1}{2} \sum_{ij} U_{im} U_{jn} \frac{K_{ij}(\Delta q_S) - K_{ij}(-\Delta q_S)}{2\Delta q_S} \tag{15.33}$$

where U_{ik} is an orthogonal matrix that diagonalizes the (mass-weighted) Hessian matrix at the mechanically stable structure K_{ij}, and $K_{ij}(\pm\Delta q_S)$ is a Hessian matrix calculated at a shifted structure along the direction of a selected mode with a shift $\pm\Delta q_S$.

Note that, in the large number of coupling elements, most are small in magnitude. Of those that are larger, most fail to meet the resonance condition

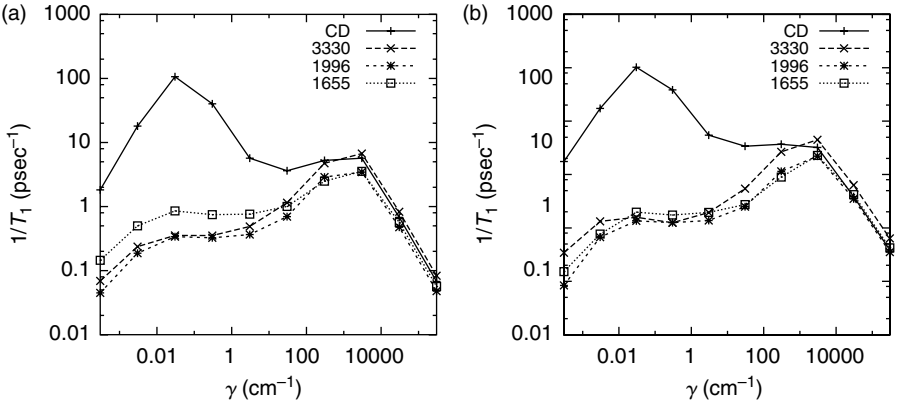

FIGURE 15.6
VER rates for the CD mode ($\omega_{CD} = 2129.1\ cm^{-1}$) and the other lower frequency modes ($\omega_{3330} = 1330.9\ cm^{-1}$, $\omega_{1996} = 829.9\ cm^{-1}$, $\omega_{1655} = 685.5\ cm^{-1}$) as a function of γ at 300 K (a) and at 15 K (b).

and do not contribute significantly to the perturbative estimate of the VER rate (see Reference 13 for the details).

15.4.4 Width Parameter

We show the width parameter γ dependence of the VER rate in Figure 15.6.[2] We consider other lower frequency modes ($\omega_{3330} = 1330.9\ cm^{-1}$, $\omega_{1996} = 829.9\ cm^{-1}$, and $\omega_{1655} = 685.5\ cm^{-1}$) as well as the CD mode ($\omega_{CD} = 2129.1\ cm^{-1}$) for comparison. From the former analysis of the frequency autocorrelation function Equation (15.12), we might be able to take $\gamma \simeq \Delta\omega \sim 3\ cm^{-1}$ for the CD mode, and we have $T_1 \simeq 0.2$ psec, which agrees with the previous result with QCFs: $T_1^{QCF} = 0.3 \sim 0.4$ psec.

We also see that the lower frequency modes have longer VER time, a few psec, which agrees with the calculations by Leitner's group employing the MF formula [15]. The main contribution to the VER rate at $\gamma = 3\ cm^{-1}$ comes from 1655th mode ($685.5\ cm^{-1}$), a heme torsion, and the 3823rd ($1443.5\ cm^{-1}$) mode, an angle bend in Met80 (~20%). Interestingly, we can conceive a peak around $\gamma = 0.03\ cm^{-1}$. Given this width parameter, the contribution from the two modes is more than 90%. We can say that 1655th and 3823rd modes are resonant with the CD mode because they satisfy the resonant condition ($|\omega_{1655} + \omega_{3823} - \omega_{CD}| \simeq 0.03\ cm^{-1}$) and the coupling elements between them is relatively large ($|A^{(2)}_{1655,3823}| \simeq 5.1\ kcal/mol/Å^3$).

This close resonance does not necessarily lead to the conclusion that it forms the dominant channel for VER of the CD stretch. There is a competing

[2]Note two limiting cases of γ dependence: $1/T_1 \propto \gamma$ when γ is very small, and $1/T_1 \propto 1/\gamma$ when γ is very large. This is easily recognized from the Lorentzian form.

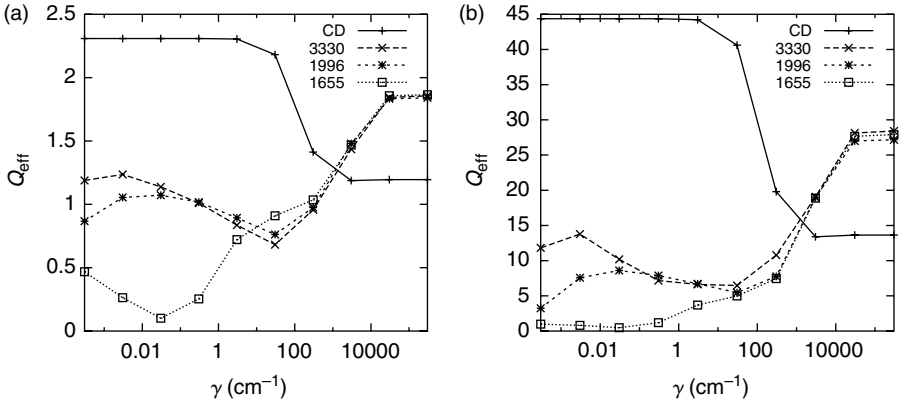

FIGURE 15.7
Effective QCF for the CD mode ($\omega_{\rm CD} = 2129.1$ cm^{-1}) and the other lower frequency modes ($\omega_{3330} = 1330.9$ cm^{-1}, $\omega_{1996} = 829.9$ cm^{-1}, $\omega_{1655} = 685.5$ cm^{-1}) as a function of γ at 300 K (a) and at 15 K (b).

near-resonance involving the 3330th mode (1330.9 cm^{-1}), an angle bending mode of Met80, and the 1996th mode (829.9 cm^{-1}), a stretch-bend mode in Met80. While the resonance is not close (it is within 31.7 cm^{-1}), the coupling element is quite large ($|A^{(2)}_{3330,1996}| \simeq 22.3$ kcal/mol/Å^3). With a larger value of $\gamma = 30$ cm^{-1}, this combination of bath modes becomes the dominant channel for VER of the CD stretch. Clearly, the uncertainty in our force field, used to compute the vibrational frequencies, and the value of γ, which is rather poorly defined, prevents us from concluding that one or another of these two channels will dominate VER of the CD stretch at room temperature.

In Figure 15.7(a), we show the effective QCF calculated from Equation (15.32) at 300 K, which is $Q_{\rm eff} \simeq 2.3$ for the CD mode with $\gamma = 3$ cm^{-1}. This value better agrees with the (normalized) HH QCF [Equation (15.10)], compared to the H–HS QCF [Equation (15.11)]. The $Q_{\rm eff}$ for the other modes are more or less unity, which indicates that these modes behave classically at 300 K.[3] In contrast, as is shown in Figure 15.7(b), $Q_{\rm eff}$ at 15 K is very large ($Q_{\rm eff} \simeq 40$), which implies that the classical VER rate becomes small because it is proportional to the temperature (see also Figure 15.8). A similar trend is found in the right of Figure 15.4, where the HH QCF ($\tilde{Q} \simeq 40$) is comparable to $Q_{\rm eff}$. On the other hand, the H–HS QCF gives an exponentially large value of $\tilde{Q}$, showing strong deviations from $Q_{\rm eff}$. We should bear in mind that different QCFs lead to significantly different conclusions at low temperatures.

[3]We notice an interesting behavior for 1655th mode, that is, $Q_{\rm eff}$ becomes very much smaller than unity at $\gamma \simeq 0.03$ cm^{-1}. In this case, we observe that $W_{\rm coll} \gg W_{\rm decay}$ because of the resonance: $\omega_{1655} + \omega_{3823} - \omega_{\rm CD} \simeq 0$ (actually 0.03 cm^{-1}). In such a case, $Q_{\rm eff}$ becomes less than unity because $W_{\rm coll} \le W^{\rm cl}_{\rm coll}$.

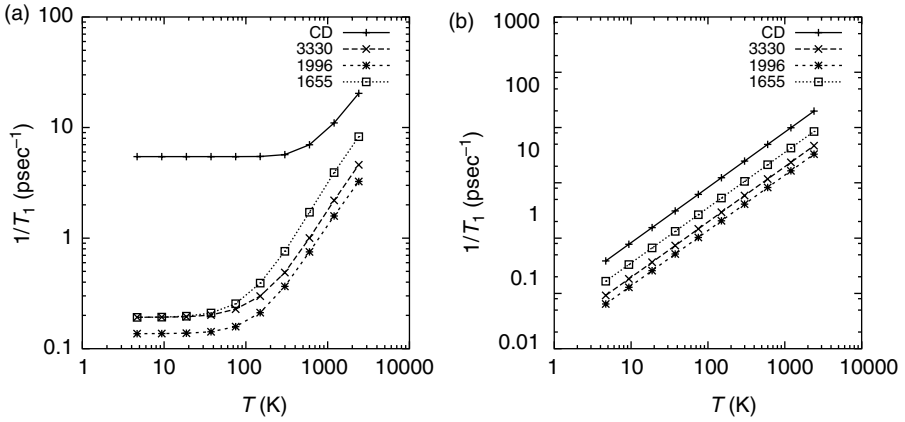

FIGURE 15.8
Quantum (a) and classical (b) VER rates for the CD mode ($\omega_{\rm CD} = 2129.1$ cm^{-1}) and the other lower frequency modes ($\omega_{3330} = 1330.9$ cm^{-1}, $\omega_{1996} = 829.9$ cm^{-1}, $\omega_{1655} = 685.5$ cm^{-1}) as a function of temperature with $\gamma = 3$ cm^{-1}.

15.4.5 Temperature Dependence

In Figure 15.8, we show the temperature dependence of the quantum and classical VER rate calculated by the MF formula and the classical limit of the MF formula. At high temperatures (∼1000 K), the quantum VER rate agrees with the classical one, but they deviate at low temperatures. The former becomes constant due to the remaining quantum fluctuation (zero point energy) whereas the latter decreases as $\propto$ (temperature). The "cross over temperature" where the VER behaves classically is smaller for the lower frequency modes compared to that of the CD mode as expected.

15.5 Discussion

15.5.1 Comparison with Experiment

Here we compare our results with the experiment by Romeberg's group [19]. They measured the shifts and widths of the spectra for different forms of cyt c; the widths of the spectra full width at half maximum (FWHM) were found to be $\Delta\omega_{\rm FWHM} \simeq 6.0 \sim 13.0$ cm^{-1}. From the discussions of Section 15.3.5, we can theoretically neglect inhomogeneous effects, and estimate the VER rate simply as

$$T_1 \sim 5.3/\Delta\omega_{\rm FWHM} \text{ (psec)} \tag{15.34}$$

which corresponds to $T_1 \simeq 0.4 \sim 0.9$ psec. This estimate is similar to the QCF prediction using Equation (15.8) (0.3 ∼ 0.4 psec) and the reduced model approach using Equations (15.20) or (15.25) (0.2 ∼ 0.3 psec). We note

that this value should be compared to the VER time of the C–H stretch in N-methylacetamide-D [$CH_3(CO)ND(CH_3)$] [26], which is also sub psec. Further experimental studies, for example, on temperature dependence of absorption spectra or on time-resolved spectroscopy, will clarify the methodology that is more applicable.

Romesberg's group studied Met80-3D (methionine with three deuteriums), while we have examined Met80-1D (methionine with one deuterium). In the case of Met80-3D, there are three peaks in the transparent region. It should be possible to consider the VER of each of the three modes, to make a more direct comparison of the predictions of our theoretical models with the results of their experimental studies.

15.5.2 Validity of Fermi's Golden Rule

We next discuss the validity of our approaches. Since our starting point is the perturbative Fermi's golden rule, our two approaches should have a limited range of validity. Naively speaking, the force applied on the CD mode should be small enough, but how small should it be?

We follow Kubo's derivation of a quantum master equation using the projection operator technique [22]. He derived an equation for the evolution of the system density operator $\sigma(t)$

$$\frac{\partial}{\partial t}\sigma(t) = -\frac{1}{\hbar^2}\int_{-\infty}^{t} d\tau [q(t)q(\tau)\sigma(\tau)\Phi(t-\tau) - q(t)\sigma(\tau)q(\tau)\Phi(-t+\tau) + \sigma(\tau)q(\tau)q(t)\Phi(-t+\tau) - q(\tau)\sigma(\tau)q(t)\Phi(t-\tau)] \tag{15.35}$$

The interaction Hamiltonian is assumed to be $\mathcal{H}_{\rm int} = -q\mathcal{F}$, as in our case, that is, q is the system coordinate and $\mathcal{F}$ contains the bath coordinates. We have defined the force autocorrelation function $\Phi(t) = {\rm Tr}_B\{\rho_B\mathcal{F}(t)\mathcal{F}(0)\} = \langle\mathcal{F}(t)\mathcal{F}(0)\rangle$. Note that Equation (15.35) is just a von Neumann equation using the projection operator technique, and it is not a master equation yet.

If $\Phi(t)$ decays fast, we can replace $\sigma(\tau)$ in the integral with $\sigma(t)$, and the dynamics becomes an approximate Markovian dynamics. If this approximation is valid, Fermi's golden rule describes the relaxation dynamics of $\sigma(t)$ [22]. The validity of the golden rule relies on the validity of the Markov approximation.

From Equation (15.35), the relaxation rate of $\sigma(t)$ can be estimated as

$$1/\tau_r \sim (\langle q^2\rangle\mathcal{F}^2/\hbar^2)\tau_c \tag{15.36}$$

where we have assumed

$$\Phi(t) \simeq \mathcal{F}^2 e^{-|t|/\tau_c} \tag{15.37}$$

The Markov approximation [$\sigma(\tau) \simeq \sigma(t)$] holds for

$$\tau_r \gg \tau_c \tag{15.38}$$

TABLE 15.1

The Parameters in Equation (15.39) for Various Molecules in AKMA Units (Unit Length = 1 Å, Unit Time = 0.04888 psec, Unit Energy = 1 kcal/mol).

	$\langle q^2 \rangle$	$\mathcal{F}^2$	τ_c	ϵ
CD in cyt c	0.01	5.0	1.0	0.5
HOD in D_2O	0.01	5.0	1.0	0.5
CN^- in water	0.002	1.0	0.5	0.01
CO in Mb	0.002	1.0	1.0	0.02

Source: The data for HOD in D_2O is taken from R. Rey and J.T. Hynes, *J. Chem. Phys.* 104, 2356 (1996); for CN^- in water from R. Rey and J.T. Hynes, *J. Chem. Phys.* 108, 142 (1998); for CO in Mb from D.E. Sagnella and J.E. Straub *Biophys. J.* 77, 70 (1999).

We have a criterion for the validity of the Markov approximation

$$\epsilon \equiv \langle q^2 \rangle \mathcal{F}^2 \tau_c^2 / \hbar^2 \ll 1 \tag{15.39}$$

In our case as well as the case of HOD in D_2O, the ratio is "just" small (see Table 15.1). Applying Fermi's golden rule to these situations should be regarded as a reasonable estimate of the VER rate. As alternative approaches that avoid this underlying Markov approximation, one can employ more "advanced" methods as mentioned in Section 15.6.

15.5.3 Higher-Order Coupling Terms

So far, we have only included the third-order coupling terms to describe the VER of the CD mode. However, we must be concerned with the relative contribution of higher-order mechanism, for example, the contribution due to the fourth-order coupling terms in Equation (15.18). This is a very difficult question. As there are many terms ($\sim 10^9$) included, we cannot directly calculate all of them for cyt c. We have found that it is not sufficient to include only the third-order coupling terms to reproduce the fluctuation of the force on the CD bond. However, this does not necessarily mean that the VER rate calculated from the third-order coupling terms is inadequate.

The main contribution from the fourth-order coupling terms to the VER rate and the force fluctuation are written as

$$\Delta\left(\frac{1}{T_1}\right) \sim \sum_{k,l,m} \frac{|H_{S,k,l,m}|^2}{\omega_k \omega_l \omega_m} \delta(\omega_S - \omega_k - \omega_l - \omega_m) \tag{15.40}$$

and

$$\Delta\langle \delta\mathcal{F}^2 \rangle \sim \sum_{k,l,m} \frac{|H_{S,k,l,m}|^2}{\omega_k \omega_l \omega_m} \tag{15.41}$$

respectively. Even if $\Delta\langle\delta\mathcal{F}^2\rangle$ becomes large, $\Delta(1/T_1)$ is not necessarily large because of the resonance condition ($\omega_S - \omega_k - \omega_l - \omega_m \simeq 0$). It is a future task how to evaluate the effects due to higher-order coupling terms. It might be interesting to compare the classical limit using the reduced model approach and the LTZ approach because there is no ambiguity about how to choose QCFs [29].

15.6 Summary

In this chapter, we have examined VER in a protein from the QCF approach and the reduced model approach, and compared the results. For the CD mode in cyt c (in vacuum) at room temperature, both approaches yield similar results for the VER rate, which is also similar to an estimate based on an experiment by Romesberg's group. Our work demonstrates both the feasibility and accuracy of a number of theoretical approaches to estimate VER rates of selected modes in proteins.

The QCF approach is appealing in that the calculation of the force autocorrelation function is straightforward and feasible, even for systems of thousands of degrees of freedom. Moreover, the classical force autocorrelation function includes all orders of nonlinearity in the interaction between the system oscillator and the surrounding bath. A weakness of the QCF approach is that we do not know which QCF to choose *a priori*. We must assume a mechanism for VER before computing the rate. Moreover, the temperature dependence of the rate of VER is sensitive to the mechanism, whether it involves few phonons or many phonons. The choice of the form of the QCF can make a significant difference in the predicted rate of VER at lower temperatures.

On the other hand, the reduced model approach is appealing in that the quantum dynamics of the reduced system is accurately treated. Using the reduced model approach, there are two ways to estimate the quantum mechanical force autocorrelation function: (1) numerical calculation of the quantum dynamics for a model Hamiltonian of a few degrees of freedom, including all orders of nonlinearity in the potential and (2) analytical solution for the quantum dynamics using perturbation theory that includes many bath modes but only the lowest-order nonlinear coupling between the system and bath modes. We have employed the latter approach through the use of the MF formula. A weakness of our reduced model approach is that the method neglects the higher-order coupling elements beyond third order, which cannot be justified *a priori* [30, 31].

We have pursued a comparative study in which we seek *consensus* in the estimates of $1/T_1$ the results of the QCF approach and the perturbation theory. A rather remarkable result of our study is that while the absolute value of the quantum corrections to the classical VER theory are large (on the order of

a factor of 40), the results of the QCF and the perturbation theory approaches are in close agreement. This is all the more remarkable given the fact that the results of the perturbation theory require a calculation of the third-order coupling constants and the estimation of the "lifetime" parameter γ. As we have shown, the dominant channel for VER, derived from the perturbation theory, depends upon the choice of γ. For smaller $\gamma = 3$ cm^{-1}, the dominant mechanism is a close resonance (within 0.1 cm^{-1}), a combination of a heme torsion and Met80 angle bending mode, with a weak coupling. For larger $\gamma = 30$ cm^{-1}, the dominant mechanism appears to be a less perfect resonance (within 31.7 cm^{-1}), a combination of a different angle bending mode and a bend-stretch mode in Met 80, with a strong coupling. Such detailed knowledge of γ is essential to predict a mechanism for VER.

Our study raises two important questions. (1) What is the optimal set of coordinates for modeling and interpreting VER in proteins? In the QCF approach, we treated the relaxing bond (CD bond) as a *local mode* that is coupled to vibrational modes of the bath. In the reduced model approach, on the other hand, we treated all the vibrational modes including the relaxing mode (CD mode) as *NMs* that are coupled to each other with the third-order nonlinear coupling terms. Our numerical results showed that the two approaches give similar results for the VER rate of the CD bond or mode, but it remains to be seen that this is a kind of coincidence or there is a theoretical ground of their equivalence (if the QCF is appropriately chosen) (2) What is the physical origin of the width parameter γ and how to calculate it? In this study, we suggested to use the relation $\gamma \simeq \Delta\omega$ where $\Delta\omega$ represents the fluctuation of the CD mode (or bond) frequency. We think this is reasonable but there is few theoretical explanation to this. If the VER rate does not significantly depend on γ, this is not a serious problem, but this is not always the case. Thus we need an "ab initio" way to derive the width parameter γ. One appealing way is to regard γ as a hopping rate between potential basins (inherent structures) [32, 33]. Recent advances may provide a theoretical underpinning for the direct calculation of the "lifetime" width parameters [34].

The results of our study are derived through the use of an approximate empirical energy function (force field), which has not been "tuned" to provide accurate frequencies of vibration for all protein modes. Our predicted rates of VER depend sensitively on the closeness of the resonance between the system and bath modes. Clearly, we must resort to the reparameterization of the empirical potential to fit with experimental data or higher levels of theory (ab initio quantum chemistry calculation) in an effort to refine our estimates of the frequencies of vibration and the details of nonlinear coupling between vibrational modes of the protein. This is a challenge for both experimental and theoretical studies.

Recent advances in experiment and theory make the present time an exciting one for the detailed study of protein dynamics. A variety of methods have been applied to examine VER in molecules, including nonequilibrium MD methods [35], time-dependent self-consistent field methods [31, 36],

mixed quantum–classical methods [37], and semiclassical methods [38, 39]. In addition, it is now possible to compute spectroscopic observables such as absorption spectra or 2D-IR signals [40, 41] as probes of protein structures and dynamics. Extensions of these studies will provide us with an increasingly detailed picture of the dynamics of proteins and its relation to structures and functions.

Acknowledgments

We thank Prof. S. Takada, Prof. T. Komatsuzaki, Prof. Y. Mizutani, Prof. K. Tominaga, Prof. S. Okazaki, Prof. F. Romesberg, Prof. J.L. Skinner, Prof. D.M. Leitner, Prof. I. Ohmine, Prof. S. Saito, Prof. R. Akiyama, Prof. K. Takatsuka, Dr. H. Ushiyama, Dr. T. Miyadera, Dr. S. Fuchigami, Dr. T. Yamashita, Dr. Y. Sugita, Dr. M. Ceremeens, Dr. J. Zimmerman, and Dr. P.H. Nguyen for helpful comments and discussions, and Prof. S. Mukamel and Prof. Y. Tanimura for informing the references related to nonlinear spectroscopy. We thank the National Science Foundation (CHE-0316551) for its generous support to our research.

References

1. N. Go, T. Noguchi, and T. Nishikawa, "Dynamics of a small protein in terms of low-frequency vibrational modes," *Proc. Natl Acad. Sci. USA* **80**, 3696 (1983); B. Brooks and M. Karplus, "Harmonic dynamics of proteins: normal modes and fluctuations in bovine pancreatic trypsin inhibitor," *Proc. Natl Acad. Sci. USA* **80**, 6571 (1983).
2. J.A. McCammon, B.R. Gelin, M. Karplus, and P.G. Wolynes, "The hinge-bending mode in lysozyme," *Nature* **262**, 325 (1976).
3. A. Kidera and N. Go, "Refinement of protein dynamic structure: normal mode refinement," *Proc. Natl Acad. Sci. USA* **87**, 3718 (1990).
4. D. Ming, Y. Kong, M.A. Lambert, Z. Huang, and J. Ma, "How to describe protein motion without amino acid sequence and atomic coordinates," *Proc. Natl Acad. Sci. USA* **99**, 8620 (2002).
5. G. Li and Q. Cui, "A coarse-grained normal mode approach for macromolecules: an efficient implementation and application to Ca^{2+}-ATPase," *Biophys. J.* **83**, 2457 (2002).
6. F. Tama, M. Valle, J. Frank, and C.L. Brooks III, "Dynamic reorganization of the functionally active ribosome explored by normal mode analysis and cryo-electron microscopy," *Proc. Natl Acad. Sci. USA* **100**, 9319 (2003).
7. Y. Mizutani and T. Kitagawa, "Direct observation of cooling of heme upon photodissociation of carbonmonoxy myoglobin," *Science* **278**, 443 (1997); "Ultrafast structural relaxation of myoglobin following photodissociation of carbon monoxide probed by time-resolved resonance Raman spectroscopy," *J. Phys. Chem. B* **105**,

10992 (2001); M.D. Fayer, "Fast protein dynamics probed with infrared vibrational echo experiments," *Ann. Rev. Phys. Chem.* **52**, 315 (2001); X. Ye, A. Demidov, and P.M. Champion, "Measurements of the photodissociation quantum yields of MbNO and MbO_2 and the vibrational relaxation of the six-coordinate heme species," *J. Am. Chem. Soc.* **124**, 5914 (2002); F. Rosca, A.T.N. Kumar, D. Ionascu, X. Ye, A.A. Demidov, T. Sjodin, D. Wharton, D. Barrick, S.G. Sligar, T. Yonetani, and P.M. Champion, "Investigations of Anharmonic Low-Frequency Oscillations in Heme Proteins," *J. Phys. Chem. A* **106**, 3540 (2002).

8. B.J. Berne, M. Borkovec, and J.E. Straub, "Classical and modern methods in reaction rate theory," *J. Phys. Chem.* **92**, 3711 (1988); J.I. Steinfeld, J.E. Francisco, and W.L. Hase, *Chemical Kinetics and Dynamics*, Prentice-Hall, New York (1989); A. Stuchebrukhov, S. Ionov, and V. Letokhov, "IR spectra of highly vibrationally excited large polyatomic molecules and intramolecular relaxation," *J. Phys. Chem.* **93**, 5357 (1989); T. Uzer, "Theories of intramolecular vibrational energy transfer," *Phys. Rep.* **199**, 73 (1991).
9. D.E. Logan and P.G. Wolynes, "Quantum localization and energy flow in many-dimensional Fermi resonant systems," *J. Chem. Phys.* **93**, 4994 (1990); S.A. Schofield and P.G. Wolynes, "A scaling perspective on quantum energy flow in molecules," *J. Chem. Phys.* **98**, 1123 (1993); S.A. Schofield, P.G. Wolynes, and R.E. Wyatt, "Computational study of many-dimensional quantum energy flow: from action diffusion to localization," *Phys. Rev. Lett.* **74**, 3720 (1995); S.A. Schofield and P.G. Wolynes, "Rate theory and quantum energy flow in molecules: modeling the effects of anisotropic diffusion and dephasing," *J. Phys. Chem.* **99**, 2753 (1995); D.M. Leitner and P.G. Wolynes, "Vibrational mixing and energy flow in polyatomics: quantitative prediction using local random matrix theory," *J. Phys. Chem. A* **101**, 541 (1997).
10. D.E. Sagnella and J.E. Straub, "A study of vibrational relaxation of B-state carbon monoxide in the heme pocket of photolyzed carboxymyoglobin," *Biophys. J.* **77**, 70 (1999).
11. L. Bu and J.E. Straub, "Vibrational frequency shifts and relaxation rates for a selected vibrational mode in cytochrome c," *Biophys. J.* **85**, 1429 (2003).
12. J.L. Skinner and K. Park, "Calculating vibrational energy relaxation rates from classical molecular dynamics simulations: quantum correction factors for processes involving vibration-vibration energy transfer," *J. Phys. Chem. B* **105**, 6716 (2001).
13. H. Fujisaki, L. Bu, and J.E. Straub, *Adv. Chem. Phys.* B **130**, 179 (2005); e-print q-bio.BM/0403019.
14. D.M. Leitner, "Vibrational energy transfer in helices," *Phys. Rev. Lett.* **87**, 188102 (2001); X. Yu and D.M. Leitner, "Vibrational energy transfer and heat conduction in a protein," *J. Phys. Chem. B* **107**, 1698 (2003).
15. D.M. Leitner, private communication.
16. K. Moritsugu, O. Miyashita, and A. Kidera, "Vibrational energy transfer in a protein molecule," *Phys. Rev. Lett.* **85**, 3970 (2000); "Temperature dependence of vibrational energy transfer in a protein molecule," *J. Phys. Chem. B* **107**, 3309 (2003).
17. D. Keilin, *The History of Cell Respirations and Cytochrome*, Cambridge University Press, Cambridge (1966); R.E. Dickerson, "Cytochrome c and the evolution of energy metabolism," *Sci. Am.* **242**, 136 (1980); G.W. Pettigrew and G.R. Moore, *Cytochromes c: Evolutionary, Structural, and Physiochemical Aspects*, Springer-Verlag, Berlin (1990).

18. S.H. Northrup, M.P. Pear, J.A. McCammon, and M. Karplus, "Molecular dynamics of ferrocytochrome c," *Nature* **286**, 304 (1980); C.F. Wong, C. Zheng, J. Shen, J.A. McCammon, and P.G. Wolynes, "Cytochrome c: a molecular proving ground for computer simulations," *J. Phys. Chem.* **97**, 3100 (1993); A.E. Carcía and G. Hummer, "Conformational dynamics of cytochrome c: correlation to hydrogen exchange," *Proteins: Struct. Funct. Genet.* **36**, 175 (1999); A.E. Cardenas and R. Elber, "Kinetics of cytochrome c folding: atomically detailed simulations," *Proteins: Struct. Funct. Genet.* **51**, 245 (2003); X. Yu and D.M. Leitner, "Anomalous diffusion of vibrational energy in proteins," *J. Chem. Phys.* **119**, 12673 (2003).
19. J.K. Chin, R. Jimenez, and F. Romesberg, "Direct observation of protein vibrations by selective incorporation of spectroscopically observable carbon-deuterium bonds in cytochrome c," *J. Am. Chem. Soc.* **123**, 2426 (2001); "Protein dynamics and cytochrome c: correlation between ligand vibrations and redox activity," *J. Am. Chem. Soc.* **124**, 1846 (2002).
20. J.S. Bader and B.J. Berne, "Quantum and classical relaxation rates from classical simulations," *J. Chem. Phys.* **100**, 8359 (1994).
21. B.R. Brooks, R.E. Bruccoleri, B.D. Olafson, D.J. States, S. Swaminathan, and M. Karplus, "CHARMM: a program for macromolecular energy, minimization, and dynamics calculations," *J. Comput. Chem.* **4**, 187 (1983); A.D. MacKerell, Jr., B. Brooks, C.L. Brooks III, L. Nilsson, B. Roux, Y. Won, and M. Karplus, "CHARMM: the energy function and its parameterization with an overview of the program," in *The Encyclopedia of Computational Chemistry*, vol 1, P.v.R. Schleyer et al., editors, John Wiley & Sons: Chichester (1998), p. 271.
22. R. Kubo, M. Toda, and N. Hashitsume, *Statistical Physics II, Nonequilibrium Statistical Mechanics*, Springer-Verlag, Berlin (1991).
23. M. Shiga and S. Okazaki, "An influence functional theory of multiphonon processes in molecular vibrational energy relaxation," *J. Chem. Phys.* **109**, 3542 (1998); "Molecular dynamics study of vibrational energy relaxation of CN^- in H_2O and D_2O solutions: an application of path integral influence functional theory to multiphonon processes," *J. Chem. Phys.* **111**, 5390 (1999).
24. A.A. Maradudin and A.E. Fein, "Scattering of neutrons by an anharmonic crystal," *Phys. Rev.* **128**, 2589 (1962).
25. V.M. Kenkre, A. Tokmakoff, and M.D. Fayer, "Theory of vibrational relaxation of polyatomic molecules in liquids," *J. Chem. Phys.* **101**, 10618 (1994).
26. P. Hamm, M. Lim, and R.M. Hochstrasser, "Structure of the amide I band of peptides measured by femtosecond nonlinear-infrared spectroscopy," *J. Phys. Chem. B* **102**, 6123 (1998).
27. R. Rey and J.T. Hynes, "Vibrational energy relaxation of HOD in liquid D_2O," *J. Chem. Phys.* **104**, 2356 (1996).
28. R. Rey and J.T. Hynes, "Vibrational phase and energy relaxation of CN^- in water," *J. Chem. Phys.* **108**, 142 (1998).
29. S. Okazaki, private communication.
30. T. Mikami, M. Shiga and S. Okazaki, "Quantum effect of solvent on molecular vibrational energy relaxation of solute based upon path integral influence functional theory," *J. Chem. Phys.* **115**, 9797 (2001).
31. R.B. Gerber, G.M. Chaban, S.K. Gregurick, and B. Brauer, "Vibrational spectroscopy and the development of new force fields for biological molecules," *Biopolymers*, **68**, 370 (2003).
32. B. Madan, T. Keyes, and G. Seeley, "Normal mode analysis of the velocity correlation function in supercooled liquids," *J. Chem. Phys.* **94**, 6762 (1991).

33. J. Cao and G.A. Voth, "A theory for time correlation functions in liquids," *J. Chem. Phys.* **103**, 4211 (1995).
34. A.A. Stuchebrukhov and R.A. Marcus, "Theoretical study of intramolecular vibrational relaxation of acetylenic CH vibration for $v = 1$ and 2 in large polyatomic molecules $(CX_3)_3YCCH$, where X = H or D and Y = C or Si," *J. Chem. Phys.* **98**, 6044 (1993); H.J. Bakker, "Vibrational relaxation in the condensed phase", *J. Chem. Phys.* **121**, 10088 (2004).
35. P.H. Nguyen and G. Stock, "Nonequilibrium molecular-dynamics study of the vibrational energy relaxation of peptides in water," *J. Chem. Phys.* **119**, 11350 (2003).
36. R.B. Gerber, V. Buch, and M.A. Ratner, "Time-dependent self-consistent field approximation for intramolecular energy transfer. I. Formulation and application to dissociation of van der Waals molecules," *J. Chem. Phys.* **77**, 3022 (1982); A. Roitberg, R.B. Gerber, R. Elber, and M.A. Ratner, "Anharmonic wave functions of proteins: quantum self-consistent field calculations of BPTI," *Science*, **268,** 1319 (1995); S.K. Gregurick, E. Fredj, R. Elber, and R.B. Gerber, "Vibrational spectroscopy of peptides and peptide-water complexes: anharmonic coupled-mode calculations," *J. Phys. Chem. B* **101**, 8595 (1997); Z. Bihary, R.B. Gerber, and V.A. Apkarian, "Vibrational self-consistent field approach to anharmonic spectroscopy of molecules in solids: application to iodine in argon matrix," *J. Chem. Phys.* **115**, 2695 (2001). For a review of the VSCF methods, see P. Jungwirth and R.B. Gerber, "Quantum molecular dynamics of ultrafast processes in large polyatomic systems," *Chem. Rev.* **99**, 1583 (1999).
37. T. Terashima, M. Shiga, and S. Okazaki, "A mixed quantum-classical molecular dynamics study of vibrational relaxation of a molecule in solution," *J. Chem. Phys.* **114**, 5663 (2001).
38. Q. Shi and E. Geva, "Semiclassical theory of vibrational energy relaxation in the condensed phase," *J. Phys. Chem.* A **107**, 9059 (2003); "Vibrational energy relaxation in liquid oxygen from a semiclassical molecular dynamics simulation," *J. Phys. Chem. A* **107**, 9070 (2003); "On the calculation of vibrational energy relaxation rate constants from centroid molecular dynamics simulations," *J. Chem. Phys.* **119**, 9030 (2003).
39. H. Kim and P.J. Rossky, "Evaluation of quantum correlation functions from classical data," *J. Phys. Chem. B* **106**, 8240 (2002); J.A. Poulsen, G. Nyman, and P.J. Rossky, "Practical evaluation of condensed phase quantum correlation functions: a Feynman-Kleinert variational linearized path integral method," *J. Chem. Phys.* **119**, 12179 (2003).
40. S. Mukamel and D. Abramavicius, "Many-body approaches for simulating coherent nonlinear spectroscopies of electronic and vibrational excitons," *Chem. Rev.* **104**, 2073 (2004).
41. T. Kato and Y. Tanimura, "Multi-dimensional vibrational spectroscopy measured from different phase-matching conditions," *Chem. Phys. Lett.* **341**, 329 (2001); K. Okumura and Y. Tanimura, "Sensitivity of two-dimensional fifth-order Raman response to the mechanism of vibrational mode-mode coupling in liquid molecules," *Chem. Phys. Lett.* **278**, 175 (1997).

16

Anharmonic Decay of Vibrational States in Proteins

Xin Yu and David M. Leitner

CONTENTS

16.1 Introduction

Normal modes of proteins provide a useful starting point for describing dynamics [1–5], thermodynamics [6–8], and for interpreting vibrational spectra [9–12]. Going beyond the harmonic approximation and exploring the limits of its validity begins with examining anharmonicity. In the limit of infinitesimally tiny atomic displacements the normal modes describe the vibrations exactly. As displacements exceed this infinitesimal limit, anharmonic corrections become increasingly important and can appreciably affect, for instance, the vibrational thermodynamic properties of a molecule [13], as well as the vibrational spectrum [9–12]. Anharmonicity also gives rise to vibrational energy transfer. The transfer and storage of vibrational energy mediate kinetics of chemical reactions [14–22], including photochemical reactions in proteins [23–27], allosteric transitions [28], and charge transfer reactions [14, 29]. A proper description of vibrational energy flow in molecules generally requires a quantum mechanical treatment. We address herein the

quantum mechanical transfer of energy among normal modes of hydrated cytochrome c and photoactive yellow protein (PYP) by anharmonic decay. The calculations provide insight into the vibrational lifetimes themselves, their temperature dependence in different spectral regions, the influence of hydration water on energy transfer, and, for the case of PYP, the influence of vibrational energy transfer on photoisomerization kinetics.

To illustrate principles of vibrational energy transfer in a protein, we examine anharmonic decay of vibrational states in cytochrome c. One particular focus of this part of the chapter is the influence of hydration water on energy transfer in a protein. The analysis here extends our recent work on myoglobin [30], as well as earlier work on bovine pancreatic trypsin inhibitor [9, 10] and other studies on myoglobin [31, 32], for which anharmonic matrix elements coupling some of the normal modes were carried out. Important insights into the role of anharmonicity in vibrational spectra and energy flow were gained from these early studies. Roitberg et al., demonstrated the importance of anharmonic corrections to vibrational spectra of low temperature proteins and their interpretation [9, 10]. Computational work by Kidera et al. on myoglobin has highlighted the important role played by Fermi resonances that spatially overlap in classical vibrational energy transfer [31, 32]. Prior to studying myoglobin [30], we calculated the anharmonic decay and dephasing rates of the vibrational states of helical and coil segments of myoglobin consisting of 10 to 24 amino acids [33–35]. This work identified a propensity for certain vibrational modes to overlap in space, depending on the range of frequency and their spatial extent (*vide infra*), a property that restricts the flow of vibrational energy in proteins. This work on vibrational energy transfer complements simulations on vibrational energy flow in myoglobin and cytochrome c, which have also provided connections between protein structure and the typically anisotropic flow of energy [36–40].

Proteins are of course aperiodic systems, a property that influences protein vibrations and energy transfer. Indeed, most normal modes of proteins are localized to a relatively small number of atoms of the protein, meaning that the vibrational amplitude for most atoms in most vibrational modes is exponentially small. It turns out that because most vibrational modes of proteins are spatially localized, the anharmonic decay rate is typically only weakly temperature dependent, as discussed below. We have observed this to be the case for the vibrational modes of myoglobin above 500 cm^{-1}, or even lower [30], and we shall see that the situation is quite similar for hydrated cytochrome c. This trend is consistent with the nearly temperature-independent anharmonic decay rates of high-frequency modes in both myoglobin [41–43] and myoglobin–CO [44] found in pump-probe studies over temperatures from 10 to 310 K.

We also examine vibrations and energy transfer in PYP. The relevance of vibrations and energy transfer to protein function is illustrated by the primary events of many photoactive proteins. In bacteriorhodopsin, for example, ultrafast experiments and simulations reveal that reorganization dynamics of the protein following the sizable charge redistribution in the chromophore

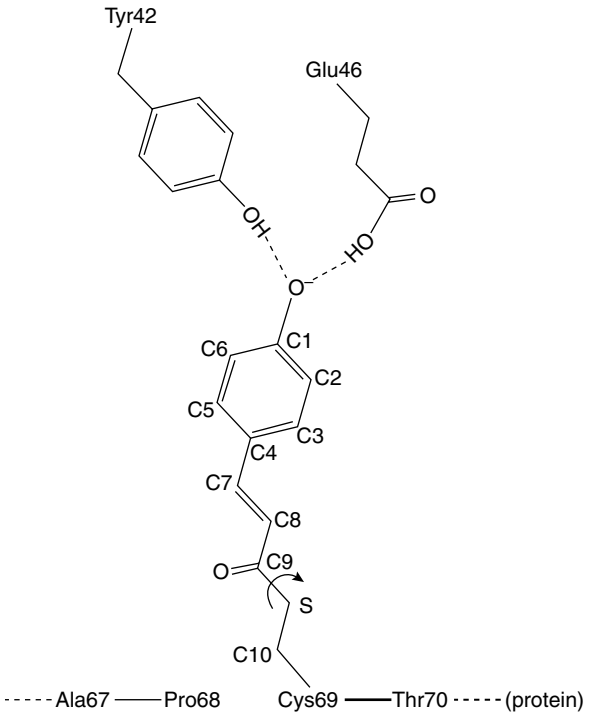

FIGURE 16.1
PYP chromophore and nearby surroundings.

upon photoexcitation occurs by numerous local, small-amplitude motions of charged groups and dipoles throughout the protein [23–25]. The protein does not have time for significant conformational change during the brief period between photoexcitation and isomerization of the chromophore; protein motions responding to charge redistribution of the chromophore are thus largely vibrational. Some of these collective oscillations are dynamically coupled to, and in effect become part of, the reaction coordinate. The dynamic coupling may appear as oscillations in fluorescence decay as the wave packet recrosses the transition state [14] during the course of conformational isomerization.

Ultrafast studies [26, 45, 46] on PYP reveal a similar picture. Mataga et al. [26, 45] have observed coherent oscillations with at least two characteristic frequencies. PYP is a small water-soluble protein of a halophilic photosynthetic bacterium, *Ectothiorhodospira halophila*, which functions as a photoreceptor for negative phototaxis, specifically avoidance of blue light [47–49]. PYP belongs to a family of blue-light receptor proteins, Xanthopsins [47–49], which contain as their light-sensitive chromophore *trans-p*-coumaric acid in PYP, a deprotonated coumaric acid thioester (Figure 16.1). The chromophore is positioned in PYP by hydrogen bonding at the head part, O^--phenyl-, and by covalent bonding at the tail part,

–CO–S–, which undergoes ultrafast twisting by flipping the thioester bond following photoexcitation [47–49]. This twisting motion is coupled to vibrations of the protein matrix. Coherent oscillations appearing in fluorescence decay curves provide information about the frequencies and the nature of these coupled vibrations. Mataga et al. [26, 45] identified coherent oscillations in the fluorescence decay of PYP of roughly 50 and 140 cm^{-1}. Site-directed mutations of the protein can shift the frequency and amplitude of the oscillation as well as the decay rate itself, and correspondingly the rate of conformational change of the chromophore. The amplitude of the lower frequency oscillation appears to be more sensitive to changes in protein environment, though both disappear when PYP is denatured [26, 45]. Mataga et al., suggest that the 140 cm^{-1} is more localized to the chromophore [26], which our analysis corroborates. Recent *ab initio* calculations on the isolated chromophore by Mataga et al. [21] provide an assignment of the 140 cm^{-1} mode. We shall see below that the twisting motion of the chromophore is in fact enhanced by coupling to the protein matrix, and that the energy transfer time from this vibration is comparable to the time for decoherence and on the same timescale as fluorescence decay. The rate of conformational change thus appears to be mediated by the rate of transfer of excess vibrational energy from modes closely associated with conformational change. We discuss how energy transfer appears to us to influence the reaction kinetics at the conclusion of this chapter.

A number of simulations [50–53] and *ab initio* studies [54, 55] on PYP have described PYP dynamics when the chromophore is in its *cis* and *trans* conformation, and how the protein aids in stabilizing the transition state [56, 57]. In the following section, we identify and characterize by analysis of normal modes and their lifetimes, the specific vibrations of PYP that appear as oscillations in fluorescence decay measurements [26]. We have recently characterized these vibrations for PYP in the absence of hydration water [27]; we consider here the effect of hydration water on the coupled vibrations of the chromophore and protein matrix.

In the following section we summarize the computational methods. In Section 16.3.1, we present results of our calculations of anharmonic decay rates of vibrational states of cytochrome c, where we discuss the influence of temperature and hydration. In Section 16.3.2, we present a normal mode analysis on hydrated PYP in the S_1 state, as well as results for the vibrational lifetimes. Concluding remarks follow in Section 16.4.

16.2 Computation of Vibrational Lifetimes

Structures for tuna cytochrome c and PYP were obtained from the Protein Data Bank. We adopt the force fields contained in the program MOIL [58] for the protein, apart from the PYP chromophore. The all-atom model for the PYP chromophore in the S_1 state has been set up with the partial charges reported in Reference 52, which accounts for the charge redistribution in the

chromophore upon photoexcitation with a dipole transition of 8.74 D. Other force field parameters were adopted from MOIL, with some modification to fit low-frequency normal modes (<200 cm^{-1}) of the isolated chromophore to *ab initio* DFT calculations (B3LYP/6-31G*) in the S_1 state, specifically for the isolated chromophore terminated with an ethyl group attached to the sulfur. We shall improve this fit to higher vibrational frequencies in future work. Values for all the force field parameters that we use to model the S_1 state of the PYP chromophore are presented in the appendix.

Each protein was then placed in a cubic box, 50 Å on each side, which was filled with water molecules and heated to 300 K over 10 psec. Five structures were then saved at each subsequent picosecond, and all but the nearest 200 water molecules to the protein were removed for normal mode analysis. Results reported here use the first structure; all were found to give similar results and the same conclusions were reached for each. We note that 200 hydration water molecules are convenient for computation. This number is likely sufficient for function, providing the protein stability and flexibility [59–61]. However, partial thermodynamic properties of these proteins may still change upon addition of more water, perhaps to 400 or 500 molecules [8, 59]. Future work will provide a more systematic study of hydration with even more waters, but in this study we already see the influence of hydration water with a substantial number of molecules.

In describing the normal modes of a protein, it is instructive to compare them conceptually with those of a simple model of a polymer, such as a chain of atoms, both periodic and aperiodic. In a harmonic periodic chain, the normal modes carry energy without resistance from one end of the 1D crystal to the other. On the other hand, the vast majority of normal modes of an aperiodic chain are spatially localized [62]. Protein molecules, which are of course not periodic, can be better characterized as an aperiodic chain of atoms, and most normal modes of proteins are likewise localized in space [1–3, 30]. If a normal mode α is exponentially localized, then the vibrational amplitude of atoms in mode α decays from the center of excitation, $\mathbf{R}_0$, as

$$|\mathbf{e}_\alpha(\mathbf{R}_n)| \propto \exp(-|\mathbf{R}_n - \mathbf{R}_0|/\xi) \tag{16.1}$$

where $|\mathbf{e}_\alpha(\mathbf{R}_n)|$ is the magnitude of the displacement of atom n, located at $\mathbf{R}_n$; ξ is the localization length; and $\mathbf{R}_0$ is the position of the atom overlapping the largest component of the normal mode vector.

We also examine the lifetimes of the normal modes. We compute the vibrational energy transfer rate from mode α, W_α, with the golden rule as we have carried out for other peptides and proteins [30, 33–35]. We consider here only cubic anharmonic terms in the potential energy written as the sum of terms that can be described as decay and collision, the former typically larger except at low frequency where both terms are comparable. Truncation at cubic terms is valid at low temperature, and gives a first estimate for mode lifetimes under other conditions. For the analysis of PYP, where we address fairly low frequency at 300 K, results that we obtain should be taken as a

rough approximation to the vibrational energy transfer rate, which may well be different due to neglect of higher-order anharmonicity. The anharmonic decay rate of vibrational mode α is then the sum of the decay and collision terms given by [63],

$$W_\alpha^{\text{decay}} = \frac{\hbar\pi}{8\omega_\alpha} \sum_{\beta,\gamma} \frac{|\Phi_{\alpha\beta\gamma}|^2}{\omega_\beta\omega_\gamma}(1 + n_\beta + n_\gamma)\delta(\omega_\alpha - \omega_\beta - \omega_\gamma) \tag{16.2a}$$

$$W_\alpha^{\text{coll}} = \frac{\hbar\pi}{4\omega_\alpha} \sum_{\beta,\gamma} \frac{|\Phi_{\alpha\beta\gamma}|^2}{\omega_\beta\omega_\gamma}(n_\beta - n_\gamma)\delta(\omega_\alpha + \omega_\beta - \omega_\gamma) \tag{16.2b}$$

where n_α is the occupation number of mode α, which at temperature T we take to be

$$n_\alpha = (\mathrm{e}^{\hbar\omega_\alpha/k_BT} - 1)^{-1}. \tag{16.3}$$

The matrix elements $\Phi_{\alpha\beta\gamma}$ appear as the coefficients of the cubic terms in the expansion of the interatomic potential in normal coordinates, computed numerically as

$$\Phi_{\alpha\beta\gamma} = (\partial^2 V/\partial Q_\alpha \partial Q_\beta|_{Q_0+\delta Q_\gamma} - \partial^2 V/\partial Q_\alpha \partial Q_\beta|_{Q_0-\delta Q_\gamma})/2\delta Q_\gamma \tag{16.4}$$

where Q_α is a mass-weighted normal coordinate, and Q_0 is the equilibrium position of the protein in normal coordinates.

16.3 Vibrational Energy Transfer in Proteins

16.3.1 Cytochrome c

Figure 16.2(a) shows the normalized density of normal modes of cytochrome c hydrated by 200 water molecules. The density is very close to that for cytochrome c without water, and we show only the density for the hydrated protein. Vibrational frequencies of cytochrome c range from about 5 to 1850 cm^{-1}, and higher frequency modes above 3000 cm^{-1} corresponding to CH, NH, and OH stretches. Only modes lying within the band of frequencies up to $\approx$2000 cm^{-1} will be considered.

In the normal mode representation, a wave packet centered at a certain frequency, ω, can diffuse throughout the entire protein if the localization length of vibrational modes of frequency $\approx\omega$ is extended. If, on the other hand, the normal modes of frequency $\approx\omega$ are localized, energy remains trapped in the region in which it is introduced until freed by anharmonic interactions. The anharmonic interactions themselves are influenced by the extent of localization of the normal modes, as discussed below, and it is therefore of interest to compute the localization length, ξ. We plot the localization length, averaged over modes of cytochrome c in 50-cm^{-1} intervals, in Figure 16.2(b).

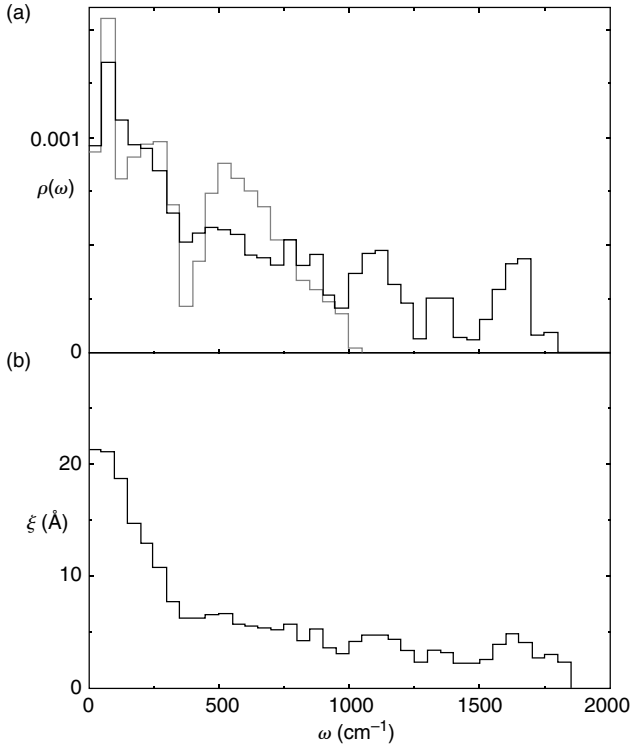

FIGURE 16.2
(a) Normal mode density for cytochrome c hydrated with 200 water molecules (black), and for water modeled by the TIP3 potential (gray); (b) localization length, ξ(Å), for hydrated cytochrome c.

To determine ξ with Equation (16.1), we calculate $\ln |\mathbf{e}_\alpha(\mathbf{R}_n)|$ for all atoms and plot it against $|\mathbf{R}_n - \mathbf{R}_0|$. A linear fit gives ξ. In this way, we have calculated ξ for all the normal modes of cytochrome c in 50 cm^{-1} intervals. At sufficiently low frequency, below about 150 cm^{-1}, the normal modes appear to be essentially delocalized over the protein, with $\xi \approx 18$ to 20 Å, comparable to the protein radius. Above 300 cm^{-1} ξ has decreased to values between 2.5 and 6 Å.

In many cases, it is difficult to assign a normal mode of hydrated cytochrome c to the protein or to the surrounding water. In Figure 16.3 we plot the projection of a normal mode onto atoms of cytochrome c as a function of mode frequency up to 2000 cm^{-1}. (We note that the frequency of the bending mode of an individual water molecule modeled by the TIP3 potential lies above 2000 cm^{-1}.) A normal mode that is uniformly distributed over both the atoms of the protein and the atoms of the water molecules would project about 0.6 onto cytochrome c. The plot reveals significant scatter in the projection with mode frequency, so we also plot a running average over ten modes to examine any trends. We observe that the vibrational modes

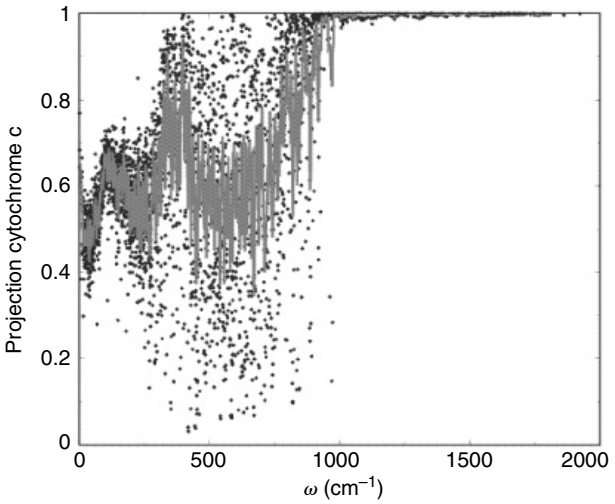

FIGURE 16.3
Projection of the normal modes of hydrated cytochrome c onto atoms of the protein (dots). A running average over 10 points is also plotted to observe trends (gray).

project around the strongly mixed value of about 0.6 up to about 300 cm^{-1}, then again from about 450 to 750 cm^{-1}. In these regions the modes typically involve vibrations of the protein and hydration waters as a whole, rather than protein atoms or water atoms, though, again, there is significant fluctuation around these averages. Between about 300 and 450 cm^{-1}, the vibrational modes project typically more strongly onto the protein. This region corresponds to a relatively low vibrational density of water, separating the higher density translational modes at low frequency, and the librational modes from about 450 to 1000 cm^{-1} (see Figure 16.2[a]) [64, 65]. Most vibrational modes above about 750 cm^{-1} can be characterized as protein modes.

In Figure 16.4 we plot the anharmonic decay rate for cytochrome c as a function of frequency at 15 and 135 K. We consider first cytochrome c without hydration water. Particularly noteworthy is the fairly weak sensitivity of the decay rates to temperature above about 500 cm^{-1}. Significant temperature dependence of the anharmonic decay rate implies that energy is flowing directly into low-frequency modes. The small temperature dependence suggests that, given the high density of low-frequency modes, matrix elements coupling a given high-frequency mode to a pair of other modes are small if the frequency of one of the pair is small. For the matrix element coupling a triple of modes to be appreciable, the three modes must overlap in space [30, 31]. As mode frequency increases, the normal mode vibrations generally become more localized. If energy in a high-frequency localized mode, α, decays into a low-frequency mode of the protein, the rest of the energy must decay into a localized mode whose frequency is similar to ω_α. However, as we shall illustrate, localized modes with similar frequencies rarely overlap in space. As a consequence, energy transfer to a localized mode with similar frequency

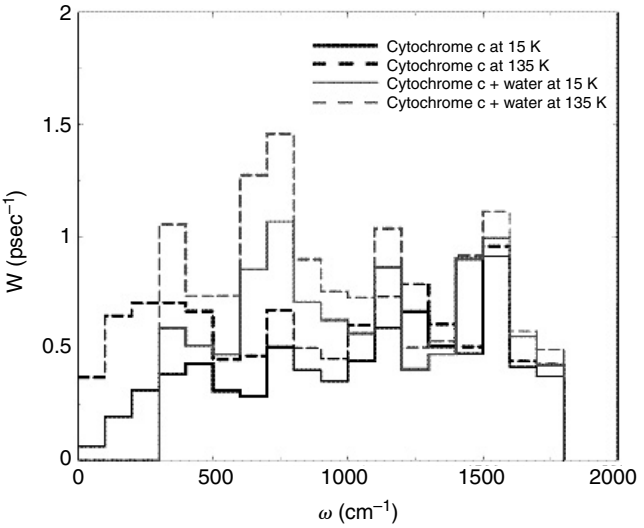

FIGURE 16.4
Rates of anharmonic decay of vibrational states of cytochrome c, averaged over 100 cm^{-1} intervals.

and the remainder to a low-frequency mode occurs slowly, and the anharmonic decay rate from high-frequency modes is only weakly dependent on temperature.

Temperature-independent anharmonic decay rates of high-frequency modes of globular proteins have been observed in time-resolved spectroscopic studies. Pump-probe vibrational spectra of the amide I band of myoglobin, between 1600 and 1700 cm^{-1}, measured at temperatures from 6 to 310 K reveal decay rates ranging only from $\approx$0.5 to 1 psec^{-1} [42], similar to the values we calculate for cytochrome c and myoglobin. Similarly, pump-probe studies on myoglobin–CO reveal that the decay of the CO stretch, about 1950 cm^{-1}, is also essentially independent of temperature over the same temperature range [44].

To examine the role of hydration on vibrational lifetimes of the protein, we have computed the anharmonic decay rate of modes of cytochrome c hydrated by 200 water molecules, and plotted the results in Figure 16.4. Modes that project largely only onto protein or water atoms are designated as protein and water modes, respectively, while others are designated as mixed. Specifically, a mode with projection of $\geqslant$0.8 onto protein atoms is a protein mode, while $\leqslant$0.2 is a water mode. Low-frequency modes are found to be strongly mixed, as already noted. In the amide I region, water only slightly affects the vibrational energy transfer rate. Direct energy transfer to water modes by, for example, a 2:1 Fermi resonance is possible but unlikely since the density of water modes is relatively small above about 700 cm^{-1} (see Figure 16.2 and Figure 16.3). There appears to be some effect of water molecules on the rate at frequencies from 1400 to 1500 cm^{-1}, due largely to the shifting of frequencies

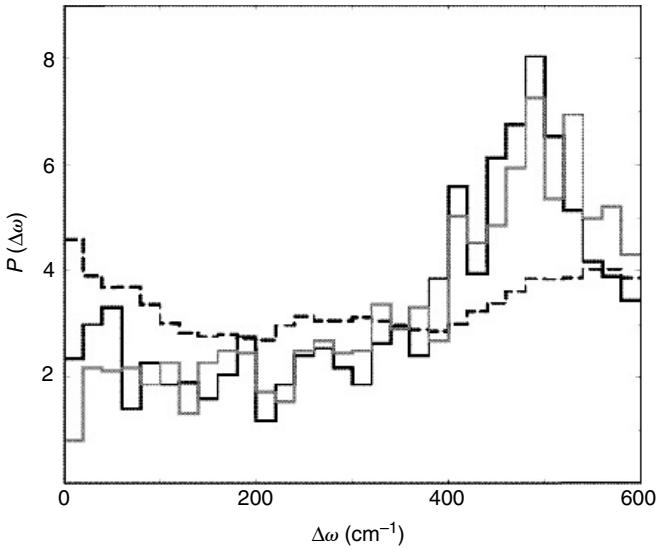

FIGURE 16.5
Probability, $P(\Delta\omega)$, of finding a pair of vibrational modes of hydrated cytochrome c with frequency difference $\Delta\omega$, when at least one of the modes is localized with frequency ω in the range $1000 < \omega < 2000$ cm^{-1}. Dashed line corresponds to any pair of modes with frequency difference $\Delta\omega$, regardless of their distance from one another in space. Solid line (black for hydrated, gray for dehydrated cytochrome c) corresponds to pairs of modes whose largest components are restricted to lie within 2 Å of each other.

of protein acceptor modes by water; the acceptor modes are more of protein character (75%) than water character. There is a noticeable rise in the anharmonic decay rate of protein modes from 300 to 1200 cm^{-1}, roughly by a factor of 2 and with a sizable temperature dependence, which we find to be due almost entirely to the presence of water acceptor modes. The density of water acceptor modes up to about 700 cm^{-1} is typically high and energy flow into them from protein modes of frequency below 1200 cm^{-1} is possible by low-order anharmonic coupling.

One important consequence of strong localization of normal modes is that frequencies of normal modes whose localization centers overlap in space are generally very different [30, 33, 66–68]. This trend gives the appearance of "repulsion" of mode frequencies between pairs of nearby localized modes. The influence of spatial localization of two normal modes in cytochrome c on the frequency difference of these vibrational modes is shown in Figure 16.5. We locate the largest component of each normal mode, α, and calculate the probability, $P(\Delta\omega)$, that for another mode, β, whose largest component lies a certain distance away from the largest component of mode α, the difference in frequency between them is $\Delta\omega = |\omega_\alpha - \omega_\beta|$. We consider only localized modes, α, whose frequency, ω_α, falls between 1000 and 2000 cm^{-1}. Probabilities are calculated for $\Delta\omega$ in intervals of 20 cm^{-1} to $\Delta\omega = 600$ cm^{-1}. The dashed histogram is an average over all pairs of modes, regardless of the distance

between the largest components of modes α and β. We observe that for any pair of modes α and β there is a somewhat greater chance that the difference between their vibrational frequencies is small, say, less than 100 cm^{-1}, than large, say, 300 to 400 cm^{-1}. However, if we only consider pairs of modes whose largest components overlap atoms that lie less than 2 Å from each other, we obtain the solid-line histogram, black for hydrated and gray for dehydrated cytochrome c. There we see that if pairs of localized modes lie close in space, there is a propensity for their frequency differences to be large, in this case around 500 cm^{-1}, rather than small, say, below 200 cm^{-1}. The propensity appears somewhat stronger for the dehydrated protein but is quite similar for the hydrated protein. The apparent mode repulsion diminishes as we consider modes whose largest components lie farther away from each other. For distances between 4 and 5 Å, for instance, we find $P(\Delta\omega)$ to be nearly the same as the dashed histogram.

16.3.2 Photoactive Yellow Protein

Our discussion of cytochrome c has addressed fairly general trends concerning how the vibrational energy transfer rate varies with vibrational mode frequency, temperature, and hydration. In our analysis of PYP, we focus instead on the dynamic interactions between the chromophore and protein matrix, energy flow rates from "chromophore" and "isomerization" modes, and the influence of hydration water. The PYP chromophore is illustrated in Figure 16.1. The projections of normal modes of PYP onto the chromophore include all chromophore atoms through C10 displayed in Figure 16.1, and projections onto the thioester group include C8, C9, S, and O.

To address dynamic interactions between the chromophore and protein matrix, we turn first to the projection of vibrational modes of PYP onto the chromophore and thioester group, plotted in Figure 16.6. The projections plotted in Figure 16.6 are a running average over 24 modes to more easily observe trends in how they vary with mode frequency. Figure 16.6(a) shows projections onto the chromophore for PYP without hydration water (gray) and with 200 water molecules (black). Normal modes of the isolated chromophore (terminated by $–SCH_2CH_3$), are indicated with asterisks. We observe, for dehydrated PYP, a sizable projection of modes of PYP onto the chromophore at frequencies that correspond quite well to the normal mode frequencies of the isolated chromophore. The situation is similar for the projections of the vibrational modes of hydrated PYP onto the chromophore, whose values we have rescaled by the ratio of all atoms in the system to just protein atoms, so that they can be compared directly with those for dehydrated PYP. We observe that for hydrated PYP the peaks in the projections are, in some cases, shifted.

Conformational change of the chromophore upon photoexcitation occurs largely at the thioester group (we include in this group the atoms S, C8, C9, and O in Figure 16.1). Thus, we also consider projections onto this group in

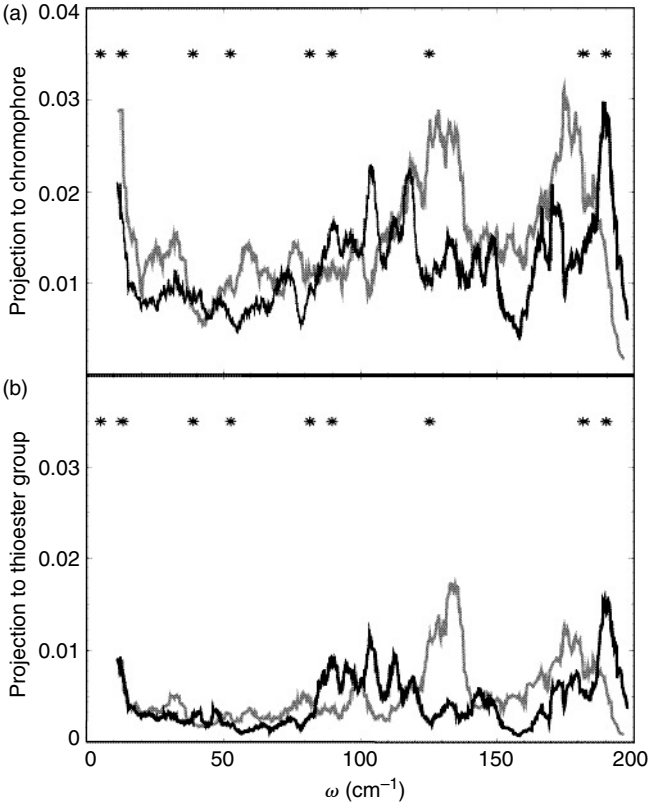

FIGURE 16.6
(a) Projection of normal modes of hydrated (black) and dehydrated (gray) S_1 PYP onto chromophore; (b) projection of normal modes of hydrated (black) and dehydrated (gray) S_1 PYP onto thioester group. Projections for the hydrated protein have been rescaled to fit the same scale as the dehydrated protein, as described in the text. Vibrational frequencies of the isolated chromophore are indicated (asterisks).

Figure 16.6(b). Turning first to dehydrated PYP, we find significant projection for normal modes near 135 cm^{-1}, not far from the 125.26 cm^{-1} mode of the isolated chromophore. The projection of these modes onto the thioester group of about 0.017 is more than three times higher than what it would be, 0.005, if the vibration were uniformly distributed over the protein. It also makes a relatively large contribution to the projection onto the whole chromophore, which is 0.028, or about 60% of the projection onto the whole chromophore. This can be compared to the projection of the nearby 125.26 cm^{-1} mode of the isolated chromophore onto the thioester group of only 19%. The vibrations of atoms involved in conformational change are thus of larger amplitude, relative to the vibrational amplitude of all the chromophore atoms, when the chromophore is embedded in the protein as opposed to isolated. Turning now to hydrated PYP, we find that this projection is shifted to lower frequency, and is also broadened over a range from about 90 to about 130 cm^{-1}.

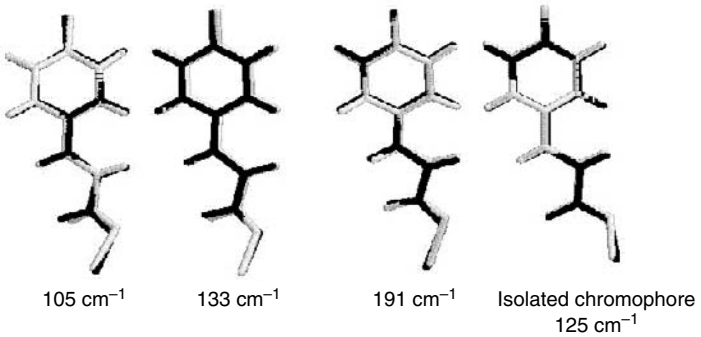

FIGURE 16.7
The direction of atomic displacements of the PYP chromophore for vibrational modes of hydrated PYP at 105, 133, and 191 cm^{-1} is shown. The minimized structure is in black and the displaced structure is in gray. Twisting of the S–C bond of the thioester group is significantly greater for the 105 and 133 cm^{-1} modes than that of a corresponding mode of the isolated chromophore at 125 cm^{-1}, also shown. The latter involves instead twisting of the phenyl ring, which moves less when the chromophore is embedded in the protein. The isolated chromophore is terminated by $–SCH_2CH_3$ (terminal methyl group not shown in the figure).

We have examined the vibrational modes themselves in the main peaks over this range, and each appears to be characteristic of an "isomerization" mode (cf. Figure 16.7 and below), quite similar to the analogous "isomerization" modes near 135 cm^{-1} of dehydrated PYP.

The direction of the displacements of the chromophore atoms of dehydrated PYP in the vibrational modes near 130 cm^{-1} is consistent with this mode being at least one of the "isomerization" modes [27]. We find similar "isomerization" modes for hydrated PYP near 130 cm^{-1}, too, but the range in frequency of such modes is broader than for dehydrated PYP, and they extend down to about 100 cm^{-1}. The direction of the displacements of chromophore atoms for two such modes is shown in Figure 16.7. Also plotted in Figure 16.7 is the nearby 125 cm^{-1} mode of the isolated chromophore. There is for this latter mode some tendency toward isomerization, but this motion is clearly enhanced when the chromophore is embedded in the protein, that is the amplitude of displacement of atoms in the direction of isomerization is enhanced. Dynamical coupling between the chromophore and protein apparently helps to guide isomerization. This is particularly so for the hindered rotation of O, which moves in a direction opposite to that of S, with the overall twisting motion in the direction of conformational change. In contrast, we see for the isolated chromophore significantly more rotation of the phenyl group, which is less pronounced when the chromophore is embedded in the protein due to anchoring by hydrogen bonds at the anion. We also plot in Figure 16.7 the direction of atomic displacements for a vibrational mode at 191 cm^{-1}, a mode that, as seen in Figure 16.6, also projects strongly onto the thioester group. In contrast to the vibrational modes from 105 to 135 cm^{-1}, we observe that the motion of O and S is in the same direction, rather than opposite. The vibrational modes near 191 cm^{-1}, despite strong projection onto the chromophore,

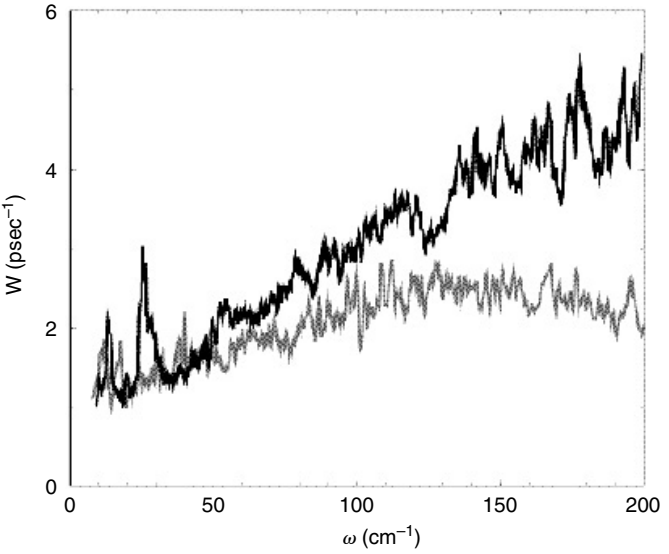

FIGURE 16.8
Energy transfer rate from normal modes of hydrated (black curve) and dehydrated (gray) PYP.

contribute less to isomerization than the modes from 105 to 135 cm^{-1}, which appear to be those that give rise to the $\approx$140 cm^{-1} oscillation observed in the fluorescence decay.

We now turn to the lifetimes of PYP vibrational modes. Vibrational energy transfer rates computed for hydrated and dehydrated PYP are plotted in Figure 16.8 at 300 K for frequencies up to 200 cm^{-1}. The results plotted are running averages over 8 modes to make more visible trends in the energy transfer rate with frequency. The energy transfer rates for the hydrated protein are typically faster than for dehydrated PYP, more so as the frequency increases toward 200 cm^{-1}. Up to this frequency, the computed lifetimes range from about 400 fsec to about 1 psec for dehydrated PYP, while they range from about 200 fsec to about 1 psec for hydrated PYP. The lifetimes of the computed $\approx$130 cm^{-1} vibrational modes are fairly similar for PYP with or without hydration water, about 300 to 400 fsec.

Excess energy in a vibrational mode of, say, 130 cm^{-1} may flow via anharmonic coupling to other modes that largely overlap the chromophore, thus keeping much of the energy in this part of the protein. The energy may also be redistributed to modes that overlap the chromophore much less. The latter case leads to cooling of the chromophore via transfer of energy to the protein matrix or water. There is of course no sharp distinction between a vibrational mode of PYP that it is a chromophore mode or not. Nevertheless, taking the peaks in projections in Figure 16.6(a) to represent bands of chromophore modes, we attempt to identify how much of the energy flows to modes within these peaks and how much flows elsewhere. We find, for example, that the

rate of energy transfer from the "chromophore" modes near 100 to 130 cm^{-1} to protein modes outside this band (and outside other bands of "chromophore" modes), amounts to about half of the total energy transfer rate from the ≈100 to 130 cm^{-1} modes computed with all accepting modes. The rest of the energy flows largely to other modes in the 100 to 130 cm^{-1} band and into a very low-frequency mode corresponding to translation of the chromophore within the protein. The time for energy to flow out of the chromophore is about half the lifetime of any vibrational mode in the 100 to 130 cm^{-1} band, so roughly 600 to 700 fsec for hydrated PYP, close to the measured 700 fsec coherence time for the 140 cm^{-1} oscillation [26].

Mataga et al. [26], also observed a second coherent oscillation in their fluorescence decay measurements. The second oscillation has a frequency of 40 cm^{-1} for wild type PYP and is quite sensitive to mutation, the shift in frequency upon mutation being considerably greater than that for the 140 cm^{-1} mode, which lies within a few cm^{-1} of this value for wild type PYP and several mutants. Mataga et al. [26], argue that this mode is more a protein matrix vibration than the mode near 140 cm^{-1}, since the damping of this oscillation appears to be more strongly affected by mutation than the oscillation near 140 cm^{-1}. Normal mode analysis reveals that this oscillation is indeed less localized on the chromophore than is the ≈140 cm^{-1} oscillation. We see in Figure 16.6 that projections onto the chromophore for modes in the range 40 to 80 cm^{-1} are smaller than the projections around 100 to 130 cm^{-1}. It is also not as easy to identify a particular oscillation that might correspond to the values reported in Reference 26; several peaks in the projection appear that roughly correspond to the isolated chromophore vibrations near 40, 50, 80, and 90 cm^{-1}. One possibility could be the vibrations near 50 for hydrated PYP, which correspond roughly to the 52.52 cm^{-1} mode of the isolated chromophore. Still, the observed oscillation in the range 40 to 80 cm^{-1} may in fact correspond to different sets of vibrations. This interpretation is consistent with that of recent *ab initio* calculations on the isolated chromophore by Mataga et al. [46]. They found that the lower frequency oscillation was difficult to characterize by a single mode of the chromophore, but suggested that it might correspond to an out-of-plane mode of the isolated chromophore near 55 cm^{-1} [46].

16.4 Concluding Remarks

We have illustrated some general properties of vibrational energy transfer in proteins by anharmonic decay with a case study of cytochrome c, as well as properties that specifically influence photoisomerization kinetics in PYP. For cytochrome c, we considered how rates of vibrational energy transfer vary with vibrational mode frequency, and how they are influenced by the spatial extent of the vibrational modes over the protein, temperature, and hydration. We analyzed the normal modes of S_1 PYP to identify vibrations

associated with isomerization, which appear as oscillations in fluorescence decay measurements [26]. We also computed energy transfer rates in PYP and vibrational cooling of the chromophore.

The normal modes of cytochrome c range from about 5 to about 1850 cm^{-1}, and again from 3000 to 4000 cm^{-1}, the latter corresponding to hydrogen atom vibrations. Most normal modes of cytochrome c, as for other globular proteins, are localized, that is, the vibrational amplitude is sizable for a relatively small number of atoms of the protein. For cytochrome c, vibrational modes above 150 cm^{-1} are localized. Energy is transferred from the localized normal modes by anharmonic coupling, and localization of these modes influences the possible pathways by which energy can flow. We have seen that two localized modes whose centers of excitation are close in space tend to have quite different frequencies, that is, localized modes at higher frequencies appear to "repel" one another. Thus modes with similar frequencies rarely overlap in space. Since energy transfer requires Fermi resonances among spatially overlapping modes in a protein, "mode repulsion" influences the pathway and rate of anharmonic decay of higher frequency, localized modes. Anharmonic matrix elements coupling, for example, two high-frequency modes and a low-frequency mode are usually small because of mode repulsion, and energy transfer from a high-frequency mode to a mode of similar frequency and the remainder to low-frequency modes often occurs very slowly. Energy flows preferably to modes of intermediate frequencies provided resonances are available. As a result, lifetimes of higher frequency modes are typically only weakly dependent on temperature. This trend is consistent with the nearly temperature-independent vibrational energy transfer rates of high-frequency modes in both myoglobin [42] and myoglobin–CO [44] from 10 to 310 K found in pump-probe studies.

The small temperature dependence of the energy transfer rate is influenced by hydration water. The influence of hydration water on the rate of vibrational energy transfer from the experimentally well-studied amide I region is small, due to a low density of water modes that can accept vibrational energy by low-order anharmonicity, but hydration water plays a greater role in energy transfer at lower frequency. Below 1200 cm^{-1}, vibrational modes of the hydration water accept vibrational energy from the protein. Even at higher frequency, in the range 1400 to 1500 cm^{-1}, we find that hydration water influences energy transfer in the protein, not so much by directly accepting energy from the protein but instead, by tuning resonances and pathways.

Our work on S_1 PYP has examined dynamical coupling between the chromophore and surrounding protein matrix and its role in guiding photoisomerization, in particular the twisting of the thioester group, by analysis of normal modes and energy transfer among them. Experimental and computational studies of fast photochemical reactions in proteins, in particular ultrafast studies and simulations on bacteriorhodopsin [23–25], reveal that a large charge redistribution in the chromophore upon photoexcitation is followed by many local, small-amplitude motions of charges and dipoles.

Charge rearrangement in the chromophore sets in motion collective oscillations of the protein, some of which couple to, and are thus part of, the reaction coordinate. Such a picture also describes the photoisomerization of PYP. The collective dielectric response of the protein appears to be coupled to coherent wave packet motion on the chromophore, which has been observed to occur with at least two characteristic frequencies in PYP and several mutants by Mataga et al. [26, 45, 46]. Our vibrational analysis on wild type PYP, summarized here, and two mutants in earlier work [27], provides information about the dynamical coupling that underlies the observed oscillations in the fluorescence decay.

We find that modes with frequencies near 100 to 130 cm^{-1} project significantly onto the thioester group where conformational change largely occurs. The vibrations appear to correspond to the oscillation observed near 140 cm^{-1} for wild type PYP and several mutants by Mataga et al. [26], which they argued substantially overlaps the chromophore. The vibrational modes near 100 to 130 cm^{-1} computed for PYP project more onto the thioester group than does the nearby 125 cm^{-1} mode of the isolated chromophore. Enhancement of the twisting motion of the thioester group for the $\approx$100 to 130 cm^{-1} modes of the protein (Figure 16.7) reveals the significance of dynamical coupling between the chromophore and protein scaffolding in guiding isomerization. This significance is further revealed by analysis in an earlier study [27] of the P68A mutant, for which we found the overlap of modes near 130 cm^{-1} onto the thioester group to be smaller, consistent with the observed [26] slower fluorescence decay of P68A.

We have also computed vibrational energy transfer rates in PYP and cooling times for the vibrational modes near 100 to 130 cm^{-1}. Vibrational energy flow mediates rates of photoisomerization [16, 20] and PYP appears to be no exception. The faster component of fluorescence decay has a time constant of 238 fsec [26], corresponding to about 130 cm^{-1}. If there is a small barrier, the excess vibrational energy that the "isomerization" modes from about 100 to 130 cm^{-1} may have following photoexcitation can assist reaction before deactivation by vibrational energy redistribution. The 3.1 psec component [26] of the fluorescence decay of PYP is on the same scale as the computed time of about 0.7 to 1 psec for vibrational energy transfer to and from isomerization modes of 100 to 130 cm^{-1}, the difference likely due to the presence of a barrier of perhaps 1 kcal mol^{-1}.

Acknowledgments

This work was supported by the National Science Foundation (NSF CHE-0112631 and CHE-0512145), a New Faculty Award from the Camille and Henry Dreyfus Foundation and by a Research Innovation Award from the Research Corporation.

Appendix: Force Field for Chromophore

The form of the potential energy function is

$$E = \frac{1}{2}\sum_{\text{bonds}} K_r(r-r^0)^2 + \frac{1}{2}\sum_{\text{angles}} K_\theta(\theta-\theta^0)^2 + \frac{1}{2}\sum_{\text{impropers}} K_\varphi(\varphi-\varphi^0)^2 + \frac{1}{2}\sum_{\text{dihedrals}} K_\phi((1+\cos(n\phi+\phi^0))) + \sum_{\substack{\text{nonbonded}\\ i-j \text{ pairs}}} \frac{q_i q_j}{R_{ij}} + \sum_{\substack{\text{nonbonded}\\ i-j \text{ pairs}}} \varepsilon_{ij}\left(\left(\frac{R_{\min,ij}}{R_{ij}}\right)^{12} - 2\left(\frac{R_{\min,ij}}{R_{ij}}\right)^{6}\right) \tag{A.1}$$

For all bonds, valence angles, and improper torsions, force constants $(K_r, K_\theta, K_\varphi)$ and equilibrium values $(r^0, \theta^0, \varphi^0)$ must be defined. For each dihedral term, three parameters are needed: the force constant K_ϕ, the periodicity n, and the phase ϕ^0. For electrostatic nonbonded interactions, each atom needs to be assigned a proper partial charge q_i [53]. The van der Waals parameters are the usual atom-type dependent parameters: well depth ε_{ij}, and minimum interaction radius, $R_{\min,ij}$.

TABLE 16.A1

Stretching Parameters for the Chromophore: Force Constant K_r (kcal mol^{-1} Å^{-2}) and Equilibrium Distance r^0 (Å).

Bond	K_r	r^0
C9–O2	570.0	1.229
C8–C9	317.0	1.493
C8–C7	317.0	1.510
C7–C4	317.0	1.510
C4–C3	469.0	1.400
C4–C5	469.0	1.400
C3–C2	469.0	1.400
C5–C6	469.0	1.400
C2–C1	469.0	1.400
C6–C1	469.0	1.400
C8–H8	367.0	1.080
C7–H7	367.0	1.080

(continued)

TABLE 16.A1

Continued

Bond	K_r	r^0
C3–H3	340.0	1.080
C5–H5	340.0	1.080
C2–H2	340.0	1.080
C6–H6	340.0	1.080
C9–S	450.0	1.364
C1–O1	450.0	1.364
S–Cβ	222.0	1.810
Cβ–Cα	260.0	1.526

TABLE 16.A2

Bending Parameters for the Chromophore: Force Constant K_θ (kcal mol^{-1} rad^{-2}) and Equilibrium Angle θ^0 (degree).

Valence angle			K_θ	θ^0
Cβ	S	C9	70.0	120.0
S	Cβ	Cα	50.0	108.6
C8	C9	S	70.0	120.0
O2	C9	S	80.0	126.0
O2	C9	C8	80.0	120.4
C9	C8	C7	63.0	120.0
C8	C7	C4	63.0	120.0
C7	C4	C3	70.0	120.0
C7	C4	C5	70.0	120.0
C4	C3	C2	85.0	120.0
C4	C5	C6	85.0	120.0
C3	C4	C5	85.0	120.0
C2	C1	C6	85.0	120.0
C3	C2	C1	85.0	120.0
C5	C6	C1	85.0	120.0
C2	C1	O1	70.0	120.0
C6	C1	O1	70.0	120.0
H8	C8	C7	35.0	120.0
H8	C8	C9	35.0	120.0
H7	C7	C8	35.0	120.0
H7	C7	C4	35.0	120.0
H3	C3	C4	35.0	120.0
H5	C5	C4	35.0	120.0
H3	C3	C2	35.0	120.0
H5	C5	C6	35.0	120.0
H2	C2	C1	35.0	120.0
H6	C6	C1	35.0	120.0
H2	C2	C3	35.0	120.0
H6	C6	C5	35.0	120.0

TABLE 16.A3

Tortional Parameters for the Chromophore: Force Constant K_ϕ (kcal mol^{-1}), Multiplicity n, and Phase ϕ^0 (degree).

Dihedral angle				K_ϕ	n	ϕ^0
Cβ	S	C9	C8	0.1	2	180
S	C9	C8	C7	2.65	2	180
O2	C9	C8	C7	0.1	3	0
C8	C7	C4	C5	2.65	2	180
C8	C7	C4	C3	2.65	2	180
C7	C4	C3	C2	5.3	2	180
C7	C4	C5	C6	5.3	2	180
C9	C8	C7	C4	2.65	2	180
C3	C2	C1	C6	2.65	2	180
C3	C2	C1	O1	2.65	2	180
C4	C3	C2	C1	5.3	2	180
H3	C3	C4	C5	0.1	2	180
H3	C3	C2	C1	0.1	2	180
H5	C5	C4	C3	0.1	2	180
H5	C5	C6	C1	0.1	2	180
H2	C2	C3	C4	0.1	2	180
H2	C2	C1	C6	0.1	2	180
H6	C6	C5	C4	0.1	2	180
H6	C6	C1	C2	0.1	2	180

TABLE 16.A4

Improper Torsion Parameters for the Chromophore: Force Constant K_φ (kcal mol^{-1} rad^{-2}) and Equilibrium Value φ^0 (degree).

Improper torsion				K_φ	φ^0
C9	C8	O2	S	100.0	0.0
C4	C3	C7	C5	90.0	0.0
C1	C2	C6	O1	150.0	0.0
C8	H8	C7	C9	45.0	0.0
C7	H7	C8	C4	45.0	0.0
C3	H3	C4	C2	145.0	0.0
C2	H2	C1	C3	145.0	0.0
C5	H5	C4	C6	145.0	0.0
C6	H6	C1	C5	145.0	0.0

References

1. Nishikawa, T. and Go, N., Normal modes of vibration in bovine pancreatic trypsin inhibitor and its mechanical property, *Proteins: Struct. Funct. Genet.* 2, 308 (1987).

2. Brooks, C.L., Karplus, M., and Pettitt, B.M., Proteins: a theoretical perspective of dynamics, structure, and thermodynamics, *Adv. Chem. Phys.* 71, 1 (1988).
3. McCammon, J.A. and Harvey, S.C., *Dynamics of Proteins and Nucleic Acids*, Cambridge University Press, Cambridge, 1987.
4. Li, G. and Cui, Q., A coarse-grained normal mode approach for macromolecules: an efficient implementation for application to Ca^{2+}-ATPase, *Biophys. J.* 83, 2457 (2002).
5. Li, G. and Cui, Q., Analysis of functional motions in Brownian molecular machines with an efficient block normal mode approach. Myosin-II and Ca^{2+}-ATPase, *Biophys. J.* 86, 743 (2004).
6. Tidor, B. and Karplus, M., The contribution of vibrational entropy to molecular association: the dimerization of insulin, *J. Mol. Biol*. 238, 405 (1994).
7. Smith, J.C., Merzel, F., Verma, C.S., and Fischer, S., Protein hydration water: structure and thermodynamics, *J. Mol. Liquids* 101, 27 (2002).
8. Yu, X., Park, J., and Leitner, D.M., Thermodynamics of protein hydration computed by molecular dynamics and normal modes, *J. Phys. Chem. B* 107, 12820 (2003).
9. Roitberg, A., Gerber, R.B., Elber, R., and Ratner, M.A., Anharmonic wave functions of proteins: quantum self-consistent field calculations of BPTI, *Science* 268, 1319 (1995).
10. Roitberg, A., Gerber, R.B., and Ratner, M.A., A vibrational eigenfunction of a protein: anharmonic coupled-mode ground and fundamental excited states of BPTI, *J. Phys. Chem. B* 101, 1700 (1997).
11. Gerber, R.B., Bauer, B., Gregurick, S.K., and Chaban, G.M., Calculation of anharmonic vibrational spectroscopy of small biological molecules, *Phys. Chem. Commun*. 5, 142 (2002).
12. Gerber, R.B. et al., Vibrational spectroscopy and the development of new force fields for biological molecules, *Biopolymers* 68, 370 (2003).
13. Calvo, F., Doye J.P.K., and Wales, D.J., Characterization of anharmonicities on complex potential energy surfaces: perturbation theory and simulation, *J. Chem. Phys*. 115, 9627 (2001).
14. Onuchic, J.N. and Wolynes, P.G., Classical and quantum pictures of reaction dynamics in condensed matter: resonances, dephasing and all that, *J. Phys. Chem.* 92, 6495 (1988).
15. Berne, B.J., Borcovec, M., and Straub, J.E., Classical and modern methods in reaction rate theory, *J. Phys. Chem.* 92, 3711 (1988).
16. Leitner, D.M. and Wolynes, P.G., Quantum energy flow during molecular isomerization, *Chem. Phys. Lett*. 280, 411 (1997).
17. Leitner, D.M., Influence of quantum energy flow and localization on molecular isomerization in gas and condensed phases, *Int. J. Quant. Chem.* 75, 523 (1999).
18. Nordholm, S., Photoisomerization of stilbene: a theoretical study of deuteration shifts and limited internal vibrational redistribution, *Chem. Phys.* 137, 109 (1989).
19. Nordholm, S. and Bäck, A., On the role of nonergodicity and slow IVR in unimolecular reaction rate theory — a review and a view, *Phys. Chem. Chem. Phys.* 3, 2289 (2001).
20. Leitner et al., Quantum energy flow and trans-stilbene photoisomerization: an example of a non-RRKM reaction, *J. Phys. Chem. A* 107, 10706 (2003).
21. Kuharski, R.A. et al., Stochastic molecular dynamics study of cyclohexane isomerization, *J. Phys. Chem.* 92, 3261 (1988).

22. Leitner, D.M., Heat transport in molecules and reaction kinetics: the role of quantum energy flow and localization, *Adv. Chem. Phys.* (in press).
23. Kennis, J.T.M. et al., Ultrafast protein dynamics of bacteriorhodopsin probed by photon echo and transient absorption spectroscopy, *J. Phys. Chem. B* 106, 6067 (2002).
24. Xu, D., Martin, C.H., and Schulten, K., Molecular dynamics study of early picosecond events in the bacteriorhodopsin photocycle: dielectric response, vibrational cooling and the J, K intermediates, *Biophys. J.* 70, 453 (1996).
25. Hayashi, S., Tajkhorshid, E. and Schulten, K., Molecular dynamics simulation of bacteriorhodopsin's photoisomerization using ab initio forces for the excited state chromophore, *Biophys. J.* 85, 1440 (2003).
26. Mataga, N. et al., Ultrafast photoinduced reaction dynamics of photoactive yellow protein (PYP): observation of coherent oscillations in the femtosecond fluorescence decay dynamics, *Chem. Phys. Lett.* 352, 220 (2002).
27. Yu, X. and Leitner, D.M., Chromophore vibrations during isomerization of photoactive yellow protein: analysis of normal modes and energy transfer, *Chem. Phys. Lett.* 391, 181 (2004).
28. Miller, R.J.D., Vibrational energy relaxation and structural dynamics of heme proteins, *Annu. Rev. Phys. Chem.* 42, 581 (1991).
29. Antoniou, D. and Schwartz, S.D., Large kinetic isotope effects in enzymatic proton transfer and the role of substrate oscillations, *Proc. Natl Acad. Sci. USA* 94, 12360 (1997).
30. Yu X. and Leitner, D.M., Vibrational energy transfer and heat conduction in a protein, *J. Phys. Chem. B* 107, 1698 (2003).
31. Moritsugu, K., Miyashita, O., and Kidera, A., Vibrational energy transfer in a protein molecule, *Phys. Rev. Lett.* 85, 3970 (2000).
32. Moritsugu, K., Miyashita, O., and Kidera, A., Temperature dependence of vibrational energy transfer in a protein molecule, *J. Phys. Chem. B* 107, 3309 (2003).
33. Leitner, D.M., Anharmonic decay of vibrational states in helical peptides, coils and one-dimensional glasses, *J. Phys. Chem. A* 106, 10870 (2002).
34. Leitner, D.M., Vibrational energy transfer in helices, *Phys. Rev. Lett.* 87, 188102 (2001).
35. Leitner, D.M., Temperature dependence of the pure vibrational dephasing rate in a heteropolymer, *Chem. Phys. Lett.* 359, 434 (2002).
36. Sagnella, D.E., Straub, J.E., and Thirumalai, D., Timescales and pathways for kinetic energy relaxation in solvated proteins: application to carbonmonoxy myoglobin, *J. Chem. Phys.* 113, 7702 (2000).
37. Sagnella, D.E. and Straub, J.E., Directed energy "funneling" mechanism for heme cooling following ligand photolysis or direct excitation in solvated carbonmonoxy myoglobin, *J. Phys. Chem. B* 105, 7057 (2001).
38. Bu, L. and Straub, J.E., Simulating vibrational energy flow in proteins: relaxation rate and mechanisms for heme cooling in cytochrome c, *J. Phys. Chem. B* 107, 12339 (2003).
39. Wang, Q., Wong, C.F., and Rabitz, H., Simulating energy flow in biomolecules: application to tuna cytochrome c, *Biophys. J.* 75, 60 (1998).
40. Yu, X. and Leitner, D.M., Anomalous diffusion of vibrational energy in proteins, *J. Chem. Phys.* 119, 12673 (2003).
41. Hamm, P., Lim, M., and Hochstrasser, R.M., Structure of the amide I band of peptides measured by fs nonlinear-infrared spectroscopy, *J. Phys. Chem. B* 102, 6123 (1998).

42. Peterson, K.A., Rella, C.W., Engholm, J.R., and Schwettman, H.A., Ultrafast vibrational dynamics of the myoglobin amide I band, *J. Phys. Chem. B* 103, 557 (1999).
43. Xie, A., van der Meer, L., Hoff, W., and Austin, R.H., Long-lived amide I vibrational modes in myoglobin, *Phys. Rev. Lett.* 84, 5435 (2000).
44. Fayer, M.D., Fast protein dynamics probed with infrared vibrational echo experiments, *Annu. Rev. Phys. Chem.* 52, 315 (2001).
45. Mataga, N., Ultrafast photoreactions in protein nanospaces as revealed by fs fluorescence dynamics measurements on photoactive yellow protein and related systems, *Phys. Chem. Chem. Phys.* 5, 2454 (2003).
46. Chosrowjan, H. et al., Low frequency vibrations and their role in ultrafast photoisomerization reaction dynamics of photoactive yellow protein, *J. Phys. Chem. B* 108, 2686 (2004).
47. Hellingwerf, K.J., Hendriks, J., and Gensch, T., Photoactive yellow protein, a new type of photoreceptor protein: will this 'yellow lab' bring us where we want to go? *J. Phys. Chem. A* 107, 1082 (2003).
48. Cusanovich, M.A. and Meyer, T.E., Photoactive yellow protein: a prototypic PAS domain sensory protein and development of a common signaling mechanism, *Biochemistry* 42, 4759 (2003).
49. van der Horst, M.A. and Hellingwerf, K.J., Photoreceptor proteins, "star actors of modern times": a review of the functional dynamics in the structure of representative members of six different photoreceptor families, *Acc. Chem. Res.* 37, 13 (2004).
50. Larsen, D.S. et al., Initial photo-induced dynamics of the photoactive yellow protein chromophore in solution, *Chem. Phys. Lett.* 369, 563 (2003).
51. van Aalten, D.M.F. et al., Concerted motions in the photoactive yellow protein, *Prot. Eng.* 11, 873 (1998).
52. Antes, I., Thiel, W., and van Gunsteren, W.F., Molecular dynamics simulations of photoactive yellow protein (PYP) in three states of its photocycle: a comparison with x-ray and NMR data and analysis of the effects of Glu46 deprotonation and mutation, *Eur. Biophys. J.* 31, 504 (2002).
53. Groenhof, G. et al., Signal transduction in the photoactive yellow protein. I. Photon absorption and the isomerization of the chromophore, *Proteins: Struct. Funct. Genet.* 48, 202 (2002).
54. Groenhof, G., Signal transduction in the photoactive yellow protein. II. Proton transfer initiates conformational changes, *Proteins: Struct. Funct. Genet.* 48, 212 (2002).
55. Thompson, M.J., Bashford, D., Noodleman, L., and Getzoff, E.D., Photoisomerization and proton transfer in photoactive yellow protein, *J. Am. Chem. Soc.* 125, 8186 (2003).
56. Yamada, A., Ishikura, T., and Yamato, T., Role of protein in the primary step of the photoreaction of yellow protein, *Proteins: Struct. Func. Bioinfo.* 55, 1063 (2004).
57. Yamada, A., Ishikura, T., and Yamato, T., Direct measure of functional importance visualized atom-by-atom for photoactive yellow protein: application to photoisomerization reaction, *Proteins: Struct. Func. Bioinfo.* 55, 1070 (2004).
58. Elber R. et al., MOIL: a program for simulations of macromolecules, *Comput. Phys. Commun.* 91, 159 (1995).
59. Rupley, J.A. and Careri, G., Protein hydration and function, *Adv. Prot. Chem.* 41, 37 (1991).
60. Steinbach, P.J. and Brooks, B.R., Protein hydration elucidated by molecular dynamics simulation, *Proc. Natl Acad. Sci. USA* 90, 9135 (1993).

61. Bizzarri, A.R. and Cannistraro, S., Molecular dynamics of water at the protein–solvent interface, *J. Phys. Chem. B* 106, 6617 (2002).
62. Ishii, K., Localization of eigenstates and transport phenomena in the one-dimensional disordered systems, *Suppl. Prog. Theor. Phys.* 53, 77 (1973).
63. Maradudin, A.A. and Fein, A.E., Scattering of neutrons by an anharmonic crystal, *Phys. Rev.* 128, 2589 (1962).
64. Pohorille A. et al., Comparison of the structure of harmonic aqueous glasses and liquid water, *J. Chem. Phys.* 87, 6070 (1988).
65. Cho, M. et al., Instantaneous normal mode analysis of liquid water, *J. Chem. Phys.* 100, 6672 (1994).
66. Fabian, J. Decay of localized normal modes in glasses: a one-dimensional example, *Phys. Rev. B* 55, R3328 (1997).
67. Fabian, J., and Allen, P.B., Anharmonic decay of vibrational states in amorphous silicon, *Phys. Rev. Lett.* 79, 1885 (1997).
68. Leitner, D.M., Vibrational energy transfer and heat conduction in a one-dimensional glass, *Phys. Rev. B* 64, 094201 (2001).

17

Collective Coordinate Approaches to Extended Conformational Sampling

Michael Nilges and Roger Abseher

CONTENTS

17.1 Introduction

Correlated motions in biological macromolecules provide a key to understanding and regulation of function. For example, binding to proteins of small molecules [1] as well as of other macromolecules [2] frequently occurs via structural rearrangements accomplished by concerted displacements of several structural elements. Thus, dynamic cross-correlations between distant sites were shown to have important implications for the design of protease inhibitors [3]. Establishing a consistent framework connecting structure, energy landscape, dynamics, and function, however, is still a challenge [4, 5]. Experiments do not offer direct access to atomic description of correlated

motion, and the experimental data need to be interpreted in the framework of an appropriate model [6–9]. The determination of correlated motions by computational means is more straightforward. They can be predicted from one representative structure using a description of intramolecular interaction at different levels of detail (normal mode analysis, Gaussian network model) [10–14] or deduced from an ensemble of structures using multivariate statistics [7,15–19]. Molecular dynamics (MD) simulation is one means of generating ensembles. However, large-scale correlated motions, in principle, amenable to simulation, pose a sampling problem [4,20], since the amplitude of significant motions is large, while the energy landscape is still rugged. This results in slow timescales of motion along these directions in conformational space.

Extrapolation of motions along collective coordinates obtained from normal mode or simplified normal mode calculations are very instructive, and examples can be found elsewhere in this book. The most important collective coordinates are in many cases astonishingly stable and similar results can be obtained with different methods or approximations. That the directions of the slowest frequency normal mode (obtained at 0 K) should be similar to those obtained from principal component analysis of MD trajectories at nonzero temperature can by no means be taken for granted, since the molecule in an MD trajectory does sample the potential energy surface close to a local minimum, which is explored by normal mode calculations (see Figure 17.1). The simple extrapolation of motion along normal modes or principal components of motion poses the additional problem that the resulting structures are necessarily distorted and hence need to be minimized. An in-detail study of the energetic landscape of the region around the native structure or of major structural transition is therefore difficult to achieve.

Schematically, one can imagine the energy surface in the direction of a low frequency mode as illustrated in Figure 17.1, being essentially flat in the native basin, with many minima and subminima.

17.2 Extended Sampling Methods

17.2.1 Principal Component Analysis

Principal coordinates of motion [16,21–23] rely on an approximation of the configurational density $\rho(\mathbf{x})$ in the vicinity of a stable structure by a multivariate Gaussian:

$$\rho(\mathbf{x}) \approx \mathcal{Z}^{-1} \exp\left[-\frac{1}{2}(\mathbf{x}-\mathbf{x}_{\text{ori}})^{\text{T}} C^{-1}(\mathbf{x}-\mathbf{x}_{\text{ori}})\right] \tag{17.1}$$

with the partition function

$$\mathcal{Z} := \int d^{3N}x \exp\left[-\frac{1}{2}(\mathbf{x}-\mathbf{x}_{\text{ori}})^{\text{T}} \mathbf{C}^{-1}(\mathbf{x}-\mathbf{x}_{\text{ori}})\right] \tag{17.2}$$

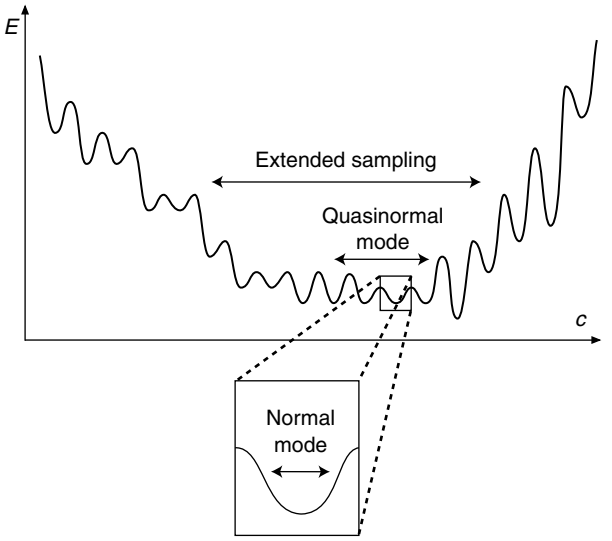

FIGURE 17.1
Schematic representation of an energy surface along a single component of motion, with regions sampled by different methods.

C is the covariance matrix:

$$\mathbf{C} = \langle (\mathbf{x} - \mathbf{x}_{\text{ori}})(\mathbf{x} - \mathbf{x}_{\text{ori}})^{\text{T}} \rangle \tag{17.3}$$

$\mathbf{x}_{\text{ori}}$ is the native structure (the reference structure), and N is the number of atoms. For principal component restraint (PCR) of protein dynamics one often uses only a subset of atoms, for example, the C^{α} atoms [16,23].

The principal components of motion (in the following also referred to as "modes") are the eigenvectors $\mathbf{v}_i, i = 1, \ldots, 3N$ of the covariance matrix **C**. They are collective coordinates and define a set of coordinate axes in conformational space. The coordinates $\mathbf{q}_k$ of a structure **x** in such a space (mode-space coordinates) are given by

$$\mathbf{q}_k = (\mathbf{x} - \mathbf{x}_{\text{ori}}) \cdot \mathbf{v}_k \tag{17.4}$$

where $\mathbf{x}_{\text{ori}}$ is the structure defining the origin of mode space, usually the average structure.

In these coordinates, the equation for the configurational density is much simplified:

$$\rho(\mathbf{x}) \approx \mathcal{Z}^{-1} \exp\left[-\frac{1}{2}\mathbf{q}^{\text{T}}\mathbf{\Lambda}\mathbf{q}\right] \tag{17.5}$$

where $\mathbf{\Lambda}$ is the diagonal matrix of the eigenvalues of **C**.

By expressing the dynamics in principal coordinates **q** a "coarse-grained" description of dynamics can be derived in a simple way: we separate the

important coordinates $\mathbf{c} = \{\mathbf{q}_1, \ldots, \mathbf{q}_D\}$ and neglect unimportant coordinates $\mathbf{s} = \{\mathbf{q}_{D+1}, \ldots, \mathbf{q}_N\}$, or, in the terminology of [16], we separate the essential subspace **c** and the near-constraints coordinates **s**. The important coordinates correspond to the D largest eigenvalues of $\mathbf{C}$ or, equivalently, to the D smallest eigenvalues of $\mathbf{C}^{-1}$. D is thus the number of coordinates necessary for our coarse-grained description, or the dimension of the essential subspace. The chapter by Liu et al. in this book describes one way of using principal components for extended sampling, by coupling them to a seperate temperature bath. The methods described in this chapter act on the motion in the direction of the principal components in a more direct way. The general procedure for these three methods is similar:

1. Obtain a description of the dynamics of molecule in the form of principal components of motions of an extensive MD trajectory.
2. Superpose the frames of the trajectory by a least-squares fitting procedure [24] onto a reference structure $\mathbf{x}_{\text{ref}}$, usually the starting structure of the trajectory. The appropriate way of fitting and possible artifacts of fitting methods were the subject of several studies [25–28]. In short, the fitting procedure can introduce artifactual correlations between distant parts in the molecule. Because of insufficient sampling of side-chain motions, only a subset of the atoms (usually only the C^{α} atoms) are included in the analysis and the definition of the principal components.
3. Select a number of principal components.
4. Calculate a new trajectory, with modified dynamics to enhance sampling.

The general aim of the three methods is similar, to obtain an increased sampling of conformational space by modifying the first principal components of motion. The methods use direct constraints or restraints (pseudo-potentials) modifying the dynamics; other possibilities are discussed elsewhere in this book.

Constraints do not modify the Hamiltonian governing the dynamics of the system since no additional potential needs to be introduced. In contrast, the conformational flooding and the PCR methods deliberately add potentials to the system to destabilize the starting conformation. There are further differences in the implementation and in the scope of possible applications.

17.2.2 Constraint Method

Berendsen and coauthors developed an approach based on constraints in the direction of principal components [29–31]. These constraints force the system to move along one or some of the first principal components (termed "essential coordinates" in the original paper). All the other coordinates move freely according to the conventional equations of motion. This results in a broader sampling of the essential subspace than in a comparable conventional MD simulation without constraints.

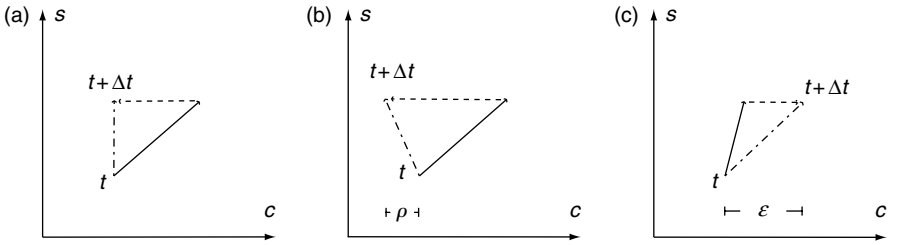

FIGURE 17.2
Schematic representation of the effect of a holonomic constraint along a single principal component of motion. The unimportant, "near-constraint" directions *s* are not affected by the constraint. The black arrow corresponds to the free dynamic step in each case, the dashed arrow to the correction applied, and the dash–dot arrow to the resulting displacement in principal coordinates. The reference structure is at the origin. (a) Simulation at constant value of the principal coordinate **c**. (b) Reduction of principal coordinate **c**. (c) Increase principal coordinate **c**.

Nonstationary holonomic (i.e., time-independent) constraints are used, such as a constant step motion along a direction in the essential subspace or a constant step expansion or contraction of the length of the radius between a fixed reference position and the actual position, both defined in the essential subspace. In a radius expansion (or reduction), the radius spanned by the coordinates along a few eigenvectors (in their paper, the authors use the first, second, and fourth) is increased (or reduced, respectively) by a small amount at each timestep (e.g., 0.004 Å). Figure 17.2 shows the principle for the application of these constraints for an expansion, reduction, and a simulation at a fixed value of the projection onto a principal direction **c**.

The authors proposed a three-phase protocol to sample conformational space:

1. An expansion phase, where the size of projection onto the eigenvector is increased; the expansion step is 5000 steps (10 psec). To do this, the projections on the eigenvectors are corrected in the radial direction of the expansion sphere in such a way that they fulfill the constraint.
2. Second, a constrained sampling phase, where the positions of the essential coordinates are fixed and 5000 steps (10 psec) of MD are performed.
3. Third, a relaxation phase, with 20 psec of free dynamics.

The procedure was then iterated, using the final structure of one cycle as the starting point and center of the expansion sphere.

In a later modification of this basic algorithm, a new position resulting from a regular MD step was only accepted if it was at least as far away from the center of the expansion sphere as the coordinates of the previous timestep, in the subspace of the first three eigenvectors. In the case where the distance decreases, a correction is applied in this subspace. This correction is applied such that the position after correction is at the same distance in the subspace

as the previous position. When the distance from the center did not increase spontaneously any more [30] or the rate of increase was very small [31], the cycle was finished and a new cycle was started with the current position as starting point and new center of the expansion sphere.

17.2.3 Conformational Flooding

The "conformational flooding" method [23] employs a biasing potential defined along the most important collective degrees of freedom, thereby deliberately destabilizing the initial conformation in order to trigger conformational transitions by lowering free energy barriers separating different stable conformations. Given an initial conformation of the system, the method is designed to identify one or more "product states," which may be separated from the initial state by high energy barriers. It provides an approximate (or at least plausible) reaction path.

An effective "coarse-grained" Hamiltonian for dynamics of the system is defined by the first principal components $\mathbf{c}$:

$$\mathcal{H}_{\text{eff}} = \tfrac{1}{2}\beta^{-1}\mathbf{c}^{\mathrm{T}}\mathbf{\Lambda}\mathbf{c} \tag{17.6}$$

The idea of conformational flooding is to destabilize the structure by adding a potential to this Hamiltonian that is localized at the stable conformation (i.e., the minimum of the effective Hamiltonian). The suggested "flooding" potential [23] is of the form:

$$V_{\text{fl}} = w_{\text{fl}} \exp\left[-\tfrac{1}{2}\mathbf{c}^{\mathrm{T}}\mathbf{\Lambda}_{\text{fl}}\mathbf{c}\right] \tag{17.7}$$

$\mathbf{\Lambda}_{\text{fl}}$ defines the shape of the potential in the space of principal coordinates, and w_{fl} is an energy constant. Since this potential is to modify $\mathcal{H}_{\text{eff}}$, one requires that $\mathbf{\Lambda}_{\text{fl}} = \mathbf{\Lambda}/(\beta w_{\text{fl}})$, which ensures that the sum $\mathcal{H}_{\text{eff}} + V_{\text{fl}}$ is quartic at the center of the conformational substate [23]. Shape and effect of this potential are schematically shown in Figure 17.3.

17.2.4 Principal Component Restraints

The structure $\mathbf{x}_{\text{ori}}$ plays a central role in the extended sampling methods described above. It defines the reference point to convert coordinates from Cartesian into collective coordinates, and it serves as a reference structure for the best-fitting procedure that needs to be applied to calculate the direction of constraints or potentials. The PCR MD method (PCR–MD) [32] is designed to reduce this role, by separating the structure $\mathbf{x}_{\text{ori}}$ defining the origin of collective coordinate space from the reference structure $\mathbf{x}_{\text{ref}}$. In particular, the $\mathbf{x}_{\text{ori}}$ is not fixed but can float freely.

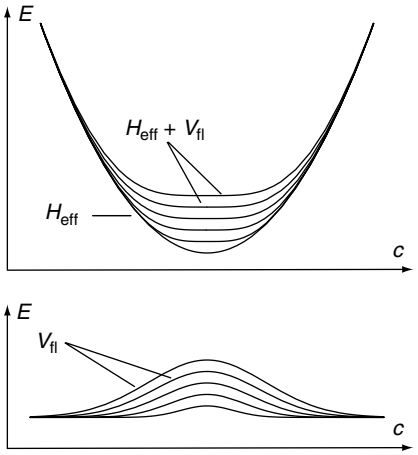

FIGURE 17.3
Schematic representation of an effective Hamiltonian along a single principal component of motion, with flooding potentials with different strengths. (Adopted from H. Grubmüller, *Phys. Rev. E* 52 [1995] 2893–2907. With permission.)

PCR–MD is a method for both efficient and tailored sampling along collective degrees of freedom. Similar to the conformational flooding method, PCR–MD uses an additional potential. This is achieved by introducing PCRs, which act on an ensemble of MD trajectories that proceed otherwise independently in parallel. In contrast to the conformational flooding method, the restraints do not act on a single trajectory — they cannot even be defined on an individual trajectory. In addition, the restraints can be used not only to destabilize the initial conformation but also to directly impose a specific variance of the projections of a conformational ensemble onto the principal components. The restraints directly specify the target variances over a structure ensemble projected onto the principal components for an arbitrary number of modes simultaneously. The PCR–MD method was first applied to study the dynamics of the PH domain of β-spectrin [33,34].

The size of the conformational space covered by a family of M structures in the kth collective coordinate may be characterized by the variance of the mode space coordinates $\mathbf{q}_{k,i}$, defined with reference to the instantaneous average structure $\langle \mathbf{x} \rangle$ of the ensemble of trajectories:

$$\mathbf{q}_{k,i} = (\mathbf{x}_i - \mathbf{x}_{\text{ori}}) \cdot \mathbf{v}_k = (\mathbf{x}_i - \langle \mathbf{x} \rangle) \cdot \mathbf{v}_k \tag{17.8}$$

where i is the index of a structure in the ensemble. The variance of a mode space coordinate is then:

$$\sigma^2(\mathbf{q}_k) = \langle \mathbf{q}_k^2 \rangle_i - \langle \mathbf{q}_k \rangle_i^2 = \frac{1}{M} \sum_{i=1}^{M} \mathbf{q}_{k,i}^2 = \frac{1}{M} \sum_{i=1}^{M} \mathbf{q}_{k,i}^2 \tag{17.9}$$

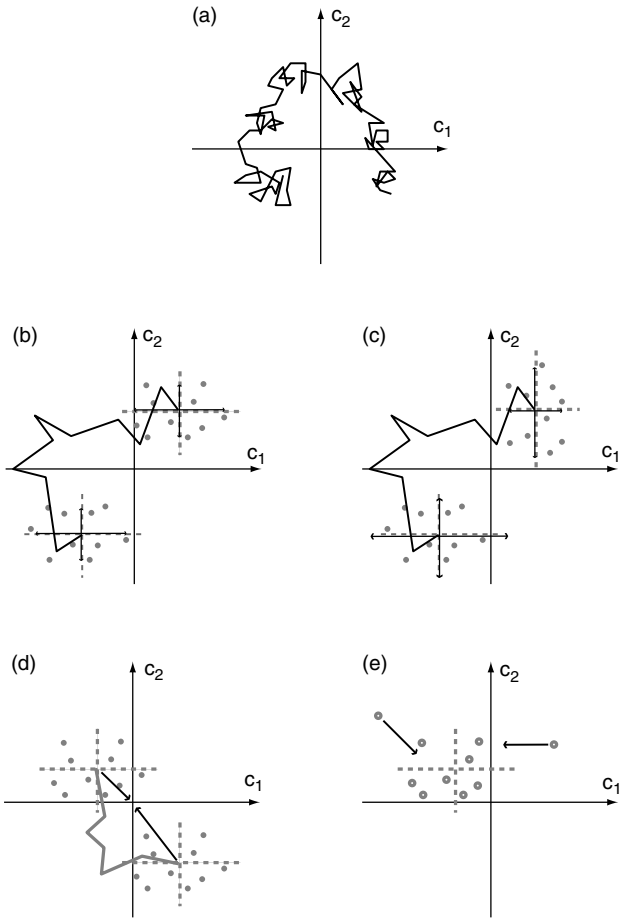

FIGURE 17.4
Schematic illustration of PCRs. (a) A single free (unrestrained) MD trajectory projected into the first two principal components. (b) An ensemble of trajectories restrained by variance PCRs to a particular variance (indicated by ellipses) is free to move in principal component space as a whole. (c) For the restraint in Equation (17.11), the shape of the ellipsoid can vary but the sum of the half-axes would remain constant. (d) In addition to the variance restraints, the location of the ensemble is restrained by the potential of Equation (17.13). (e) The restraint defined in Equation (17.12) acts only if one or several members of the ensemble are more than a specified distance from the center of the ensemble. For clarity, force arrows are only shown for these, whereas differentiation of Equation (17.12) gives forces for all members.

since the average mode space coordinate $\langle \mathbf{q}_k \rangle_i$ vanishes. PCRs are implemented as a set of potentials E_{PCR}, restraining different functions of the variances of D collective coordinates, and of other functions of the projections onto principal coordinates. The actions of the different restraint terms are illustrated in Figure 17.4.

The variance restraint is harmonic in the difference of the variances $\sigma^2(\mathbf{q}_k)$ and target values λ_k:

$$E_{\text{var}} = w_{\text{var}} \sum_{k=1}^{D} \{\langle \mathbf{q}_{k,i}^2 \rangle_i - \lambda_k\}^2 = w_{\text{var}} \sum_{k=1}^{D} (\sigma^2(\mathbf{q}_k) - \lambda_k)^2 \tag{17.10}$$

where w_{var} is a weighting factor for the variance term. In contrast to the "conformational flooding" [23] and the constraint [29–31] methods, the reference structure $\mathbf{x}_{\text{ref}}$ enters the restraints only indirectly in the best-fitting of the ensemble, to re-calculate the average structure $\langle \mathbf{x} \rangle$ at every MD or minimization step. PCRs in this form do not impose any structural restraints but restrain exclusively the variance of an ensemble (i.e., the distance from the instantaneous average) and not the distance from a reference structure. The ensemble of structures may be seen as a cloud in conformational space free to move as a whole, and it is only the size of the cloud along selected directions that is restrained.

Instead of using a separate restraint for each eigenvector direction, the cumulative variance in several directions can be restrained. In this case, the modes and the eigenvalues are not assumed to be known exactly, and one only imposes a restraint on the "essential subspace" as a whole:

$$E_{\text{cum}} = w_{\text{cum}} \left(\sum_{k=1}^{D} \sigma^2(\mathbf{q}_k) - \sum_{k=1}^{D} \lambda_k \right)^2 \tag{17.11}$$

A third type of restraint enforces the homogeneity of the structural ensemble and prevents outliers by imposing a maximum size of the projection for each structure in the ensemble:

$$E_{\text{ext}} = w_{\text{ext}} \sum_{k=1}^{D} \sum_{i=1}^{M} \Theta[(\mathbf{q}_{k,i}) - n_\sigma \sigma(\mathbf{q}_k)][(\mathbf{q}_{k,i}^2) - n_\sigma \sigma^2(\mathbf{q}_k)]^2 \tag{17.12}$$

where n_σ is the maximum deviation from the average structure, specified as number of variances, and Θ is the Heaviside step function. Another type of restraint can be used to tie the average structure to a reference point in mode space [32], effectively restricting the location of the cloud to the vicinity of a reference structure $\mathbf{x}_{\text{ref}}$.

$$E_{\text{avg}} = w_{\text{avg}} \sum_{k=1}^{D} [(\langle \mathbf{x} \rangle - \mathbf{x}_{\text{ref}}) \cdot \mathbf{v}_k]^2 \tag{17.13}$$

PCRs are used in conjunction with standard MD simulation, very similar to conformational flooding. In the implementation in X-PLOR [35], we use the Langevin dynamics option with an explicit friction and random force term to simulate at constant temperature. The potential energy is composed of a

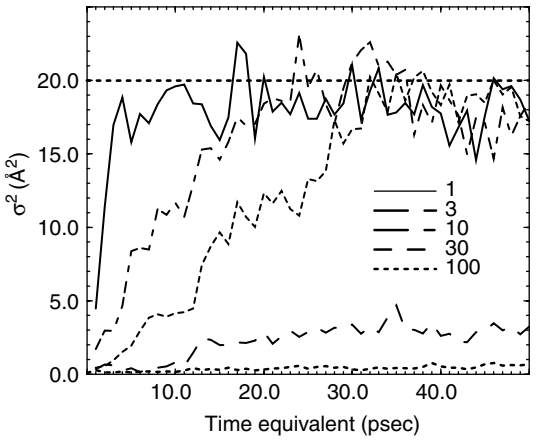

FIGURE 17.5
Mode-specific response to PCR. A target variance of 20 Å^2 was applied with a weight of 0.1 kcal mol^{-1} Å^{-4} to mode 1, 3, 10, 30, or 100, respectively. The resulting variances in mode space are shown as a function of simulation time. The target variance is shown as a straight dotted line. (Adopted from R. Abseher and M. Nilgee, *Proteins* 26 [1996] 314–322. With permission.)

standard MD force field E_{phys} and the PCR energy terms:

$$m_{i,l}\frac{\mathrm{d}^2}{\mathrm{d}t^2}\mathbf{x}_{i,l}(t) = -\frac{\partial}{\partial \mathbf{x}_{i,l}}(E_{\text{phys}}[+w_{\text{var}}E_{\text{var}} + w_{\text{avg}}E_{\text{avg}} + \cdots]) + f_{i,l}(t) - m_{i,l}b_{i,l}\frac{\mathrm{d}}{\mathrm{d}t}\mathbf{x}_{i,l}(t) \tag{17.14}$$

where $\mathbf{x}_{i,l}(t)$ are the Cartesian coordinates of atom i in ensemble member l at time t, $m_{i,l}$ the atom mass, $f_{i,l}(t)$ a random force, and $b_{i,l}$ the friction coefficient.

The weights on the different terms need to be set empirically. In the study of the PH domain, w_{var} was set to 0.1 kcal mol^{-1} Å^{-4}. This value was applied successfully also with systems other than the PH domain for calculations *in vacuo*. Below 0.03 kcal mol^{-1} Å^{-4}, the target diversity was not reached within 100 psec time equivalent even for the softest modes. Computational experiments like the one illustrated in Figure 17.5 may be used to further optimize w_{var}.

The target diversities λ were chosen to be equal or comparable to the eigenvalues of a covariance matrix of the 9 nsec reference trajectory. In general, the choice will depend on the application; whether the native state diversity should be reproduced or large-scale transitions be triggered. The native state variances depend on the system, system size, and the simulation method.

The method is implemented in a modified version of the program X-plor [35] and will be available in X-plor–NIH [36] in the near future. An ensemble of trajectories can be calculated with ease in X-plor by switching off any interactions in the force field E_{phys} between different members in the ensemble in

the same way as it is implemented [37] in Chemistry of Harvard Molecular Mechanics (CHARMM) [38].

17.3 Applications

The advantage of using only the first principal components to define the constraint forces or additional potentials is that the perturbation to the energetics of the system is small. This was tested for the constraint method and the PCR–MD method by calculating standard structure validation parameters with PROCHECK [39], which showed that the quality of the structures in constrained or restrained trajectories were virtually identical to those of reference simulations without additional forces.

17.3.1 Characterization of the Free Energy Surface Around the Native Structure

One of the first applications of the extended sampling techniques was the characterization of the "free energy basin" around the native structure of HPr from *Escherichia coli* by the constraint method [31]. The analysis defined the boundaries of the free energy basin in the space of principal components of motion. The motions in the essential subspace within this basin showed a diffusion-like behavior. Using the conformational flooding method for a model protein, Grubmüller [23] derived acceleration rates and estimates of transition rates. He also suggested using the conformational flooding method to examine the stability of structures (experimental structures or homology models). The advantage would be that instabilities could appear much faster than in standard MD calculations [40].

The PCR–MD method was used to characterize the energy surface surrounding the native structure of the β-spectrin PH domain by probing the resistance of the structure to PCRs in different directions [32]. A clear separation of soft and stiff modes could be demonstrated, and the order of the rates of reaction to restraints corresponded to the eigenvalues of the original 9 nsec MD trajectory. This result could be used to design a new method to *define* the essential subspace — the directions in collective coordinates where the system is "softest," that is, where the system reacts easiest to an external force.

17.3.2 Rapid Conformational Sampling

The PCR method has been applied extensively to the more modest goal of rapid conformational sampling [41] (see Figure 17.6). The advantage of perturbations in the direction of large amplitude collective coordinates is that they are (by definition) of low energy.

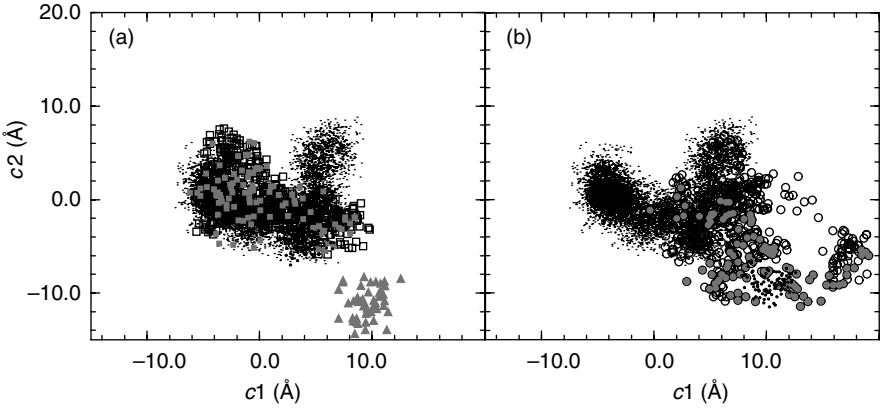

FIGURE 17.6
Conformational sampling using PCR–MD of an ensemble of 10 spectrin PH domains. The restraint-free 9 nsec reference trajectory of a single PH domain molecule that had been used for the determination of modes is displayed in both Figures (small black dots). (a) PCR–MD run with both mode space variance and position restraints; sampling during the first 10 psec (gray squares) and during further 40 psec (empty squares). A 100 psec subtrajectory of the 9 nsec trajectory (same computational effort as 10 psec PCR–MD of an ensemble of 10 structures) is shown as small circles. The NMR structure ensemble (pdb access code 1 mph) is indicated as triangles. (b) PCR–MD run with variance restraints only; sampling during the first 10 psec (gray circles) and during further 40 psec (empty circles). 10 psec MD of an ensemble of 10 structures without PCRs (larger dots) starting from the same initial conditions. (Adapted from R. Absecher and M. Nilgres, *Proteins* 39 [2000] 82–88.).

As the other methods, PCR–MD assumes the knowledge of principal components and variances from an initial restraint-free trajectory. This limits its use for "rapid" conformational sampling. The PCR summation restraint (Equation 17.11) does not require this level of detail; it suffices to specify a number of eigenvector directions that one wants to restrain and the sum of the target variances along these directions. In order to use PCR–MD to sample conformational space, the true variances need not be known and one can simply use a value larger than the current value.

A calculation with prion protein [42] solvated in a shell of water illustrates the use of PCR–MD for sampling. In this case, the first ten eigenvectors calculated from a reference trajectory were used as target directions. All calculations were performed with the CHARMM19 force field with TIP3P water, force shifting and a nonbonded cutoff of 14 Å. Ten trajectories were run in parallel. The calculations were run in cycles, where every cycle consisted of 1 psec PCR–MD followed by 1 psec free MD. The target value for the sum of the projections for the next cycle was set to twice the value at the end of 1 psec free MD. No PCR term was used in the first cycle, and a total of 50 cycles were calculated. The weight on the PCR term was recalculated at the beginning of each cycle such that the PCR energy had a specified value. Four calculations were run with energies of 500, 200, 100, and 0 kcal mol^{-1},

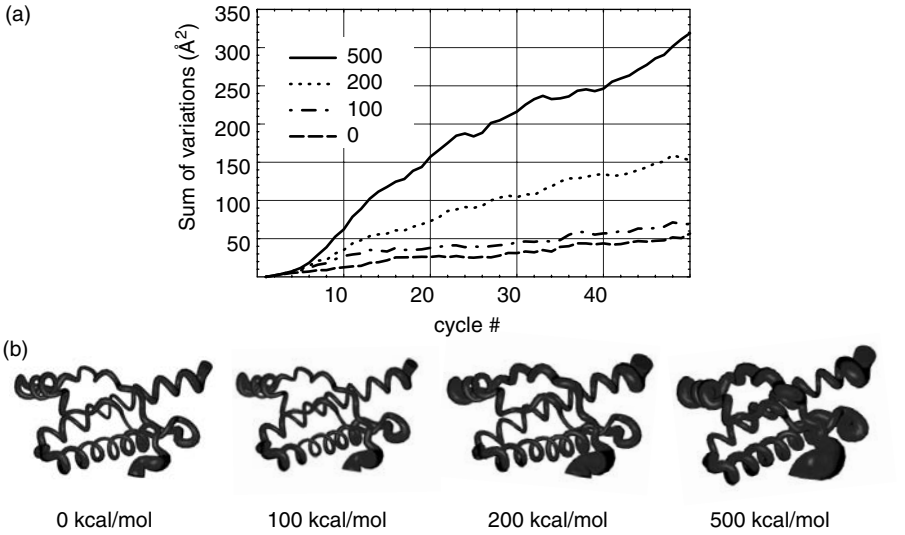

FIGURE 17.7
Conformational sampling with the cumulative PCRs of Equation (17.11). The calculations were performed at "constant energy"; at the beginning of each cycle, the weight on the PCRs was adjusted such that the PCR energy had a specified value (0, 100, 200, or 500 kcal mol^{-1}). (a) The sums of the variances along the ten principal components at the end of each cycle consisting of 1 psec restrained dynamics and 1 psec free relaxation, against the cycle number. (b) Structure ensembles after cycle 20. The structure plots were generated with MolMol [43].

respectively. Figure 17.7 shows the sum of the variances at the end of each cycle, and the structures at the end of cycle 50. In a similar way, using standard PCRs, the PCR–MD method was used extensively to presample protein conformations for rigid-body protein–protein docking calculations [41].

17.3.3 Large Conformational Motions: Allosteric Transitions, Unfolding, Folding

One of the original applications of conformational flooding was the identification of distant minimum conformations in a model protein [23]. In principle, all methods described in this chapter can be applied to identify and study allosteric transitions or other large conformational changes that have so far been studied with other methods, such as the conformational transition between Ras–GDP and Ras–GTP [44–46].

Protein folding and unfolding are highly cooperative processes. One can therefore presume that collective motions play an important role in folding and unfolding. The results of one study [47] have evidenced a clear correlation between the directions of the deformation motions that occur in the first stage of the unfolding process and a few specific essential motions characterizing the 300 K dynamics of the protein.

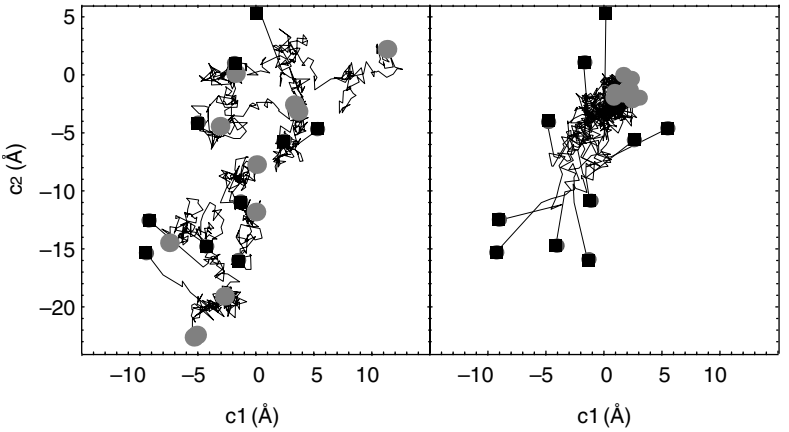

FIGURE 17.8
Projections of conformational space onto the first to first two principal components of motion derived from a standard MD trajectory of the same system. The initial state is an ensemble of ten partially "denatured" SH3 domain structures from Src, obtained by heating the x-ray crystal structure to 1000 K. The starting structures are indicated by the black squares, the final structures by gray disks. (a) Projections of standard MD trajectories, run at 300 K, onto the principal components. The trajectories sample the conformational space around the starting structures but do not get closer to the native x-ray crystal structure (at position 0,0). (b) Projections of an ensemble of trajectories, using only PCRs on variance (Equation [17.10]). Although the restraints act only on the instantaneous average and do not use the knowledge of the x-ray crystal structure, the final structures cluster around the native structure.

The PCR–MD method was used to study the folding from structures of src-homology 3 (SH3) domains showing various degrees of disorder [48] (see Figure 17.8). Several increasingly disordered structural ensembles obtained by thermal unfolding or randomization of the coordinates of the native structure of the domain were used as starting points. In combination with a standard MD force field the PCRs were sufficient to generate native structure in disordered structural ensembles. The study clearly demonstrated the important role of the reference structures $\mathbf{x}_{\text{ref}}$ and $\mathbf{x}_{\text{ori}}$ on the results of the calculations. In the PCR–MD method the bias is small since $\mathbf{x}_{\text{ori}}$ is always the instantaneous average over the structure ensemble. In a similar spirit, the constraint method was applied to study folding at atomic detail and to obtain a folding landscape for cytochrome C [49]. These folding simulations allow an exploration of the folding funnel in the wider vicinity of the minimum represented by the native structure.

17.4 Conclusions

The main use of the discussed methods will be the exploration of conformational space around the native structure. Since the forces or constraints act along the principal components of motion (by definition low energy directions), these methods have the advantage that small forces are sufficient to provoke large conformational differences, and that the structures therefore remain in energetically favorable regions of conformational space. Structures obtained from simple projections onto normal modes or principle components are, in contrast, locally distorted and need to be minimized (e.g., [50]). The PCR–MD method has been used to take into account flexibility in protein–protein docking [41], but the approaches may also be useful for small-molecule docking. However, little use has been made of these methods up to now, outside the groups that had originally proposed them.

The convergence achieved with the PCR–MD method for folding simulations, when used to reduce the variance of a structure ensemble, toward the correct structure from rather distorted initial structures indicates that applications of extended sampling methods are possible in cases of structure refinement with sparse data, and structure prediction. One would expect improvements with better implicit solvent models (e.g., the generalized Born model [51–54]). Similarly, the method may be useful as a refinement approach for structures from *ab initio* 3D structure prediction.

Acknowledgments

MN thanks Arnaud Blondel for a critical reading of the manuscript.

References

1. S. Remington, G. Wiegand, and R. Huber, Crystallographic refinement and atomic models of two different forms of citrate synthase at 2.7 and 1.7 Å resolution, *J. Mol. Biol.* 158 (1982) 111–152.
2. P.A. Boriack-Sjodin, S.M. Margarit, D. Bar-Sagi, and J. Kuriyan, The structural basis of the activation of ras by sos, *Nature* 394 (1998) 337–343.
3. R.B. Rose, C.S. Craik, and R.M. Stroud, Domain flexibility in retroviral proteases: structural implications for drug resistant mutations, *Biochemistry* 37 (1998) 2607–2621.
4. H. Frauenfelder, and D.T. Leeson, The energy landscape in non-biological and biological molecules, *Nat. Struct. Biol.* 5 (1998) 757–759.
5. H. Frauenfelder, and B. McMahon, Dynamics and function of proteins: the search for general concepts, *Proc. Natl Acad. Sci. USA* 95 (1998) 4795–4797.

6. S. Sunada, N. Go, and P. Koehl, Calculation of nuclear magnetic resonance order parameters in proteins by normal mode analysis, *J. Chem. Phys.* 104 (1996) 4768–4775.
7. D.M.F. van Aalten, D.A. Conn, B.L. de Groot, H.J.C. Berendsen, J.B.C. Findlay, and A. Amadei, Protein dynamics derived from clusters of crystal structures, *Biophys. J.* 73 (1997) 2891–2896.
8. J.R. Tolman, J.M. Flanagan, M.A. Kennedy, and J.H. Prestegard, Nmr evidence for slow collective motions in cyanometmyoglobin, *Nat. Struct. Biol.* 4 (1997) 292–297.
9. C.B. Arrington, L.M. Teesch, and A.D. Robertson, Defining protein ensembles with native-state nh exchange: kinetics of interconversion and cooperative units from combined nmr and ms analysis, *J. Mol. Biol.* 285 (1999) 1265–1275.
10. I. Bahar, B. Erman, R.L. Jernigan, A.R. Atilgan, and D.G. Covell, Collective motions in HIV-1 reverse transcriptase: examination of flexibility and enzyme function, *J. Mol. Biol.* 285 (1999) 1023–1037.
11. M.M. Tirion, Large amplitude elastic motions in proteins from a singleparameter and atomic analysis, *Phys. Rev. Lett.* 77 (1996) 1905–1908.
12. M. Levitt, C. Sander, and P.S. Stern, Protein normal-mode dynamics: trypsin inhibitor and crambin and ribonuclease and lysozyme, *J. Mol. Biol.* 181 (1985) 423–447.
13. B. Brooks, and M. Karplus, Harmonic dynamics of proteins: normal modes and fluctuations in bovine pancreatic trypsin inhibitor, *Proc. Natl Acad. Sci. USA* 80 (1983) 6571–6575.
14. N. Gō, T. Noguti, and T. Nishikawa, Dynamics of a small globular protein in terms of low-frequency vibrational modes, *Proc. Natl Acad. Sci. USA* 80 (1983) 3696– 3700.
15. T. Ichiye, and M. Karplus, Collective motions in proteins: a covariance analysis of atomic fluctuations in molecular dynamics and normal mode simulations, *Proteins* 11 (1991) 205–217.
16. A. Amadei, A.B.M. Linssen, and H.J.C. Berendsen, Essential dynamics of proteins, *Proteins* 17 (1993) 412–425.
17. B.L. de Groot, D.M.F. van Aalten, A. Amadei, and H.J.C. Berendsen, The consistency of large concerted motions in proteins in molecular dynamics simulations, *Biophys. J.* 71 (1996) 1707–1713.
18. R. Abseher, L. Horstink, C. Hilbers, and M. Nilges, Essential spaces defined by nmr structure ensembles and molecular dynamics simulation show significant overlap, *Proteins* 31 (1998) 370–382.
19. B.L. de Groot, D.M.F. van Aalten, R.M. Scheek, A. Amadei, G. Vriend, and H.J.C. Berendsen, Prediction of protein conformational freedom from distance constraints, *Proteins* 29 (1997) 240–251.
20. M.A. Balsera, W. Wriggers, Y. Oono, and K. Schulten, Principal component analysis and long time protein dynamics, *J. Phys. Chem.* 100 (1996) 2567–2572.
21. M. Karplus and J.N. Kushick, Method for estimating the conformational entropy of macromolecules, *Macromolecules* 14 (1981) 325–332.
22. J. Schlitter, Estimation of absolute and relative entropies of macromolecules using the covariance matrix, *Chem. Phys. Lett.* 215 (1993) 617–621.
23. H. Grubmüller, Predicting slow structural transistions in macromolecular systems: conformational flooding, *Phys. Rev. E* 52 (1995) 2893–2907.
24. W. Kabsch, A solution for the best rotation to relate two sets of vectors, *Acta Crystallogr. Sect.* A 32 (1976) 922–923.

25. P.H. Hünenberger, A.E. Mark, and W.F. van Gunsteren, Fluctuation and cross-correlation analysis of protein motions observed in nanosecond molecular dynamics simulations, *J. Mol. Biol.* 252 (1995) 492–503.
26. M. Karplus and T. Ichiye, Comment on "fluctuation and cross-correlation analysis of protein motions observed in nanosecond molecular dynamics simulations," *J. Mol. Biol.* 263 (1996) 120–122.
27. R. Abseher and M. Nilges, Are there non-trivial dynamic cross-correlations in proteins? *J. Mol. Biol.* 279 (1998) 911–920.
28. U. Schieborr and H. Rüterjans, Bias-free separation of internal and overall motion of biomolecules, *Proteins* 45 (2001) 207–218.
29. A. Amadei, A.B.M. Linssen, B.L. de Groot, D.M.F. van Aalten, and H.J.C. Berendsen, An efficient method for sampling the essential subspace of proteins, *J. Biomol. Struct. Dyn.* 13 (1996) 615–625.
30. B.L. de Groot, A. Amadei, D.M.F. van Aalten, and H.J.C. Berendsen, Towards an exhaustive sampling of the configurational spaces of the two forms of the peptide hormone guanylin, *J. Biomol. Struct. Dyn.* 13 (1996) 741–751.
31. B.L. de Groot, A. Amadei, R.M. Scheek, N.A.J. van Nuland, and H.J.C. Berendsen, An extended sampling of the configurational space of hpr from E. coli, *Proteins* 26 (1996) 314–322.
32. R. Abseher and M. Nilges, Efficient sampling in collective coordinate space, *Proteins* 39 (2000) 82–88.
33. M.J. Macias, A. Musacchio, H. Ponstingl, M. Nilges, M. Saraste, and H. Oschkinat, Structure of the pleckstrin homology domain from β-spectrin, *Nature* 369 (1994) 675–677.
34. M. Nilges, M. Macias, S.I. O'Donoghue, and H. Oschkinat, Automated NOESY interpretation with ambiguous distance restraints: the refined nmr solution structure of the pleckstrin homology domain from β-spectrin, *J. Mol. Biol.* 269 (1997) 408–422.
35. A. Brünger, *X–PLOR. A System for X-ray Crystallography and NMR*, Yale University Press, New Haven, CT, 1992.
36. C.D. Schwieters, J.J. Kuszewski, N. Tjandra, and G. Clore, The Xplor–NIH NMR molecular structure determination package, *J. Magn. Reson.* 160 (2003) 65–73.
37. A. Miranker and M. Karplus, Functionality maps of binding sites: a multiple copy simultaneous search method, *Proteins* 11 (1991) 29–34.
38. B.R. Brooks, R.E. Bruccoleri, B.D. Olafson, D.J. States, S. Swaminathan, and M. Karplus, CHARMM: a program for macromolecular energy and minimization and dynamics calculations, *J. Comput. Chem.* 4 (1983) 187–217.
39. R.A. Laskowski, M.W. MacArthur, D.S. Moss, and J.M. Thornton, Procheck: a program to check the stereochemical quality of protein structures, *J. Appl. Crystallogr.* 26 (1993) 283–291.
40. H. Fan, and A.E. Mark, Relative stability of protein structures determined by x-ray crystallography or nmr spectroscopy: a molecular dynamics simulation study, *Proteins* 53 (2003) 111–120.
41. R. Gruenberg, J. Leckner, and M. Nilges, Complementarity of structure ensembles in protein–protein binding, *Structure* 12 (2004) 2125–2136.
42. F. Lopez-Garcia, R. Zahn, R. Riek, and K. Wüthrich, NMR structure of the bovine prion protein, *Proc. Natl Acad. Sci USA* 97 (2000) 8334–8339.
43. R. Koradi, M. Billeter, and K. Wüthrich, MOLMOL: a program for display and analysis of macromolecular structures, *J. Mol. Graph.* 14 (1996) 51–55.
44. J.F. Diaz, B. Wroblowski, J. Schlitter, and Y. Engelborghs, Calculation of pathways for the conformational transition between the gtp- and gdp-bound states of the

ha-ras-p21 protein: calculations with explicit solvent simulations and comparison with calculations in vacuum, *Proteins* 28 (1997) 434–451.
45. J. Ma and M. Karplus, Ligand-induced conformational changes in ras p21: a normal mode and energy minimization analysis, *J. Mol. Biol.* 274 (1997) 114–131.
46. J. Ma and M. Karplus, Molecular switch in signal transduction: reaction paths of the conformational changes in ras p21, *Proc. Natl Acad. Sci. USA* 94 (1997) 11905–11910.
47. D. Roccatano, I. Daidone, M.A. Ceruso, C. Bossa, and A.D. Nola, Selective excitation of native fluctuations during thermal unfolding simulations: horse heart cytochrome c as a case study, *Biophys. J.* 84 (2003) 1876–1883.
48. R. Abseher, and M. Nilges, Protein folding in mode space: a collective coordinate approach to structure prediction, *Proteins* 49 (2002) 365–377.
49. I. Daidone, A. Amadei, D. Roccatano, and A.D.D. Nola, Molecular dynamics simulation of protein folding by essential dynamics sampling: folding landscape of horse heart cytochrome c, *Biophys. J.* 85 (2003) 2865–2871.
50. A. Taly, M. Delarue, T. Gruetter, M. Nilges, N.L. Novère, P.-J. Corringer, and J.-P. Changeux, A quaternary twist model for the nicotinic receptor gating, *Biophys. J.* 59 (2005) 662–672.
51. W.C. Still, A. Tempczyk, R.C. Hawley, and T. Hendrickson, Semianalytical treatment of solvation for molecular mechanics and dynamics, *J. Am. Chem. Soc.* 112 (1990) 6127–6129.
52. M. Schaefer and M. Karplus, Comprehensive analytical treatment of continuum electrostatics, *J. Phys. Chem.* 100 (2001) 1578–1599.
53. G.D. Hawkins, C.J. Cramer, and D.G. Truhlar, Parametrized models of aqueous free energies of solvation based on pairwise descreening of solute atomic charges from a dielectric medium, *J. Phys. Chem.* 100 (1996) 19824–19839.
54. D. Bashford and D.A. Case, Generalized born models of macromolecular solvation effects, *Annu. Rev. Phys. Chem.* 51 (2000) 129–152.

18

Using Collective Coordinates to Guide Conformational Sampling in Atomic Simulations

Haiyan Liu, Zhiyong Zhang, Jianbin He, and Yunyu Shi

CONTENTS

18.1 Introduction

18.1.1 Biomolecular Simulations and Enhanced Conformation Sampling

The atomic simulation of biomacromolecular systems has become an indispensable tool in structural biology [1]. In general, such simulations involve solving the Newton's equations of motion:

$$\begin{aligned} \frac{\mathrm{d}\vec{x}_i}{\mathrm{d}t} &= \vec{v}_i, \\ \frac{\mathrm{d}\vec{v}}{\mathrm{d}t} &= \frac{\vec{f}_i}{m_i} = -\frac{\vec{\nabla}_i V(\vec{x}_1, \vec{x}_2, \ldots, \vec{x}_{\mathrm{Na}})}{m_i}, \quad i = 1, \ldots, N_\mathrm{a} \end{aligned} \tag{18.1}$$

where $\{\vec{x}_i, i = 1, \ldots, N_\mathrm{a}\}$ are the atomic coordinates, N_a the number of atoms, and $V(\vec{x}_1, \vec{x}_2, \ldots, \vec{x}_{\mathrm{N_a}})$ the potential energy function. As a result, we obtain the trajectory of the system, $\{\vec{x}_i(t), i = 1, \ldots, N_\mathrm{a}\}$, for a period of time $t = [0, t_\mathrm{tot}]$.

For any specific biological question, it is well known that the adequateness of this tool persistently relies on two issues (1) whether the potential energy function $V(\vec{x}_1, \vec{x}_2, \ldots, \vec{x}_{\mathrm{N_a}})$ is of appropriate accuracy for the question, and (2) whether the parts of the conformational space relevant to the question can be sufficiently sampled within the time period $t = [0, t_\mathrm{tot}]$, so that reliable ensemble averages can be obtained.

The above two issues are closely related: more detailed potential energy functions (hopefully with higher accuracy) usually require more expensive computations for each energy and energy derivative evaluation of a single conformation, resulting in shorter t_tot or, equivalently, more restricted sampling in the conformational space given the same amount of computation. Thus, depending on the problem at hand, we frequently need to trade accuracy for efficiency, or *vice versa*.

During the last few decades, tremendous progresses have been made to address both the model accuracy and sampling efficiency issues in atomic simulations of protein dynamics. Some of the techniques have been developed for specific purposes, while others with a general purpose that atomic simulations employing them can address problems of wider range and with more biological significance. Among them, techniques achieving enhanced conformational sampling have found wide applications.

18.1.2 A Qualitative Picture of the Conformational Energy Landscape

To rationalize different strategies to accelerate conformational sampling, we start from the following well-known qualitative features of protein energy landscapes [2–4].

First, at ambient temperature, only a tiny fraction of the entire space spanned by all the atomic degrees of freedom is physically accessible to a macromolecule.

Second, using k_BT as a measure of the energy barriers separating different local minima, the energy landscape within the accessible regions dictates numerous local conformational states. The activation barriers separating the numerous potential energy minima within each local state are much lower than k_BT, while the activation barriers separating different local conformational states are much higher than k_BT. Thus, in a molecular dynamics (MD) simulation, the timescales required to achieve equilibrium sampling within individual local conformational states and between different local states are widely separated. At typical timescales accessible by atomic simulations, we may observe excessive sampling within local conformational states (diffusive relaxations), and rarely observe transitions between different local states, although the latter processes are often of more functional significance [5, 6].

Third, there may be dominating paths (associated with lower activation barriers than other paths) for the rare transitions between local states, and identifying such paths often produces important insights into mechanisms.

18.1.3 Objectives and Basic Strategies for Enhanced Conformation Sampling

In enhanced sampling simulations, one major objective is to achieve the frequent observation of conformational transitions between local conformational states, which usually take place at much longer timescales and thus are rarely observable in conventional simulations.

Besides this objective, for some problems we may also be interested in obtaining information about the thermodynamically dominating transition paths connecting different local states. Not all enhanced sampling techniques have been designed with the latter goal in mind. We note that a number of progresses have been made to address the specific question of identifying transition paths and obtaining the associated activation barriers [7, 8]. A discussion of these techniques is out of the scope of this chapter.

The fundamental principle behind ideas to achieve accelerated transition is the transition state theory, according to which the frequency or rate of transition is proportional to $e^{-\Delta G^{\neq}/k_BT}$, in which $\Delta G^{\neq}$ is the free energy of activation and k_BT the Boltzmann constant times the temperature. Given the total amount of computational costs, two basic strategies can be employed to accelerate the escape from local conformational states in a simulation: simulating the system at higher temperatures [9, 10], or deforming the potential energy function [11–15]. With each strategy, a number of techniques have been developed, each having its advantages and disadvantages in the different aspects discussed in the next two paragraphs. Frequently, these strategies are integrated with parallel simulations of multiple copies of the system [9, 10, 16–18].

For an enhanced sampling technique to be practically useful, the acceleration of rare transitions is necessary but not sufficient. As we have already mentioned, only a tiny fraction of the space spanned by all degrees of freedom are physically accessible to the system. Thus, for any method adopting either of the abovementioned strategies, an additional key to achieve efficient enhancement is to avoid overexpanding the accessible conformational space while increasing the transition rate in the transformed simulation. Otherwise, the majority of the conformations sampled in the transformed simulation would be physically irrelevant for the system at ambient temperature.

Besides the above, the disturbance on the equilibrium within the local conformational states should also be minimized.

Thus, we have the following aspects to consider in developing and choosing enhanced sampling techniques for particular goals: the degree of acceleration of conformational transitions rarely observable in conventional simulations; the proportion of physically relevant conformations among all the sampled conformations; the degree of disturbance of the equilibrium within local conformational states; and in some cases, the correspondence between the sampled transition paths and the dominating transition paths in the physical process of interest.

In this chapter, we will focus on those enhanced sampling techniques that employ collective coordinates obtained from (quasi-) harmonic approximations of protein dynamics, with specific emphasis on the amplified collective motion (ACM) technique described by us recently [19].

18.2 Using Collective Coordinates for Enhanced Conformation Sampling

18.2.1 Collective Coordinate Descriptions of Protein Dynamics

We refer to other chapters (e.g., Chapter 17 by Nilges and Abseher) in this book for an introduction of collective coordinates and protein dynamics. For our discussions, we classify these collective coordinate models into three types (1) The traditional normal mode analysis (NMA) of obtaining eigenvectors and eigenvalues of the Hessian matrix at a strict minimum on the potential energy surface [20]; (2) Essential dynamics (ED) analysis or principle component analysis (PCA) of a predefined group of conformations [4, 5, 21], usually obtained from MD simulation trajectories or determined under different experimental conditions; (3) The coarse-grained Gaussian elastic network model (GNM) [22–25] and its anisotropic version (ANM) [26]. Recently, Ming et al. have developed a quantized elastic deformational model [27, 28] that combines and enhances the ANM and the vector quantization method for computing intrinsic deformation motions of protein structures by using low-resolution electron density maps.

The reason for employing collective coordinates to enhance sampling can be readily understood. It has been repeatedly demonstrated that within each local state, dynamics along the few lowest frequency (the softest few) collective coordinates often accounts for the majority of the conformational fluctuations. The higher frequency coordinates are strongly restricted and large deformations along these degrees of freedom are highly unfavorable. Qualitatively speaking, transforming the set of atomic coordinates into an appropriate set of collective coordinates partitions the conformational space into two subspaces; fluctuations in one correspond to larger scale motions that may lead to transitions into different local conformational states and in the other to conformational equilibration in the same local conformational states. Thus proper usage of collective coordinate may achieve efficient sampling with a balance among the aspects discussed above: the acceleration of minimum escaping, the expansion of the accessible conformational space, the disturbances on local conformational equilibriums, and the distortions on transition paths.

18.2.2 Enhanced Sampling Methods Employing Collective Coordinates

Collective coordinates have been employed as basis sets for efficient sampling in a number of studies, including Monte Carlo simulations using normal modes as variables so that sampling step size could be scaled by normal mode amplitudes [29]. The Berendsen group developed an "essential dynamics" simulation method. In this method, protein motions are constrained to move along the essential collective modes, while the motions along the other degrees of freedom obey the usual equations of motions [30]. De Groot et al. have applied this technique in the study of a 13-residue peptide hormone guanylin [31] and an 85-residue protein HPr [32]. The region of conformational space obtained from the essential dynamics sampling includes the area sampled by the normal MD and extends beyond.

Collective coordinates can also be applied to guide the design of a deformed potential energy function. In the conformational flooding scheme [11] and chemical flooding methods [14] (see also Chapter 17 by Nilges and Abseher in this book) according to the collective modes obtained from short MD simulations, a coarse-grained description of conformational substate is derived, from which bias potential can be constructed. The bias potential destabilizes the initial conformation and lowers free energy barriers of structural transitions, as in umbrella sampling [15]. Thus complex conformational transitions and chemical reactions may be observed and followed in a simulation.

Collective coordinates have been combined with ensemble sampling by Abseher and Nilges [18]. These authors applied restraints in essential subspace on an ensemble of MD trajectories that proceed, otherwise independently in parallel. The results show that weak restraints on the ensemble variance suffice for an increase in sampling efficiency along collective modes by two orders of magnitudes.

18.3 The Amplified Collective Motion Method

18.3.1 The Weak Coupling Method for Constant Temperature MD Simulations

The temperature in an atomic simulation is controlled by coupling to external thermostats. At time t, the kinetic energy of the molecular system is

$$K(t) = \sum_{i=1}^{N_a} \frac{1}{2} m_i \vec{v}_i^{\,2}(t) \tag{18.2}$$

and the instantaneous temperature of the system is

$$T(t) = \frac{2K(t)}{N_{dof} k_B} \tag{18.3}$$

where, m_i and $\vec{v}_i(t)$ are atomic mass and velocity of atom i, respectively. N_a is the number of atoms, N_{dof} the number of unconstrained degrees of freedom in the simulation, and k_B the Boltzmann constant. In an equilibrated simulation the thermodynamic temperature of the system corresponds to the average of $T(t)$ over time.

Different thermostats can be applied to control the temperature of the system so that the simulation samples a canonical ensemble at constant temperature. For our purpose, we describe the weak-coupling method briefly [33]. This thermostat is one among the most commonly used in MD simulations of macromolecules. In this thermostat, we assume that the relaxation of the system temperature toward the temperature of the external bath (T_0) follows the first-order kinetics:

$$\Delta T(t) = T(t) - T_0 = \Delta T(0) e^{-t/\tau_T} \tag{18.4}$$

in which τ_T is the temperature relaxation time, a larger τ_T indicating a weaker coupling. The exchanges of energy between the system and the thermostat are represented by applying a scaling factor s on the atomic velocities

$$\vec{v}_i^{\,\text{scaled}}(t) = s\vec{v}_i^{\,\text{unscaled}}(t), \quad i = 1, \ldots, N_a \tag{18.5}$$

The scaled velocities are employed to integrate the equations of motions. It can be derived that the scaling factor should be

$$s = \sqrt{1 + \frac{\Delta t}{\tau_T}\left[\frac{T_0}{T(t)} - 1\right]} \tag{18.6}$$

where Δt is the MD time step, if the scaling factor s is uniformly applied on all degrees of freedom and the temperature relaxation follows Equation (18.4). In the case of simulations with constraints, for example, bond lengths constrained by SHAKE [34], the scaling factor is computed after applying constraints on the velocities in a timestep, which are then employed to rescale the unconstrained velocities of the next time step.

18.3.2 The ACM Scheme

In the ACM scheme, we couple the motions in the lower frequency subspace to a higher temperature. This is done according to the scheme shown in Figure 18.1.

Since we will be representing the lower frequency subspace by residue degrees of freedom instead of atomic degrees of freedom (see the later section), first we obtain the center-of-mass velocities of individual residues $\{\vec{v}_\alpha^{\,\mathrm{res}}, \alpha = 1, \ldots, N_\mathrm{r}\}$ from the atomic velocities $\{\vec{v}_i, i = 1, \ldots, N_\mathrm{a}\}$, where N_r is the number of residues in the protein.

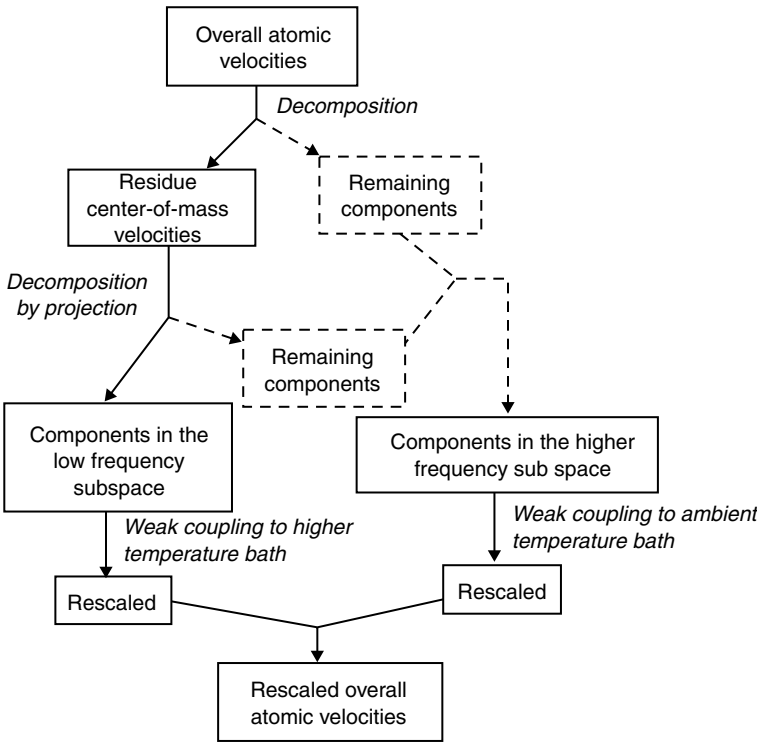

FIGURE 18.1
A schematic representation of the amplified collective motion simulation algorithm. See text for detailed descriptions.

Now, suppose that a n_1-dimensional lower frequency subspace Π is spanned by an orthonormal basis set $\{\vec{y}^{\,l}_{\alpha}, \alpha = 1, \ldots, N_r, l = 1, \ldots, n_1\}$, the projection of $\{\vec{v}^{\,res}_{\alpha}\}$ onto Π gives $\{\vec{v}^{\,res}_{\alpha,\Pi}\}$, the desired velocity components to be coupled to the higher temperature:

$$\vec{v}^{\,res}_{\alpha,\Pi} = \sum_{l=1}^{n_1} c_l \vec{y}^{\,l}_{\alpha} \tag{18.7}$$

$$c_l = \sum_{\beta=1}^{N_r} (\vec{v}^{\,res}_{\beta} \cdot \vec{y}^{\,l}_{\beta}) \tag{18.8}$$

The dot product in Equation (18.8) is carried out with respect to the three Cartesian components of $\{\vec{v}^{\,res}_{\beta}\}$ and $\{\vec{y}^{\,l}_{\beta}\}$ for residue β.

Now, for each atom i of residue α, we finish the decomposition of its velocity $\{\vec{v}_i, i \in \alpha\}$ into lower and higher frequency subspaces by

$$\begin{aligned} \vec{v}_i &= \vec{v}^{\,slow}_i + \vec{v}^{\,fast}_i \quad \text{with } \vec{v}^{\,slow}_i = \vec{v}^{\,res}_{\alpha,\Pi} \\ \vec{v}^{\,fast}_i &= \vec{v}_i - \vec{v}^{\,slow}_i, \quad \forall i \in \alpha, \ \alpha = 1, \ldots, N_r \end{aligned} \tag{18.9}$$

We apply the weak-coupling method to these two parts of the velocities, separately. For $\{\vec{v}^{\,slow}_i\}$ and $\{\vec{v}^{\,fast}_i\}$, the reference temperatures of the thermostats are T_l and T_h, respectively. The corresponding temperature scaling factors s_l and s_h can be computed separately according to Equation (18.6), and the scaled velocities obtained as

$$\vec{V}^{\,scaled}_i = s_l \vec{V}^{\,slow}_i + s_h \vec{V}^{\,fast}_i, \quad i = 1, \ldots, N_a \tag{18.10}$$

The above ACM scheme is quite different from conventional simulations at elevated temperatures. There, the acceleration of transitions between different local conformational states is achieved at the cost of destabilizing local interactions and extending the accessible conformational space. As the overall density of states increases rapidly with increased temperature, unselectively putting all degrees of freedom at higher temperature usually decreases the overall efficiency of the sampling, because the majority of the sampled conformations is irrelevant to the physically allowed conformations at ambient temperature. ACM increases the chance of escaping a local trap by increasing the temperature of only a few collective modes supposed to dominate conformational transitions. With this, sampled configurations are dominated by the physically allowed ones.

To our knowledge, the idea of accelerating sampling by coupling different degrees of freedom to different temperature baths has been first proposed for the molecular dynamics docking (MDD) method [35, 36]. There, by employing a higher temperature bath for overall translation and rotational degrees of freedom and ambient temperature bath for the internal degrees

of freedom of the substrate, an efficient search in the translational and rotational subspace of the substrate is achieved without disturbance of its internal structure. The Berendsen thermostat has been employed in these studies. In another novel MD simulation, the protein and solvent have been simulated at different temperatures [37] using the Nose–Hoover thermostat [38, 39], not for enhanced sampling, but to demonstrate the key roles of solvent in controlling functionally important fluctuations.

As in conventional constant temperature simulations, usage of the weak-coupling thermostat in ACM is one among a number of possible choices. Other thermostats such as the Nose–Hoover [38, 39] or Nose–Hoover chain [40] can be used as well. Both the weak-coupling and the Nose–Hoover thermostats require sufficient energy exchanges between different degrees of freedom coupled to the same temperature bath for efficient thermodynamics equilibriation. As the lower frequency subspace is spanned by only a few degrees of freedom and as there may not be enough mixing within this lower-dimensional subspace, the Nose–Hoover chain thermostat may be a more appropriate choice.

In practice, there are enough energy exchanges between different modes in the lower frequency space to establish thermoequilibrium, and that makes the weak-coupling scheme appropriate even for this lower-dimensional subspace. The sources of mixing include that the higher and lower frequency subspaces are not completely decoupled, and that there exists mixing of modes between the lower and higher frequency motions as the conformation evolves. Both factors cause ACM to produce a perturbed ensemble in which the actual averaged temperature of motions in the lower frequency subspace is lower than the targeted temperature of the thermostat, and a narrow spectrum of modes that have frequencies just above the lower frequency subspaces to have temperatures higher than the ambient temperature.

A weakness of ACM is that so far there is not yet any strict theory on how to obtain exact thermodynamic averages from this ensemble. Empirically, we may expect that the transition frequencies observed in the ACM simulation could be related to true transition rates after corrections with respect to the elevated temperature of the motions in the lower frequency subspace. To obtain exact free energy barriers, the ACM paths can be used to derive reaction coordinates for more strict methods, such as umbrella sampling. Because only a small number of modes are separated out, the averaged temperature of the system as a whole is solely dependent on the thermostat coupled to the higher frequency subspace. The above rationalizations are consistent with observations in example simulations discussed in this chapter.

18.3.3 Using ANM to Guide Atomic Simulations in the ACM Scheme

A significant simplification in previous approaches using collective coordinates as a basis set for enhanced sampling is to fix the basis set for the low

frequency subspace during sampling and ignore its dependence on conformational states. This is largely because the basis set is either from strict NMA or from PCA of a predefined set of conformations. By such approaches to update, the low frequency subspace either requires local energy minimization first or requires a prior knowledge of the dominating fluctuations of the conformations to be sampled.

In ACM, we employ simplified NMA, which does not require minimization, but does not assume conformation independence of the modes. In the ACM method, the collective modes obtained by the coarse-grained model ANM [26] are employed to guide the atomic-level MD simulation. By ANM, the collective modes are estimated using a single protein conformation without carrying out a long simulation. These modes can be updated frequently during the simulation since computation of the collective modes using the ANM is rapid, which allows us to give up the severe assumption that the essential dynamics subspace is invariant in the conformational space.

Usage of ANM to obtain the lower frequency subspace in the ACM scheme also relies on previous observations that the subspace is usually insensitive to the details of the model for describing the intramolecular interactions [5, 25, 41]. Thus, this subspace obtained by coarse-grained ANM can be reasonably used to guide simulations employing atomic molecular mechanics force field. In fact, in the T4 lysozyme example discussed below, the three slowest ANM modes obtained from a single conformation also cover more than 80% of the first two principle components obtained using a set of about 40 crystal structures [19].

Compared to conventional MD, the additional computational costs in the ACM algorithm mainly involve the diagonalization of the ANM Hessian matrix. For residue-based analysis, the computational cost of the algorithm is $O(N_r^2)$ [42]. The updation of the ANM modes does not need to be carried out for every time step. For one of the examples discussed later in this chapter, the S-peptide analog, the additional computational cost is ignorable, and for another example, the T4 lysozyme, the computational cost is increased by about 10% compared to conventional MD in ACM with the ANM modes updated every 100 time steps [19].

18.3.4 The Amplified Collective Motion-Assisted Minimum Escaping (ACM-AME) Scheme

One problem when the ACM scheme is applied that some degrees of the system are always at higher temperature. And because the higher and lower frequencies subspaces are not completely decoupled with the true molecular mechanics Hamiltonian, there are continuous exchanges of energies between the higher and lower temperature parts. In the ACM-AME scheme [44], a simulation is partitioned into alternative excitation and relaxation phases. The ACM method is only applied in an excitation phase to drive the system out of a minimum to correspond to a local conformational state. The system

is reequilibrated (probably in a different local conformational state) by a conventional simulation at ambient temperature in the subsequent relaxation phase.

For the switching between the relaxation phase and the excitation phase, we use the root mean square (RMS) deviation of the current time-averaged [43] structure from a reference structure representing the local minimum in a coarse-grained sense as our criterion. The reason to use the current time-averaged structure instead of the current structure is to remove large instantaneous fluctuations in this RMS deviation so that it can be employed as a robust criterion. Using a time-averaged structure filters out the contributions of higher frequency fluctuations to the RMS deviations. Such fluctuations are small for individual degrees of freedom but within a local minimum contribute significantly to the overall RMS deviations because there are a large number of such degrees of freedom.

In enhanced sampling, we do not know in advance, which local minima the system would fall into during the simulation. Thus the reference structure is not fixed but time-dependent. In fact, it corresponds to a time-averaged structure determined at some previous time point.

We start from a relaxation phase and the starting structure is the initial reference structure $\{\vec{x}_i^{\,p}, i = 1, \ldots, N_\mathrm{a}\}$. At time t, the current time-averaged structure $\{\vec{x}_i^{\,\tau}(t), i = 1, \ldots, N_\mathrm{a}\}$ is computed as

$$\vec{x}_i^{\,\tau}(t) = \vec{x}_i^{\,\tau}(t - \Delta t)\mathrm{e}^{-\Delta t/\tau} + \vec{x}_i(t)(1 - \mathrm{e}^{-\Delta t/\tau}), \quad i = 1, \ldots, N_\mathrm{a} \tag{18.11}$$

Here, $\{\vec{x}_i(t), i = 1, \ldots, N_\mathrm{a}\}$ are the coordinates at time t, and τ the timescale covered by the averaging. Then we compute the RMS deviation of $\{\vec{x}_i^{\,\tau}(t)\}$ from $\{\vec{x}_i^{\,p}(t)\}$,

$$\delta(t) = \sqrt{\frac{\sum_{i=1}^{N_\mathrm{a}} |\vec{x}_i^{\,\tau}(t) - \vec{x}_i^{\,p}|^2}{N_\mathrm{a}}} \tag{18.12}$$

The overall translations and rotations are eliminated by superimposing both $\{\vec{x}_i^{\,\tau}(t - \Delta t)\}$ and $\{\vec{x}_i^{\,p}(t)\}$ onto $\{\vec{x}_i(t)\}$ before applying Equations (18.11) and (18.12).

As the simulation goes on in a relaxation phase, $\delta(t)$ would increase gradually through diffusive relaxation until the system falls into a trapped local conformational state. We assume that if in a predefined time period $t_\mathrm{relaxation}$, $\delta(t)$ increased to greater than a predefined threshold δ_min, the system has been going through the diffusive relaxation process in the conformational space and we update the reference structure, that is, replacing the old $\{\vec{x}_i^{\,p}\}$ by $\{\vec{x}_i^{\,\tau}(t)\}$. If not, we assume the system has reached equilibrium in a local conformational state and the simulation switches into the excitation phase. The excitation phase ends until $\delta(t)$ exceeds δ_max, roughly the displacements required for the system to escape a local minima.

The physical meanings of τ, $\delta_{\min}$, and $t_{\text{relaxation}}$ are the following: τ corresponds to the cutoff in the frequency filter for eliminating the instantaneous fluctuations in the RMS deviations; $\delta_{\min}$, in an average sense, represents the size of a local conformational minimum measured by the filtered RMS deviations; and $t_{\text{relaxation}}$, also in an average sense, represents the relaxation time for reaching equilibrium within a local conformational state. $\delta_{\max}$ is roughly the displacement required for the system to escape a local minima.

Because of the above physical meanings and the two type of processes (namely, fluctuations within the same local conformational state and transitions across different conformational states) that take place in widely separated time scales, cover different frequency ranges and corresponds to different amplitudes of conformational change, the parameters τ, $\delta_{\min}$, and $t_{\text{relaxation}}$ need only to be chosen within their respective physical ranges and their exact values are not critical.

For a particular system, these parameters can be estimated by short trial simulations before the ACM-AME scheme is employed for lengthy sampling. First, to determine τ, we can compare the fluctuations of the filtered RMS deviation $\delta(t)$ computed with different values of τ. With τ increasing, $\delta(t)$ as a function of time gets smoother. At a physically meaningful value of τ, higher frequency fluctuations of $\delta(t)$ have been eliminated so that $\delta(t)$ becomes an essentially monotonically increasing function of time at small t and then reaches a plateau value, which is almost constant (i.e., without rapid fluctuations). Then, in a short trial simulation, larger than necessary values for $t_{\text{relaxation}}$ and $\delta_{\min}$ can be used, so that the relaxation phases are sufficiently long and $\delta(t)$ can increase to its plateau values within each relaxation phase. Then $t_{\text{relaxation}}$ can be chosen as the approximate time for $\delta(t)$ to reach its plateau value, and $\delta_{\min}$ can be chosen as slightly larger than the observed plateau value of $\delta(t)$. $\delta_{\max}$ is not critical as long as it is large enough to ensure a high probability for the system to escape from the previous local state, while it is still of reasonable magnitude so that the simulation does not inefficiently spend too long in the excitation phases.

18.4 Examples

18.4.1 Interdomain Motions of Bacteriophage T4 Lysozyme

Bacteriophage T4 lysozyme (T4L) consists of two domains, the *N*-terminal and *C*-terminal domains, connected by a long α-helix. Between the two domains there is a deep cleft, corresponding to the binding site for the enzyme's substrate, oligosaccharide [45].

Experimental structures [46, 47] as well as theoretical studies [48], have revealed a hinge-bending type domain motion opening or closing up the cleft. The first two largest amplitude collective modes determined from the MD trajectories of T4L have been identified as being the closure and twisting modes [48].

Starting from a crystal structure of T4L determined at 1.7 Å resolution [49], we carried out simulations on this molecule in a box of explicit water with both conventional MD simulations and ACM simulations. Both simulations started from the same equilibrated configuration and lasted for 3 nsec each. Details of the calculations have been presented elsewhere [19].

The conventional MD at 300 K (S_{300}) was performed using an isothermal–isobaric simulation algorithm [33]. The ACM simulation (S_{ACM}) was otherwise the same as the control simulation, except for modifications to the temperature-coupling scheme according to ACM.

In ACM, we selected the three slowest collective modes obtained from ANM analyses ($n_l = 3$), which were done every 100 time steps according to the new current configuration of the protein. These three degrees of freedom were coupled to a higher temperature bath ($T_h = 800$ K), and the other modes coupled to an ambient temperature bath ($T_l = 300$ K). The actual average temperatures were 751 and 299 K for the collective modes and the rest, respectively. As the number of degrees of freedom at higher temperature is negligible compared to the total number of degrees of freedom, the temperature averaged over all degrees of freedom of the system in S_{ACM} is almost the same as in S_{300}.

Comparing ACM and conventional MD, the ACM simulations produce larger fluctuations as measured by the root-mean-square fluctuations (RMSF) of the C^α atoms from residues 1 to 162 in the two simulations (Figure 18.2[a]). More importantly, the increased motions mainly come from the interdomain motion. While the C^α atom RMS deviations from the starting structure for the overall protein (residues 1 to 162) is larger in the ACM simulation (Figure 18.2[b]), the RMS deviations computed separately for the *N*-terminal domain (residues 13 to 65, Figure 18.2[c]) and *C*-terminal domain (residues 75 to 162, Figure 18.2[d]) are comparable in the ACM as in the conventional simulation. We also showed that the secondary structures as well as the structures of each domain have been well maintained in both simulations.

The trajectories from both simulations can be visualized on a two-dimensional plane spanned by the first two eigenvectors obtained by PCA analysis. The analysis has been performed on a cluster of 38 x-ray crystallographic structures, which may be representatives of accessible conformations of T4L under physiological conditions [47]. The first mode corresponds to a closure motion and the second mode to a twisting of the two domains. Along the first mode there seem to be two distinct clusters of the x-ray structures: structures to the left are open structures and structures to the right closed. The two eigenvectors contribute about 90% to the total positional variations among the experimental structures [48]. Figure 18.3 shows that the MD simulation (S_{300}), which started with a closed structure, sampled mostly in an intermediate region between the two clouds of the x-ray structures, without reaching positions corresponding to either the most open or the most closed configurations in the x-ray cluster. The ACM simulation (S_{ACM}), sampled a significantly wider area in the plane than the normal MD and the x-ray clusters.

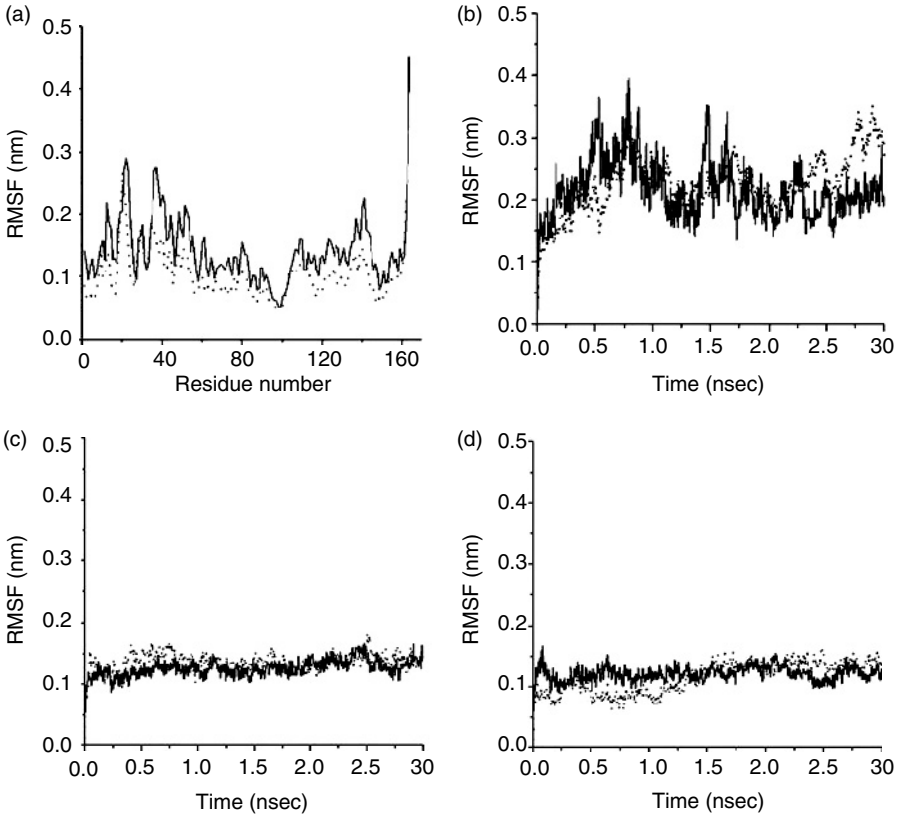

FIGURE 18.2
Properties of the conventional constant temperature (dotted lines) and the ACM (solid lines) simulations of the bacteriophage T4 lysozyme. (a) RMS fluctuations of C^{α} atoms from residues 1–162; (b) atomic positional RMS deviations from the starting structure of the C^{α} atoms from residues 1–162; (c) RMS deviations of the C^{α} atoms of the *N*-terminal domain (residues 13–65); and (d) RMS deviations of the C^{α} atoms of the *C*-terminal domain (residues 75–162). (Reproduced from Zhang, Z., Shi, Y. and Liu, H., *Biophys. J.*, 84, 3583, 2003. With permission.)

18.4.2 Folding of an S-Peptide Analog

A 15-residue α-helical analog of Ribonuclease A S-peptide [50], the native structure of this peptide consists of α-helix (residues 4 to 12), *N*-terminal (1 to 3), and *C*-terminal (13 to 15) random coils. Simulations of this peptide at lower temperature (278 K) maintained its stable helical native structure, while at a higher temperature (358 K), a 20 nsec simulation completely unfolded the peptide [51].

Four groups of simulations of this peptide in solution (solvent effects described by an implicit generalized Born/surface area (GB/SA) model [52,53]) were carried out [19] (1) conventional simulations at 274 K; (2) ACM simulations starting from its native structure (noted as NA and NA_ACM, respectively); (3) conventional simulations at 274 K; and (4) ACM simulations

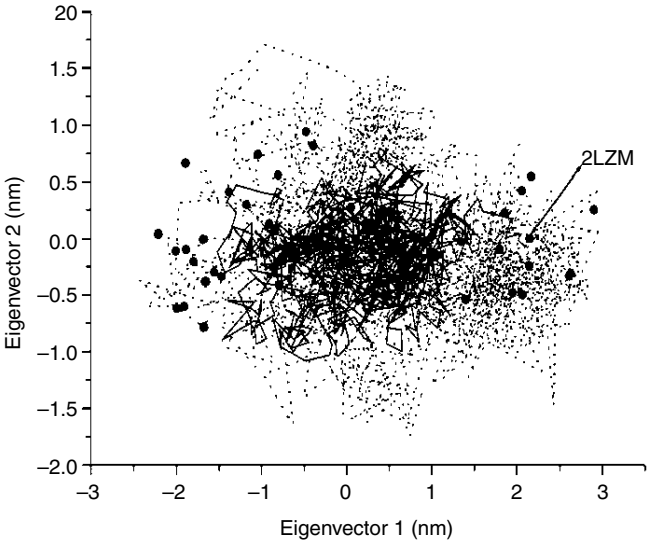

FIGURE 18.3
Two-dimensional projections of the T4L structures from x-ray (solid circles), and both the conventional (solid line) and the ACM (dotted line) simulation trajectories. The plane projected onto is defined by the "closure" and the "twist" mode obtained by PCA on 38 crystal structures. The starting structure of the simulations (PDB ID 2LZM) is indicated by an arrow. (Reproduced from Zhang, Z., Shi, Y., and Liu, H., *Biophys. J.*, 84, 3583, 2003. With permission.)

starting from the unfolded conformations (noted as UN and UN_ACM, respectively). In the ACM simulations, either the slowest 3 or the slowest 5 ANM modes were coupled to the higher temperature ($T_h = 358$ K), the other modes coupled to the lower temperature ($T_l = 274$ K). The collective modes were recalculated either every 10 or every 25 time steps according to the new current configuration of the peptide. Multiple simulations within each group produced similar results, and results of one simulation from each group are discussed briefly here.

The helix is stable during the NA simulations (Figure 18.4[a]). The NA_ACM simulations also kept the native α-helix well, although with significantly larger structural fluctuations (Figure 18.4[b]). In the UN simulations, the peptide maintains persistently large RMS deviations (Figure 18.4[c]), no transitions to native-like helical structures could be observed. In eight of ten UN_ACM simulations with varying number of slower modes, varying intervals in updating the slower modes, and different initial velocities, the unfolded peptide refolds into the native helix (Figure 18.4[d]). The refolding time (the first time when the RMS derivations from the native structure is below 0.1 nm) ranged from 20 to 90 nsec. After refolding, the UN_ACM simulations are similar to the NA_ACM simulations (Figure 18.4[b]). In two UN_ACM simulations, refolding has not been observed within 100 nsec.

For this peptide, the average effective potential energy (including the GB/SA effective free energy of solvation) of the denatured structures

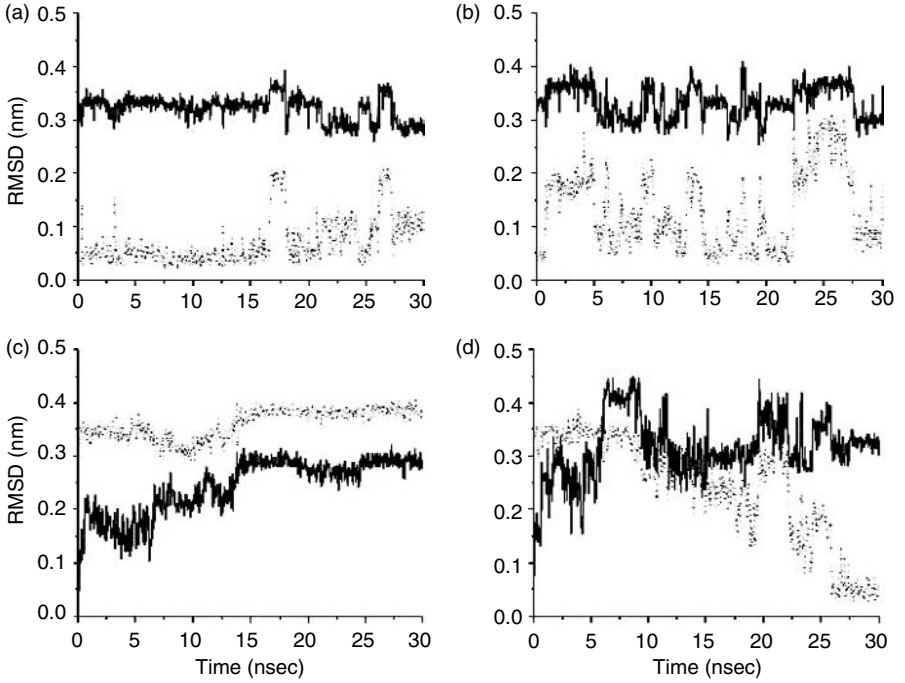

FIGURE 18.4
RMS deviations of the backbone atoms of residues 4 to 12 from the native structure (dotted lines) and from a denatured starting structure (solid lines) in different groups of the simulations. (a) A conventional simulation starting from the native structure (NA); (b) an ACM simulation starting from the native structure (NA_ACM); (c) a conventional simulation starting from the denatured structure (UN); and (d) an ACM simulation starting from the denatured structure (UN_ACM). (Reproduced from Zhang, Z., Shi, Y., and Liu, H., *Biophys. J.*, 84, 3583, 2003. With permission.)

(-2808.2 ± 30.6 kJ mol^{-1}) is higher than that of the native structures (-2831.3 ± 29.8 kJ mol^{-1}). The energies averaged over the ACM simulations (-2828.2 ± 31.1 kJ mol^{-1} for NA_ACM and -2814.9 ± 32.1 kJ mol^{-1} for UN_ACM) have only slightly larger fluctuations than that in the conventional simulations, likely caused by a few collective modes that have been coupled to a higher temperature. However, the average energy values in the ACM simulations are still in a reasonable range.

These results are consistent with our purpose in designing the ACM method, that is, to assist the system to escape unfolded local conformational states by expanding the sampling region selectively, without stepping into irrelevant high-energy regions of the conformational space.

The refolding processes repeatedly observed in UN_ACM simulations give some implications on the folding/unfolding pathways of the peptide. The forming and breaking of five native $i + 4 \rightarrow i$ hydrogen bonds (Phe8: NH-Ala4: CO [HB_1], Leu9: NH-Ala5: CO [HB_2], Arg10: NH-Ala6: CO [HB_3], Glu11: NH-Lys7: CO [HB_4], and His12: NH-Phe8: CO [HB_5])] were observed

to correspond well with the folding/unfolding process. They were more stable in NA than in NA_ACM simulations, and remained unformed in UN simulations. In UN_ACM simulations, the hydrogen bonds near the *N*-terminal formed earlier than those near the *C*-terminal in refolding processes. Consistently, in a higher temperature-driven unfolding simulation, the latter hydrogen bonds have been observed to break earlier in unfolding processes [51].

18.4.3 ACM-AME Sampling of Peptide Conformations

We compared ACM-AME with conventional simulations as well as an alternative scheme that elevates the temperature of all degrees of freedom during the excitation phase (amplified overall motion-assisted minimum escaping, or AOM-AME) [44]. Simulations on four peptides starting from nonnative extended or all helical structures with difference schemes were performed. Among the four systems tested, the native structures of the S-peptide analog and the E6-interacting peptide are helical, while the β-peptide is two β-strands connected by a turn, and the villin headpiece subdomain (HP-36) is a small alpha protein containing three secondary structural elements. The following aspects of the results were looked at in detail: the energies of sampled conformations, the diversity of sampled conformations, and the deviations of the sampled conformations to the corresponding native structures. Details of the results have been reported elsewhere [44] and we summarize the results below.

(1) *Energies*: We consider the effective energies consisting of intramolecular potential energy and the effective free energy of solvation computed by the GB/SA model, that is, $E_{\text{tot}} = E_{\text{intra-mol}} + E_{\text{solvation}}$. In the normal MD simulation starting from extended structures, the energies always dropped rapidly during the initial phase of the simulations, soon becoming flat and fluctuating around at values obviously higher than the averaged energies of the native simulations. The ACM-AME simulations, however, produced much larger fluctuations in energies, occasionally sampling conformations with instantaneous energies lower than the averages of the native simulations. This has been observed in the simulations on the S-peptide analog, the β peptide, and HP-36 (starting from a all helical conformation). That is, the ACM-AME scheme does introduce much more frequent escaping from local energy minima. Comparisons between the ACM-AME energies and the normal MD energies as functions of simulation time also indicate that the increase in sampling in the ACM-AME scheme is not trade-off by excessive sampling in nonrelevant, high-energy regions. This is contrary to the AOM-AME scheme, by which although the simulations do not seem to be trapped in any energy minimum, much of the sampling is within uninteresting higher energy regions of the conformational spaces. Our study also indicated that for longer chains that fold into several secondary structure segments, applying

ACM-AME to an extended starting structure may not be a good choice; there the initial local contacts formed from the extended starting structure may dominate the low frequency subspace in the initial phase of the simulation, thus destabilized by the ACM scheme.

(2) *Conformation Clusters*: The number of conformation clusters (clustered on the atomic positional RMS deviation basis) as functions of simulation time should directly reflect the degree of enhancement in sampling. In the ACM-AME simulations, the number of clusters formed by sampled conformations increased almost at a constant rate, with the sampled conformations relatively evenly distributed in different clusters. Only at very later phases of the ACM-AME simulations the rate slows down, as certain conformation clusters were being revisited, rather than that the systems have been trapped in local minima. For the S-peptide analog we seem to observe near convergence of the ACM-AME simulations, because the sampled conformations are more evenly distributed in different conformational clusters and the rate of sampling new conformations are very slow near the end of the simulations. For the simulations in the other systems our simulations did not seem sufficiently long to explore the entire low energy parts of their conformational spaces and the rates of sampling new conformations remained high at the ends of the simulations. In the normal MD simulations, the same number of conformation clusters quickly reach a plateau value and rarely increase with the length of the simulation. This is not unexpected for a frustrated landscape, on which the escape from local minima may take orders of magnitude of longer simulation time than we performed. Thus the majority of sampled conformations belong to a few clusters, not diversely distributed among different conformational clusters.

(3) *Near Native Conformations*: Successful *ab initio* folding of a peptide or protein requires both an accurate energy function and sufficient exploration of the energy landscape. For the S-peptide analog, the smallest C^{α} RMS deviation from the native structure is below 2 Å. We also observed correlations between the energies and RMS deviations from the native structure, both as functions of simulation time. We believe that for this particular short peptide, the global minimum of our energy function correspond to the native helical structure. The simulations of the other systems sampled near native conformations with 2 to 4 Å backbone RMS deviations from the native structure, but we cannot tell the near native structure from the trajectories by the effective energies.

18.5 Summary

Based on a general qualitative picture of protein energy landscape, we emphasize that there are the following major considerations in enhanced conformation sampling techniques: to accelerate rare conformational transitions;

to avoid sampling in the mass of irrelevant higher energy part of the conformational space; to avoid disturbing the local conformational equilibriums; and in some cases, to sample along the dominating transition paths. Collective coordinates obtained from various NMA technologies reflect the local landscape, the lower frequency space leading to pathways along which to deform the local conformational states is the easiest. Various enhanced strategies have been developed to take advantages of this property.

We discussed in detail the ACM scheme, in which the lower frequency modes obtained from the coarse-grained ANM model are employed to guide the sampling in atomic simulations. The main advantage brought about by the ANM model is that we can update the lower frequency subspace locally as the system samples different part of the conformational landscape. We further described the ACM-AME scheme, in which the ACM is applied repeatedly to assist minimum escaping in the simulation. The examples discussed include applying ACM to interdomain motions of lysozyme, unfolding and refolding of a short helical peptide, and applying ACM-AME to conformational searching of a number of small peptides.

As an enhanced sampling technique, the ACM method may be used to explore large-scale functional motions of proteins. As it increases the efficiency of conventional molecular dynamics with little additional computational burden, its applications may include providing alternative conformations for structure-based inhibitor design or molecular docking, generating conformations better satisfying experimental constraints, or producing low-activation-barrier transition pathways between different conformational states from which new insights into the mechanisms of function-related protein dynamics can be obtained.

Acknowledgments

The authors gratefully acknowledge the Chinese Natural Science Foundation and the Chinese Academy of Sciences for financial supports to their research. We also thank Professor WF van Gunsteren for providing the GROMOS96 [54] program package.

References

1. Karplus, M. and McCammon, J.A., Molecular dynamics simulations of biomolecules, *Nat. Struct. Biol.*, 9, 646, 2002.
2. Frauenfelder, H., Sligar, S.G., and Wolynes, P.G., The energy landscapes and motions of proteins, *Science*, 254, 1598, 1991.
3. Garcia, A.E., Large-amplitude nonlinear motions in proteins, *Phys. Rev. Lett.*, 68, 2696, 1992.

4. Kitao, A., Hayward, S., and Go, N., Energy landscape of a native protein: jumping-among-minimum model, *Proteins,* 33, 496, 1998.
5. Kitao, A. and Go, N., Investigating protein dynamics in collective coordinate space. *Curr. Opin. Struct. Biol.,* 9, 164, 1999.
6. Berendsen, H.J.C. and Hayward, S., Collective protein dynamics in relation to function, *Curr. Opin. Struct. Biol.,* 10, 165, 2000.
7. Elber, R., Meller, J., and Olender, R., Stochastic path approach to compute atomically detailed trajectories: application to the folding of C peptide, *J. Phys. Chem. B.*, 103, 899, 1999.
8. Bolhuis, P.G. et al., Transition path sampling: throwing ropes over rough mountain passes, in the dark, *Annu. Rev. Phys. Chem.*, 53, 291, 2002.
9. Hansmann, U.H.E. and Okamoto, Y., Prediction of peptide conformation by multicanonical algorithm-new approach to the multiple-minima problem, *J. Comput. Chem.*, 14, 1333, 1993.
10. Nakajima, N., Nakamura, H., and Kidera, A., Multicanonical ensemble generated by molecular dynamics simulations for enhanced conformational sampling of peptides, *J. Phys. Chem. B*, 101, 817, 1997.
11. Grubmuller H., Predicting slow structural transitions in macromolecular systems — conformational flooding, *Phys. Rev. E*, 52, 2893, 1995.
12. Huber, T., Torda, A.E., and van Gunsteren, W.F., Local elevation — a method for improving the searching properties of molecular-dynamics simulation, *J. Comput. Aid. Mol. Des.*, 8, 695, 1994.
13. Pak, Y. and Wang, S., Folding of a 16-residue helical peptide using molecular dynamics simulation with Tsallis effective potential, *J. Chem. Phys.*, 111, 4359, 1999.
14. Muller, E.M., de Meijere, A., and Grubmuller, H., Predicting unimolecular chemical reactions: chemical flooding. *J. Chem. Phys.*, 116, 897, 2002.
15. Bartels, C. and Karplus, M., Probability distributions for complex systems: adaptive umbrella sampling of the potential energy, *J. Phys. Chem. B*, 102, 865, 1998.
16. Huber, G.A. and McCammon, J.A., Weighted-ensemble simulated annealing: faster optimization on hierarchical energy surfaces, *Phys. Rev. E*, 55, 4822, 1997.
17. Huber, T. and van Gunsteren, W.F., SWARM–MD: searching conformational space by cooperative molecular dynamics, *J. Phys. Chem. A*, 102, 5937, 1998.
18. Abseher, R. and Nilges, M., Efficient sampling in collective coordinates space, *Proteins,* 39, 82–88, 2000.
19. Zhang, Z., Shi, Y., and Liu, H., Molecular dynamics simulations of peptides and proteins with amplified collective motions, *Biophys. J.,* 84, 3583, 2003.
20. Brooks, B.R., Janezic, D., and Karplus, M., Harmonic analysis of large systems. I. Methodology, *J. Comput. Chem.*, 16, 1522, 1995.
21. Amadei, A., Linssen, A.B.M., and Berendsen, H.J.C., Essential dynamics of proteins, *Proteins*, 17, 412, 1993.
22. Kloczkowski, A., Mark, J.E., and Erman, B., Chain dimensions and fluctuations in random elastomeric networks. 1. Phantom Gaussian networks in the underformed state, macromolecules, *Macromolecules,* 22, 1423, 1989.
23. Erman, B., Kloczkowski, A., and Mark, J.E., Chain dimensions and fluctuations in random elastomeric networks. 2. Dependence of chain dimensions and fluctuations on macroscopic strain, *Macromolecules,* 22, 1432, 1989.
24. Haliloglu, T., Bahar, I., and Erman, B., Gaussian dynamics of folded proteins, *Phys. Rev. Lett.,* 79, 3090, 1997.

25. Bahar, I., Atilgan, A.R., and Erman, B., Direct evaluation of thermal fluctuations in proteins using a single parameter harmonic potential, *Fold. Des.*, 2, 173, 1997.
26. Atilgan, A.R. et al., Anisotropy of fluctuation dynamics of proteins with an elastic network model, *Biophys. J.*, 80, 505, 2001.
27. Ming, D. et al., Domain movements in human fatty acid synthase by quantized elastic deformational model, *Proc. Natl Acad. Sci. USA*, 99, 7895, 2002.
28. Ming, D. et al., How to describe protein motion without amino acid sequence and atomic coordinates, *Proc. Natl Acad. Sci. USA*, 99, 8620, 2002.
29. Noguti, T. and Go, N., Efficient Monte Carlo method for simulation of fluctuating conformations of native proteins, *Biopolymers*, 24, 527, 1985.
30. Amadei, A. et al., An efficient method for sampling the essential subspace of proteins, *J. Biomol. Struct. Dyn.*, 13, 615, 1996.
31. de Groot, B.L. et al., Towards an exhaustive sampling of the configurational spaces of the two forms of the peptide hormone guanylin, *J. Biomol. Struct. Dyn.*, 13, 741, 1996.
32. de Groot, B.L. et al., An extended sampling of the configurational space of hpr form *E. coli*, *Proteins*, 26, 314, 1996.
33. Berendsen, H.J.C. et al., Molecular dynamics with coupling to an external bath, *J. Chem. Phys.*, 81, 3684, 1984.
34. Ryckaert, J.P., Ciccotti, G., and Berendsen., H.J.C., Numerical integration of the cartesian equations of motion of a system with constraints: molecular dynamics of n-alkenes, *J. Comput. Phys.*, 23, 327, 1977.
35. Di Nola, A., Roccatano, D., and Berendsen. H.J.C., Molecular dynamics simulation of the docking of substrates to proteins, *Proteins*, 19, 174, 1994.
36. Mangoni, M., Roccatano, D., and Di Nola, A., Docking of flexible ligands to flexible receptors in solution by molecular dynamics simulation, *Proteins*, 35, 153, 1999.
37. Vitkup, D. et al., Solvent mobility and the protein "glass" transition, *Nat. Struct. Biol.*, 7, 34, 2000.
38. Nose, S., A molecular dynamics method for simulation in the canonical ensemble, *Mol. Phys.*, 52, 255, 1984.
39. Hoover, W.G., Canonical dynamics: equilibrium phase–space distributions, *Phys. Rev. A*, 31, 1695, 1985.
40. Martyna, G.J., Klein, M.L., and Tuckerman, M.E., Nose–Hoover chains: the canonical ensemble via continuous dynamics, *J. Chem. Phys.*, 97, 2635, 1992.
41. Tirion, M.M., Large amplitude elastic motions in proteins from a single-parameter, atomic analysis, *Phys. Rev. Lett.*, 77, 1905, 1996.
42. Dhillon, I., A new $O(n^2)$ algorithm for the symmetric tridiagonal eigenvalue/eigenvector problem, Computer Science Division Technical Report No. UCB//CSD-97-971, UC Berkeley, 1997.
43. Torda, A.E., Sheek, R.M., and van Gunsteren, W.F., Time-averaged nuclear Overhauser effect distance restraints applied to tendamistat, *J. Mol. Biol.*, 214, 223, 1990.
44. He, J. et al., Efficiently explore the energy landscape of proteins in molecular dynamics simulations by amplifying collective motions, *J. Chem. Phys.*, 119, 4005, 2003.
45. Anderson, W.F. et al., Crystallographic determination of the mode of binding of oligosaccharides to T4 bacteriophage lysozyme: implications for the mechanism of catalysis, *J. Mol. Biol.*, 147, 523, 1981.

46. Faber, H.R. and Matthews, B.W., A mutant T4 lysozyme displays five different crystal conformations, *Nature*, 348, 263, 1990.
47. Zhang, X.J., Wozniak, J.A., and Matthews, B.W., Protein flexibility and adaptability seen in 25 crystal forms of T4 lysozyme, *J. Mol. Biol.*, 250, 527, 1995.
48. de Groot, B.L. et al., Domain motions in bacteriophage T4 lysozyme: a comparison between molecular dynamics and crystallographic data, *Proteins,* 31, 116, 1998.
49. Weaver, L.H. and Matthews, B.W., Structure of bacteriophage T4 lysozyme refined at 1.7 Å resolution. *J. Mol. Biol.*, 193, 189, 1987.
50. Tirado-Rives, J. and Jorgensen, W.L., Molecular dynamics simulations of an a-helical analog of ribonuclease A S-peptide in water, *Biochemistry*, 30, 3864, 1991.
51. Zhang, Z., Zhu, Y., and Shi, Y., Molecular dynamics simulations of urea and thermal-induced denaturation of S-peptide analogue, *Biophys. Chem.,* 89, 145, 2001.
52. Still, W.C. et al., Semianalytical treatment of solvation for molecular mechanics and dynamics. *J. Am. Chem. Soc.,* 112, 6127, 1990.
53. Zhu, J., Shi, Y., and Liu, H., Parametrization of a generalized born/solvent-accessible surface area model and applications to the simulation of protein dynamics, *J. Phys. Chem. B*, 106, 4844, 2002.
54. Van Gunsteren, W.F. et al., *Biomolecular simulation: The GROMOS96 Manual and User Guide*. Zurich, Switzerland: Vdf Hochschulverlag, 1996.

Index

A

B

C

D

E

F

G

H

I

J

K

L

M

N

O

P

Q

R

S

T

U

V

W

X

Y

Z

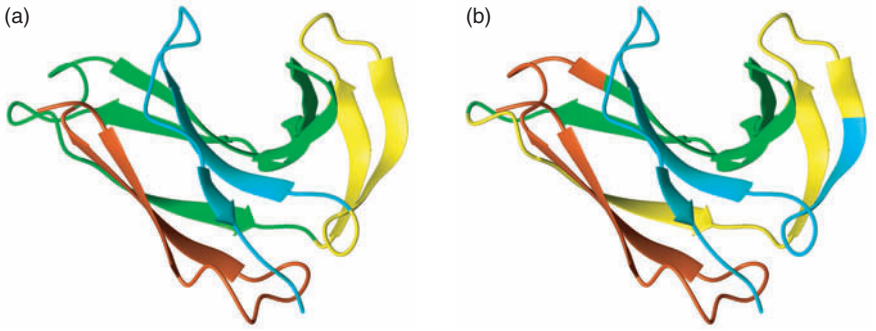

FIGURE 2.3
Structure of NCS. (a) Partition of the protein according to its secondary structure elements. (b) Subdivision of the protein in four equal parts of 237 atoms without any structural considerations. Each part of the protein is presented by a different color.

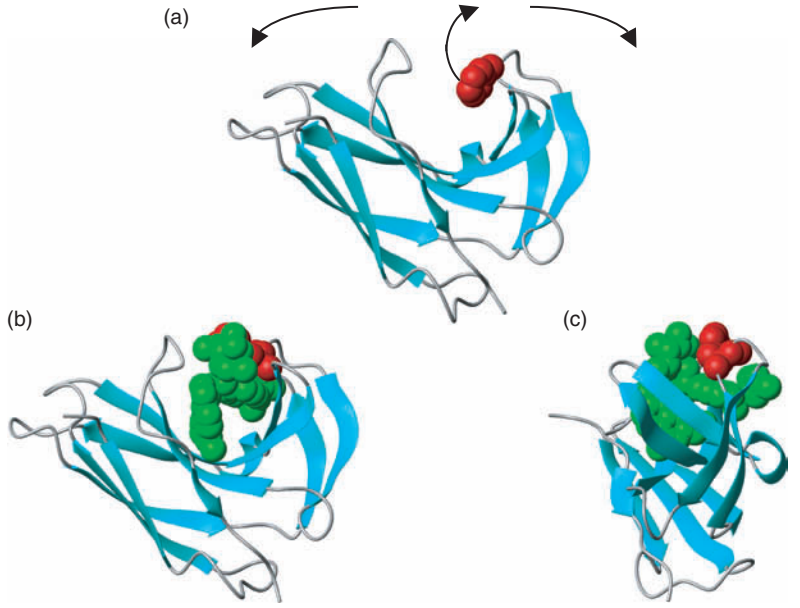

FIGURE 2.8
Crystal structures of apo (a) and holo-NCS containing a chromophore (b and c); residue Phe 78 is shown in red and the chromophore in green. In (a) the arrows indicate the motion along mode 9, in the opening direction of the cleft, which is coupled to the upward motion of Phe 78. In (b) holo-NCS is presented in the same orientation as (a) while in (c) it is rotated by 90°.

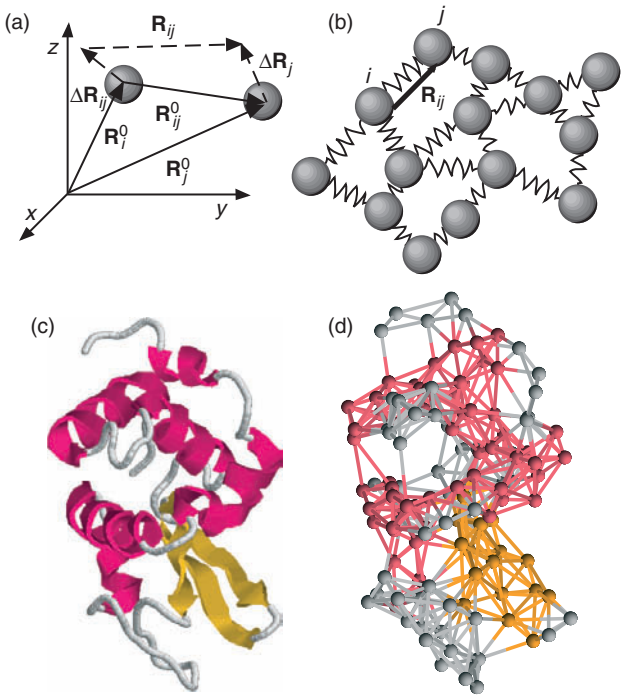

FIGURE 3.1
Description of the GNM. (a) Schematic representation of the equilibrium positions of the ith and jth nodes, $\mathbf{R}^0_i$ and $\mathbf{R}^0_j$, with respect to a laboratory-fixed coordinate system (xyz). The instantaneous fluctuation vectors, $\Delta\mathbf{R}_i$ and $\Delta\mathbf{R}_j$, are shown by the dashed arrows, along with the instantaneous separation vector $\mathbf{R}_{ij}$ between the positions of the two residues. $\mathbf{R}^0_{ij}$ is the equilibrium distance between nodes i and j. (b) In the EN of GNM every residue is represented by a node and connected to spatial neighbors by uniform springs. These springs determine the $N-1$ degrees of freedom in the network and the structure's modes of vibration. (c) Three dimensional image of hen egg white lysozyme (PDB file 1hel [46]) showing the C^α trace. Secondary structure features are indicated by pink for helices and yellow for β-strands. (d) Using a cutoff value of 10 Å, all connections between C^α nodes are drawn for the same lysozyme structure to indicate the nature of the EN analyzed by GNM.

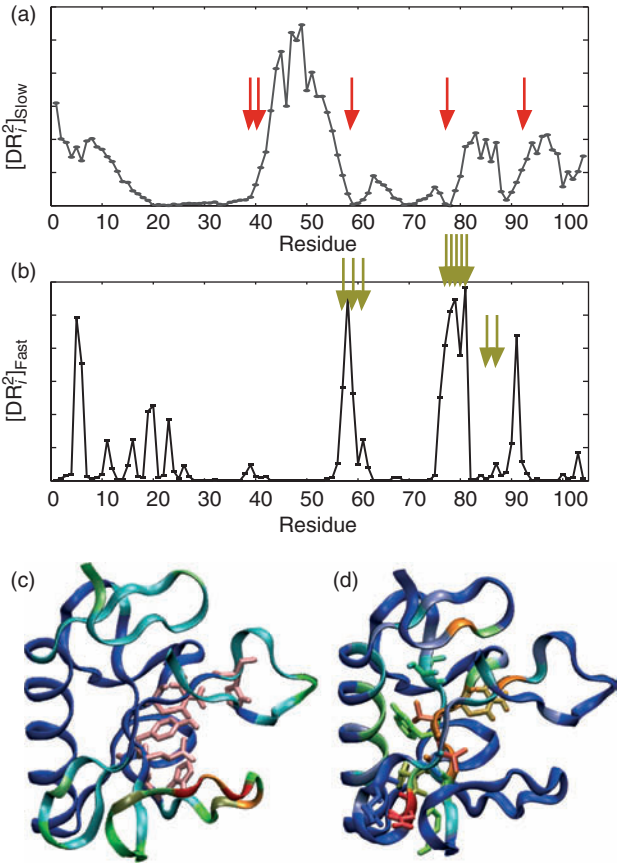

FIGURE 3.3
Physical meaning of slow and fast modes in GNM. (a) Distribution of squared displacements of residues in the slowest mode as a function of residue index for ribonuclease T1 (RNase T1). The red arrows identify local minima that correspond to five experimentally identified catalytic residues: Tyr38, His40, Glu58, Arg77, and His92. (b) Distribution of squared displacements averaged over the ten fastest modes for the same protein. Here the arrows indicate the residues shown by hydrogen/deuterium exchange to be the most protected and thus important for reliable folding. A majority of these critical folding residues appear as peaks in the fast modes. (c) Color-coded mapping of the slowest mode (a) onto the 3D C^{α} trace of RNase T1 (PDB file: 1bu4 [53]) where red is most mobile and blue least mobile. The side chains of the five catalytic residues are shown in pink surrounding the nucleotide binding cavity. (d) A similar color-coded mapping of the fluctuations of the ten fastest modes (b) onto the C^{α} trace. Here the side chains of the ten most protected residues from hydrogen deuterium exchange experiments are drawn explicitly showing that most of them are calculated to be mobile (red). The images in c and d were generated using VMD [74].

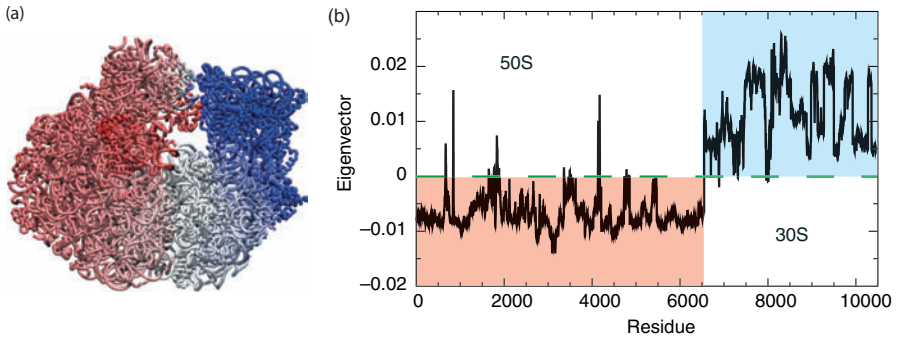

FIGURE 3.4
Application of GNM to the 70S ribosome structure. The calculations were performed on the wild type 70S ribosome from *E. coli* (PDB files 1pnx and 1pny [59]). (a) The slowest nonzero mode for the 70S ribosome colored from −1 (red) to +1 (blue) is mapped onto the 3D structure indicating a dramatic break at the interface between the two subunits (50S and 30S). This image was generated using VMD [74]. (b) The slowest nonzero mode plotted vs. the residue number. Residues in the 50S subunit (blue) exhibit one direction of motion that is opposed to the motion in the 30S subunit (red).

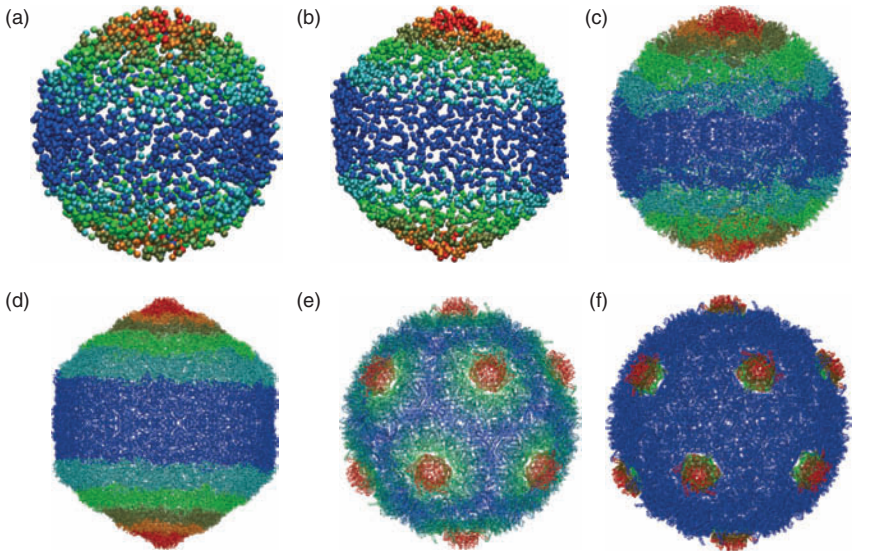

FIGURE 3.5
Application of GNM to the HK97 bacteriophage viral capsid. (a) The ms fluctuations from the slowest (threefold degenerate) mode for the prohead viral capsid coarse-grained by retaining only every 35th residue are colored from most mobile (red) to least mobile (blue). (b) The results for the slowest (threefold degenerate) mode of the head viral capsid calculated using a similar coarse-grained procedure of retaining every 35th residue. Both identify pentamer-centered regions at opposite poles as the most mobile regions suggesting an expansion or puckering of these residues. (c) The ms fluctuations for the slowest mode calculated over the entire (107,520 residue) prohead capsid structure (PDB file 1if0 [62]) and (d) entire (117,600 residue) head capsid structure (PDB file 1fh6 [61]) also demonstrate this high degree of mobility at the poles. (e) The weighted summation of the 11 slowest modes identifies the 12 pentamers as the most mobile regions responsible for expansion from the prohead to head form. (f) The slowest nondegenerate, symmetric mode, mode 31, also identifies these pentamers as highly mobile. These images were generated using VMD [74].

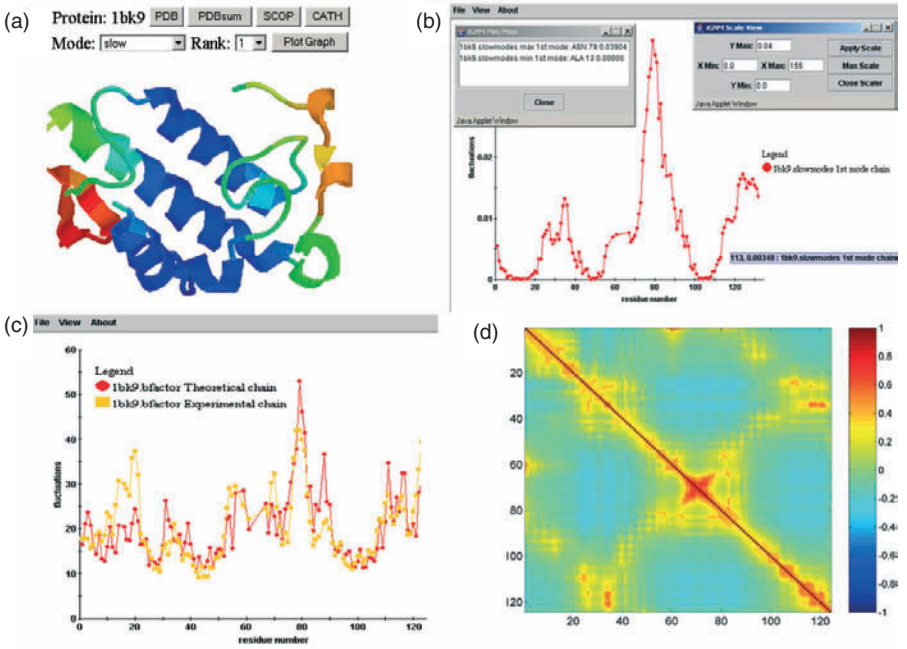

FIGURE 3.6
Visualization of dynamics data stored in the iGNM DB. The results shown are of the example phospholipase A2 (PDB:1bk9 [75]). (a) The slowest motions (slow1) are color-coded and mapped on structure of 1bk9 in dark blue, green, orange to red in the increasing order of mobility. (b) The window shows the mobility of the slowest mode with scalable range of view, max/min value info window and pop-up tag that shows the residue number and coordinates. (c) The experimental and predicted *B*-factors are compared. (d) The cross-correlation of residue pairs of all modes. The perfect concerted motion (+1) is colored dark red while the perfect anticorrelated motion (−1) is colored dark blue.

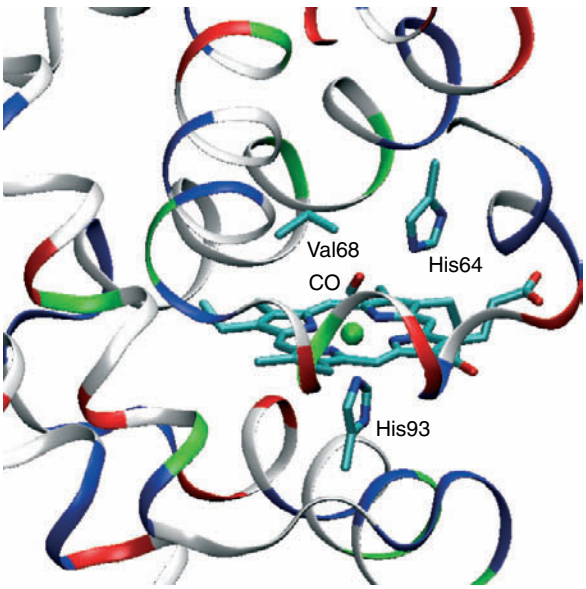

FIGURE 4.1
Active site of CO bound myoglobin. The heme and CO are shown in the line form, and part of the protein is shown in the ribbon form; the protein is color-coded based on the amino acid type (red — acidic, blue — basic, green — polar, and white — nonpolar).

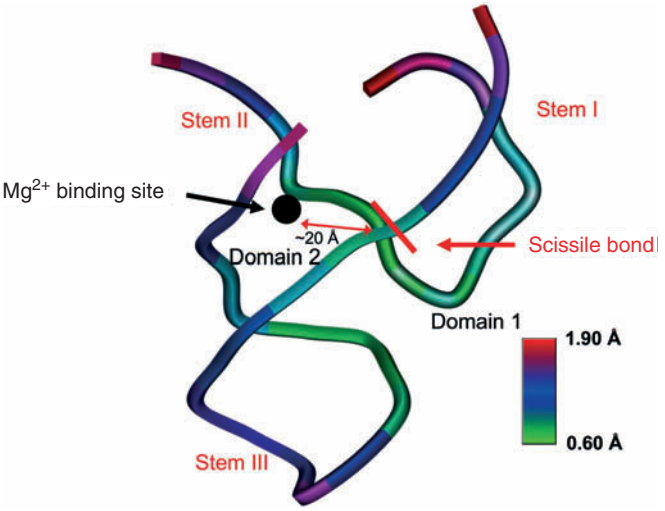

FIGURE 4.2
Computed RMS fluctuation using classical NMA mapped onto the structure of the hammerhead ribozyme. The structural domains and approximate location of the second metal binding site relative to the scission site are also shown.

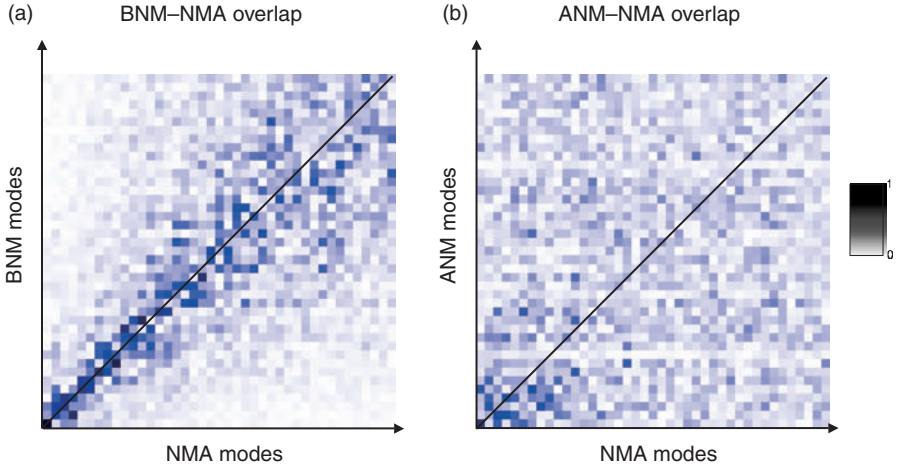

FIGURE 4.4
Overlap between (a) BNM–NMA and (b) ANM–NMA eigenvectors for the hammerhead ribozyme.

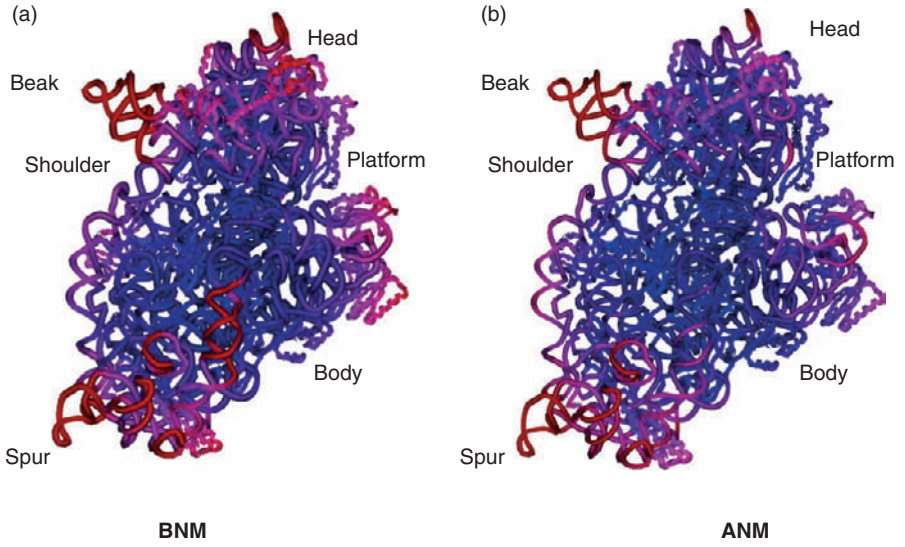

FIGURE 4.5
Computed RMS fluctuation using (a) BNM and (b) ANM mapped onto the structure of the 30S ribosome subunit (PDB code 1J5E). The red region has higher fluctuations.

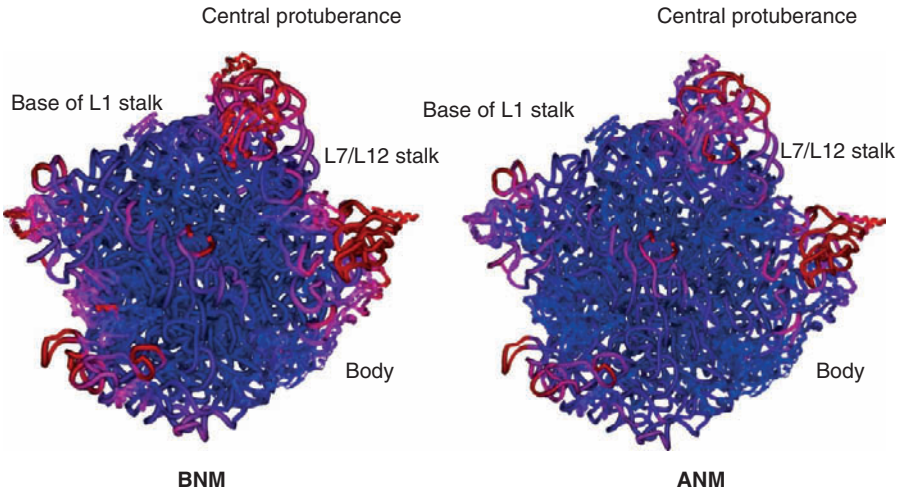

FIGURE 4.6
Computed RMS fluctuation using (a) BNM and (b) ANM mapped onto the structure of the 50S ribosome subunit (PDB code 1JJ2). The red region has higher fluctuations.

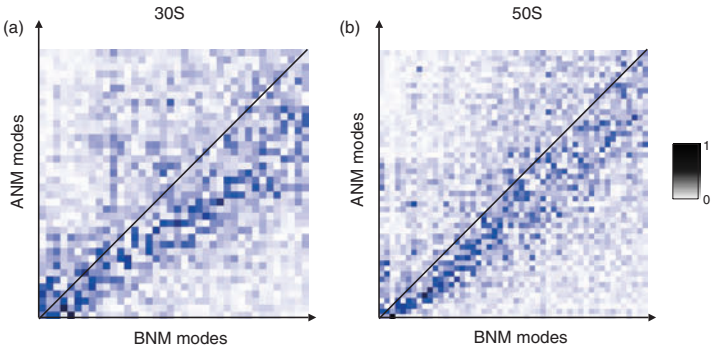

FIGURE 4.8
Overlap between BNM and ANM eigenvectors for (a) 30S and (b) 50S ribosome subunits.

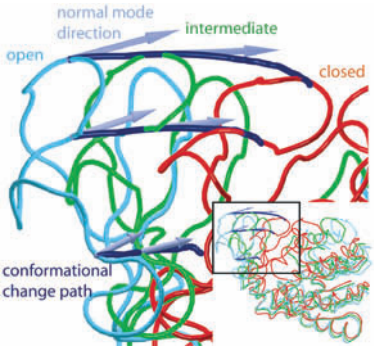

FIGURE 6.1
Nonlinear conformational change between the open and closed forms of the adenylate kinase the linear normal mode directions.

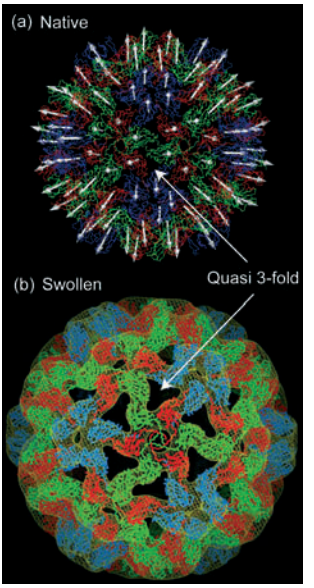

FIGURE 6.2
Elastic NMA of the viral capsid proteins of CCMV. (a) Amplitude and direction of motion for CCMV as obtained from expansion along the breathing mode. (b) Electron density fitting with the estimated model for swollen CCMV as obtained from NMA. All the graphics were produced using VMD [62].

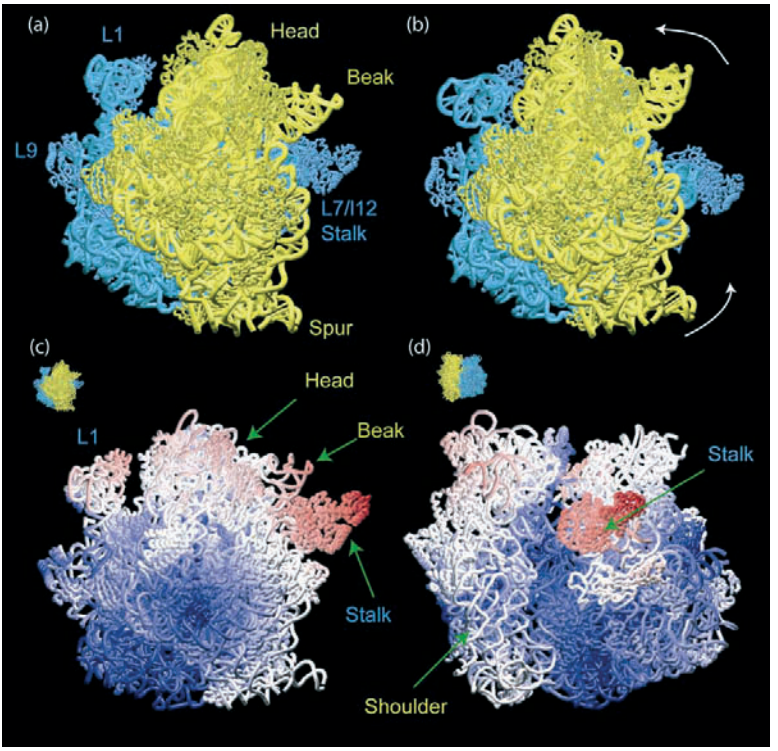

FIGURE 6.3
Elastic network NMA of the 70S ribosome. (a) The x-ray structure of the 70S ribosome (the 30S subunit in yellow and the 50S in blue). (b) Rearrangements of the 70S ribosome after displacement along the ratchet-like mode. (c) and (d) Two different views, as indicated by thumbnails, of the atomic displacements along the ratchet-like mode. The atoms are colored according to their amplitude along the mode. The scale ranges from red (largest conformational rearrangements) to blue (no motions).

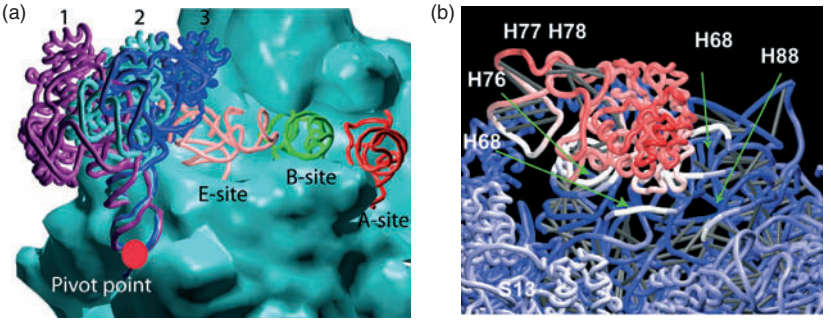

FIGURE 6.4
Elastic network NMA of the 70S ribosome. The structural rearrangements of the L1 stalk along the mode 1. (a) This displacement occurs around a pivotal point and several positions of the L1 stalk along this mode are represented (1) the outer, (2) x-ray structure, (3) the inner. (b) The magnitude of the structural rearrangements correlated with the L1 stalk motion, with red color indicating large motion and blue color indicating no motion. Small rearrangements are observed in H68, which is connected with H69. H69 is known to interact with the tRNA at A, P, and E sites.

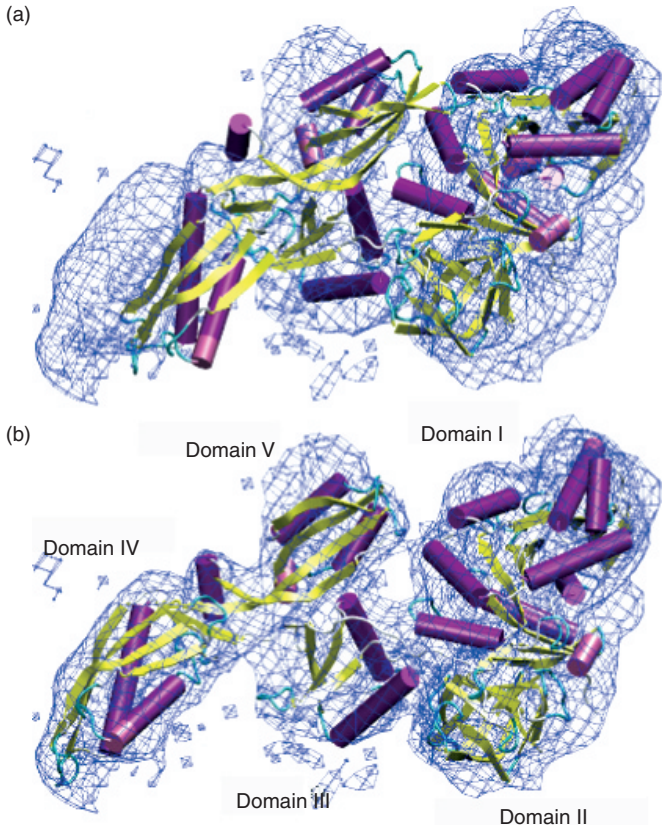

FIGURE 6.7
Flexible fitting using all-atoms at 10 Å resolution of Elongation G bound to the ribosome with NMFF. Rigid-body fitted structure (with Situs package) [56] into simulated EM map of the other conformational state. (b) The final flexibly fitted structure.

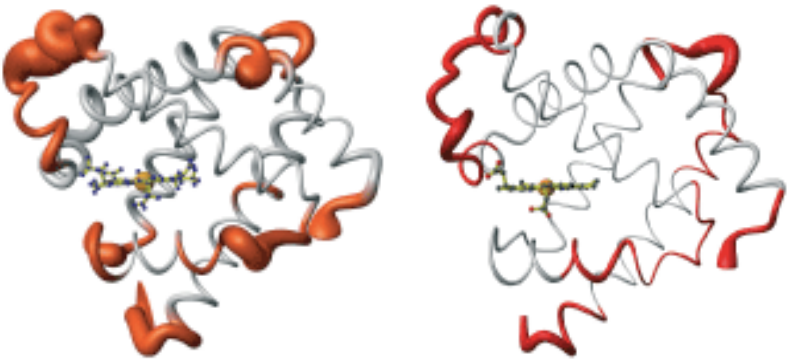

FIGURE 8.1
Comparison of the variation within an ensemble derived from NMR (left) and x-ray crystallography (right). The plot shows an expanded backbone representation in proportion to the RMS deviations within each ensemble. The regions of mobility overlap well.

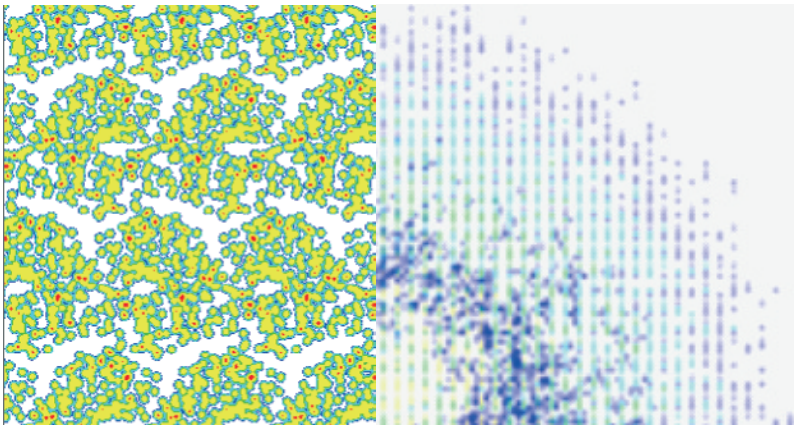

FIGURE 8.3
On the left is a constructed segment of a 3D lattice of a crystal of the enzyme, adenylate kinase, and on the right is the calculated reciprocal-space slice showing the calculated Bragg and diffuse x-ray scattering assuming independent motions within each molecule.

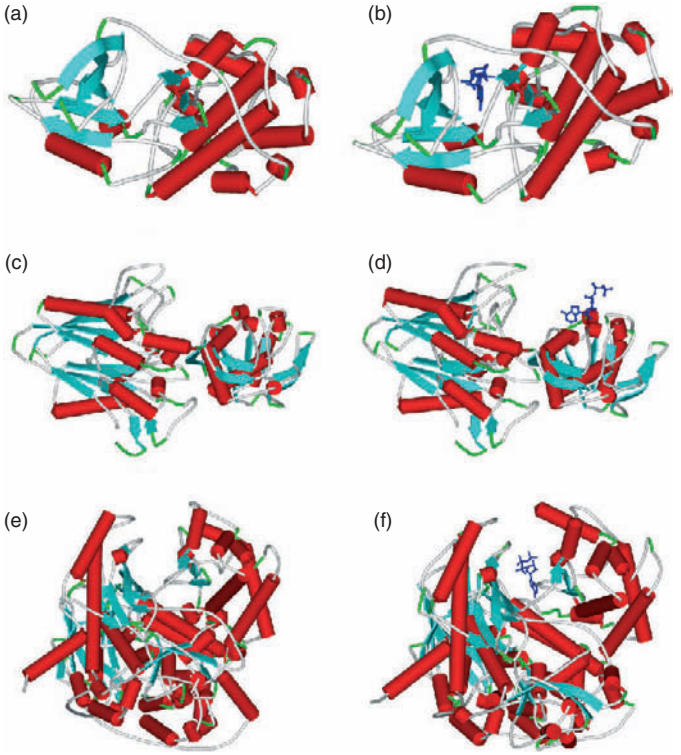

FIGURE 9.1
Three-dimensional representations of representative ATP-binding proteins (a) 1HCL, (b) 1HCK, (c) 1USH, (d) 1HP1, (e) 1E8Y, and (f) 1E8X. The proteins are colored according to their secondary structures using Accelrys DS ViewerPro 5.0. The ATP-bound conformers are shown in the right column. Their unbound counterpart is in the left column. ATP molecules are given with blue stick representations.

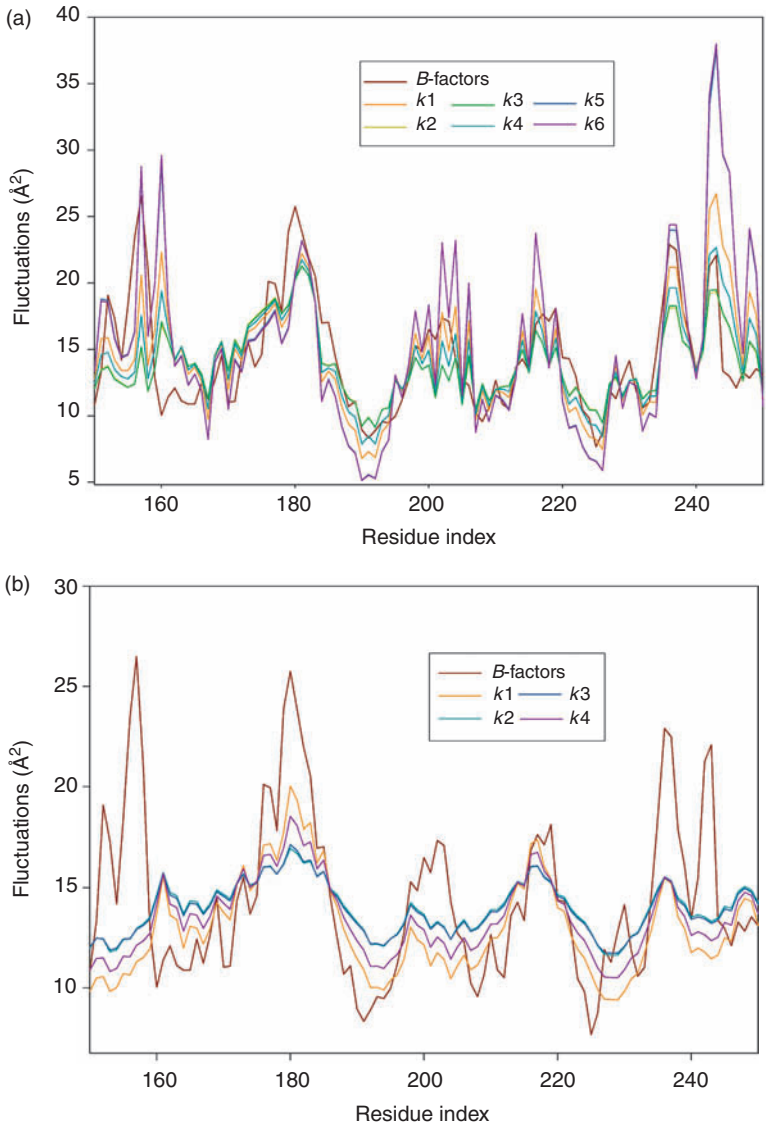

FIGURE 9.5
Comparison of mean-square fluctuations with *B*-factors for 1HP1 with different spring constants at (a) 7 Å and (b) 35 Å cutoff distances.

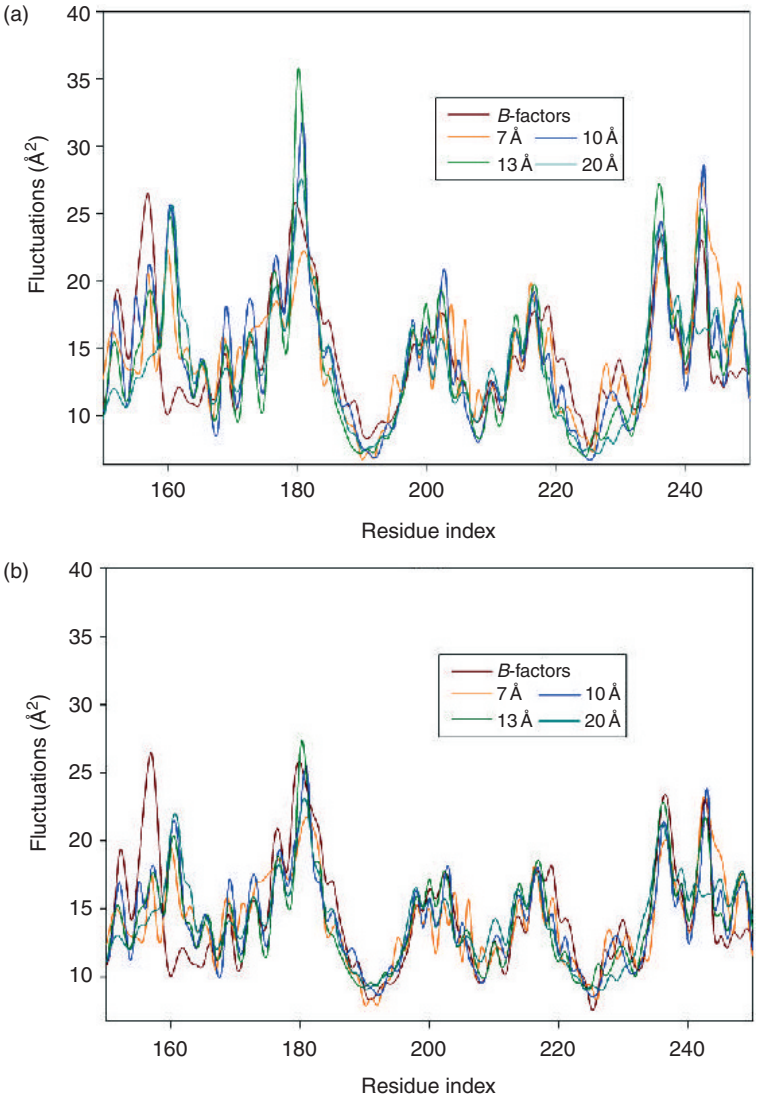

FIGURE 9.6
Comparison of mean-square fluctuations in the case of 1HP1 at (a) $k = 1$ and (b) $k = 4$.

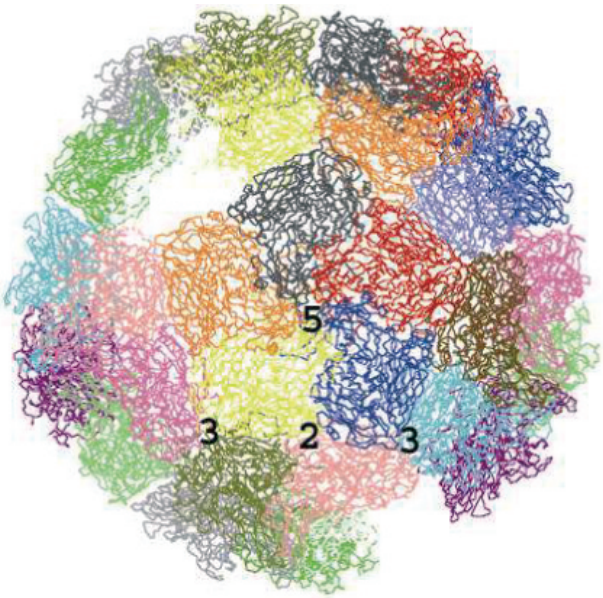

FIGURE 11.3
Top view of the C_α-trace of the poliovirus capsid, in which protomers are shown in different colors. The locations of a 2-fold, two 3-fold, and a 5-fold symmetry axis are indicated.

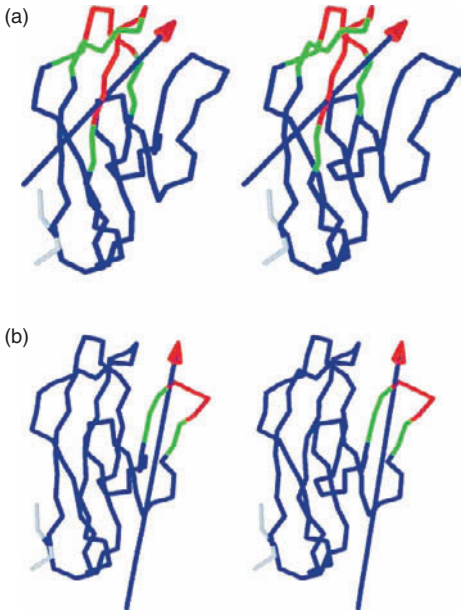

FIGURE 12.2
Dynamic domain motions in (a), the first and (b) second JAM mode in free human CD2. The residues shown in blue, red, and green represent fixed-domain, moving-domain, and bending residues, respectively, as determined by DynDom (Hayward S., and Berndsen H.J. *Proteins*, 30, 144, 1998). The arrows represent the axes of domain motions. The moving-domains rotate around these axes. The figure created by using the programs DynDom (de Groot B.L., Hayward S., van Aalten D.M., Amadei A., and Berendsen H.J. *Proteins,* 31, 116, 1998) and Rasmol (Sayle R., and Milner-White E.J. *Trends Biochem. Sci.,* 20, 374, 1995). (Reproduced from Kitao A., and Wagner G. *Proc. Natl Acad. Sci. USA,* 97, 2064, 2000. With permission.)

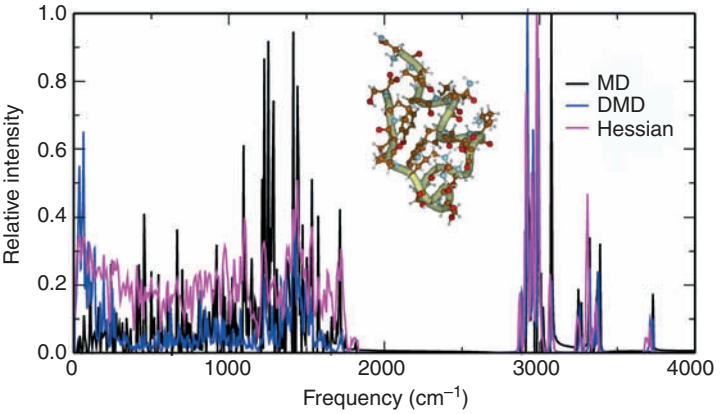

FIGURE 14.2
Distributions of frequencies calculated by standard NMA (Hessian), MD simulations with and without the driving terms (DMD and MD, respectively). In the Trp-cage structure the backbone trace is shown as a yellow tube.

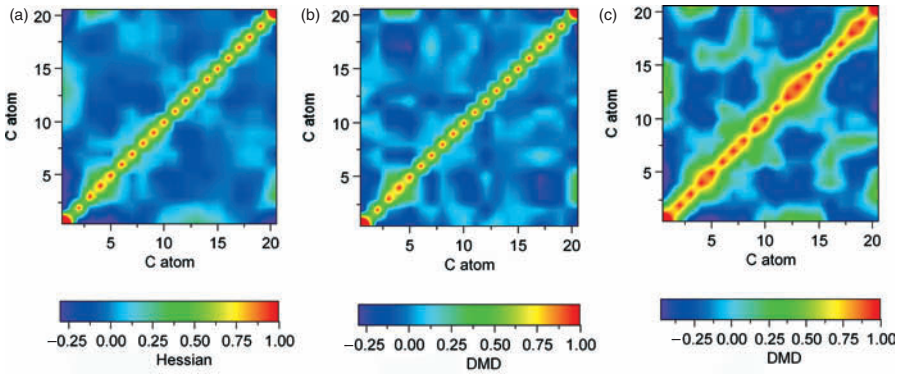

FIGURE 14.5
Cross-correlation maps for C_α atoms from (a) Hessian normal modes and frequencies, (b) DMD normal modes at exact Hessian frequencies, and (c) DMD normal modes at frequencies obtained from the high resolution DMD calculation.

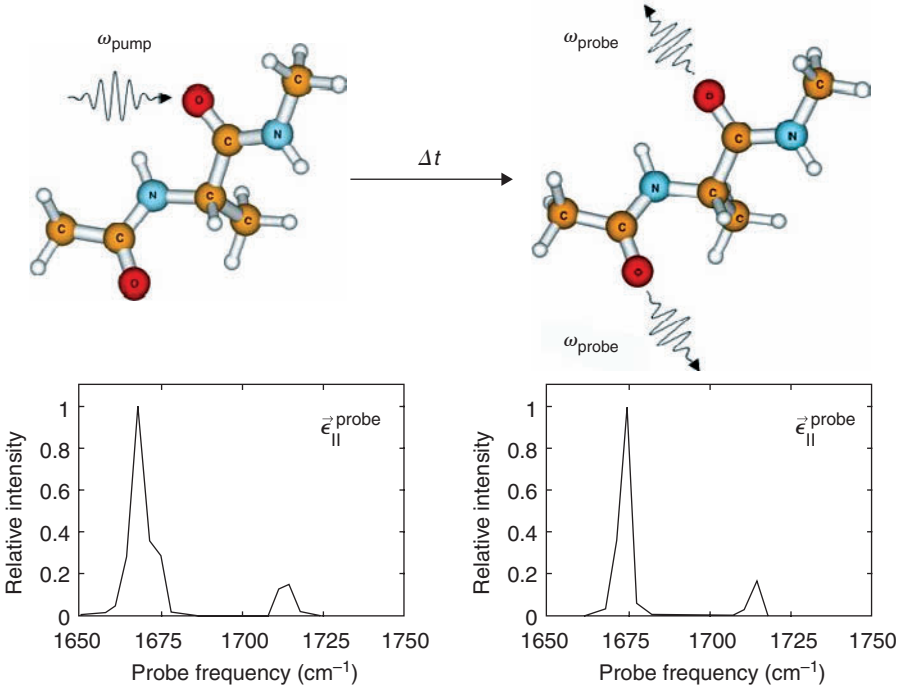

FIGURE 14.7
Scheme of the 2D-IR experiment for dialanine using the DMD dipole-driving method. The spectrum and structure was recorded at $\Delta t = 4.0$ psec with perpendicularly polarized pump and probe pulses.

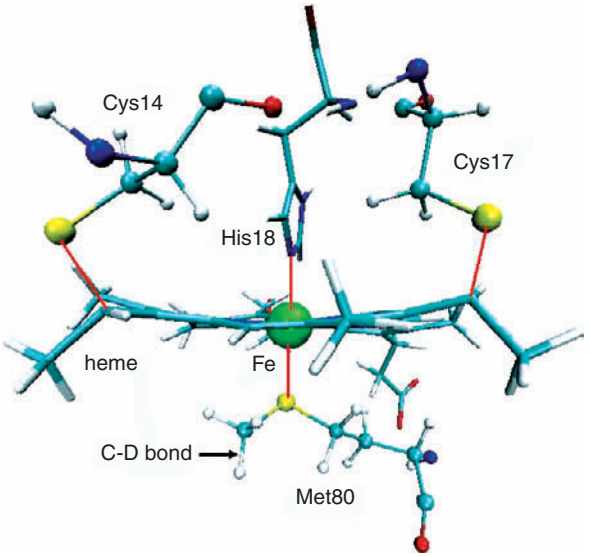

FIGURE 15.1
The structure of cytochrome c in the vicinity of the heme group, showing the thioether linkages and nonplanar heme geometry.

Chapman & Hall/CRC
Mathematical and Computational Biology Series

Rapid developments in experimental techniques continue to push back the limits in the resolution, size, and complexity of the chemical and biological systems that can be investigated. This challenges the theoretical community to develop innovative methods for better interpreting experimental results. Normal mode analysis (NMA) is one such technique. Capable of providing unique insights into the structural and dynamical properties of complex systems, it is now finding a wide range of applications in chemical and biological problems.

From the fundamental physical ideas to cutting-edge applications and beyond, this book presents a broad overview of normal mode analysis and its value in state-of-the-art research. The first section introduces NMA, examines NMA algorithm development at different resolutions, and explores the application of those techniques in the study of biological systems. Later chapters cover method developments based on or inspired by NMA but going beyond the harmonic approximation inherent in standard NMA techniques.

Normal mode analysis complements traditional approaches with computational efficiency and applicability to large systems that are beyond the reach of older methods. This book offers a unique opportunity to learn from the experiences of an international, interdisciplinary panel of top researchers and explore the latest developments and applications of NMA to biophysical and chemical problems.

Quang Cui is an assistant professor in the Department of Chemistry at the University of Wisconsin-Madison, USA

Ivet Bahar is Chair of the Department of Computational Biology at the University of Pittsburgh, Pennsylvania, USA.

C472X

ISBN 1-58488-472-X

90000

9 781584 884729

Chapman & Hall/CRC
Taylor & Francis Group
www.taylorandfrancisgroup.com

6000 Broken Sound Parkway, NW
Suite 300, Boca Raton, FL 33487
270 Madison Avenue
New York, NY 10016
2 Park Square, Milton Park
Abingdon, Oxon OX14 4RN, UK